Tectonic Evolution of the Eastern Mediterranean and its Implications for the Messinian Salinity Crisis

by

© Pınar Güneş

A thesis submitted to the

School of Graduate Studies

in partial fulfilment of the

requirements for the degree of

Doctor of Philosophy

Department of Earth Sciences

Memorial University of Newfoundland

April 2017

St. John's Newfoundland

Abstract

The interpretation of a comprehensive set of high-resolution multi-channel seismic reflection profiles, multibeam bathymetry data and the litho- and bio-stratigraphic information from exploration wells across the Antalya Basin and Florence Rise revealed important conclusions on the Miocene to Recent tectonic evolution and the Messinian Salinity Crisis depositional history of the eastern Mediterranean Basin.

This study clearly demonstrated the presence of a 4-division Messinian evaporite stratigraphy in the eastern Mediterranean, similar to that observed in the western Mediterranean, suggesting the existence of a similar set of depositional processes across the Mediterranean during the Messinian Salinity Crisis. However, the stratigraphic and depositional similarities of the evaporites between the eastern and western basins do not necessitate synchroneity in their depositional histories. The fact that the only saline water source for the eastern Mediterranean is the Atlantic Ocean and that the Sicily sill creates a physical barrier between the eastern and western Mediterranean impose several critical conditions. A simple 2-D model is developed which satisfies these conditions. The model suggests that the eastern and western basin margins experienced a nearly synchronized gypsum deposition associated with the initial drawdown of the Mediterranean level, followed by the resedimentation in the deep basins of the terrigenous and early evaporite deposits as the drawdown intensified. The synchroneity of evaporite deposition across the eastern and western basins broke down as the Sicily Gateway became largely subaerial during a period when the Calabrian Arc area experienced uplift associated with slab break-off: the Sicily sill must have remained within a "goldilocks" zone to allow the right amount of saline water inflow into the eastern Mediterranean so that evaporites (massive halite) could be deposited. During this time, the sea level in western Mediterranean was at the breach-level of the Sicily sill, thus no evaporite deposition took place there. The model suggests that further restriction of the inflow occurred across the Betic and Rif gateways as these regions also largely became subaerial associated with the uplift of the Gibraltar Arc region caused again by the

lithospheric slab break-off. However, similar to the Sicily Gateway, the Betic and Rif gateways must also have remained within the "goldilocks" zone to allow the right amount of saline water inflow into the western Mediterranean so that massive halite could be deposited. The re-opening of the Betic and Rif gateways reflooded the western Mediterranean first, then the eastern Mediterranean allowing the deposition of a mixed evaporite-siliciclastic unit, followed by the transgressive sediments with a distinctive brackish water *Lago Mage* fauna.

The interpretation and mapping of the tightly-spaced high-resolution multichannel seismic reflection profiles clearly improved our understanding of the Late Miocene–Recent tectonic and kinematic evolution of the Antalya Basin and Florence Rise and it is relationship with Cyprus-Eratosthenes collision zone, along the plate boundary between the African Plate and the overriding Aegean-Anatolian Microplate.

The pre-Messinian Miocene structural architecture of the Antalya Basin and its southwestern extension into the Florence Rise is characterized by a very prominent broadly northwest-southeast striking and largely southwest verging fold thrust belt, with occasional northeast verging back-thrusts. During the Messinian a number of prominent thrusts remained active; however, numerous thrusts which were active during the pre-Messinian Miocene became inactive. During the Pliocene–Quaternary the stain was partitioned into five broadly northwest-southeast trending morpho-tectonic domains, each delineated by a distinctive seafloor morphology: (a) a domain across the inner and western Antalya Basin is dominated by extensional faults, (b) a domain immediately south of the extensional faults, is characterized by contractional structures, (c) a halokinetic zone in southwestern Antalya Basin north of the foothills of the Anaxagoras Mountain is characterized by numerous positive flower structures beneath a corrugated seafloor, (d) a domain across the crestal portion of the Florence Rise is dominated by prominent inversion structures, and (e) a domain across the northeastern and southwestern margins of the Florence Rise characterized by positive flower structures.

Acknowledgements

First of all I would like to thank my supervisors Ali Engin Aksu and Jeremy Hall. Thank you for the possibility to work on this challenging topic, for your continues support and guidance, several insightful discussions, for sharing your passion and enthusiasm on all earth science related aspects and for giving me the opportunity of personally involving in every step of this project including seismic data collecting, processing and interpretation and thank you both for teaching me and advising me how to grow as a geoscientist.

Data for this thesis was acquired through collaboration with Dokuz Eylül University in Izmir, Turkey. A big thank you goes to Dokuz Eylul University Seis Lab. Thank-you to all the staff, ship crew, scientific crew and students for their help with the data acquisition. Funding for this project has been made possible through NSERC Discovery Grants to Ali Aksu and Jeremy Hall and the processing software was kindly provided by Landmark Graphics. Thank you to TPAO for kindly providing deep seismic data collected along the Antalya Basin and Mediterranean Ridge.

I would further like to thank Tom Colon for his valuable contribution in this study. Thank you James Conliffe for your support and encouragement and feedback throughout the editing process. Thank you Statoil St. John's Canada geosciences team for two great summer internship experiences which gave me a great break with working on offshore Newfoundland with using my seismic interpretation background I developed during this dissertation. Thank you to all the students, staff, and professors in the Earth Sciences Department who have helped me along the way, especially those affiliated with the Eastern Mediterranean Research Group; Melanie Barnes, Heather King. A special thank you goes out to Peter Bruce and Sharon Deemer for all your help and support on the technical side of things. Also a big thank you goes to AGU, AAPG and SEG for giving me the opportunity of presenting my work I have done in this thesis and financially supporting my participation in many important geoscience related short courses and networking conferences and additional thanks for giving me the opportunity of meeting with many valuable geoscientist all over the world.

I truly enjoyed the company of very nice friends who kept my motivation up whenever I feel down during this process: Rooz, Bahar, Tugce, Reza, Erkan, Anne, Edgards, Semra, Deniz and Michelle.

Finally and most deeply I thank my husband Guillermo Zambrano and my family; Cevriye Gunes, Aliyar Gunes, Funda Gunes and Aydan Gunes. Thank you for your patience and your endless support.

Contents

List of Tables

List of Figures

Chapter 1

Introduction

1.1 Aim of this thesis

This thesis aims at achieving a deeper understanding of the Miocene to Recent interrelations between the structural, morphological and stratigraphic features of the northwestern sector of the eastern Mediterranean in relation to thick-skinned–thin-skinned tectonics, including halokinesis and the events that are associated with the Messinian Salinity Crisis. More specifically, this thesis aims (a) to outline the stratigraphic framework of the study area, (b) to describe the distribution of the Messinian evaporite successions, which will be used to develop a stratigraphic model to understand the Messinian depositional history of the study area in the content of the entire Mediterranean Sea, (c) to determine the Miocene–Recent structural framework of the study area, (d) to delineate the overall style of deformation in the uppermost Messinian–Quaternary successions and to explain how and when the deformation formed, and what controls its distribution in the western Cyprus Arc.

The aims of the thesis have been met by detailed mapping from seismic reflection data in an area of the eastern Mediterranean previously lacking such information. By filling this hole in knowledge, I have been able answer some unresolved questions of the Miocene-Recent geology, especially I have been able to provide a much better resolved picture of the variation in thickness, depth and internal

stratigraphy of the Messinian evaporites allowing me to develop an improved concept of the regional variation from the western to eastern Mediterranean. In addition, my mapping has enabled me to provide a more thorough examination of the regional structure and its dynamic interpretation.

Why the eastern Mediterranean?

The Mediterranean Sea and its surrounding land mass have long been recognized as an excellent "natural laboratory" for the study of fundamental plate tectonic processes, including rifting, passive margin development, contraction and associated subduction, ophiolite emplacement and orogenesis (Figs. 1.1, 1.2; Robertson, 1998; Aksu et al., 2005a). Numerous previous studies have documented the ubiquitous occurrence of thick evaporite successions across the eastern Mediterranean (e.g., Hsü et al., 1973; Cita et al., 1978a,b; Gradmann et al., 2005; Unit 2 of Hall et al., 2005a,b; and Işler et al., 2005; Netzeband et al., 2006; Lofi and Berné, 2008; Ryan, 2009; Garcia-Castellanos et al., 2009; Urgeles et al., 2010; Garcia-Castellanos and Villaseñor, 2011), thus the region is regarded as a world class example of salt deposition and the associated halokinesis. The evaporites were deposited during the desiccation of the Mediterranean associated with the "Messinian Salinity Crises" (e.g., Cita et al., 1978a,b). The deep basins of the eastern Mediterranean Sea are also used for studying (a) thick-skinned tectonics with irregular geodynamics and (b) salt tectonics with extensive salt deposition and its implications on post-salt and pre-salt activities (e.g., Hsü et al., 1978; Dixon and Robertson, 1984; Kastens et al., 1990; Emeis et al., 1996; Robertson, 1998; McClusky et al., 2000; Sellier et al., 2013a,b).

Today, the tectonic framework of the eastern Mediterranean is characterized by the last phase of convergence between the African and Eurasian plates and the displacement of the smaller Arabian and Aegean-Anatolian microplates (Figs. 1.1, 1.2; McKenzie, 1972; Dewey and Şengör, 1979; Dewey et al., 1986; Le Pichon and Kreemer, 2010). The boundary between the African Plate and the Aegean-Anatolian Microplate is delineated by the Hellenic Arc and the Pliny-Strabo Trenches in

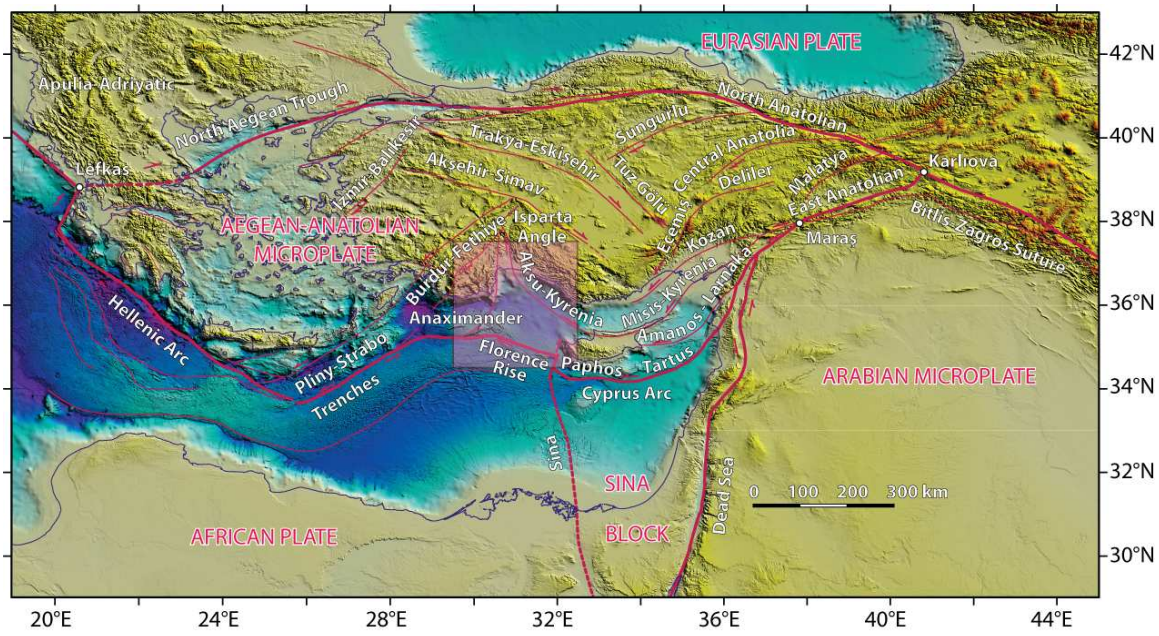

Figure 1.1: Simplified tectonic map of the broader eastern Mediterranean region showing the prominent fault zones (thin red lines), plate boundaries as defined by the position of the hard boundary of the overriding lithosphere (thick red lines, from Aksu et al., 2009), and the triple junctions (small white circles). The topography is compiled using GeoMapApp (Ryan et al., 2009), and shaded using Global Mapper. The multibeam bathymetry from the high-resolution EMODnet (European Marine Observation and Data Network, Portal for Bathymetry, http://www.emodnet-hydrography.eu/). The coastline is taken from the International Bathymetric Charts of the Mediterranean (IOC, 1981). Pink inset = study area, half arrows = transform/strike-slip faults (modified from Aksu et al., 2009).

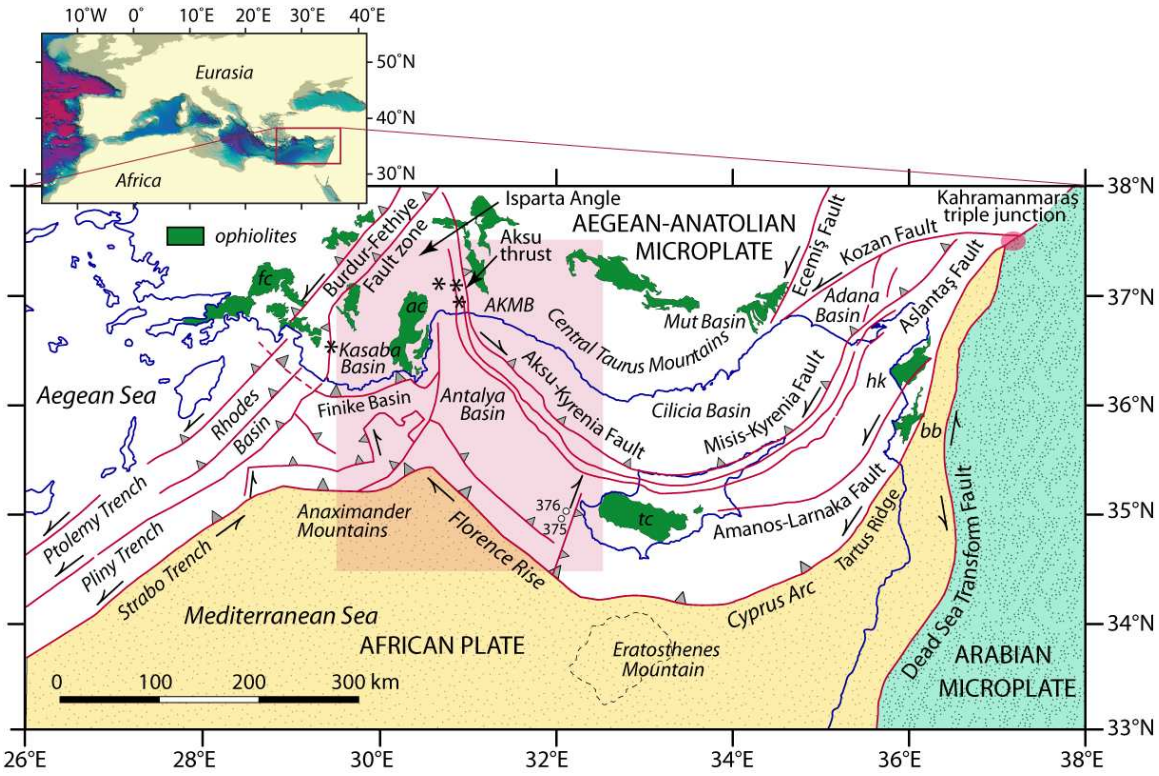

Figure 1.2: Simplified tectonic map of the eastern Mediterranean Sea and surrounding regions, showing major plate/microplate boundaries and ophiolitic rocks, ac= Antalya Complex, bb= Baër Bassit Complex, fc= Fethiye Complex, hk= Hatay–Kızıldağ Complex, tc= Troodos Complex. Small white circles= DSDP Sites 375 and 376, half arrows= transform/strike–slip faults, pink inset = study area.

the west and the Florence Rise, and Cyprus Arc in the east (Figs. 1.1, 1.2; Le Pichon and Kreemer, 2010). The Florence Rise forms a prominent bathymetric high that connects with the Anaxagoras Mountains towards the northwestern end of the Cyprus Arc (i.e., the eastern boundary at the level of crystalline basement between the African Plate and the Aegean–Anatolian microplate) and separates two main salt-bearing basins, the Antalya Basin in the north and the Herodotus Basin in the south (Figs. 1.1, 1.2; Robertson et al., 1998b). The Antalya Basin is a predominantly marine depocentre, situated in a forearc setting between Florence Rise in the south and the Taurus Mountains of southern Turkey in the north (Figs. 1.1, 1.2).

The kinematics and structural setting of the eastern Mediterranean varies considerably in both time and place, reflecting the rate of the plate convergence, subducting slab geometry (angle of the subducting slab) and the thickness of sediments above the crystalline basement. Those aspects related to the structural complexity of the eastern Mediterranean are further influenced by the variable thickness and lateral extent of evaporites resulting from the Messinian desiccation of the Mediterranean Sea. Despite the fact that numerous studies have been carried out on the style and timing of deformation and depositional process in the eastern Mediterranean, significant controversy exists regarding the Miocene-Recent tectonic and sedimentary evolution of the area, including (i) the determination of the structural elements and the age of the deformation along the western Cyprus Arc, (ii) the delineation of the uppermost Messinian-Quaternary structural and deformation style and (iii) the determination of Miocene-Recent depositional history of the eastern Mediterranean, including the Messinian Salinity Crisis. My work has provided new seismic data and geological interpretation in the southern Antalya Basin, the Florence Rise and Anaximander mountains enabling me to fill a significant knowledge gap in the Messinian story and so allowing me to come to new conclusion on the Messinian-Recent history of this part of the Mediterranean and it is implications for the regional evolution of the entire Mediterranean Sea. This PhD thesis provides new multi-channel high resolution seismic data and interpretation from the Florence Rise and Antalya Basin in western

Cyrus Arc, which are used (a) to better understand the Miocene-Recent structural and depositional history of the eastern Mediterranean and (b) to better define the responses of the eastern Mediterranean environment to the Messinian Salinity Crisis event, from a stratigraphic and structural point of view as well as from a salt tectonics point of view.

This thesis presents new results on:

- The strain pattern through time along and across the Florence Rise and Anaxagoras Mountain.
- The relationship of the Messinian in two areas, Antalya Basin and Herodotus Basin, separated by the Florence Rise..
- Explaining why the lower mobile unit (halite) in the Messinian is much thicker in the eastern Mediterranean Sea than its counterpart in the western Mediterranean Sea.
- A new model of the Mediterranean-wide depositional history of the Messinian that can account for the observed lithologies and chronologies of the successions associated with the Messinian Salinity Crisis in the west and east.

1.2 Specific scientific objectives

The specific scientific objectives of this thesis can be classified under the following three broad categories:

Seismic stratigraphy

- to construct a detailed seismic stratigraphic framework for the Antalya Basin and Florence Rise and provide correlations between the offshore seismic stratigraphy and offshore and onshore boreholes and outcrop in eastern Mediterranean;

- to produce detailed isopach maps for the uppermost Pliocene–Quaternary and Messinian successions, so to determine the regional distribution and variation of the stratigraphic sequences within the study area;

Messinian Salinity Crisis

- to delineate the main stratigraphic characteristics of the evaporites and the overlying uppermost Pliocene–Quaternary successions across the eastern Mediterranean, so as to develop a sequence stratigraphic model that will explain the fractionation of the evaporite facies between different paleo-bathymetric settings that will permit prediction of the temporal evolution of the sediments associated with the Messinian Salinity Crisis across the Mediterranean basins;

- to determine the relationship between different stages of the Messinian Salinity Crisis and global events, particularly of sea level changes, so as to develop a "desiccating deep basin model" for the Messinian Salinity Crisis in the eastern Mediterranean;

Tectonics and kinematics

- to produce detailed tectonic maps of the pre-Messinian Miocene, Messinian and uppermost Pliocene–Quaternary, so as to delineate the tectonic and kinematic evolution of the eastern Mediterranean since the Miocene;

- to identify the geometric characteristics and regional distribution of halokinetic structures and the relationship between the ductile top salt and the overlying brittle cover so as to develop a model for the evolution of the localized dissolution structures, and to explain how and when they formed, and what controls their distribution in the western Cyprus Arc area..

1.3 Thesis Layout

The thesis is divided into seven chapters, three of which are the main result chapters (Chapters 3, 4 and 5). These represent a logical series of arguments relating to the structural and sedimentary evolution of the eastern Mediterranean.

Chapter 1 reviews the geological setting of the study area, including the background geology with the structural and morphological elements and Messinian Salinity Crisis event of the eastern Mediterranean and general geological uncertainties in the eastern Mediterranean. Chapter 1 also points out the aim of this PhD thesis and the thesis layout. Chapter 2 reviews the data and methods used for this research. This includes the 2D multi-channel seismic data collecting and processing and how it is interpreted. There is also a summary of the various types of mapping and the seismic-to-well correlation methods used for this study.

Chapter 3 describes the Miocene-Recent stratigraphy and within the study area.

Chapter 4 focuses on seismic and sequence stratigraphic analysis of the Messinian evaporite deposits and describes their temporal and spatial distribution with new high resolution seismic reflection data collected from the western Cyprus Arc, eastern Mediterranean and discusses the consequences and correlations with the global sea-level variations.

Chapter 5 describes regional distribution and variation of the geological structures and the stratigraphic sequences from Late Miocene to Recent within the study area. In this chapter I used structural analysis of multichannel seismic data to produce the several structural maps to delineate the main structural and morphological domains (extensional, translational and contractional). This chapter also describes the primary driving mechanism of the deformation style and its distribution in the uppermost Messinian-Quaternary sedimentary cover. I used structural analysis of multichannel seismic data and uppermost Messinian-Quaternary structural maps to evaluate the implication of regional tectonics and salt tectonics (including both salt dissolution and gravitational loading) and their impact on stratigraphic and structural deformation in the uppermost Messinian Quaternary

succession.

Chapter 6 draws together the conclusions of Chapter 3 and 5. The discussion distinguishes: (i) the role of thick-skinned tectonics depending on the local geodynamic settings and its influence on the thin-skinned tectonics of the study area, (ii) distinguishes the summary of structures from the southern fringes of the Mediterranean Ridge across the entire forearc region into Taurus Mountains of southern Turkey and focusses on the uppermost Messinian–Recent (i.e., Unit 1) tectonic evolution along the western Cyprus Arc.

A final overview based on the structural evolution of the eastern Mediterranean presented in this thesis and its placement in a broader scientific context is given in this discussion chapter. Finally, the implications, and limitations of the research are discussed and proposals for future work conclude the chapter.

Chapter 7 draws together the conclusions of Chapter 3 and 4 and discusses the temporal and spatial seismic facies variations of the Messinian evaporites across the study area and a depositional model of the Messinian Salinity Crisis event in the eastern Mediterranean. A final overview based on the sedimentary evolution of the eastern Mediterranean during the Messinian Salinity Crisis and its placement in a broader scientific context is given in this chapter. Finally, the implications, and limitations of the research are discussed and proposals for future work conclude the chapter.

Chapter 8 lists the salient conclusions of the thesis.

1.4 Tectonic and kinematic evolution

1.4.1 Geological Background of the Eastern Mediterranean

The tectonic and stratigraphic evolution of the eastern Mediterranean began in the late Paleozoic, during the opening of the Neo-Tethys Ocean (Dewey et al., 1973; Dewey and Şengör, 1979; Şengör et al., 1985; Le Pichon et al., 1982; Dewey et al., 1986; Robertson et al., 1991; Schattner, 2010).

A period of rifting started at the northern margin of Gondwana in the Late Permian and continued throughout the Early Triassic. In the Middle to Late Triassic, the final breakup of Gondwana took place, initiating the opening of the southern portion of the Neo-Tethys Ocean. During the Jurassic and Early Cretaceous, ocean-floor spreading continued while the margins of the southern Neo-Tethys Ocean experienced passive margin development and subsidence. The opening of the South Atlantic Ocean resulted in the convergence of the African and Eurasian plates during the Cretaceous and the development of two subduction zones: a southerly, intra-oceanic subduction zone, and a northerly subduction zone below the Eurasian continental margin (Livermore and Smith, 1985). During the Eocene, the remaining Neo-Tethys Ocean was subducted beneath the Eurasian Plate and the northerly-directed subduction persisted under the south-central segment of the Eurasian Plate (which later became southeastern Turkey) through the latest Paleocene (Fig. 1.3; Dewey et al., 1973; Şengör et al., 1985; Dercourt, 1986; Robertson et al., 1998a; Montadert et al., 2010).

The post-Eocene tectonic framework of the eastern Mediterranean is characterised by the collision between the African and Eurasian plates, and the development and displacement of smaller Aegean-Anatolian and Arabian microplates (Figs. 1.1, 1.2; Dewey et al., 1973; Şengör and Yılmaz, 1981; Şengör et al., 1985; Sage and Letouzey, 1990; Robertson et al., 1998b; Vidal et al., 2000). Today, the boundary between the Arabian Microplate and the African Plate is delineated by the north-south trending sinistral Dead Sea Transform Fault zone (Fig. 1.1), which developed as the result of the onset of the rifting/drifting in the Red Sea during the Oligocene-Miocene (Fantozzi and Sgavetti, 1998; Watchorn et al., 1998). The northward movement of the Arabian Microplate and its eventual collision with the Eurasian Plate in the Late Miocene-Early Pliocene resulted in the closure of the southwestern arm of the Neo-Tethys Ocean (i.e., the Bitlis Sea) and the suturing along the Bitlis-Zagros zone of southeast Turkey and northwest Iran (Şengör and Yılmaz, 1981). This collision initiated the westward tectonic escape of the Aegean-Anatolian Microplate along two major transform fault systems: the North and East Anatolian Transform faults (Fig. 1.2; Şengör et al.,

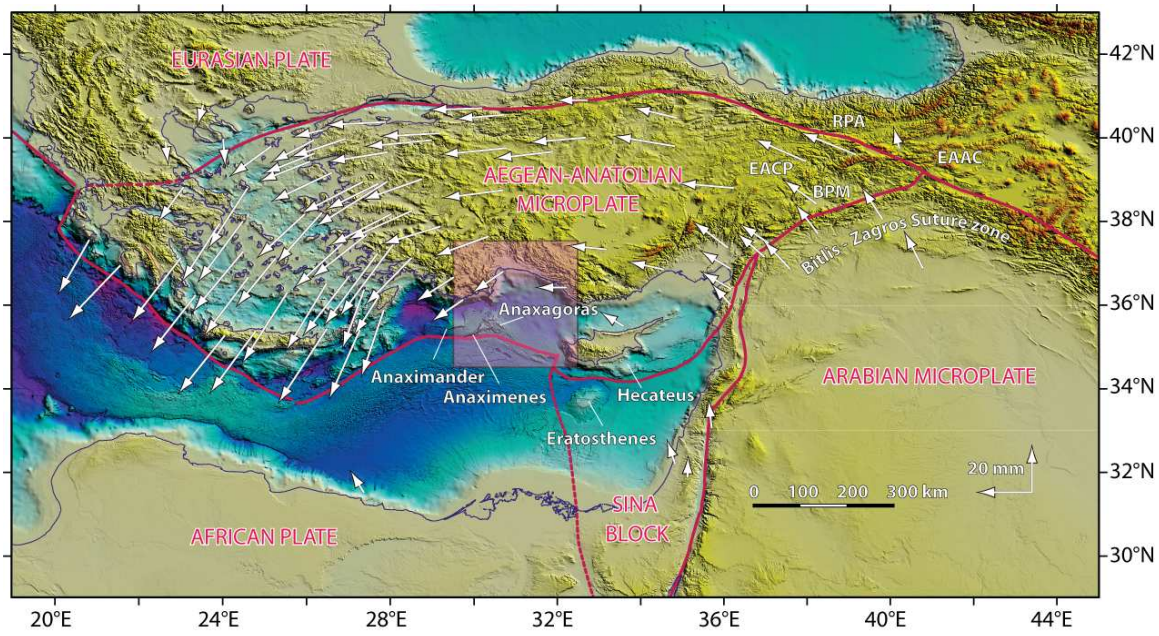

Figure 1.3: Physiography of the eastern Mediterranean Sea showing the GPS vectors, relative to a fixed Eurasia, redrawn from McClusky et al. (2000). The topography is compiled using GeoMapApp (Ryan et al., 2009), and shaded using Global Mapper. The multibeam bathymetry are from the high-resolution EMODnet (European Marine Observation and Data Network, Portal for Bathymetry, http://www.emodnet-hydrography.eu/). BPM= Bitlis-Pütürge Massif, EAAC= east Anatolian accretionary complex, EACP= east Anatolian contractional province, RPA= Rhodope–Pontide Arc. The coastline is taken from the International Bathymetric Charts of the Mediterranean (IOC, 1981). Plate boundaries are from Aksu et al. (2009). Pink inset = study area.

1985).

The North Anatolian Fault zone extends from the Karlıova triple junction in eastern Turkey westward into the Marmara Sea and then to the northern Aegean Sea, forming a gently arcuate dextral strike-slip fault system delineating the boundary between the Aegean-Anatolian Microplate and the Eurasian Plate (Figs. 1.1, 1.2). The sinistral East Anatolian Fault zone defines the boundary between the Aegean-Anatolian and the Arabian Microplates (Figs. 1.1, 1.2). It extends from the Karlıova triple junction in eastern Turkey toward the southwest, tracing the northwestern fringes of the Bitlis-Zagros suture. This fault zone meets the sinistral Dead Sea Fault zone and the northeast continuation of the Cyprus Arc, the Amanos Fault zone, at the Maraş (sometime referred to as the Kahramanmaraş) triple junction (Figs. 1.1, 1.2; Şengör et al., 1985).

The deformation front along the boundary between the Aegean-Anatolian Microplate and the African Plate is defined by two large crustal-scale arcuate structures: the Cyprus Arc in the east and the Hellenic Arc in the west (Fig. 1.1). This double arc system forms a good example of imminent continental collision governed by promontories and irregularities at the plate boundary (Woodside et al., 2002; ten Veen et al., 2004). The Cyprus Arc forms the boundary between the Aegean-Anatolian Microplate in the north, and the African Plate in the south. The Cyprus Arc is connected to the Hellenic Arc in the west and to the Dead Sea Fault and East Anatolian Fault zones in the east, and comprises several distinct morphological domains. To the west, the Cyprus Arc is delineated by the southeast-northwest-trending Florence Rise (Figs. 1.1, 1.2; Hsü et al., 1978; Woodside et al. 2002).

South of the Cyprus Arc, the Eratosthenes Seamount forms a prominent bathymetric high situated on the northern edge of the African Plate (Fig. 1.1). International Ocean Discovery Program (IODP) results show that the Eratosthenes Seamount consists of Cretaceous-Miocene carbonate successions, which overly an intermediate-thickness attenuated continental crust (Robertson et al., 1998a). Robertson inferred that Eratosthenes Seamount is a continental fragment developed along the northern margin of the African Plate during the rifting of the Neo-Tethys Ocean. The progres-

sive subduction of the African Plate beneath the Cyprus Arc was significantly disrupted during the Late Pliocene–Early Pleistocene by the collision of the Eratosthenes Seamount and the Cyprus Arc (Fig. 1.1; Robertson et al., 1998a; Kempler, 1998). Cessation of subduction south of Cyprus, and the continued northeastward motion of the African Plate changed the deformation style, and initiated a low rate of relatively oblique convergence between the Aegean-Anatolian Microplate and the African Plates (Figs. 1.1, 1.2; Le Pichon et al., 1995; Kahle et al., 2000; McClusky et al., 2000). Along the eastern Cyprus Arc, the collision has been accommodated by localized sinistral shearing, while to the west of the arc, dextral shearing along the Florence Rise has been accommodating the collision between the two plates (Woodside et al., 2002). The now-sutured Hecataeus Ridge north of the Cyprus Trench and the Mamonia and Troodos Complexes suggest that the process of microplate accretion has been a common process in the evolution of the island of Cyprus (Robertson, 1998).

1.4.2 Present-day GPS vectors

Present day Global Positioning System (GPS) vectors show that in regions where the convergence is orthogonal, the strain is defined by subduction and related processes, whereas in regions where the convergence is oblique, the strain is controlled by strikeslip deformation (Fig. 1.3; Reilinger et al., 1997; McClusky et al., 2000; 2003). GPS vectors calculated relative to a fixed Eurasian Plate show the details of the deformation within the Aegean-Anatolian Microplate (Fig. 1.3). North of the Eastern Anatolian Fault zone the GPS vectors are oriented toward the northwest with slip velocities of generally less than 10 mm year^{-1}. Across the central Anatolia there is a visible increase in the GPS velocities to 10-20 mm year^{-1} with vectors broadly oriented in a westerly direction. Farther west across the northern Aegean Sea, there is notable swing of the GPS vectors toward the southwest, and a clear increase to velocities of 20-30 mm year $^{-1}$. The GPS velocities continue to increase toward the Hellenic Arc $>$40 mm year $^{-1}$. This velocity structure is interpreted as the result of the tectonic escape of the Aegean–Anatolian Microplate following the collision of the Ara-

bian Microplate with Eurasia in Late Miocene. So, the Aegean-Anatolian Microplate is pushed west along the dextral North Anatolian Fault and sinistral East Anatolian Fault (Fig. 1.3). To the west, the Aegean-Anatolian Microplate is colliding with the Apulia-Adriatic block (Figs. 1.1, 1.3; Underhill, 1989), forcing it to progressively rotate counterclockwise and swing toward the free face along the Hellenic Arc (Mann, 1997). The westward displacement and counterclockwise rotation of the Aegean-Anatolian Microplate are driven by the north-northwest push of the Arabian Microplate and the pull of the subducting African Plate beneath the Hellenic Arc (McClusky et al., 2003). The motion between the Arabian Microplate and African Plate is accommodated by the sinistral Dead Sea Fault. The boundary between the African Plate and Aegean-Anatolian Microplate is delineated by the Hellenic Arc and the Pliny-Strabo Trenches in the west and the+ Florence Rise and Cyprus Arc in the east (Sellier et al. 2013a,b; Schattner and Lazar, 2014). The western segments of the two arcs are perpendicular to the motion of the African Plate relative to the Aegean-Anatolian Microplate, forming the subduction-collision zones whereas the Pliny-Strabo Trenches and the Tartus Ridge are sub-parallel to the slip vector, with a mainly sinistral motion (Vidal et al., 2000; Mascle et al., 2000; Woodside et al., 2002; Zitter et al., 2003). The Eratosthenes Seamount–a microcontinental block on the northern margin of the African Plate–is presently choking the subduction zone south of Cyprus: thrusting has already jumped south of Eratosthenes (Welford et al., 2015). An earlier block–the Hecateus Ridge–may already sutured with Cyprus, causing the uplift of the island. Thus, the transition from subduction of oceanic crust to collision of continental lithosphere is taking place by downthrusting of continental lithosphere resistant to subduction, overthrusting and uplift of the overriding lithosphere and complex shunting of continental blocks in the broadening subduction and/or collisional zone.

1.4.3 Structural and Morphological Elements of the Eastern Mediterranean

Various morpho-tectonic features observed in the eastern Mediterranean reflect the complexity of the region. The regional distribution and character of these features are prominent in the analysis of the tectonic processes since they comprise evidence of previous and recent tectonic activity (Figs. 1.1, 1.3).

Hellenic Arc

The Hellenic Arc defines the western boundary of the convergence between the African Plate and the Aegean-Anatolian Microplate. The evolution of the Hellenic Arc began during the initiation of subduction of the African Plate beneath the Aegean Anatolian Microplate in Late Miocene (Mascle et al., 1986). Subduction beneath the Hellenic Arc can be traced along the Ionian Trench which extends from the Ionian Sea in the northwest, encircles the southern shores of Crete and swings to the northeast, where it is linked with Cyprus Arc by three prominent sinistral strike-slip fault systems along the Ptolemy, Pliny and Strabo trenches and by the prominent Anaximander Mountains (Figs. 1.1, 1.2; Şengör and Yılmaz, 1981; Ryan et al., 1982; Dewey et al., 1986; Sage and Letouzey, 1990; ten Veen et al., 2004; Aksu et al., 2009). The Ptolemy, Pliny and Strabo trenches represent the eastern portion of the Hellenic trench system (the physiographic expression of central Hellenic Arc) and each consists of several southwest-northeast–trending elongate depressions. The Ptolemy and Pliny trenches are very prominent with depths varying from 2000–3630 m and 2000–4450 m, respectively. The Strabo Trench is less pronounced with a shallower depth in the southwest ($\sim$2800 m) that becomes deeper ($\sim$3200 m) towards the northeast, where it gradually plunges into the deep Rhodes Basin, $\sim$4700m (Figs. 1.1, 1.3). The Pytheus Trench is defined by a chain of southeast elongate depressions, and lies south of the Rhodes Basin, Anaximander Seamounts and Florence Rise, linking the Cyprus Trench (the physiographic expression of central Cyprus Arc) to Tartus Ridge (Figs. 1.1, 1.2). The Cyprus Trench is situated between Cyprus and the Eratosthenes Seamount and extends

eastward where it merges into the >1000 m deep Cyprus Basin (Fig. 1.1).

Cyprus Arc

The Cyprus Arc forms the boundary between the Aegean-Anatolian Microplate in the north, and the African Plate in the south (Figs. 1.1, 1.2). The Cyprus Arc is connected to the Hellenic Arc in the west and to the Dead Sea Fault and East Anatolian Fault zones in the east, and comprises several distinct morphological domains. To the west, the Cyprus Arc is delineated by the southeast-northwest trending Florence Rise (Hsü et al., 1978; Woodside et al., 2002; Sellier et al., 2013a,b), which connects to the greater Anaximander Mountains through the eastern Anaxagoras Mountain, forming a notable east-west trending bathymetric feature that rises from the abyssal plain to a depth of 1559 m (Fig. 1.1).

Florence Rise

Sage and Letouzey (1990) described the Florence Rise as the expression of a pre-Messinian accretionary wedge which contained many north-dipping reflectors. However, recent work by Sellier et al. (2013a,b) indicated that the uplift of the Florence Rise to the south may be post-Messinian in age, and that it may be possibly related to the salt tectonics. Giermann (1966, 1969) pointed to the structural and sedimentological similarities between the Florence Rise and the Kyrenia Range and argued that they were parts of a once continuous arc. However, subsequent studies showed that the Kyrenia Range extended toward the northeast linking with the Misis Mountains of southern Turkey (e.g., Aksu et al., 2005a; 2014a,b; Walsh-Kennedy et al., 2014) as well as toward the northwest linking with the Aksu Thrust of the onland Antalya Basin (Işler et al., 2005; Hall et al., 2014a), forming a prominent arcuate belt, often referred to as the Misis-Kyrenia-Aksu fault zone. These studies clearly documented that the Florence Rise is a separate entity south of the Misis-Kyrenia-Aksu fault zone (Aksu et al., 2005; 2014a,b; Işler et al., 2005; Hall et al., 2014a; Walsh-Kennedy et al., 2014).

Deep Sea Drilling Project (DSDP) Sites 375 and 376 (Hsü et al., 1978) sampled the upper sedimentary successions across the Florence Rise (Fig. 1.2). Seismic reflection data and the results from the DSDP Site 375 show that the Messinian-lowermost Pliocene evaporites are either missing or very thin across the Florence Rise, and that the structure was a pre-Messinian high which must have stood above the depositional base of the Messinian evaporites (Fig. 1.4; Sage and Letouzey, 1990; Woodside et al., 2002; Sellier et al., 2013a,b).

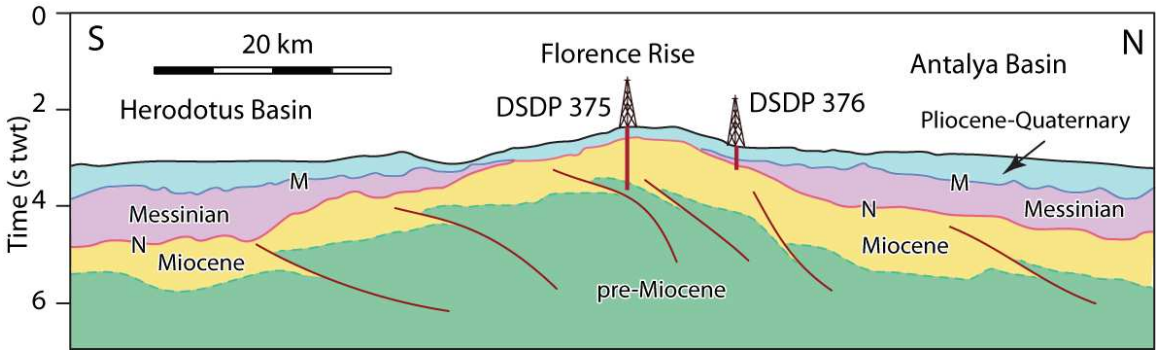

Figure 1.4: Line drawing of a deep-penetrating seismic line across the Florence Rise (redrawn from Sellier et al., 2013a; which is modified from Sage and Letouzey, 1990).

Previous studies suggested that the principal relief of the Florence Rise is caused by flower structures in post-Miocene sediments to the southwest of the ridge (Woodside et al., 2002; Zitter et al., 2003). Traced from the Herodotus Basin toward the Florence Rise (i.e., from south to north), the Messinian-lowermost Pliocene evaporites pinch out across the core of the rise (Fig. 1.4; Woodside et al., 2002). Güneş (2009) showed that further to the north, the Messinian evaporites form a north-thickening wedge which is nestled on the northern fringes of the Florence Rise. Thus, the Messinian evaporites are absent over the crustal region of the Florence Rise, where the major erosional M- and N-unconformities converge to form a prominent composite unconformity. At the southern part of the Florence Rise, a fold belt domain appears on seismic data (Güneş, 2009), which can be correlated with the Mediterranean Ridge.

Anaximander Mountains

The Anaximander Mountains (*sensu lato*) are located at the junction of the Hellenic and Cyprus arcs, southwest of the Antalya Basin, immediately south of the Finike Basin and northwest of the Florence Rise (Fig. 1.1, 1.2, 1.3). They consist of three main morpho-tectonic elements that rise ∼2000 m above the deep abyssal plain of the Antalya and Herodotus Basins, reaching relatively shallow depths of less than 1000 m. These are the Anaximander Mountain (*sensu stricto*) in the northwest, the Anaxagoras Mountain in the east, and the Anaximenes Mountain in the southwest (Fig 1.3). The Anaximander Mountain (*sensu stricto*) and the Anaximenes Mountain formed during the Pliocene–Quaternary, due to reactivation, uplift and rotation of a linked, thick-skinned pre-Messinian imbricate thrust fan (Aksu et al., 2009). Aksu et al. (2009) argued that the morphology of the submarine mountains was accentuated in both regions by the development of back thrusts, and the Anaximenes Mountain experienced a progressive counter clockwise rotation, while the Anaxagoras Mountain and the Florence Rise experienced a clockwise rotation. They concluded that these tectonic events were responsible for the present-day arrowhead-shaped morphology of the Anaximander Mountains (*sensu lato*).

Antalya Basin

The Antalya Basin is a deep depocentre situated between the foothills of the Taurus Mountains in the north and the Florence Rise in the south (Figs. 1.1–1.3). To the east it is connected to the Outer Cilicia Basin through the Anamur–Kormakiti zone, whereas in the west it is bounded by the Kemer Peninsula. The continental shelf around the Antalya Basin is very narrow, ranging between 2 and 6 km. The shelf-slope break occurs at ∼100–150 m depth, and steep slopes lead to the continental rise and abyssal plain. There is no multibeam data from the Antalya Basin, but the available bathymetry maps with 200 m isobaths show that the slope face is dissected by numerous submarine canyons, presumably feeding submarine fans, similar to those seen in continental slopes around the

western Mediterranean (Droz et al., 2001; Lastras et al., 2002). The continental rise occurs between 1800 and 2000 m water depth, where the slope gradient decreases considerably. The abyssal plain occurs at ∼2200–2400 m water depth: the maximum depth of ∼2600 m is observed as a near-circular depression in a central location within the Antalya Basin.

Previous studies have documented the complex tectonic architecture of the Antalya Basin and its role in the Miocene–Recent kinematic evolution of the eastern Mediterranean (Glover and Robertson, 1998a,b; Işler et al., 2005; Sage and Letouzey, 1990; Woodside et al., 2002; Hall et al., 2014a). Işler et al. (2005) outlined a two phase history for the Miocene–Recent kinematic evolution of the Antalya Basin. The first phase, during the Miocene, was dominated exclusively by compressional tectonism. This phase of deformation affected the entire Antalya Basin and is represented by several major northwest–southeast-striking, and predominantly north-dipping and south-verging thrust culminations. These thrust culminations created a series of elongated to tear-drop-shaped piggy-back basins within which thick Pliocene–Quaternary successions developed. A fundamental change in kinematic regime occurred during the transition from the Miocene to the Pliocene–Quaternary, when the strain was partitioned into discrete domains and the broad fold–thrust belt was overprinted by extensional/transtensional faults in the northeastern Antalya Basin, while transpression dominated the southwestern Antalya Basin. Hall et al. (2014a) suggested that the Miocene–Recent kinematic evolution of the western Antalya Basin occurred in three phases based on structures and their associations observed in the seismic reflection profiles. Phase 1 (pre-Messinian Miocene) is characterized by structures developed during a period of protracted contractional deformation. The deformation associated with Phase 1 also extends eastward toward the Kyrenia Range of northern Cyprus and southward toward the Florence Rise. During Phase 2 (Messinian) the entire Antalya Basin became a deep largely sub-aerially exposed basin, with very shallow water depth. Most of the Miocene thrust activity ceased during Phase 2, with Miocene thrusts terminating at or below the M-reflector (top of Messinian evaporites) and the absence of growth strata development within the evaporite suc-

cession. Phase 3 (Pliocene–Quaternary) deformation is spatially partitioned and characterized by transtension and transpression, partly reactivating older structures.

1.4.4 Segmentation of the NE Mediterranean Miocene basins

The evolution of the Miocene basins in the eastern Mediterranean is controlled by the development of a large, nearly east–west-trending foredeep in front of the Tauride fold–thrust belt (Williams et al., 1995; Aksu et al., 2009; Hall et al., 2009). The Tauride culmination was characterized by an arcuate thrust front that delineated a broad syntaxis, comprising several smaller thrust culminations which developed in the foredeep itself. There are remarkably similar marine Aquitanian–Tortonian successions in the onland Mut and Adana basins (Eriş et al., 2005; Şafak et al., 2005), Aksu, Köprüçay and Manavgat basins (Poisson et al., 2003a,b; Deynoux et al., 2005; Karabıyıkoğlu et al., 2005) and the Mesaoria Basin of central Cyprus (Robertson and Woodcock, 1986). The depositional similarities further continue into the fold–thrust panels of the Misis Mountains (Gökçen et al., 1988) and the Kyrenia Range (Calon et al., 2005a,b), the Aksu Thrust (Poisson et al., 2003a,b), as well as the marine Cilicia, Iskenderun, Antalya and Finike basins (Figs. 1.1, 1.4; Uffenorde et al., 1990; Aksu et al., 2005a,b, 2009, 2014c; Işler et al., 2005). These strong regional depositional similarities suggest the presence of a single large basin in the Early Miocene which encompassed what are now seemingly isolated basins in the eastern Mediterranean. This large ancestral basin probably extended from the Karsantı and Maraş basins in the east (Calon et al., 2005a; Hall et al., 2005a; Ilgar and Nemec, 2005; Satur et al., 2005; Hüsing et al., 2009) into the Antalya and Kasaba basins in the west (Işler et al., 2005; Çiner et al., 2008). The development of crustal-scale thrust culminations (e.g., the Misis–Kyrenia–Anamur lineament;(Aksu et al., 2014a,b)), the Amanos–Larnaka fault zone (Hall et al., 2005a; Aksu et al., 2005b) and the Tartus ridge (Hall et al., 2005b), are perhaps associated with the onset of escape tectonics related to the final collision of the Arabian and Aegean–Anatolian microplates in the latest Miocene and Pliocene–Quaternary (Şengör et al., 1985), which essentially

split the foredeep into several large piggy-back basins: the Mut–Adana–Cilicia basin complex, the Iskenderun–Latakia–Mesaoria basin complex, and the Cyprus, Antalya, Finike and Rhodes basins (e.g., Calon et al., 2005a; Hall et al., 2005a, 2009; Aksu et al., 2005a,b). While the origins of these basins lie in Miocene contraction, extensional structures are overprinted on them in many places, especially during the Pliocene to Recent, reflecting regionally-variable transtension. Within this context, the Antalya Basin forms a predominantly marine depocentre, situated in a forearc setting between the Florence Rise and the Taurus Mountains of southern Turkey to the north (Fig. 1.1, 1.4).

1.4.5 Structural Relationship with Onshore Fault Zones

The geodynamic and kinematic evolution of the Eastern Mediterranean region and the correlations of the offshore and onshore structures are currently the focus of much debate (McClusky et al., 2000; Woodside et al., 2002; Aksu et al., 2009; Hall et al., 2009; Sellier et al., 2013a,b). Several horsetail-like sinistral strike-slip faults splay from the East Anatolian Fault zone and extend toward the southwest from the Maraş triple junction (Fig. 1.1, 1.3). The Amanos Fault zone is one of the most prominent of these splays, and defines the eastern boundary of the Amanos Mountains (Taymaz et al., 1991; Beydoun, 1999; Westaway, 2004). It can be readily traced to the eastern shores of the Mediterranean Sea where it joins with the prominent arcuate Amanos-Larnaka Fault zone, where the structure enters the Island of Cyprus (Hall et al., 2005a). From here, the Amanos-Larnaka Fault zone is traced across the southern margin of the Troodos Complex, swinging to the northwest and possibly extending into the Antalya Basin (Calon et al., 2005a,b). The onland Misis-Andirin Fault Zone is another important splay of the East Anatolian Fault zone and extends toward the southwest into the Misis Mountains of southern Turkey (Figs. 1.1, 1.3). This structure can be readily traced into the prominent northeast trending Misis-Kyrenia Fault zone (Aksu et al., 1992, 2005a) and then to the east-west trending Kyrenia Range of northern Cyprus (Calon et al., 2005a; Aksu et al., 2014a,b; Walsh-Kennedy et al., 2014). Further west the Misis-Kyrenia Fault swings toward the northwest

and continues into the Antalya Basin, linking with the onland Aksu Fault Zone (Işler et al., 2005; Hall et al., 2014a). The Misis-Kyrenia-Aksu and the Amanos-Larnaka-Troodos lineaments form two crustal-scale arcuate zones running parallel to the general trend of the Cyprus Arc, indicating that the deformation in the forearc setting extended 250–350 km north of the arc (Figs. 1.1–1.3).

1.5 Messinian Salinity Crises

The Messinian Salinity Crisis refers to a series of events that occurred between ∼5.97 and 5.33 Ma, which resulted in the reduction/cessation of water inflow from the Atlantic Ocean into the Mediterranean Sea, creating widespread evaporite precipitation across the Mediterranean basins. During this period the base-level of the Mediterranean Sea dropped considerably below its present level. In the western Mediterranean a ∼1500 m deep river valley incision occurred and propagated at least ∼300 km inland from the coast. Karst systems that were formed in association with the Messinian canyons of the Ardèche and Rhône rivers suggesting that the base level dropped to -1500 m (Loget et al., 2006; Mocochain et al., 2006; Urgeles et al., 2010). In the eastern Mediterranean several erosional surfaces are observed in seismic profiles along the Egyptian margin at a depth between -2500 and -3000 m (Gargani and Rigoller, 2007). These authors argued that the Pliocene–Quaternary subsidence ranges between 750–1000 m, thus, the erosional surfaces must have been formed during the Messinian Salinity Crisis at depths of 1500–2250 m below the present-day base level. Successions across the Afiq Canyon in the Levant margin show similar sea-level lowering during the Messinian (Druckman et al., 1995).

1.5.1 Why did the Mediterranean became isolated from the global ocean?

During the Eocene, the Mediterranean Sea constituted the western sector of the Tethys Ocean (sometime referred to as the Neotethys Ocean) which was situated between the African and Eurasian plates (Fig. 1.5). The protracted contraction between these two plates progressively closed the Tethys

Ocean, creating the largely inland Mediterranean Sea (Fig. 1.5). Plate tectonics played a pivotal role in the development of the Messinian Salinity Crisis in the Mediterranean region. The tectonic evolution of two regions are critical in the events that led to the complete isolation of the Mediterranean Sea from the global ocean: (a) the closure of the Bitlis Ocean (sometime referred to as the Bitlis-Zagros Ocean) and the collision and suturing of the Arabian Microplate with the southern fringes of the Eurasian Plate during the late Miocene in the east (e.g., Hüsing et al., 2009) and (b) the progressive closure and uplift of the Gibraltar region during the latest Miocene in the west (e.g., Rosenbaum et al., 2002; Garcia-Castellanos and Villaseñor, 2011). During the Middle-Late Miocene, the Mediterranean Sea (*sensu stricto*) was also connected in the north to the Pannonian and Dacic basins of eastern central Europe, as well as to the greater Black Sea and the Caspian Sea (Popov et al., 2004, 2006). However, these water bodies were not independently connected to the world ocean, except via the Mediterranean Sea (Popov et al., 2004, 2006). The only other possible watermass communication between the Mediterranean Sea and the global ocean during the Middle-Late Miocene was via the Red Sea to the south. The tectonic evolution of the Red Sea occurred in two-stages: major rifting took place during the Eocene, followed by seafloor spreading in the late Eocene and early Oligocene (Stern and Johnson, 2010). The rift phase was followed by a period of 30 Ma of no motion, during which a large amount of evaporites were deposited across the Red Sea. Activity restarted in the latest Miocene as shown by the magnetic anomalies across the Red Sea formed during the last 5 Ma (Stern and Johnson, 2010). Thus, during the Late-Middle Miocene, there was no watermass communication between the Mediterranean Sea and the embryonic Red Sea (Popov et al., 2004, 2006).

Therefore, it is clear that there are only two gateways during the Middle-Late Miocene that formed the connection of the Mediterranean Sea (senso lato) to the world ocean: the Bitlis gateway in the east and the Betic and Rif gateways in the west. The timing and tectonic causes for the closures of these two gateways are summarized below to provide a better understanding of the

Figure 1.5: Paleogeographic maps of the Early Eocene, Late Oligocene and Middle Miocene. Adopted from Ron Blakey, Colorado Plateau Geosystems, Arizona, USA, Paleogeography of Europe.

Messinian Salinity Crisis.

1.5.2 Tectonics of the Bitlis gateway – eastern Mediterranean

Geodynamic and geological context

The continental collision of the African Plate–Arabian Microplate with the Eurasian Plate resulted in a tectonic collage in eastern Anatolia, including: (a) the eastern Rhodope–Pontide Arc in the north; (b) the east Anatolian accretionary complex consisting of an ophiolitic mélange overlain by Paleocene to upper Oligocene sediments; and (c) the Bitlis–Pötürge Massif tectonically overlying the northern part of the Arabian margin (Fig. 1.3; Şengör and Yılmaz 1981; Yılmaz 1993; Tüysüz and Erler 1995; Robertson 2000; Şengör et al. 2003; Agard et al. 2005). During the closure of the Bitlis Sea (or Bitlis-Zagros gateway) a series of major geodynamic processes took place along the northern Arabian promontory, which accommodated the tectonic responses to the Arabian Microplate–Eurasian Plate collision. At $\sim$30 Ma, the northern fringes of the Arabian Microplate started to collide with eastern Anatolia and the western Iran regions of the Eurasian Plate (Jolivet and Faccenna, 2000; Bellahsen et al., 2003). This early collision caused the Arabian Microplate to progressively rotate in a counterclockwise sense leading to diachronous collision eastward from southeastern Anatolia towards the Persian Gulf (Hessami et al., 2001). As the north–south shortening continued between the converging Eurasian Plate and the Arabian Microplate, the east Anatolian accretionary complex took up most of the initial post-collisional convergent strain by shortening and thickening (Yılmaz et al., 1998). During the Late Miocene, around 13–11 Ma, eastern Anatolia experienced rapid uplift and widespread volcanism (Dewey et al., 1986; Pearce et al., 1990; Keskin 2003; Şengör et al., 2003), which has been associated with detachment of a northward dipping subducted lithospheric slab (Keskin, 2003; Faccenna et al., 2006; Hafkenscheid et al., 2006; also see the tomographic studies below). From this moment onward, the ongoing northward motion of Arabian Microplate (McClusky et al., 2000; Reilinger et al., 2006; Allmendinger et al., 2007), and

the retreat of the Hellenic subduction zone to the southwest (Berckhemer, 1977; Le Pichon et al., 1982; Jolivet 2001) resulted in the westward tectonic escape of Anatolia along the North and East Anatolian Faults (Fig. 1.3; Dewey and Şengör 1979; Şengör et al., 1985). Thus, the region that comprised the eastern Tethys gateway during the Eocene–Middle Miocene has thus been subjected to plate convergence and subduction during the Late Miocene. Şengör et al. (2003) suggested that this subduction led to southward migrating accretion of nappes and the overlying deep marine flysch and molasse successions that were deposited within the foreland. A foredeep likely remained present until continent–continent collision and subsequent slab break-off stalled the convergence and the collision zone is dramatically uplifted during the Late Miocene, closing the marine gateway between the Mediterranean Sea and the Tethys Ocean by $\sim$11 Ma (Hüsing et al., 2009).

P-wave tomographic studies

The east Anatolian contractional province occupies the eastern portion of Anatolia, and it is characterized by north-south convergence between the Arabian Plate to the south and the Eurasian Plate to the north (Fig. 1.3). Following the closure of the southern branch of the Tethys Ocean (i.e., the Bitlis Sea) during the middle Miocene the ensuing contraction gave way to the formation and widespread distribution of left- and right-lateral conjugate strike-slip faults during the early Pliocene ($\sim$5 Ma; Fig. 1.3). Recent geophysical investigations in the region revealed the presence of a thin crust and mantle lithosphere beneath the Eastern Anatolian Plateau (Türkelli et al., 1996; Sandvol et al., 1998; Gök et al. 2000; Al-Lazki et al., 2003; Zor et al., 2003; Angus et al., 2006; Özacar et al., 2008, 2010; Biryol et al., 2011). These geological studies and the associated geochemical data on igneous rocks exposed across the eastern Anatolia indicated that the sustained uplift of the plateau is associated with the steepening and break-off of the northward subducting Arabian lithosphere. Hüsing et al. (2009) have dated the youngest sediments underneath subduction-related thrusts at $\sim$11 Ma, which suggests that this age must correspond to the end of underthrusting in the Maraş triple junc-

tion region (Figs. 1.1, 1.3; i.e., the end of subduction of Arabian slab beneath the Eurasian Plate, now the easternmost sector of the Aegean-Anatolian Microplate). The geophysical studies further suggested that the upwelling hot asthenosphere replaced the slab, giving way to recent volcanism and supporting the 2 km elevation of the eastern Anatolia (sometime referred to as the Eastern Anatolian Plateau; Keskin 2003; Şengör et al., 2003). This event also marks a dramatic change in the stress field throughout the eastern Anatolia, as suggested by Koçyiğit et al. (2001) and Örgülü et al. (2003). Teleseismic tomography studies indicated the presence of a detached slab located at depths of $\sim$600 km beneath the eastern Anatolia, immediately north of the Bitlis-Zagros suture zone (Figs. 1.1, 1.3; Zor, 2008).

In the tomographic modelling studies there is an intriguing low velocity anomaly beneath the northwestern part of the Arabian Microplate from 100 km down to 300 km depth (Figs. 1.6, 1.7; Toksöz et al., 2010). This low velocity anomaly spread out at the lower mantle, suggesting that the hotspot may be the surface manifestation of a broad mantle upwelling connected to the African Super Plume in the lower mantle beneath southern Africa (Benoit et al., 2006). In the tomographic model of Toksöz et al. (2010), the subduction along the Bitlis-Zagros suture zone is well imaged (Figs. 1.6, 1.7). Here, pronounced high velocity anomalies with a southward dip angle are detected in the upper mantle (above 410 km discontinuity) and earthquakes are confined above 150 km depth in the fast structures (Toksöz et al., 2010). The south-dipping slabs in the upper mantle is interpreted by these authors as the result that the Arabian Plate has overridden itself during post-collision between Arabian and Eurasian plates, similar to what has been observed at the Indian Plate and Eurasian Plate collision (Li et al., 2006). The north-dipping slab of the Arabian Microplate in the upper mantle appears to disconnect with the fast structures in the lower mantle (Toksöz et al., 2010).

The P-wave tomographic model of Biryol et al. (2011) shows an abrupt eastern termination of the Cyprus slab along the 33–34^{o}E longitudes (Figs. 1.8, 1.9). To the east of this zone, there is a relatively homogeneous slow velocity anomaly beneath the eastern Anatolian Plateau, which

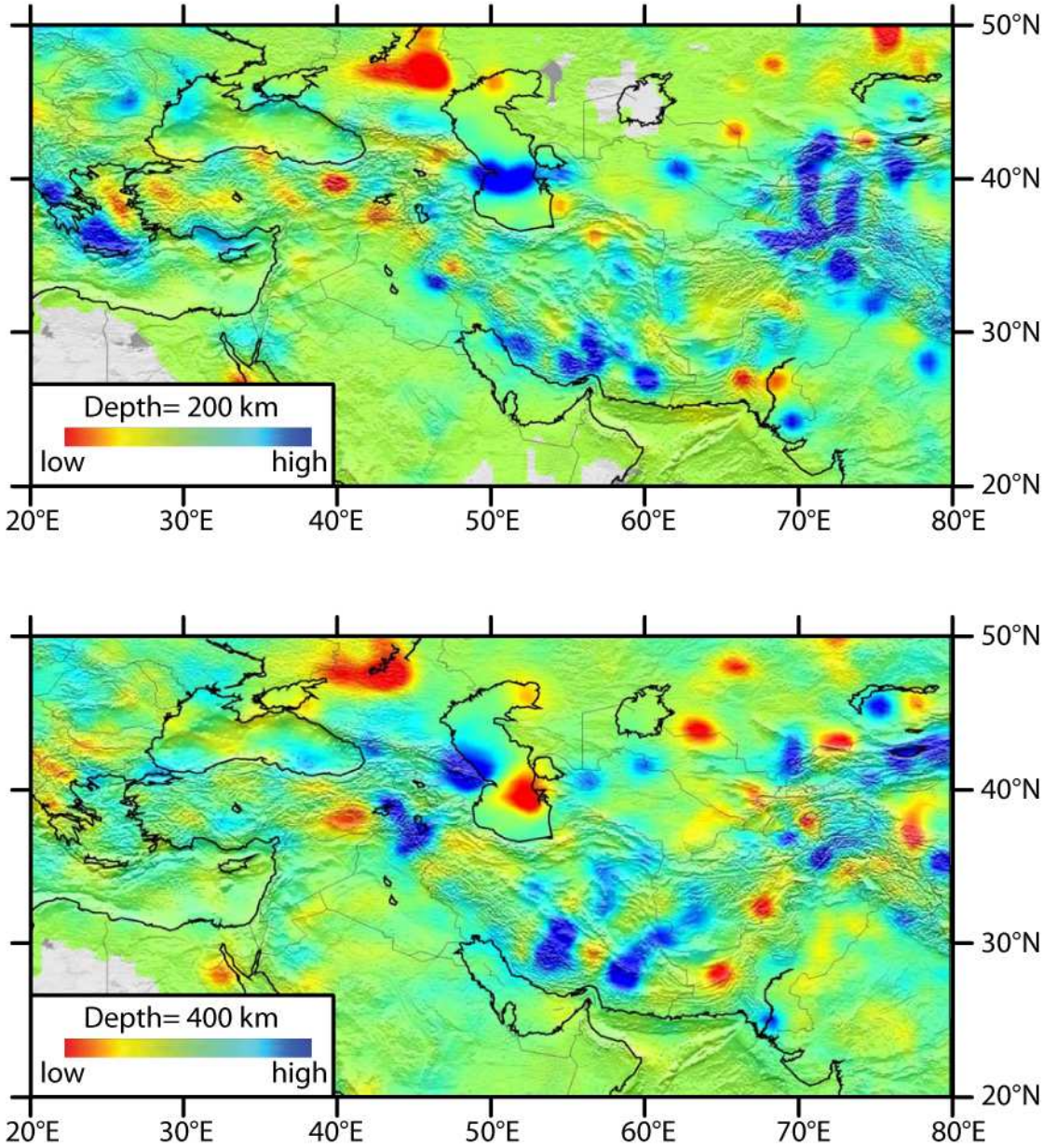

Figure 1.6: P wave velocity profile at 200 km and 400 km depths across the eastern Mediterranean and the Middle East. Adopted from Toksöz et al. (2010).

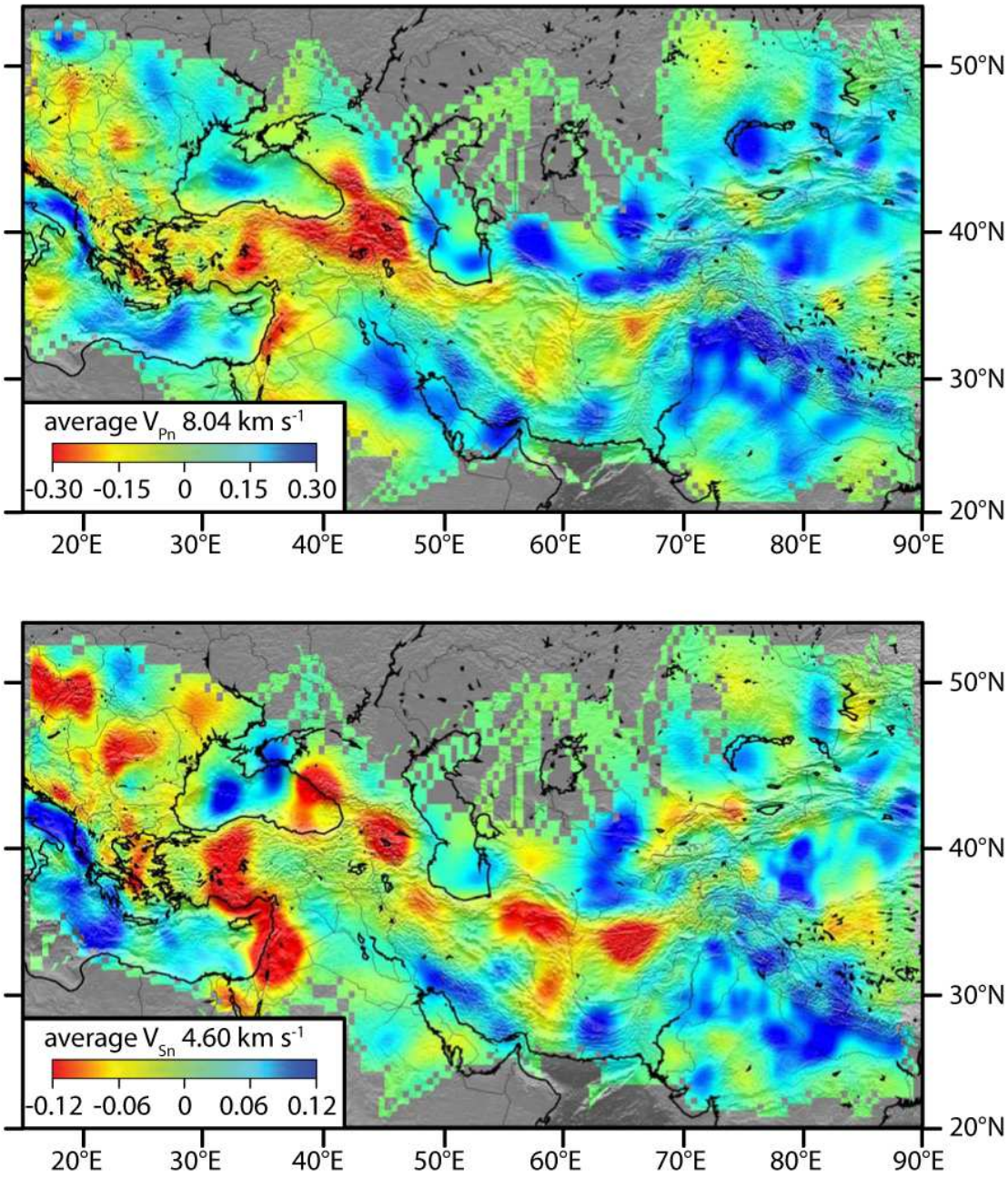

Figure 1.7: Imaged Pn (top) and Sn (bottom) velocity lateral variations across the eastern Mediterranean and the Middle East. The average Pn and Sn velocities are 8.04 km s^{-1} and 4.60 km s^{-1}, respectively. Red represents lower velocity than average and blue denotes higher velocity. Adopted from Toksöz et al. (2010).

extends as deep as 400 km beneath the plateau. This slow velocity anomaly is also delineated by several previous studies (e.g., Al-Lazki et al. 2003, Gans et al., 2009). In all these studies, the low velocity anomaly is interpreted to be associated with the asthenosphere that ascended and was emplaced beneath the plateau after the detachment of the northward subducting Arabian oceanic lithosphere (Keskin 2003, Şengör et al. 2003, Al-Lazki et al. 2003, Gans et al., 2009, Toksöz et al., 2010, Biryol et al., 2011). The models presented by Toksöz et al. (2010) and Biryol et al. (2011) clearly outline the 3-dimensional extent of this hot, buoyant asthenospheric body that is believed to be supporting the relatively thin ($\sim$2 km) crust of the eastern Anatolian high plateau (Şengör et al., 2003; Zor et al., 2003; Özacar et al., 2008, 2010). The P-wave tomograms presented by Biryol et al. (2011) also show that the eastern termination of the Cyprus slab (i.e., the eastern edge of the subducting African lithosphere) and the western tip of the emplaced asthenosphere nearly align with the boundary between the eastern Anatolian contractional province (EACP in Figs. 1.8, 1.9) to the east and the central Anatolian Province to the west (Figs. 1.8, 1.9). This alignment was also suggested by the Pn velocity observations of Gans et al. (2009). The western extent of the east Anatolian contractional province roughly aligns with the northward projection of the Dead Sea Transform Fault (Barka and Reilinger, 1997), which delineates the boundary between the African Plate and Arabian Microplate (Figs. 1.3, 1.8, 1.9). Reilinger et al. (1997) suggested that the crust of eastern Anatolia is hot and weak due to the presence of hot buoyant asthenosphere beneath the region (Keskin, 2003), and that this weak crust accommodates the N-S convergence between the Eurasian Plate and the Arabian Microplate across the eastern Anatolian contractional province (Figs. 1.8, 1.9). This is in agreement with the distribution of the slow anomalies delineated in the P-wave tomographic model of Biryol et al. (2011). These authors remark that the broad alignment of the western edge of the slow anomaly associated with eastern Anatolia lies along the eastern Anatolian contractional province–central Anatolian province transition with the northward projection of the Dead Sea Transform Fault (Figs. 1.8, 1.9).

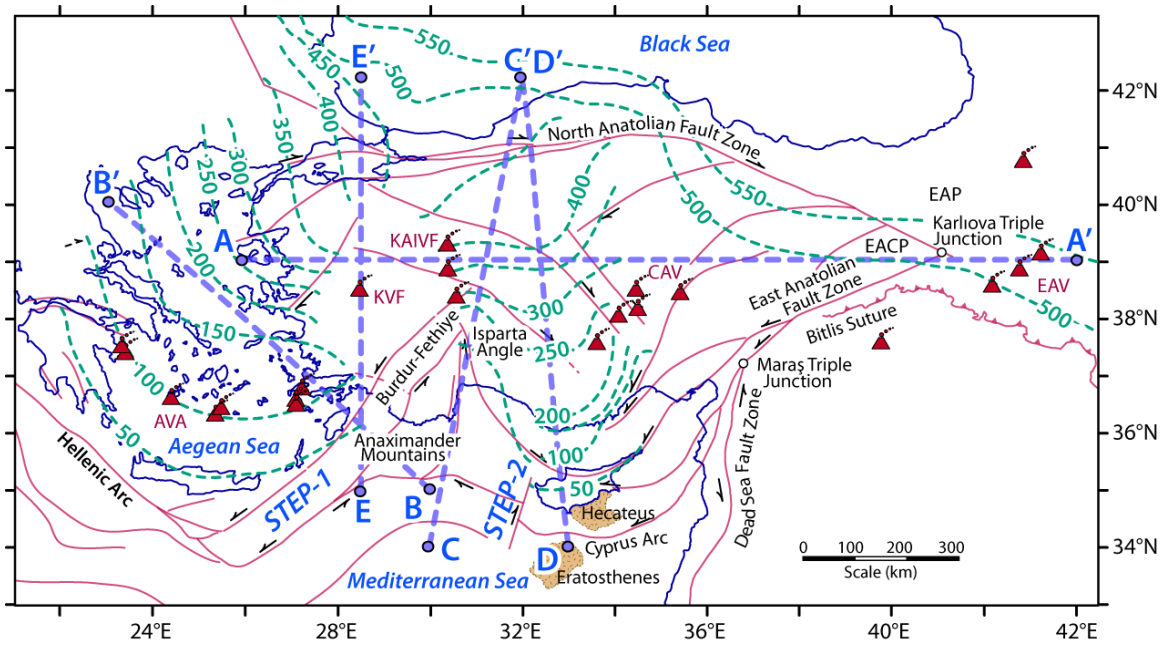

Figure 1.8: Map showing the depth of the subducted slabs beneath the Aegean and Cyprus arcs (dashed aquamarine contours). Also shown are the locations of the P-wave tomographic cross sections illustrated in Figure 1.9. Redrawn from Biryol et al. (2011).

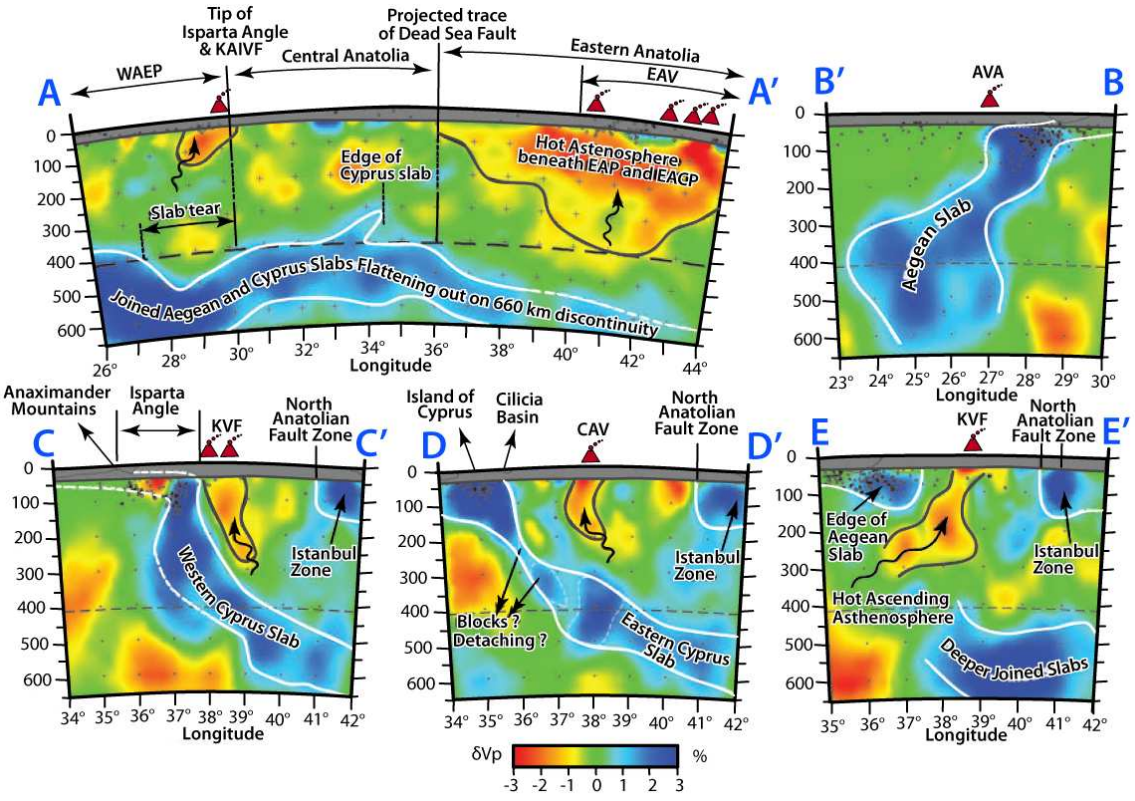

Figure 1.9: P-wave tomographic cross sections across the Aegean-Anatolian Microplate. Note that the slab(s) consumed beneath the Aegean and Cyprus arcs becomes flattened at ∼400-500 km depth (profile A-A'). Also note the hot astenosphere beneath the east Anatolian contractional province (EACP in profile A-A'). WAEP= west Anatolian extensional province, KAIEF= Kirka-Afyon-Isparta volcanic field, EAV= eastern Anatolian volcanic, EAP= eastern Anatolian province, AVA= Aegean arc volcanic, KVF= Kula Volcanic Field, CAV= central Anatolian volcanic. Redrawn from Biryol et al. (2011).

The above discussion clearly shows that by the Late Miocene (∼11 Ma; Hüsing et al., 2009) the Arabian Microplate already collided with Eurasian Plate and that it was sutured, closing the marine gateway that connected the Tethys Ocean in the east and the Mediterranean Sea in the west (Fig. 1.5). The only remaining watermass communication link between the Mediterranean Sea (*sensu lato*) and the global ocean was the Betic and Rif gateways across the present-day Strait of Gibraltar, which is discussed below.

1.5.3 Tectonics of the Betic, Rif and Sicily gateways – western Mediterranean

Geodynamic and geological context

During the Oligocene, ∼30 Ma, the northwestern margin of the Mediterranean Sea consisted of several terrains, including the Betic and Rif Cordilleras, the Balearic Islands, the Kabylies, Corsica, Sardinia and Calabria. (Fig. 1.10; Rosenbaum et al., 2002). A prominent subduction zone existed immediately south of these terrains where the African plate was being consumed beneath the western portion of the Eurasian Plate. During the Late Oligocene, roll back of the subduction zone created widespread extension in the Alps and in the western Mediterranean region (Fig. 1.10; Rosenbaum et al., 2002). This extension on the overriding plate, formed the foundation of the development of the western Mediterranean basins, including the Gulf of Lion and Valencia Trough (Fig. 1.10; Rosenbaum et al., 2002). Extension continued in the Early Miocene and led to breakup and drifting of continental fragments formerly attached to southern France and Iberia. During the opening of the "Ligurian Sea, Gulf of Lion and Valencia Trough", the Balearic Islands, Corsica, Sardinia and Calabria experienced block rotations. During the Burdigalian, subduction roll back continued and caused intense tectonic activity across northwest Africa (Fig. 1.10; Rosenbaum et al., 2002). The breakup between Balearic Islands and Kabylies caused the opening of the Algerian Basin and the subsequent emplacement of the Rif onto the African margin. Between ∼18 and 15 Ma ago, the Kabylies blocks drifted south in response to further southward rollback of the subduction zone until

they collided and accreted to the African margin (Fig. 1.10, 1.11; Rosenbaum et al., 2002). The Alboran Sea formed during the west ward migration of the subduction hinge when rapid rollback was compensated by wholesale extension in the overriding thinned continental crust (Fig. 1.11; Rosenbaum et al., 2002). The final accretion of the Rif-Betic Cordillera occurred at $\sim$10 Ma, when the subduction zone rolled back as far west as the present-day Strait of Gibraltar (Fig. 1.11; Rosenbaum et al., 2002; Garcia-Castellanos and Villaseñor, 2011). During the Messinian the western part of the Mediterranean around the Alboran Sea was very shallow or largely sub-aerially exposed: the uplift of the Gibraltar Arc created the necessary conditions for the isolation of the Mediterranean Sea from the Atlantic Ocean (Garcia-Castellanos and Villaseñor, 2011). The eastern segment of the prominent subduction zone that delineated the Kabylies and the Maghrebites also experienced south- and southeast-directed roll back. The Tyrrhenian Sea which is the youngest basin in the western Mediterranean formed in the Tortonian ($\sim$9 Ma) as the result of a southeastward rollback of subduction systems near the margins of the Adriatic plate (Malinverno and Ryan, 1986). The Tyrrhenian Sea opened in two stages: 9-5 Ma opening of the northern Tyrrhenian Sea, followed by a 5-0 Ma opening of the southern Tyrrhenian Sea (Fig. 1.10; Rosenbaum et al., 2002). During the Early Pliocene extension ceased in the northern Tyrrhenian Sea and migrated southward to the southern Tyrrhenian Sea (Fig. 1.11; Rosenbaum et al., 2002). During the same time, crustal shortening occurred in the southern Apennines and in Sicily accompanied by counterclockwise block rotations across the Apennines and clockwise rotations in Sicily. These processes have been controlled by rapid roll back of Ionian oceanic lithosphere beneath the Calabrian Arc.

The development of the southern Apennines and Sicily north and west of the east-concave Calabrian Arc has serious implications for the history of the Messinian Salinity Crisis. Today, this region defines a major bathymetric barrier which separates the eastern and western Mediterranean seas. The evolution of the Calabrian Arc and its subduction zone since the Serravallian-Tortonian has been characterized by rollback of the Ionian lithosphere associated with opening of the Tyrrhenian

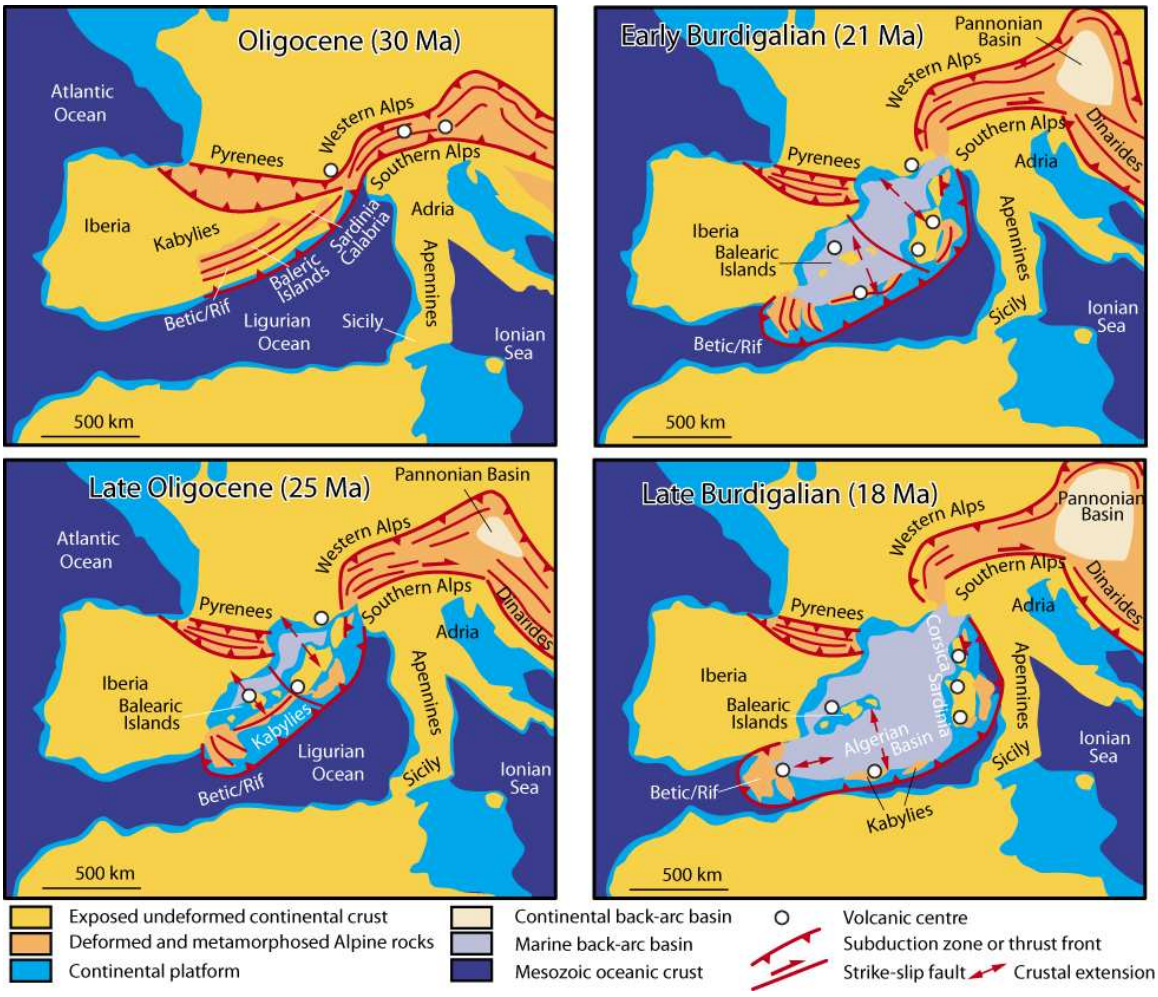

Figure 1.10: Oligocene–Late Burdigalian reconstruction and tectonic evolution of the western Mediterranean, adopted from Resenbaum et al. (2002).

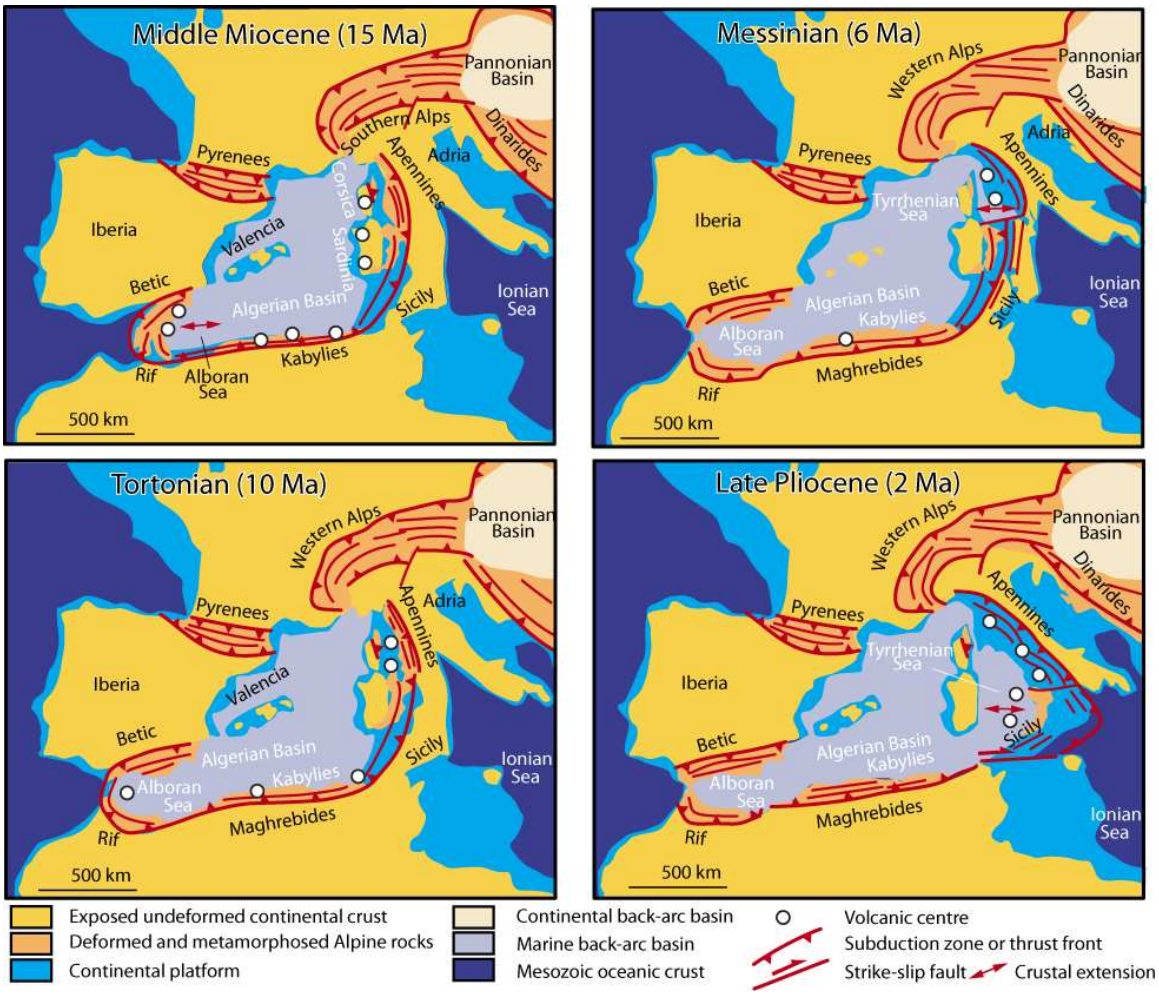

Figure 1.11: Middle Miocene–Late Pliocene reconstruction and tectonic evolution of the western Mediterranean, adopted from Resenbaum et al. (2002).

Sea as a back-arc basin (Malinverno and Ryan, 1986; Mattei et al., 2007; Cifelli et al., 2007). During the Late Miocene there were distinct episodes of tears and break-off along the Tyrrhenian slab (e.g., Chiarabba et al., 2008; Argnani, 2009). The first episode occurred from 8.5 to 4.0 Ma and affected the segment of the slab located in the Sardinia Channel. The second episode occurred between 2.5 and 1.6 Ma, affecting the segment of slab located north of Sicily, and was proceeded by rifting in the Strait of Sicily (Argnani, 2009; D'Agostino et al., 2011)

P-wave tomographic studies

Lithospheric slab detachment and roll back has previously been suggested as the possible cause for protracted Gibraltar Arc uplift which initiated the Messinian Salinity Crisis (Duggen et al., 2003; Garcia-Castellanos and Villaseñor, 2011). Geodynamic interpretation of the tomographic data results invokes the lateral migration of a tearing of the lithospheric slab originally attached to the south Iberian margin at the end of Miocene (Fig. 1.12; Garcia-Castellanos and Villaseñor, 2011). Similarly, the lithospheric slab detachment and roll back across the Calabrian Arc, and the subsequent uplift of the southernmost Apennines and Sicily created a major topographic block separating the eastern and western Mediterranean seas (e.g., Chiarabba et al., 2008). This region has considerable importance as the Sicilian sill is believed to have controlled the saline water influx from the western to the eastern Mediterranean seas (Blanc, 2000).

During the latest Miocene $\sim$6 Ma ago, progressive tectonic restriction and subsequent closure of the two Mediterranean-Atlantic gateways: one through northern Morocco (Rif Corridor) and the other through southern Spain (Betic Corridor) (Fig. 1.13; Platt and Vissers 1989; Rosenbaum et al., 2002) led to extreme salinity fluctuations in the Mediterranean Sea, which resulted in the deposition of thick evaporite successions in a relatively brief period of $\sim$0.63 Ma (Montadert et al., 1970; Hsü et al., 1973; Lofi et al., 2005; Hilgen et al., 2007, Gaullier et al., 2010). The sea level drop during the Messinian Salinity Crisis represents the most striking environmental change in the Cenozoic history

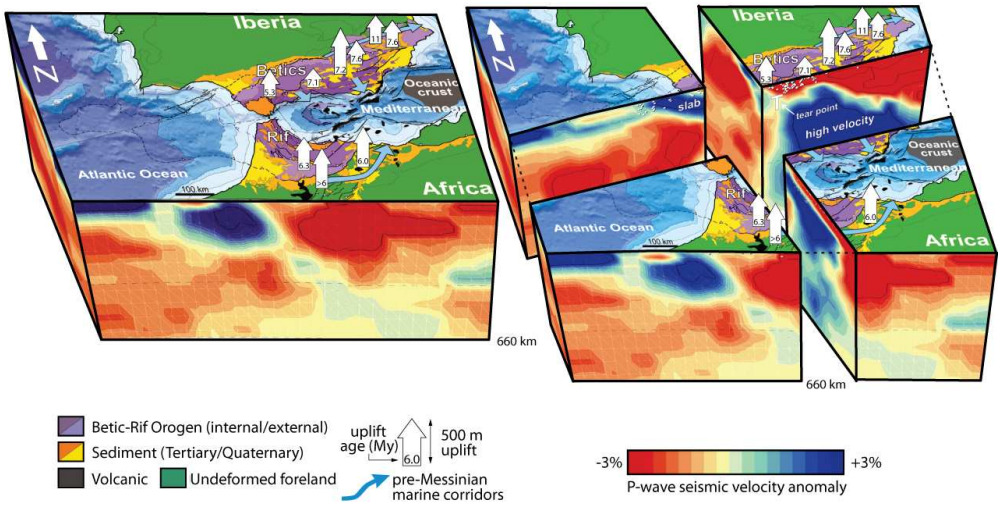

Figure 1.12: Geological map of the Betics and the Rif (South Spain, North Africa) combined with tomographic images of the Earth's interior, reaching ∼660 km depth. Vertical white arrows= crustal uplift horizontal blue arrows = marine corridors. Adopted from Garcia-Castellanos and Villaseñor (2011).

of the Mediterranean Sea. During this event, rapid sea level drop resulted in increased seawater salinity and the deposition of evaporites within shallow marginal basins (Lofi et al., 2011a,b). The dramatic sea-level lowering exposed the continental margin to subaerial erosion while thick evaporite successions deposited within the physiographically deep Mediterranean basins, but at shallow water depths (e.g., Ryan, 2009). During this interval the top of the accretionary wedge as well as the frontal portion of the subduction zones also experienced considerable erosion (Hsü et al., 1973; Montadert et al., 1978; Clauzon, 1982; Tay et al., 2002; Ryan, 2009). The end of the Messinian Salinity Crisis was marked by rapid refilling of the Mediterranean basins during latest Miocene/early Pliocene and re-connection of the Mediterranean Sea and the Atlantic Ocean.

Deposition of the evaporite successions during the Messinian Salinity Crisis was complex, thus the stratigraphy of Messinian evaporites varies throughout the Mediterranean region (Rouchy and Caruso, 2006; Roveri et al., 2008a; Lofi et al. 2011a,b; Manzi et al., 2013, 2014; Roveri et al., 2014a,b,c). The distribution of the Messinian deposits results from the superimposition of regional

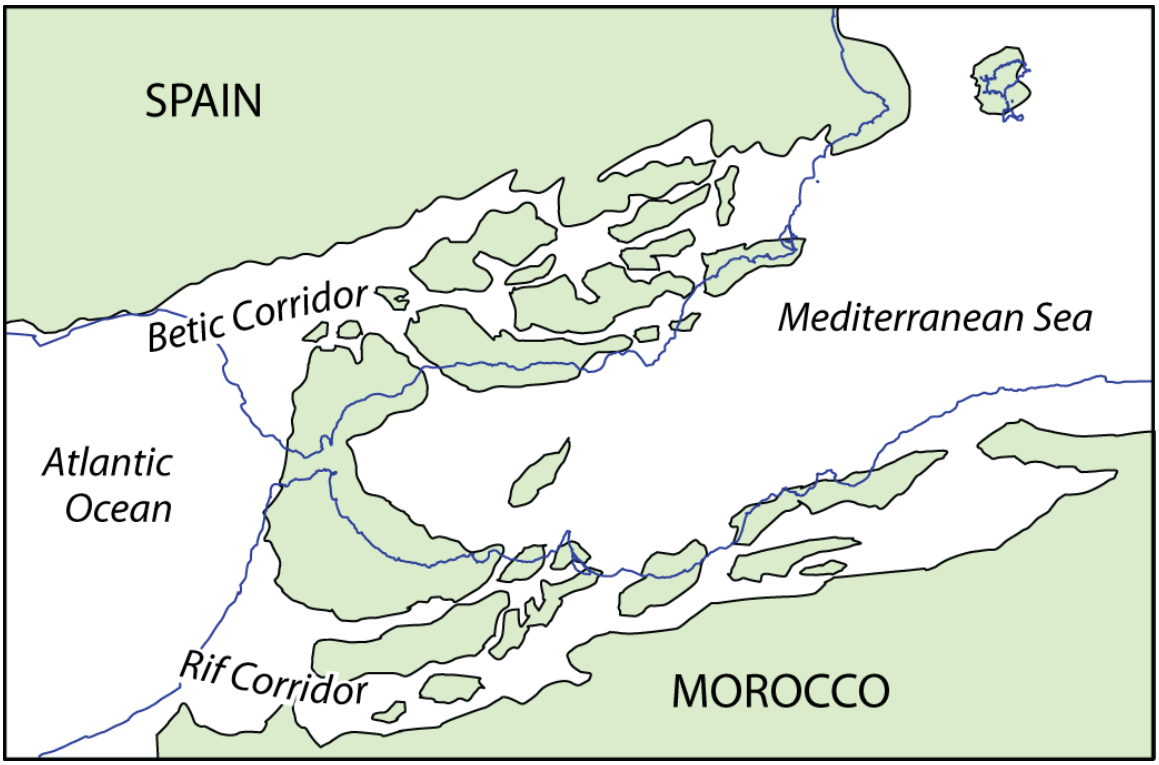

Figure 1.13: Schematic map of the western Mediterranean region showing the position of the Betic and Rif corridors that formed the gateway between the Atlantic Ocean and the Mediterranean Sea during the Late Miocene, prior to the Messinian Salinity Crisis (redrawn from http://www.paleo.bris.ac.uk/~ri5774/research.html). The present-day coastline is taken from the International Bathymetric Charts of the Mediterranean (IOC, 1981).

controlling factors related to the Messinian Salinity Crisis and local controlling factors related to the structural and geodynamical evolution both of the eastern and western Mediterranean basins (Rouchy and Caruso, 2006). Seismic data have shown that the base and top of the Messinian evaporites are marked by two strong reflectors, the N reflector at the base and the M reflector at the top. These reflectors correspond to two regional seismic events traditionally defining the erosion surfaces associated with the huge drop of sea level and subsequent deposition of the Messinian evaporites (Finetti and Morelli, 1973; Hsü et al., 1973; Ryan et al., 1973; Ryan and Cita, 1978; Bertoni and Cartwright, 2006, 2007). The N reflector has been defined as a tectonic unconformity in the Cyprus Arc area (Hall et al., 2005b).

1.6 Geological uncertainties in the eastern Mediterranean

There are several uncertainties in our geological understanding of the eastern Mediterranean region, which require a brief explanation in this chapter as they are critical in the development of the ideas in this study. These are explained below.

1.6.1 Geodynamics of the Hellenic and Cyprus "Double Arc System"

Previous studies have described the geodynamic evolution of the eastern Mediterranean region and the complex interaction of crustal-scale tectonics associated with the Hellenic and Cyprus Arc systems. Nur and Ben-Avraham (1978) and Rotstein and Kafka (1982) suggested that the Hellenic and Cyprus arcs may once have formed a single arc system, which must have extended into the Bitlis Ocean, prior to the collision of the Arabian Microplate with the Eurasian Plate in the Late Miocene. The vestige of this former ocean is now incorporated in the thrust panels of the Bitlis-Zagros suture (Bozkurt, 2001). The current configuration, with a broadly east-west-trending double arc system, is related to the final collision and suturing of the Arabian Microplate with the Eurasian Plate along the Bitlis–Zagros fold-thrust belt, and the west-directed tectonic escape of the Aegean-Anatolian

Microplate (Şengör and Yılmaz, 1981, Taymaz et al., 1991, Le Pichon et al., 1995, Robertson, 1998, Bozkurt, 2001). The irregularities along the plate margins and the oblique lithospheric convergence play an important role in subduction-zone dynamics and in the development of complex fault patterns. The junction between the Hellenic and Cyprus arcs has been considered enigmatic as far as the relationship between subduction zone dynamics and observed crustal deformation is concerned (Woodside et al., 2002; Zitter et al., 2003; ten Veen et al., 2004; Aksu et al, 2009; Hall et al. 2009).

The tectonic setting and seismic activity along the Cyprus Arc indicated a relative northeast-southwest plate motion across the arc (Wdowinski et al., 2005). The extreme eastern portion of the Cyprus Arc is oriented sub-parallel to relative convergence vectors, thus it is dominated by transcurrent tectonism. The western portion of the Cyprus arc is oriented almost normal to relative plate motion and is subjected to convergent processes (Wdowinski et al., 2005). Variations in the level and depth of seismic activity along the western Cyprus arc suggest that the northwestern section of the arc represents a subduction boundary, whereas the southeastern section represents a collision boundary (Wdowinski et al. 2005). Observations on active faulting along the Cyprus Arc showed that these two tectonic domains of the western arc are separated by a northeast-southwest trending lithospheric tear, which produces large earthquakes, such as the M_W=6.8 1996, Paphos Earthquake (STEP-2 in Fig. 1.14; Arvidsson et al., 1998; Aktar et al., 2000; Pilidou et al., 2004) used seismic tomography to study the deep structure of the Aegean-Anatolian Microplate–African Plate boundary at the junction between the Hellenic and Cyprus arcs. These authors interpreted this region as a Subduction Transform Edge Propagator (STEP-1 in Fig. 1.14; Wortel and Spakman, 1992; Govers and Wortel, 2005; Yıldırım and Sandvol, 2009). This STEP-1 fault zone separated the northern fringe of the subducting African Plate into two slabs; the Hellenic slab beneath the Hellenic Arc and the Cyprus slab beneath the Cyprus Arc (Fig. 1.14). They further suggested that the deep structure of the eastern part of the Cyprus Arc, which exhibits a broad zone of sinistral deformation at the surface, is very similar to the eastern segment of the Hellenic subduction zone. Salaun et al. (2010) used new

tomographic results to show that a vertical slab tear with a narrow ∼160 km horizontal extent exists between the eastern termination of the Hellenic slab and the Cyprus slab.

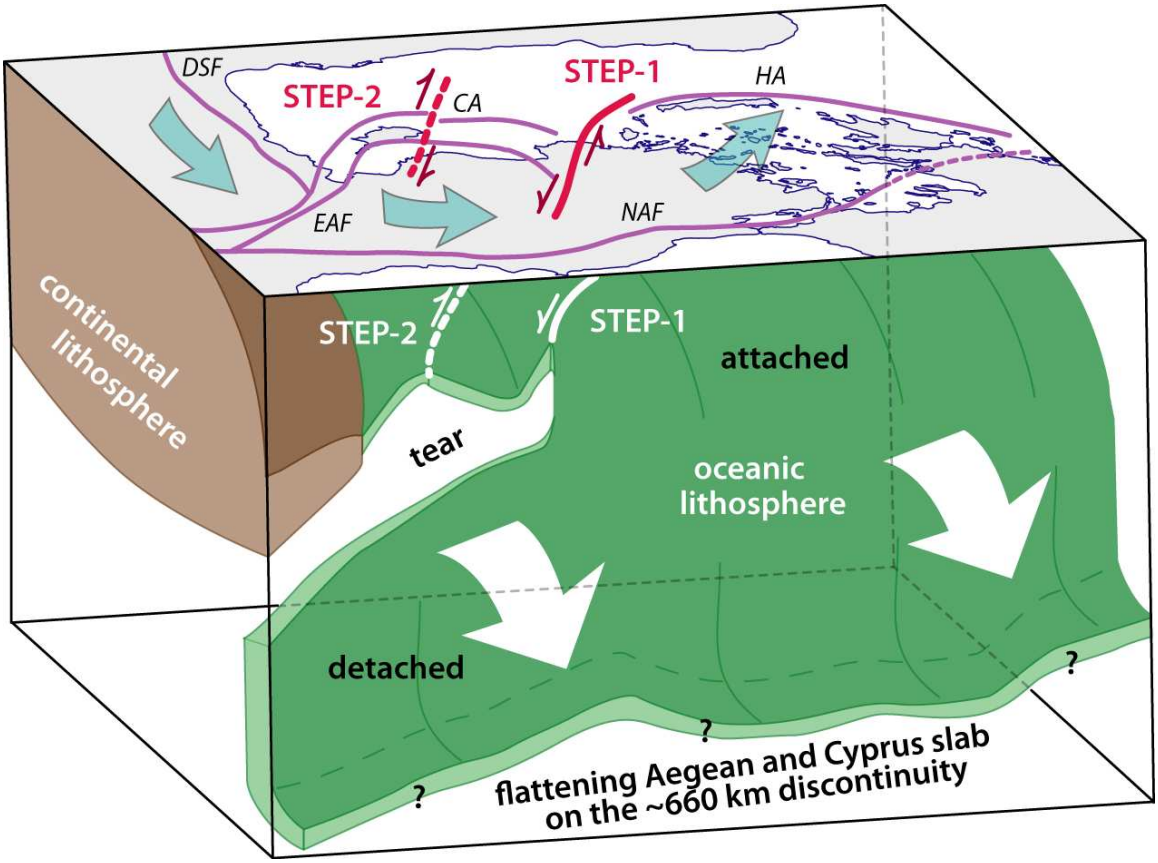

Figure 1.14: Schematic 3D block diagram showing the development of lithospheric tear associated with the subduction of the African lithosphere beneath the Aegean–Anatolian Microplate (inspired from Barka and Reilinger (1995), Govers and Wortel (2005) and Biryol et al., 2011). CA= Cyprus Arc, DSF= Dead Sea Fault zone, EAF= East Anatolian Fault zone, HA= Hellenic Arc, NAF= North Anatolian Fault zone. STEP-1 and STEP-2 represent the litospheric tears that developed across the Pliny-Strabo Trenches and the Paphos Fault zone, respectively (explained in text).

The current geodynamics of the Cyprus Arc are largely controlled by the post-Messinian collision of Eratosthenes Seamount with the Island of Cyprus (Robertson et al., 1998a). Active subduction

beneath the Cyprus Arc appears to have ceased with the arrival of the Eratosthenes Seamount at the subduction zone (Robertson et al., 1998a, Glover and Robertson, 1998a,b). Woodside et al. (2002) suggested that most features of subduction zones, such as volcanism, bathymetric trenches, accretionary prism, and high and focussed seismicity are lacking along the Florence Rise. In addition, the fast retreat of the Hellenic Slab towards the south may have played a major role in the evolution and dynamics of the system (Woodside et al., 2002). Marine geophysical surveys south and west of the Cyprus Arc have documented the predominantly north-south convergence and the geological structures associated with north-south convergence across the arc (Robertson et al., 1998a; Woodside et al., 2002). Woodside et al. (2002) and Sage and Letouzey (1990) showed that the western Florence Rise part of the Cyprus Arc is under compression, where oblique convergence created a major strike-slip fault zone after the Messinian. In contrast, the central portion of the Cyprus Arc immediately north and northeast of the Eratosthenes Seamount is mainly characterised by transpressional features (Ivanov et al., 1992; Kempler, 1994; Limonov et al., 1996). The eastern Tartus Ridge segment of the Cyprus Arc is delineated by structures associated with a sinistral strike-slip system, which further to the east links with the Dead Sea Fault zone (Kempler and Ben-Avraham, 1987; Girdler, 1990; Kempler and Garfunkel, 1994).

Numerous authors have described the evolution of the Anaximander Mountains at the junction of the eastern Hellenic and western Cyprus arcs (Woodside et al., 2002; Zitter et al., 2003; ten Veen et al., 2004; Aksu et al, 2009; Hall et al. 2009). Woodside et al. (2002) argued that the Florence Rise is presently acting as a transpressive right-lateral fault zone, with two oppositely shearing arc segments, and complex strain patterns at the junction between the Hellenic and Cyprus Arcs. Ten Veen et al. (2004) argued that the sense and rate of relative motion between the African Plate and Aegean-Anatolian Microplate changes close to the junction between the Hellenic and Cyprus Arcs. They suggested that the Miocene–Quaternary in the western part of the Anaximander Mountains was characterised by sinistral shear, with NW-SE striking faults cut by several NE-SW striking faults. This

was marked by the onset of extension on normal faults which formed long graben-like depressions, and was related to the opening of the Rhodes and Finike basins during the transtensional tectonics that affected southwest Turkey since the Pliocene. Ten Veen et al. (2004) also suggested that the eastern part of the Anaximander Mountains has affinities with the Florence Rise, and is characterised by a normal and/or oblique normal fault zone with no evidence for strike-slip deformation.

In contrast, Aksu et al. (2009) and Hall et al. (2009) proposed a much more complex geodynamic model for the evolution of the Anaximander Mountains. They found no evidence for normal faulting in the Anaximander Mountains, with the exception of a small area in the southwestern margin of the Antalya Basin. Their data suggested a protracted Miocene contractional tectonic phase that culminated during the Messinian. This was replaced in the early-mid Pliocene by a tectonic regime dominated by transpression and probably rotation. Aksu et al. (2009) speculated that this change in tectonic regimes was due to the westward propagation of the North Anatolian Fault zone and the progressive counterclockwise rotation of the western segment of the Aegean-Anatolian microplate during the Pliocene–Quaternary. These authors also suggested that the formations of the Finike Basin (Aksu et al., 2009; 2014c) and the adjacent Rhodes Basin (Hall et al., 2009; 2014b) were related to the thrusting and lithospheric loading of the western Taurus Mountains during the Pliocene–Quaternary and associated flexure resulting in subsidence in these basins.

1.6.2 Tectonic transition and accretionary processes in eastern Mediterranean

Shortening styles, kinematics and the accretionary process of the eastern Mediterranean basins depend on the areal extent and the composition (thus the rheology) of the evaporite successions. The tectonic evolution in the eastern Mediterranean is generally divided into two periods separated by the deposition of thick evaporitic sequences during the Messinian (Costa et al., 2004). Chaumillon and Mascle (1997) describe two accretionary wedges in the Mediterranean Ridge south of the Hellenic Arc, an older wedge developed prior to deposition of Messinian evaporites, and a younger

wedge developed during the Pliocene–Quaternary. Messinian evaporites created a layer with low basal friction, low cross sectional taper and anomalous width, thus forming a *décollement* surface beneath the younger wedge (Polonia et al., 2002).

In the Levantine Basin of the eastern Mediterranean, the main detachment of the post-Messinian wedge is located at the base of the thick and viscous Messinian salt layer along the Mediterranean Ridge (Costa et al., 2004). Their physical modeling results show that a viscous (salt) *décollement* would produce thrusting trending normal to the shortening direction, but boundary conditions affect structural trends even more than stress and/or movement direction. Both strain partitioning and the formation of major strike-slip faults within the post-Messinian wedge are prevented by the high angle of convergence between the African and Aegean plates as well as by the low intraplate friction. Furthermore they show that curved and anastomosing thrust fronts are reflected in the topography of the Mediterranean Ridge. They also argued that extension may occur in the central Mediterranean Ridge as a result of the geometry of the plate boundaries. This extension is considered as a possible cause of mud volcanism and mud diapirism.

The western Florence Rise segment of the Cyprus Arc has also been described as an accretionary wedge by a number of authors (Sage and Letouzey, 1990; Woodside et al., 2002; Sellier et al., 2013a,b). However, unlike the Mediterranean Ridge to the south, it is still not clear whether or not the accretionary wedge has been active since the Messinian. Woodside et al. (2002) argued that modern day tectonics in the Florence Rise are compressional, with subduction having ceased or stalled due to the collision of the Eratosthenes Seamount with the Island of Cyprus. Therefore, these authors argued that all accretionary processes should have stopped during the post-Messinian and that mud volcanism south of the Florence Rise must be due to overpressure in the pre-Messinian accretionary wedge activated by modern strike slip faulting (Woodside et al., 2002). In addition, recent work by Sellier et al. (2013a,b) also argued that post-Messinian compression south of the Florence Rise is very similar to that observed across the Mediterranean Ridge. These authors also

interpreted the Florence Rise as a post-Messinian accretionary wedge, which is strongly influenced by salt tectonics and the sedimentation associated with the Nile delta fan.

1.6.3 Uncertainties in Messinian evaporite precipitation and distribution

The Messinian Salinity Crisis is a prominent series of events that has profoundly modified the Mediterranean within a relatively limited time span, and led to the deposition of thick evaporite successions in basins that are presently located both onland and offshore (e.g., Lofi et al., 2011b, and references therein). The depositional environment of evaporite successions have been described in three models: (1) shallow basin and shallow water model: where in a shallow evaporative basin limited connection to the open ocean allows the salt water inflow, (2) deep basin and shallow water model: where the deep basin is isolated from the global oceans and evaporates, (3) deep basin and deep water model: where excessive evaporation at the ocean surface allows brines to develop and downwell to deep levels (Fig. 1.15).

Previous regional studies based on outcrop, well and 2D seismic data have demonstrated that during the Messinian Salinity Crisis the Mediterranean region was characterised by a complex and highly diversified stratigraphy of evaporite deposition as a result of morphological, geodynamical and isostatic responses of the deep offshore basins and marginal shallower basins (Montadert et al., 1978; Garfunkel and Almagor, 1984; Gorini et al., 1993; Gradmann et al., 2005; Rouchy et al., 2006; Roveri et al., 2008a,b,c, 2014a,b,cs). It is broadly accepted that the period of widespread evaporite precipitation in the Mediterranean region spanned from 5.97 to 5.33 Ma, but it is not known how the events recorded in strata correlate between the shallow marginal basins and the deep Mediterranean basins. Evaporites in shallow marginal basins are exposed onshore and have been extensively studied (Krijgsman et al., 2001, 2002, 2004; Lofi et al., 2011a,b; Manzi et al., 2013, 2014). However, these form incomplete Messinian successions that are geometrically disconnected from the offshore basins (e.g., Schreiber et al., 1976; Rouchy, 1982; Butler et al., 1995; Clauzon et al., 1996; Riding et al.,

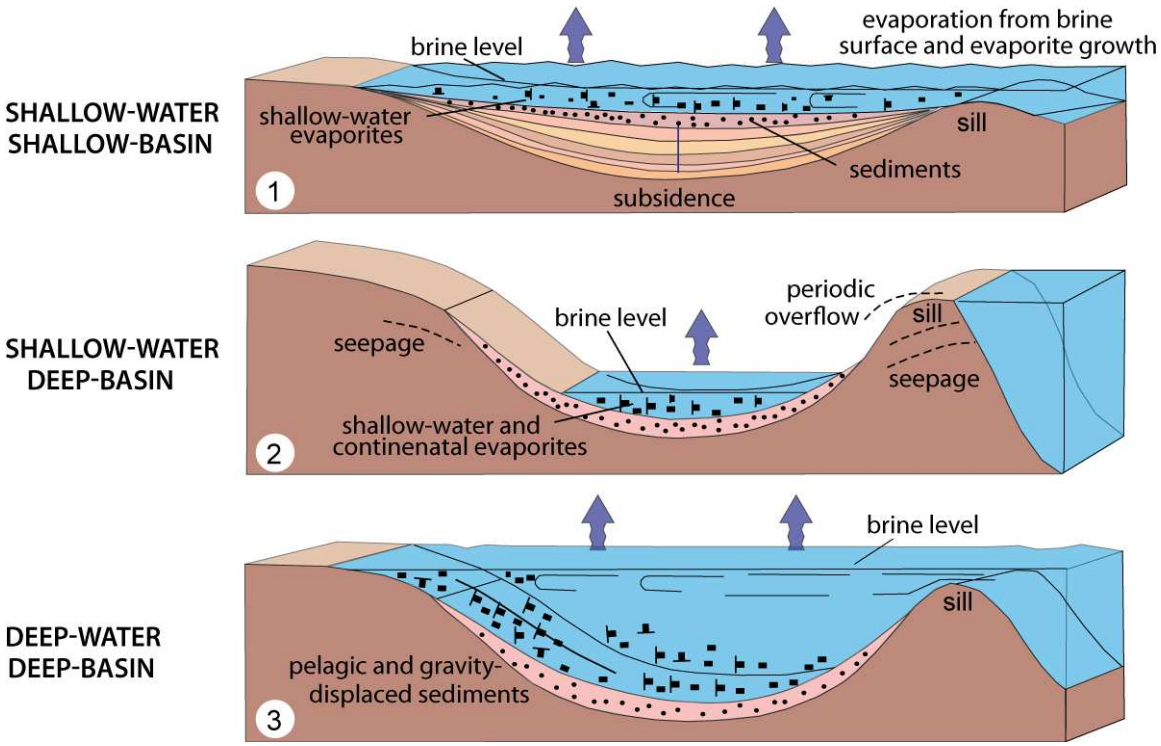

Figure 1.15: Models for the depositional environment of evaporite successions. Redrawn after http://www.britannica.com/EBchecked/topic/197000/evaporite.

1998; Krijgsman et al., 1999). The knowledge of the correlative deep and thick offshore evaporites in the eastern Mediterranean has so far been hampered due to lack of complete calibration of the stratigraphy of the Messinian Salinity Crisis record from scientific boreholes and the absence of high resolution seismic data to image and explore the entire Messinian Salinity Crisis event as a continuous process in the deep offshore basins.

Within in the eastern Mediterranean, most previous research on the successions associated with the Messinian Salinity Crisis in deep basins has focussed on the Nile Deep Sea Fan and the Levantine Basin, which have been investigated in relation to the development of giant salt diapirs (Mart and Ben Gai, 1982; Garfunkel and Almagor, 1987; Cohen, 1993; Loncke et al., 2004, 2006; Gradmann et al., 2005; Bertoni and Cartwright, 2006; Netzeband et al., 2006; Bertoni and Cartwright, 2007; Hübscher and Netzeband, 2007). Hübscher and Dümmong (2011) focused on the successions of evaporites and overlying formations which show a complex deformation pattern due to a combination of thick-skinned plate-tectonic convergence and thin-skinned disharmonic deformation related to the mobile evaporite-bearing unit in the eastern Cyprus Arc. The western part of the Cyprus Arc has been the subject of number of previous studies focused on post- and pre-evaporitic structural deformation (Woodside et al, 2002; Sellier et al., 2013a). A recent synthesis based on the stratigraphic framework of the Messinian Salinity Crisis across the entire Mediterranean region has been proposed by Lofi et al. (2011a, b). However their synthesis of the distribution of the sedimentary successions deposited during the Messinian Salinity Crisis across the western Cyprus Arc, covering the Florence Rise and the Antalya Basin has not been clearly presented due to lack of available data. According to Lofi et al. (2011b) the typical successions of Lower Evaporites, Salt, and Upper Evaporites that occur across the western Mediterranean are not present in the eastern Mediterranean. They suggest that the Messinian Salinity Crisis is largely recorded by a single salt-bearing seismic unit. More recently, an attempt at correlating western and eastern Mediterranean Messinian seismic units has been suggested by Manzi et al. (2014). However, their results show that the recently established

western Mediterranean stratigraphy applies to only the marginal basins of eastern Mediterranean.

1.6.4 Halokinetic/structural uncertainties in uppermost Messinian-Quaternary

In the eastern Mediterranean, the thick Messinian-lowermost Pliocene evaporite layer has a significant impact on the evolution of the host basin. The interplay between halokinesis, salt tectonics and sedimentation occurs at many different scales due to many different triggering factors. During the last 2–3 decades interests in the evaluation of evaporite basins and in salt tectonics have led to improved understanding of the halokinetic processes controlling stratigraphic architecture in areas such as the Gulf of Mexico, the North Sea and the west African continental margin. The most significant factor in this improved understanding is the recognition that halokinesis is often a response to regional tectonics and salt tectonics, commonly triggered by tectonic deformation of the overburden (Vendeville and Jackson, 1992a,b; Jackson, 1995).

Previous studies have shown that both thick-skinned plate tectonics and thin-skinned salt tectonics have a significant control on the structural dynamics and morphologic architecture of the Mediterranean basins (dos Reis et al., 2005; Gaullier et al., 2008; Reiche et al., 2015). However, relatively few previous studies have focussed on identifying the salt-related structures and determining their geometry and distribution, the associated structural features in the overburden and their surface expressions, in order to better understand the interaction between sedimentation, salt tectonics and structural pattern (e.g., Costa et al., 2004; Bertoni and Cartwright 2005). In contrast, the stratigraphic and structural evolution of the eastern Mediterranean has been increasingly studied during the last decade (Aksu et al., 2014; Hall et al., 2014; Walsh-Kennedy et al., 2014; Blanco 2015). Our knowledge of the Neogene structural evolution of the Cyprus Arc has been considerably improved recently (Aksu et al., 2005a; Calon et al., 2005a,b; Hall et al., 2005a,b), with the identification of two major phases of deformation. The earlier phase (pre-Miocene to Late Miocene) is compressional and affects pre-Miocene and Messinian units, whereas the younger phase (upper-

most Pliocene–Quaternary), which affects all stratigraphic units, is predominantly contractional, but accompanied by strike-slip with minor superficial extension.

Even at geologically rapid strain rates, salt is mechanically weak and flows like a fluid (Hudec and Jackson, 2007, CIESM, 2008). This rheology and the incompressibility of salt make it inherently unstable under a wide range of geologic conditions. Salt is extremely mobile and may displace and deform in response to differential loading which may be induced by gravitational forces, by forced displacement of the boundaries of a system or by a thermal gradient (CIESM, 2008). Gravitational loading can generate flow if the load represented by the overburden is unevenly distributed. The interaction between fluids and salt also causes suberosion and subsequent surface collapses with potential impact on deformation of overburden. This is called salt/evaporite dissolution and is considered an important process in many evaporite-bearing basins worldwide (e.g., Warren 1999). Examples of evaporite dissolution have been described in the North Sea (Lohmann 1972; Jenyon 1983; Cartwright et al., 2001), western Canada (Anderson and Knapp 1993), Gulf of Mexico (Rezak et al., 1985; Hossack 1995), US Permian Basin (Anderson and Kirkland, 1980) and west Africa (Hudec and Jackson, 2002). However, in the eastern Mediterranean previous analyses of salt related deformation in the Pliocene–Quaternary sediment were mostly explained by salt–sediment interaction stemming from vertical movements associated with overburden. Maillard et al. (2011) undertook a study aiming specifically at the salt tectonic framework, focusing on the deformed Messinian markers in the western Cyprus Arc. They hypothesized that a thin-skinned phase of compressional deformation during the late Miocene affected the entire MSC unit, overlain by undeformed Pliocene–Quaternary layers. A second thin-skinned phase, well expressed in the bathymetry, occurred from the Pliocene to Recent, resulting in extensional gravity gliding within the evaporites and the Pliocene–Quaternary sequence (Maillard et al., 2011). Costa et al. (2004) presented the experiments simulating the physical and structural parameters to investigate the structural expression of the convergence in the Eastern Mediterranean at a regional scale. Sellier et al. (2013b) also presented similar experiments to

discuss probable kinematics of the basement structural highs (e.g., Florence Rise and Eratosthenes Seamount) whether presently active or inactive, and how they influence the deformation and displacement patterns of the salt and its overburden. According to these studies, deformation of the Messinian evaporites and their Pliocene–Quaternary overburden is controlled by both deep-seated, thick-skinned tectonics, and gravitational, salt-related thin-skinned tectonics. A recent study by Bertoni and Cartwright (2007) described the morphology of the structures and the associated overburden, allowing the reconstruction of their origin and development in the Levantine Basin. They proposed that evaporite dissolution led to the collapse of the weakly lithified overburden, and this deformed with a series of concentric extensional faults. However, these studies and models are not always able to entirely explain the structural features in the overburden and their surface expressions, to be able to understand the interaction between sedimentation, salt tectonics, structural pattern and neotectonics in the Florence Rise and Antalya Basin.

1.7 Questions arising from the above literature summary

The literature review above leads to a series of questions which form the basis of the objectives of this thesis described earlier.

- Did the active subduction beneath the Cyprus Arc cease with the arrival of the Eratosthenes Seamount?
- Why are features typical of subduction zones, such as volcanism, bathymetric trench, and intense and focussed seismicity lacking along the Florence Rise?
- Are the Florence Rise and the Mediterranean Ridge to the south part of a broad accretionary prism? Is mud volcanism directly related to the accretionary process along the Cyprus Arc?
- What is the strain pattern through time along and across the Florence Rise and Anaxagoras Mountain?

- Do the eastern and western Mediterranean seas have the same depositional history during the Messinian Salinity Crisis? Why is the lower mobile unit (halite) much thicker in the eastern Mediterranean Sea than its counterpart in the western Mediterranean Sea?
- Is it possible to determine a Mediterranean-wide depositional history that can account for the observed lithologies and chronologies of the successions associated with the Messinian Salinity Crisis in the west and east?

Chapter 2

Data And Methods

This Chapter presents the information on the methods used in the acquisition, processing and interpretation of ∼10.000 km of high-resolution seismic reflection data (∼3000 km of which processed by the author) collected from the western Cyprus Arc, eastern Mediterranean (Fig. 2.1). Isochron maps and seismic cross-sections are correlated with borehole information from the DSDP Leg XLII Sites 375 and 376, the onland Aksu-1, Manavgat-1, Manavgat-2 wells in Antalya region and the Xeri borehole in Cyprus, as well as onshore successions in the eastern Mediterranean region. Other data used during this project include various multibeam bathymetric data previously collected by IFREMER (French Research Institute for Exploration of the Sea) and several deep-penetrating seismic reflection profiles kindly provided by the Turkish Petroleum Corporation (TPAO). The following is a detailed account of the methods used in this study, including a full discussion on 2D marine seismic data acquisition with the survey geometry and the specific survey parameters, data processing steps, both the general theory of data processing and its applications used in this study. The method of geological interpretation of the 2D marine seismic data and their applications are also presented in this chapter.

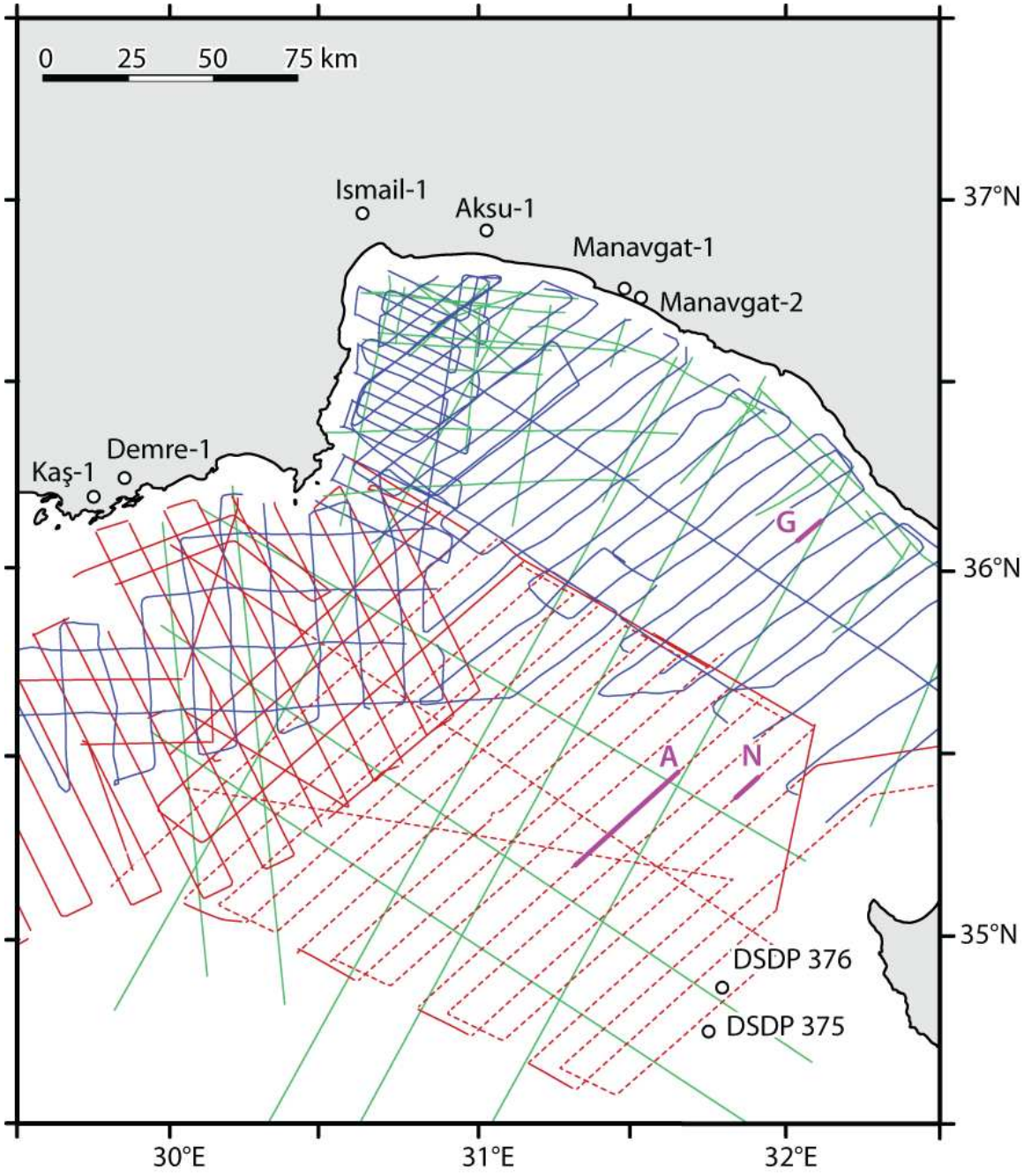

Figure 2.1: kMap showing the locations of the multi-channel seismic reflection profiles used in this study. Blue lines= 1992, 2001, 2008 vintages, red lines= 2007, 2010 vintages, green lines= Turkish Petroleum Corporation profiles. Thicker purple lines are illustrated in text figures. Red dashed lines are processed by the author. The coastline is from the International Bathymetric Charts of the Mediterranean (IOC, 1981).

2.1 Seismic Reflection Method

The seismic reflection method is an important geophysical technique that uses echo-sounding to estimate the properties of large volumes of rock beneath the Earth's surface from reflected seismic waves (Yılmaz, 2001). The general principle of seismic reflection is to create images of subsurface structure from surface recordings resulting from the emission of a pulse of energy into the Earth (using an energy source, e.g., air gun, water gun, sparker, vibrator, etc.), where each layer within the Earth reflects a portion of the wave's energy back and allows the rest to refract through (Fig. 2.2). Waves are reflected from subsurface interfaces that represent a change in acoustic impedance due to variation in rock properties (Fig. 2.3a). This reflected energy is detected by receivers, such as hydrophone arrays and geophone arrays for the marine and land surveys, respectively. In the marine environment, hydrophones convert pressure changes into electrical signals. The time it takes a seismic wave to travel from the source to the receiver is measured and it represents the amount of time it took the sound to reach the reflecting surface plus the time to be reflected back up. This is the reflection time, also called two-way travel time (twt). Each receiver's response in time to a single shot is known as a "trace" and is recorded onto a data storage device, then the shot location is moved along and the process is repeated. The trace can refer to the information from one shot that was received by one group hydrophones, as on a monitor record, or it can be the information from a set of traces combined into one. The traces may be displayed in the form of wiggle traces, as on a monitor record. Traces from a number of shots are combined by common depth point (CDP) stacking to enhance the signal. A large number of these stacked traces are placed side by side to make a seismic section. There are usually hundreds of overlapping traces on a section.

Acoustic impedance, represented by the symbol Z, is the product of the velocity (υ) and density (ρ) of a rock layer (Kearey et al., 2002). Contrast in the acoustic impedance across a boundary gives rise to a strong reflection dependent on fluid content, texture, porosity and composition (Equation 2.1; see below).

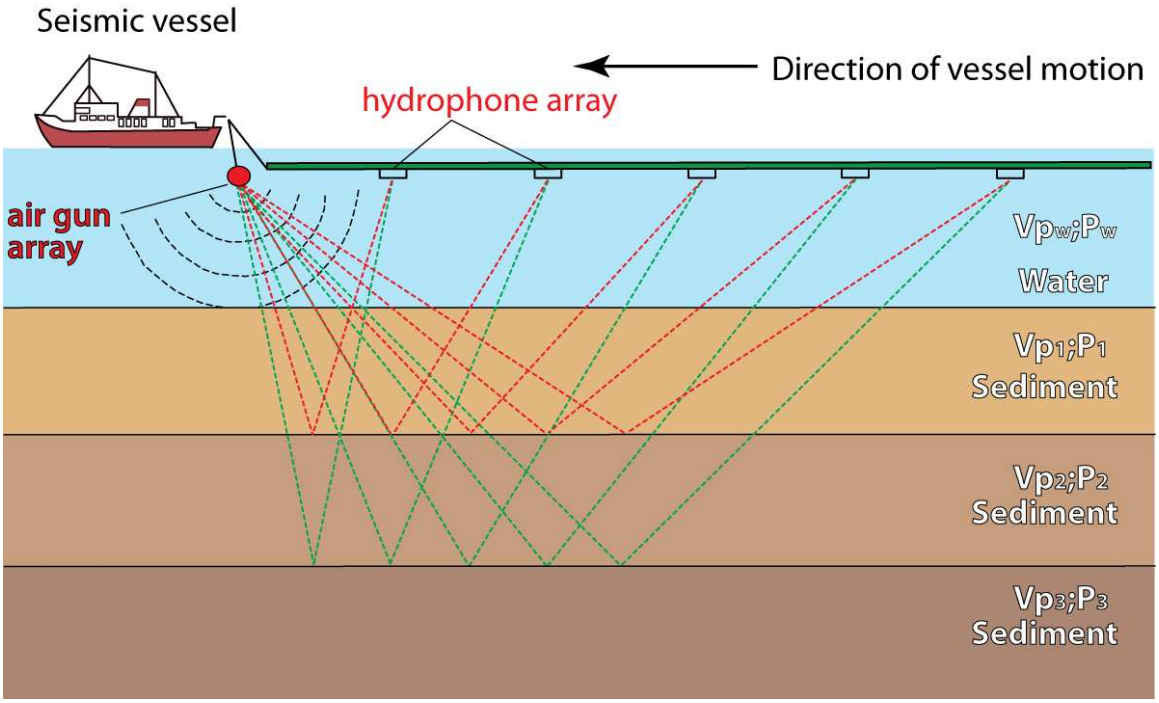

Figure 2.2: Simplified cartoon showing the ray path of the P-waves emanating from the airgun array reflecting from various interfaces to arrive at the hydrophone array.

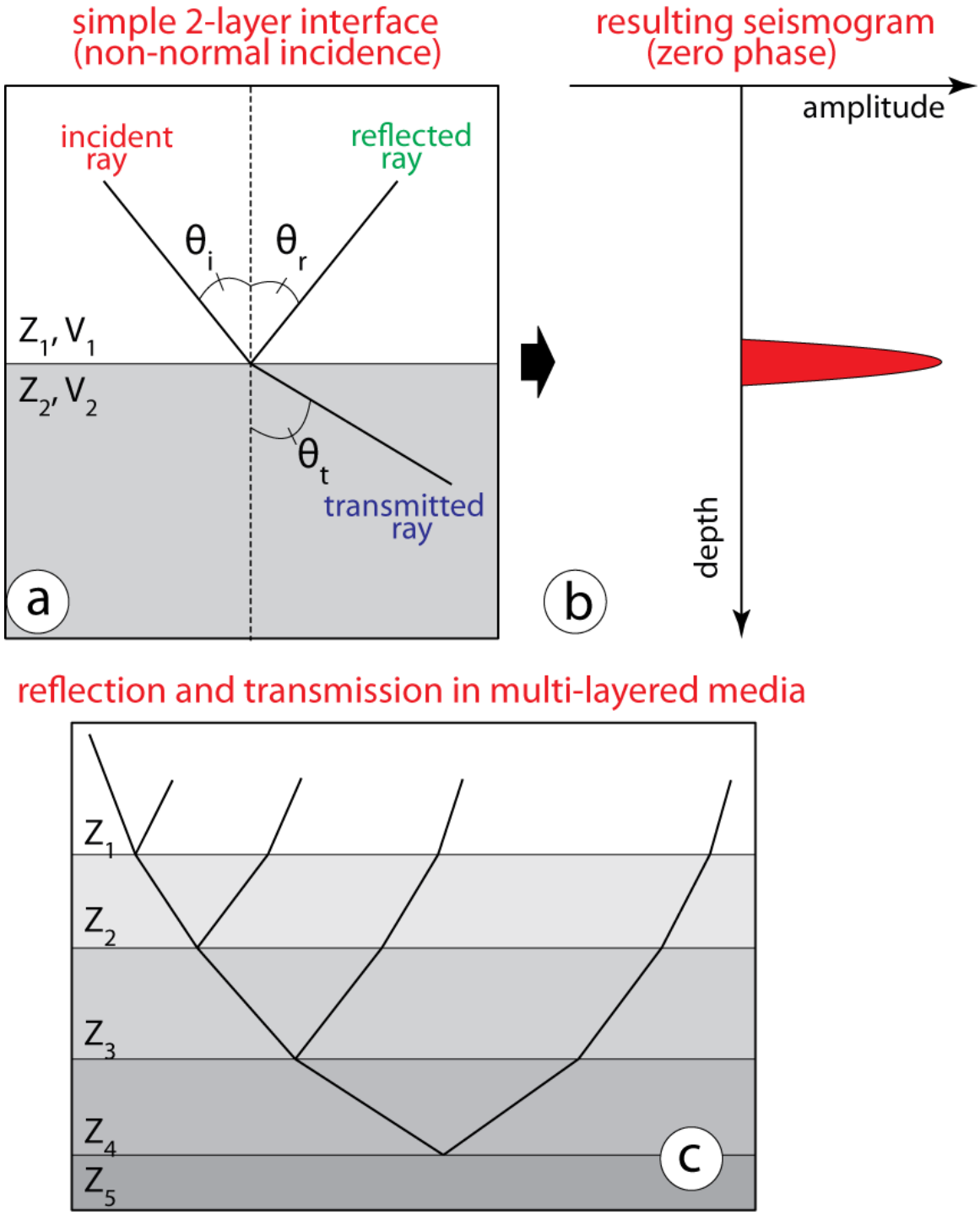

Figure 2.3: Simplified diagram showing the Snell ray path in 2-layer interface and multilayer interfaces. $Z_1, V_1, Z_2, V_2, a, \theta_i, \theta_r$ and $Z_1 - Z_5$ are explained in text.

Equation 2.1 $Z = \upsilon\rho$

The jumps in acoustic impedance across an interface are recorded as reflection wavelets on a vertical trace (Fig. 2.3b; Kearey et al., 2002). The amplitude and polarity of the reflected energy is proportional to the acoustic impedance contrast (Z) across the boundary (Yılmaz, 2001). The reflectivity coefficient (RC) determines the amount of seismic energy which will be reflected from an interface and can be expressed as a function of acoustic impedances. The reflection coefficient depends upon angle of incidence. For normal incidence, it is described by Equation 2.2 where $\rho_1\upsilon_1$ and $\rho_2\upsilon_2$ are the acoustic impedance of layers 1 and 2, respectively.

Equation 2.2 $RC_{12} = (\rho_2\upsilon_2 - \rho_1\upsilon_1)/(\rho_2\upsilon_2 + \rho_1\upsilon_1)$

Acoustic impedance contrasts which generate strong reflections usually arise from geologically significant interfaces such as bedding surfaces separating contrasted lithologies, fault planes, pore fluid contacts, mineral phase changes. However, seismic records may also show events which are artifacts such as multiples, diffractions, or returns from out-of-plane geology. Special care must be taken to ensure these artifacts are not interpreted as geology.

The "Law of Reflection" states that the incident ray is reflected at the same angle as it was incident on the interface ($\theta_i = \theta_r$) where θ_i is the angle of the incident ray and θ_r is the angle of the reflected ray (Fig. 2.3a). The remaining wave energy is transmitted, or refracted, into the second layer according to the Snell's Law:

Equation 2.3 $sin\ \theta_i/V_1 = sin\ \theta_t/V_2$

where θ_t is the angle of the transmitted ray, V_1 is the velocity of the first layer and V_2 is the velocity of the second layer. As layering increases (e.g., Fig. 2.3b), reflection and refraction continue at each interface allowing imaging of all layers.

When a P-wave encounters a boundary where there is a significant change in acoustic impedance, some energy is reflected back to the surface, while some is transmitted into the next layer (Fig. 2.3a).

2.2 2D Marine Seismic Data Acquisition and Survey Geometry

In a conventional 2D marine seismic reflection survey, the vessel tows the source and the receiver arrays behind it at a near constant speed (Fig. 2.4). Maintaining relatively constant speed is important for maintaining various survey parameters. The typical source used on marine seismic vessels is the airgun. The airgun works by controlling the movement of high-pressure air through its chamber to send a large burst of pressured air into the water. Source signatures for single airguns are oscillatory and can generate significant late bubble pulses. To minimize this effect, airguns of varying sizes are often mounted in arrays with each gun contributing to the overall source signature. The pressure in the airgun(s) is maintained by on-board compressors and shots are fired at fixed intervals. The distance between successive shots is called the shot interval. Seismic vessels require reliable navigation tools, such as global positioning system (GPS) and differential GPS (DGPS) to accurately map the location of each shot fired. The receivers consist of hydrophone groups which are uniformly spaced at the group interval and embedded in a long streamer, towed behind the ship just below the sea. Because S-waves do not travel through fluids, such as water, conventional hydrophones will only receive P-waves. Digitizers, located in the streamer near the hydrophones, convert the analog signal to digital form at a set sampling interval, referred to as the sample rate, and relay the digital signal back to ship via fiber optic cables. Depth controllers are often used to maintain the streamer at a constant depth below the sea surface to minimize noise from near-surface turbulence (propeller noise, waves etc) and to provide a strong signal from subsurface reflectors. The convention is to tow the streamer at one quarter of the wavelength of the dominant source frequency, so that the upcoming reflection constructively interferes with the reflection from the air-sea interface, thus a streamer at the surface would record zero signal from the subsurface. Seismographs are located onboard and record the incoming digital signals on a separate channel for each hydrophone group. The data are monitored for quality and possible problems with the streamer and/or guns.

The data used in this study were collected during five separate surveys that were carried out using

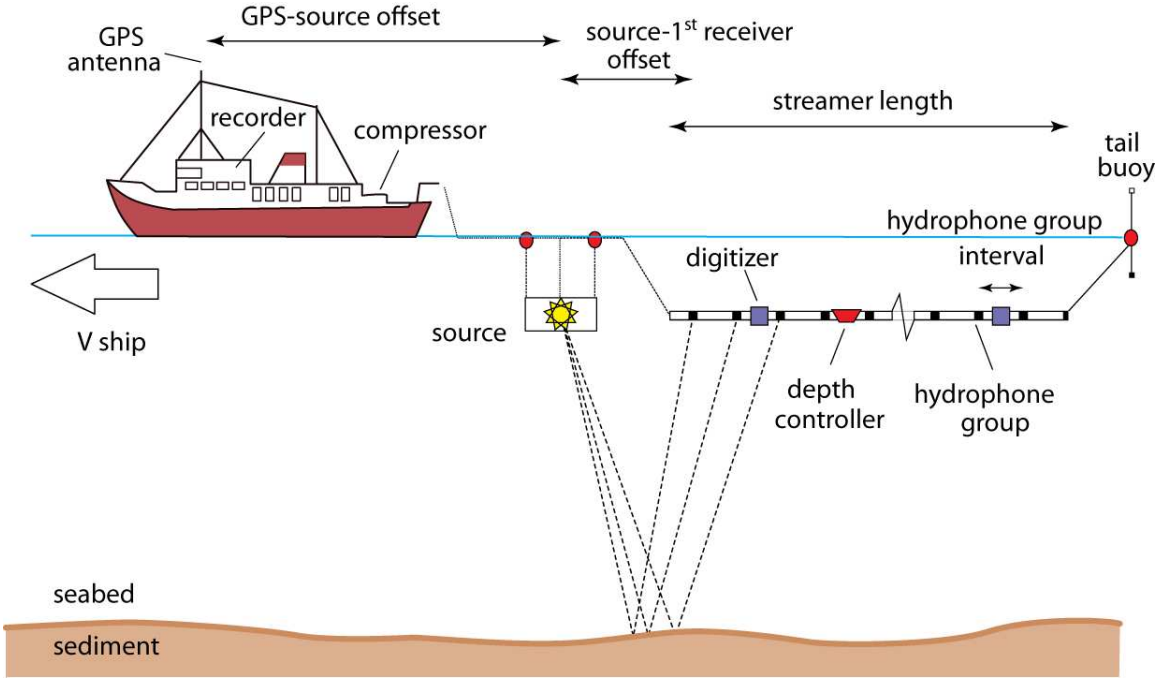

Figure 2.4: Simplified cartoon showing the various survey parameters discussed in text.

various combinations of the multichannel seismic data acquisition gear that resides at the Memorial University of Newfoundland (MUN) and the Seismic Laboratory (SeisLab) facility of the Institute of Marine Sciences and Technology at the Dokuz Eylül University (IMST). The equipment was used aboard the RV *Koca Piri Reis* of the IMST. For example, during the 1992 and 2001 surveys only the MUN seismic acquisition system was used; whereas, during the 2007, 2008 and 2010 surveys the source of the MUN system and the streamer and seismograph of the Seismic Laboratory (SeisLab) facility were used. During the 1992 and 2001 surveys $\sim$7300 km of multichannel data were collected across the northeastern sector of the eastern Mediterranean Sea. During the 2007, 2008 and 2010 surveys $\sim$9400 km of multichannel reflection seismic data were collected along the western Cyprus Arc between the Antalya, Rhodes, Finike and Herodotus basins in the eastern Mediterranean. The locations of all the reflection profiles were carefully chosen with lines running broadly perpendicular to the general trend of the prominent structures with several cross lines and tie lines to facilitate

correlation between seismic profiles (Fig. 2.1). Satellite navigation and GPS were used during the 1992 and 2001 surveys, respectively, whereas navigation was accomplished using an onboard GPS system during the 2007, 2008 and 2010 surveys.

The flow chart describing the detail cruise set-up for the multi-channel seismic surveys is shown in Figure 2.5. The source for the MUN multichannel data consisted of a Halliburton sleeve gun array, employing gun sizes of 40, 20 and 10 cubic inch (656, 328 and 164 cm^3), with the total volume varying during maintenance cycling of the guns, but typically 200 cubic inch (3277 cm^3). Shots were fired every 25 m, and reflections were detected by the last 12 channels of the 48 channel streamer (group intervals = 12.5 m) in 1992, the full 48 channels (group intervals = 12.5 m) in 2001, the 72-channel (group interval = 6.25 m) in 2007, the 96-channel (group intervals = 6.25 m) in 2008 and the 216 channels (group interval = 6.25 m) in 2010. The resultant data consisting of 3-fold in 1992, 12-fold in 2001 and 2008, 9-fold in 2007 and 27-fold in 2010 were recorded digitally for 3–7 s (with delay dependent on water depth on early surveys) at 1 ms sample rate, using an DFS-V in 1992, OYO DAS-1 in 2001 and Hydrosciences NTRS2 seismographs in 2007, 2008 and 2010. The geometry of the surveys is provided in Figure 2.4 and details of the acquisition geometry are given in Table 2.1.

After the data collection, the raw data needed to be processed to provide final images of sub-surface structure and to increase the quality and resolution by spatially distributing reflection points correctly and eliminating unwanted events (e.g., Yılmaz, 2001).

2.3 CDPs, CMPs, and Seismic Data Fold

Before describing the 2D seismic data processing steps it is useful to understand the method of stacking of common mid-points (CMP). The process of sorting the data using the CMP method provides multiple coverage of each point sampled in the subsurface (i.e., every point is sampled >1). Thus, sorting the data using the CMP method creates redundancy of the sampled points, and

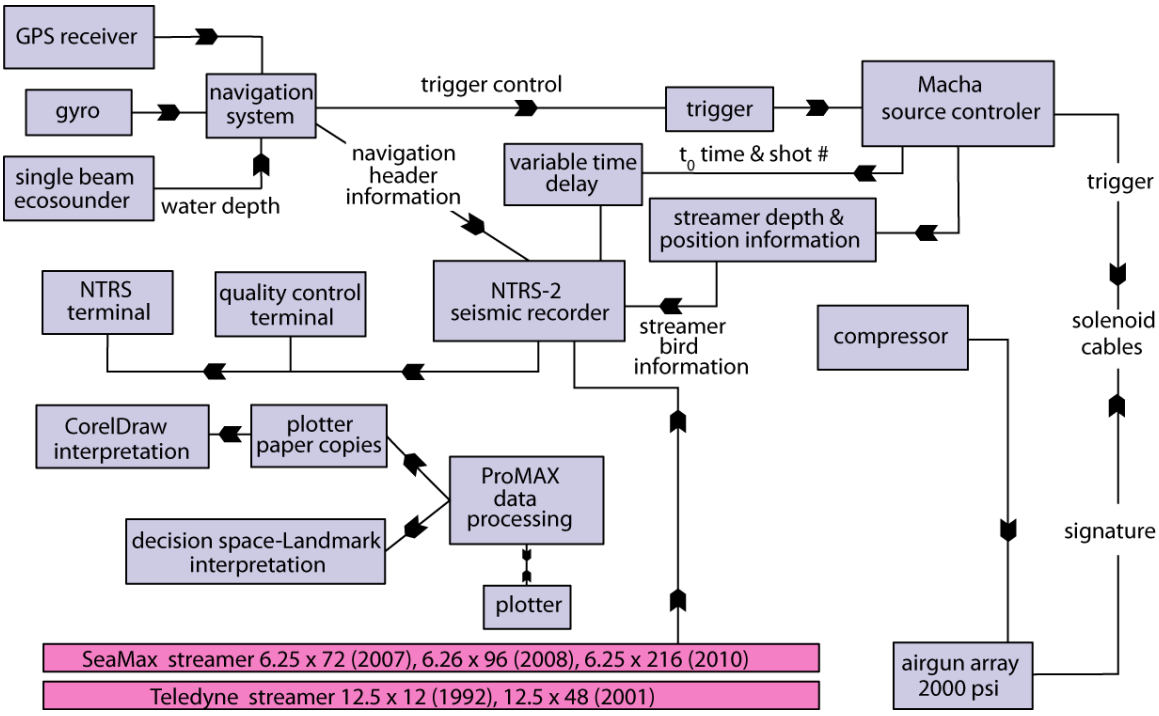

Figure 2.5: Flow chart showing the relationships between the navigation, source, receiver and recorder used during the acquisition of the multichannel seismic reflection data used in this study (adopted from http://web.deu.edu.tr/seislab/eng_index.html)

Table 2.1: Sismic survey and data acquisition geometry.

	emed-1992	emed-2001	emed-2007	emed-2008	emed-2010
stern to source (X1)	40 m	37 m	50 m	50 m	50 m
source to center of first hydrophone group (X2)	95 m	95 m	80 m	80 m	70 m
hydrophone group interval (X3)	12.5 m	12.5 m	6.25 m	6.25 m	6.25 m
channel number	12	48	72	96	216
active streamer length	150 m	600 m	450 m	600 m	1350 m
source and streamer depth (Y1)	3 m	3 m	3 m	3 m	3 m
shot interval	25 m	25 m	25 m	25 m	25 m
fold	3	12	9	12	27

integrating the repeated traces increases the signal to noise ratio and ultimately enhances the quality of the seismic image (Fig. 2.6a). This process is called CMP sorting where each trace is assigned a midpoint for a source receiver pair and all traces that correspond to a given midpoint create a CMP gather (Figs. 2.6a). The number of traces in a CMP gather represents the redundancy of each sampled point by any of the hydrophone groups and defines the fold of the dataset.

Equation 2.4 $$fold = \frac{1}{2}(number\ of\ channels)(group\ interval/shot\ interval)$$

A higher fold results in higher sampling of subsurface points and improves the quality of the final image. The point on the subsurface that has been sampled several times by different source-receiver pairs is called a CMP. Spacing of the CMPs, assuming horizontal reflectors, is calculated by:

Equation 2.5 $$CMP\ Spacing = \frac{1}{2}(group\ interval)$$

Note that when the subsurface reflectors are not horizontal, CMPs are not equivalent to CDPs (Fig. 2.6b). The assumption of CMP and CDP equivalency in the CMP sorting process creates arti-

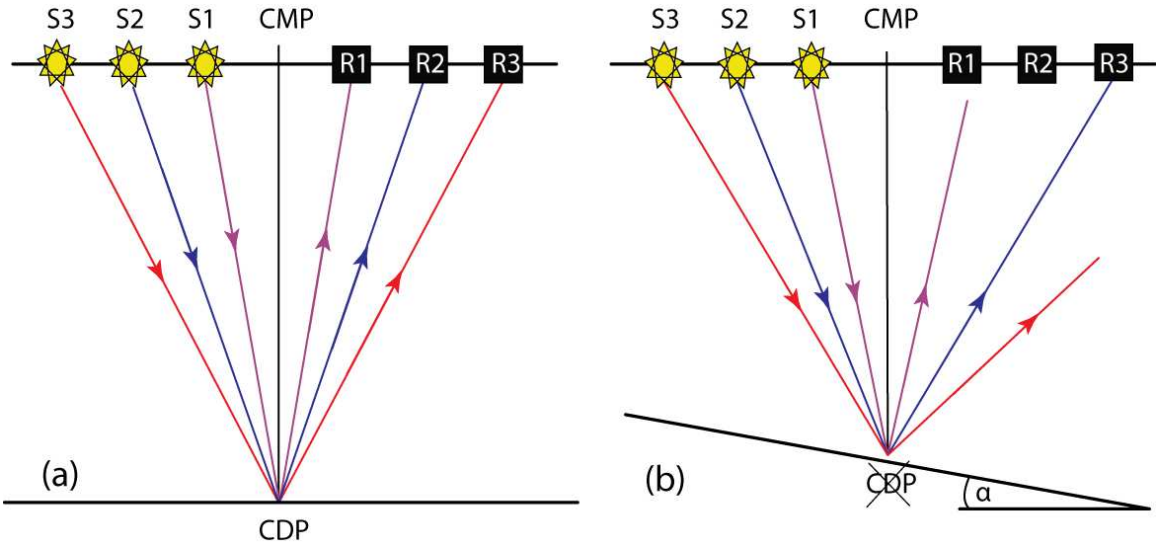

Figure 2.6: Illustration of CMP and CDP non-equivalency (adopted from King, 2014).

facts on the seismic record and requires an extra processing step to restore true subsurface locations of dipping reflectors (i.e., migration, discussed later in this Chapter).

2.4 Seismic Data Processing

The aim of seismic data processing is to enhance the signal to produce interpretable seismic sections that are closest to the true image of the subsurface structures or singularities. A conventional marine seismic reflection data processing flow generally includes: analysis of shot records, frequency filtering, gain control, application of geometry and CMP sorting, CMP gather (CMP is used interchangeably as CDP), velocity analysis, normal move out (NMO) correction, deconvolution, stack and migration (Fig. 2.7).

The success of each process in the data processing flow depends on the reliability of the previous stages as well as the parameters defined within each step. A seismic record contains random and coherent noise as well as primary reflection. The random noise can originate from various sources including electrical noise from the recording instruments, strumming noise caused by the vibration

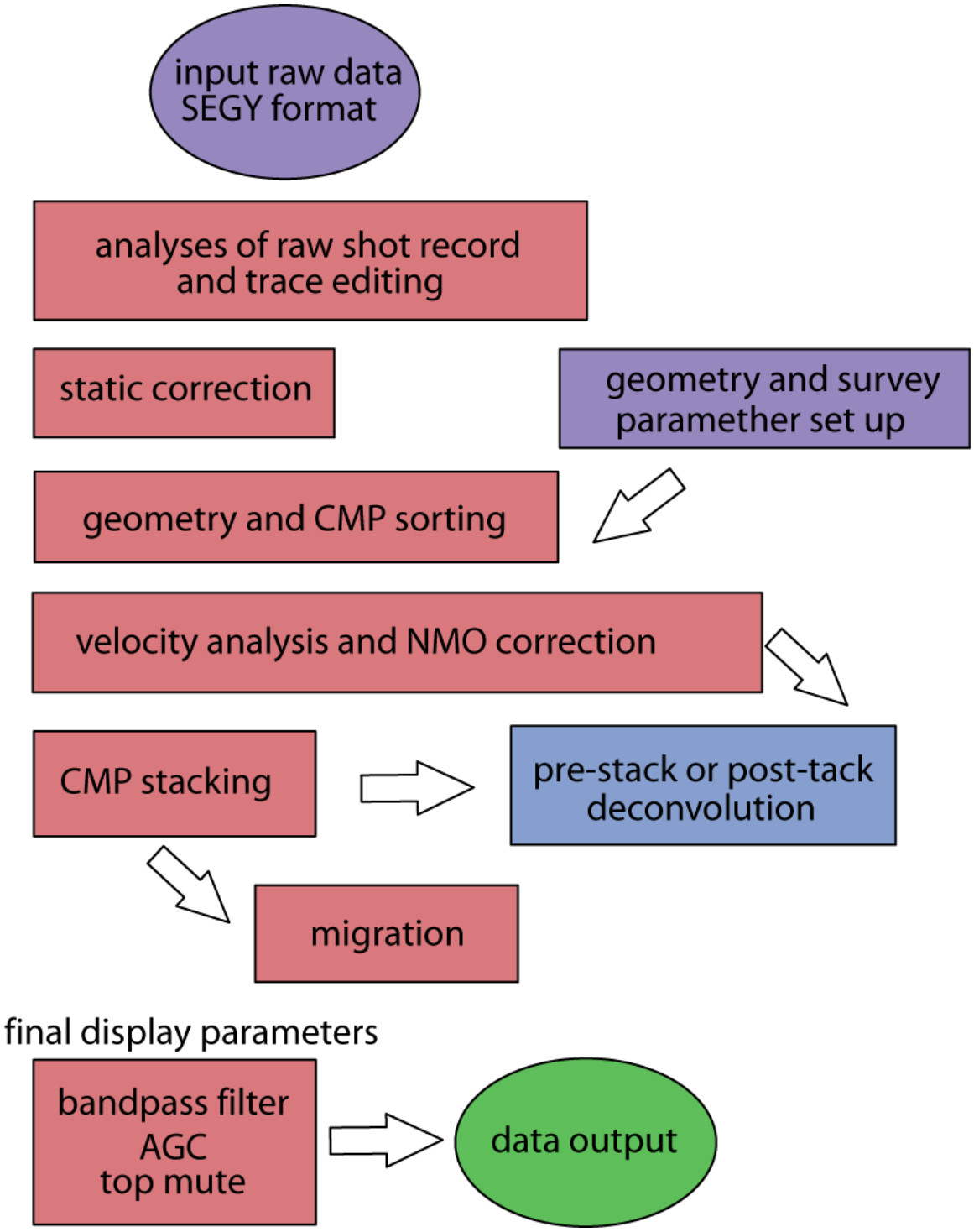

Figure 2.7: Flow chart showing the sequences of the seismic processing steps used in this study.

of the streamer in water due to towing speed, general vessel noise originating from propellers, generators, compressors and the wave noise caused by rough sea conditions. The coherent noise, on the other hand, occurs most commonly in the form of multiple reflections originating from secondary reflections from the interfaces, monofrequency waves generated by alternating current electrical power lines, and low frequency waves originating from the streamer cable.

One of the most important aspects of data processing is to suppress the noise in order to increase the signal-to-noise ratio. The most common noise suppression methods are filtering, deconvolution and stacking. After the noise component is minimized and stacking is performed, migration is applied to the data to move the dipping reflectors to their true subsurface locations and to collapse diffraction hyperbolae. Care must be taken, as combinations of different choices of processing parameters can produce quite different results. In addition, there are some other common processing operations that should be applied before the main procedures. Preprocessing, noise attenuation and filtering and static corrections are some of these. Before explaining the main processing steps, the preprocessing operations are briefly summarized. Pre-processing is required to convert the format of the seismic data. Usually, the data is acquired in SEG-D (Society of Exploration Geophysicists D format) and in order to process it, the data need to be converted to SEG-Y (Society of Exploration Geophysicists Y format), which is a standard format for seismic data processing (Sheriff and Geldart 1995; Dentith and Mudge 2014). The geometry of the seismic line should be set up. Accurate coordinates of source and receivers must be defined since these play an important role in static corrections and stacking of the data correctly.

Seismic reflection data processing has been carried out using ProMAX© software by Landmark. Approximately 3000 km seismic data has been processed for this Ph.D. thesis collected across the western Cyprus Arc area of the eastern Mediterranean (Fig. 2.1). The other lines used for interpretation were acquired during the 2001 survey and previously processed at Memorial University of Newfoundland. In this study all seismic data processing except the data provided by TPAO was

completed at Memorial University of Newfoundland using the StarPak© software (1992 and 2001 vintages) and the Landmark ProMAX© software (2007, 2008, 2010 vintages). The ProMAX© 2D multichannel seismic data processing flow was used to process all lines from the shot domain to final migration and is provided in Figure 2.7. The processing steps are described in greater detail below with specific references to the 2007 and 2010 seismic reflection profiles which were processed by the author.

2.4.1 Analysis of Shot Records/Display

The analysis of the shot records involves the examination of the raw data using all channels, paying attention to the frequency content, amplitude variations in the data. A shot record contains the data recorded on all available channels following a single shot (Fig. 2.8). A typical shot record will contain both signal (i.e. hyperbolic primary reflections) and noise (e.g. linear direct wave, noisy traces, refractions, lowfrequency noise from equipment, multiples, etc.). The display application in ProMAX© is a very useful tool for analysing the shot records. It is used to display the data on the screen for visual inspection during processing. By analysing the trace display for each line it is possible (i) to determine optimal filter parameters, (ii) to perform trace editing and correct time delays if necessary, and (iii) to apply an appropriate gain control. The display flow is also used to create paper-plots that are printed at various steps during processing for data quality control and to produce the final bitmap images.

Initially, the raw data is loaded into ProMAX© work space using the SEG-Y input application. Next, the shots are displayed using all channels (Fig. 2.9) and as a single channel/near trace gather (Fig. 2.10) to examine the trace display of the raw data along with the corresponding amplitude spectrum, which involves running of a spectral analysis. This process allows an initial determination of the signal and noise for the data set.

First inspection of the raw data shows that the signal to noise ratio in the 2007 (e.g. Fig. 2.11) and

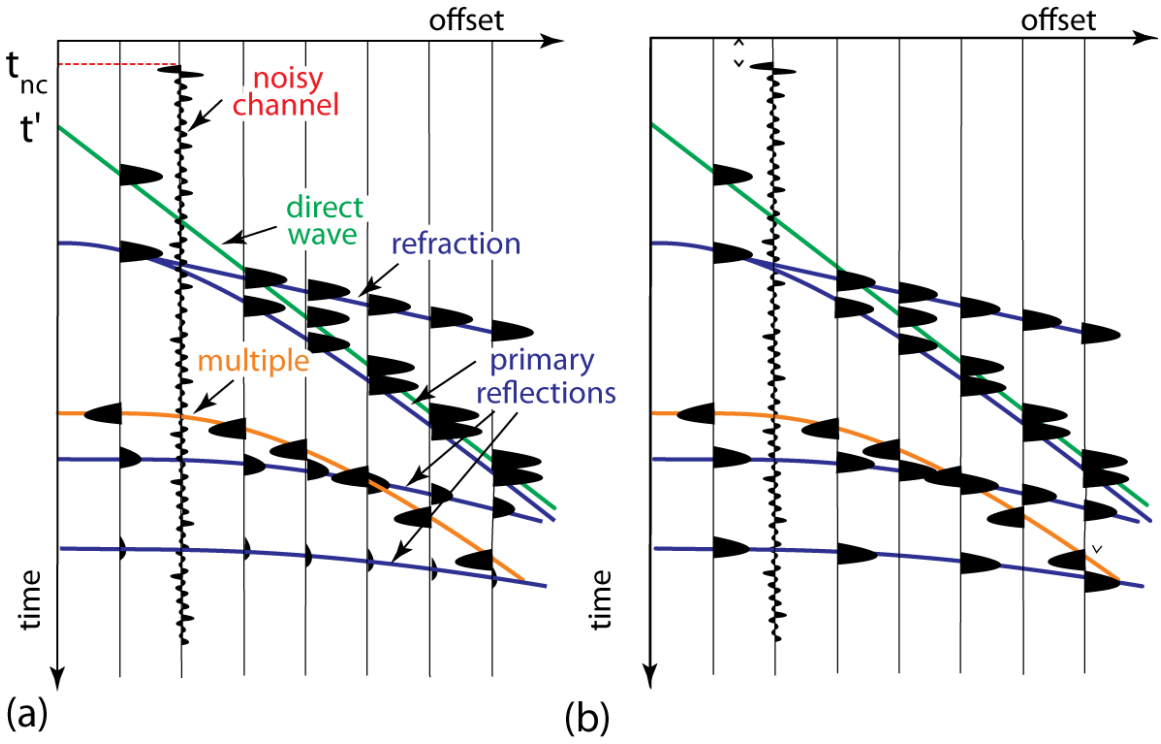

Figure 2.8: **(a)** Illustration of a marine shot record (bandpass filter applied, no AGC) showing several features including the direct wave, primary reflections, seabed multiple and a noisy channel. *Tnc* = time associated with the onset of the first pulse of a near-offset noisy channel, t' = actual arrival time of the direct wave. Note how the amplitude of reflections diminishes significantly with depth except the amplitude of the seabed multiple which remains very strong. Also note how the seabed multiple has the opposite polarity relative to the seabed reflector (i.e., first primary reflection). On the noisy channel, a large pulse can be seen shortly after the assumed zero-time, which indicates the time of shot (real zero-time) and therefore the static correction that must be made to the data. **(b)** Same shot record, but with AGC applied. Note how the stronger, shallower reflections are slightly scaled down and the weaker, deeper reflections are scaled up (adopted from King, 2014).

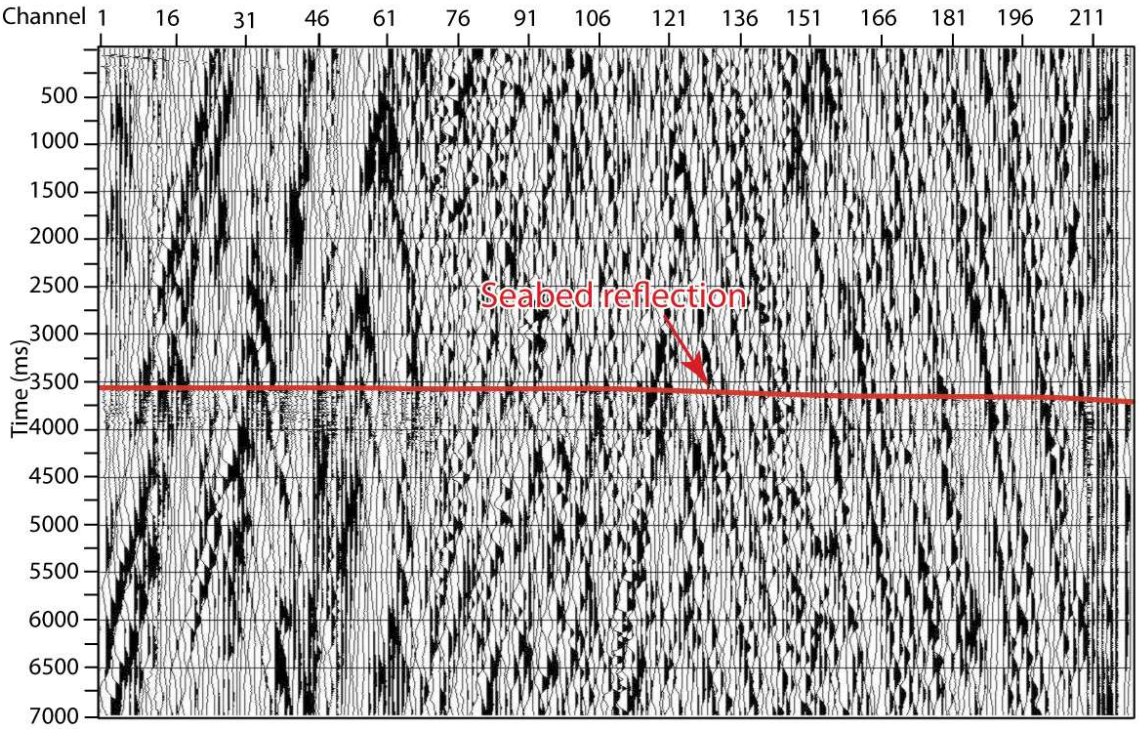

Figure 2.9: Trace display of the raw data using all channels.

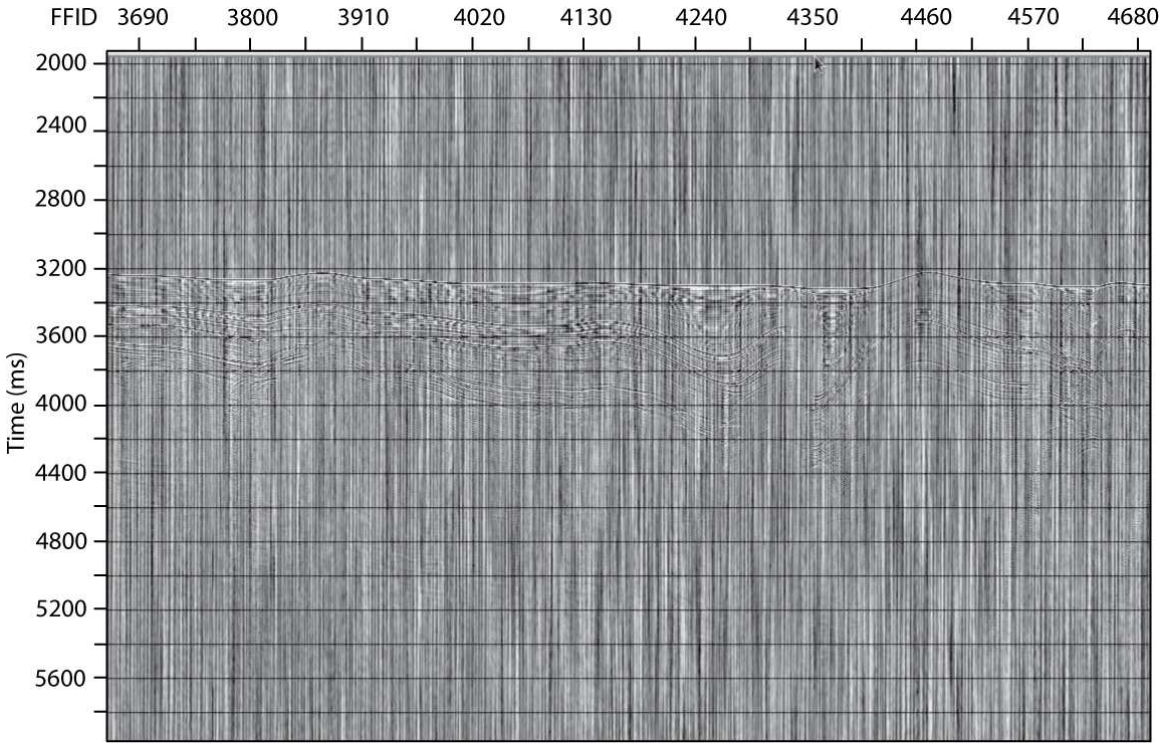

Figure 2.10: Trace display of 2010 raw data using a single channel/near trace gather display option.

2010 data is very low and it is hard to distinguish primary reflections. The seabed reflection can be distinguished at ~500-3000 ms, but it is strongly masked by high levels of noise (e.g. Fig. 2.11). The amplitude spectrum of the raw data graphically represents the amplitudes of the various frequencies of the seismic signal and it is a direct indicator of the low signal to noise ratio for this dataset.

Frequency Filtering and Spectral Shaping

A frequency filtering technique is applied within the frequency range of the data set following the inspection of the raw data. This technique is used to eliminate the low and high frequency noise while enhancing the primary energy to increase the signal to noise ratio in order to give the operator a clearer image of the data and its frequency content. Frequencies of primary reflectors can be estimated from the raw shot gather:

Equation 2.6 $$Fr = 1/Tr$$

where *Fr* is the dominant frequency of the reflection and Tr is the period of the waveform. This information can be used to construct a filter which will retain only this desired frequency range and attenuate the noise contained outside this range. A filter that retains certain frequencies while rejecting others is called a *bandpass filter*. One common bandpass filter is the Ormsby filter which uses four input frequencies, $f1 - f2 - f3 - f4$ to form a 4-sided polygon in F-K space: $f1$ = low-cut frequency, $f2$ = low-pass frequency, $f3$ = high-pass frequency and $f4$ = high-cut frequency (Fig. 2.12b). The range $f2 - f3$ is the bandpass and $f1$ and $f4$ determine how abruptly to cut off the filter. The sharp discontinuities at either shoulder of the filter can result in ringing in the filtered image. Special cosine filters can be applied to the upper corners of the polygon creating smoother ramps to reduce the ringing effect in the filtered image.

In this step both Ormsby and Butterworth filters were tested using the trial and error method, by altering the filter and phase values to develop the best possible filter for 2007 and 2010 data sets on the filtering application in ProMAX© (Fig. 2.12a, b). Based on the observed frequencies on the shot

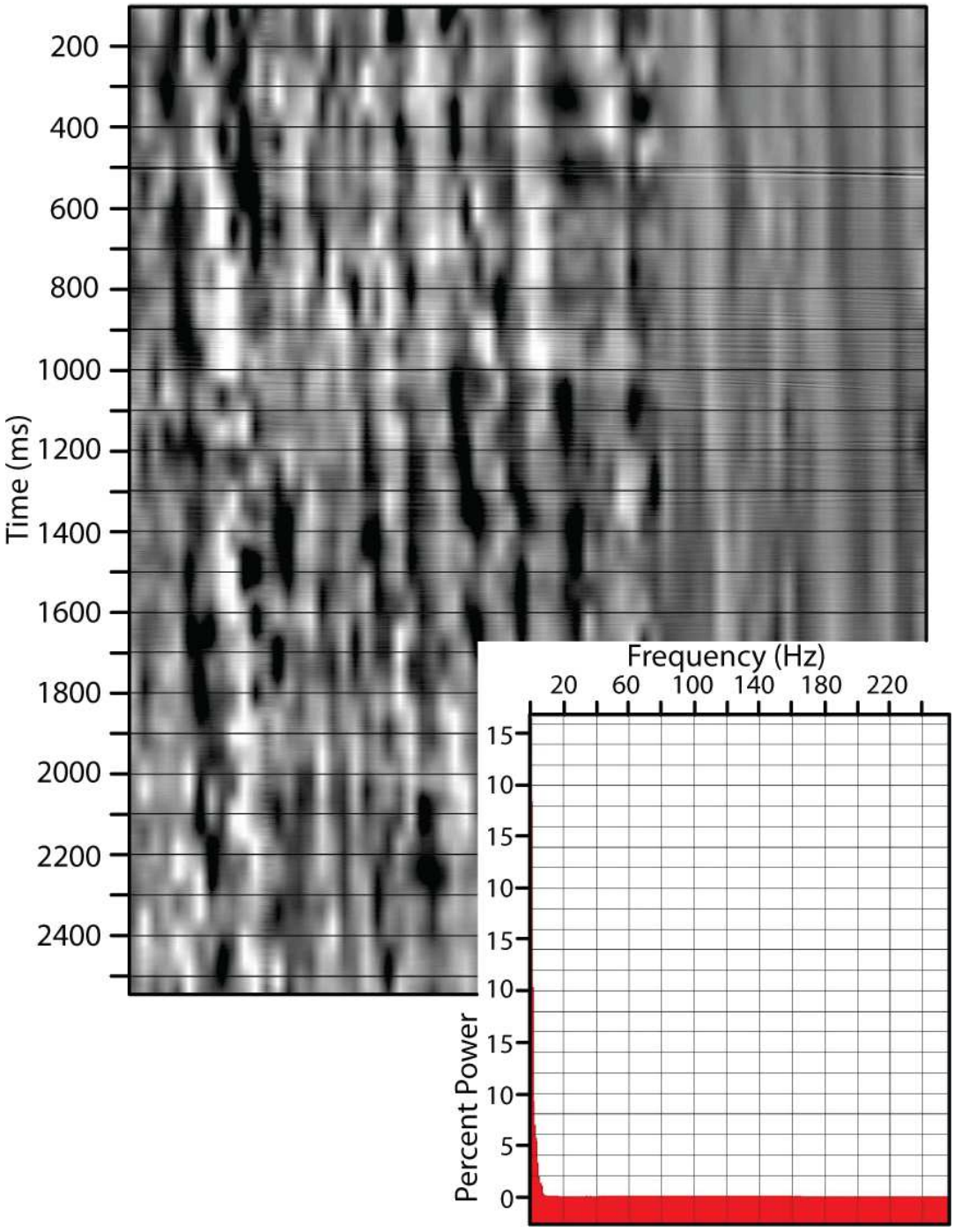

Figure 2.11: **(a)** Trace display of 2007 raw data using all channels. The red line highlights the seabed reflection at ∼500 ms and **(b)** the amplitude spectrum of the raw data. Notice that the primary signal is dominated by noise and that there is a significant low frequency peak ≤10 Hz.

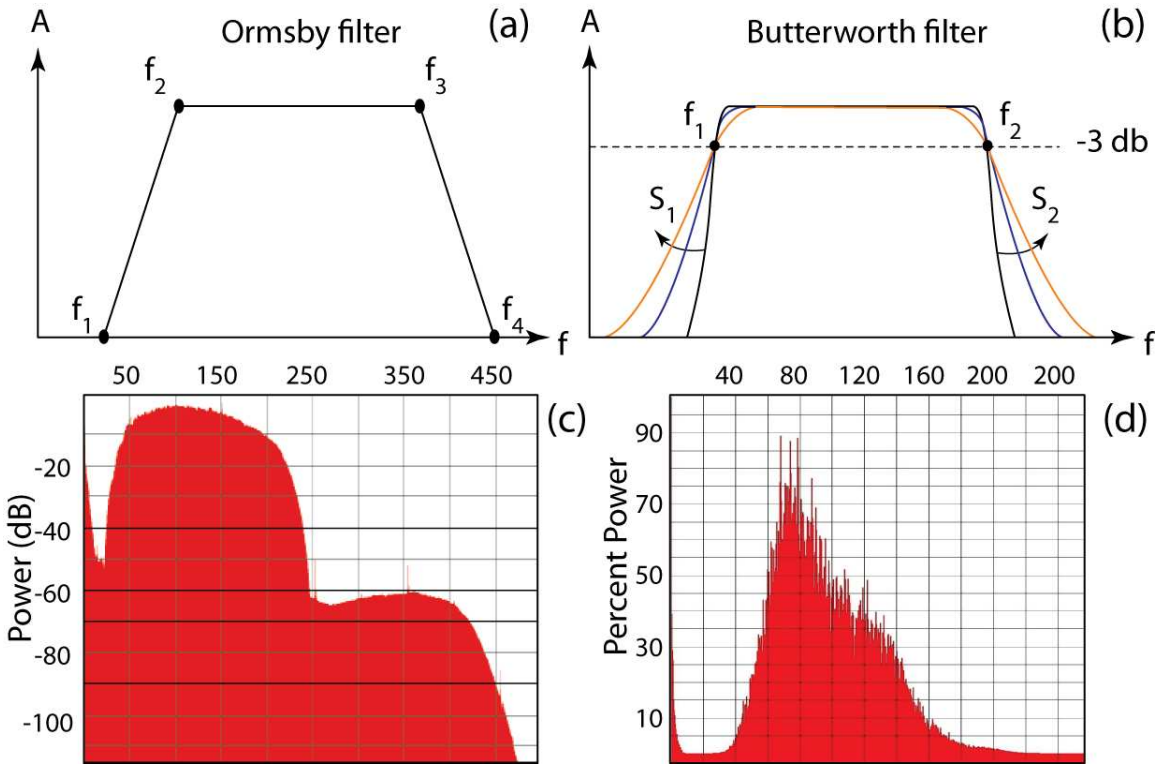

Figure 2.12: **(a)** Ormsby filtering method, **(b)** Butterworth filtering method, **(c)** after applying a 20 - 60 - 200 - 250 Hz Ormsby frequency filter, the 50 - 250 Hz signal is amplified for 2010 data, **(d)** amplitude spectrum after a bandpass filter was applied to 2007 data. Note that at (d) although the signal has been amplified the large peak of low frequency noise has not been eliminated by the filter on 2007 data.

gather the most favourable filter is determined to be an Ormsby filter, a trapezoidal bandpass filter for 2010 data set, using the following parameters: low-cut frequency of 40-60 Hz, high-cut frequency of 200 Hz, low- and high-frequency slopes cutting the frequency axis at 20 Hz, and 220-250 Hz, respectively (Fig. 2.12a,c). For 2007 data set, Butterworth bandpass filtering method used with the following parameters: 40-220 Hz. It is important to remember that applying a permanent filter at this early stage of processing can lead to removal of frequency content which can adversely affect the quality of the final image.

The filtered data shows significant improvements in the signal to noise ratio for both 2007 and 2010 data sets. However the low frequency noise is clearly visible through the filtered 2007 and 2010 profiles of the north-western portion of the study area. The large peak of low frequency noise at $\sim$10 Hz continues to dominate the spectrum, reaching values $>$95% power (Fig. 2.12d). In order to eliminate the low frequency spike, the spectral shaping process was necessary. This process balances frequency content by applying a spectral shaping algorithm to all input traces (ProMAX© Users Manual). Spectral shaping in the frequency domain scales and multiplies all frequency components by a specified contour with no effect on the original phase of the data. The shaping function is defined by a series of frequency-amplitude pairs, where amplitudes are given as a percentage of the maximum amplitude. The low frequency spike is completely eliminated from the amplitude spectrum with the best shaping contours for the 2010 data set (Fig. 2.13a and b). It is important to point out that both bandpass filter and spectral shaping are used for display purposes only and are never applied permanently to the data. This step provided the operator the necessary information to determine if further trace editing is required, such as the removal of noisy and/or dead traces, and time delay corrections.

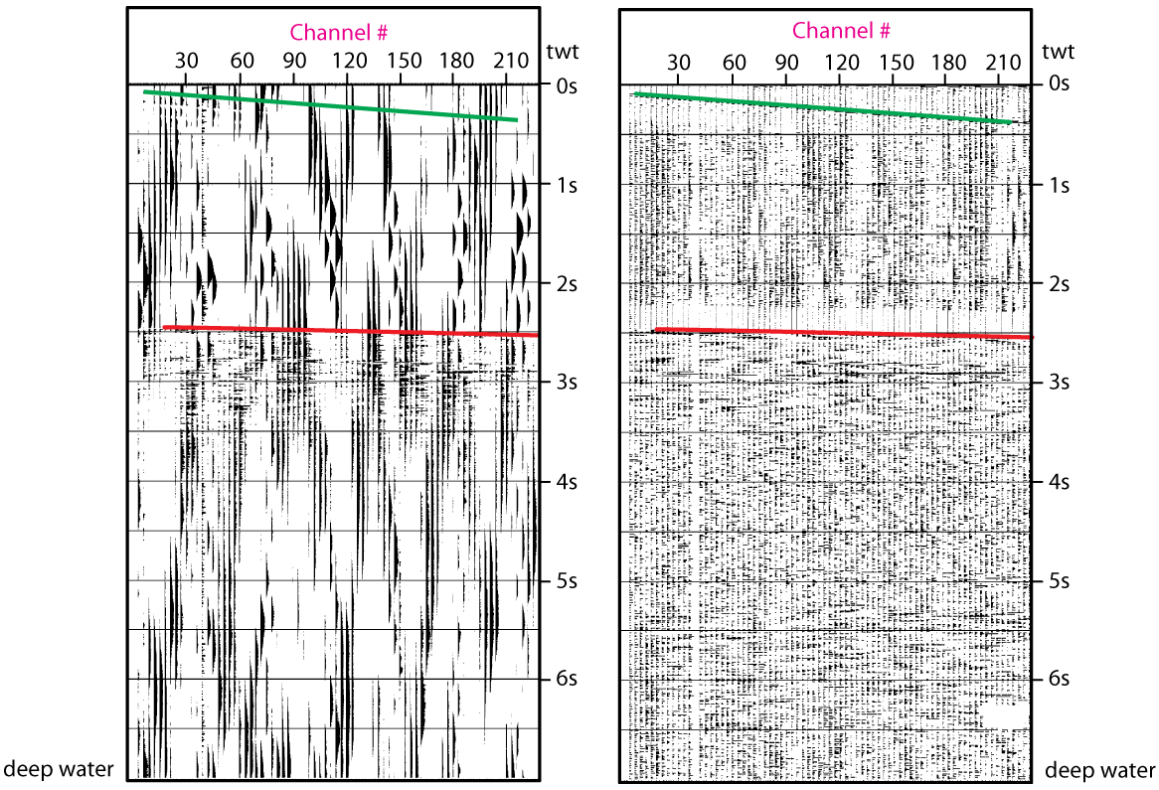

Figure 2.13: **(a)** Segment of the 2007 data showing the shot records before the application of the frequency filtering, where the low-frequency noise dominates the shot record, **(b)** Segment of the 2007 data showing the shot gathers after the frequency filtering, trace editing and AGC applications: here the low amplitude deeper reflections have been enhanced.

i. Trace Editing

The trace editing process of seismic data has been used in this study includes two steps: (1) removing bad traces (Fig. 2.14a), (2) time delay corrections (Fig. 2.14b; static corrections).

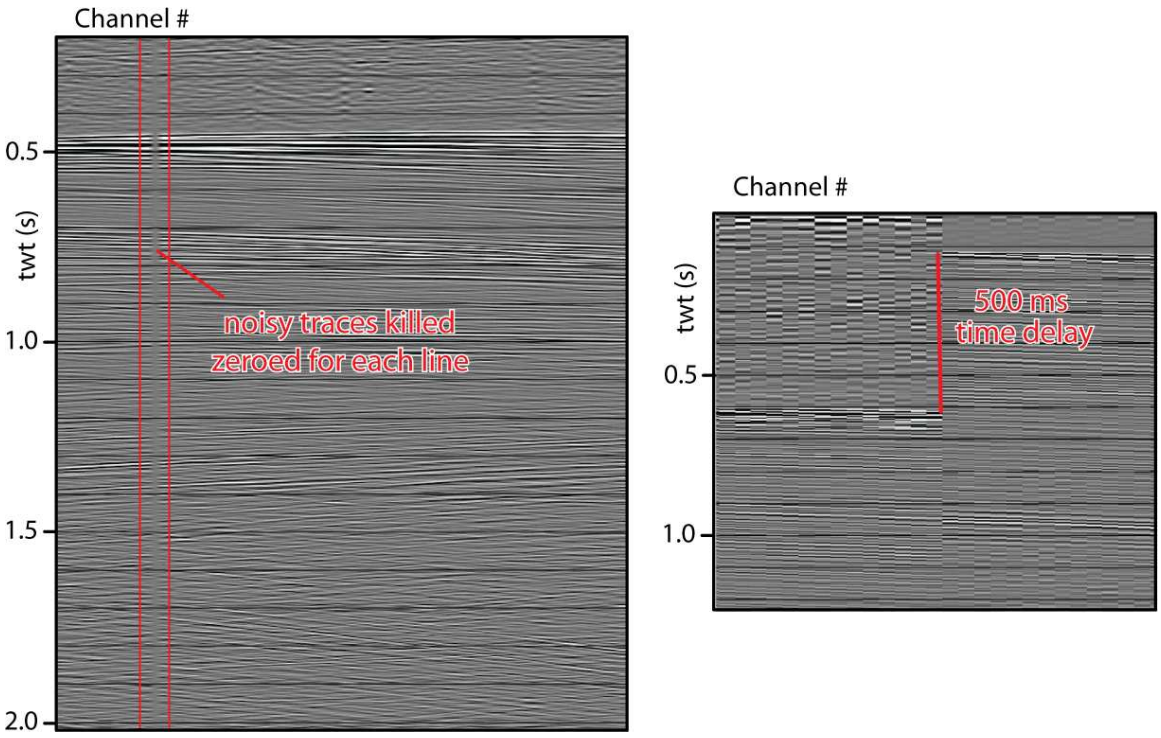

Figure 2.14: **(a)** Segment of the 2007 data showing the application of trace editing with zeroed Channel#13, **(b)** shows the 500 ms delay change on the profile.

(1) Removing bad traces: An inspection of the trace display (e.g., Figs. 2.9, 2.10) confirms that there was 1 noisy trace in 2007 and 3 noisy traces in 2010 data set randomly distributed along the streamer. The noise was probably generated within the hydrophone array either associated with the portions of the streamer exposed on the sea-surface due to rough sea conditions or malfunctioning birds (streamer depth controller), garbage trapped around birds or air bubbles trapped within the streamer. These traces were zeroed before further processing was carried

out. In spite of the fact that deleting the traces decreases the fold on the stacked section, a compromise had to be made to achieve a reasonable signal-to- noise ratio (Fig. 2.14a).

(2) Time delay corrections: This process was only applied on the 2007 data set because there was no time delay used in the 2010 data set. Because of the short shot cycle time, and the time required to write the data to the storage device in 2007, it was necessary to use delayed recording to maximize the recorded information from the seabed and below. This process starts with checking each trace of the near trace gather individually to ensure the correct field file identification (FFID) number is determined for each delay change on display application of ProMAX©. In order to determine the exact FFID where the delay was applied it was necessary to zoom in and inspect each trace individually (Fig. 2.14b). A ProMAX© processing application "hand-statics" is used to shift the time-delayed data back to its original position. Record time delays varying between 500-3000 ms (depending on the water depth) were applied during data acquisition in deep water regions in order to maximize the amount of sub-seafloor data that was recorded at all times. The data were shifted downward with the amount of the delay to place the reflections to their original arrival times (Fig. 2.15a,b).

ii. Automatic Gain Control (AGC)

AGC is a function that attempts to correct for amplitude attenuation with depth by using a sliding window to scale-down higher amplitudes and scale-up lower amplitudes (e.g., Fig. 2.8). The choice of window is extremely important for the AGC function: a window that is too small will make strong reflections indistinguishable from weak reflections and all amplitude information is lost; a window that is too large will not scale amplitudes enough and amplitude of deeper reflections may still be too low. AGC does not discriminate between signal and noise and will amplify both equally. Permanent application of the AGC function means all original amplitude information is lost; such a function should not be applied to the data early in the processing flow. AGC was used in the gain functions

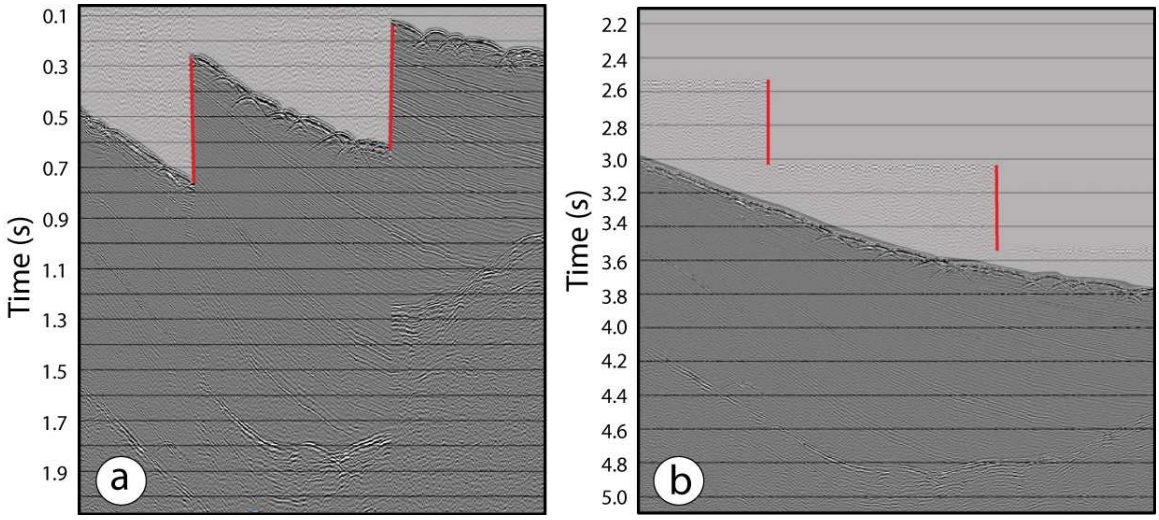

Figure 2.15: **(a)** Segment of the 2007 data showing the trace display with a number of delay changes, **(b)** shows the trace display after hand statics correction applied. Note that the delays are now corrected and the sea bed is shifted to its correct position.

on ProMAX© to process the 2007 and 2010 data sets. The width of the window was selected as 500 ms because a broad sampling interval has been sufficient to give the desired result – an overall even signal level but retaining local high amplitudes of stronger reflections. Figures 2.13 a,b shows that the data before and after the application of AGC. It is important to note that applying a gain function permanently alters the true amplitude information, thus caution must be exercised when using a gain function. During data processing the AGC function was not applied permanently to the data and was used for display purposes only.

2.4.2 Geometry and CMP Sorting

Because the survey grid lines are very nearly straight , specific survey navigation coordinates were not required for processing this data set. Instead, the survey geometry was entered into ProMAX's *2D Marine Geometry Spreadsheet* and headers were created using relative floating coordinates. CDPs imaged by different shot-receiver pairs were grouped together (Fig. 2.16). Note that the CDPs re-

ferred to in this context are actually CMPs (or common mid points). Processing these CMPs as though they were CDPs creates artifacts on the seismic record from mis-positioned reflectors. Repositioning of the true locations of subsurface depth points does not occur until after stacking (further discussed below); however, for the purpose of this discussion it will be assumed that CDP $\approx$ CMP.

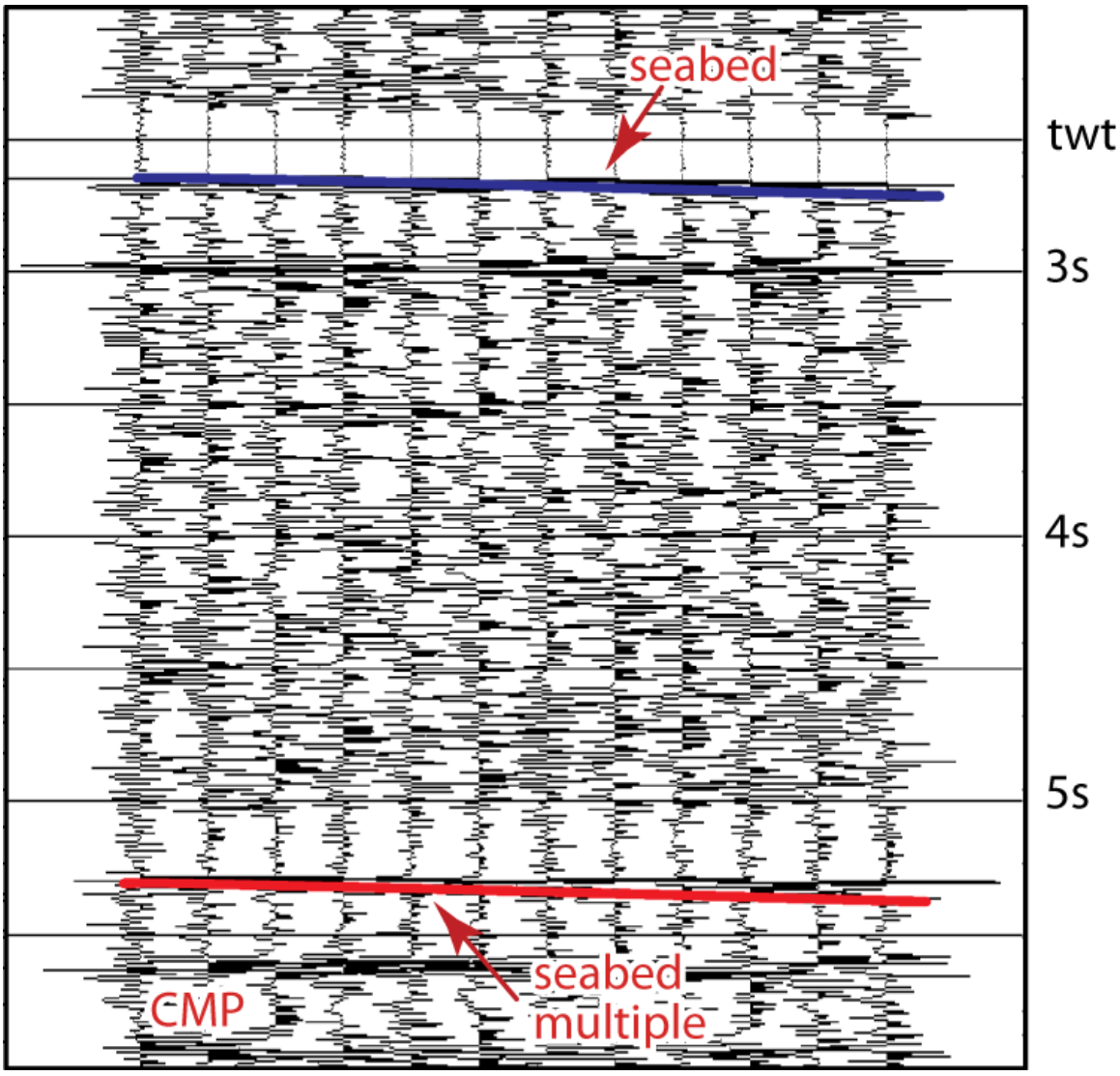

Figure 2.16: CDPs imaged by different shot receiver pairs grouped together. The seabed is highlighted in purple; seabed multiple is highlighted in red.

The geometry information of the seismic data, including the positions of the source and receivers, were defined by carefully determining several parameters including the minimum and maximum offset, the shot and receiver intervals, and the sailing azimuth. This information carries the data used for further processing for the velocity analysis and common midpoint (CMP) stacking (Figs. 2.16–2.19). The shooting geometry for the 2007 and 2010 survey was applied to the dataset using the ProMAX© 2D auto function to create a *2D Marine Geometry Spreadsheet*. After the geometry information was incorporated with the data, the originally acquired shot and receiver coordinates were transformed to midpoint and offset coordinates by assigning each trace to the midpoint between the associated shot and receiver locations, a process known as CMP sorting. Sorting the data using the CMP method creates multiple coverage of each point sampled in the subsurface, increases the signal to noise ratio and ultimately enhances the quality of the seismic image (Figs. 2.6, 2.16). Consequently, traces corresponding to the same midpoint were assembled to form a CMP gather. The number of traces in a CMP gather represents the redundancy of each sampled point and defines the fold of the dataset. By applying the correct geometry to the data set it was possible to create a binning spreadsheet which assigns each trace to a CMP. The CMP gathers created were further used to determine the staking velocities during the velocity analysis (Figs. 2.17–2.19). After the shooting geometry was applied to the data, by applying the geometry information to the individual trace headers, it was necessary to do some trace quality control by carefully examining the final geometry spreadsheet to ensure that each channel corresponds to the correct CMP.

2.4.3 Velocity Analysis and Normal Moveout (NMO) Correction

The quality of seismic imaging depends highly on the accuracy of the velocity analysis used during processing. Velocity analysis is one of the most important processes used to ensure the following steps of the processing such as, NMO correction, stacking and migration, are successful. Velocity analysis is performed based on the variation of NMO with travel time with the assumption of hy-

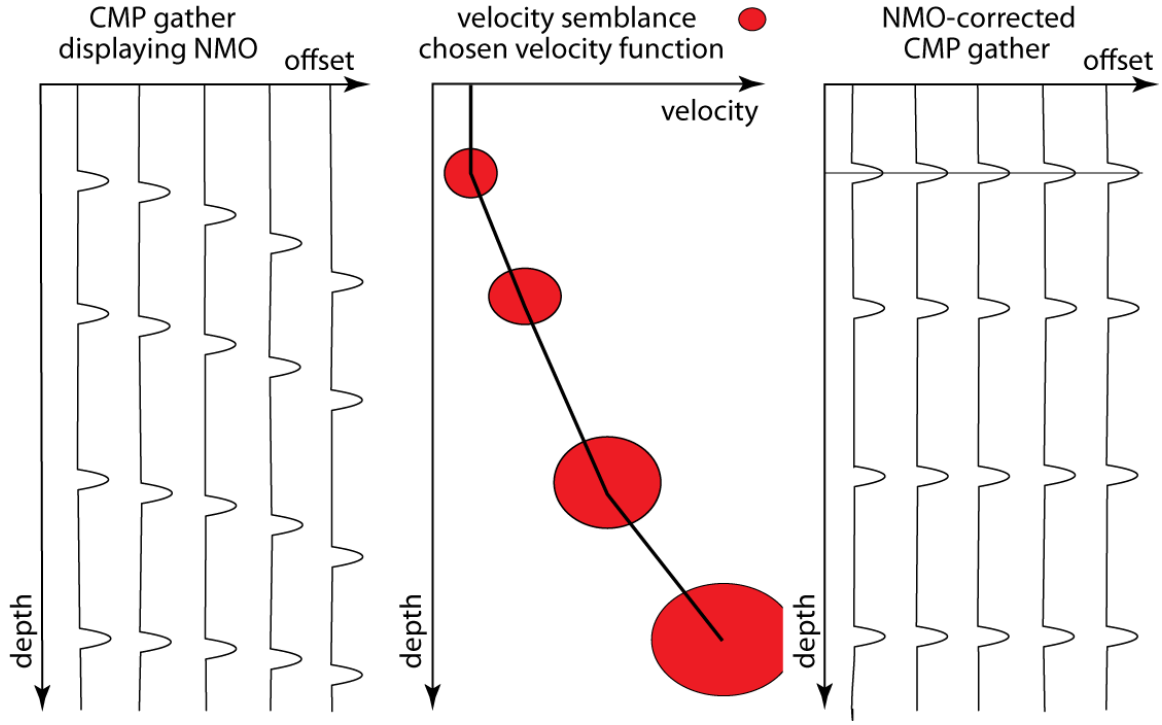

Figure 2.17: Cartoon depicting the velocity analysis using semblance and the subsequent NMO correction of the CMPs (adopted from King, 2014).

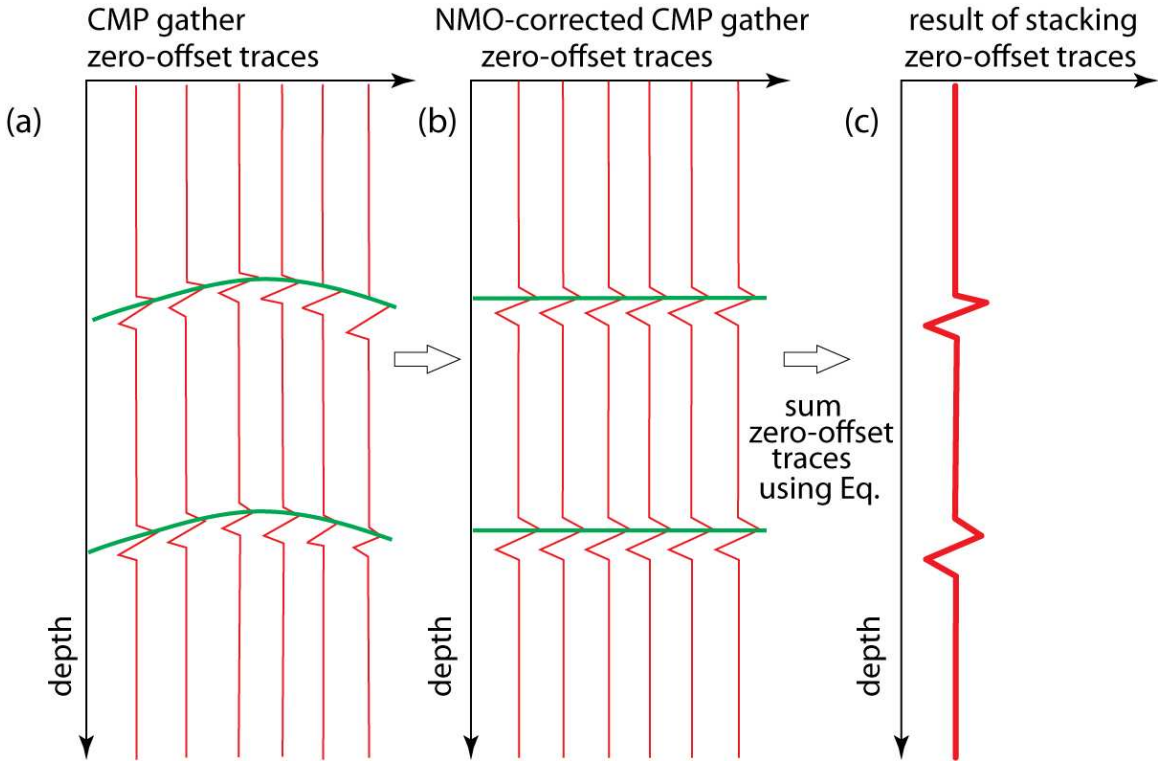

Figure 2.18: A series of seismographs showing CMP gathers with **(a)** hyperbolic NMO response, **(b)** events that have been corrected for NMO and **(c)** a stacked seismic trace (modified after Yılmaz, 2001).

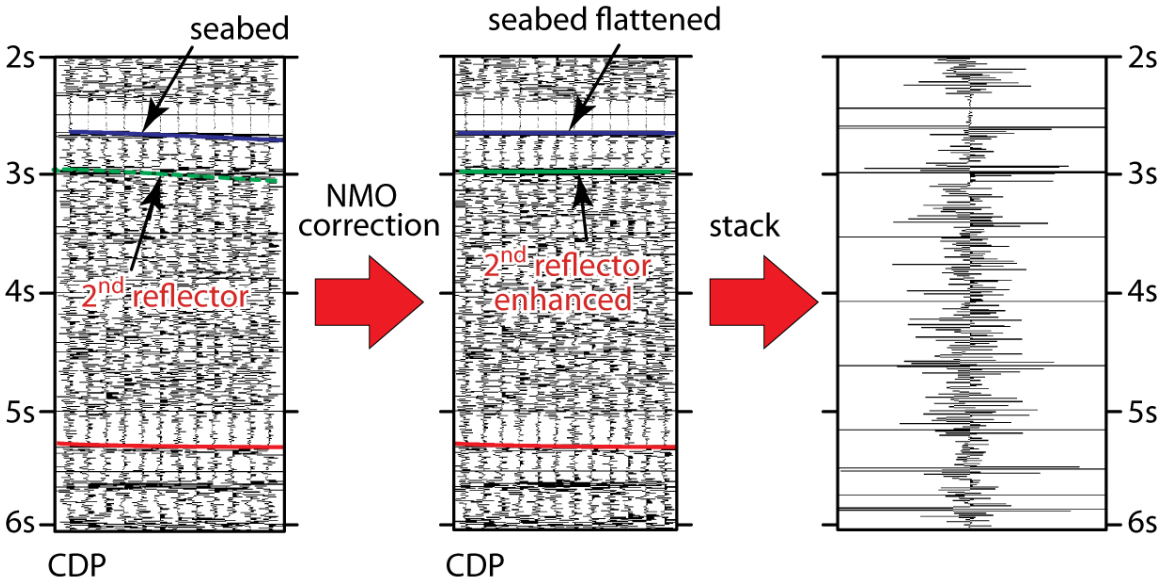

Figure 2.19: NMO-corrected CDP gathers are stacked to increase the signal/noise ratio.

perbolic reflection $t - x$ trajectories. It is usually applied to CDP gathers before stacking by using the primary velocity function. The estimated velocities are then used to eliminate the time delay associated with the finite distance between the source and the receiver in the CDP gather, a process known as the NMO correction. The NMO correction is applied to the CDP gathers before stacking by using the primary velocity function (Figs. 2.17–2.19).

There are several methods used to determine the stacking velocities from seismic data, including the semblance spectra, constant velocity stack, and the constant velocity gathers (Yılmaz, 2001, ProMAX© Users Manual). The semblance spectrum is a contour plot of stacked reflection strengths (actually semblance) against time and velocity calculated for a wide range of time and velocity. The point in the spectra with the maximum coherence or semblance ("bull's eye") is the best NMO velocity provided that the event is a primary reflection (Yılmaz, 2001). This technique is based on the correlation of traces rather than the lateral continuity of stacked events, the semblance velocity spectrum panel yields good resolution in both velocity and time and allows the identification of multiple reflections as well as providing a reasonable stacking velocity function. The display is usually in the form of semblance contours on a time-versus- velocity graph, where the peaks indicate the maximum coherence, from which the optimum stacking velocities can be derived for an event at a given time. The gather panel is achieved by forming a common-offset-stacked gather of a number of CDPs and observing the effect of NMO correction using a specified range of velocities (Figs. 2.17, 2.20, 2.21). If the velocities used in the removal of normal moveout are greater (or smaller) than the primary stacking velocities then hyperbolae corresponding to events appear undercorrected (or overcorrected) (Figs. 2.22, 2.23). Finally, the velocities, which are able to flatten the hyperbolae on the gather, are picked as the stacking velocities (Figs. 2.20, 2.21).

During the processing of the 2007 and 2010 data sets, it was important to spend a considerable amount of time on the velocity analysis of each profile. The velocity analysis was carried out creating the CMP supergathers by summing together several adjacent CMPs, in order to increases the

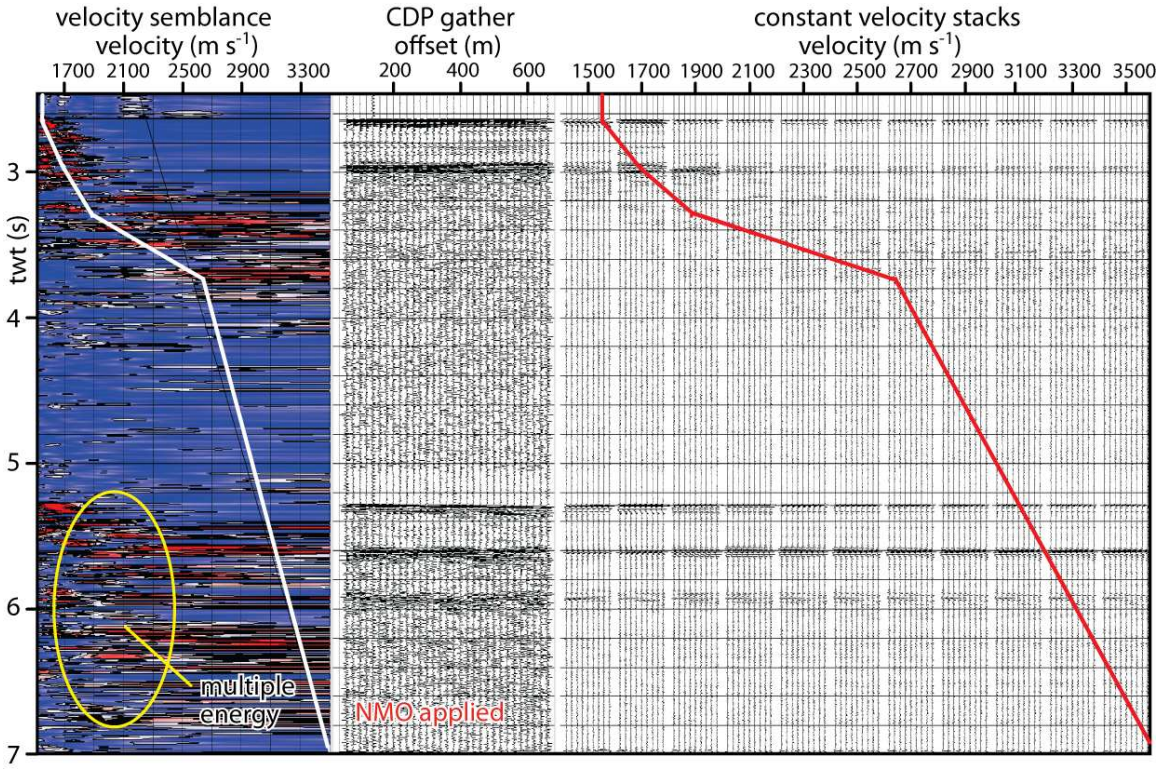

Figure 2.20: Segment of the 2010 data showing the velocity analysis with **(a)** the velocity color spectrum, **(b)** CDP gather and **(c)** constant velocity stacks used to determine the stacking velocities.

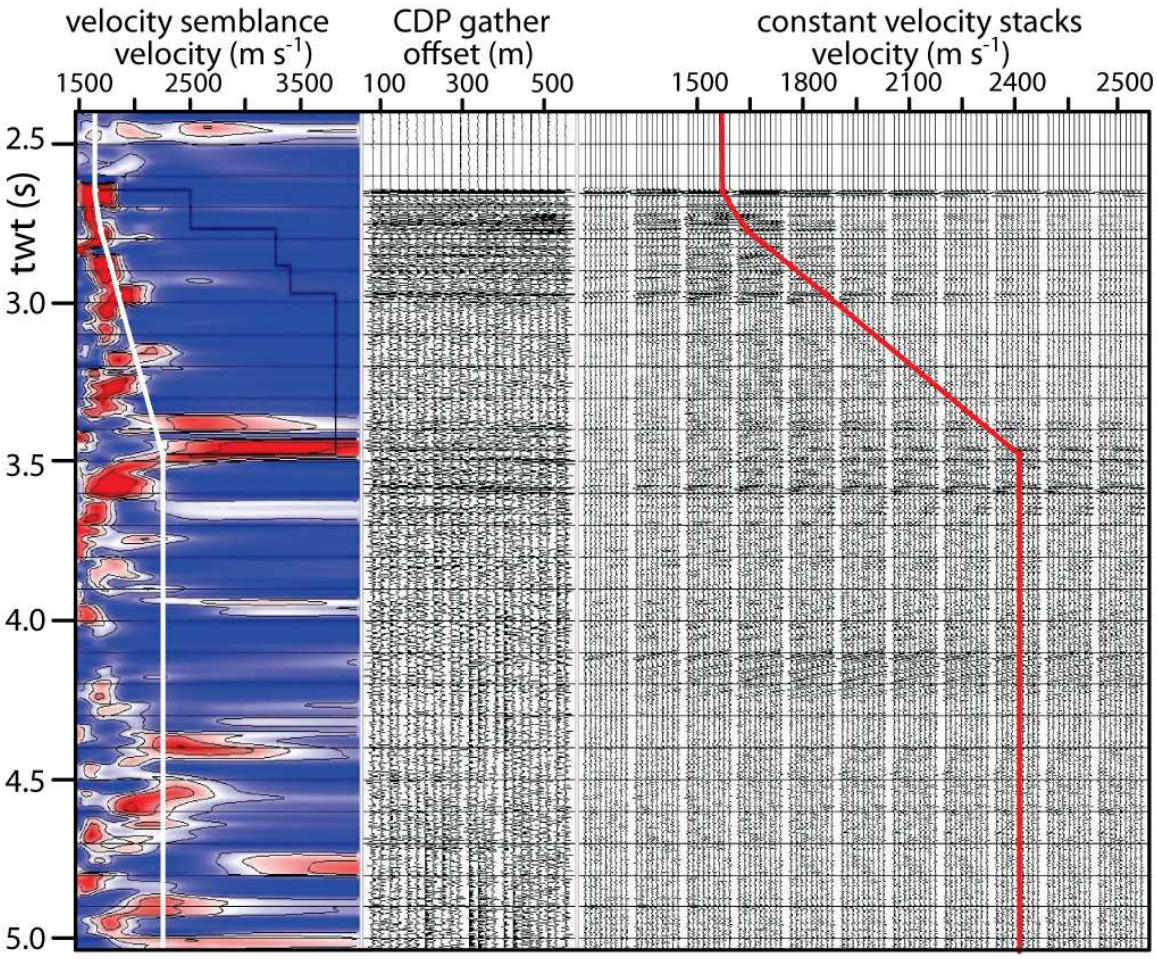

Figure 2.21: Segment of the 2007 data showing the velocity analysis with **(a)** the velocity color spectrum, **(b)** CDP gather and **(c)** constant velocity stacks used to determine stacking velocities. Note that there is decrease in velocity resolution starting at 3.8 s and extending to 5.0 s.

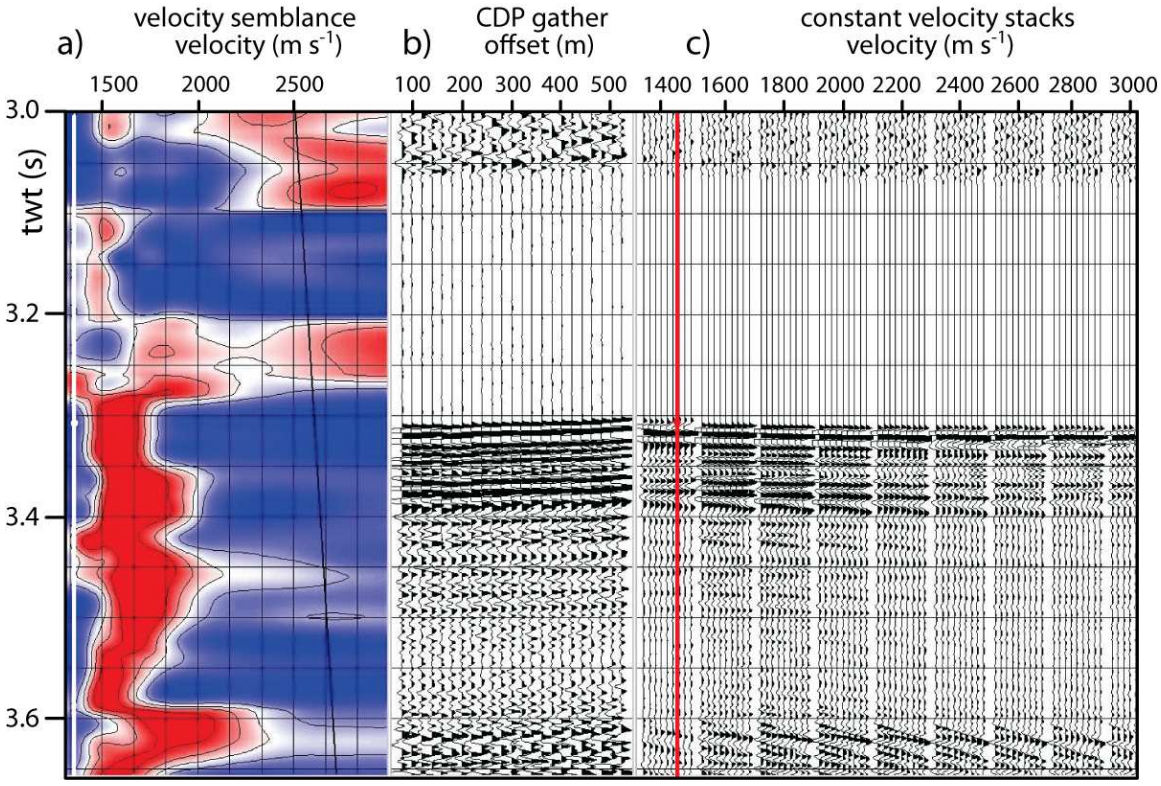

Figure 2.22: **(a)** Velocity semblance spectra with a velocity pick where the velocity is too low **(b)** the NMO is over-corrected on the CMP gather, with events curving up, **(c)** the data are not stacking on the constant velocity stacks.

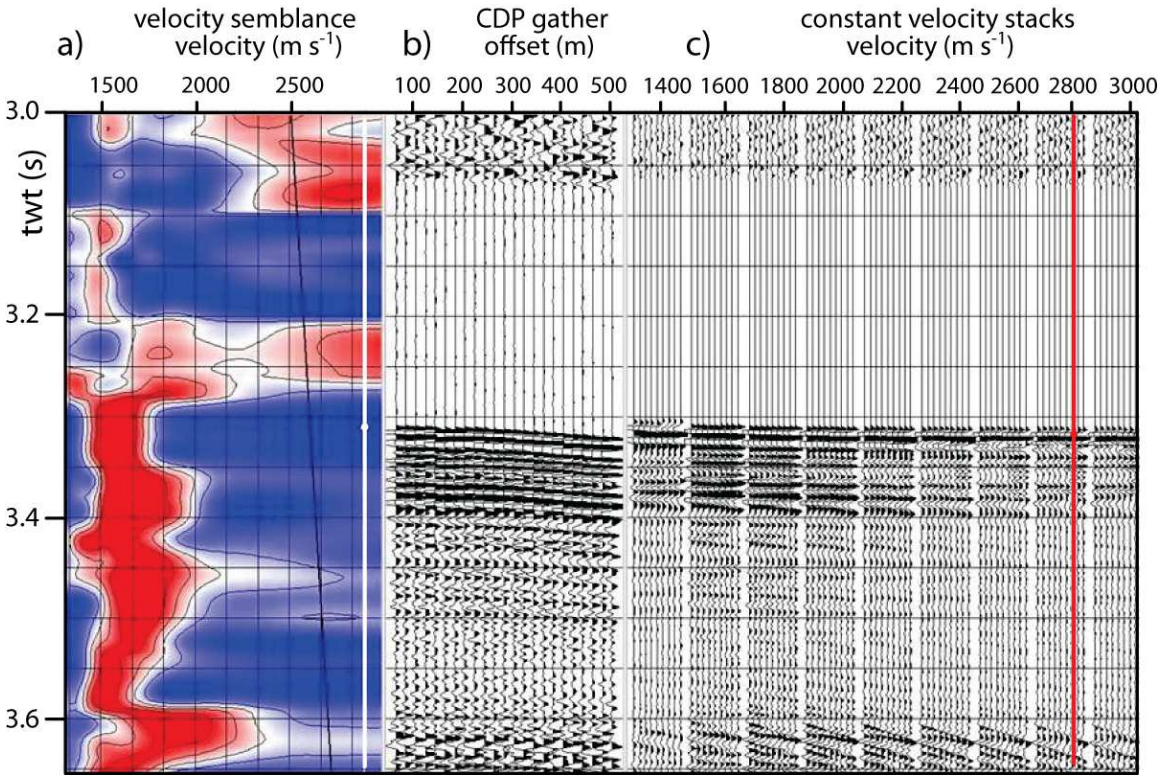

Figure 2.23: **(a)** Velocity semblance spectra showing a velocity pick where the velocity is too high **(b)** the NMO is under-corrected on the CMP gather, with events curving down **(c)** the data are not stacking in on the constant velocity stacks.

quality of the semblance spectra. The supergathers provide the location and range of CMPs packed together into ensembles for the velocity analysis (ProMAX© Users Manual). During this step the 2D supergather formation application has been used in ProMAX© to determine the velocities that produce the best NMO correction (Fig. 2.20).

During the velocity analysis of the profiles from the Florence Rise and its environs the minimum and maximum expected stacking velocities were defined as 1480 m s^{-1} and 2500 m s^{-1}, respectively. These velocities were defined according to the past experiences in the study area and also preliminary testing. The lateral sampling interval was selected to be every 500^{th} CMP, and was increased in areas where more velocities were needed depending on the complexity of the area for a reasonable lateral resolution on the semblance panel. An example of a possible velocity trend is delineated by the white dots located at the semblance peaks in Figure 2.20. The semblance window also has the option to use the interval velocity tool, shown as a black downward stepping line on the velocity spectra (Fig. 2.21). Using the interval velocity function increases your confidence when picking, with the general assumption that velocity increases with depth (except when Messinian evaporate deposits are present, see Chapters 4 and 5). Reliable estimates of the interval velocities are also useful for converting reflection times to depth.

The length of the streamers used for the data collection of this study has a major impact on velocity analysis. The fact that the streamer length is small compared to the water depth yields only small moveouts, resulting in an overall fairly broad range of velocities that are able to stack the events. The velocity analysis sample window corresponding to the 72-channel 2007 data and the 216-channel 2010 data are displayed in Figures 2.21 and 2.22, respectively. On the 2010 data, the sharp semblance peaks, the well aligned hyperbolas and the high amplitude, continuous appearance of events, are recognized in the shallow portions of the data due to greater moveout at shallow depths. Note that there is decrease in velocity resolution starting at 4300 ms and extending to 5000 ms in 2010 data while there is higher decrease in velocity resolution starting at 3800 ms and extending to

5000 ms in 2007 (Figs. 2.21, 2.22). The poor constraints on the velocities below 3800 ms decreases confidence for making good velocity picks at greater depths on the semblance analysis alone, but it was possible to integrate the semblance analysis with the CMP gathers and constant velocity stacks and use all three to make the best possible pick (Figs. 2.20, 2.21). The constant velocity stack, is done by correcting the normal moveout of a specified number of CMPs using either a set of constant velocities or time-variant velocity functions and then stacking them. And, the CMP gather displays the common offset stacked supergather for the specified CMPs (Fig. 218, 2.19). It was possible to see if each pick was under- or over-corrected for the NMO velocity by using the interactive NMO application to the CMP gather. When the velocity pick is too low and over-corrected for NMO the event will curve up (Fig. 2.22). If the pick is too high and is under-corrected for NMO the event will curve down (Fig. 2.23). Finally, when the NMO velocity is correct the given reflection in the gather will appear flat in time (Fig. 2.24). Integrating these three velocity analysis methods significantly increased confidence when picking velocities.

After the velocity picking was complete it was necessary to display the output velocity field and edit the function using the velocity viewer/point editor (Fig. 2.25a,b). The velocity viewer/point editor tool allows velocity picks to be manipulated and the new velocity function is output and saved. The velocity editing tool was also used to delete unwanted CMPs from the velocity function and to do some minor smoothing where sharp edges occurred (Fig. 2.25b). Editing the velocity function for stacking was not critical because the water levels are relatively deep and the data stacked quite well over a wide range of velocities. However, velocity editing was very important when choosing the correct velocities for migrations. Migration velocities will be discussed in greater detail later in this chapter.

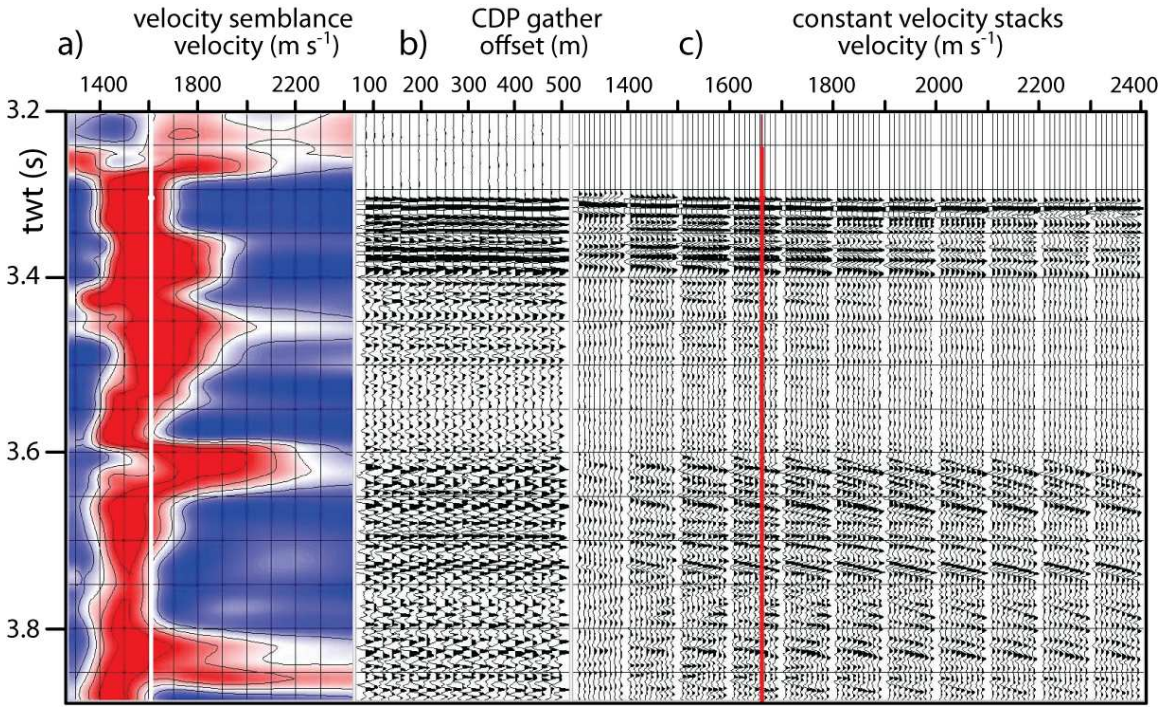

Figure 2.24: **(a)** Velocity spectrum showing a good velocity pick at a semblance peak on the velocity color spectrum, **(b)** the normal move out is corrected, with the events flattened on the CMP gather, **(c)** the data are stacking in on the constant velocity stack.

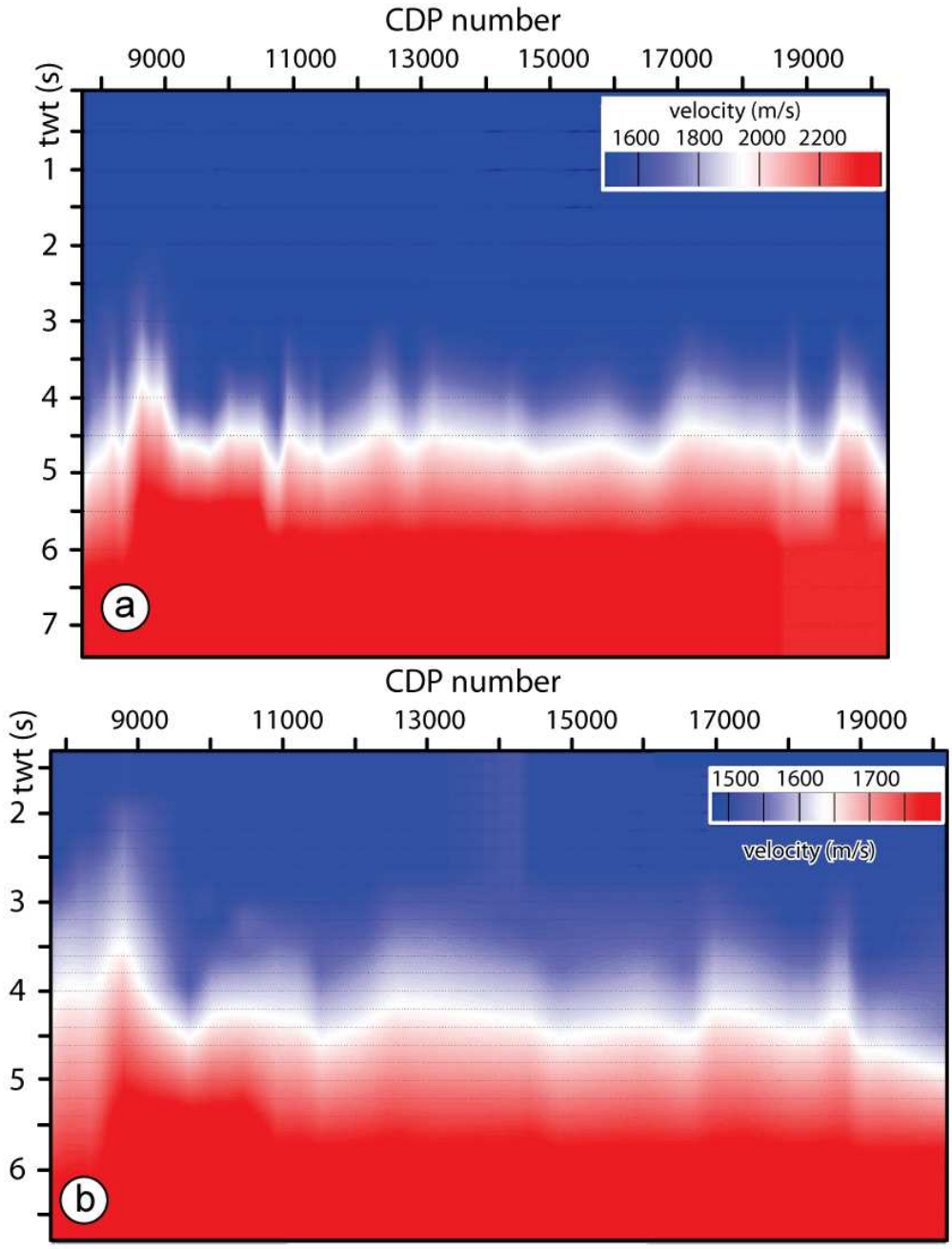

Figure 2.25: Velocity viewer/point editor with **(a)** output velocity function created from picking the NMO stacking velocities: here notice the sharp edges on the dipping structures, **(b)** velocity function post velocity editing where there are less CDP's and the velocity function has been slightly smoothed in comparison to the original velocity function in (a).

2.4.4 Common Midpoint (CMP) Stacking

Stacking is one of the most efficient steps in data processing in terms of improving the data quality. The stacked seismic sections show a significant increase in the signal to noise ratio, but the image is distorted by the diffraction hyperbolas and migration is required. The stacking process involves summing together each trace in the NMO corrected CMP gather and dividing the sum by the total number of traces in the gather to produce a single stacked trace (see Equation 2.6; Fig. 2.18).

Equation 2.7 $$Stack = \sum_0^t (1/n \sum_1^n S(t))$$

The traces in a CMP gather corresponding to various offsets are summed at each time sample to give a single trace, equivalent to zero offset, on the stacked section. Stacking not only compresses the dataset but also attenuates both random and coherent noise (Figs. 2.18, 2.19). The primary reflections tend to have less NMO than the multiple reflections. For a primary and multiple reflection arriving at the receiver at zero offset at the same time, the NMO of the primary reflection is less than the multiple because a greater portion of the travel path of a multiple reflection is confined to the shallow part of the subsurface. Hence, its propagation velocity is lower compared to the primary reflection, which penetrates into the deeper, higher velocity media. As a result of NMO correction using the velocities estimated via velocity analysis, the hyperbolae corresponding to the primary reflections are flat in time while the multiple reflections remain undercorrected. During CMP stacking, the aligned primary reflections add up constructively, yielding high amplitudes, while the undercorrected multiple reflections do not show amplitudes that stand out on the stacked section. The random noise, because of its uncorrelatable character from trace to trace, is also attenuated by the stacking process (i.e., the signal-to- noise ratio being enhanced by $n^{1/2}$ where n is the stacking fold).

Stacked data is displayed as zero-offset data set assuming normal-incident P-waves reflected on horizontal layers (i.e., CDPs are treated as CMPs). This results in distortion of dipping reflectors. Dipping reflectors are imaged to be longer and less steep than they really are (Fig. 2.26a,b). Geological features like anticlines, synclines, and faults are distorted in the stacked section. Anticlines

appear broader and display reflector cut-off at either limb (Fig. 2.26c,d). Synclines appear narrower and may display "bow-tie" geometry (Fig. 2.27a,b). Faults, sharp edges and dipping surfaces appear as a series of diffractions on the seismic profile (Fig. 2.27c,d). In order to correct for this distortion, the data must be migrated.

A near trace gather and a stack section of a range of shots are displayed in Figure 2.28. Note that, on the stack section reflectors stand out more distinctly and an improvement in the signal-to-noise ratio is recognized.

2.4.5 Migration

The goal of migration is to focus the seismic image. The image is inherently out of focus when we observe it at the surface. The migration focuses the image by some form of downward continuation of the wave field observed at the surface down to the point of origin of the reflection or diffraction. That is why, for instance, an out of focus point diffraction is collapsed to a point source during migration. On a stacked seismic image, dipping reflectors appear at slightly incorrect locations with respect to the location of the sources and receivers, and diffraction hyperbolae occur where there are discontinuities along the reflectors. Migration is the processing technique used for collapsing these diffraction hyperbolae, moving dipping reflections to their correct locations, increasing the spatial resolution that accurately illustrates the geological setting of the subsurface (Figs. 2.28b,c, 2.29). Thus, the migration process focuses the final seismic image, making detailed structural and stratigraphic interpretations possible. The accuracy of the migration is controlled by a number of factors such as: the proximity of stacked section to zero-offset section, the signal/noise ratio, and the quality of the velocities used during migration.

Migration can be performed either pre- or post- stack. Where geology is complex, pre-stack migration produces better signal-retention, but the computational cost is high. Migration can be executed in either in time or in depth. Depth migration requires accurate interval velocity information

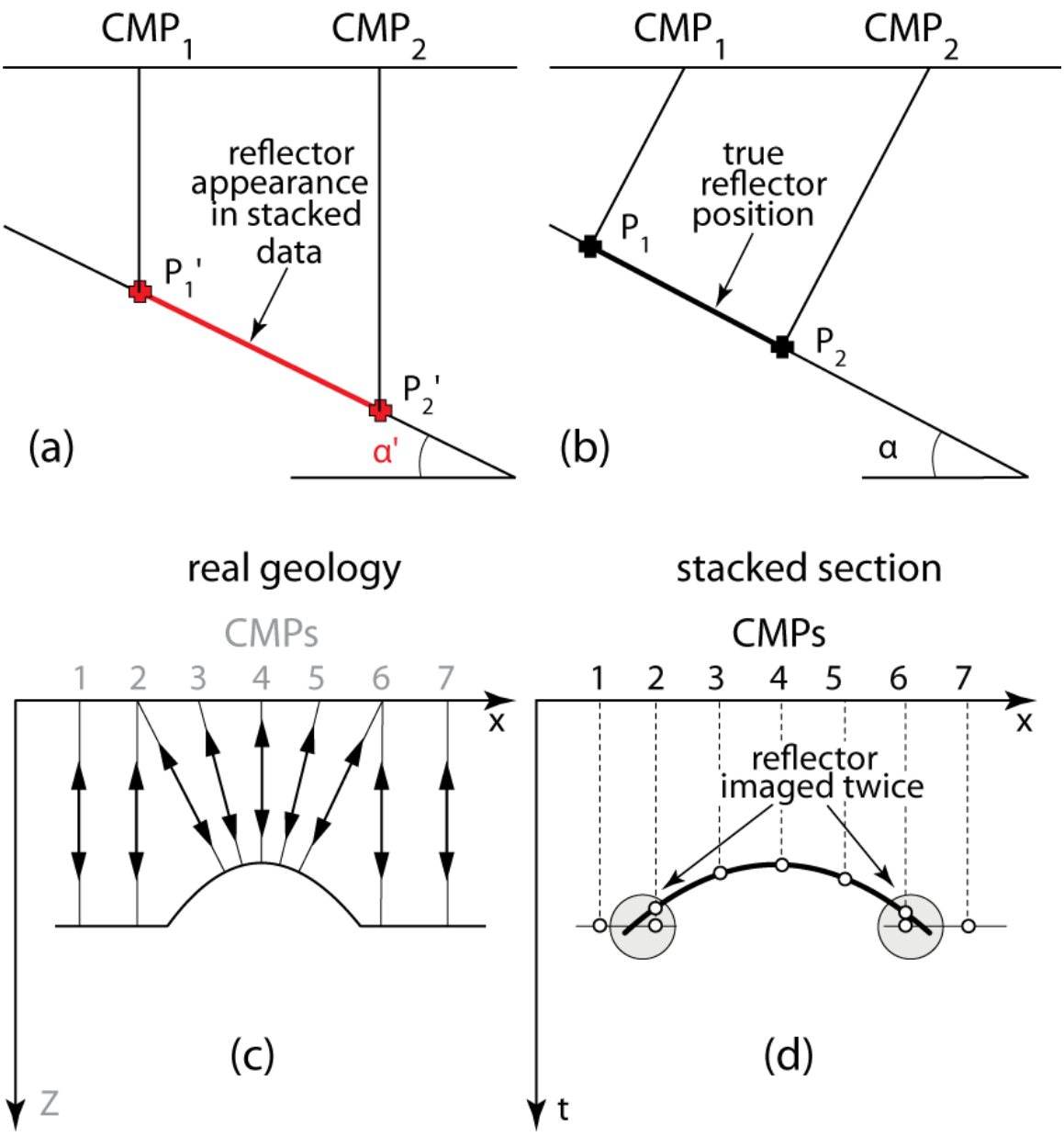

Figure 2.26: On a CMP stack, dipping reflectors are imaged longer and less steeply than they really are. **(a)** Imagined positions of P_1 and P_2 on reflector with apparent dip = α', **(b)** true subsurface position of P_1 and P_2 on reflector with true dip = α, **(c)** actual subsurface anticline, **(d)** because of the curved surface, two reflections originating from the same reflector are recorded at CMPs 2 and 6. Note how the anticline appears broader on the CMP stack section (adopted from King, 2014).

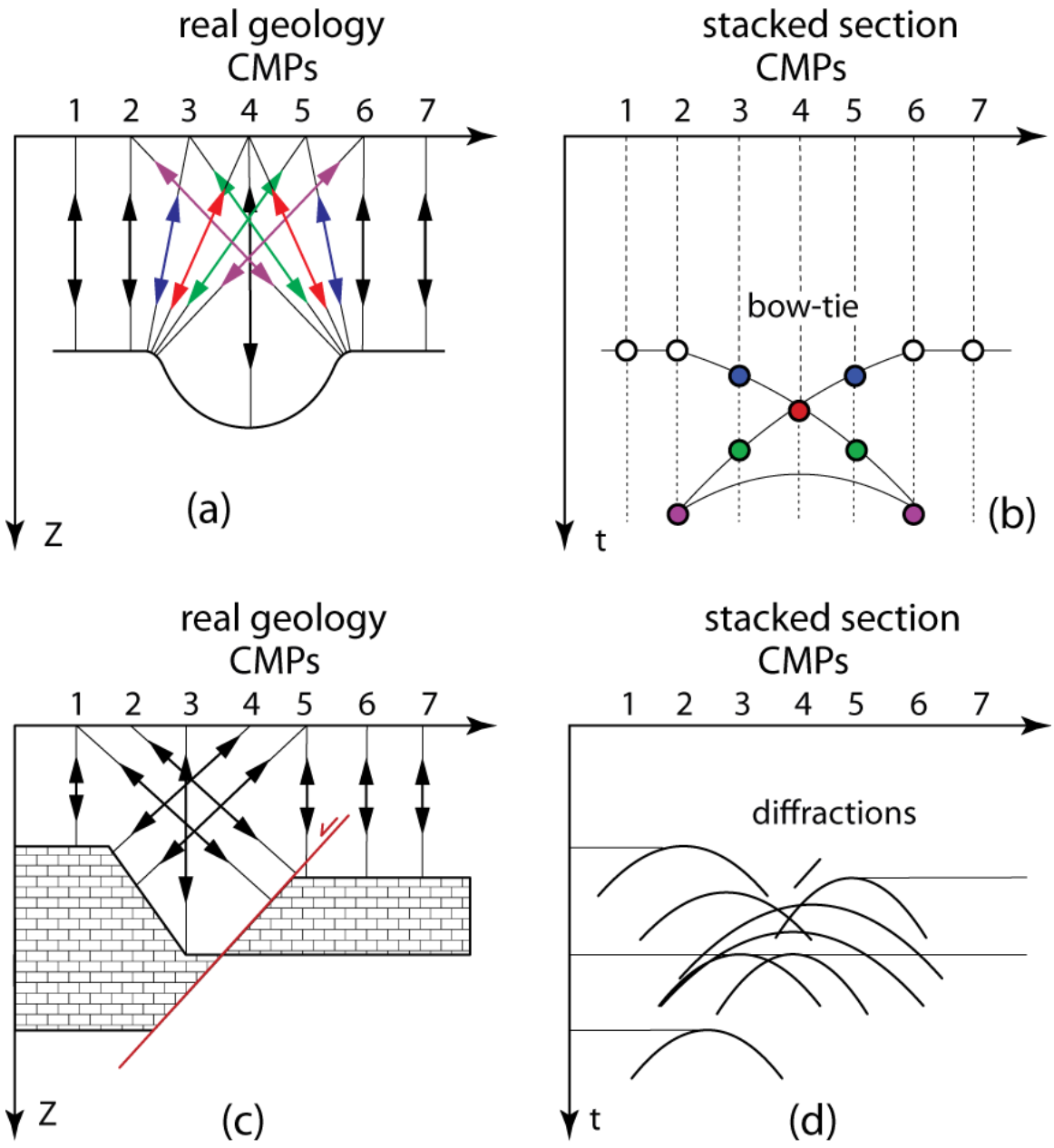

Figure 2.27: **(a)** Actual subsurface syncline, **(b)** the reflector is imaged several times at the CMPs because of the curvature, resulting in bow-tie geometry in the stacked section. Note how the syncline appears compressed in the stacked section. **(c)** Actual geology of a dipping reflector and an extensional fault, **(d)** diffractions generated in stacked section (adopted from King, 2014).

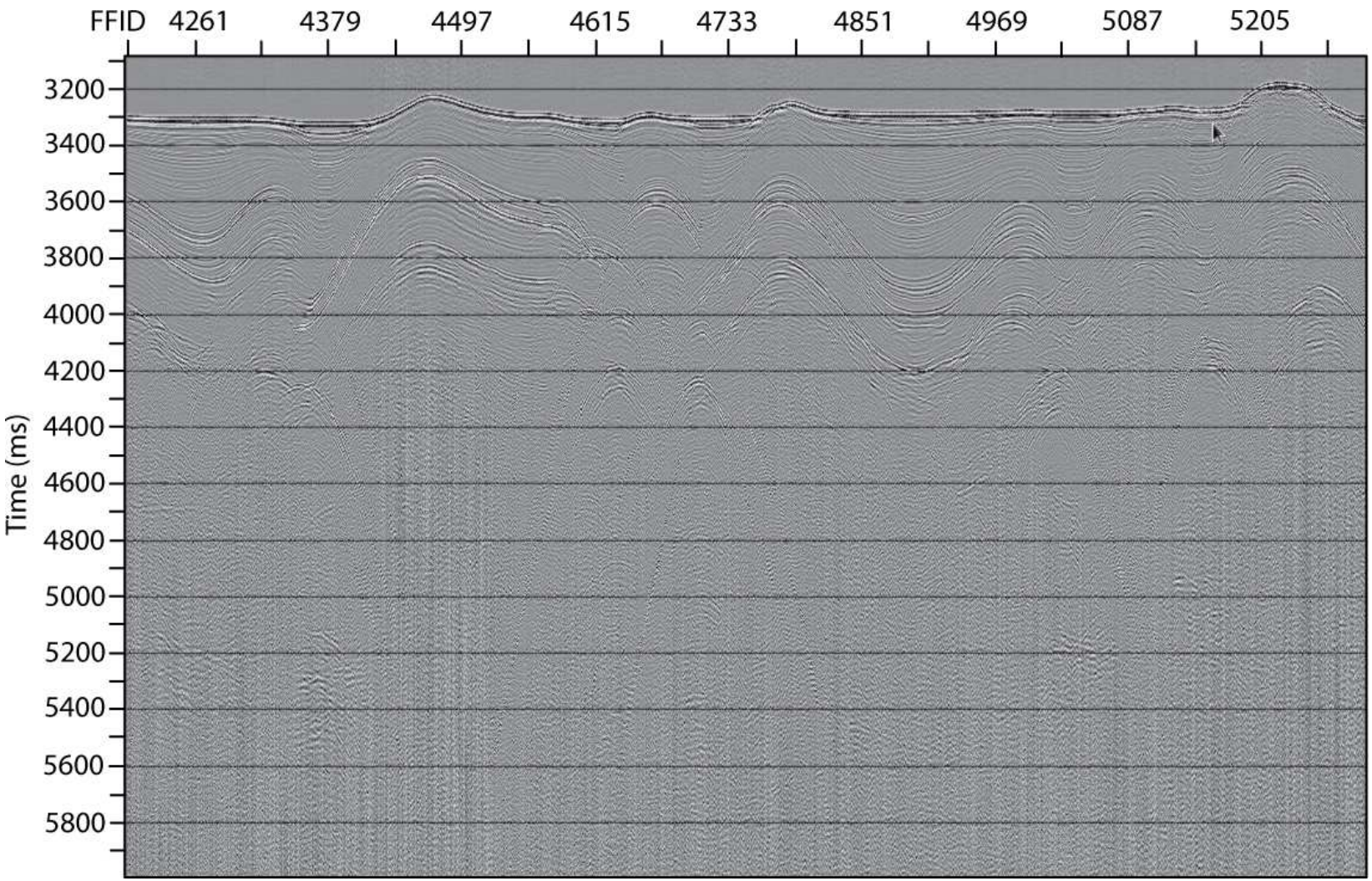

(a)

Figure 2.28: Trace display shows 2010 data before the stacking process.

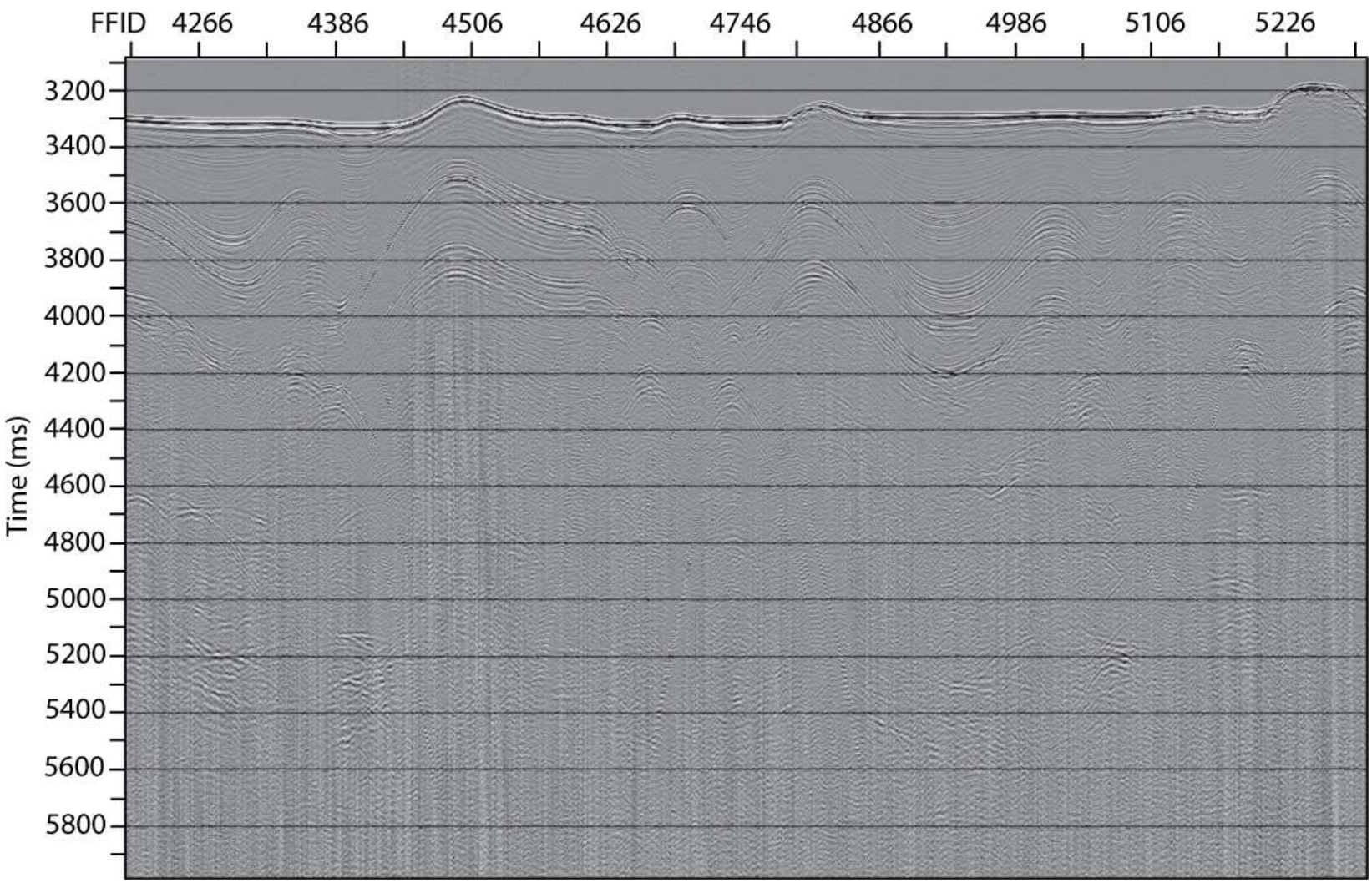

(b)

Figure 2.28: Trace display shows 2010 data after the stacking process.

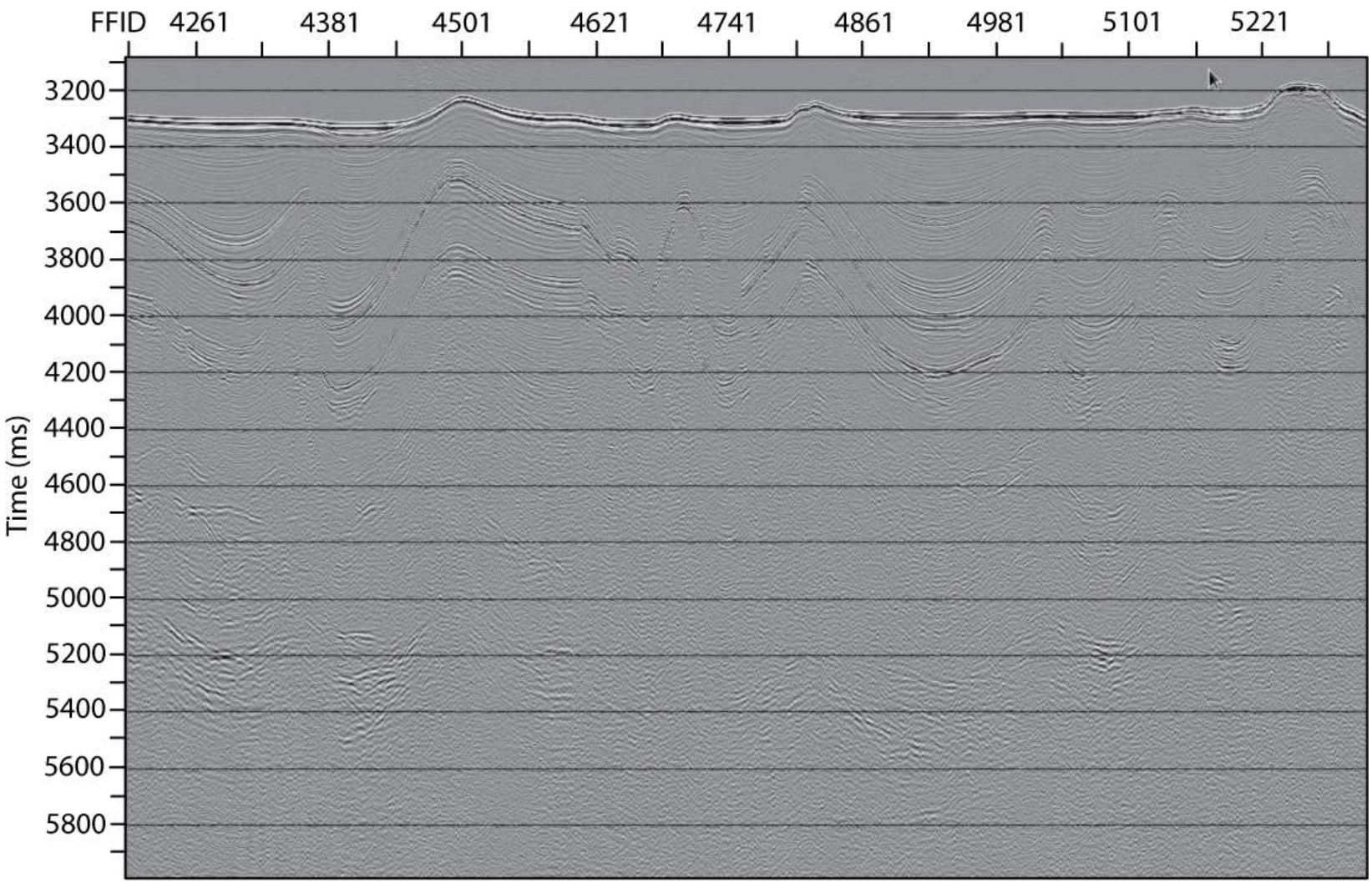

(c)

Figure 2.28: Trace display shows 2010 data after the migration process.

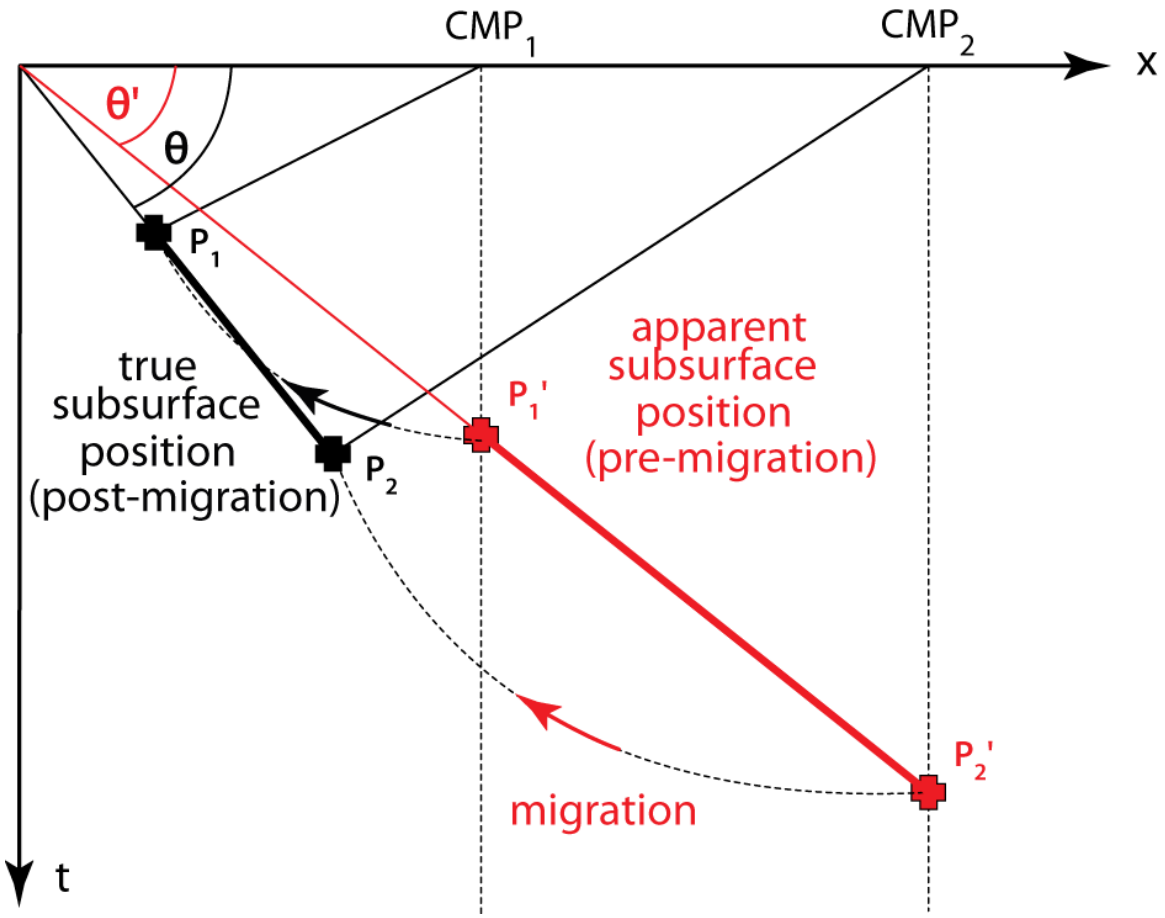

Figure 2.29: Illustration of migration principles. Note that after migration, the reflector is shortened, dip is increased (i.e., $\theta < \theta'$), and reflector is moved up-dip (modified from King,2014).

and therefore, time migration is commonly used for interpretation purposes, especially in deep water surveys like the present study, where velocity is not well constrained. Time migration assumes diffractions are hyperbolic and uses this to collapse diffractions while depth migration uses a known velocity model to more-correctly approximate diffraction shapes.

In this study post-stack time migration techniques are used to be able to make detailed structural and stratigraphic interpretation possible for the 2007 and 2010 seismic reflection data. To estimate accurate migration velocities, the Stolt (constant and variable velocity) and 2D Kirchhoff time migrations techniques were applied to the post-stack data on proMAX© sofware.

i. Constant Velocity Stolt Migration

Stolt constant-velocity migration is a very fast migration, using a transformation into the frequency domain, migration operation and inverse transformation. However, the end-result is not as good as other migration algorithms in the time domain because it does not handle complex structures and lateral variations in velocity well. This step of migration was only used to estimate the proper velocities for the subsequent migration techniques.

In this study for both 2007 and 2010 data set, F-K Stolt constant velocity migration were applied and printed with the velocity values of 1500, 1600 and 1700 m s^{-1} to generate constant velocity plots. Working on paper copies made it easier to compare the sections and identify the best velocities for the variable velocity Stolt migrations and Kirchhoff migration.

ii. Variable Velocity Stolt Migration

Variable-velocity Stolt migration was used next to give a better image than the constant-velocity Stolt migration, while still suffering from the same disadvantages.

Kirchhoff Time Migration

The Kirchhoff migration algorithm is a much more accurate migration procedure than Stolt, but takes a lot longer to compute. It collapses the diffraction hyperbolae visible on stacked sections by summing the amplitudes of the diffraction hyperbolae of all the secondary sources and placing them at the appropriate apex (Fig. 2.30). The technique has the advantages of: (1) migrating events with steep dips up to 90°, (2) being efficient when velocity varies vertically.

During the migration of the study area profiles, the Kirchhoff time migration was performed as a final migration step. The stacking (or RMS) velocities obtained through velocity analysis, when used in migration, resulted in over-migrated hyperbolas particularly at deeper portion of the section. The appropriate migration velocities, which were successful in collapsing the hyperbolas, were determined by performing a number of tests. Figures 2.31a and b provide example of a stacked section and its associated final Kirchhoff migration.

2.4.6 Multiple Attenuation

Deconvolution and stacking are the two most effective multiple removal tools. There are two types of deconvolution techniques, spiking deconvolution and predictive deconvolution. Spiking deconvolution (also called spectral whitening) increases the temporal resolution of the data by collapsing the seismic wavelet to a spike, which is closer to the true geological response. Strictly speaking, the spiking deconvolution operator is the inverse of the wavelet. The process is carried out using both the inverse and the least-squares statistical filters and is dependent on the length of the filter and whether the seismic wavelet is minimum phase or not (Yılmaz, 2001, proMAX Users Manual). The unwanted response of the source, receiver and instruments are treated as linear filters and inverse filters are designed to attenuate these effects. The success of the deconvolution rests on the assumption that (i) the seismic wavelet is minimum phase, and (ii) the information on the original form of the wavelet is known, or can be estimated from the recorded trace. In this study, a spiking deconvolution

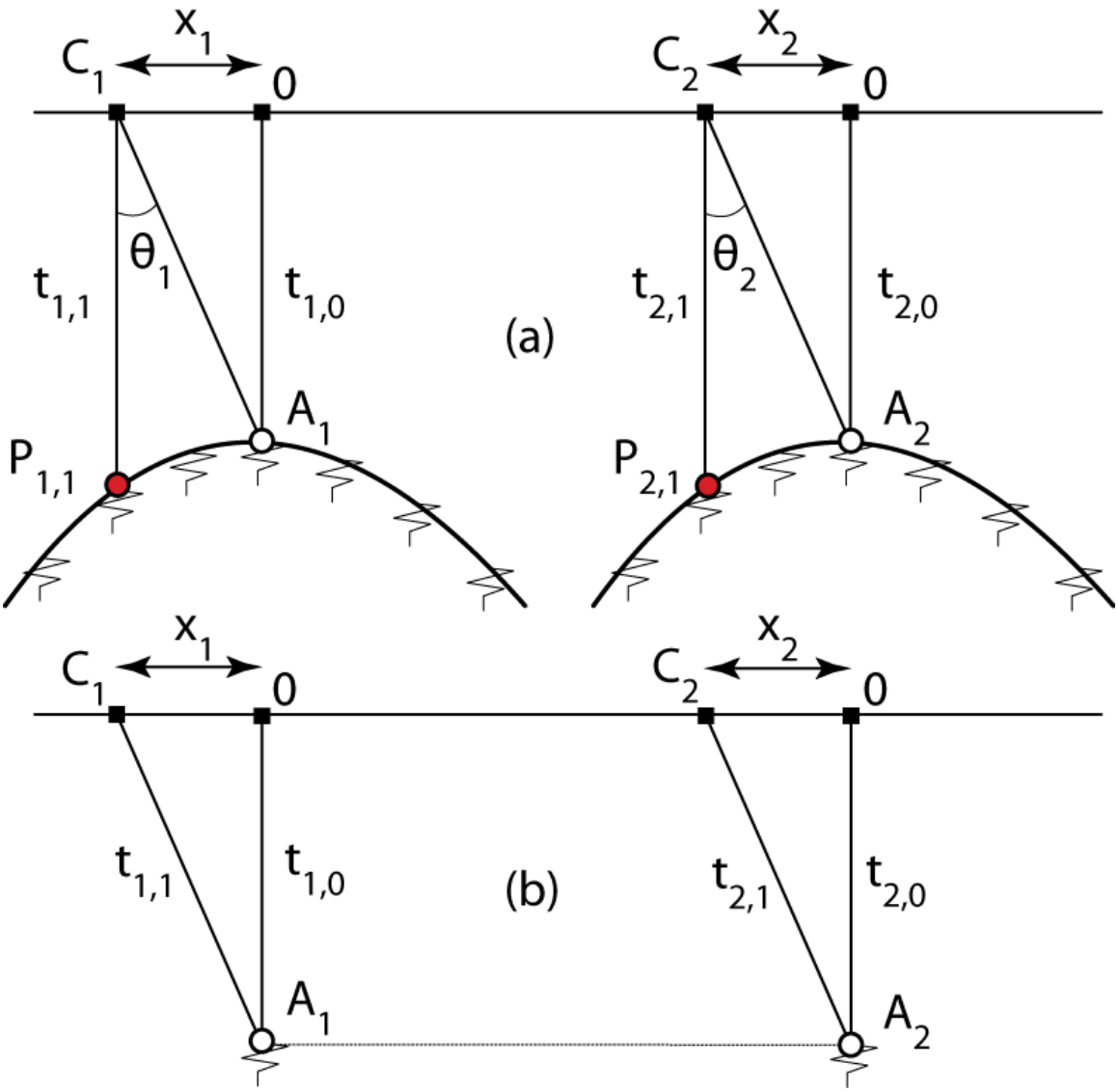

Figure 2.30: Illustration of the Kirchhoff migration principles. **(a)** Zero-offset stacked section, **(b)** Kirchhoff migration maps the amplitude at points $P_{1,1}$ or $P_{2,1}$ to apexes A_1 and A_2, respectively.

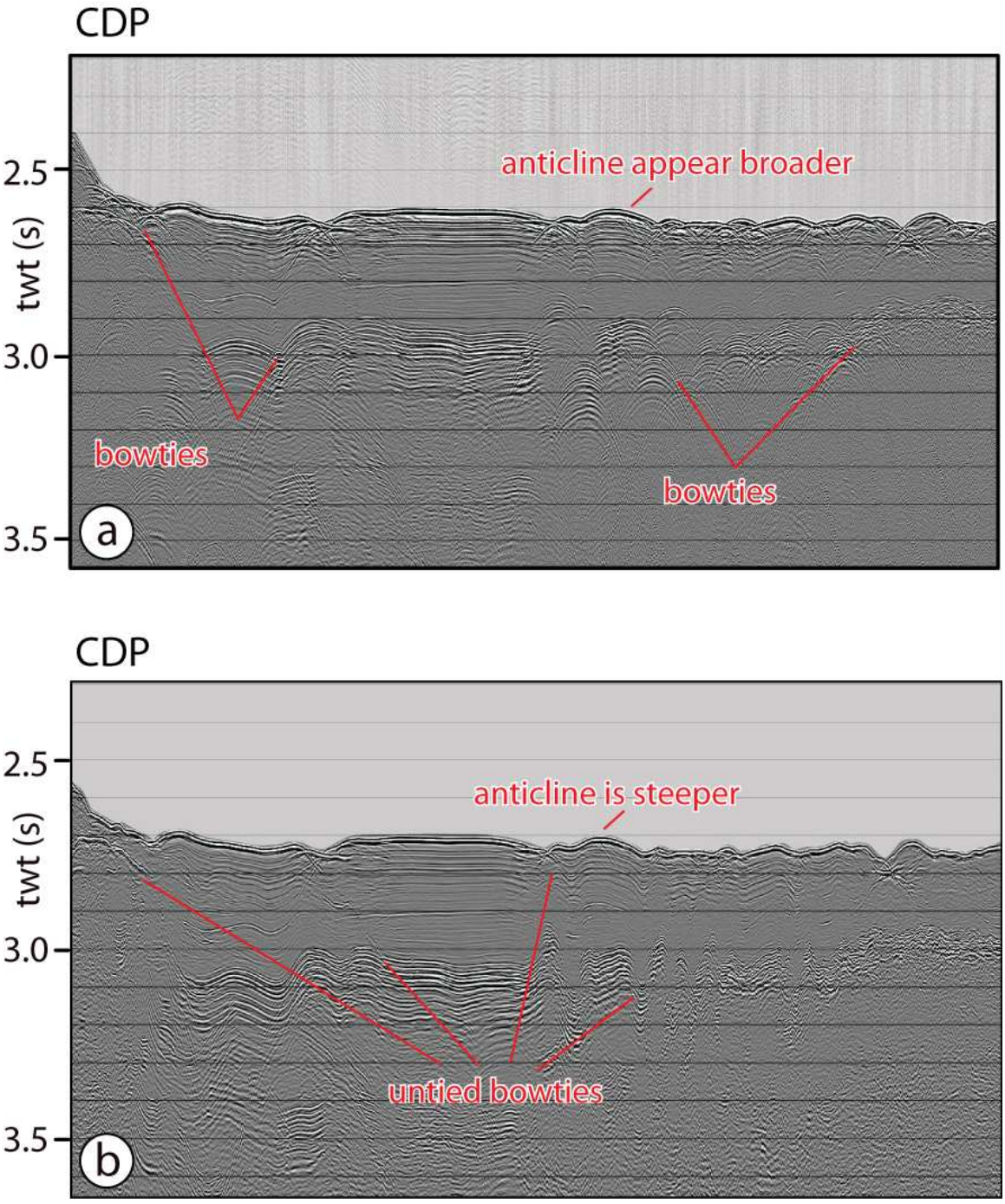

Figure 2.31: **(a)** The stacked section shows bowties and reflectors dip at incorrect angles, whereas **(b)** the migrated section shows that diffraction hyperbolae are collapsed and reflectors are repositioned nearer to their true subsurface locations.

technique was attempted to compress the seismic wavelet and increase the temporal resolution of the data however, this pre/post stack technique failed to be efficient because it introduced more high frequency energy to the seismic data.

A predictive deconvolution process is designed by analysing the autocorrelation for a given trace to determine the parameters required for deconvolution (Lines, 1996). The correct parameters (the prediction distance and the deconvolution operator length) of the predictive deconvolution removes the predictable part of the wavelet (the multiples) and only primary reflectors are left behind. The predictive deconvolution technique was also tested after the application of migration process to try to attenuate the seabed multiple both for 2007 and 2010 data sets. This deconvolution application only partially removed the sea bed multiple due to the presence of complex sea floor morphology and less than two multiple repetitions within the prediction window. Other types of multiple removal processes include frequency-wavenumber (FK) - domain multiple removal and the wave equation multiple removal (WEMR). However, neither of these techniques (FK and WEMR) proved to be particularly beneficial for this data set.

The application of a deep low velocity layer in migration was attempted to try and suppress the migration smiles coming from the residual sea bed multiples. Following the addition of the low velocity layer, the multiple was still over-migrated, but the smiles that penetrated up through the section were drastically reduced (Fig. 2.32a,b). In the end applying a trace mix to attenuate diffraction smiles from migration was also beneficial. Weighted trace mixes using of 5, 7, 9 or 11 traces were performed in different areas through the study area to reduce the diffraction smiles.

For the final display image of a seismic section a top-mute 20 ms above the seabed was constructed for each seismic reflection profile. This ensured a cleaner-looking final image. Before final output, the top-mute was applied to the data along with the 20-50-200-250 Ormsby bandpass filter and the 500 ms AGC filter. The final display for the fully processed profile is shown in Figure 2.33.

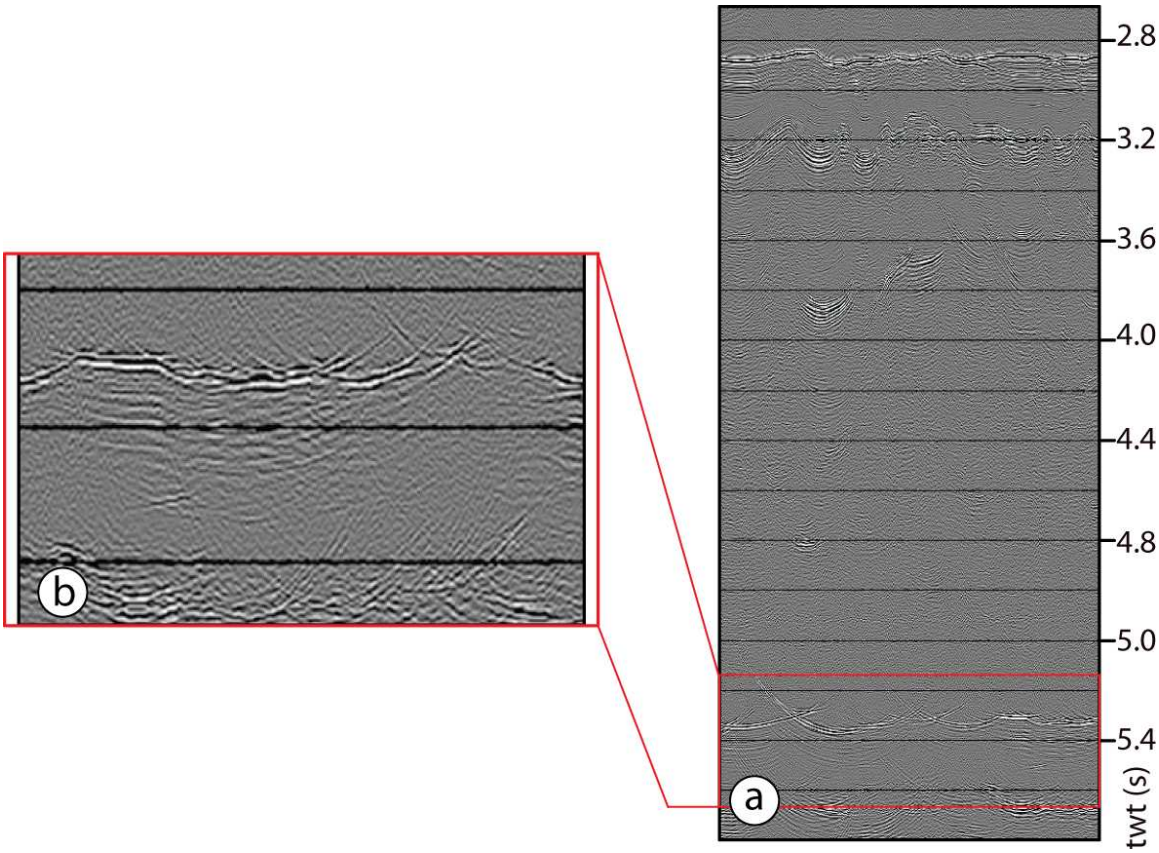

Figure 2.32: **(a)** Trace display of a final migration with no low velocity layer, **(b)** final migration with the application of a low velocity layer.

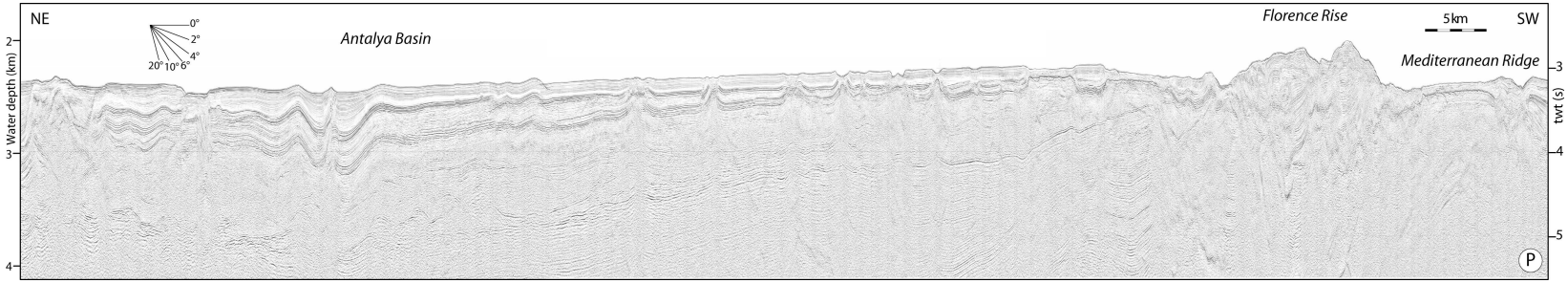

Figure 2.33: Fully processed Line A with final display parameters which include a 20 ms top-mute, a 20-50-200-250 Hz Ormsby bandpass filter and a 500 ms AGC. EMED10 (fix 1814-1904)

2.5 Interval Velocity Determination and Time-Depth Conversion

Accurate interval velocities are needed in order to carry out time – depth conversions. Although seismic reflection profiles are not depth-converted in this thesis, the average interval velocities are calculated for the upper Messinian–Quaternary and Messinian succession to allow accurate litho-stratigraphic interpretation and the correlations between well and seismic data. For this thesis it was assumed that $V_{NMO} \approx V_{RMS}$ (methodology for determining V_{NMO} described in previous section). The determination of the RMS velocities allows the calculation of interval velocity, V_{INT}, between one reflection with velocity V_{RMS_1} and a second reflection with velocity V_{RMS_2} using the Dix Equation:

Equation 2.8 $$V_{INT} = \{[(V_{RMS_2}^2 t_2/2) - (V_{RMS_1}^2 t_1/2)]/[(t_2/2) - (t_1/2)]\}^{1/2}$$

where t_1 and t_2 are the zero-offset TWT for the first and second reflectors, respectively. Once the interval velocity is determined, depth can be calculated using the simple relation

Equation 2.9 $$d = d_0 + V_{INT}(t_2 - t_1)$$

where d_0 is the depth to the first reflector (note that $V_{INT}(t_2 - t_1)$ gives the thickness of the layer). This process can be extended to calculate depth for multi-layered systems.

The sonic velocity data from the exploration wells and interval velocities from the seismic data processing show that the velocities in the upper Messinian–Quaternary sediments increase from $\sim$1500 m s^{-1} at the sediment–water interface to 2000–2300 m s^{-1} at the base of the succession, Miocene siliciclastic successions have interval velocities of 3000–3500 m s^{-1} and the Messinian evaporites of Unit 2 in the study area exhibit values ranging between 4200 and 4800 m s^{-1} (Fig. 2.34). The thickness of the MSC succession is calculated based on a constant velocity of 4200 m s^{-1} and we use a 2100 m s^{-1} constant velocity for the Pliocene-Quaternary succession.

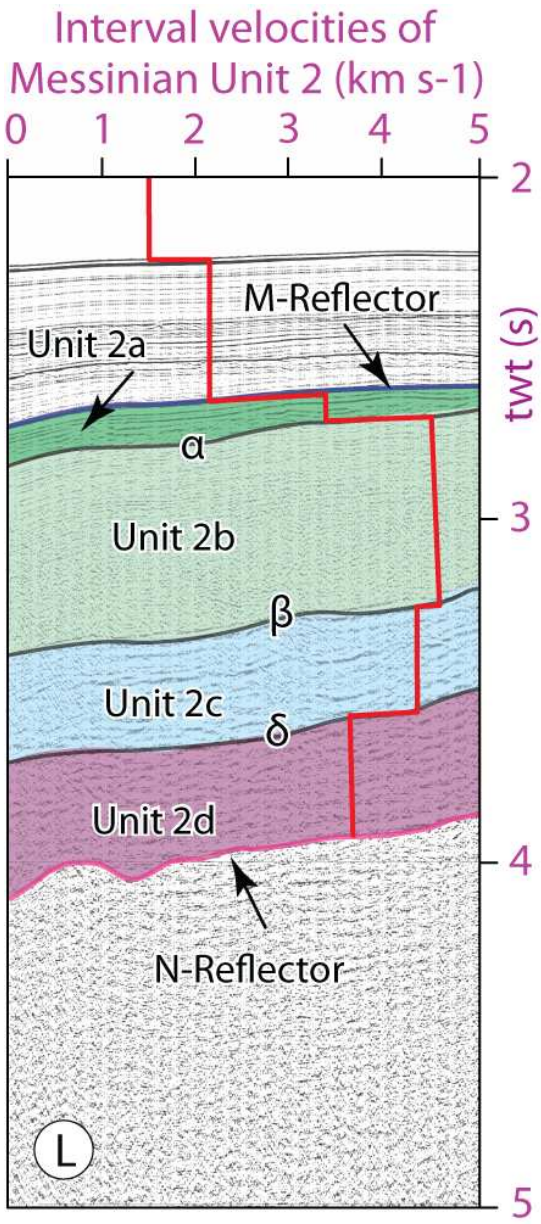

Figure 2.34: Segment of the high-resolution multi-channel seismic reflection profile L showing the interval velocity profile across the uppermost Messinian–Quaternary of Unit 1 and the Messinian evaporites of Unit 2. Note the notable velocity increases across the M- and α-reflectors and smaller velocity decreases across the β- and δ-reflectors. Location is shown in Figure 4.1. EMED10 (fix 1967-1971)L

2.6 Interpretation of 2D Seismic Data

Seismic interpretation is the science of inferring the subsurface geology from the processed seismic reflection profiles. Seismic interpretation consists of the distinction, tracing and correlation of relevant reflectors. Two basic elements of the seismic reflection data are very important: (a) the time of arrival of any reflection (or refraction) from a geological surface and (b) the actual depth to this surface which is a function of the thickness and velocity of overlying rock layers. The character of a particular reflection interval includes the strength and distribution of the reflections within it, , what frequencies it contains, and how the frequencies are distributed over the interval. This information can often be used to infer lithologic interpretation of the seismic reflector interval being evaluated.

In this study the major issues of geological interpretation are (a) establishing a litho- and chronostratigraphic framework by identifying and mapping important marker reflectors across the study area and (b) generating models which explain both structural and stratigraphic evolution of these features on a regional scale. During the seismic interpretation of the seismic reflection data, the following sequence is taken into consideration: (a) available subsurface geological data are used to acquire information on the acoustic characteristics of the subsurface and to evaluate the boundaries along which strong acoustic impedance contrast creates good mapping surfaces, and (b) various such markers are picked in the seismic reflection profiles where stratigraphic units are correlated and structures delineated across the study area.

The process of the interpretation of the seismic reflection profiles is divided into two interrelated categories: (a) stratigraphic interpretation and (b) structural interpretation. Structural interpretation is directed toward the creation of structural maps of the subsurface from the observed three-dimensional configuration of arrival times. Seismic sequence stratigraphic interpretation relates the pattern of reflections observed to a model of cyclic episodes of deposition. In this study lithology interpretation is aimed at determining changes in lithology from the available seismic data and its correlation with available well and outcrop data under the stratigraphic interpretation process for

the area of interest. The process of interpreting seismic data is performed both manually on paper copies of the seismic reflection profiles as well as in the workstation environment using the software DecisionSpace® by Landmark. The workstation offers advantages in data management, manipulation, and display however; interpretation on paper was more convenient and useful to have better correlation throughout the 2D seismic data set used in this study because of the long distance between the seismic profiles.

2.6.1 Approach to stratigraphic interpretation

The process of interpreting seismic data started with printing paper copies of the original seismic reflection profiles collected from the eastern Mediterranean during the research cruises in 2001, 2007 and 2010 from digital data files. The next step is inspecting the dataset to have a general idea about the basin setting, major structural components, and major stratigraphic components and major unconformities. After inspection, major faults are picked as a guide to establishing the dominant structural style and stratigraphic packages. Two prominent reflectors are identified: the M- and N-reflectors (Fig. 2.35) which divided the successions imaged in the seismic reflection profiles into three distinct seismic stratigraphic units (Units 1, 2, 3). Similarly less prominent reflections, α, β, γ, and δ allowed the seismic reflection profiles to be are divided into several subunits (Fig. 2.35). Next, distinctive seismic reflections, in particular those defining regional unconformities, are highlighted. Following this, unconformities are re-traced as precisely as possible and correlated throughout the seismic grid to ensure agreement at cross-over points. Unconformities are delineated on the basis of reflection terminations in seismic reflection profiles, particularly by onlap, downlap, toplap and erosional truncation (Fig. 2.36). The M- and N-reflectors and where possible the α, β, γ, and δ reflectors are traced through the seismic reflection data grid. The most critical step of the interpretation process was comparing how horizons and faults tie at line intersections. This process was strictly followed which allowed a reliable stratigraphic framework to be established across the study area.

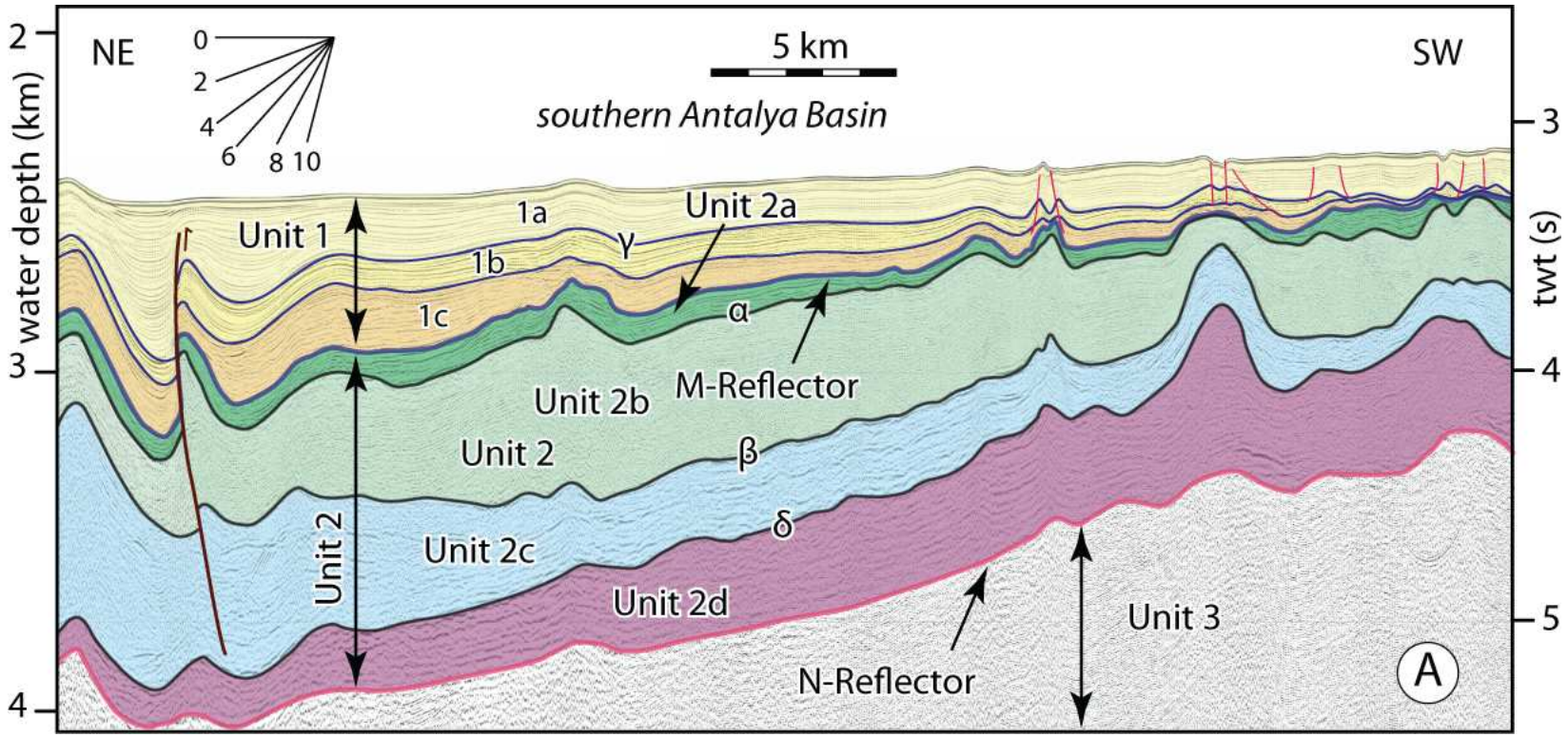

Figure 2.35: High-resolution multichannel seismic reflection profile (A) showing the prominent M- and N-reflectors that divides the stratigraphy into three units: Units 1–3. Also note the less prominent reflectors γ and an un-labeled reflector which divide the uppermost Messinian–Quaternary of Unit 1 into three subunits (1a–1c), and the α, β, and δ reflectors which define the bounding surfaces of the sub-units 2a–2d of the Messinian evaporite successions of Unit 2. Location is shown in Fig. 2.1 EMED10 (fix 1953-1978)

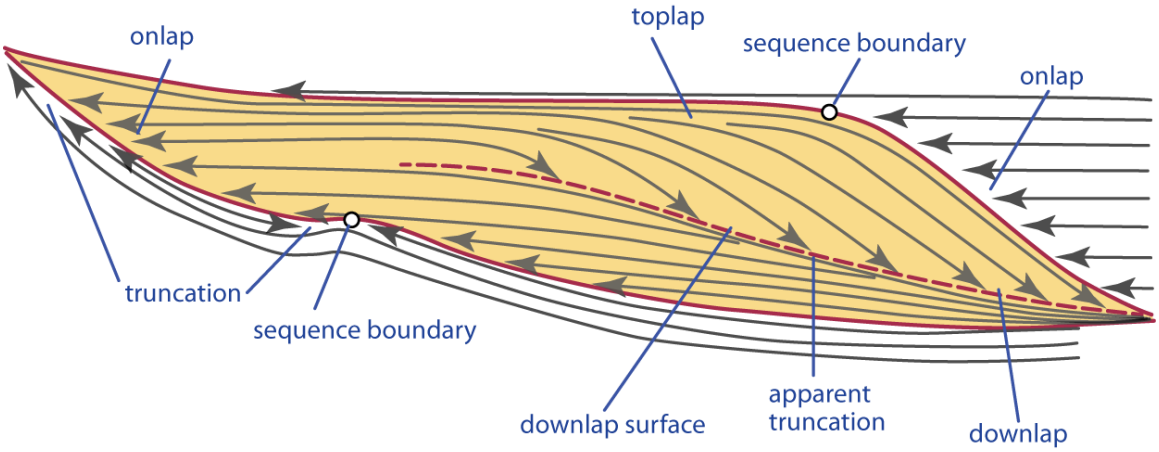

Figure 2.36: Schematic line drawing showing the reflection terminations that define the depositional sequence boundaries, where a depositional sequence is defines as a bundle of genetically-related reflectors that are bounded at their tops and bases by unconformities. Note that unconformities are defines by the reflection terminations of onlap, toplap, downlap and erosional truncation (adopted from Mitchum et al., 1977, also see http://www.oocities.org/znajeeb2000/geo.htm).

In the present study of the western Cyprus Arc region, the results of the interpretation of high resolution seismic reflection data are summarized with isochron maps, chronostratigraphic correlation chart, and the Messinian Salinity Crisis depositional model for the geologic time intervals of interest (i.e., Miocene to Recent). These are further described in Chapters 3 and 4.

2.6.2 Approach to Structural Interpretation

The structural interpretation of the available seismic data required a basic understanding of what tectonic influences and depositional systems occurred within the study area. Basins, ridges, salt structures and faults (both normal and reverse) were identified in this study. Identification of these structures are carried out at two levels: (a) direct observations of structural elements, such as faults where there is visible offset of distinct reflectors or reflector bundles, and/or the vertical trace of the fault planes are clearly visible in the seismic reflection profiles, and (b) indirect observations

of structures, such as blind faults, salt diapirs where the faults or salt diapirs are not readily visible in the seismic reflection profiles, but the presence of these structures are inferred on the basis of the secondary structures created by the them, such as the structures associated with thrusts: ramp anticlines consisting of asymmetric folds with short, steeply dipping forelimbs and long, gently dipping backlimbs, and growth strata wedges that developed associated with the faults (and also with halokinetic structures) (Fig. 2.37).

High-resolution multi-channel seismic reflection profiles often require vertical exaggeration so that the details of the structural and stratigraphic architectures can be clearly seen. Vertical exaggeration of seismic reflection profiles is a definite complicating factor for interpretation, because all structures are notably distorted (e.g., Fig. 2.38). For example, thrusts that are observed at low angles of $<10^{\circ}$ in the field studies appear nearly 70-80° in the vertically exaggerated sections. However, vertical exaggeration of the high-resolution seismic reflection profiles is a necessary "evil" and all seismic vintages required $\sim 7\times$ vertical exaggeration. Thus, during the interpretation special attention was paid to the fact that the sections are vertically exaggerated. Migration often improved the definition of complicated structures from areas where there has been major tectonic disturbance such as complex fault patterns and halokinetic movements. Finally, an angle scale showing the corresponding values of the exaggerated angles, a horizontal scale and an approximate vertical scale are presented in all figures showing the seismic reflection profiles to assist in the understanding of the dimensions and geometric relationships of stratigraphic and structural elements illustrated in the profiles. Chapters 4–6 contain full descriptions of the architecture structure across the Antalya Basin and western Cyrus Arc area of the eastern Mediterranean.

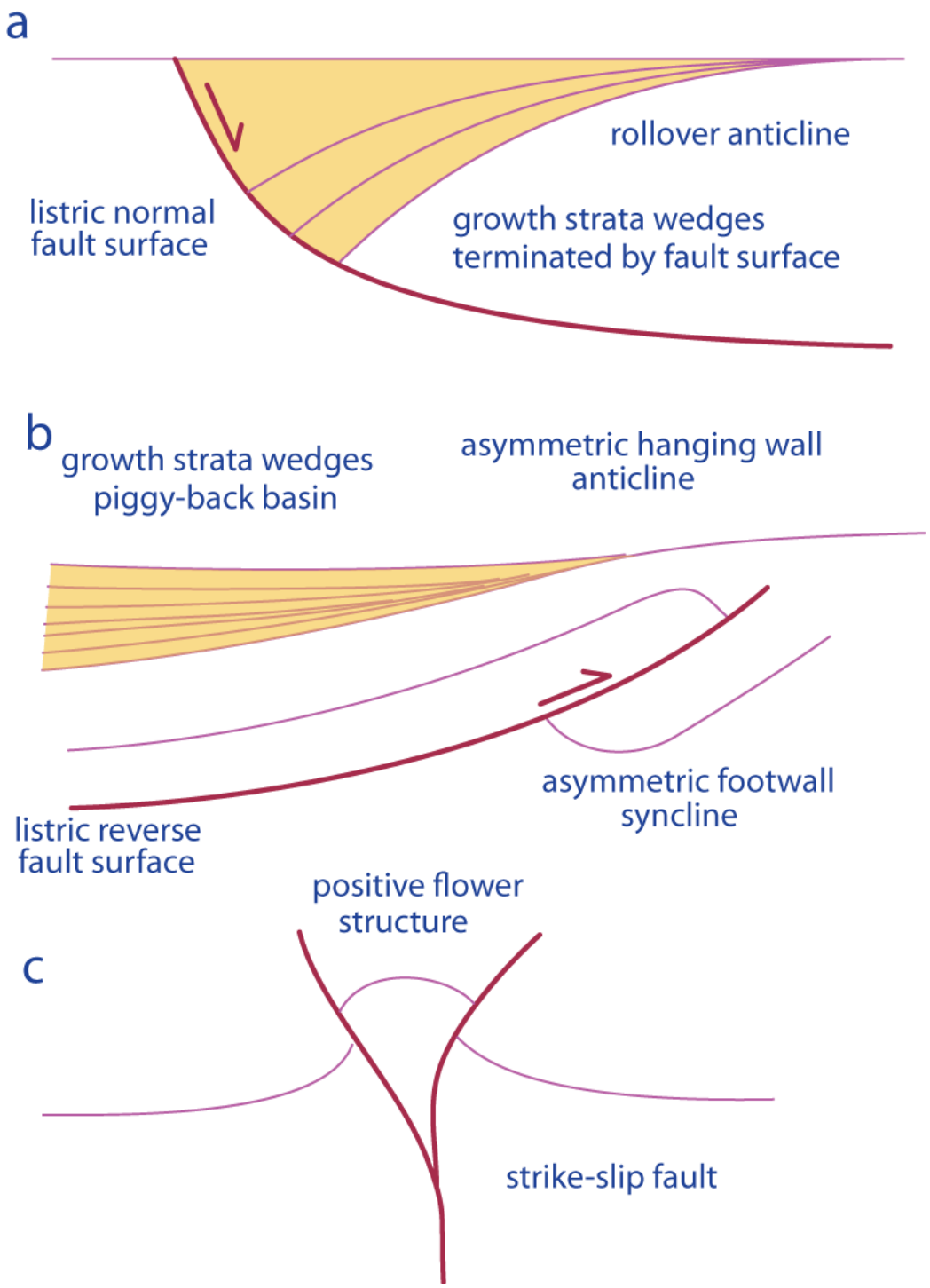

Figure 2.37: Cartoon showing the geometric relationships in the development of secondary structures associated with (a) listric normal faults, (b) thrusts, and strike- slip faults (c) (adopted from Hall et al., 2009).

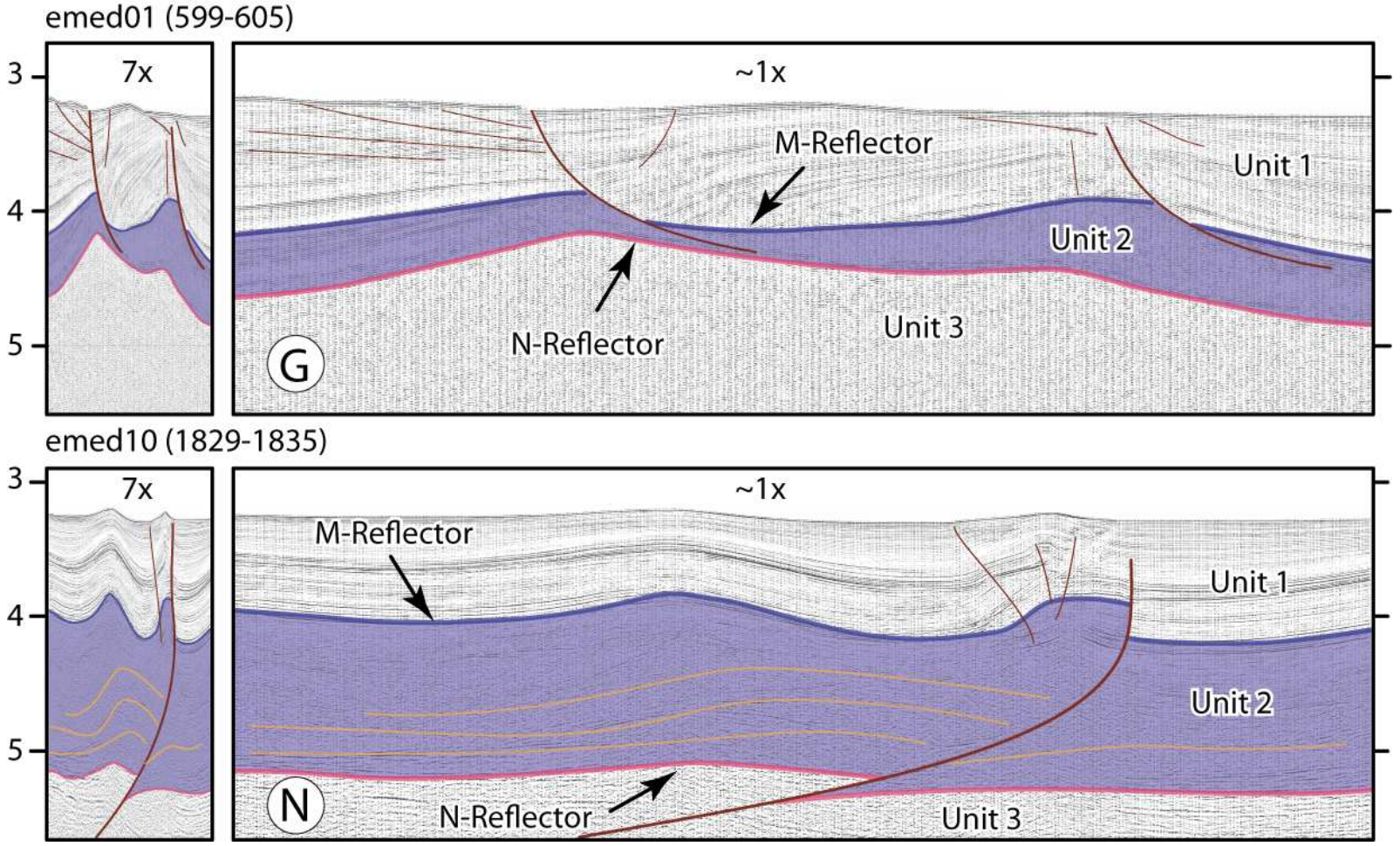

Figure 2.38: High-resolution multichannel seismic reflection profiles (B, C) showing the effects of vertical exaggeration. Note that the profiles on the left are 7× vertically exaggerated to show the exquisite stratigraphic and structural detail in the profile, whereas the profiles on the right are stretched to make the vertical exaggeration ∼1×. Also note how the listric fault trajectories (a) and the listric thrust trajectory (b) are notably steeper in the vertically exaggerated profiles. EMED01 (599-605) EMED10 (1829-1835)

Chapter 3

Miocene–Recent Stratigraphy and Chronology

This chapter describes the general stratigraphic and chronologic framework of the study area from the Miocene to the Recent. The seismic reflection profiles across the western Cyprus Arc, including the Florence Rise and the Antalya Basin show three seismic stratigraphic units (Unit 1, Unit 2 and Unit 3), separated from each other by the prominent M- and the N-reflectors. Each unit is distinguished by its acoustic character, reflection strength and reflection continuity. The lithostratigraphic composition and chronology of these seismic stratigraphic units are done using seismic stratigraphy and correlation with offshore Deep Sea Drilling Project, Leg XLII, Sites 375 and 376 and four exploration wells drilled in the onland Aksu, Köprüçay and Manavgat basins: Aksu-1, Ismail-1 Manavgat-1 and Manavgat-2 (Fig. 3.1).

3.1 Lithostratigraphy and Chronology of DSDP Sites 375 and 376

Two deep boreholes (Sites 375 and 376) were drilled on the Florence Rise by the Deep Sea Drilling Project (Shipboard Scientific Party, 1978; Fig. 3.1). The sediments encountered in these boreholes

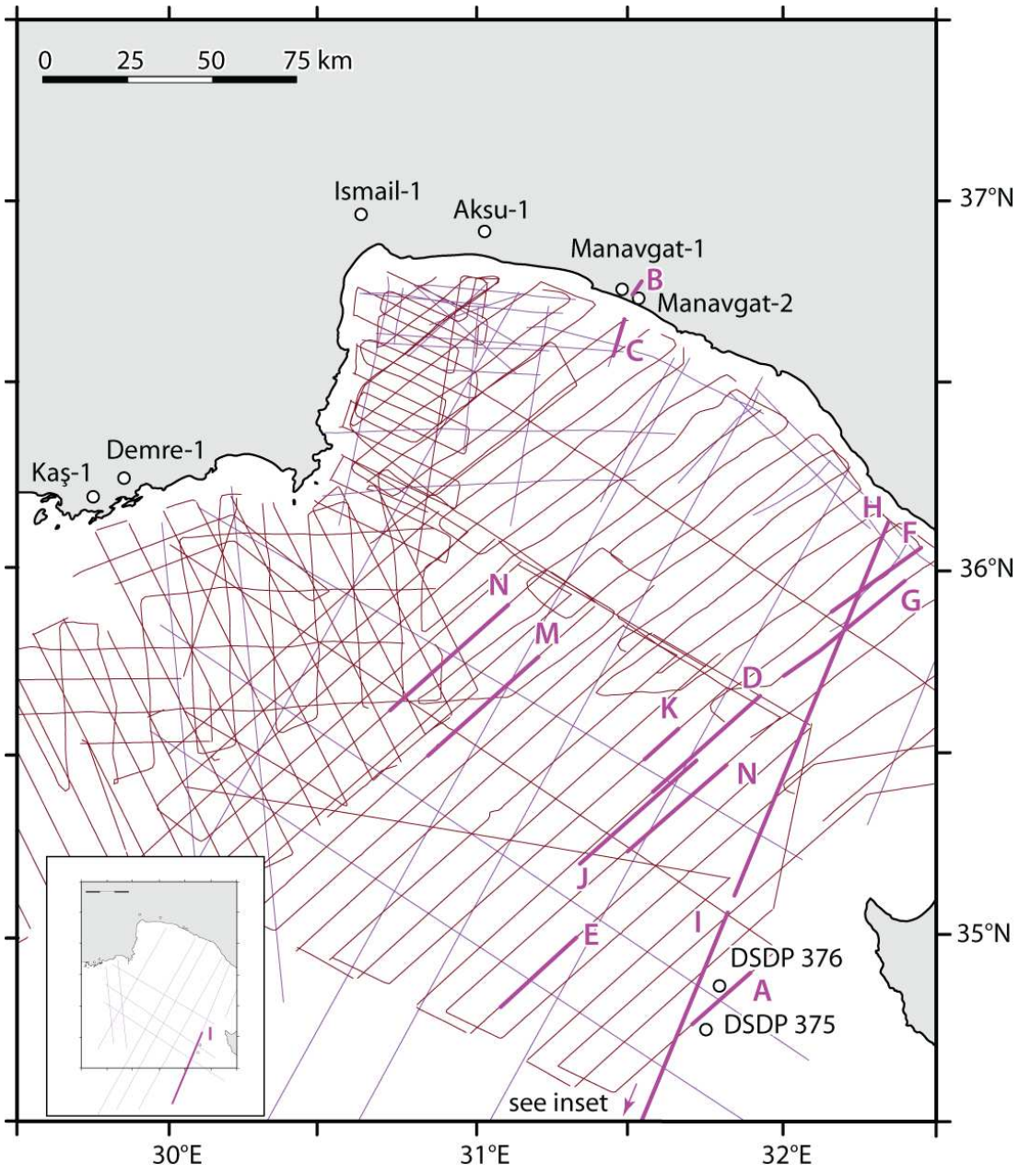

Figure 3.1: Map showing the locations of the seismic reflection profiles illustrated in this chapter. Also shown are the locations of the DSDP Sites 375 and 376 and the exploration wells Aksu-1, Ismail-1, Manavgat-1 and Manavgat-2 in the Aksu, Köprüçay and Manavgat basins, and the Demre-1 and Kaş-1 wells in the Kasaba Basin. The coastline is taken from the International Bathymetric Charts of the Mediterranean (IOC, 1981).

are described here in detail to form the basis for correlations between the lithostraigraphic units and the seismic reflection profiles used in this study. Site 375 had a total drill depth of 821.5 m with spot coring (Shipboard Scientific Party, 1978). A predominantly pre-evaporite succession was recovered at this site. Site 376 was offset $\sim$13 km to the north and was cored continuously into the Messinian evaporate succession. Eleven lithologic units have been distinguished at this site: four units in the Pliocene-Quaternary pelagic successions, two in the late Miocene evaporite and post evaporate successions, a flysch-type unit in the Tortonian, and four units in the pre-Tortonian to Early-Middle Miocene sediments (Shipboard Scientific Party, 1978; Fig. 3.2). These units are described below.

Unit I: nannofossil marl with interlayered sapropel and tephra

Unit I is of Quaternary age and consists of soft nannofossil marls with minor, thin interbeds of sapropelic marl and volcanic ash (Shipboard Scientific Party, 1978; Fig. 3.2). Nannofossil marls consist chiefly of clay minerals and nannofossils. Unit I is a hemipelagic sequence, which was deposited in an environment which fluctuated between a stagnant and highly reducing environment (sapropel layers), and a slightly oxidized environment (light brown layers). The absence of burrowing and the predominant drab gray color of the marlstones suggest that slightly reducing conditions prevailed during the deposition of this unit.

Unit II: gray nannofossil marls

Unit II consists of nannofossil and foram-nannofossil marls with generally dull colors and a soft, but firm texture (Shipboard Scientific Party, 1978; Fig. 3.2). It is Late Pliocene in age. The upper part of the unit contains scattered small pyrite nodules. Burrows appear to be absent, except for slight burrowing at the base of the unit. The depositional setting of Unit II appears to have been similar to that for Unit I: generally reducing bottom conditions with periodic and short lived intervals of strong

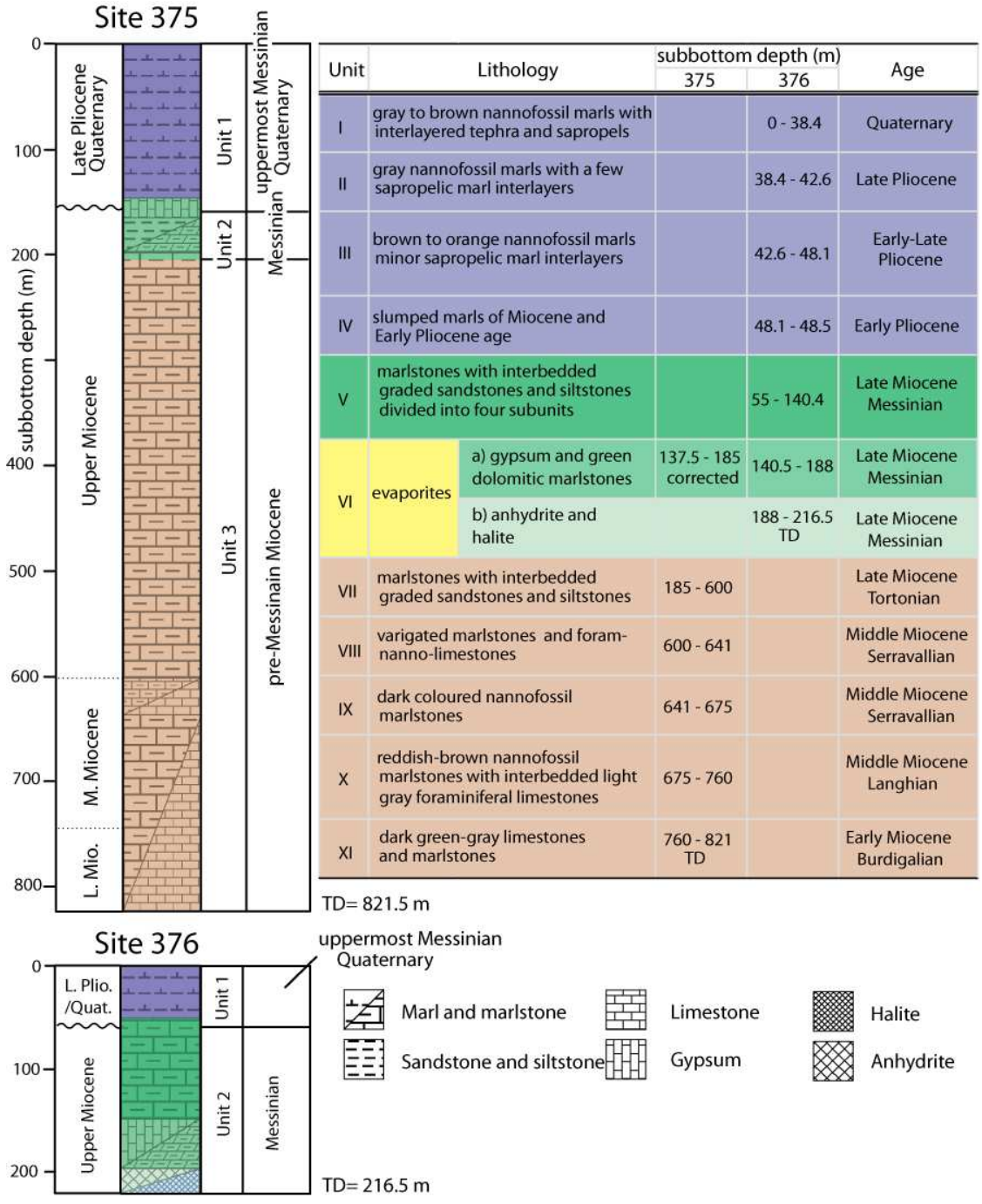

Unit	Lithology		subbottom depth (m) 375	subbottom depth (m) 376	Age
I	gray to brown nannofossil marls with interlayered tephra and sapropels			0 - 38.4	Quaternary
II	gray nannofossil marls with a few sapropelic marl interlayers			38.4 - 42.6	Late Pliocene
III	brown to orange nannofossil marls minor sapropelic marl interlayers			42.6 - 48.1	Early-Late Pliocene
IV	slumped marls of Miocene and Early Pliocene age			48.1 - 48.5	Early Pliocene
V	marlstones with interbedded graded sandstones and siltstones divided into four subunits			55 - 140.4	Late Miocene Messinian
VI	evaporites	a) gypsum and green dolomitic marlstones	137.5 - 185 corrected	140.5 - 188	Late Miocene Messinian
		b) anhydrite and halite		188 - 216.5 TD	Late Miocene Messinian
VII	marlstones with interbedded graded sandstones and siltstones		185 - 600		Late Miocene Tortonian
VIII	varigated marlstones and foram-nanno-limestones		600 - 641		Middle Miocene Serravallian
IX	dark coloured nannofossil marlstones		641 - 675		Middle Miocene Serravallian
X	reddish-brown nannofossil marlstones with interbedded light gray foraminiferal limestones		675 - 760		Middle Miocene Langhian
XI	dark green-gray limestones and marlstones		760 - 821 TD		Early Miocene Burdigalian

Figure 3.2: Lithostratigraphy of the DSDP Sites 375 and 376 (adopted from Shipboard Scientific Party, 1978). Also shown are the seismic stratigraphic units and their assigned ages used in this study (see text for detail).

stagnation and a few episodes when the bottom waters were oxidized.

Unit III: brown to orange nannofossil marls

Unit III is characterized of nannofossil marls with bright colors (such as light brown, pale yellowish-brown, yellowish-gray, moderate brown and very pale orange) indicative of oxidizing conditions (Shipboard Scientific Party, 1978; Fig. 3.2). It is Early to Late Pliocene in age. The unit is well bedded and contains numerous thin layers which are moderately burrowed and apparently enriched in iron oxides, giving them a darker brown color than the surrounding sediment.

Unit IV: slumped marls

Unit IV consists of light to medium gray marls of Early Pliocene to Late Miocene in age (Shipboard Scientific Party, 1978; Fig. 3.2). It comprises two chaotically deformed subunits. ***Subunit IVa***; consists of medium gray nannofossil marls mixed with light brown marls, with a sharp and undeformed upper contact with Unit III. ***Subunit IVb***; consists of light brown to pale yellowish-brown nannofossil marls. Lithologically this marl is identical to the brownish, oxidized marls of Unit III above. Unit IV is interpreted as a slump succession.

Unit V: nannofossil dolomitic marlstone, interbedded sandstones, siltstones

Unit V consists of nannofossil marlstones and dolomitic marlstones of latest Miocene age. Siltstones and sandstones within this upper marl and marlstone unit are interpreted as turbidites (Shipboard Scientific Party, 1978, Fig. 3.2). In Unit V, a supply of fresh or brackish waters from continental sources is also indicated by isotopic data (McKenzie and Ricchiuto, 1978; Ricchiuto and McKenzie, 1978; Pierre and Fontes, 1982). Marine microfossils, such as oligotypic planktonic foraminifera and cysts of marine planktonic algae have been identified in several horizons, which also suggest the occasional influx of marine waters into this predominantly brackish "*Lago Mare*" environment. Unit V is com-

posed of four subunits which invariably contain the Cyprideis pannonica fauna, and is interpreted as latest Messinian in age (Shipboard Scientific Party, 1978). Four subunits are recognized based on color differences, mineralogical composition, and on the relative proportions of marlstones and clastic sedimentary rocks. ***Subunit Va*** mainly contains slightly silty nannofossil dolomitic marlstone, with minor amounts of interbedded siltstones and sandstones, including sapropelic layers. ***Subunit Vb*** consists of interbedded silty nannofosil dolomitic marlstones, siltstones and sandstones. It differs from Subunit Va in having a higher percentage of interbedded clastics and in containing no sapropelic layers. ***Subunit Vc*** contains thinly bedded inter-layered laminated siltstones and marlstones of probably turbiditic origin. ***Subunit Vd*** differs from the others in containing gypsum often as gypsiferous sandstone layers.

Unit VI: Mediterranean evaporites

Unit VI contains gypsum, green dolomitic marlstone, anhydrite and halite which are identified as Messinian in age (Shipboard Scientific Party, 1978; Fig. 3.2). It is composed of two subunits. ***Subunit VIa*** uncomfortably underlies Unit V and contains olive gray to light gray gypsum. The unit includes crudely layered and recrystallized gypsum, coarse selenitic gypsum crystals, coarsely crystalline recrystallized gypsum with roughly equant and traced anhydrite and elongate selenitic "swallow-tail" gypsum crystals, set in a matrix of gypsiferous greenish-white marlstone. ***Subunit VIb*** contains from top to base: (i) numerous small pieces of clear, coarsely crystalline halite with thin wavy interlayers of finely crystalline gypsum; (ii) larger fragments of white nodular anhydrite with large and small inter-oolitic folds and occasional chicken-wire structure with considerable amounts of gypsum; (iii) fragments of banded anhydrite, in which thin dark brown, organic-rich laminae separate up to 1 cm thick bands of nodular anhydrite with occasional chicken-wire structure and (iv) banded halite with 2 to 4 cm thick layers of clear coarsely crystalline halite separated by 0.5 cm thick, brown, fine-grained gypsum layers containing rare anhydrite (see Chapter 5 for detail

explanation and correlation of Messinian evaporites).

Unit VII: marlstones with interbedded graded siltstones and sandstones

This unit consists of a predominantly dark colored, partly dolomitic marlstone sequence (Shipboard Scientific Party, 1978; Fig. 3.2). It is upper Miocene (Tortonian) in age. Typically, the sequence shows a distinct cyclicity, with each cycle consisting of three members instead of subunits. Member A is a fine-grained terrigeneous arenite and siltstone with a sharp lower boundary. It grades upwards into of the structureless, occasionally finely-laminated, dolomitic nannofossil marlstone with rare sand and volcanic glass. This succession is in turn, overlain by marlstones with sparse burrowing.

Unit VIII: variegated nannofossil marlstones to foram-nanno limestones

Unit VIII consists of variegated mudstones, nannofossil marlstones and foram-nanno limestones, which exhibit cyclic centimeter- to decimeter-scale alternations of dark mudstones and marlstones and light-colored foram-nanno limestones (Shipboard Scientific Party, 1978; Fig. 3.2). The dark layers are characterized by a sharp lower boundary. They gradually pass upwards into the light colored more calcareous and foraminifer-rich marlstone and limestones. The unit is Serravallian in age. Unit VIII represents an episode of slower deposition of distal turbidites and hemipelagic marls in a slightly more oxidizing environment between the dark marlstones of Unit IX (see below) and the dark greenish turbiditic facies of Unit VIII.

Unit IX: dark colored nannofossil marlstones

The Unit consists of dark colored mudstones and nannofossil marlstones interlayered with lighter colored, more calcareous nannofossil marlstones (Shipboard Scientific Party, 1978; Fig. 3.2). The age of the Unit IX recovered is Serravallian. The main difference between Unit IX and the underlying Unit X and overlying Unit VIII is mainly the change of colors, which range from medium dark gray

to grayish-brown. The sequence shows a cyclic development, similar to the ones in Unit VIII and X, with darker-colored argillaceous lithologies grading into lighter-colored calcareous lithologies. The darker units show sharp lower boundaries and faint parallel lamination and occasionally graded and cross laminated layers of fine sand and silt are present at the base. The light colored lithologies contain traces of terrigenous silt.

Unit X: nannofossil marlstones, interbedded foraminiferal limestones

Unit X is composed of reddish-brown dolomite-bearing nannofossil marlstones with interbedded grayish-blue green to greenish-gray nannofossil marlstones and hard, well cemented, very light colored gray to bluish-white foraminiferal limestones (Shipboard Scientific Party, 1978; Fig. 3.2). The age of Unit X is Langhian. In Unit X various kinds of cycles can be observed. Cycles similar to the ones described in Units VIII and XI consist of grayish-blue-green to greenish-gray and dark greenish-gray marlstone with sharp lower boundaries. Another type of cycle is composed of very light gray and bluish-white to pale blue, hard cemented foraminiferal limestones with sharp lower boundaries which grade into gray or red marlstones.

Unit XI: dark green-gray limestones and marlstones

Unit XI is composed of hard grayish-olive limestones and green marlstones (Shipboard Scientific Party, 1978; Fig. 3.2). It is Langhian in age. Recovery of samples from this unit is very poor. The limestones include planktonic foraminifera filled with a ferroan calcite cement and greenish-gray foraminifera-rich nannofossil-limestone, which are interbedded with greenish-black marlstones.

3.2 DSDP Site 375 and 376 Sonic Velocity Data

Figure 3.3 shows sounds velocity vertical and horizontal measurement through the sediments recovered at Sites 376 and 375 by the Shipboard Scientific Party (1978). Very little physical property

data were obtained at Site 375 primarily because coring did not begin until the drill bit reached the evaporite layer at 137.5 meters. High velocities (4.5 to 4.9 km s^{-1}) were measured through pieces of coarsely crystalline gypsum recovered from between 139 and 194 m sub-bottom (Fig. 3.3). Slightly higher values (5.5 km s^{-1}) were measured through pieces of thin, hard, laminated limestone layers recovered from 733 to 736 m sub-bottom. Some velocities measured in dolomitic marlstones and nannofossil marlstones cored intermittently between 653 to 736 m sub-bottom ranged from 2.49 to 2.79 km s^{-1}. Lower velocities (1.98 to 2.02 km s^{-1}) are characteristic of dolomitic nannofossil marlstones recovered near 250 and 570 m sub-bottom (Fig. 3.3; Shipboard Scientific Part, 1978).

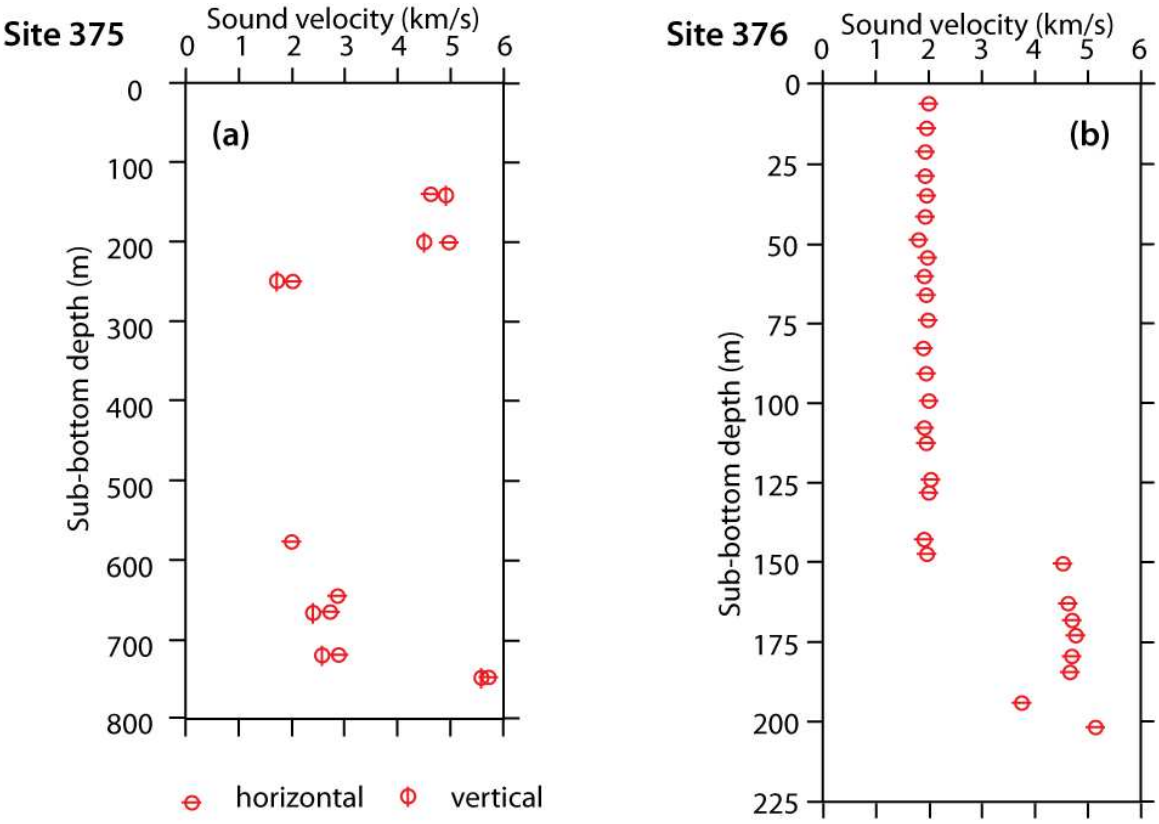

Figure 3.3: Sound velocity values measured in the horizontal (red circles with horizontal bars) and vertical (red circles with vertical bars) directions on sediments recovered at Sites 375 and 376 (adopted from Shipboard Scientific Party, 1978).

Site 376 sonic velocity data are summarized in Figure 3.3b (Shipboard Scientific Part, 1978). Immediately apparent in this figure is the very small velocity increase from about 1.5 km s^{-1} at the sea floor to about 1.7 km s^{-1} at 140 m sub-bottom. Velocities determined through pieces of gypsum recovered from below 140 m were high (4.4 to 5.2 km s^{-1}). A single velocity measurement through a piece of siltstone recovered from 186.4 m gave an intermediate velocity of 3.64 km s^{-1}. The very low seismic velocity and its constancy with depth above the evaporite layer are unusual features, in view of the rather well-consolidated sediments recovered at this site (Fig. 3.3). The increases noted in bulk wet density is poorly reflected in the velocity profile, and in fact the significant density decrease observed at 65 m coincides with a subtle velocity increase. The approximate constancy of the thermal conductivity data with depth is also in general agreement with the velocity data (Shipboard Scientific Part, 1978).

3.3 Correlation of seismic reflection profiles with DSDP Sites 375 and 376

DSDP Sites 375 and 376 are located over the crest of the southeastern segment of the Florence Rise, which is a marked bathymetric feature extending from south of the Island of Cyprus to the Anaximander Mountains (*sensu lato*), and separating the Antalya Basin from the Mediterranean Ridge (Figs. 3.1; Shipboard Scientific Party, 1978). A critical multichannel seismic reflection profile (i.e., EMED07-02) transect the Florence Rise in a northeast-southwest direction, allowing correlations to be made with the sedimentary successions drilled at the DSDP Sites 375 and 376 (Figs. 3.4, 3.5). This profile is located 2.9 km southeast and 3.4 km northwest of the DSDP Sites 376 and 375, respectively. The lithologies described in DSDP Sites 375 and 376 are grouped into three distinct chrono-stratigraphic units: (1) uppermost Messinian–Quaternary siliciclastics; (2) Messinian evaporites with interbedded siliciclastics; and (3) pre-Messinian Miocene siliciclastics and carbonates.

These three chrono-stratigraphic units are correlated with the seismic stratigraphic units identified across the Florence Rise and the Antalya Basin: seismic Unit 1 is correlated with the uppermost Messinian–Quaternary siliciclastic successions; seismic Unit 2 is correlated with the Messinian evaporite and interbedded siliciclastic successions, and seismic Unit 3 is correlated with the pre-Messinian Miocene siliciclastics and carbonates (Figs. 3.4, 3.5).

In order to correlate the sedimentary successions drilled in the DSDP wells and the seismic reflection profiles the thicknesses encountered in the wells had to be converted to depth in milliseconds. The following interval velocities of 1700-1800 m s^{-1}, 3500-5000 m s-1 and 2500-3000 m s^{-1} are used to convert the thicknesses of the uppermost Messinian–Quaternary siliciclastics, Messinian evaporate succession and the pre-Messinian upper Miocene successions, respectively.

Unit 1 is the youngest sedimentary succession in the study area and contains uppermost Messinian–Quaternary siliciclastic rocks. Drilling at Sites 375 and 376 showed that the uppermost Messinian–Quaternary siliciclastics succession across the crest of the Florence Rise is $\sim$137.5 meters thick (Shipboard Scientific Party, 1978; Fig. 3.2). Calculations using the above interval velocities suggest that the thickness of the uppermost Messinian–Quaternary succession in line EMED07-02 (i.e., Fig. 3.4) is $\sim$160 m. At the DSDP Sites 375 and 376 the Messinian evaporites are $\sim$ 48 m and 68 m thick, respectively. Similar calculations suggest that there must be $\sim$19–39 ms-thick Messinian succession corresponding to Unit 2 is imaged in seismic profile EMED07-02 (Figs. 3.4, 3.5). Unit 2 is composed of siliciclastic and carbonate successions interbedded with evaporites arising from the cyclical near desiccation of the eastern Mediterranean during the Messinian. Underlying the Messinian evaporites a $\sim$485 m succession of Tortonian and Serravalian marls and turbidites of Unit 3 were drilled at Site 375 (Fig. 3.2; Shipboard Scientific Party, 1978). Calculations using the above interval velocities suggest that there must be a $\sim$415 m-thick pre-Messinian strata must be present in seismic profile EMED07-02 (Figs. 3.2, 3.4). Seismic profile EMED07-02 shows that the thick Messinian evaporite successions of Unit 2 in southern Antalya Basin and northern portion of

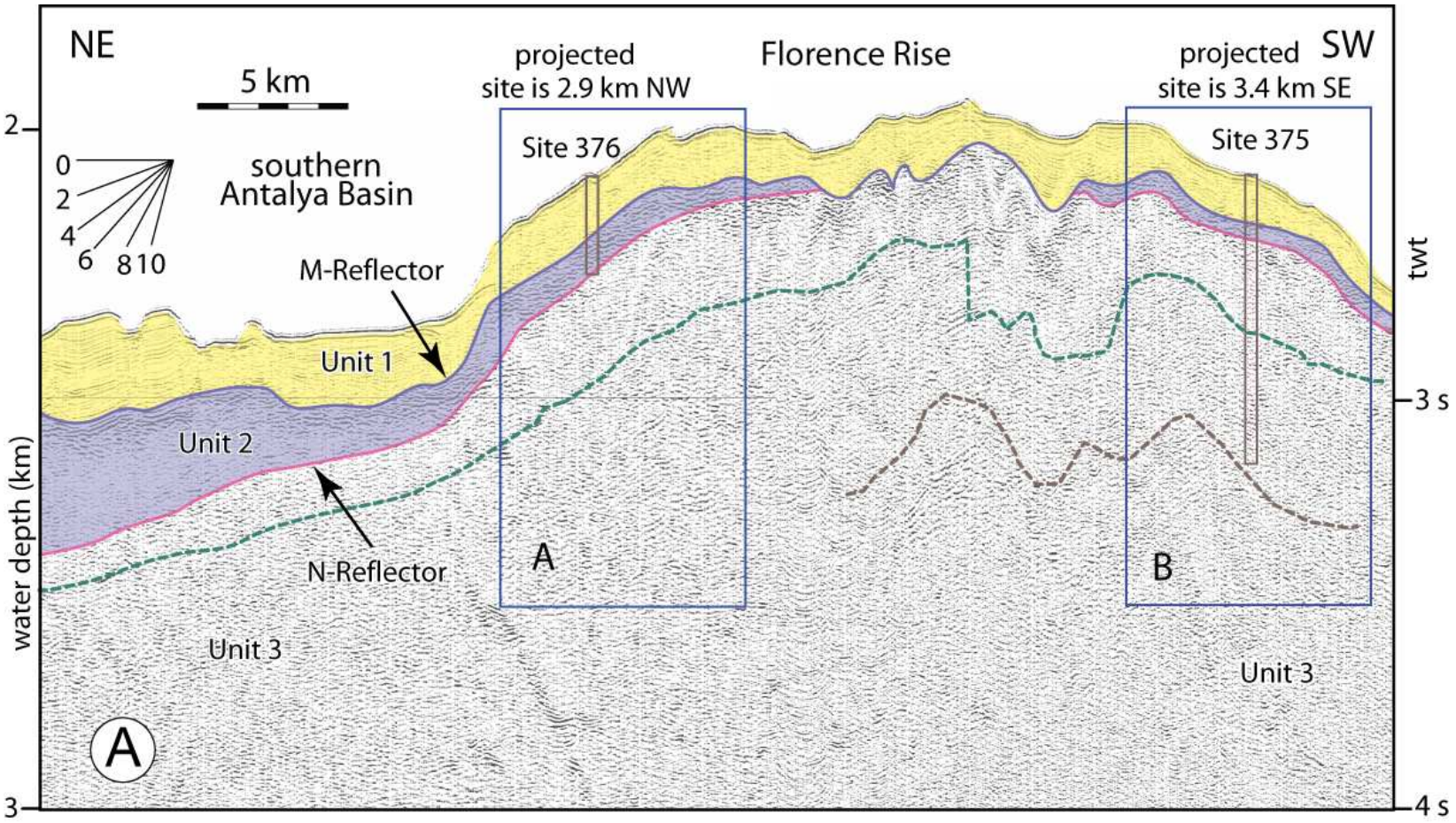

Figure 3.4: High-resolution seismic reflection profile A showing the broad morphology of the Florence Rise and the locations of the DSDP Sites 375 and 376. Red insets are shown in Figure 3.5. Location is shown in Figure 3.1. EMED07 (fix 0167-0183)

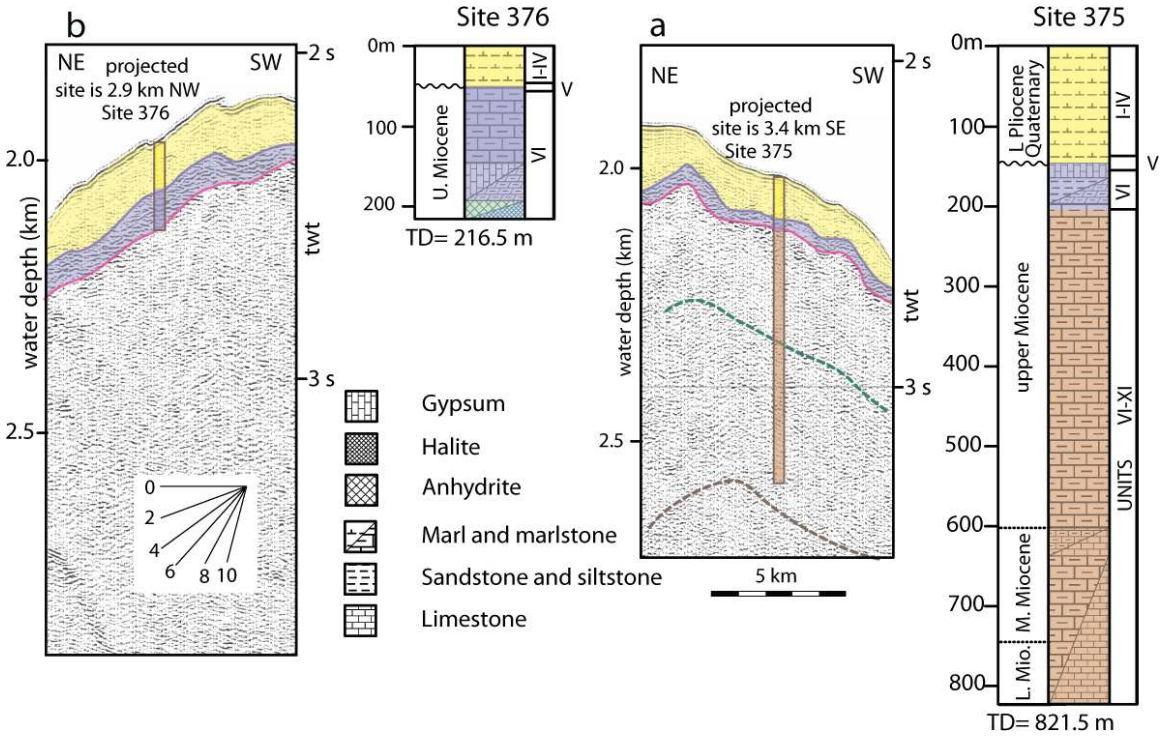

Figure 3.5: Seismic stratigraphic correlation between section (a) and (b) of profile (A) and the DSDP Sites 375 and 376. See Figure 3.2 for detail lithological information from the wells (from Shipboard Scientific Party, 1978). Location of the seismic profile and the wells are shown in Figures 3.1 and 3.4.

the Mediterranean Ridge pinch out along the northern and southern sectors of the Florence Rise, bringing the pre-evaporitic layers (Unit 3) closer to the sea floor, below a thin cover of uppermost Messinian–Quaternary sediments of Unit 1 (Figs. 3.4, 3.5).

3.4 Stratigraphic and chronologic correlation with onshore wells

Stratigraphic and chronologic correlation between the onshore and offshore study area has been performed on the basis of exploration well data from onshore extension of the Antalya Basin. Previous work studied the entire onshore Antalya Neogene basin, which is subdivided in three sub-basins from east to west: the Manavgat, Köprüçay and Aksu sub-basins (Bizon et al., 1974; Akbulut, 1977; Monod, 1977; Gutnic et al., 1979; Dumont, 1976; Poisson et al., 1983, 1984, 2003a,b; Akay et al., 1985; Akay and Uysal, 1985; Karabıyıkoğlu et al., 1997, 2000, 2005; Tuzcu and Karabıyıkoğlu, 2001; Deynoux et al., 2005; Çiner et al., 2008). The Manavgat and Köprüçay basins are separated by the north-south striking Kırkavak fault, and the Köprüçay and Aksu basins by the north-northwest–south-southeast striking Aksu thrust. There are four exploration wells drilled in the onland Aksu, Köprüçay and Manavgat basins: Manavgat-1, Manavgat-2, Aksu-1 and Ismail-1 (Fig. 3.1).

The chronology of the Manavgat-2 well in the onland Manavgat basin is critical for this study because the successions encountered in the Manavgat-2 well can be readily correlated with the seismic stratigraphic units identified in the seismic reflection profiles (Fig. 3.6). The Manavgat-2 well was drilled to a total depth of 2565 m (Figs. 3.6, 3.7; Turkish Petroleum Corporation, unpublished data). The well recovered $\sim$ 204 m of loosely consolidated to unconsolidated claystone with few sandstone interbeds. These sediments are assigned to the Pliocene–Quaternary Yenimahalle Formation. Below this upper veneer, there is a 290 m thick siliciclastic succession composed of sandstones and shales with several volcanic tuff horizons (Fig. 3.7). Although the sediments drilled in the Manavgat-2 well did not include any evaporites (such as the gypsum, anhydrite and evaporitic carbonates seen

on outcrops; Deynoux et al., 2005; Çiner et al., 2008), this succession is correlated with the Late Miocene Taşlık Formation on the basis of biostratigraphic information. The Taşlık Formation is the lateral equivalent of the evaporitic deposits of the Gebiz Formation, associated with the Messinian Salinity Crisis (e.g., Garrison et al., 1978). It is conformably underlain by a 445 m thick siliciclastic succession consisting of sandstone, siltstone and claystone interbeds, which is correlated with the Tortonian Karpuzçay Formation (Fig. 3.7; Turkish Petroleum Corporation, unpublished data). Below the Karpuzçay Formation the well recovered a 436 m thick siliciclastic succession with several well-defined limestone beds (Fig. 3.7), correlated with the Aquitanian–Serravallian Geceleme Formation. This succession is underlain by a 171 m-thick prominent limestone unit, which is referred to in the Aksu, Köprüçay and Manavgat basins as the Oymapınar Formation (Akay and Uysal, 1985; Akay et al., 1985). At the base of the Oymapınar Formation the well encountered a 575 m thick sequence of Geceleme Formation sediments, clearly indicating a repetition of stratigraphy (Fig. 3.7). A northeast–southwest trending industry seismic reflection profile explains this age reversal: the Manavgat-2 well drilled through a broadly northeast-verging thrust at $\sim$1.1 second depth where a strongly reflective seismic package is clearly duplicated (Figs. 3.6, 3.7). The Manavgat-1 well a few km to the northwest was drilled away from the thrust, and so does not include the duplication seen in the Manavgat-2 well. The Manavgat-2 well recovered an additional 128 m of siliciclastic successions with carbonate interbeds, which are correlated with the Aquitanian–Burdigalian Aksu Formation (Figs. 3.6, 3.7).

Ismail-1 and Aksu-1 wells located west and east of Antalya respectively (Fig. 3.1). The Ismail-1 well intersected 250 m of Quaternary limestone of the upper Tufa Formation, and then recovering $\sim$100 m of Upper Mesozoic chert, limestone and shale (Çatal Tepe nappe; Yenice Boğazı unit) and Mesozoic peridotites of the Antalya Complex (Özbey and Bagnasco, 1960). Tertiary deposits are absent in this well and this probably means that the border of the Antalya Neogene basin remained located further to the east, during the Miocene and Pliocene times (Poisson et al., 2011). By con-

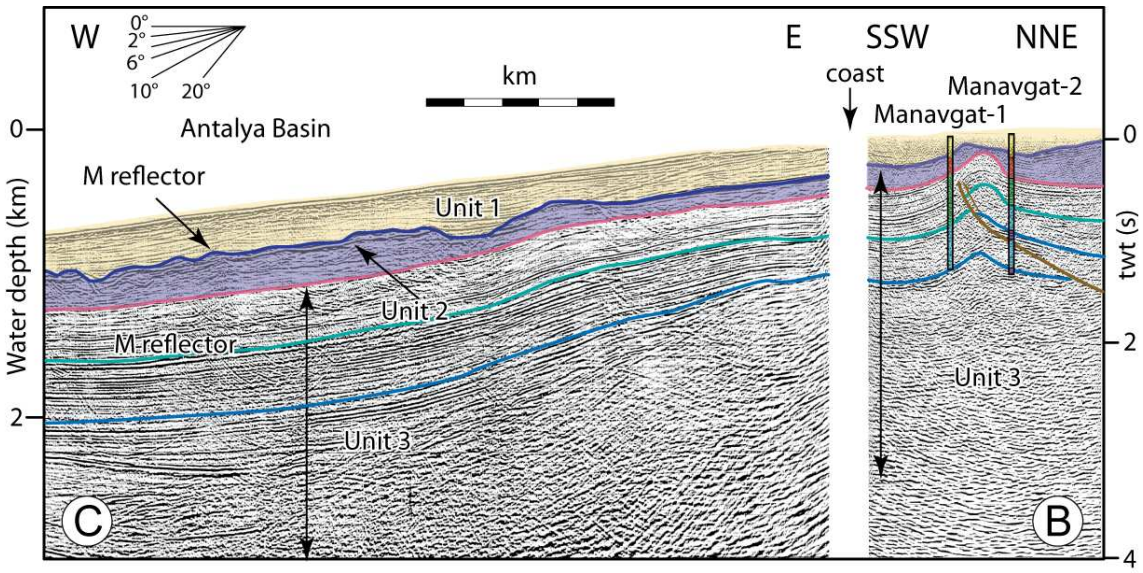

Figure 3.6: Industry seismic reflection profiles (B and C) showing the projected locations of theManavgat-1 andManavgat-2 exploration wells, and the seismic stratigraphic correlation into the northern Antalya Basin. Note that there is a major NE-verging thrust that produced a duplication of the lower Miocene successions in the Manavgat-2 well. Profile is kindly provided by the Turkish Petroleum Corporation. Location of the seismic profile and the wells are shown in Figures 3.1 and 3.4. TP2 & TP11

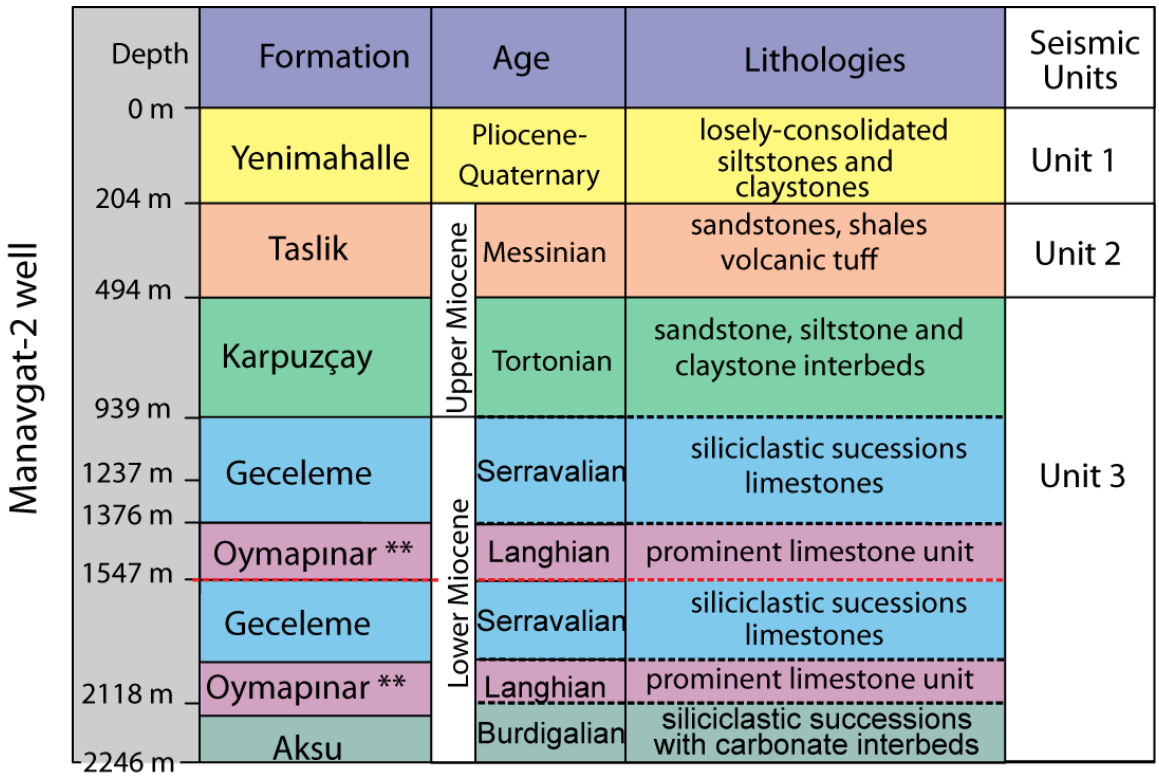

Figure 3.7: Lithologies recovered in the Manavgat-2 exploration well with their approximate thicknesses and ages. Note the stratigraphic age reversal at 1547 m depth; this is interpreted by the Turkish Petroleum Corporation as evidence that a major Miocene thrust is intercepted by the Manavgat-2 exploration well. Data kindly provided by the Turkish Petroleum Corporation.

trast, the Aksu-1 well is deeper (2856 m) and crosses only the Quaternary and Tertiary deposits (Fig. 3.8). The Aksu-1 well recovered ∼131 m thick of Quaternary alluvium, consisting of clay, silt, sand, and gravel left by flowing streams in a river valley or delta (surface rather than subsurface; Şenel, 1997a,b). The alluvium is uncomfortably underlying by ∼550m thick siliciclastic succession consisting of claystone which is correlated with lower Pliocene Yenimahalle Formation (Turkish Petroleum Corporation, unpublished data). The Aksu-1 well revealed the existence of a duplication in the Burdigalian-Langhian sequences above the fragments of the Antalya Complex (Fig. 3.8; Şenel, 1997a,b; Poisson et al., 2011). This duplication is interpreted as the western leading thrusts of the Aksu thrust system (Poisson et al., 2011).

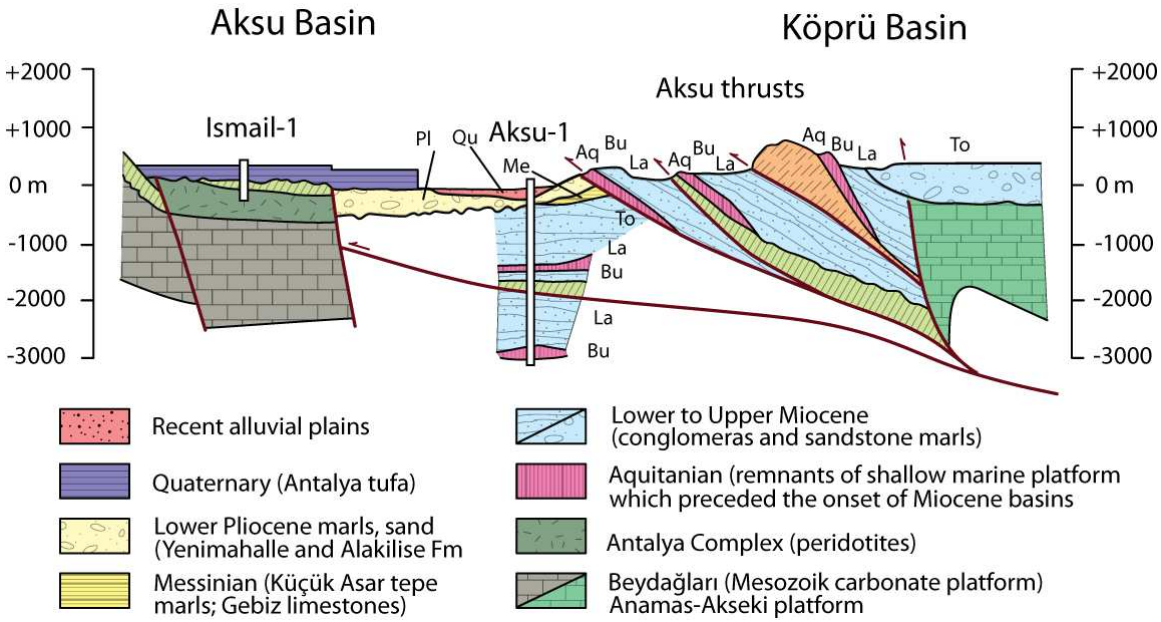

Figure 3.8: Interpretative W-E transverse cross section across the onland central part of the Antalya Basin from the Aksu Basin to the west to the Köprüçay Basin to the east (modified from Poisson et al., 2011). Two exploration deep wells give data for the interpretation of the deep structure of the basin: the Ismail-1 and Aksu-1 wells (Şenel, 1997a,b) revealed the existence of a duplication of the Miocene sequence with fragments of Antalya nappes at 2000 m below the surface interpreted as a blind thrust related to the Aksu phase of deformation (Poisson et al., 2011).

3.5 Description of seismic stratigraphic units and their bounding surfaces

On the basis of acoustic character, stratigraphic position and location of the M and N unconformities, three distinct seismic units are identified in the marine Antalya Basin: (a) Unit 1: uppermost Messinian–Quaternary siliciclastic successions; (b) Unit 2: Messinian evaporites and interbedded siliciclastic successions and (c) Unit 3: the undifferentiated pre-Messinian siliciclastic and carbonate successions (Fig. 3.9). The lithostratigraphic composition and chronology of these units are determined through correlation with onshore and offshore exploration wells discussed in detail above (Figs. 3.2, 3.5–3.8, 3.10). These units are further correlated with sedimentary successions identified in the adjacent Adana, Mesaoria, Cilicia, Latakia basins and the onshore Antalya basin (discussed below).

3.5.1 Description of M- and N-reflectors

The M- and N-reflectors observed in seismic reflection profiles across the eastern Mediterranean Sea represent distinctive regional unconformities. The M-reflector is first described by Ryan (1969), as well as many subsequent studies (e.g., Işler et al., 2005, Aksu et al., 2005, 2009, 2014a–c, Hall et al., 2009, 2014a,b). The M-reflector marks the erosional surface which developed during the Late Miocene (Messinian) when the closing and re-opening of the Gibraltar Strait caused a cyclic, nearly-complete desiccation of the entire Mediterranean Sea (e.g., Garcia-Castellanos and Villaseñor, 2011). In most of the previous studies, the M-reflector is commonly defined as a major unconformity separating the latest Miocene sequences from the oldest Pliocene sedimentary successions (e.g., Hsü et al., 1978; Robertson, 1998, Işler et al., 2005, Aksu et al. 2005, 2009, Hall et al. 2009). However, seismic stratigraphic interpretations and their correlations with both onshore and offshore well data presented in this study and in Walsh-Kennedy et al. (2014) indicate that the

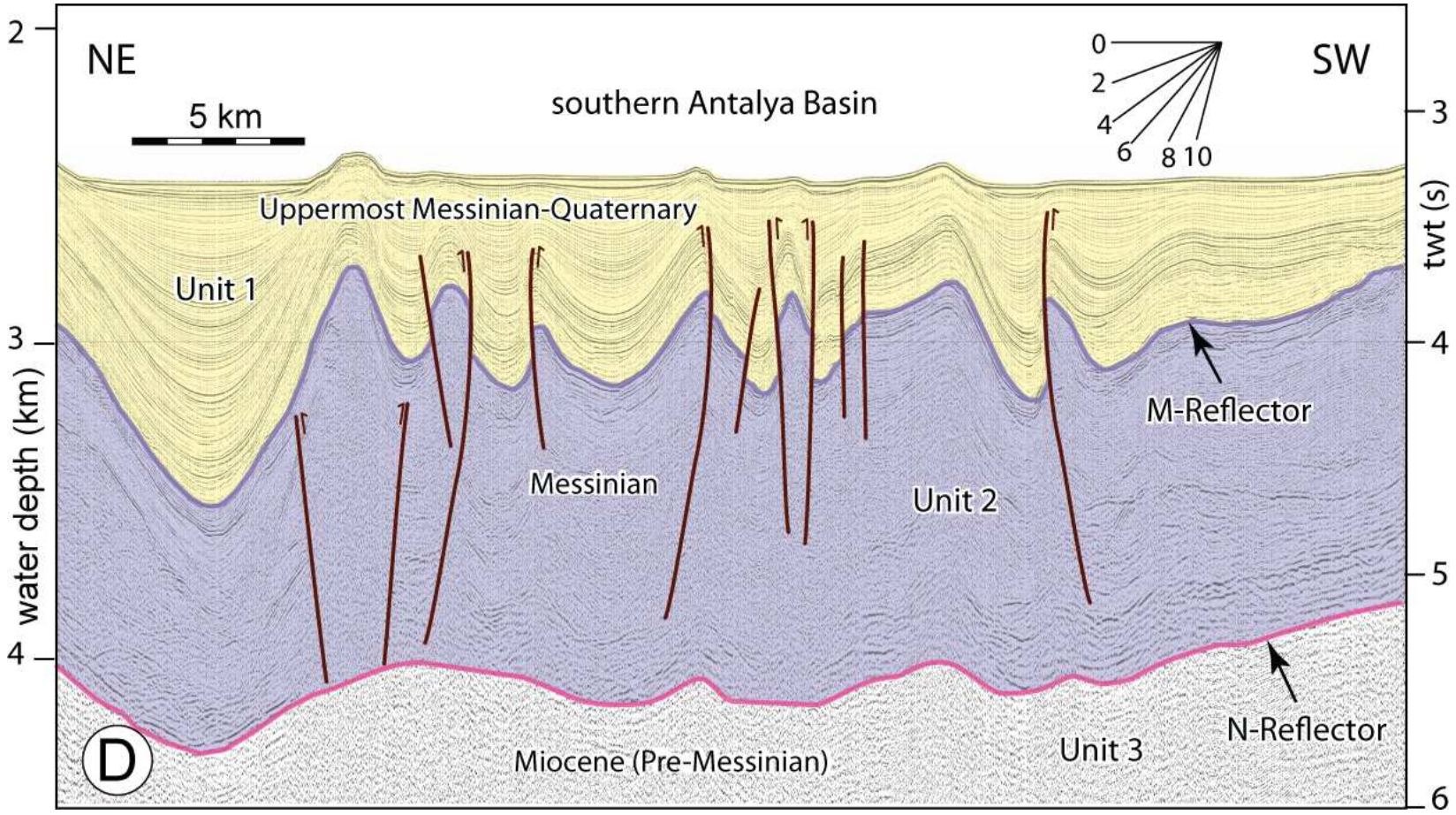

Figure 3.9: High-resolution multichannel seismic reflection profile D showing the architecture of seismic stratigraphic units described in text. The prominent M and N reflectors define the top and base of the evaporite successions of Unit 2, respectively. EMED10 (fix 1972-1998)

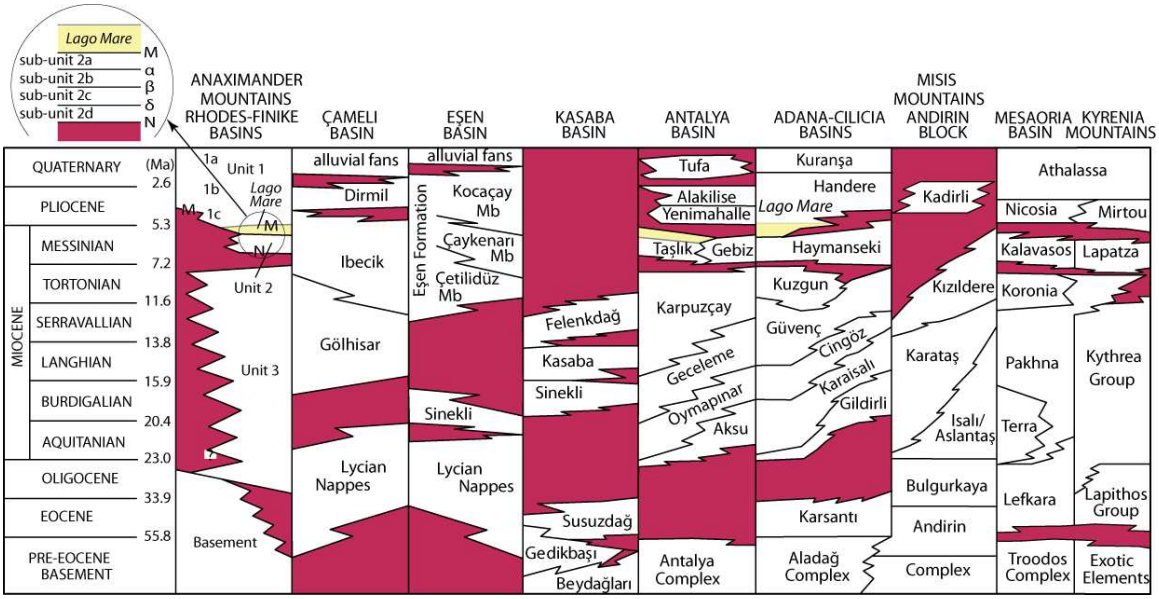

Figure 3.10: Stratigraphy of the Florence Rise and Antalya Basin showing the correlations between seismic stratigraphic units and the sedimentary successions on land, compiled from: (a) Adana and Cilicia basins, Andirin Block= Yalçın and Görür (1984), Kozlu (1987), Yılmaz et al. (1988), Gökçen et al. (1988), (b) Mesaoria Basin and Kyrenia Range= Weiler (1969), Cleintaur et al. (1977), Robertson et al. (1995), (c) Aksu, Köprüçay and Manavgat basins= Akay and Uysal (1985), Akay et al. (1985), Flecker et al. (1998), Karabıyıkoğlu et al. (2000, 2005), Kasaba Basın= Hayward (1984), Şenel (1997a,b), Şenel and Bölükbaşı (1997), Çameli Basin = Elitez and Yaltırak (2014), Eşen (Çay) Basin = Alçiçek et al. (2006); Alçiçek (2007). Stratigraphy of the Manavgat-1 and Manavgat-2 wells is from the Turkish Petroleum Corporation (unpublished data). Units 1 through 3 and M and N are reflectors delineating the top and base of the Messinian successions, discussed in text.

M-reflector corresponds to the bounding erosional surface marking the top of the Messinian Salinity Crisis evaporite deposits of Late Miocene, separating these evaporites from the uppermost Messinian where the post-evaporitic *Lago-Mare* sediments exist (Fig. 3.10). The M-reflector is imaged as a bright, laterally continuous acoustically strong marker on almost all seismic reflection profiles and serves as an important stratigraphic marker across the Florence Rise and Antalya Basin (e.g., Figs. 3.11, 3.12). It is laterally traceable in to the Messinian Erosional Surface which developed around basin margins during the Messinian lowstand, beginning at $\sim$5.97 Ma.

In the northwestern Antalya Basin and southwestern Florence Rise, extensive deformation of the subsurface makes the usually prominent M-reflector more difficult to discern. In this area, the placement of the M-reflector is inferred using stratigraphic cut-offs and the thicknesses and acoustic character of the overlying and underlying sedimentary sequences (Figs. 3.13, 3.14).

The N-reflector marks the base of Unit 2 in regions where the Messinian evaporites successions are present. In the Florence Rise and the Antalya Basin, the N-reflector is imaged as a bright, continuous marker in the seismic reflection profiles, where it usually displays an opposite polarity to the M-reflector (Figs. 3.9–3.11, 3.13, 3.14). In these areas, the N-reflector separates the Messinian evaporite sequences from the Tortonian and older Miocene successions. The M- and N-reflectors are further discussed in Chapters 4 and 5.

3.5.2 Unit 1: Uppermost Messinian–Quaternary

Unit 1 comprises the youngest succession recognized within the Antalya Basin, Florence Rise and its environs. Unit 1 is characterized by a regularly reflective sediment package that consists of acoustically strong reflectors. These reflectors show excellent lateral continuity throughout the study area, and reflectors from Unit 1 display the highest frequency content recorded in the seismic profiles (Fig. 3.9). The base of this unit is marked by a major angular unconformity. On the basis of its acoustic character and stratigraphic position at the base of the upper unit, this unconformity is cor-

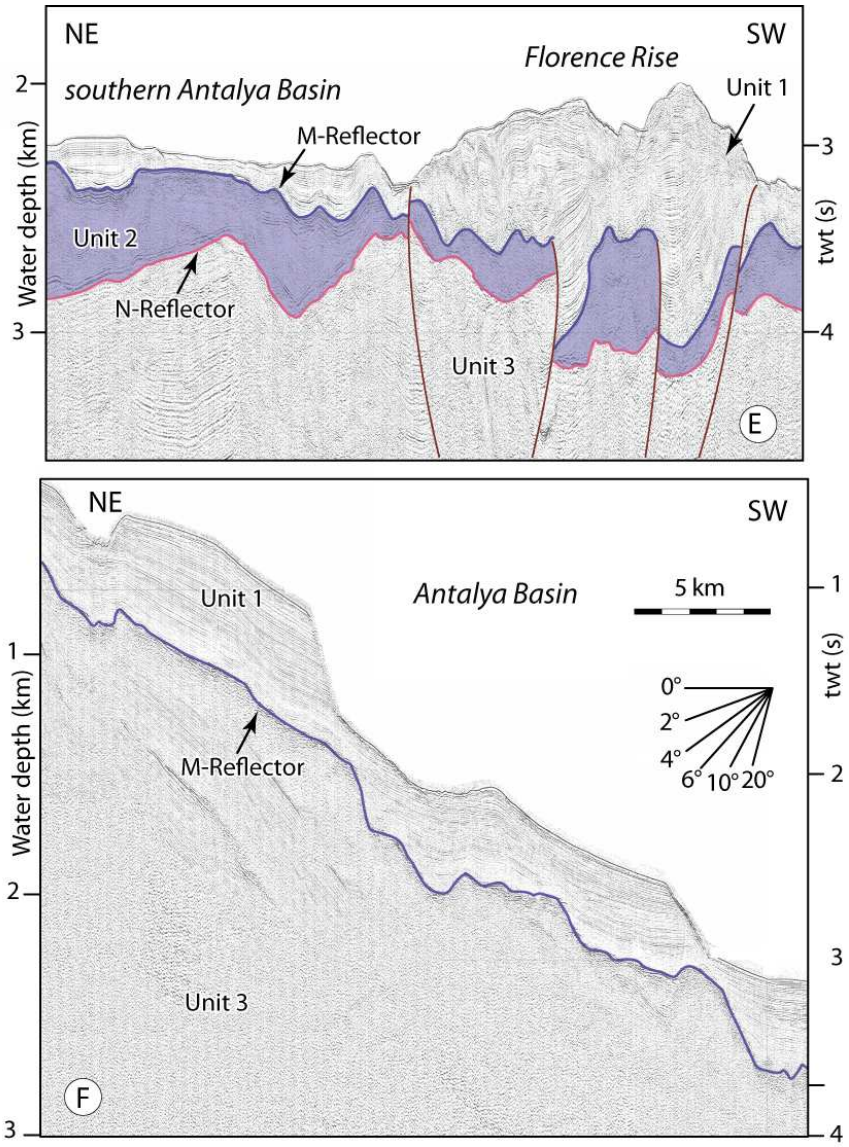

Figure 3.11: High-resolution seismic reflection profiles E and F showing the acoustic character of the M- and N-reflectors across the study area. Note that in regions where the Messinian evaporite and siliciclastic successions of Unit 2 are missing, the M-reflector is imaged as a prominent composite unconformity. Locations are shown in Figure 3.1. EMED92 (fix 1778-1798), EMED10 (fix 1875-1895)

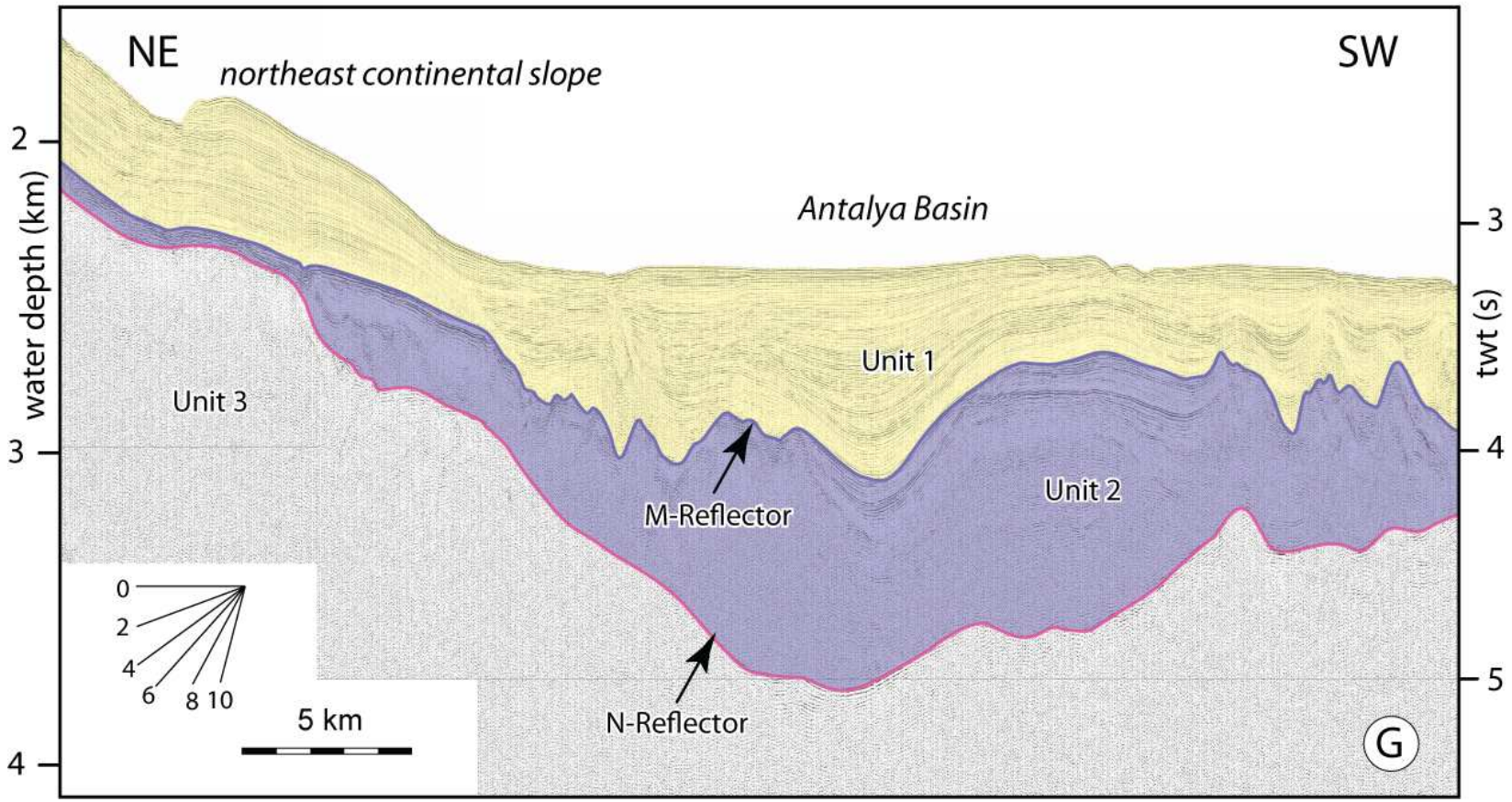

Figure 3.12: High-resolution multichannel seismic reflection profile (G) showing the architectures of the M- and N-reflectors which define the top and base of the evaporate successions of Unit 2, respectively. EMED01 (fix 1778-1798)

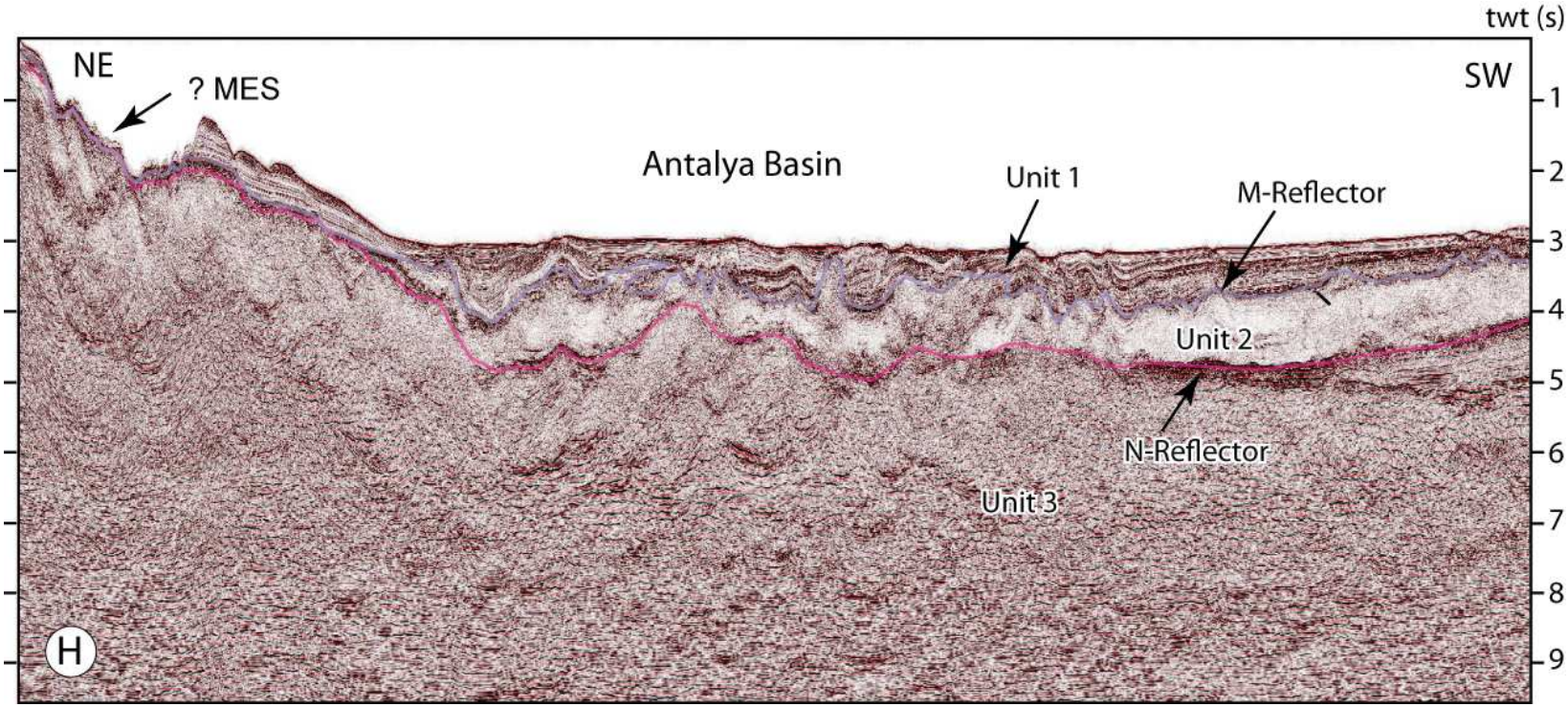

Figure 3.13: Industry multi-channel seismic profile (H) showing the acoustic character and stratigraphic architecture of the M- and N-reflectors. Across most of the northern continental margin of the Antalya Basin, and over the crestal region of the Florence Rise, Unit 2 is absent, thus the M-reflector defines a prominent composite unconformity. In this region, the M-reflector probably correlates with the Messinian Erosional Surface (MES; e.g., Lofi et al., 2011b). Location is shown in Fig. 3.1. TPAK07 (11218-20820)

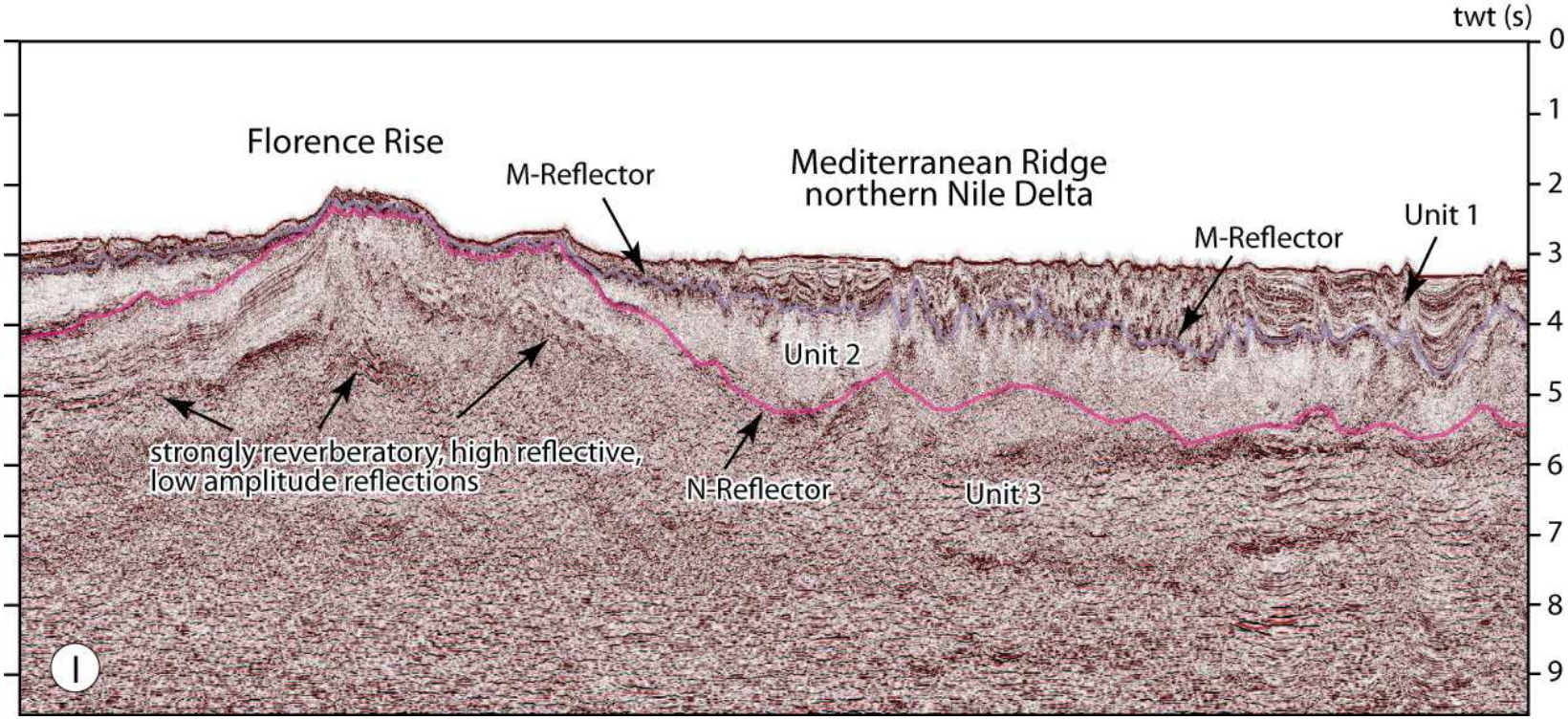

Figure 3.14: Industry multi-channel seismic profile (I) showing the acoustic character and stratigraphic architecture of the M- and N-reflectors. Note that extensive deformation of the subsurface makes the usually prominent M-reflector more difficult to discern. Location is shown in Fig. 3.1. TPAK07 (15-10818)

related with the M-reflector (Figs. 3.9–3.11, 3.13, 3.14), which represents the ultimate desiccation of the Mediterranean basin during the Messinian (Ryan et al., 1966; Hsü et al., 1978).

According to data from the DSDP Sites 375-376, onshore wells from the Antalya Basin and schematic stratigraphic cross-sections from southern Cyprus basins (Shipboard Scientific Party, 1978; Orszag-Sperber et al., 2009; Manzi et al., 2013, 2014), Unit 1 has been correlated with the predominantly Pliocene–Quaternary siliciclastic successions (Fig. 3.10). In a regional context, Unit 1 is correlated with: Kuranşa and Handere formations of the Adana and Cilicia basins, the Anthalassa and Nokosia formation of the Mesaoria Basin, and the Mirtou Formation of the Kyrenia Mountains of northern Cyprus.

The thickness of the uppermost Messinian–Quaternary succession of Unit 1 varies across the study area from $<$100 ms in the shallow nearshore regions to $>$2000 ms in northwest-southeast trending, elongated, tear-drop-shaped basins in deep Antalya Basin (Fig. 3.15). In general, Unit 1 is thickest along the center of the Antalya and Finike basins, but dramatically thins towards the bathymetric highs (e.g., Florence Rise and Anaxagoras Mountain) and along the Turkish continental shelf and slope. A broadly north-south trending elongated lobe of uppermost Messinian–Quaternary sediments (800–1000 ms thick) is also found in the northwestern Antalya Basin (Fig. 3.15). The relationship between the distribution and thickness variations of the uppermost Messinian–Quaternary and controlling factors are discussed in further detail in Chapter 7.

Unit 1 is divided into three subunits (1a–1c) on the basis of its internal seismic character and stratigraphic architecture (Figs. 3.9, 3.16). Table 3.1 summarized the inferred ages of the uppermost Messinian–Quaternary subunits in the study area. These ages are derived from the seismic reflection profiles using the assumption that (a) in the deepest portion of the basins, the uppermost Messinian–Quaternary succession includes no discernible hiatus, (b) the base of the uppermost Messinian–Quaternary Subunit 1c is delineated by the M-reflector, and that this reflector represents the end of the Messinian evaporite depositions associated with the Messinian Salinity Crisis, (c) the top

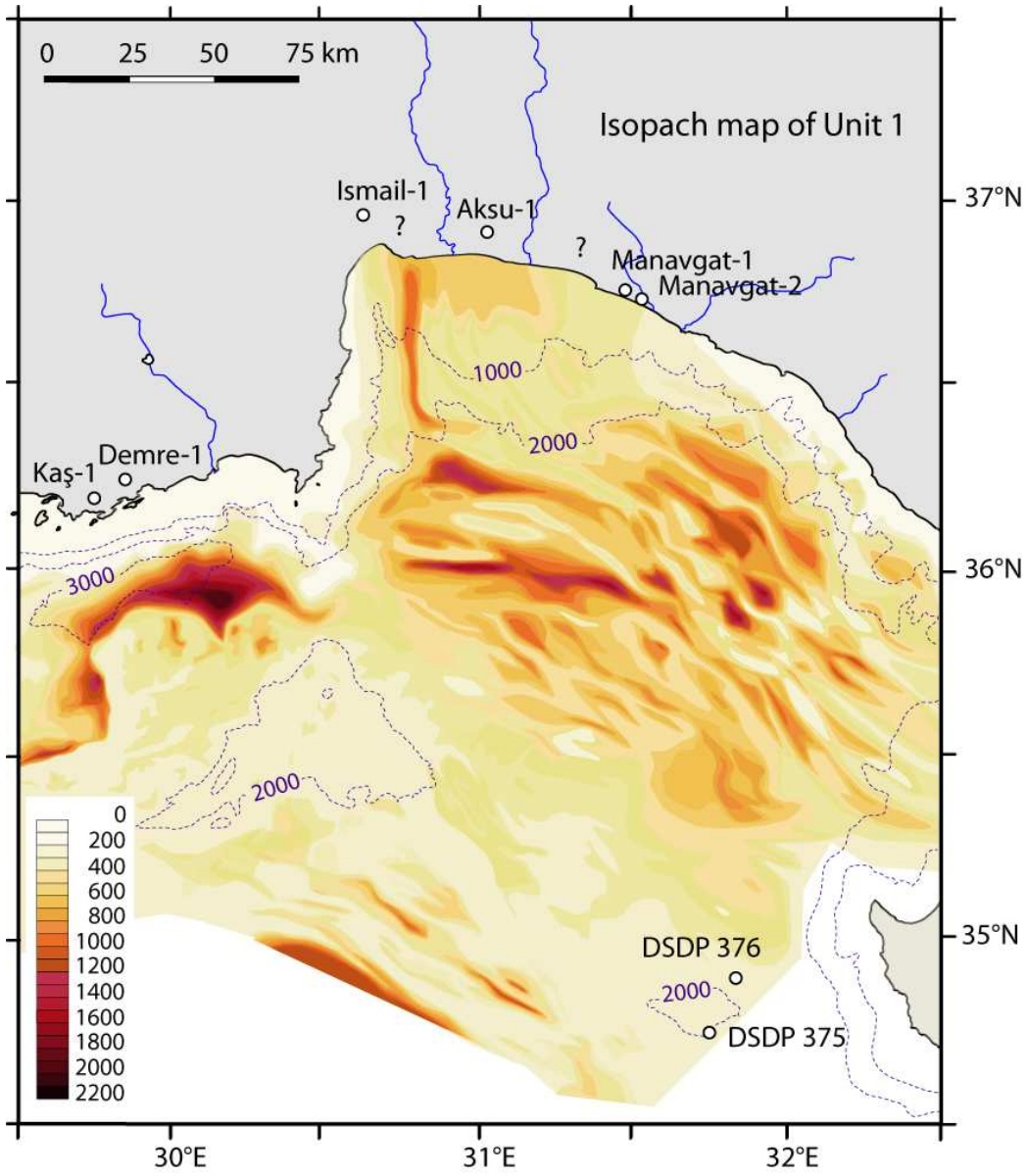

Figure 3.15: Isochron map of the Pliocene–Quaternary succession of Unit 1 (in millisecond two-way time= twt) in Antalya Basin, Florence and environs. Isobaths contours 1000 m, 2000 m and 3000 m are taken from the International Bathymetric Charts of the Mediterranean (IOC, 1981). Note that the continental slope have a very thin veneer of Unit 1 sediments, whereas the broad Antalya Basin and the deep Finike Basin contains in excess of 2000 ms of Unit 1 sediments. Also note that Unit 1 is notably thin across the Sırrı Erinç Plateau, Anaximander Mountains as well as the Florence Rise.

of Subunit 1a at the seafloor represents the contemporary deposition at 0 Ma, and (d) the sedimentation rate during the uppermost Messinian–Quaternary was nearly constant. Provided that these assumptions are correct, a back-of-the-envelope calculation can be made by linear interpolation along lines drawn orthogonal to the reflectors in selected seismic profiles from deep basins that contain a complete uppermost Messinian–Quaternary succession (e.g., Fig. 3.9). The results of this exercise show that Subunits 1a, 1b and 1c represent deposition from approximately 0 to 2 Ma, 2 to 3 Ma and 3 to 5.42 Ma, respectively (Table 3.1).

Table 3.1: The seismic units and subunits identified in the Antalya Basin and Florence Rise survey area and their infered ages based on a simple linear interpolation of vertical stratigraphic thickness.

Stratigraphic (Seismic) Unit		**Infered Age (Ma)**
Unit 1	Subunit 1a (Upper Pliocene - Quaternery)	$\sim$2.0-0
	Subunit 1b (Middle Pliocene)	$\sim$2.0-3.0
	Subunit 1c (uppermost Messinian - Lower Pliocene)	$\sim$3.0-5.0
Unit 2 (Messinian)		$>$5.0

Subunit 1a

The uppermost Subunit 1a is characterized by parallel and continuous reflectors giving it a highly stratified appearance in seismic section (Figs. 3.16, 3.17). It is also mapped as a prominent subunit in the Cyprus Basin (Hall et al., 2005b) and the Antalya Basin (Işler et al., 2005) and Cilicia and Adana Basins (Walsh-Kennedy et al., 2014). A prominent transparent zone with occasional weak and discontinuous parallel reflections occurs near the base of subunit 1a. In many places, the base of Subunit 1a is a mild but conspicuous erosional unconformity (Fig. 3.18), and reflectors within subunit 1a show near vertical offsets where the deformation clearly affects the seafloor morphology,

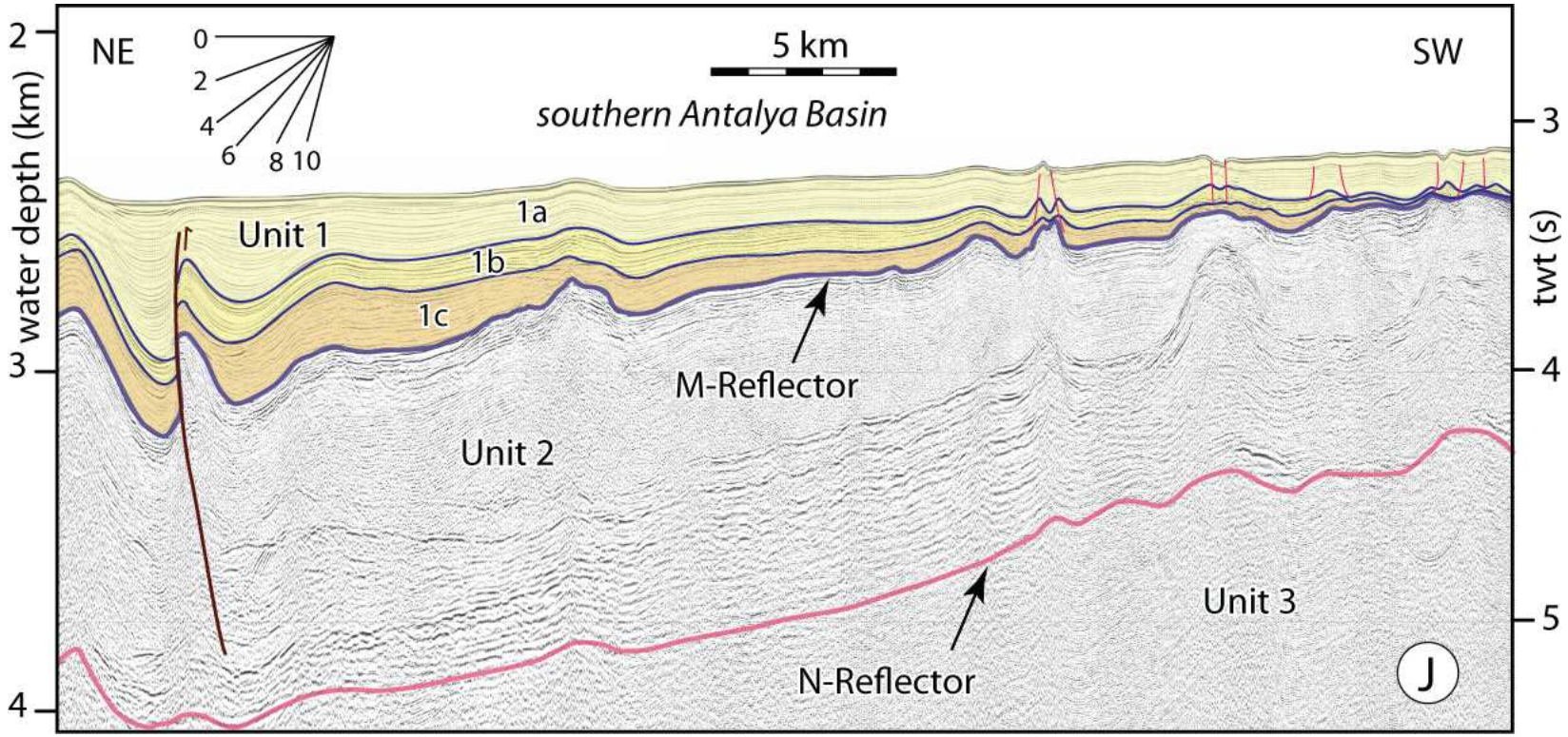

Figure 3.16: High-resolution multichannel seismic reflection profile (J) showing the subunits 1a–1c of the uppermost Messinian–Quaternary of Unit 1. Note that two laterally continuous distinct reflectors define the subunit boundaries. Location is shown in Fig. 3.1 EMED01 (fix 1778-1798)

creating small steps on the seabed (see Chapter 6).

Subunit 1a is correlated with the Quaternary to late Pliocene Units I and II of the DSDP Sites 375 and 376. Subunit 1a is further tentatively correlated with the shallow marine and terrestrial Apolos and Kakkaristra formations in the Mesaoria Basin (Fig. 3.10; Cleintuar et al., 1977; McCallum and Robertson, 1990; Robertson, 1998; Hall et al., 2005a; Calon et al., 2005a,b), as well as the Pleistocene Antalya Tufa and Belkış conglomerate in southwestern Turkey (Fig. 3.10; Akay and Uysal, 1985; Akay et al., 1985; Karabıyıkoğlu et al., 2000).

Subunit 1b

Subunit 1b generally has a stratified acoustic character, with a series of continuous parallel reflections and good lateral continuity (Figs. 3.16, 3.17). It is correlated with the Early-Late Pliocene Unit III and Unit VI of the DSDP Sites 375 and 376 (Fig. 3.2; Shipboard Scientific Party, 1978). Subunit 1b is tentatively correlated with the Middle-Upper Pliocene marls of the Athalassa Formation of the Mesaoria Basin (Figs. 3.10; Cleintuar et al., 1977; McCallum and Robertson, 1990; Robertson, 1998; Calon et al., 2005a,b; Hall et al., 2005a,) and the Alakilise Formation in southwestern Turkey (Fig. 3.10; Akay and Uysal, 1985; Akay et al., 1985; Karabıyıkoğlu et al., 2000).

Subunit 1c

A strong and conspicuous reflector separates Subunits 1b and 1c and the base of seismic Subunit 1c is marked by the M-reflector (Figs. 3.16, 3.17). Subunit 1c corresponds to Early Pliocene uppermost Messinian. It is characterized by moderate to weak transparent, discontinuous reflections, and can be further subdivided into an upper and lower portion. The upper portion of Subunit 1c is correlated with early Pliocene slumped marl successions of lithostratigraphic Unit IV of the DSDP Sites 375 and 376 (Figs. 3.10, 3.16, 3.17; Shipboard Scientific Party, 1978). It is tentatively correlated with the Nikosia and Mirtou formations of the Mesaoria Basin and Kyrenia Mountains respectively (Fig. 3.10;

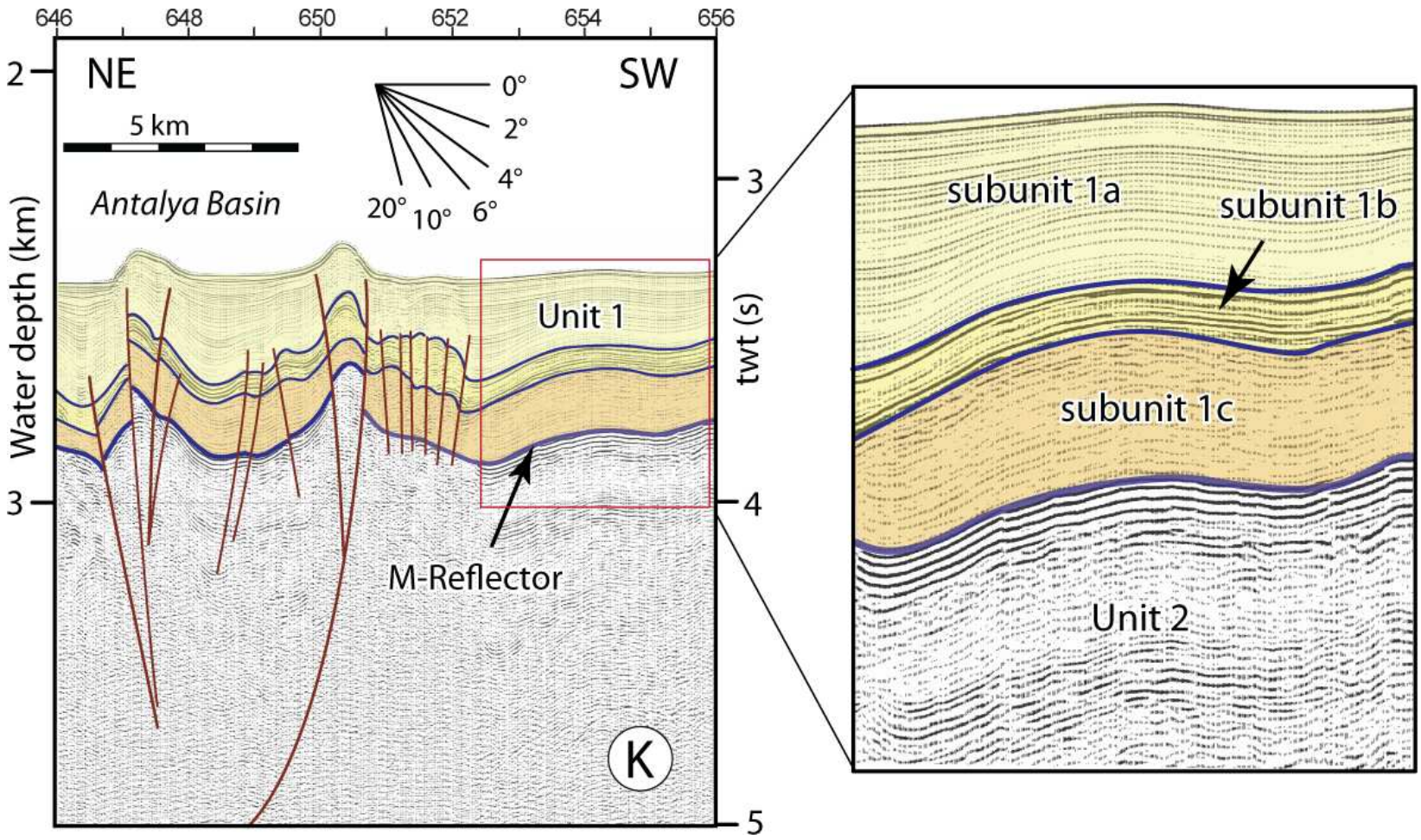

Figure 3.17: High-resolution multichannel seismic reflection profile (K) showing the architectures and the seismic characteristics of subunits 1a–1c. Location is shown in Fig. 3.1 EMED07 (fix 646-656)

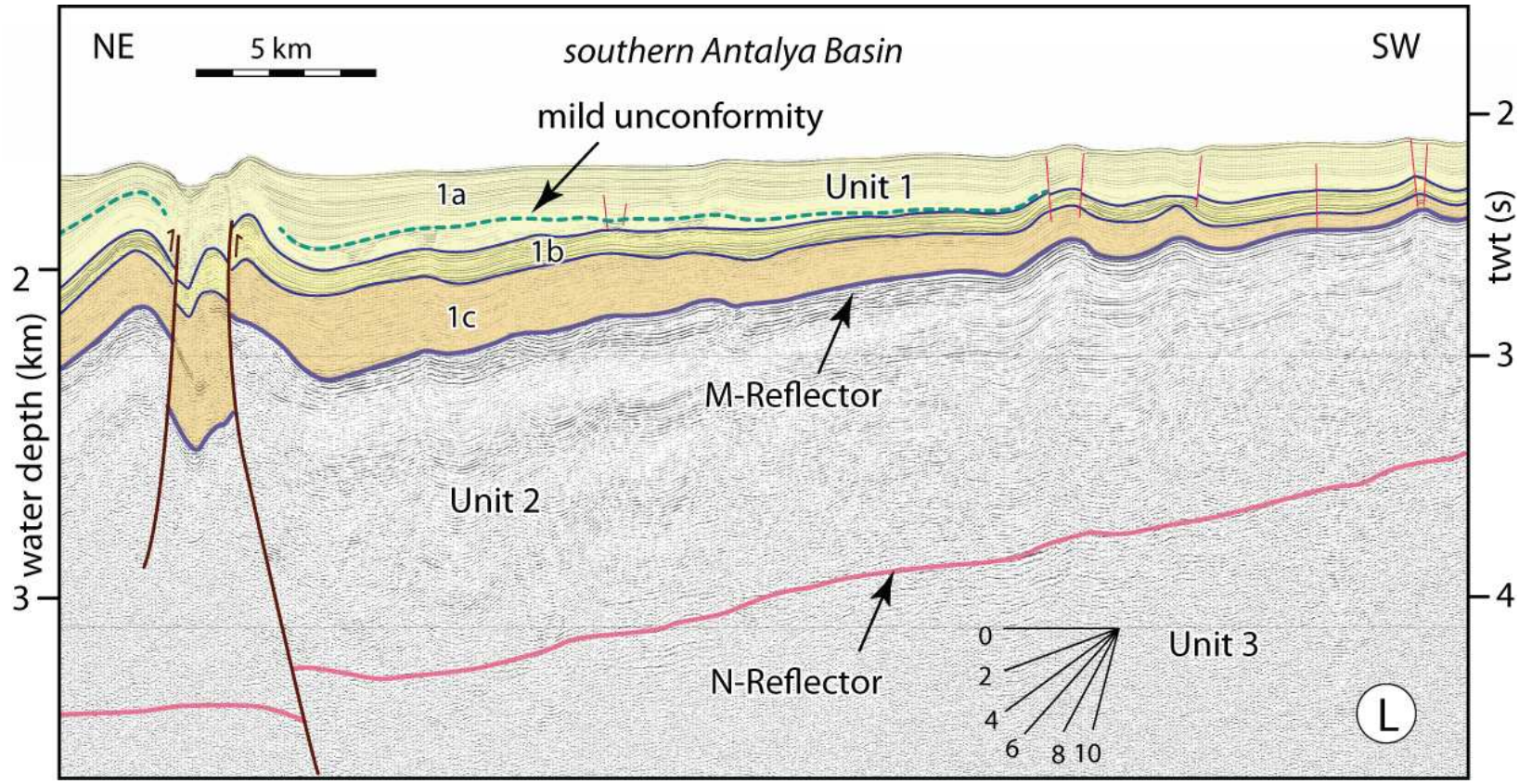

Figure 3.18: High-resolution multichannel seismic reflection profile (L) showing the subunits 1a–1c, and the mild angular unconformity that developed within the lower portion of subunit 1a. Location is shown in Fig. 3.1 EMED07 (fix 572-602)

Cleintuar et al., 1977; McCallum and Robertson, 1990; Robertson, 1998; Calon et al., 2005a,b), as well as the Yenimahalle Formation in the Antalya region (Fig. 3.10; Akay and Uysal, 1985; Akay et al., 1985; Karabıyıkoğlu et al., 2000).

The lowermost portion of Subunit 1c is generally characteristic by partially transparent appearance along the study area. However, it is occasionally characteristic by very thin and continues reflective package in the southern Antalya Basin (e.g., Fig. 3.17). The lowermost portion of Subunit 1c is tentatively correlated with the marlstones and interbedded graded sandstones and siltstones of middle to upper Unit V of the DSDP Sites 375-376 (i.e., *Lago Mare*).

The "*Lago Mare*" sediments of uppermost Messinian-Early Pliocene deposits of lowermost portion of the Subunit 1c is interpreted as it is in transition between the uppermost portion of Unit 2 and lowermost portion of Unit 1. In seismic reflection profiles, it is often difficult to separate this transition zone from the rest of the Subunit 1c because of their similar acoustic characteristics (both of these deposits consist mostly of siliciclastic successions). The "*Lago Mare*" event and its chronostratigraphic correlation and distribution are discussed in further detail in Chapter 5.

3.5.3 Unit 2: Late Miocene (Messinian)

Unit 2 is characterized by strong and continuous reflections at the top and base of the unit and a low reflectivity package with weak and often discontinuous reflections in the middle of the succession (Figs. 3.1, 3.9,). It is correlated with Messinian evaporites and the siliciclastic successions associated with the Messinian Salinity crisis. Between the southern Antalya Basin and the Florence Rise and between the Florence Rise and the north eastern Mediterranean Ridge, the succession is most often dominated by a thick transparent appearance delineated by only a low reflectivity package with weak and often discontinuous reflections with a corrugated geometry. It is readily distinguished by its strongly reflective top (M-reflector) and its less reflective and more discontinuous base (N-reflector). In areas where Unit 2 is absent, the M-reflector is a strong horizon representing an

erosional surface that defines a composite unconformity, which includes the M- and N-reflectors. In these regions, units above and below the M-reflector are interpreted as the uppermost Messinian–Quaternary (Unit 1) and pre-Messinian (Unit 3), respectively.

Based on the DSDP Sites 375 and 376 drill hole data (Figs. 3.2, 3.5; Shipboard Scientific Party, 1978) Unit 2 is correlated with gypsiferous marls, and evaporitic successions intercalated with marls and chalks of lower Unit V and anhydrite, halite, gypsum and green dolomitic marlstones of the entire Unit VI. Unit 2 is also correlated with other Messinian bedded pebblestone, sandstone, gypsiferous and fossiliferous limestone successions in the Aksu and Manavgat Basins (Fig. 3.10; Akay et al., 1985; Karabıyıkoğlu et al., 2000), as well as the similar evaporate lithologies of the Kalavasos and Lapatza formations of the Mesaoria Basin and Kyrenia Mountains (Fig. 3.10).

In the DSDP Sites 375 and 376, there is a gradational transition from Miocene lithostratigraphic lower Units V to VI. This boundary is generally delineated in the seismic reflection profiles, therefore lowermost part of the Unit V and entire Unit VI are lumped together in seismic stratigraphic Unit 2. Unit 2 is subdivided into four subunits (2a–2d) according to its internal acoustic characteristics (Figs. 3.19, 3.20). Unit 2 varies in thickness from 20-1500 ms. The interaction of faulting and diapirism control the thickness variations throughout the study area (Figs. 3.19, 3.20). The details of the internal architecture and chronology of the subunits 2a–2d, and the regional distribution of the Messinian successions of Unit 2 are discussed in detail in Chapter 4.

3.5.4 Unit 3: Miocene (pre-Messinian)

Unit 3 comprises of the oldest succession(s) imaged in the Florence Rise and Antalya Basin. In most of the study area (western and central Antalya Basin, southern and central Florence Rise) the seismic reflection profiles show that Unit 3 is characterized by a series of strongly vibrated, high reflective, low amplitude reflections with significant lateral continuity (Figs. 3.13, 3.14). In regions which have undergone intense deformation, these reflections have moderate lateral continuity. The

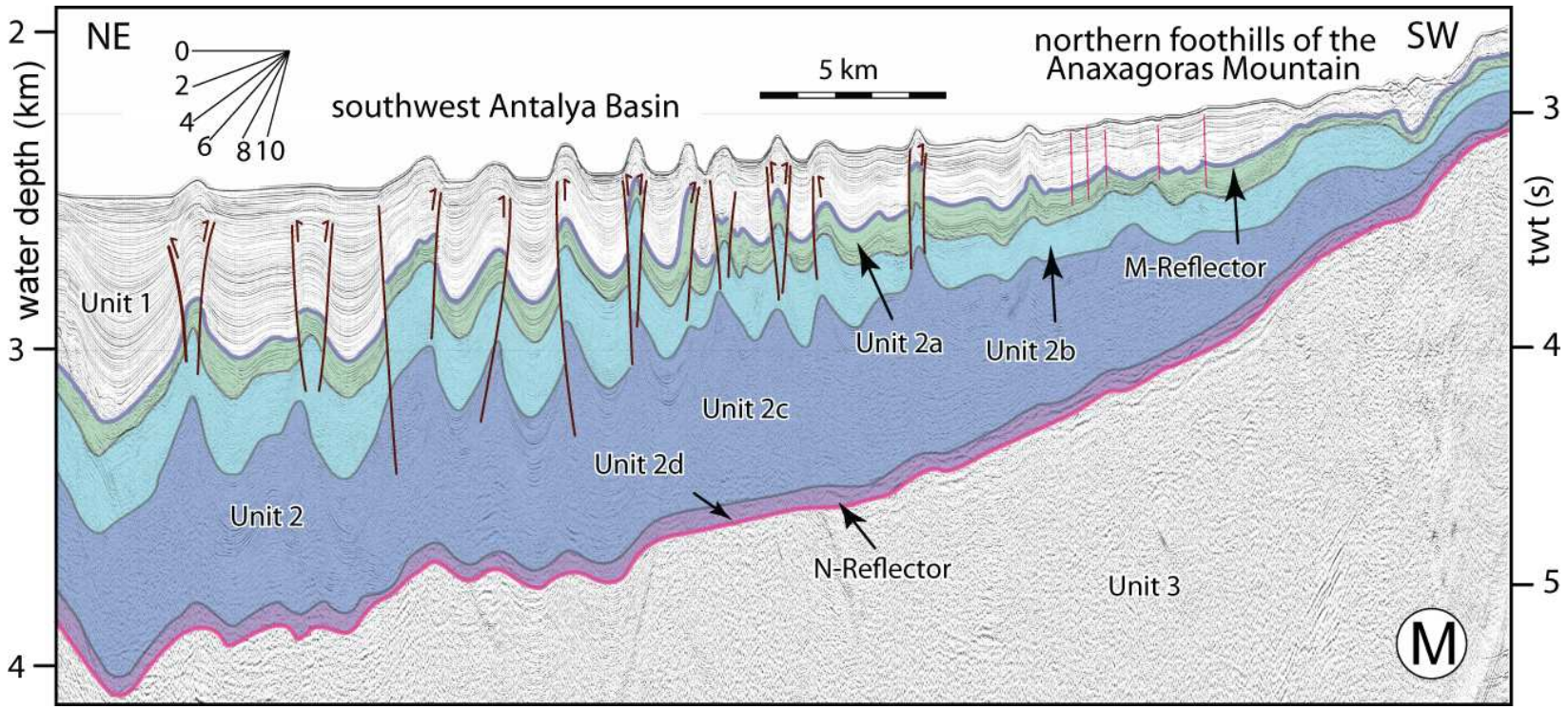

Figure 3.19: High-resolution multichannel seismic reflection profile (M) showing the thickness variation of Unit 2 and its subunits in the south western Antalya Basin and south eastern flank of the Anaxagoras Mountain. Location is shown in Fig. 3.1 EMED10 (fix 1351-1381)

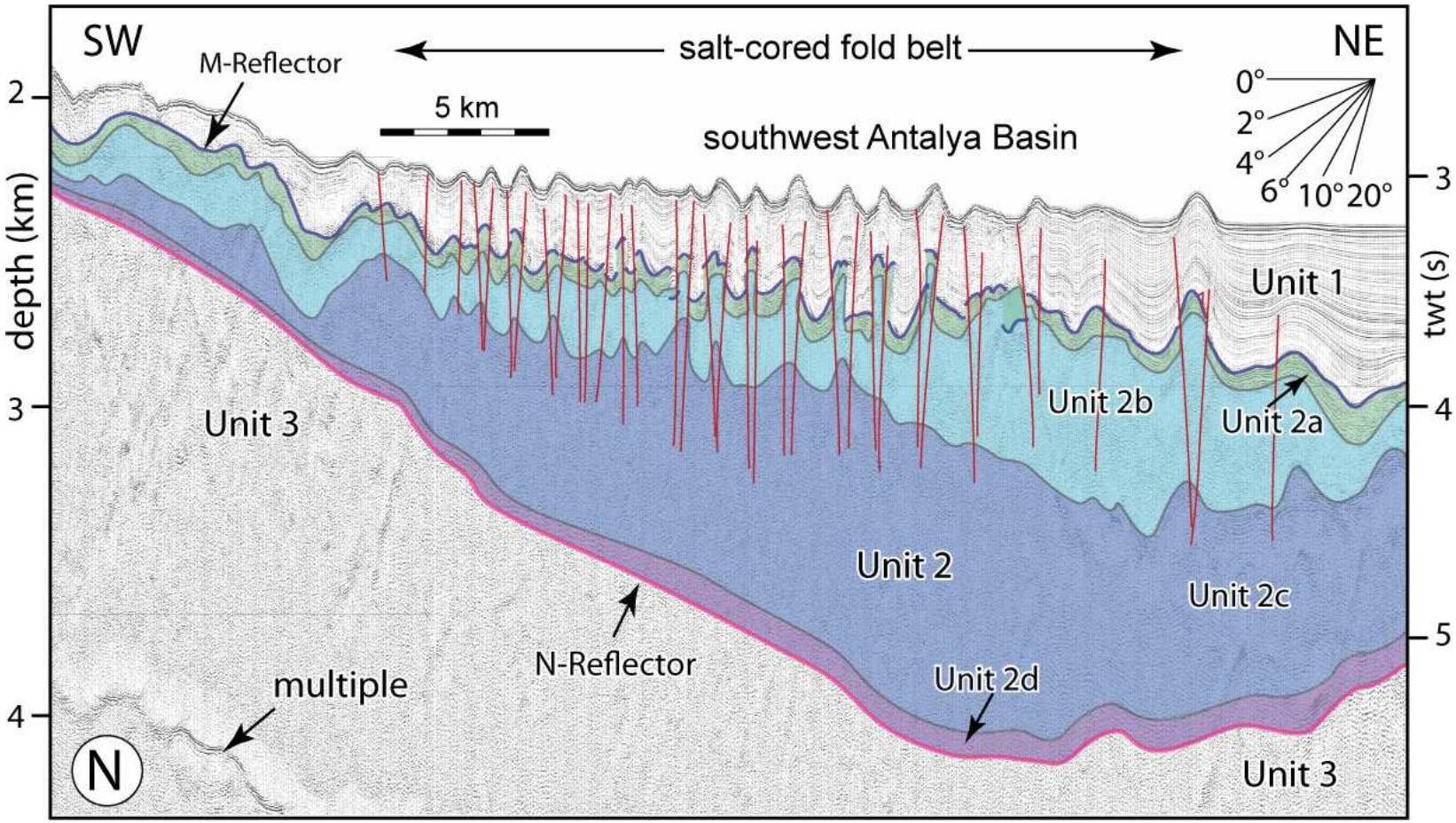

Figure 3.20: High-resolution multichannel seismic reflection profile (N) showing the thickness variation of Unit 2 and its subunits in the south western Antalya Basin and south eastern flank of the Anaxagoras Mountain. Location is shown in Fig. 3.1 EMED10 (fix 1496-1523)

upper boundary of the pre-Messinian Miocene package is delineated by the M-reflector in regions where Unit 2 is absent or the N-reflector where Unit 2 is present. The lower boundary of Unit 3 is never clearly imaged in the high-resolution seismic reflection profiles, but is clearly imaged in the deep-penetrating industry seismic data (Figs. 3.13, 3.14).

The lithology and chronology of Unit 3 has been investigated using correlations with the Manavgat-1 and Manavgat-2 wells and DSDP Site 375 (c, 3.6, 3.7). Based on these correlations, Unit 3 is inferred to be composed of a diverse assemblages of pre-Messinian (Miocene) and older siliciclastic and carbonate successions. It is subdivided into three subunits: 3a–3c.

The uppermost portion of Unit 3 (i.e., Subunit 3a) can be readily correlated with Unit VII at DSDP Site 375 (Figs. 3.2, 3.5; Shipboard Scientific Party, 1978). Subunit 3a is also correlated with the Upper Miocene Tortonian Karpuzçay Formation (Fig. 3.10). The middle segment of Unit 3 (i.e., Subunit 3b) is correlated with the marlstone and limestone successions of DSDP Site 375 Middle to Late Miocene Units (VIII to XI) (Figs. 3.2, 3.5; Shipboard Scientific Party, 1978). Subunit 3b is further correlated with the Middle to Lower Miocene Geceleme, Oymapınar and Aksu Formations of the Aksu, Köprüçay and Manavgat Basins (Fig. 3.10; Akay and Uysal, 1985; Akay et al., 1985; Flecker et al., 1998; Karabıyıkoğlu et al., 2000). The lower portion of Unit 3 may include regional lithostratigraphic units ranging from the lower Mesozoic to upper Oligocene in age. This portion of Unit 3 is seen in the industry seismic reflection profiles but not in the MUN 2001, 2007 and 2010 EMED surveys because the source volume of the MUN surveys were not large enough to image these succession (Figs. 3.13, 3.14).

In a regional sense, Unit 3 is further correlated with the Pakhna Formation (including the Koronia, Terra members) of the Mesaoria Basin, the Kythrea Group of the Kyrenia Mountains in Northern Cyprus (Bagnall, 1960; Follows and Robertson, 1990); and also the Elekdağ, Kasaba and Sinekli formations of the Kasaba Basin (Şenel, 1997a,b; Şenel and Bolukbaşı, 1997; Fig. 3.10). According to DSDP Site 375 well data results reflections below structural highs (i.e., the core of the Florence

Rise and Anaxagoras Mountain) are believed to be cored by Unit 3; however strata in these locations show a significant amount of intense internal deformation and reflector correlation is challenging.

Chapter 4

Seismic Stratigraphic Approach to Eastern Mediterranean Deep Basin Messinian Salinity Crisis Deposits

In this chapter, an integrated scenario that revives the key points of the previous models with new statements about the depositional settings is proposed. This scenario is derived mainly from seismic and sequence stratigraphic analysis of the Messinian evaporite deposits and their temporal and spatial distribution with new high resolution seismic reflection data collected from the western Cyprus Arc, eastern Mediterranean (Fig. 4.1) and the consequences of, and correlations with global environmental changes. Isochron maps and seismic cross-sections are correlated with borehole information from DSDP Leg 42 Sites 375 and 376, ODP Sites 965 and 968, the onland Aksu-1, Manavgat-1, Manavgat-2 wells in the Antalya region and the Xeri borehole in Cyprus, as well as onshore successions in the eastern Mediterranean. This framework is then used to describe temporal and spatial seismic facies variations across the Antalya Basin and Florence Rise. The most significant contribution of this chapter to the Mediterranean geology is the documentation that the Messinian successions

of Unit 2 in the eastern Mediterranean are composed of four seismic stratigraphic sub-units. Until now, no such subdivision for Unit 2 was presented from the eastern Mediterranean. The presence of these four sub-units imposes strict environmental and sedimentological constraints for the deposition of the Messinian evaporites during the Messinian Salinity Crisis (also see Chapter 3). In this chapter, thorough acoustic and proxy-sedimentary descriptions of these sub-units are provided and depositional frameworks for these successions are delineated. These new findings are later (in Chapter 7) set in the context of the whole of the Mediterranean Basin allowing me to formulate a new concept for the relationships of the Messinian in the eastern and western Mediterranean.

4.1 Introduction

At the end of the Miocene approximately 6 Ma, progressive closure of the straits connecting the Mediterranean Sea with the Atlantic Ocean triggered the desiccation of the Mediterranean Sea (e.g., Garcia-Castellanos and Villaseñor, 2011). This caused significant amounts of evaporation across the Mediterranean Sea in a relatively brief period of $\sim$0.63 Ma, and led to a series of events, which are known as the Messinian Salinity Crisis (Hsü et al., 1973; Hilgen et al., 2007). The dramatic sea level drop during the Messinian Salinity Crisis represents the most striking environmental change in the Cenozoic history of the Mediterranean Sea (e.g., Ivanovic et al., 2014). During the Messinian Salinity Crisis, rapid evaporation of the Mediterranean Sea resulted in increased seawater salinities and the deposition of evaporites within shallow water marginal basins, followed by massive erosion at the continental margins and deposition of thick evaporite successions in deep Mediterranean basins (Hsü et al., 1973; Montadert et al., 1978; Clauzon, 1982; Ryan, 2009; Lofi et al., 2011b). Following the re-opening of the Strait of Gibraltar and the re-connection of the Mediterranean Sea with the Atlantic Ocean during latest Miocene/earliest Pliocene, the Mediterranean basins were rapidly refilled, which marked the end of the Messinian Salinity Crisis.

The Messinian Salinity Crisis is a prominent series of events that has profoundly modified the

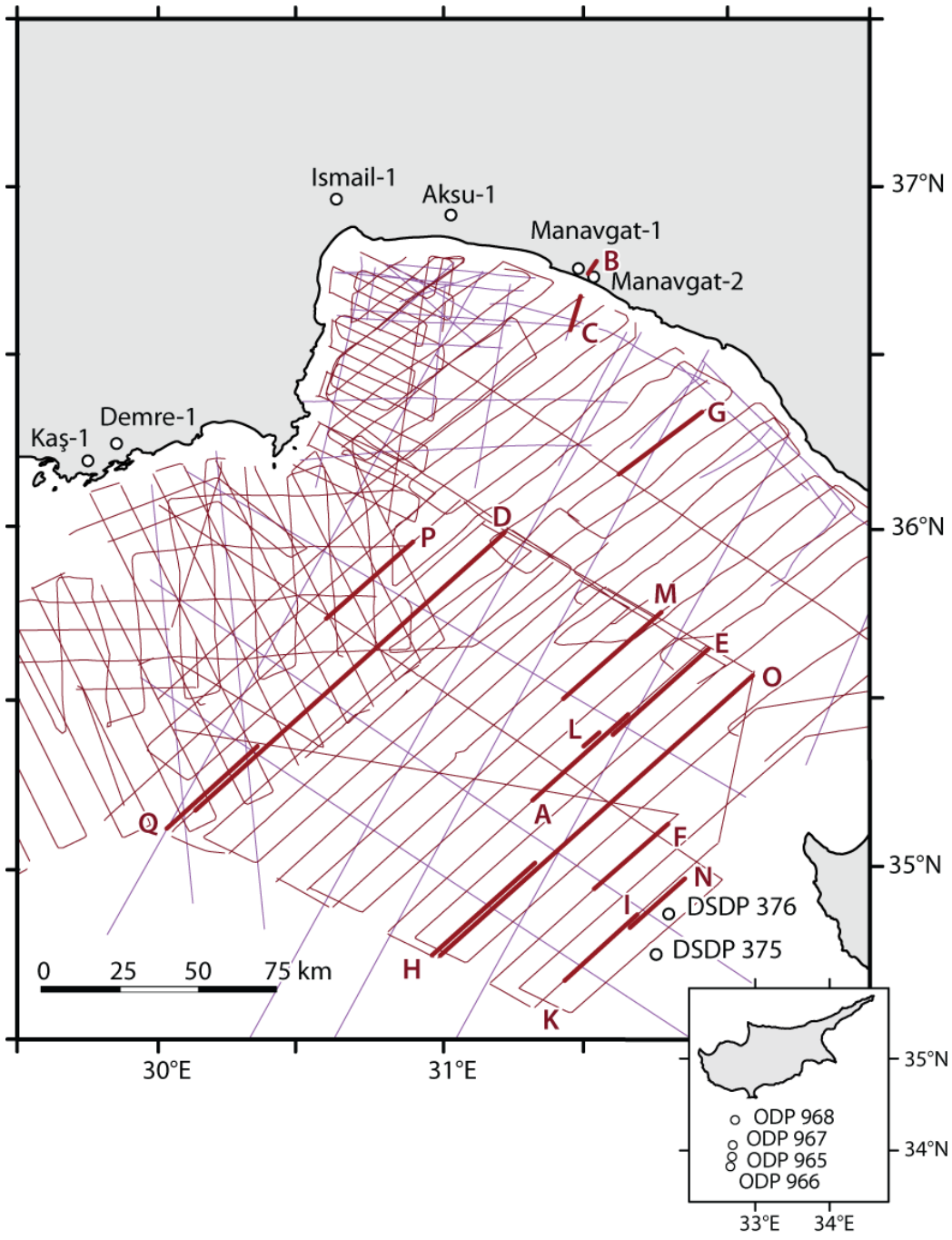

Figure 4.1: Map of the eastern Mediterranean Sea and environs, showing the locations of the high-resolution multichannel seismic reflection profiles used in this study. Heavy lines are figures illustrated in this chapter. The coastline is from the International Bathymetric Charts of the Mediterranean (IOC, 1981).

Mediterranean within a relatively limited time span, and led to the deposition of thick evaporite successions in basins that are presently located both onland and offshore (e.g., Lofi et al., 2011b, and references therein). The depositional environment of evaporite successions has been described in three models: (1) shallow basin and shallow water depth model, where evaporites were deposited in a shallow evaporative basin with limited connection to the open ocean, (2) deep basin and shallow water depth model, where the deep basin was isolated from the global oceans, quickly evaporates to great depths, leaving only a shallow evaporative basin across the seafloor, (3) deep basin and deep water depth model, where excessive evaporation at the ocean surface allows brines to develop and downwell to the deeper waters allowing the precipitation of evaporites (Fig. 4.2). Previous regional studies based on outcrop, borehole and 2D seismic reflection data have demonstrated that during the Messinian Salinity Crisis, the Mediterranean was subject to complex and highly diversified evaporite deposition which resulted from morphological, geodynamical and isostatic responses of the deep offshore basins and marginal shallower basins (Montadert et al., 1978; Garfunkel and Almagor, 1984; Gorini et al., 1993; Gradmann et al., 2005; Rouchy and Caruso, 2006; Roveri et al., 2008a–c, 2014a, b). It is generally accepted that the period of widespread evaporite precipitation in the Mediterranean spanned from 5.97 to 5.33 Ma, but it is not known how the events recorded in sedimentary successions correlate between the shallow marginal and deep basins across the Mediterranean region. The evaporites in shallow marginal basins are largely exposed onshore, and thus, have been extensively studied (Krijg sman et al., 2001, 2002, 2004; Lofi et al., 2011a, b; Manzi et al., 2013, 2014). However, these successions are often incomplete and they are geometrically disconnected from the Messinian evaporite successions found in the deep offshore basins (e.g., Schreiber et al., 1976; Rouchy, 1982; Butler et al., 1995; Clauzon et al., 1996; Riding et al., 1998; Krijgsman et al., 1999). Thus, correlations between the thick offshore evaporites and those exposed onland across the eastern Mediterranean are tentative at best.

Within the eastern Mediterranean, most previous research on the Messinian Salinity Crisis in

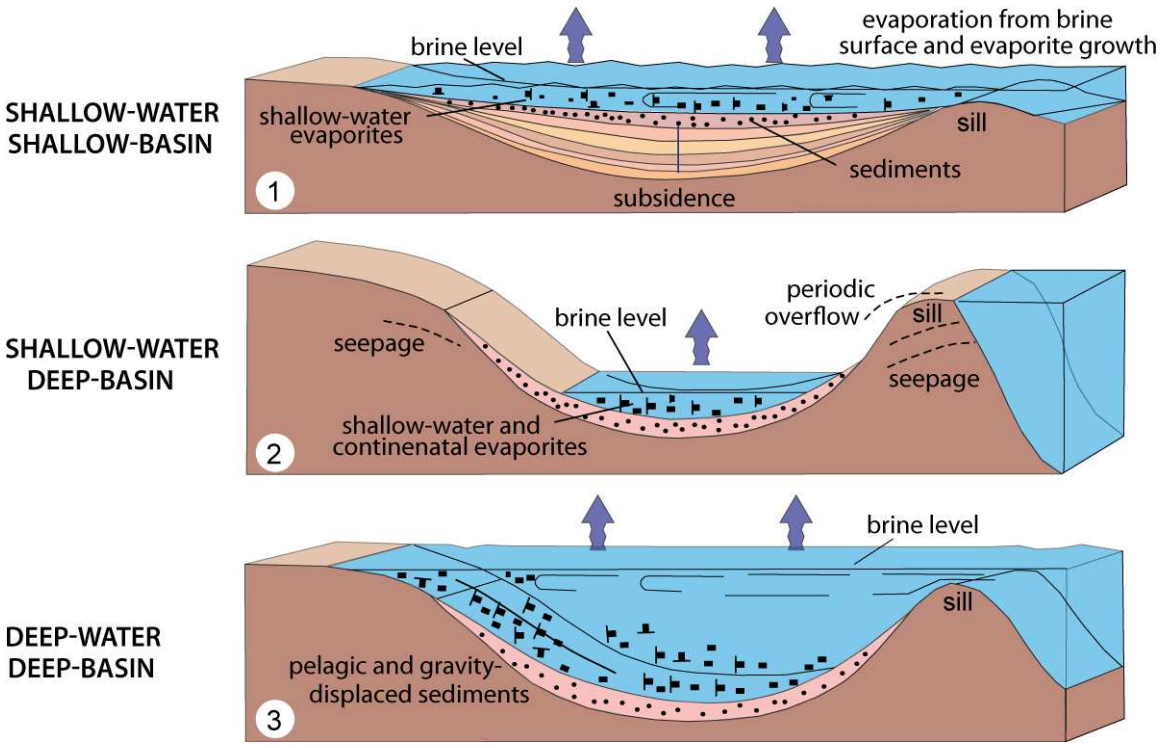

Figure 4.2: Three potential depositional models for evaporites, adopted from http://www.britannica.com/EBchecked/topic/197000/evaporite.

deep basins has focused on the Nile deep sea fan and the Levantine Basin, which have been investigated in relation to the development of giant salt diapirs (Mart and Ben Gai, 1982; Garfunkel and Almagor, 1987; Cohen, 1993; Loncke et al., 2004, 2006; Gradmann et al., 2005; Bertoni and Cartwright, 2006; Netzeband et al., 2006b; Bertoni and Cartwright, 2007; Hübscher and Netzeband, 2007). Dümmong and Hübcher (2011) focused on the Messinian Salinity Crisis evaporites and overlying formations which show a complex deformation pattern due to a combination of thick-skinned plate tectonic convergence and thin-skinned disharmonic deformation related to the mobile evaporite-bearing unit in the eastern Cyprus Arc. The western part of the Cyprus Arc has been the subject of a number of previous studies focused on post- and pre-evaporitic structural deformation (Woodside et al, 2002; Sellier et al 2013a,b). A recent synthesis based on stratigraphic framework of the Messinian Salinity Crisis in the entire Mediterranean has been proposed by Lofi et al, (2011b). However, in their synthesis of the eastern Mediterranean, the distribution of the successions associated with the Messinian Salinity Crisis in the western Cyprus Arc region, including the Florence Rise and the Antalya Basin, is presented in an abstract fashion because these authors did not have a sufficiently high density of high-resolution multichannel seismic reflection data from this region. Lofi et al. (2011b) indicated that the typical successions of Lower Evaporites, Salt, Upper Evaporites observed in the western Mediterranean region is not present in the eastern Mediterranean where the Messinian Salinity Crisis is largely recorded by a single salt-bearing seismic unit. More recently, a tentative correlation for the Messinian successions across the western and eastern Mediterranean has been proposed by Manzi et al. (2014). However, a detailed examination of their results suggests that this correlation may only apply to the marginal basins of the eastern Mediterranean.

4.2 Previous Messinian Salinity Crisis scenarios

The timing and environment of deposition of the successions associated with the Messinian Salinity Crisis in deep Mediterranean basins are in a state of flux and controversial. Three main hy-

potheses have been proposed to account for the chronology of the major evaporitic stages which are mostly established for the western Mediterranean basins (Fig. 4.3). The first (Fig. 4.3a) is a stratigraphic model, with synchronous deposition of Messinian Lower Evaporites (at 5.97 $\pm$ 0.02 Ma) in all Mediterranean basins (shelves, slopes and deep basins) before the rapid sea level fall (Figs. 4.3, 4.4; Hsü et al., 1973; Krijgsman et al., 1999). Detailed cyclostratigraphic studies showed that the oldest Sicilian evaporites in these sub-basins have all formed synchronously at an age of $\sim$5.98 Ma (Hilgen and Krijgsman, 1999). Astronomically calibrated chronology for the Mediterranean Messinian age based on an integrated high-resolution stratigraphy and 'tuning' of sedimentary cycle patterns to variations in the Earth's orbital parameters also showed that evaporite deposition in Spain, Greece and Cyprus took place at approximately the same age of 5.96 $\pm$0.02 Ma (Krijgsman et al., 1999, 2002), demonstrating that, at the resolution of a precessional cycle, the onset of evaporite deposition was synchronous throughout the eastern and western Mediterranean basins. The second model proposes that a slight diachroneity on the onset of the evaporite deposition (Figs. 4.3b, 4.4). This model suggests that the Messinian stratigraphy of the marginal shallow-water areas is not time equivalent to that of deep basinal areas and implies a major two-stage evaporite deposition (i.e., the lower and the upper evaporites) (Fig. 4.4; Rouchy and Caruso, 2006). In this model, the distribution and the fractionation of the evaporite deposits are controlled by the paleogeographic configuration of the basin, consisting of several smaller sub-basins of different size and depth and by the role of the thresholds that controlled the water exchanges between these sub-basins (Fig. 4.4). Thus, these minor constraints introduced a slight diachronism of the beginning of the evaporite deposition at each stage and in the different sub-basins (Butler et al., 1995; Clauzon et al., 1996; Rouchy and Caruso, 2006). The third model suggests a diachroneous deposition of evaporites and the associated sediments during the Messinian Salinity Crisis (Figs. 4.3c, 4.4). Recent studies favor the diachroneous deposition model which introduces three stages of desiccation (Fig. 4.4, 4.5; CIESM, 2008; Roveri et al., 2008a,b; Lugli et al., 2010; 2014a; Manzi et al., 2014). Stage 1 (Fig. 4.4, 4.5;

5.97–5.62 Ma; Krijgsman et al., 1999; Lofi et al., 2005; Manzi et al., 2014) involved minor sea-level drawdown with early evaporite precipitation. In the shallow marginal basins this stage is marked by the deposition of the "Primary Lower Gypsum", whereas in the deeper basins only organic-rich shale and carbonate deposition took place (de Lange and Krijgsman 2010; Lugli et al. 2010, Roveri et al., 2008b). The second stage is short lived (5.60–5.53 Ma) and involves a combination of base-level drop, tectonic uplift and variation in the sedimentation rate of evaporites (Manzi et al., 2014), but records the peak of the Messinian Salinity Crisis (Fig. 4.4, 4.5). During Stage 2, the shallow-water peri-Mediterranean areas were exposed to subaerial erosion and evaporite deposition moved to the deeper basins with the widespread deposition of primary halite and clastic gypsum-carbonate deposits. These clastic evaporites are referred to as the "Lower Evaporites" (Roveri et al., 2008a, 2014a), and were derived from the resedimentation of the primary lower gypsum. The end of Stage 2 is marked by a basal unconformity (Fig. 4.4, 4.5) which corresponds to the Messinian erosional surface (MES) and reflects a phase of increased tectonic activity, leading to uplift and erosion of the primary lower gypsum (Pierre et al., 2002, 2007; Natalicchio et al., 2014). The final stage of Messinian Salinity Crisis, Stage 3 (5.53–5.33 Ma; Hilgen et al., 2007; Manzi et al., 2009), includes the deposition of evaporites in both shallow and deep basin settings. It is characterized by gypsum and marl deposits of the *Lago Mare* facies (Lugli et al., 2013; Roveri et al., 2014, Fig. 4.4, 4.5), which represent sedimentation in a brackish to fresh water environment (Gignoux, 1950; Ruggieri, 1962; Cita and Colombo, 1979; Bertini et al., 1995; Orszag-Sperber et al., 2006). The author of this dissertation also favors the third model, which is adopted across the Antalya Basin and Florence Rise, as further discussed below.

4.3 Messinian Salinity Crisis – base level changes and paleogeography

The Messinian salinity crisis can be defined as an ecological crisis caused by large amplitude environmental changes which developed in the Mediterranean at the end of the Miocene as a result of

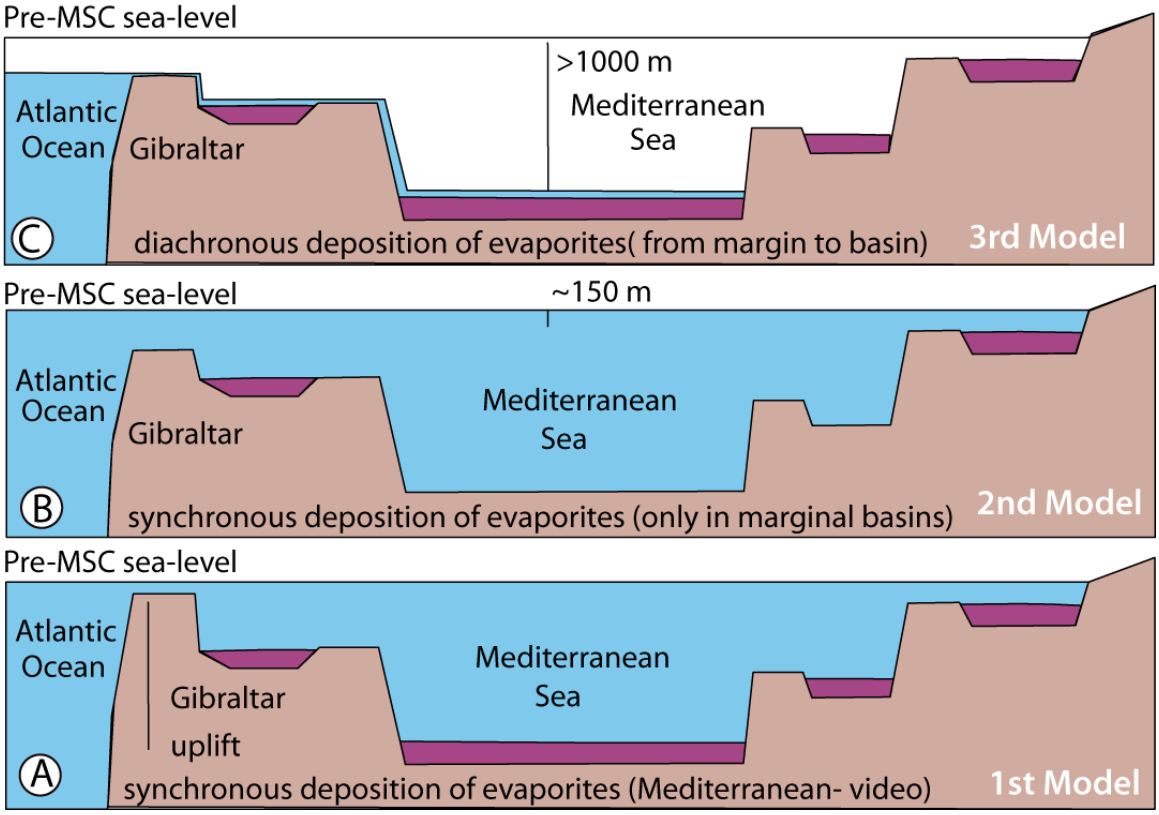

Figure 4.3: Three main hypotheses proposed to account for the chronology of the major evaporitic stages established for the western Mediterranean basin, adopted from Krijgsman, et al., 2008.

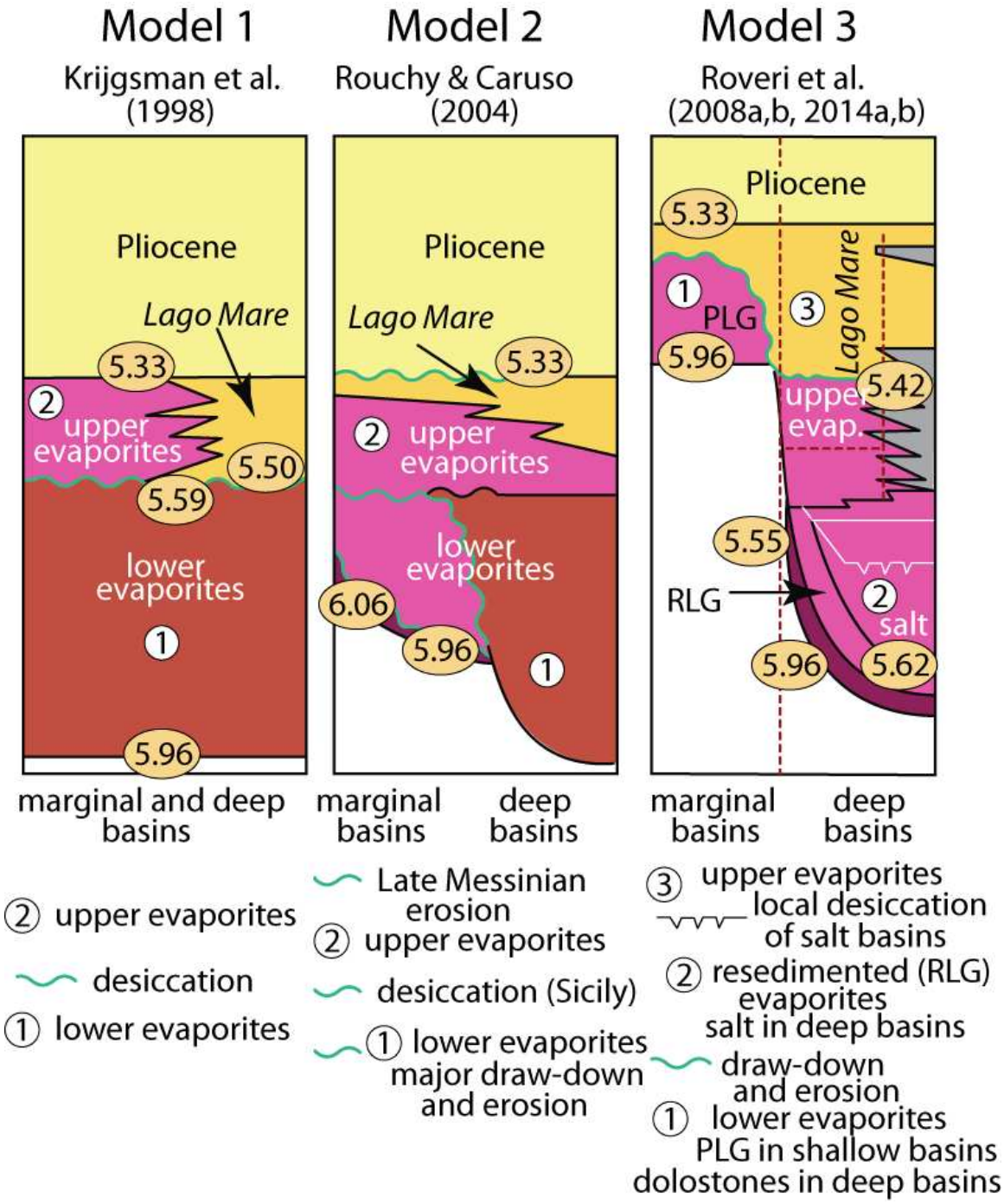

Figure 4.4: Comparison of chronologies proposed by Butler et al. (1995), Clauzon et al., (1996), Riding et al. (1998), Krijsgman et al. (1998), Rouchy and Caruso (2004) and Roveri et al. (2008a,b) for the successions associated with the Messinian Salinity Crisis.

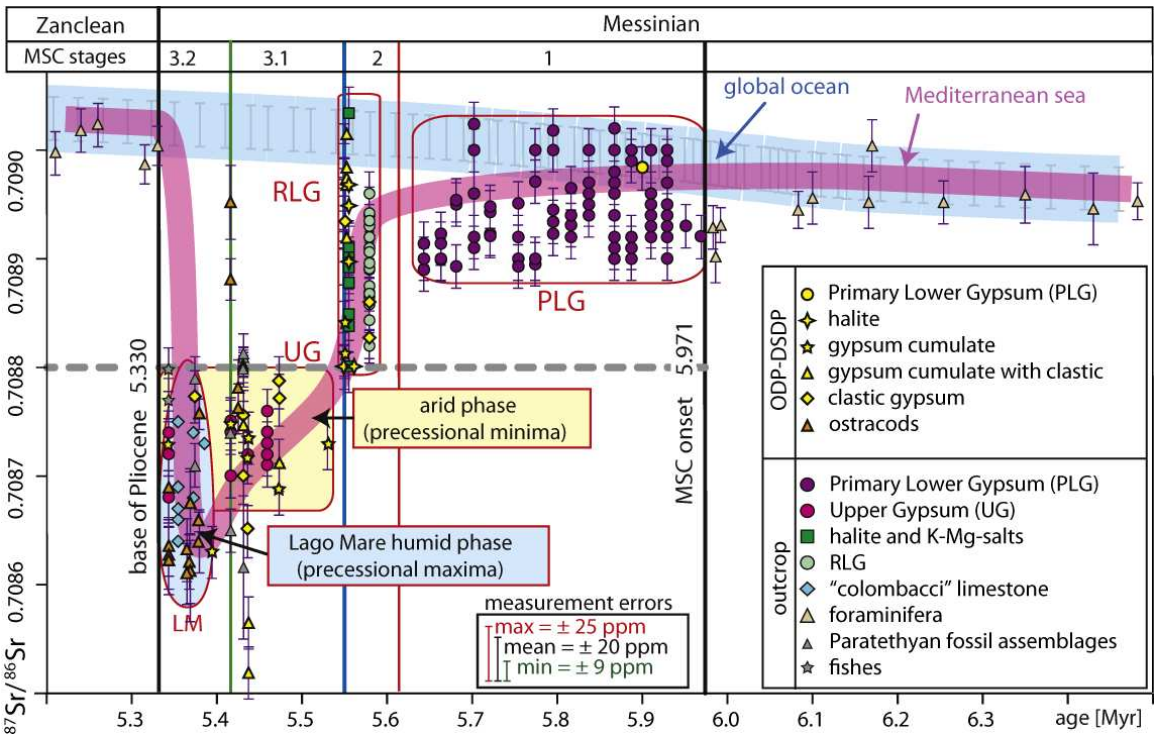

Figure 4.5: Sr isotope curve of Roveri et al. (2014a,b). Note the progressive change in the isotopic composition of Mediterranean waters during the Messinian salinity crisis; the three MSC stages can be clearly differentiated; with no overlapping values in stages 2 and 3. PLG= Primary Lower Gypsum; RLG= Resedimented Lower Gypsum; UG= Upper Gypsum; LM= *Lago Mare*.

coeval effects of geodynamic and climatic forcing and their feedbacks.

Offshore observations suggest that base-level changes during the Messinian Salinity Crisis were complex and cannot be considered as a single continuous lowering and refilling event (CIESM, 2008; Roveri et al., 2014a,b). This complexity may result from the presence of several topographic sills disconnecting the different Mediterranean basins and sub-basins during the Messinian Salinity Crisis. Ryan (2009) proposed a scenario of the crisis stressing the importance of some Mediterranean sills (e.g., Sicilian, Apennine and Suez) in the control of temporary base-levels and in the timing of precipitation of the halite in the Mediterranean. Using numerical modeling involving the uplift of the Betic and Rif (i.e., Gibraltar) and the Sicily straits, Gargani and Rigollet (2007) proposed that numerous sea-level falls of short duration occurred before the final major drawdown. At this point, the number, location, paleo-depth of the sills which played critical roles in the water mass budgets of the Mediterranean basins and base-level variations are clearly very important. The knowledge of the paleogeography of the Mediterranean and Paratethys during the Messinian Salinity Crisis is also essential for restoring the paleo-connections among the basins during higher sea levels (Clauzon et al., 2005, 2008; Krijgsman et al., 2010).

A Mediterranean base-level fall of $\geq$1500 m is envisaged in the western Mediterranean (Hsü and Cita, 1973; Ryan, 1976; Blanc, 2002; Lofi et al., 2005). This is based on the interpretation of the shallow water nature of the offshore Upper Unit, inferred from its aggradational geometry onlapping the basin margins and the erosion at its top (Maillard et al., 2006) and the subaerial origin of the widespread erosional features and associated drainage patterns observed along the Mediterranean slopes (Ryan, 1978; Lofi et al., 2005) which have been correlated with the Messinian erosional surface (MES) onshore. In addition, deep incision of long canyons and valleys such as the Rhône and Nile is thought to have been driven by the adjustment of river profiles to an exceptional base-level fall in the Mediterranean (Chumakov, 1967, 1973; Barber, 1981; Clauzon, 1982). An indirect argument supporting the idea of a high-amplitude drawdown is the development of giant pockmark

fields caused by pore-fluid overpressure and large-scale fluid venting, recently discovered at the base or within the Messinian salt unit in the Levant basin (Lazar et al., 2012; Bertoni et al., 2013). However, based on a different interpretation of some evaporitic facies, the occurrence of high-amplitude base-level changes during the Messinian Salinity Crisis has been questioned by several authors (Busson, 1990; Martinez del Olmo, 1996; Manzi et al., 2005; Roveri et al., 2008 a–d, 2009).

In the eastern Mediterranean basins, estimates of base-level fall of 800 m have been proposed for the Levant margin (Druckman et al., 1995; Cartwright and Jackson, 2008). Lugli et al. (2013) pointed out the presence of fully subaqueous clastic evaporites in the infill of the main Messinian canyons and suggested that the estimates of sea-level drop previously proposed may be not correct. Much greater base-level fall is proposed for the Nile delta fan region (Gargani and Rigollet, 2007). These authors used 3–5 erosional surfaces observed in the seismic reflection profiles along the Egyptian margin at a depth between -2500 and -3000 m depth, and estimated a subsidence of 750–1000 m since the Pliocene-Quaternary to conclude that these erosional surfaces must have formed during the Messinian Salinity Crisis at a depth of 1500–2250 m beneath the present-day sea level of the eastern Mediterranean Sea (Gargani and Rigollet, 2007). Views on the timing of Mediterranean sea-level fall has changed through time (Ryan, 2009). Exactly when the base-level fall occurs has important implications for the origin and nature of the basinal evaporite units. Following the model of Blanc (2000), Lofi et al. (2005) suggested a two-step base level fall in the western Mediterranean basins controlled by a Sicily–Tunisia sill. In their model, the first step in the order of 400–600 m caused slope instability and the deposition of gravity flow deposits which formed a large part of the Lower Unit. The thick evaporites of the Mobile Unit and Upper Unit then formed respectively during and immediately after a second, higher amplitude drop in base-level. Most commonly, the maximum sea-level fall has been placed within or (Ryan 2009) at the end of the deposition of the Mobile Unit in the deep western and eastern Mediterranean basins (Lofi et al. 2005, 2011a,b; Bertoni and Cartwright, 2007; Ryan, 2009), i.e., at the end of Messinian Salinity Crisis stage 2 (Fig. 4.3). Other authors (i.e.

Bache et al., 2009, 2012) consider the whole deep basin evaporitic suite as having been deposited after the main sea-level drop, requiring a continuous input of marine waters to an almost desiccated basin.

Ryan (2008, 2009) proposed that strong net evaporation concentrated Mediterranean seawater prior to drawdown, resulting in the rapid precipitation of halite during sea level fall. In this scenario, the Mobile Unit would have started accumulating in a relatively deep-water setting and ended its deposition in an almost desiccated basin (Lofi et al., 2011b). The Top Erosion Surface observed in the Levant Basin at the top the Mobile Unit is interpreted by some authors as a phase of subaerial erosion during the last stage of the crisis (Ryan, 1978; Bertoni and Cartwright, 2007). Yet others (e.g., Roveri et al., 2001, 2014a,b), suggested that halite accumulated in a fully subaqueous environment during the peak of the Messinian Salinity Crisis.

The rise of sea level after the peak of the Messinian Salinity Crisis is considered to have occurred almost instantaneously (Meijer and Krijgsman, 2005; Garcia-Castellanos et al., 2009), more progressively with large-scale fluctuations related to precession-controlled hydrological changes (Fortuin and Krijgsman, 2003) or in a stepped way (Lofi et al., 2005; Bache et al., 2009, 2012; Just et al., 2011; Lofi et al., 2011a,b). Lofi et al. (2005, 2011b) suggested that the Sicily–Tunisian sill may have generated temporary base-level still stand in the western Mediterranean during the refilling phase. A stepped base-level rise during the final Messinian Salinity Crisis stage has also been suggested by Just et al. (2011), based on the observation of terraced surfaces at constant depth along Messinian paleo slopes. These features would record a sea-level still stand in the western Mediterranean which persisted until the water level in the eastern Mediterranean basins transgressed the Sicily–Tunisia sill. Bache et al. (2009, 2012) consider a moderate initial rise in base-level, associated with the deposition of the deep basin evaporites and the development of a transgressive ravinement surface, followed by a rapid sea-level rise (up to 900 m) resulting from the collapse of the Gibraltar channel. In their model, the rapid sea-level rise occurred well before the Mio-Pliocene boundary, at $\sim$5.46 Ma,

i.e., during the *Lago Mare* phase. They proposed that, were this to be the case, the eustatic sea-level rise associated with a small-scale deglaciation occurred during the latest Messinian (Bache et al., 2009, 2012) and could explain, at least in a part, the transgressive trend observed in the onshore stage 3 deposits. This would indicate a Mediterranean base-level already rising well before the base of the Pliocene.

4.4 Messinian Salinity Crisis Stratigraphic Framework

During the Late Miocene, the Mediterranean Sea and portions of the present-day landmass were segmented into a mosaic of interconnected sub-basins of various depth and size inherited from a complex assemblage of different structural domains and separated to each other by sills (Fig. 4.6, Roveri et al., 2014). During the Messinian Salinity Crisis, the drawdown provided a new configuration to the Mediterranean sub-basins and created a succession of morphological and sedimentological changes. A major contrast existed between the margins and the deep basins: the former have been deeply eroded whereas the latter have accumulated thick evaporite and clastic sediments that have been eroded from the adjacent continental margin. The Messinian deepest basins of $>$1500 m of depth roughly coincide with the extent of the present-day abyssal plains although the paleobathymetry changed locally in response to geodynamical constraints. Widespread evidences for deep-water conditions before and after the Messinian Salinity Crisis has been observed as the presence of psychrospheric ostracod and benthic foraminiferal assemblages, which usually live at depths of 1000–1300 m (Benson, 1973a,b, 1978; Cita, 1973; Sprovieri et al., 1996a,b, 1999; Sgarrella et al., 1997). The close similarities in thickness and composition of the Messinian sedimentary succession in the deepest eastern and western Mediterranean basins imply similar evolution of the hydrological changes in these basins, confirming their close genetic relationships (Figs 4.6, 4.7; CISEM, 2008; Roveri et al., 2014).

During the Messinian Salinity Crisis, the depositional history of the Messinian successions was

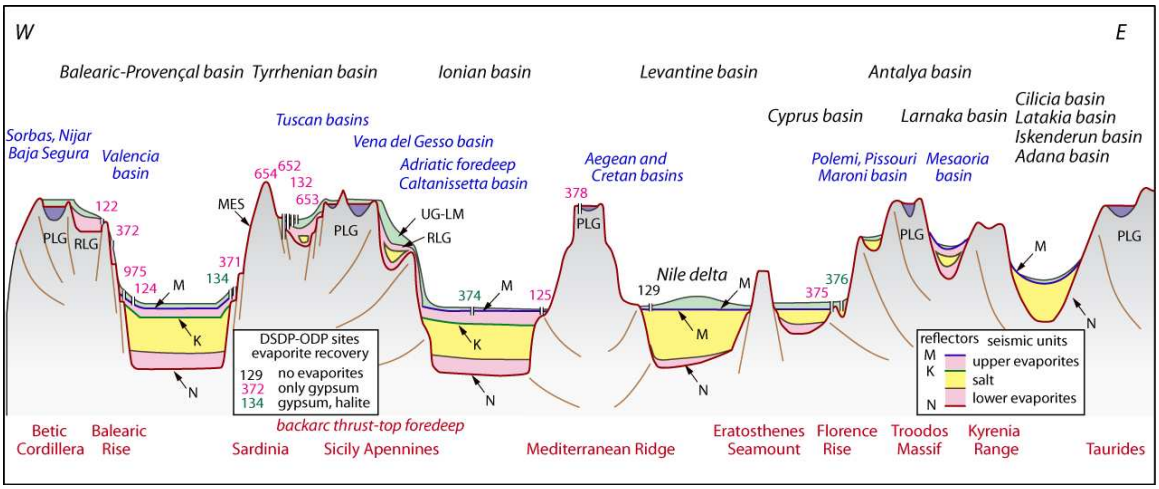

Figure 4.6: Distribution of Messinian deposits and seismic units across the Mediterranean basins along a schematic west to east cross-section showing the location of the main onshore outcrops and of the DSDP–ODP (adopted from Roveri et al., 2014a,b). Drilling sites are also reported: in pink the sites where only sulfate evaporites have been recovered; in green the sites where halite has been recovered. Onshore units: PLG= Primary Lower Gypsum; H= halite; RLG= Resedimented Lower Gypsum; UG= Upper Gypsum; LM= *Lago Mare*; Offshore units: LE= Lower Evaporites; LU= Lower Unit; H= Messinian Salt; MU= Mobile Unit; UE= Upper Evaporites=UU, Upper unit Surfaces: MES= Messinian erosional surface/marginal erosional surface. Base of Messinian evaporites: horizon N = BES, basal erosional surface/BS, basal surface; Top of the Messinian evaporites: horizon M= TES, Top erosional surface/Top Surface.

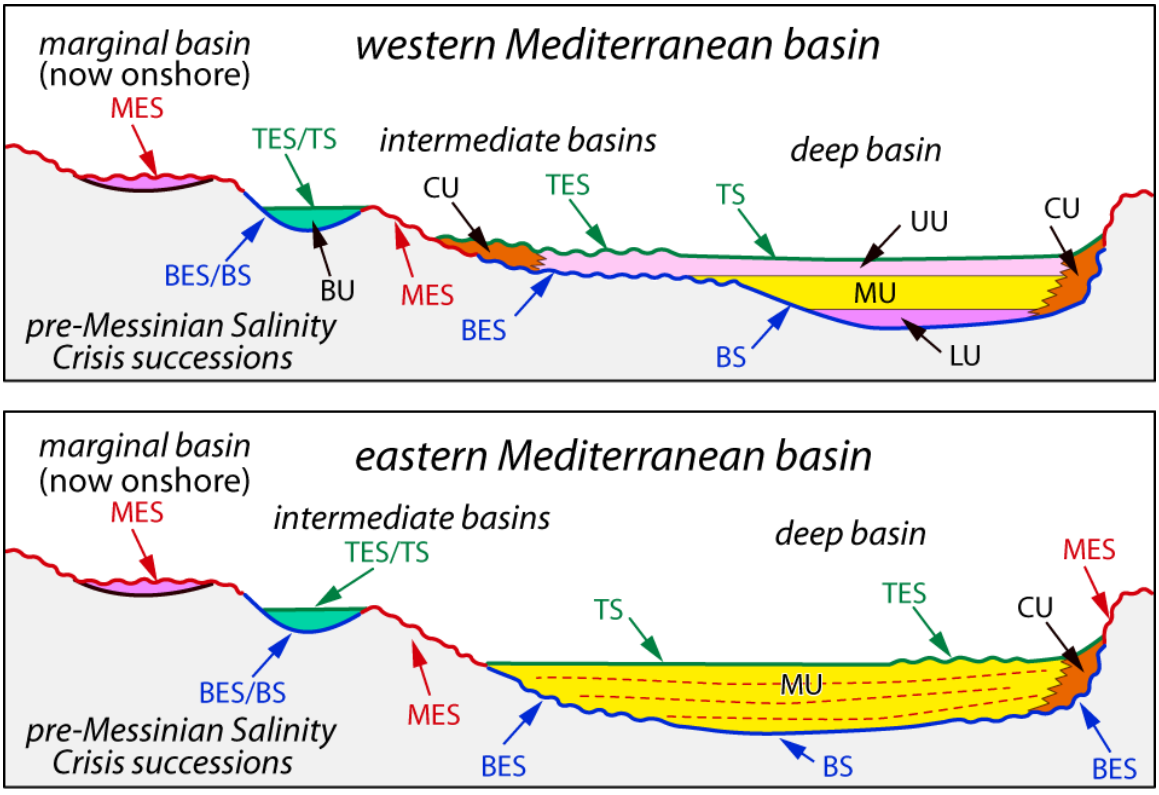

Figure 4.7: Schematic conceptual sketches across the western (a) and eastern (b) Mediterranean basins, illustrating the organization of the Messinian Salinity Crisis seismic markers from the margins down to the deep basins at the end of the Messinian Salinity Crisis (adopted from Roveri et al., 2014a,b). Abbreviations are given in Figure 4.6.

complex and its stratigraphy varied throughout the Mediterranean region (Hsü et al., 1973; Lofi et al. 2011a,b). The distribution of the Messinian deposits resulted from the superimposition of regional controlling factors related to the Messinian Salinity Crisis and local controlling factors related to the structural and geodynamical evolution of the basins (Rouchy and Caruso, 2006).

In the Mediterranean region, the classic Messinian successions were first described from Sicily (Decima and Wezel, 1973). Here the successions start with cyclic alternations of open marine marls and sapropels, pass via diatomites into the "Lower Evaporites" (evaporitic limestone, gypsum, marls and halite), and end, above an erosional surface and sometimes angular unconformity, with the "Upper Evaporites" (gypsum, marls) and fresh to brackish water deposits of *Lago Mare* facies (Figs. 4.4–4.7; Lofi et al., 2005; Rouchy and Caruso, 2006; Roveri et al., 2006; Krijgsman et al., 2008 and references in it). In the western Mediterranean, the stratigraphy of the successions associated with the Messinian Salinity Crisis is well constrained and a new global and consistent terminology for the Messinian seismic surfaces and depositional units have been provided (CIESM 2008, Lofi et al., 2011a,b). In the deep western Mediterranean basins the thickness of the evaporite deposition reaches $\sim$1600 m and Messinian Salinity Crisis seismic markers include six bounding surfaces, separating five depositional units (Fig. 4.7). In contrast, the stratigraphic and lithological history of the successions associated with the Messinian Salinity Crisis in the eastern Mediterranean region is less well constrained. In the deep eastern Mediterranean basins, evaporates successions of up to 3500 m have been observed (e.g., Mediterranean Ridge and Herodotus Basin), which is considered to be the result of an over thickening of the evaporites caused by tectonics and downslope gliding (Rouchy and Caruso, 2006). Messinian evaporites in the eastern Mediterranean basins are generally composed of a single complex mobile unit (CMU) which is classically subdivided into lower and upper layers (Bertoni and Cartwright, 2006; Loncke et al., 2011; Maillard et al., 2011; Lofi et al., 2011a,b; Figs. 4.6, 4.7). In the Levantine Basin the mobile unit of the Messinian successions includes up to four distinct internal reflections (Fig. 4.7; Réhault et al., 1984; Garfunkel,

1984; Rouchy and Saint Martin, 1992; Polonia et al., 2002; Gradmann et al., 2005; dos Reis et al., 2005). Three explanations have been given for these reflections: (a) interbedded shales, (b) layers of different evaporites, and (c) several depositional cycles.

Previous studies have described the Late Miocene sedimentary successions from measured sections in Cyprus and the onshore Antalya Basin (Akay et al., 1985; Karabıyıkoğlu et. al., 2000, Orszag-Sperber et al., 2009; Manzi et al., 2014, Turkish Petroleum unpublished data), boreholes from the DSDP Leg 42 Sites 375 and 376 in the Florence Rise (Fig. 4.1; Baroz et al., 1978), and the previous seismic surveys (PRISMED II, P/V Atalante, Woodside et al, 2001; Black, R/V Le Suroît, Benkhelil, et al., 2005), as well as the Ocean Drilling Program Leg 160, Sites 965–968 across the Eratosthenes Seamount (Robertson, 1998b). However, little is known about the stratigraphy in the offshore Antalya Basin and other deep basins in the eastern Mediterranean. (This thesis provides a new stratigraphy for the offshore Antalya basin, for comparison with studies elsewhere in the Mediterranean.)

In the onshore Antalya Basin, the Messinian was described from the Manavgat Basin along the eastern side of the regionally extensive onland Antalya Basin by Bizon et al. (1974), then by Flecker (1995). As indicated in Chapter 3 (see Section 3.4), the sediments drilled in the Manavgat-2 well did not include any Messinian-age gypsum, anhydrite and evaporitic carbonates that are seen on outcrops (Deynoux et al., 2005; Çiner et al., 2008). On the basis of biostratigraphic data, this succession is correlated with the Late Miocene Taşlık Formation, which is the lateral equivalent of the evaporitic successions of the Gebiz Formation, associated with the Messinian Salinity Crisis (e.g., Garrison et al., 1978). In the Aksu Basin, along the western side of the Antalya Basin recent studies show that the Messinian successions are present in the Gebiz area and also southwards, along the eastern part of the basin (Akay et al., 1985). However, Messinian evaporites are not encountered in the Aksu-1 well (Turkish Petroleum Corporation, unpublished data) and also do not exist in the central part of the basin (Poisson et al., 2003b, 2011). The Gebiz section across the eastern part of the Aksu

Basin consists of two units: a basal unit consisting of marls, sandstones and micro-conglomerates, which is unconformably overlain by the upper Gebiz limestone. The Gebiz limestone is subdivided into five members: (a) basal conglomerate, (b) lower limestone unit, (c) intermediate marls, (d) upper limestone composed of bioclastic calcilutites and calcarenites and (e) breccias and stromatolitic limestone, which separated from the upper limestone unit by deep erosional surface (Poisson et al., 2003b). In the absence of biostratigraphic markers the Gebiz limestone have been attributed to Late Miocene (Bizon et al., 1974), Early Pliocene (Poisson, 1977), Messinian (Akay et al., 1985; Akay and Uysal, 1985), Tortonian (Glover, 1995; Glover and Robertson, 1998a,b), Late Tortonian-Messinian (Tuzcu and Karabıyıkoğlu, 2001; Karabıyıkoğlu et al., 2005) and Late Messinian-Early Pliocene (Poisson et al., 2003b). However, new stratigraphic data provided a precise Messinian age for the Gebiz limestone (Poisson et al., 2011). These authors indicated that the Messinian successions are topped by an erosional surface indicating a break in the marine sedimentation between the Messinian and the Lower Pliocene, related to the sea level drawdown across the eastern Mediterranean Sea.

In northern Cyprus, the Lapatza Formation of the Mesaoria Basin and its late Miocene evaporite depositions are essentially dominated by gypsum (Fig. 4.8, 4.9; Baroz et al., 1974, Manzi et al., 2014). However, $\sim$300 m of rock salt are recovered in the Xeri borehole across the central portion of the Mesaoria Basin (Figs. 4.8, 4.9; Gass, 1960). Evaporites of the Lapatza Formation generally have been subdivided into two members: Lower Gypsum and Upper Gypsum. The Lower Gypsum is $\sim$70 m thick and is composed of selenite and laminated gypsum (Fig. 4.8; Robertson et al., 1995). The Upper Gypsum is $\sim$60 m thick and it is lithologically variable, consisting of gypsum layers alternating with chalks and siliciclastics containing marine microfossils (Robertson et al., 1995). The presence of marine microfossils suggests the occasional influx of marine waters into predominantly brackish *Lago Mare* environment. In southern Cyprus the Kalavasos Formation records the whole Messinian Salinity Crisis: it is subdivided into three sub-units (Fig. 4.8; Rouchy, 1982; Robertson et al., 1995; Orszag-Sperber et al., 2009). These are from the bottom: (a) the Lower Gypsum; (b) the

Intermediate Breccia; and (c) the *Lago Mare* deposits and Upper Gypsum (Fig. 4.8). The Lower Gypsum is up to 70 m thick (Robertson et al., 1995), and is described as a composite unit including selenitic, laminar (locally known as "marmara" gypsum), clastic and nodular gypsum (Rouchy, 1982). A discontinuous unit known as "barre jaune", a carbonate breccia including stromatolitic deposits and fragments of primary gypsum (Fig. 4.8; Rouchy, 1982; Orszag-Sperber et al., 2009), is commonly present at the base of the lower unit. The Intermediate Breccia is up to 20 m thick (Robertson et al., 1995), and is composed of polygenic and heterometric breccia made up of gypsum clasts and blocks in a carbonate/gypsarenite matrix (Rouchy, 1982). According to Robertson et al. (1995) the gypsum clasts are derived from different gypsum facies including both twinned selenite crystals and laminar gypsum. These authors suggest that this complex unit resulted from large-scale tectonically induced mass-failures within the Mesaoria Basin. The Upper Gypsum unit is up to 60 m thick (Robertson et al., 1995), and is lithologically very variable. According to Rouchy (1982), this unit includes up to six gypsum beds characterized by different facies, mainly selenitic in the lower three beds, and mainly laminar gypsum associated with clastic and minor selenitic gypsum in the upper three-beds. These gypsum beds are separated by marl horizons characterized by the presence of the typical *Lago Mare* brackish water faunal assemblages (Fig. 4.8; Roveri et al., 2008a and references therein) of Parathetyan affinity, including mollusks (*Limnocardiine*, *Melania*, *Melanopsis*), ostracods (*Cyprideis*) and foraminifers (*Ammonia beccarii*). In the Pissouri Basin the interval comprised between the uppermost gypsum bed and the Messinian-Zanclean boundary consists of a lower marl unit with *Lago Mare* ostracods and gastropods capped by an alternation of conglomerate, calcarenites and paleosoils (Figs. 4.8, 4.9; Rouchy et al., 2001, Manzi et al., 2014). The final stage of the Messinian Salinity Crisis is marked by deposition of the Upper Gypsum and "*Lago Mare*" units (Orszag-Sperber et al., 2009).

The Messinian sedimentary successions in the marine areas were cored during DSDP Leg 42 at Sites 375 and 376 on the Florence Rise (Shipboard Scientific Party, 1978), as well as during the ODP

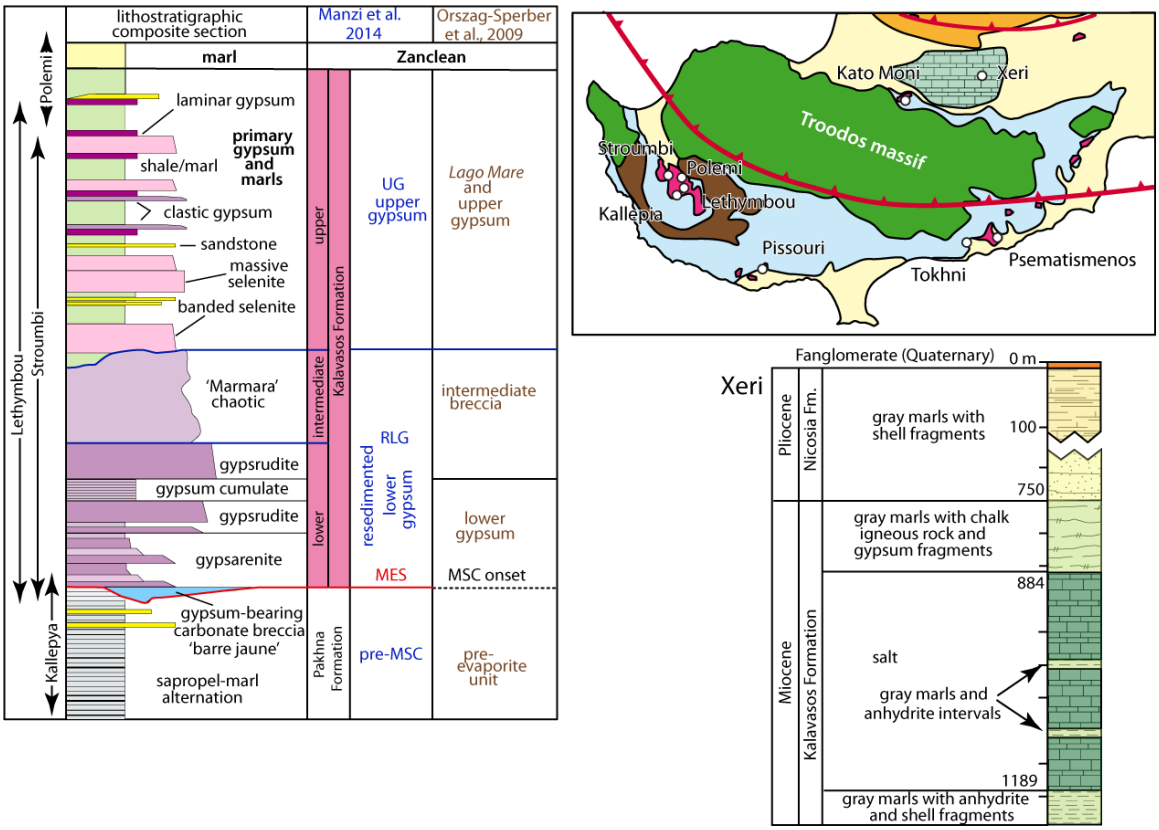

Figure 4.8: Stratigraphic composite section of the Polemi Basin (adopted from Manzi et al., 2014). The subdivisions adopted in the Orszag-Sperber et al. (2009). The stratigraphy of the central Mesaoria basin (adopted from Manzi et al., 2014), the Xeri borehole (adopted from Gass, 1960).

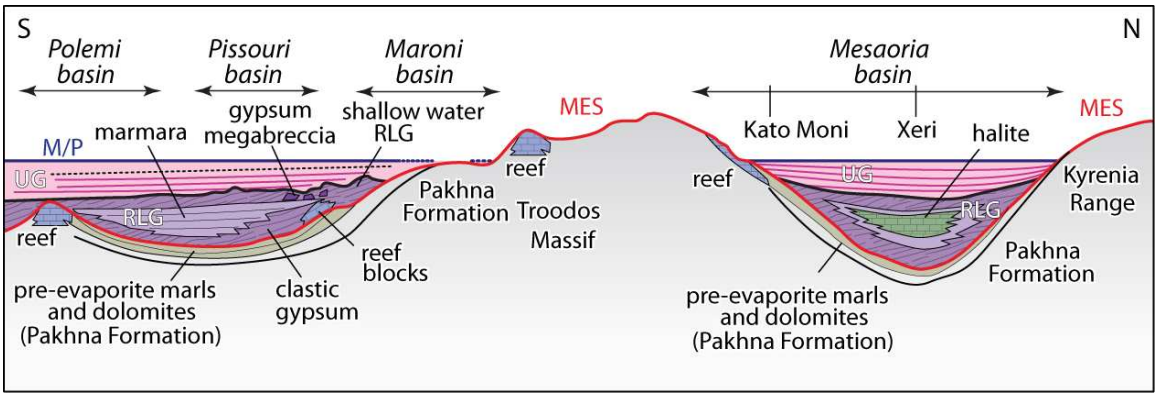

Figure 4.9: N-S schematic geological section along the southern Island of Cyprus across the Troodos Massif (adopted from Roveri et al., 2014, who has modified from Robertson et al., 1995).

Leg 160 at Sites 965, 968 (Fig. 4.1; Shipboard Scientific Party, 1996). Site 375 (TD 821.5m) was located near the top of the Florence Rise and intermittently cored a sediment sequence, Burdigalian to Quaternary in age. Site 376 (TD 216.5m) was located $\sim$13 km to the north, at the southern margin of the Antalya Basin and near the pinch-out of the salt layer (Figs 4.1, 4.10, also see Fig. 3.5 § Chapter 3) The sites complement each other and combined provide a standard section for correlation with onshore sequences in Cyprus (Figs. 3.5, 4.10).

The thickness of Messinian evaporites is less than 50 m at Site 375 and more than 76 meters at Site 376. Site 375 only represents the uppermost part of the sequence, and is characterized by gypsum and green dolomitic marlstone. At Site 376, two units are identified as Messinian in age; Unit V and Unit VI, and these correspond to the Lapatza Formation and Kalavasos Formation of Cyprus (Fig. 4.10; Shipboard Scientific Party, 1978). The Messinian units are briefly described below:

- Unit V consists of nannofossil dolomitic marlstones, with intercalations of siltstones and sandstones. It is subdivided into four sub-units. Sub-units Va and Vb are two successions of a slightly silty nannofossil dolomitic marlstone, with minor amounts of interbedded siltstones and sandstones. Sub-unit Vc contains thinly bedded inter-layered laminated siltstones and marlstones, probably of turbiditic origin. Finally, Sub-unit Vd is characterized by abundant detrital gypsum, and greenish sandstones and siltstones. Marine microfossils, such as planktonic foraminifers and cysts of marine planktonic algae have been identified in several horizons. Their presence suggests the occasional influx of marine waters into this predominantly brackish "*Lago Mare*" environment. Parts of Unit V have also been recognized at Site 375; however, its thickness there is unknown. Seismic data show that Unit V increases markedly in thickness towards the Antalya Basin (Fig. 4.10; Shipboard Scientific Party, 1978).

- Unit VI is composed of gypsum, green dolomitic marlstone, anhydrite and halite. It is divided into two sub-units. Sub-unit VIa underlies Unit V and contains olive grey to light grey

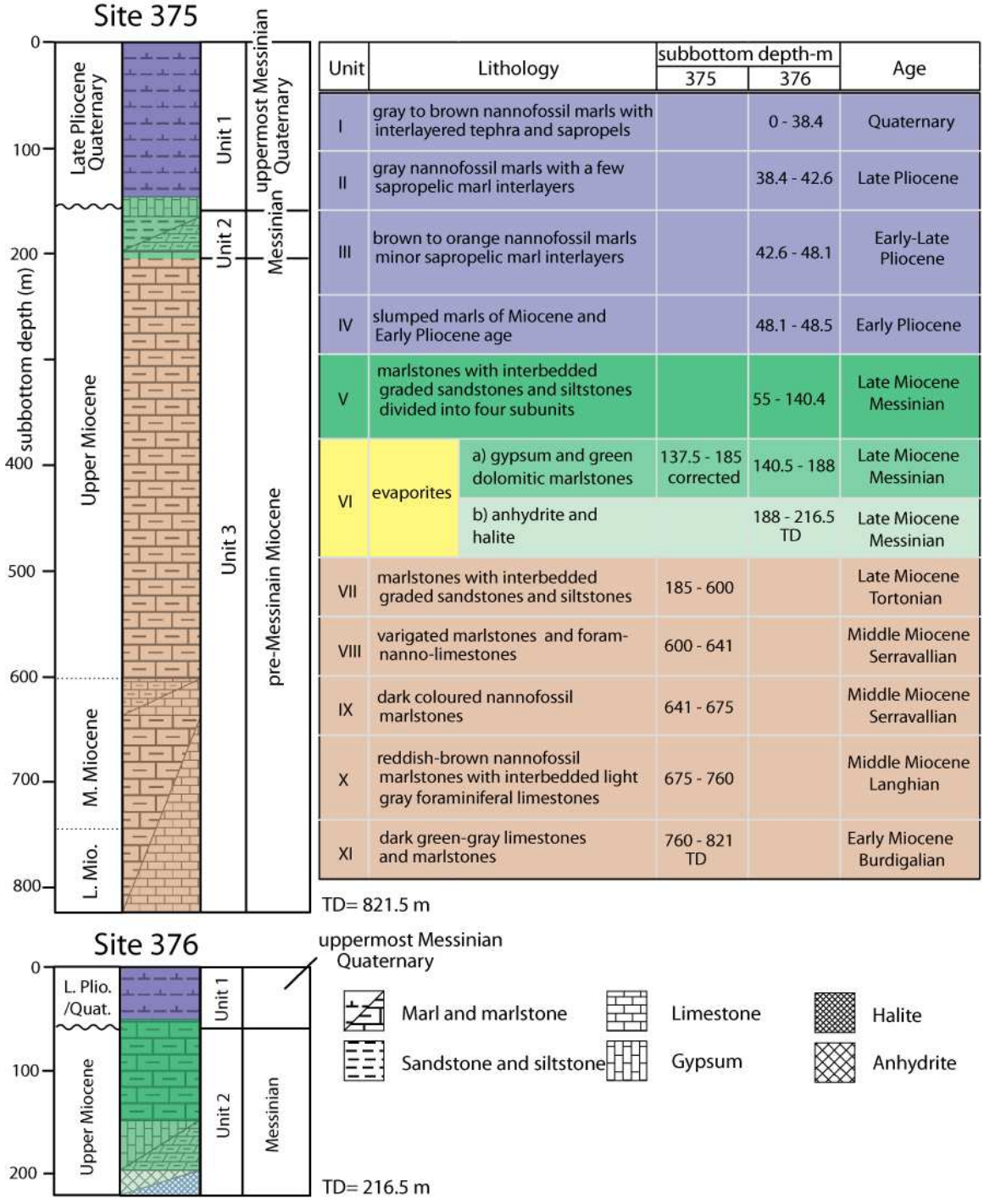

Figure 4.10: Simplified lithostratigraphy of the Deep Sea Drilling Project Leg XLII, Sites 375 and 376 (adopted from Shipboard Scientific Party, 1978).

gypsum. The Sub-unit includes crudely layered and recrystallized gypsum, coarse selenitic gypsum crystals, coarse recrystallized gypsum with roughly equant and traced anhydrite and elongate selenitic "swallow-tail" gypsum crystals, set in a matrix of gypsiferous greenish-white marlstone. Sub-unit VIb is mainly composed of anhydrite and halite, and contains from top to base: (i) clear, coarsely crystalline halite with thin wavy interlayers of finely crystalline gypsum; (ii) white nodular anhydrite with large and small enter-oolitic folds and occasional chicken-wire structure with considerable amounts of gypsum; (iii) banded anhydrite, in which thin dark brown, organic-rich laminae separate up to 1 cm thick bands of nodular anhydrite; and (iv) banded halite with 2 to 4 cm thick layers of clear coarsely crystalline halite separated by 0.5 cm thick, brown, fine-grained gypsum layers containing rare anhydrite (Fig. 4.10; Shipboard Scientific Party, 1978).

In this dissertation Sub-unit VIa has been interpreted as the deep and margin lateral equivalent of Upper Evaporites and Sub-unit VIb has been interpreted as deep basinal lateral equivalent of the Lower Evaporites (Lower Gypsum) identified from the marginal basins (Hsü et al., 1978, Rouchy, 1982).

Messinian-age sediments are also recovered during the drilling of the Ocean Drilling Program Leg 160 Sites 965 and 968A (Shipboard Scientific Party, 1996). Sites 965 and 968 are critical for this study. The upper Messinian succession recovered at Ocean Drilling Program Hole 968A on the Cyprus lower slope (Fig.4.1) was generated under brackish conditions (*Lago Mare*), as deduced from sedimentological and paleontological data. Gypsum that displays marine signatures (stable isotope composition of gypsum and monospecific nannoplankton included in gypsum crystals) is interbedded within this series and interpreted as being reworked from earlier Messinian evaporite deposits, such as those present onshore in Cyprus (Blanc-Valleron et al., 1996).

The sedimentary sequence recovered at Site 968A is assigned to three lithostratigraphic units (Shipboard Scientific Party, 1996). Unit I corresponds to 143 m of early Pliocene to late Pleistocene

age nannofossil clay, nannofossil silty clay, and clayey nannofossil ooze. Several ash layers occur in the upper 55 m, and about 80 sapropels are present within the upper 116 m. Unit II (143—167 mbsf) consists of nannofossil clay, clayey nannofossil ooze, clay, and calcareous silty clay. Down to 153.8 mbsf the series is of early Pliocene age, but below it may be early Pliocene to Miocene(?) in age. Unit III (167-302.7 mbsf) is composed of calcareous silty clay, silt, and sand. Some gypsum occurs, as millimeter- to centimeter-thick layers, at approximately 215 mbsf. Paleontological evidence suggests that this interval is Messinian in age (Shipboard Scientific Party, 1996).

Hole 965 penetrated 250.4 m of calcareous ooze and clays overlying limestones, where the sediments are divided into three lithostratigraphic units (Shipboard Scientific Party, 1996). The unconsolidated material is principally nannofossil clay with limited intervals of foraminifer-bearing nannofossil clay and nannofossil ooze. Intercalated within the calcareous muds are several decimeter-thick, dark-colored sapropels that contain disseminated organic matter and pyrite in addition to the common components of the muds. Unit I extends from 0 to 23 mbsf and consists of nannofossil ooze, clayey nannofossil ooze, nannofossil clay, and foraminiferal sand, all characterized by random alternations of color bands through a range of browns, grays, and greenish grays. Unit II directly underlies Unit I and consists of a 6.3 m thick mottled clays that contain clasts of chalky calcite. It is early Pliocene in age. Underlying the clay of Unit II is a continuous sequence of limestone that occupies the section to total depth of the hole at 250.4 mbsf. The calcareous muds overlie a 5.9 m-thick clay layer that rests unconformably on limestone. The limestone varies from oosparites at the top through a range of biosparites and biomicrites to the bottom of the unit, where. Biostratigraphic data show that Unit III is Miocene in age (Shipboard Scientific Party, 1996).

Previous seismic studies have shown that the thickness of the Messinian evaporites in the Eastern Mediterranean reaches to 2000 m in basins such as Levantine Basin and Herodotus Basin (Netzeband et al., 2006). In the Florence Rise area, the Messinian evaporites pinch out across the core of the rise and are absent over the crestal region of the Florence Rise (Woodside et al., 2002), where the

major erosional M- and N-reflectors converge to form a prominent composite unconformity. The Messinian evaporite successions gradually increase in thickness away from the core of the Florence Rise, both toward the Antalya Basin and the Mediterranean Ridge (Hsü et al, 1978; Woodside et al., 2002; Özer, 2009; Sellier et al, 2013b). Özer (2009) showed that further to the north, the Messinian evaporites form a north-thickening wedge which is nestled on the northern fringes of the Florence Rise toward the Antalya Basin. The internal stratigraphy of the Messinian evaporites in the Florence Rise and the Antalya Basin has not been well constrained by previous studies. Limited seismic reflection data collected during PRISMED II seismic survey (R/V Atalante; Mascle, 1998) identified one depositional unit (termed the Mobile Unit), and the six depositional surface markers identified in this part of the eastern Mediterranean (Lofi et al., 2011a, Loncke et al., 2011).

4.5 *Lago Mare*

The *Lago Mare* has long been considered a unique chronostratigraphic unit overlying the Messinian evaporites (Hsü et al., 1973) generated by a rapid flow of low salinity waters from the Atlantic and Paratethyan basins into the almost completely desiccated Mediterranean Basin (Fig. 4.11; Cita et al., 1978a,b).

Lago Mare is a key to the understanding of the geodynamics of the Mediterranean: depth before and after the Messinian Salinity Crisis, connections with Atlantic and Paratethys domains, significance of the erosional phases observed during the Messinian. It documents the onset of the modern marine circulation in the Mediterranean after the reflooding ending the Messinian Salinity Crisis (Do Couto et al., 2014). It widely accepted that the final stage of the Messinian Salinity Crisis is marked by deposition of the Upper Gypsum and *Lago Mare*, overlying the erosional surface. The *Lago Mare* unit corresponds to a very short time interval that separates the marine Lower Evaporite unit from the marine Pliocene sediments. It is predominantly characterized by brackish to fresh water environment at the Miocene–Pliocene boundary. The presence of brackish micro-organisms is

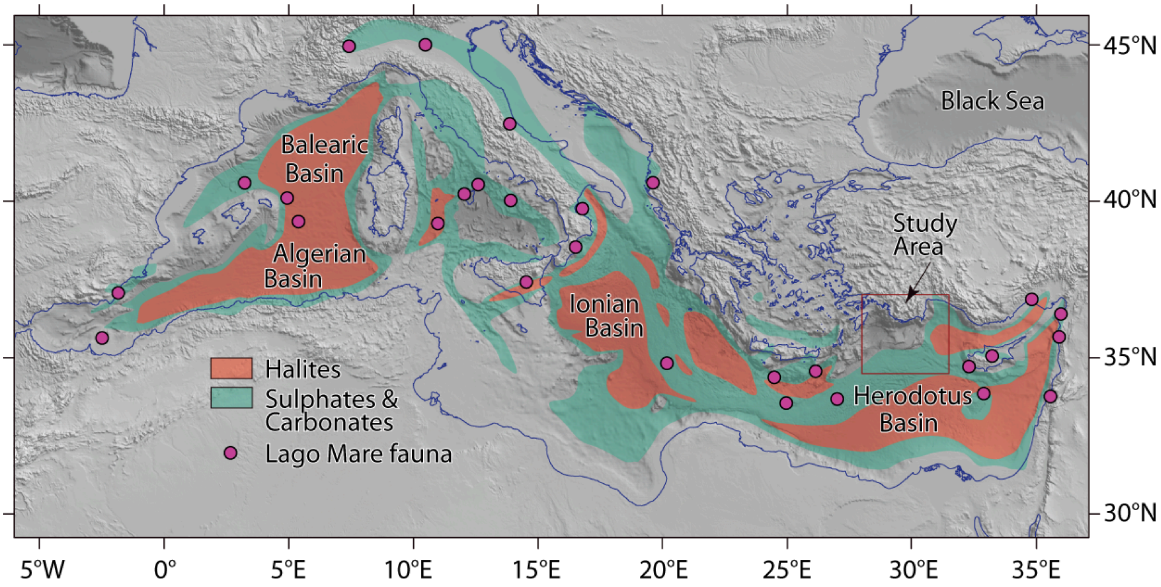

Figure 4.11: Distribution today of the Messinian-age salt and evaporites, and *Lago Mare* fauna identified in drill sites (adopted from Ryan, 2009).

considered to be the consequence of the mixing of faunas due to an exchange of water masses during the very rapid transition from continental to marine conditions at the Miocene–Pliocene boundary (Orszag-Sperber, 2006). Guerra-Merchán et al. (2010) also proposed that near the Strait of Gibraltar, the palaeontological data and the palaeomagnetic results obtained in both the *Lago Mare* unit and the overlying Pliocene marine sediments restrict the age of the former to the post-evaporitic latest Messinian. They correlate these deposits based on the age and the environmental conditions with the *Lago Mare* event that diachroneously by rapidly occurred throughout the Mediterranean before the rapid and widespread marine flooding of the Mediterranean at the beginning of the Pliocene.

The biofacies of the *Lago Mare* deposit are characterized by molluscs and/or ostracods and/or dinoflagellate cysts of Paratethyan-type (Gignoux, 1950; Ruggieri, 1962; Cita and Colombo, 1979; Bertini et al., 1995; Orszag-Sperber et al., 2006). The Mediterranean ostracod assemblages of the post-evaporitic Messinian showed that the *Lago Mare* facies was widespread across the entire Mediterranean region, from Spain and France in the west to Cyprus, Syrian and Levant coastline

in the east (Fig. 4.11; Rouchy et al., 2001; Orszag-Sperber et al., 1989 2000; Cipollari et al., 1999; Gliozzi et al., 2002, 2007; Bassetti et al. 2006; Roveri and Manzi, 2006; Grossi et al., 2008, Manzi et al., 2014).

Both outcrop and borehole data show that the *Lago Mare* type-facies is present across the Mediterranean region, both in the exposed onland basins as well as in the deep parts of the Mediterranean, above the marine evaporites and just beneath the marine Zanclean reflooding (Fig. 4.11). A brackish fauna is described in different ODP sites, particularly at Sites 974 (Tyrrhenian Sea) and 975 (Balearic Basin) in the western Mediterranean (Iaccarino and Bossio, 1999), but also at Sites 965 and 968 (Eratosthenes Seamount; Blanc-Valleron et al., 1996). Records of the *Lago Mare* environment in the deep basins of the western Mediterranean were already described at the ODP Site 652, eastern Sardinia (Cita et al., 1990) and at the DSDP Site 372 on the Minorca Rise (Benson, 1978). Also, the Upper Gypsum and *Lago Mare* units, overlying erosional surfaces and covered by marine Pliocene in the western Mediterranean, display a marked cyclicity, comprising seven–ten sedimentary cycles in the Upper Gypsum of Sicily (Decima and Wezel, 1971; van der Laan et al., 2006; Hilgen et al., 2007; Manzi et al., 2009), the post-evaporitic deposits of northern Italy (Vai, 1997; Roveri et al., 2009, 2014a,b) and the Zorreras/Feos units of southeast Spain (Fortuin and Krijgsman, 2003; Bassetti et al., 2006; Omodeo-Salé et al., 2012).

In the eastern Mediterranean detailed studies of the Pliocene–Miocene boundary in Cyprus and its correlation with western Mediterranean were carried out in the Polemi, Pissouri, Maroni/ Psematismenos and Mesaoria basins (Rouchy et al., 2001; Dupoux, 1983; Ellion, 1983; Orszag-Sperber et al., 1989, 2000, 2009; Manzi et al., 2014). Southern Cyprus basins, such as the Pissouri and Polemi basins, are tectonically controlled depressions oriented NNW–SSE, which widen in the direction of the deep Mediterranean Sea. In the Polemi and Pissouri basins, synthetic stratigraphic sections of the Messinian sedimentary succession observed by Orszag-Sperber (2006) show that the Upper Gypsum includes brackish to fresh water fauna occurring in both basins. Manzi et al. (2014)

proposed a tentative correlation and tuning of the Upper Gypsum of stage 3 units of the Messinian Salinity Crisis in Cyprus, Sicily and northern Apennines (Fig. 4.4). Original tuning was proposed, respectively, by Manzi et al. (2009), for the Upper Gypsum of Sicily, and by Roveri et al. (2008c), for the evaporite-free units of northern Apennine (Fig. 4.12).

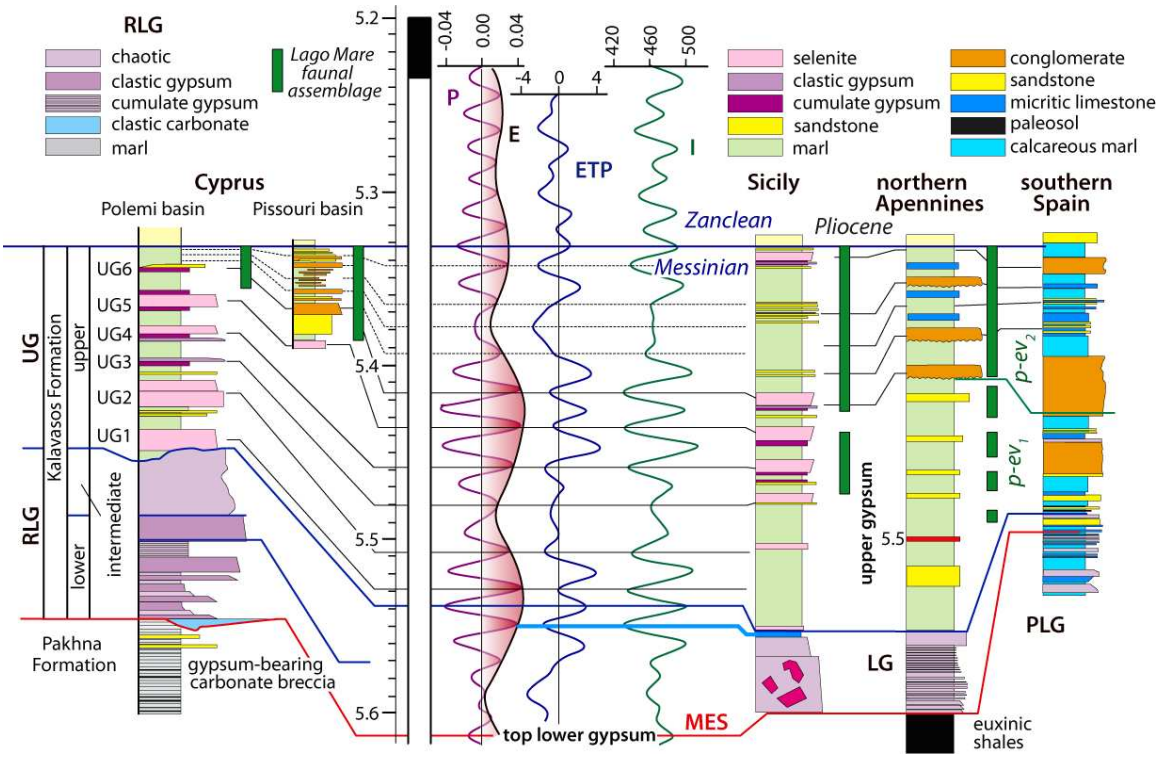

Figure 4.12: Tentative correlation and tuning of the stage 3 units of the Messinian Salinity Crisis of Cyprus, Sicily and Northern Apennines (adopted from Manzi et al., 2014).

Drilling data from west of Cyprus (Florence Rise, DSDP sites 375, 376) show that horizons with marine foraminifera possibly indicate occasional marine influxes within the *Lago Mare* sediments, (e.g., Cita et al., 1978a,b; Blanc-Valleron et al., 1996). Also drilling results of the Eratosthenes Seamount, south of Cyprus (ODP Sites 965, 968) show that sediments across the Miocene–Pliocene transition include faunal assemblages distinctive of *Lago Mare* (Blanc-Valleron et al., 1996; Robert-

son, 1998).

4.6 New seismic data from Messinian successions (Antalya Basin and Florence Rise); Seismic character and distribution of Messinian Salinity Crisis Markers

In this study, the Messinian Salinity Crisis seismic markers have been recognised over the Antalya Basin and Florence Rise area offshore domain, presented in Table 4.1. The identified seismic markers of the Messinian Salinity Crisis correspond to erosion surfaces, depositional units and associated bounding surfaces (Table 4.1 and Fig. 4.13). The main seismic characteristics and distribution of those seismic markers are described briefly below.

Table 4.1: The Messinian Salinity Crisis seismic sequnces and their charactheristics

	This study		MSC Seismic Atlas Lofi et al. (2010)		Seismic Characteristics of MSC subunits This study (Antalya Basin, Florence Rise)
MSC sequences in the deep eastern Mediterranean basin	Subunit 2a Upper Evaporites		Upper Unit		strong seismic expression with lateral continuity high amplitude parallel reflectors with locally internal unconformaties chaotic facies changes
	Subunit 2b	Salt Layer	Mobile Unit 1	Mobile Unit	low reflective, semi transparent high amplitude highly deformed, largely regionally discontinuous reflection packages
	Subunit 2c		Mobile Unit 2		weak and transparent seguence, with less strong internal reflection packages
	Subunit 2d Lower Evaporites		Lower Unit		group of high amplitude low frequency reflections, more or less continuos

In this chapter the terminology used to describe depositional units and surface markers in the Messinian Salinity Crisis is based on the new synthesis of Lofi et al. (2011a). Based on the seismic

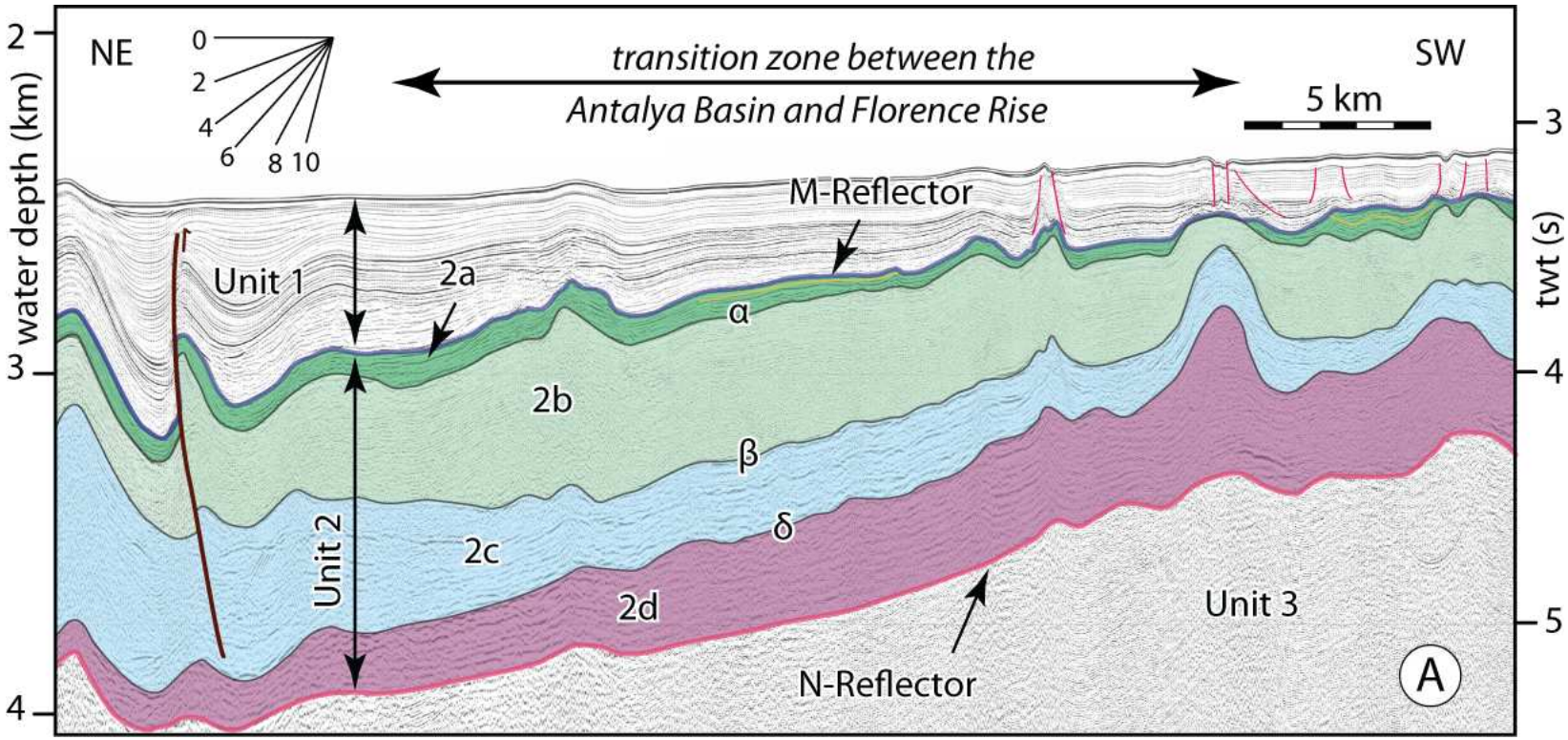

Figure 4.13: High-resolution multi-channel seismic reflection profile A showing the internal architecture of Unit 2 associated with the deposition during the Messinian Salinity Crisis. Note that the prominent M- and N-reflectors define the top and base of Unit 2, respectively and that less prominent reflectors α, β and δ define the bounding surfaces of the sub-units 2a–2d. The correlation of the subunits 2a–2d with the lithostratigraphic units identified in the DSDP Leg XLII, Sites 375 and 376 are given in Figure 4.10, the correlation of these subunits with the Messinian Salinity Crisis units described in Lofi et al. (2011b) are presented in Table 4.1. Location is shown in Figure 4.1. EMED10 (fix 1953-1978)

data presented in this thesis four correlative packages in Unit 2 are identified in deep Antalya Basin for the first time. These sub-units are: sub-unit 2a (Upper Unit, Lofi et al., 2011b), sub-unit 2b (Mobile Unit 1, named by Maillard et al., 2011), sub-unit 2c (Mobile Unit 2, name by Maillard et al., 2011) and sub-unit 2d (Lower Unit, Lofi et al., 2011b; Table 4.1, Figs. 4.7, 4.14). Five seismic reflectors are identified in the study area, bounding the above seismic stratigraphic sub-units: M- and N- and the internal α-, β-, and δ-reflectors (Table 4.1, Figs. 4.13, 4.14, 4.15). A detailed description of the seismic characteristics of each of these seismic sub-units and internal α-, β-, and δ-reflectors is presented below, and correlations are made between these sub-units and Messinian Salinity Crisis successions in deep basin DSDP drill holes and shallow marginal basins.

Based on the drill hole data from DSDP Sites 375 and 376 (Fig. 4.10; Shipboard Scientific Party, 1978) the Messinian Salinity Crisis deposits and their correlation with seismic units in the Antalya Basin and Florence Rise corresponding to lowermost portion of Unit 1 (lower Sub-unit 1c, uppermost Messinian) and entire Unit 2 (Messinian). These successions are correlated with the marlstones and interbedded graded sandstones and siltstones of Unit V, and the anhydrite, halite, gypsum and green dolomitic marlstones of Unit VI. In the DSDP boreholes, there is a gradational transition between Miocene lithostratigraphic Units V to VI and this transitional boundary is also seen in the seismic reflection profiles (Figs. 4.10, 4.13). Unit 2 is also correlated with siliciclastic series interbedded with anhydrite-bearing and/or gypsiferous and carbonaceous sediments as well as the terrestrial coarser siliciclastic sediments of the Taşlık, Eskiköy and Gebiz formations in the onland Aksu and Manavgat Basins (Figs. 4.16, 4.17; Akay et al., 1985; Karabıyıkoğlu et al., 2000), the Kalavasos and Lapatza formations of the Polemi Basin in southern Cyprus, the Mesaoria Basin and Kyrenia Mountains in northern Cyprus, and the Haymanseki and Vakıflı formations of Hatay and Iskenderun basins (Tekin et al., 2010), as well as the typical of thin, marginal facies of the evaporite basins, respectively (Figs. 4.8, 4.16; Hsü et al., 1973, 1978; Shipboard Scientific Party, 1978; Orszag-Sperber et al., 1980a,b, 2009; Rouchy and Orszag-Sperber, 1980; Ellion, 1983; Dupoux, 1983; Roberstson et al., 1995;

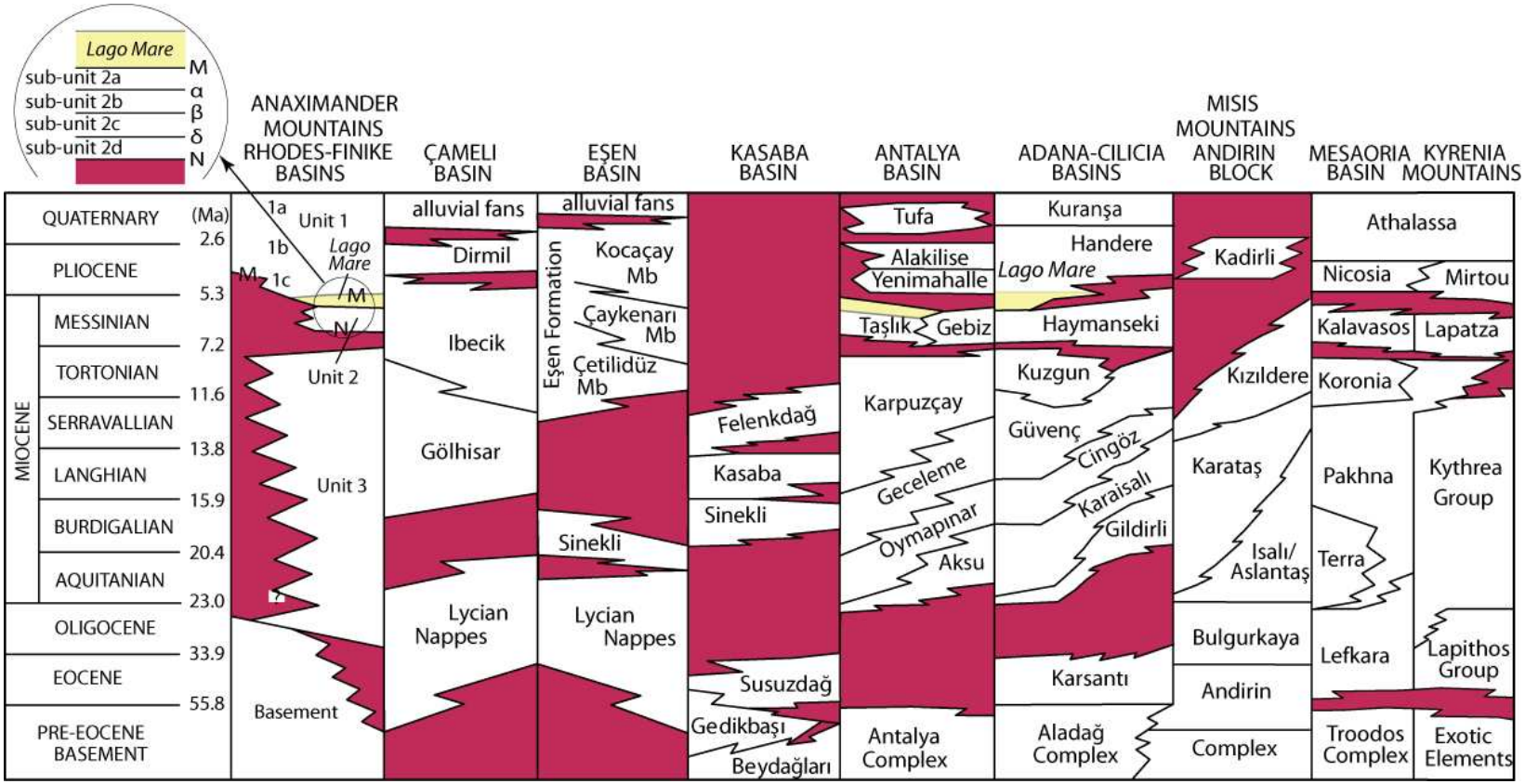

Figure 4.14: Stratigraphy of the Florence Rise and Antalya Basin showing the correlations between seismic stratigraphic units and the sedimentary successions on land, compiled from: (a) Adana and Cilicia basins, Andirin Block= Yalçın and Görür (1984), Kozlu (1987), Yılmaz et al. (1988), Gökçen et al. (1988), (b) Mesaoria Basin and Kyrenia Range= Weiler (1969), Cleintaur et al. (1977), Robertson et al. (1995), (d) Aksu, Köprüçay and Manavgat basins= Akay and Uysal (1985), Akay et al. (1985), Flecker et al. (1998), Karabıyıkoğlu et al. (2000, 2005), Kasaba Basın= Hayward (1984), Şenel (1997a,b), Şenel and Bölükbaşı (1997), Çameli Basin = Elitez and Yaltırak (2014), Eşen (Çay) Basin = Alçiçek et al. (2006); Alçiçek (2007). Stratigraphy of the Manavgat-1 and Manavgat-2 wells is from the Turkish Petroleum Corporation (unpublished data). Unit 2 is delineated by the prominent M- and N-reflectors. Also shown are the α, β and δ reflectors which define the bounding surfaces of the sub-units 2a–2d.

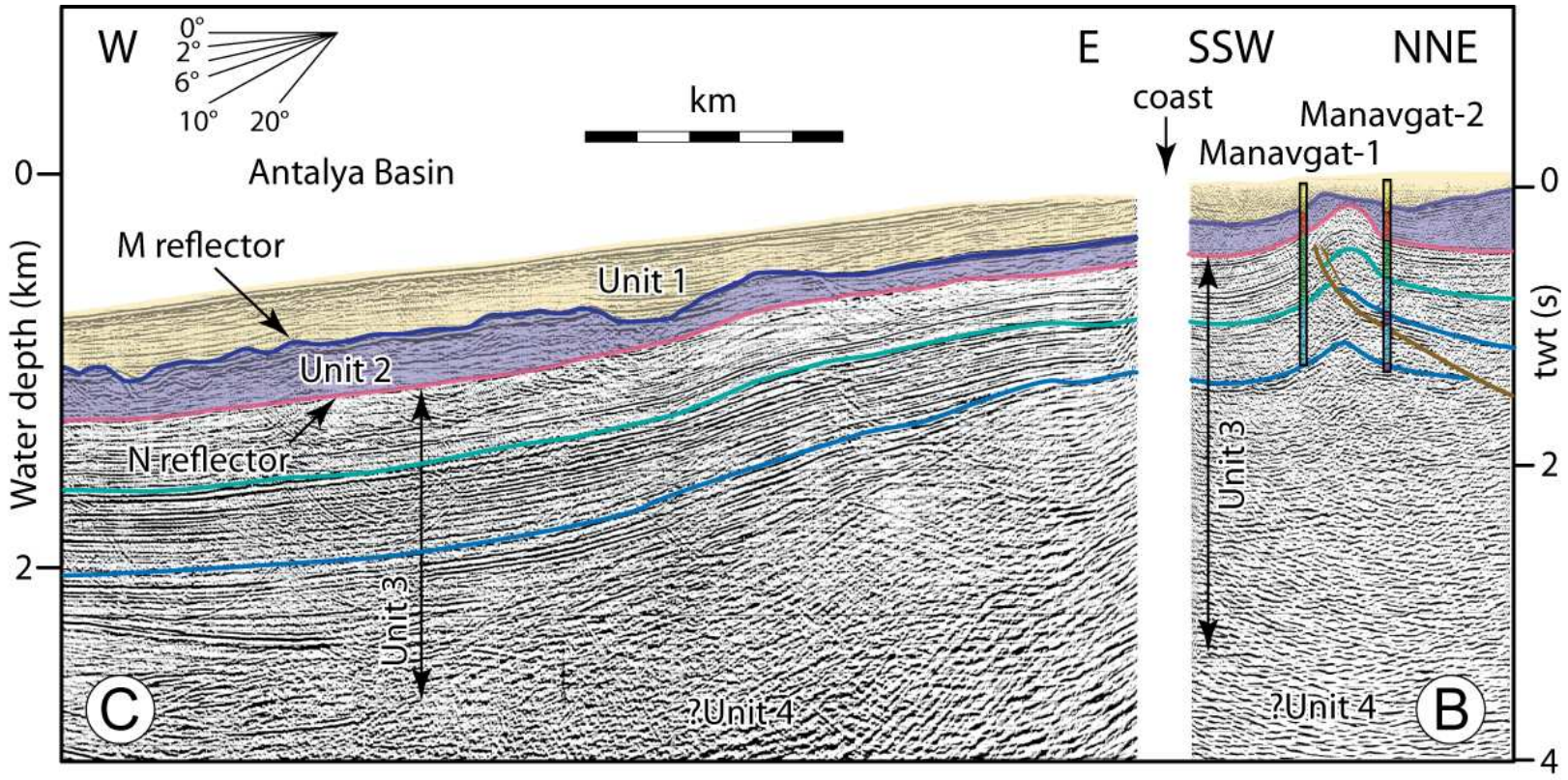

Figure 4.15: Industry seismic reflection profiles (B and C) showing the projected locations of the Manavgat-1 and Manavgat-2 exploration wells, and the seismic stratigraphic correlation into the northern Antalya Basin. Profile is kindly provided by the Turkish Petroleum Corporation. Location of the seismic profile and the wells are shown in Figure 4.1. TP2 & TP11

Manzi et al., 2014).

4.6.1 Sub-unit 2d (Lower Unit)

The lowest sub-unit 2d is characterized by a group of high amplitude, low frequency reflections which are more or less continuous (Fig. 4.15). Sub-unit 2d is bounded below by the pre-Messinian Unit 3 and above by sub-unit 2c. The lowermost reflectors of sub-unit 2d onlap onto the N-reflector (e.g., Fig. 4.18), which corresponds to the Bottom Erosional Surface (BES) of Maillard et al. (2006) and Lofi et al. (2011a). In the study area, the boundary between sub-units 2d and 2c is delineated by the δ-reflector, which laterally shows two distinctly different acoustic characters: (a) a very smooth apparently concordant surface in the transition zone between the Florence Rise and the Antalya Basin, and (b) a very disturbed and erosional surface in the inner and central portions of the Antalya Basin (Figs. 4.18, 4.19). The areal extent and thickness of sub-unit 2d vary throughout the eastern Mediterranean basins. Based on the interpretations of the seismic reflection profiles EMED10-57, EMED10-53, and EMED10-51 across the central segment of the Antalya Basin the thickness of sub-unit 2d varies between $\sim$250 and $\sim$400 ms twt (Figs. 4.13, 4.18, 4.19). The thickness of this sub-unit decreases toward the middle portion of the northern continental slope of the Antalya Basin, where the sub-unit eventually pinches out with no onlap over the N-reflector (Figs. 4.20). Traced from the southern Antalya Basin across the Florence Rise, the sub-unit also shows a notable decrease in thickness and it is absent over the core of the Florence Rise (Fig. 4.13, 4.21–4.24). It is hard to distinguish sub-unit 2d across the southern regions of the Florence Rise, along the western Cyprus Arc and the northern entrance of the Levantine Basin, because the entire seismic Unit 2 shows a very complex geometry. High amplitude low frequency reflections are interfered with by low amplitude high frequency reflections in this part of the study area (Figs. 4.23, 4.24). This complex unit shows largely post-depositional plastic deformation and mobilization along the southern outer part of the Florence Rise.

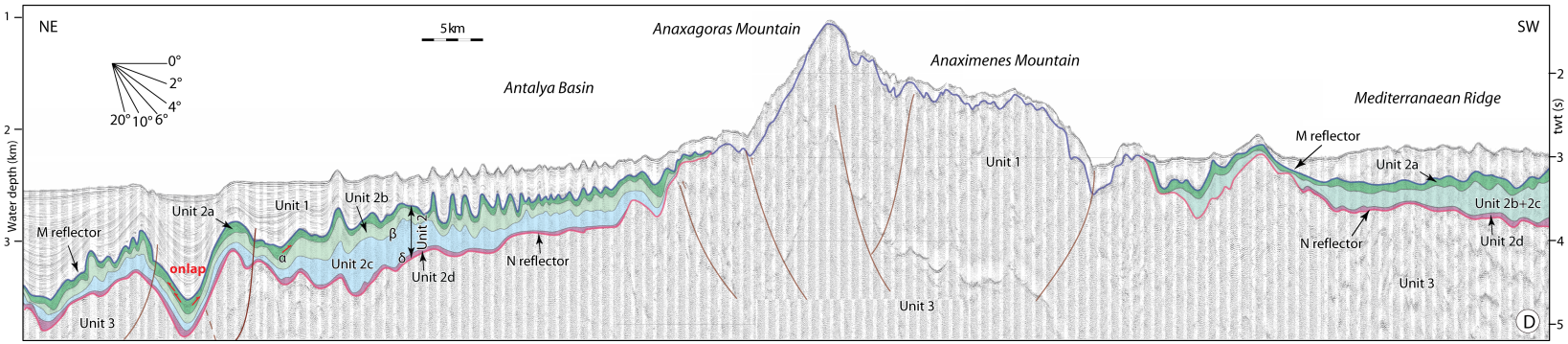

Figure 4.16: High-resolution multi-channel seismic reflection profile D showing the internal architecture of Unit 2 across the southwestern Antalya Basin and the Anaxagoras and Anaximenes Mountain. Reflectors α, β and δ defining the bounding surfaces of the sub-units 2a–2d are discussed in text. Location is shown in Figure 4.1. EMED10 (fix 1451-1536)

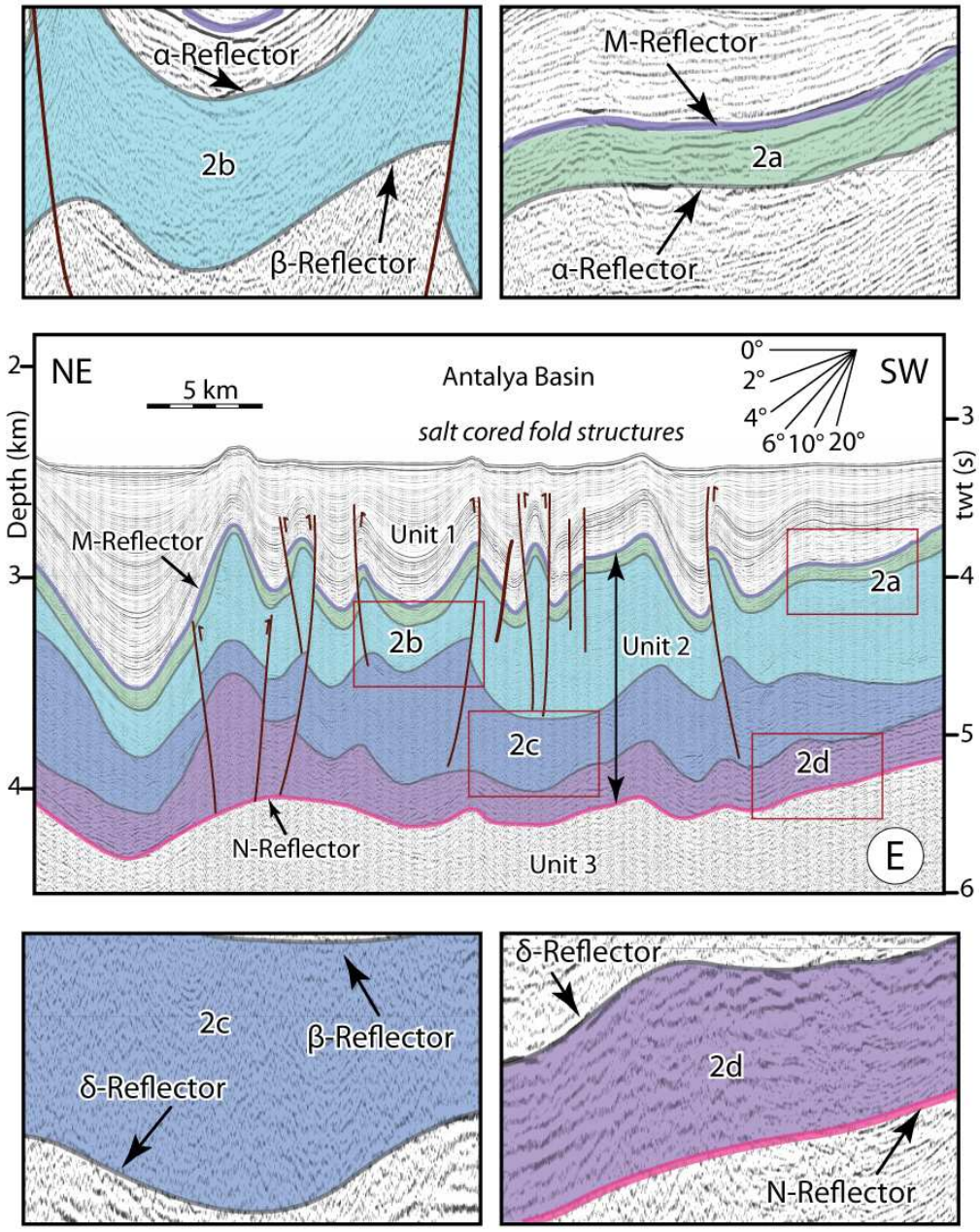

Figure 4.17: High-resolution multi-channel seismic reflection profile E showing the internal architecture of Unit 2 associated with the deposition during the Messinian Salinity Crisis. Note that the prominent M- and N-reflectors define the top and base of Unit 2, respectively and that less prominent reflectors α, β and δ define the bounding surfaces of the sub-units 2a–2d. Insets show the acoustic characteristics of sub-units 2a–2d. Location is shown in Figure 4.1. EMED10 (fix 1972-1998)

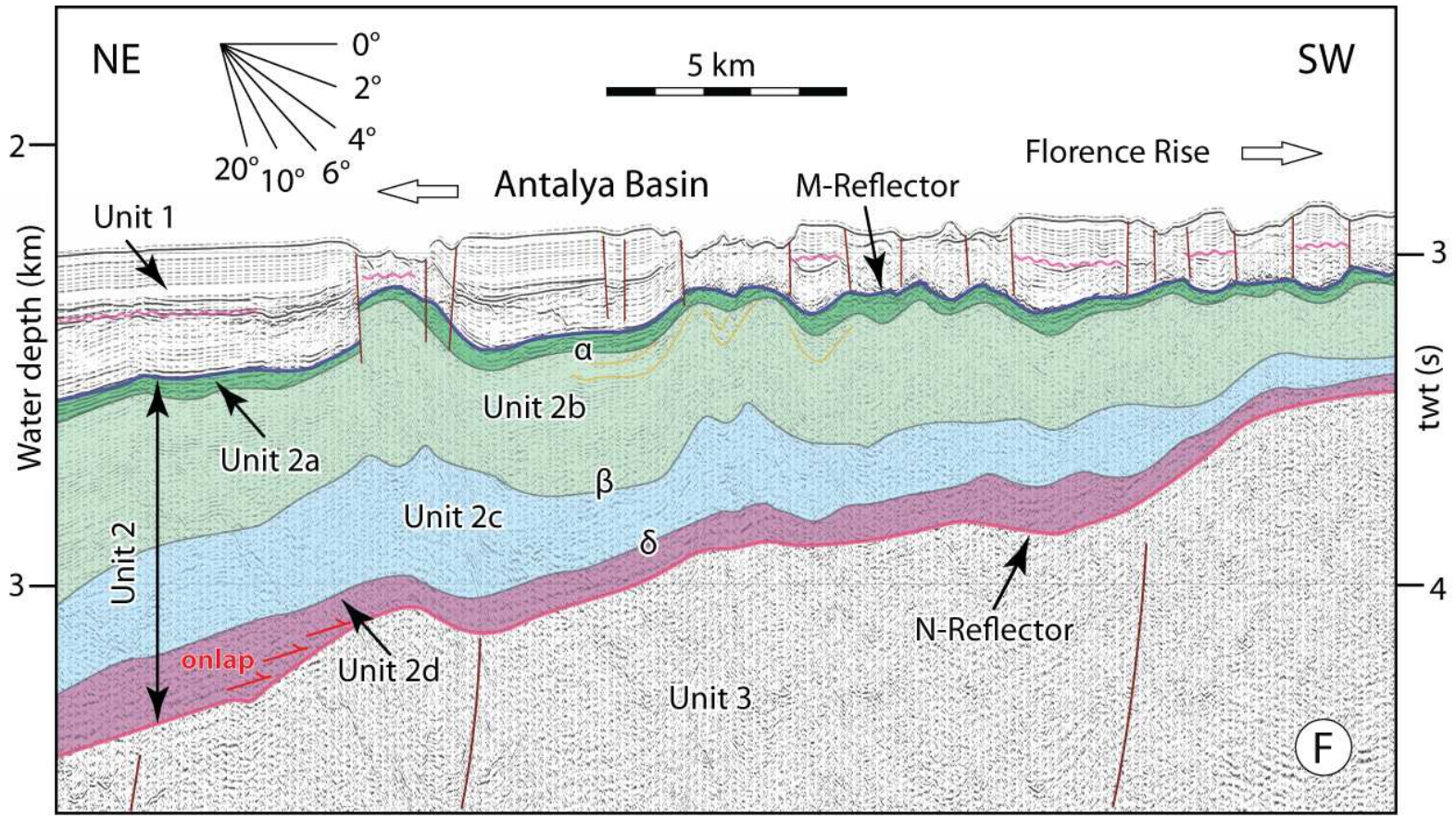

Figure 4.18: High-resolution multi-channel seismic reflection profile F showing the internal architecture of Unit 2 associated with the deposition during the Messinian Salinity Crisis. Note that the prominent M- and N-reflectors define the top and base of Unit 2, respectively and that less prominent reflectors α, β and δ define the bounding surfaces of the sub-units 2a–2d. Location is shown in Figure 4.1. EMED10 (fix 2122-2142)

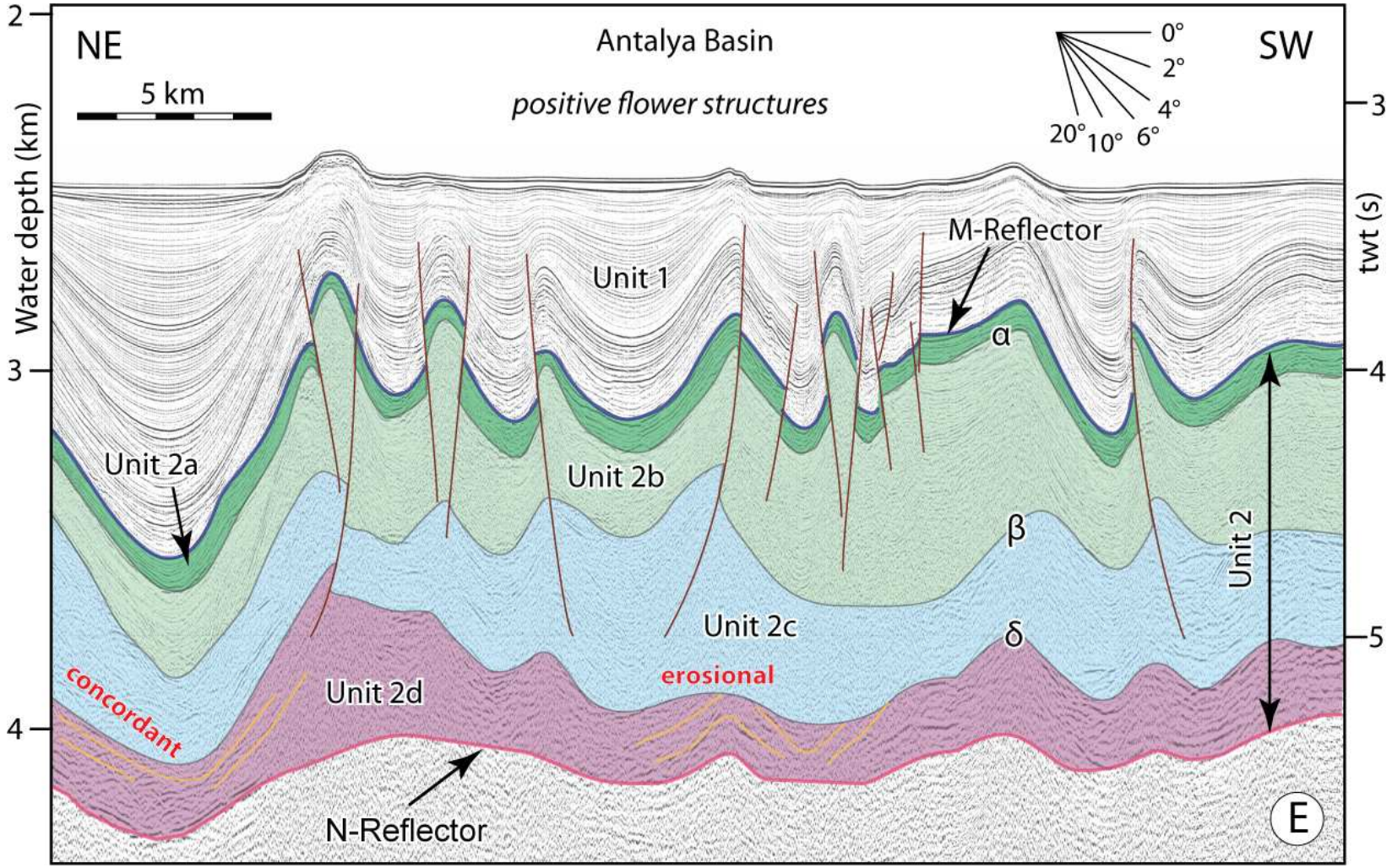

Figure 4.19: High-resolution multi-channel seismic reflection profile E showing the internal architecture of Unit 2 associated with the deposition during the Messinian Salinity Crisis. Note that the prominent M- and N-reflectors define the top and base of Unit 2, respectively and that less prominent reflectors α, β and δ define the bounding surfaces of the sub-units 2a–2d. Location is shown in Figure 4.1. EMED10 (fix 1976-1996)

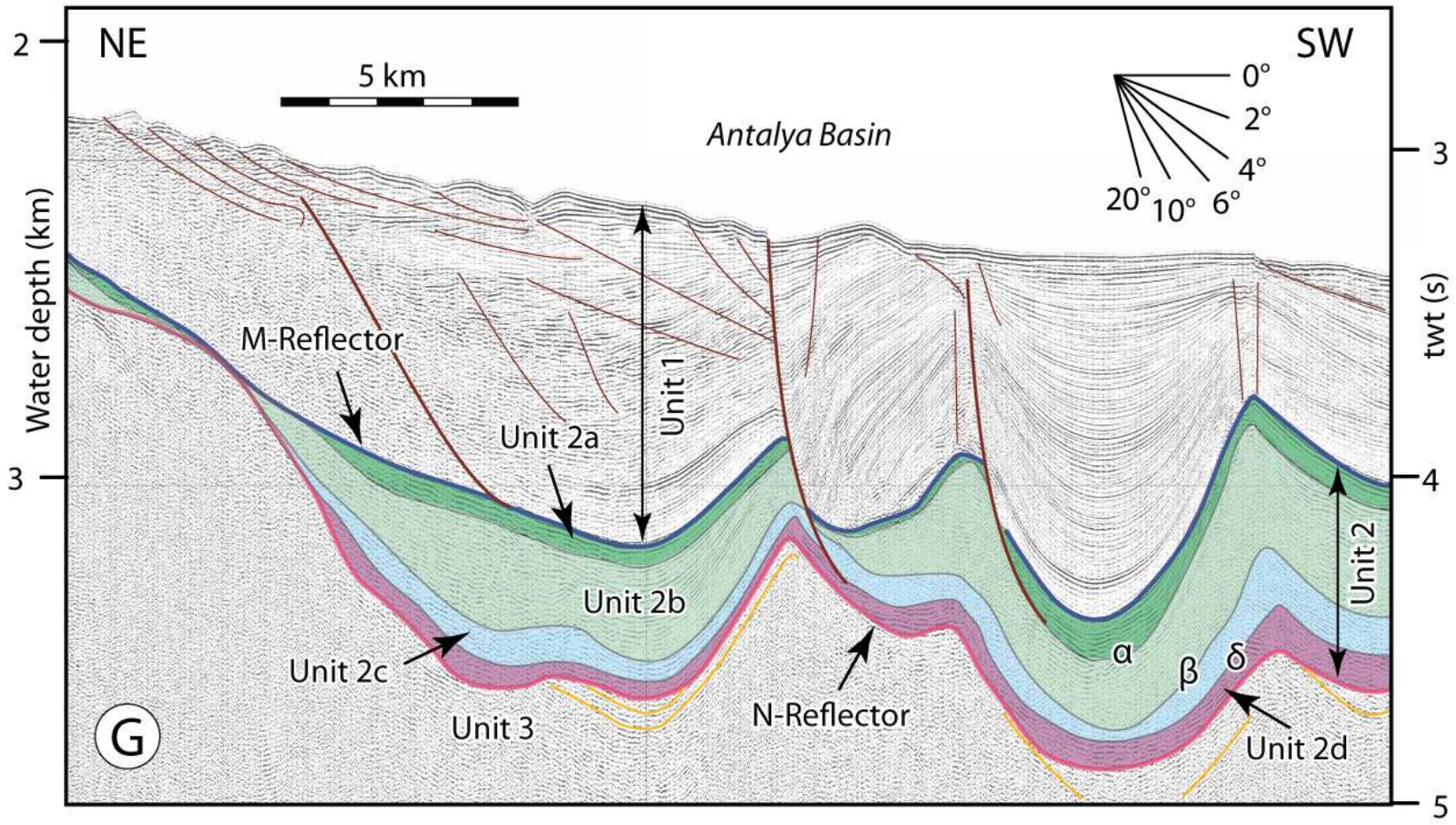

Figure 4.20: High-resolution multi-channel seismic reflection profile G showing the internal architecture of Unit 2 associated with the deposition during the Messinian Salinity Crisis. Note that the prominent M- and N-reflectors define the top and base of Unit 2, respectively and that less prominent reflectors α, β and δ define the bounding surfaces of the sub-units 2a–2d. Location is shown in Figure 4.1. EMED01 (fix 490-510)

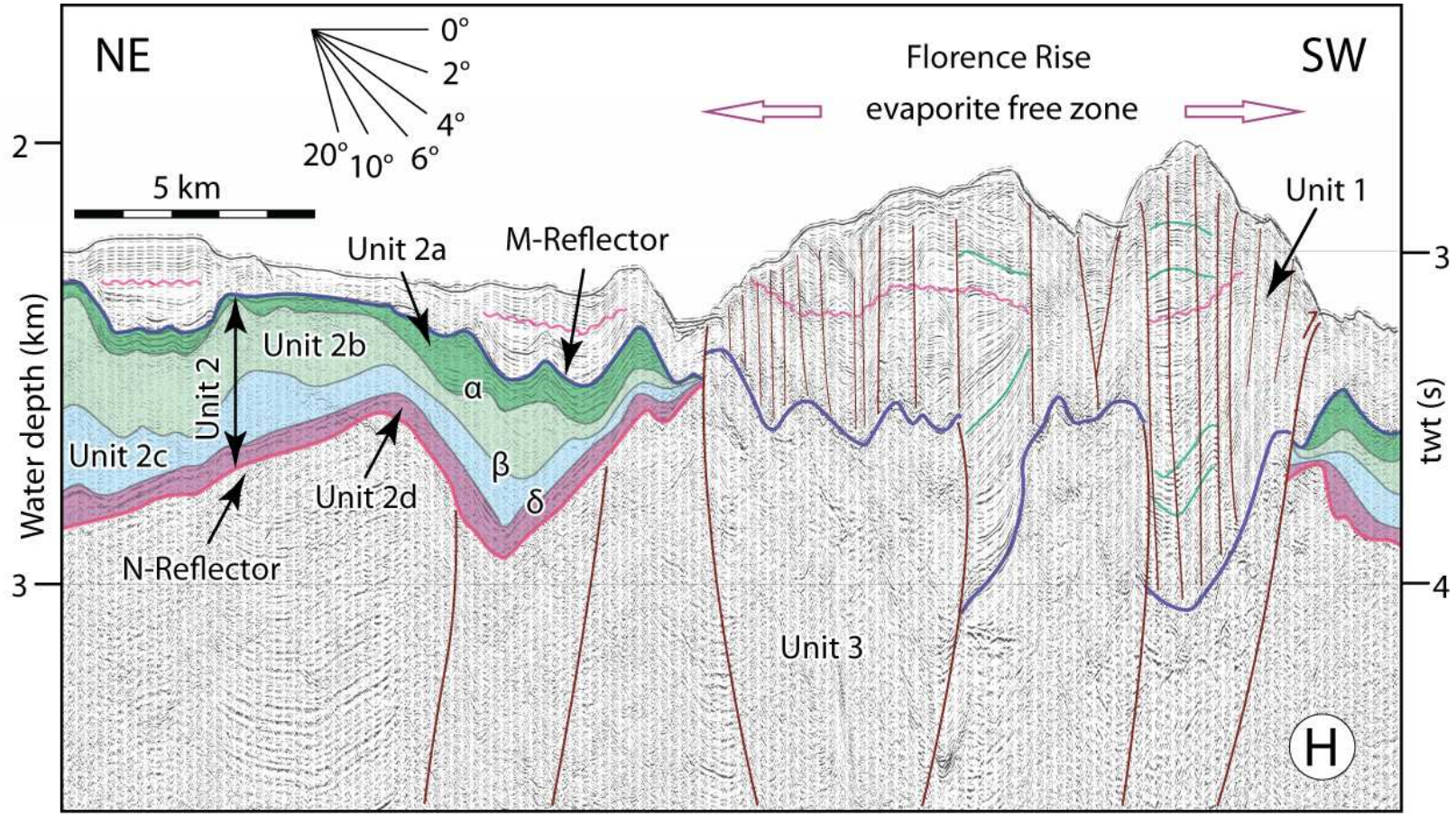

Figure 4.21: High-resolution multi-channel seismic reflection profile H showing the internal architecture of Unit 2 associated with the deposition during the Messinian Salinity Crisis. Note that the prominent M- and N-reflectors define the top and base of Unit 2, respectively and that less prominent reflectors α, β and δ define the bounding surfaces of the sub-units 2a–2d. Location is shown in Figure 4.1. EMED10 (fix 1875-1895)

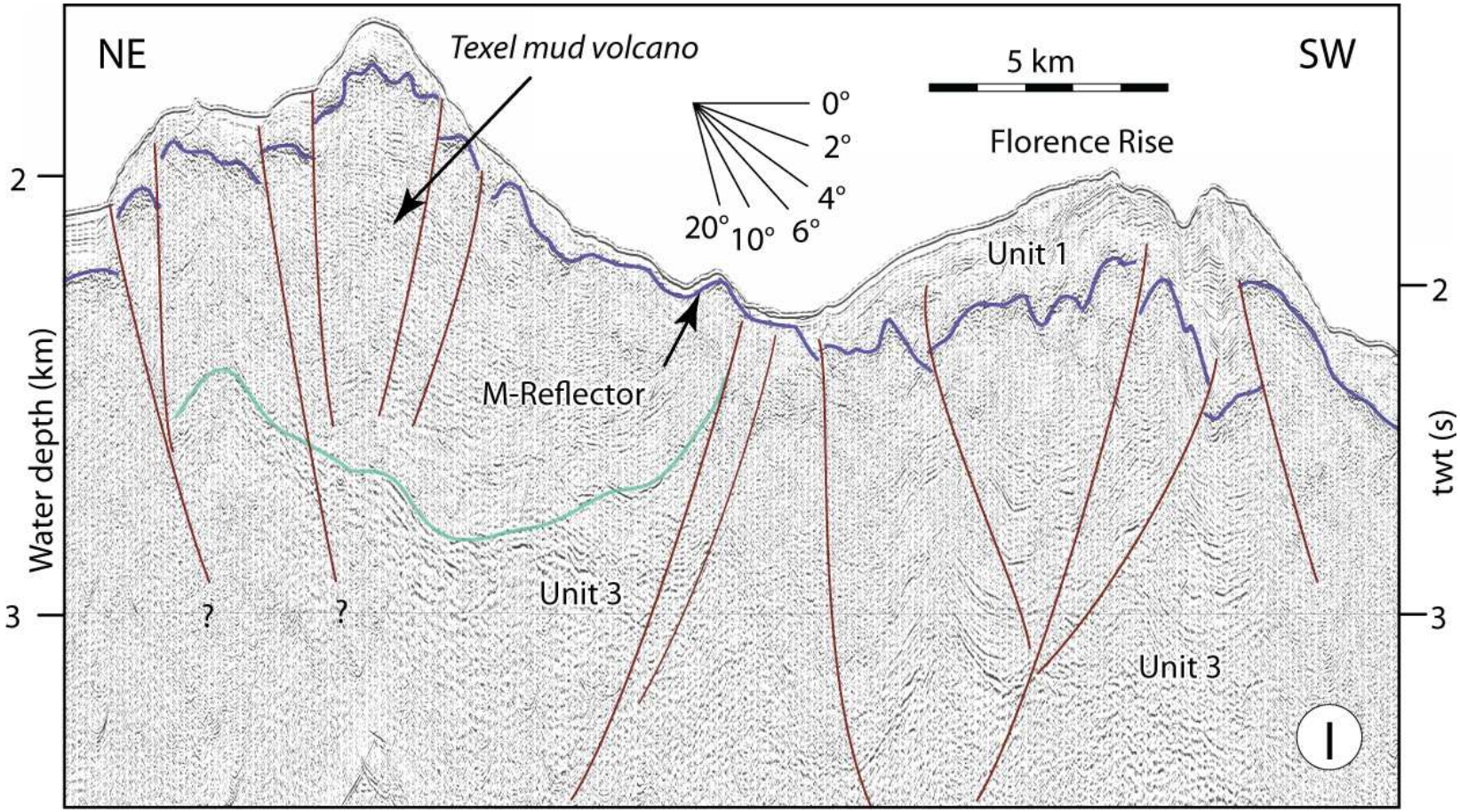

Figure 4.22: High-resolution multi-channel seismic reflection profile I showing the internal architecture of Unit 2 associated with the deposition during the Messinian Salinity Crisis. Note that the prominent M- and N-reflectors define the top and base of Unit 2, respectively and that less prominent reflectors α, β and δ define the bounding surfaces of the sub-units 2a–2d. Location is shown in Figure 4.1. EMED10 (fix 2056-2076)

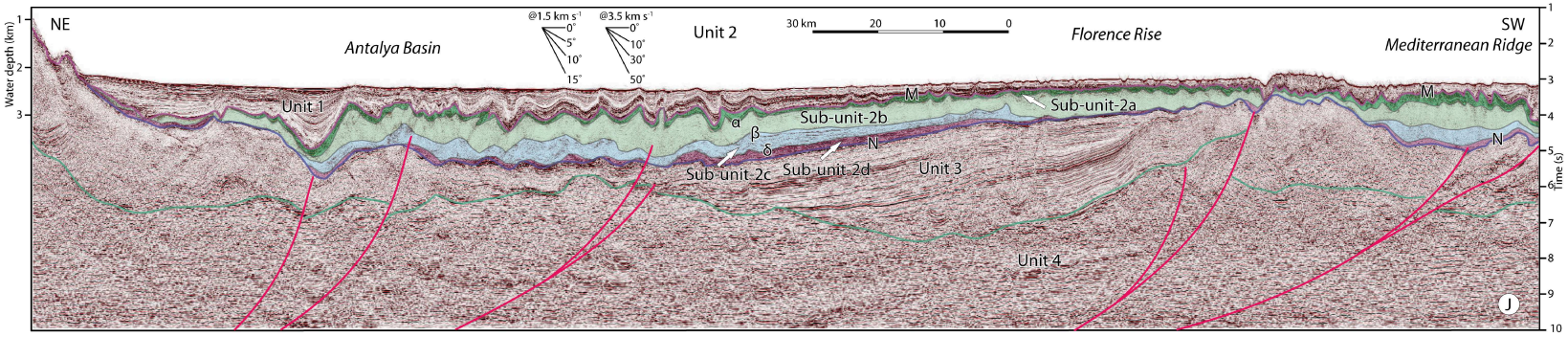

Figure 4.23: High-resolution multi-channel seismic reflection profile J showing the internal architecture of Unit 2 associated with the deposition during the Messinian Salinity Crisis. Note that the prominent M- and N-reflectors define the top and base of Unit 2, respectively and that less prominent reflectors α, β and δ define the bounding surfaces of the sub-units 2a–2d. Location is shown in Figure 4.1. TPAK071-06

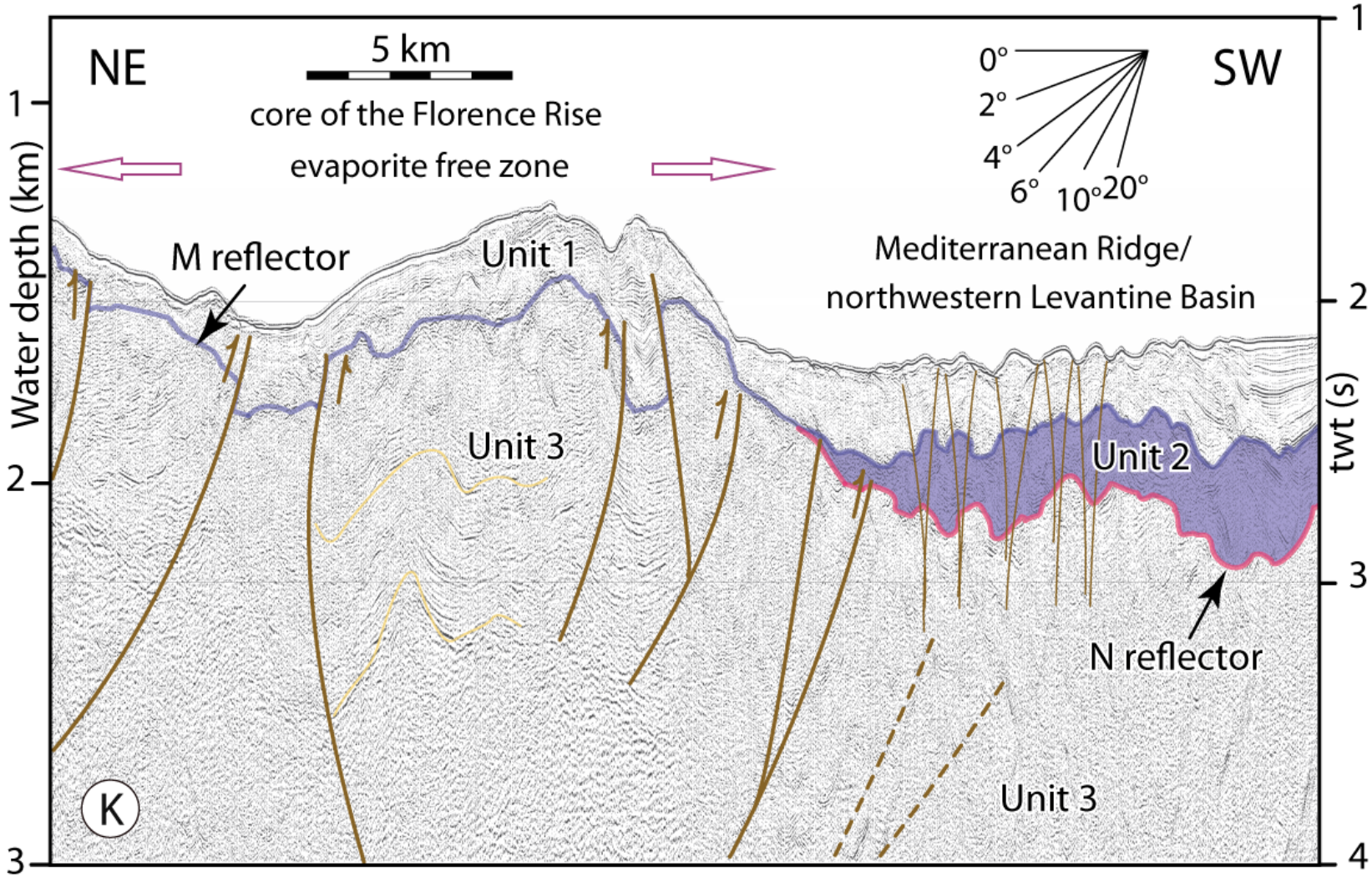

Figure 4.24: High-resolution multi-channel seismic reflection profile K showing the internal architecture of Unit 2 associated with the deposition during the Messinian Salinity Crisis. Note that the prominent M- and N-reflectors define the top and base of Unit 2, respectively and that less prominent reflectors α, β and δ define the bounding surfaces of the sub-units 2a–2d. Location is shown in Figure 4.1. EMED10 (fix 2063-2084)

The age, lithological characteristics and the depositional environment of lowermost sub-unit 2d of the Messinian evaporite successions is very speculative, because it has never been drilled in the deep Antalya Basin. Here the seismic characteristics of sub-unit 2d and the general chronostratigraphic history of the evaporite deposition across the eastern Mediterranean suggest that sub-unit 2d possibly corresponds to deposition of detrital sediment and re-deposition of the shallow water primary lower gypsum (Resedimented Lower Gypsum), related to intensive subaerial erosion immediately after the onset of the fast and major Messinian sea-level drawdown. However, it is important to note that sub-unit 2d in the Antalya Basin may not be the correlative successions of the primary lower evaporites found along the marginal basins across the eastern Mediterranean (CIESM, 2008; Roveri et al., 2014a,b). The stratigraphic and chrono-stratigraphic correlations in this study further suggest that sub-unit 2d in the deep Antalya Basin does not correspond to the onset of the Messinian Salinity Crisis.

At the northern lower slope of the Antalya Basin the base of sub-unit 2d is a regional unconformity, locally showing angular discordance, which is related to the erosion and resedimentation of primary evaporites, dominated by the Messinian-age gypsum turbidites deposited during the first stage of the Messinian Salinity Crisis (Fig. 4.20). The correlation with outcrop and borehole data from Cyprus show that the primary gypsum of the lower evaporites in southern Cyprus marginal basins and the resedimented gypsum of the lower evaporites in northern Cyprus intermediate basins are not correlated in terms of their geological ages and the depositional environments (Gass, 1960; Manzi et al., 2011, 2014; Roveri et al., 2008a, c; Roveri et al., 2014a,b).

4.6.2 Sub-units 2c and 2b (Mobile Units 1 and 2)

Sub-units 2c and 2b represent the Messinian salt deposited in the deep basins and display the greatest thickness variations throughout the study area (Figs. 4.13, 4.19–4.21). They are absent across the upper and middle slopes of the Antalya Basin and very thin at the lower slope region of the basin

(Fig. 4.20). Sub-units 2c and 2b thicken to ∼1.5 s twt within the center of the Antalya Basin, then thin towards the Florence Rise, pinching out along the north foothills of the Florence Rise, but thickening once more toward the northern Levantine Basin (Figs. 4.19, 4.21). Seismic interval velocities range between 4200 and 4800 m s^{-1} across sub-units 2c and 2b: the acoustically transparent regions exhibit interval velocities of up to 4800 m s^{-1}, while the more stratified regions exhibit lower velocities (Fig. 4.25). These internal stratifications indicate vertical facies changes in the evaporites of sub-unit 2b and 2c, possibly with intercalated siliciclastics and/or trapped fluids. Fluid escape structures have been frequently reported from the eastern Mediterranean Sea, possibly linked to fluids emanating from the accretionary prism above the subduction zone. In the Antalya Basin and Florence Rise (except for the core of the Florence Rise), the mobile salt layer is ascribed to sub-unit 2c (Mobile Unit 1; Lofi et al., 2011b) and sub-unit 2b (Mobile Unit 2; Lofi et al., 2011b) (Figs. 4.13, 4.18, 4.23). However, from the southern flank of the Florence Rise to the Levantine Basin, these two sub-units are often shown as a single complex mobile sub-unit (i.e., Complex Mobile Unit of Lofi et al., 2011b) (Figs. 4.23, 4.24).

Sub-unit 2c immediately underlies sub-unit 2b and it is bounded at its base by the δ-reflector. In seismic reflection profiles sub-unit 2c is characterized by both a low reflectivity, semi-transparent acoustic facies (Fig. 4.15) and an alternating layered facies with several locally continuous and/or discontinuous and highly deformed high amplitude reflection packages (Fig. 4.19). The geometry of this sub-unit shows that it experienced syn-sedimentary deformation and deformation associated with fluid escape (Figs. 4.13, 4.18–4.24). The thickness of this sub-unit differs along the study area; it is thick in the Antalya Basin (∼500 ms twt), thicker in the transition zone between the Antalya Basin and the Florence Rise (∼700 ms twt), but thins toward the northern flank of the Florence Rise to ∼200 ms twt). Sub-unit 2c is possibly lithologically composed of halite intervals with interbedded anhydrite, Mg and K salts and siliciclastic inputs similar to those observed within the Kalavasos and Lapatza formations (Fig. 4.8).

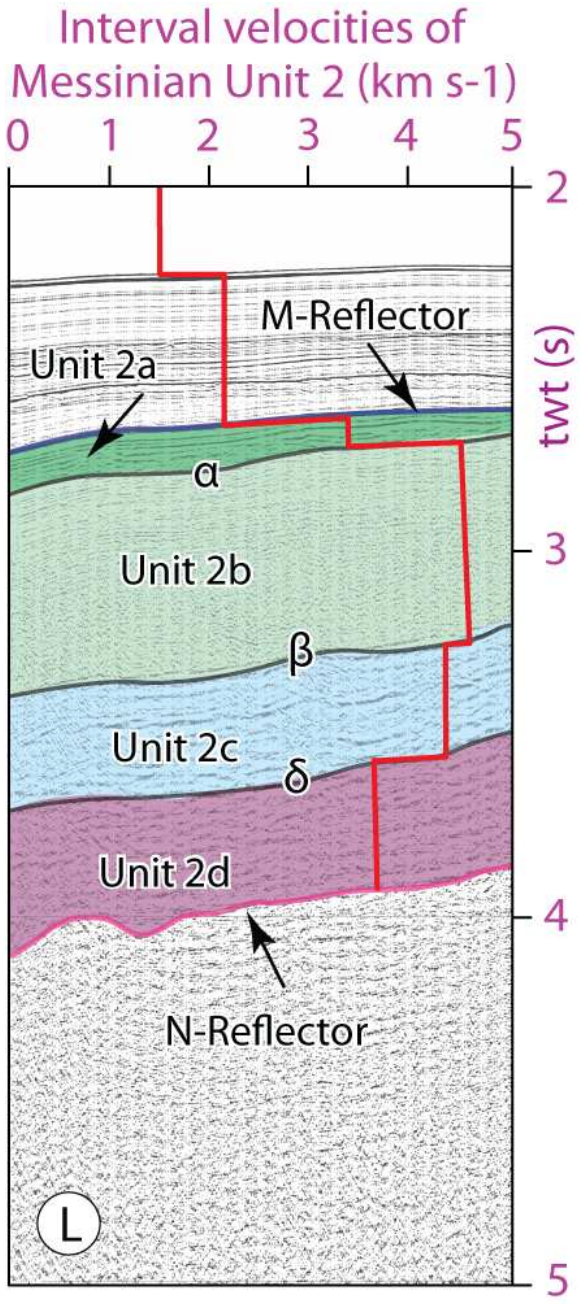

Figure 4.25: Segment of the high-resolution multi-channel seismic reflection profile L showing the interval velocity profile across the uppermost Messinian–Quaternary of Unit 1 and the Messinian evaporites of Unit 2. Note the notable velocity increases across the M- and α-reflectors and smaller velocity decreases across the β- and δ-reflectors. Location is shown in Figure 4.1. EMED10 (fix 1967-1971)

Sub-unit 2b comprises of a weakly stratified to transparent sequence, which underlies sub-unit 2a (Figs. 4.13, 4.18–4.24, 4.26). Sub-unit 2b exhibits an internal reflection configuration that is less strong than that observed in sub-unit 2c. The boundary between sub-units 2c and 2b is delineated by the β-reflector in places where both sub-units are present. However, in places where sub-unit 2c is absent, sub-unit 2b immediately overlies sub-unit 2d (Fig. 4.23). Sub-unit 2b is interpreted as a massive and relatively pure salt deposit and is the most representative facies of the Messinian evaporite successions in eastern Mediterranean deep and its intermediate basins (Lofi et al., 2011b). Sub-unit 2b is $\sim$300–700 ms thick in the northern part of the Antalya Basin, it reaches $\sim$800 ms across the transition zone between the Florence Rise and the Antalya Basin, but pinches out along the northern and southern fringes of the Florence Rise and northern and southern slope of the Anaxagoras Mountains (Figs. 4.13, 4.19, 4.24, 4.27–4.29). Within sub-unit 2b, the internal reflection packages clearly show that the brittle deformation observed in the folded and faulted portion of the Antalya Basin extends towards the Florence Rise and Anaxagoras Mountain (Fig. 4.1, 4.28, 4.29). According to the seismic interval velocities and litostratigraphic correlations, the lithologies associated with sub-unit 2b are most likely dominated by halite with less siliciclastic and anhydrite beddings than sub-unit 2c (Fig. 4.25).

In the southern Florence Rise and Anaxagoras Mountain, towards the northern part of the Levantine Basin the entire Messinian mobile succession (i.e., sub-units 2b and 2c) is made up of mixed seismic facies with transparent seismic facies and very unclear discontinuous reflections that could be either sub-unit 2b or sub-unit 2c (Figs. 4.26, 4.30). Thus, this succession is labeled as sub-unit 2b+2c. The seismic reflection characteristics of this complex sub-unit show plastic deformation and mobilization along the northern Levantine Basin and it is thinner at the southern flank of the Florence Rise and it thickens towards the south through the Levantine Basin (Figs. 4.23, 4.24).

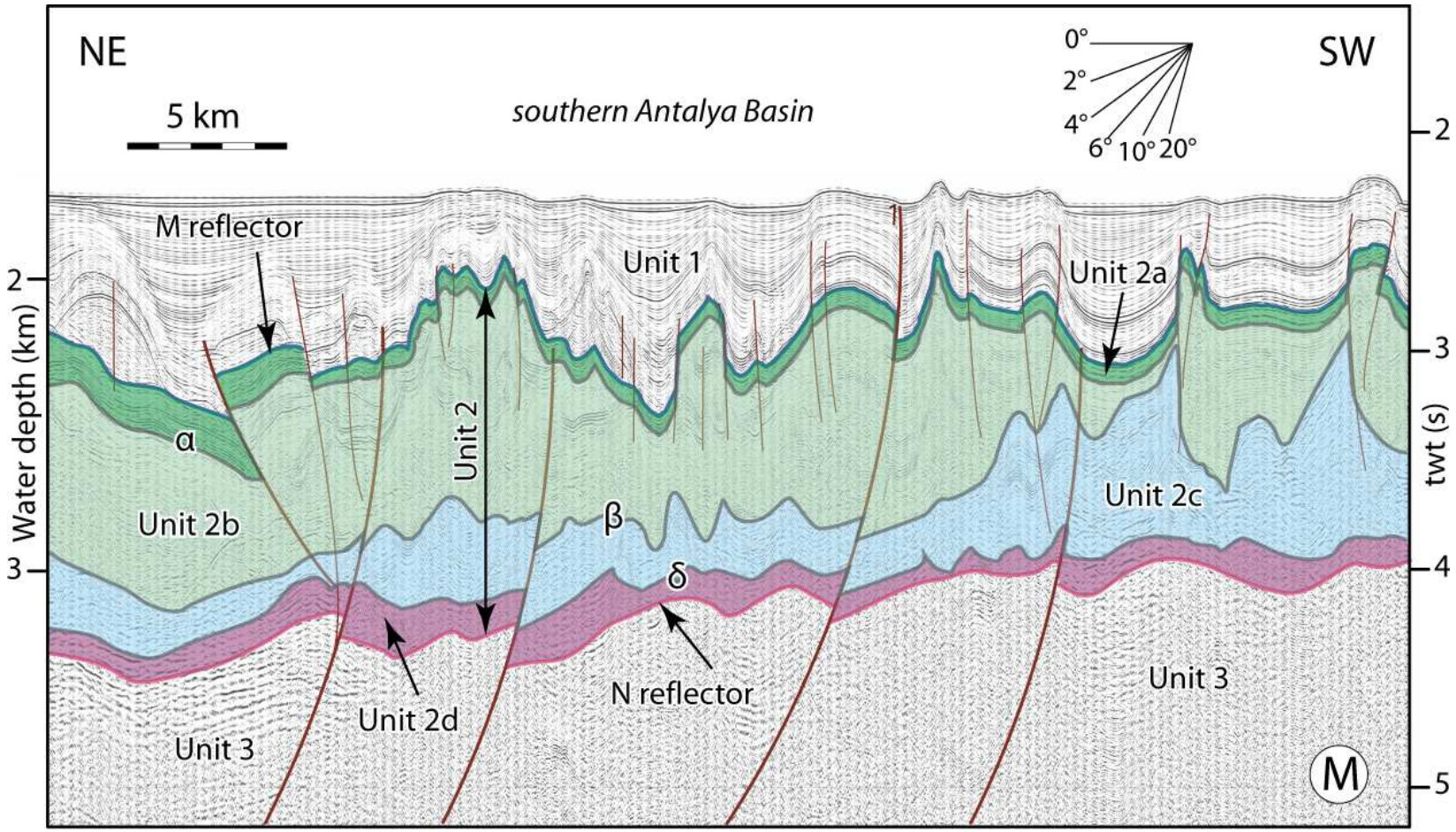

Figure 4.26: High-resolution multi-channel seismic reflection profile M showing the internal architecture of Unit 2 associated with the deposition during the Messinian Salinity Crisis. Note that the prominent M- and N-reflectors define the top and base of Unit 2, respectively and that less prominent reflectors α, β and δ define the bounding surfaces of the sub-units 2a–2d. Location is shown in Figure 4.1. EMED10 (fix 1577-1604)

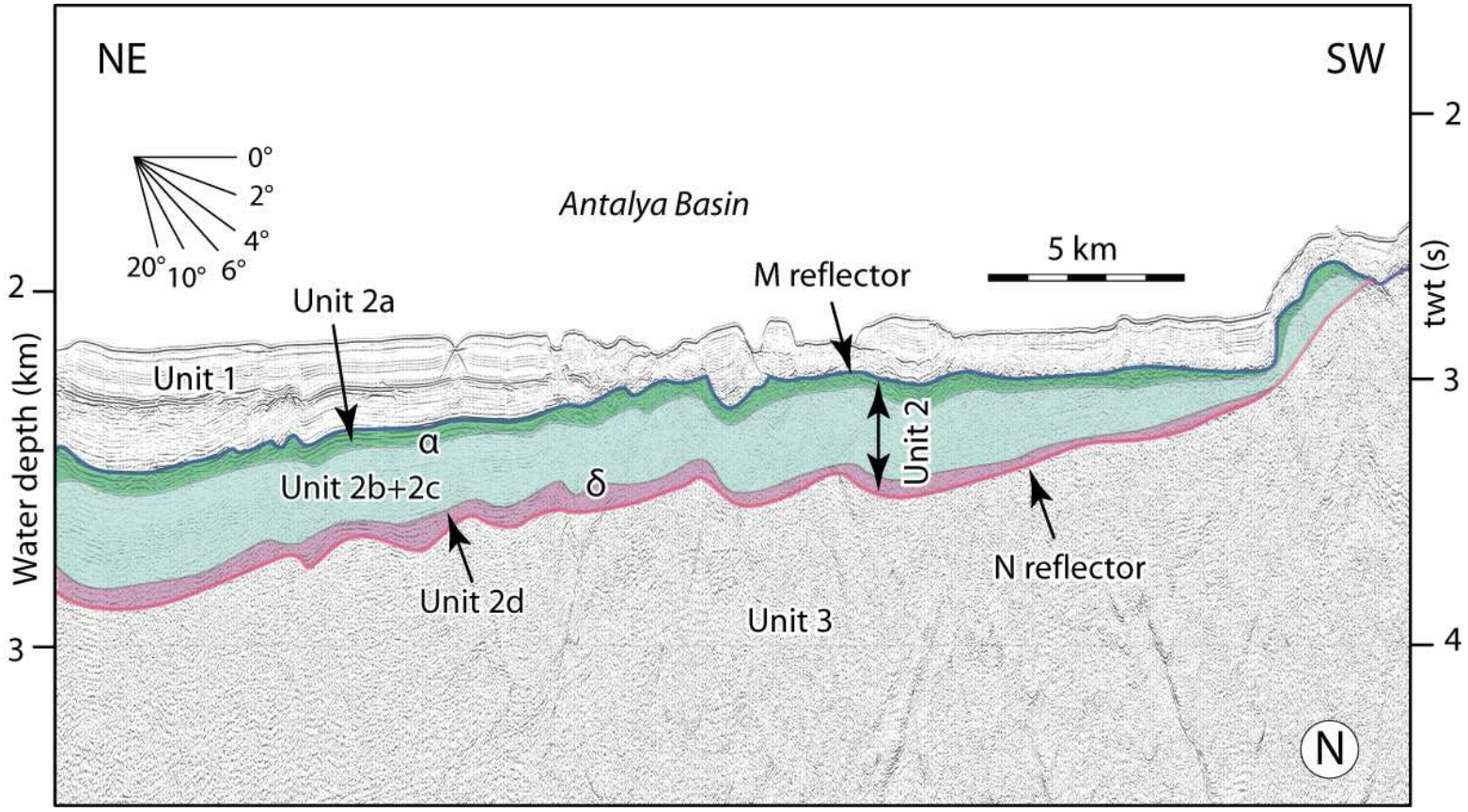

Figure 4.27: High-resolution multi-channel seismic reflection profile N showing the internal architecture of Unit 2 across the Mediterranean Ridge. Note that reflectors α and δ can be identified but the , β–reflector cannot be readily identified in this region. Location is shown in Figure 4.1. EMED10 (fix 2045-2060)

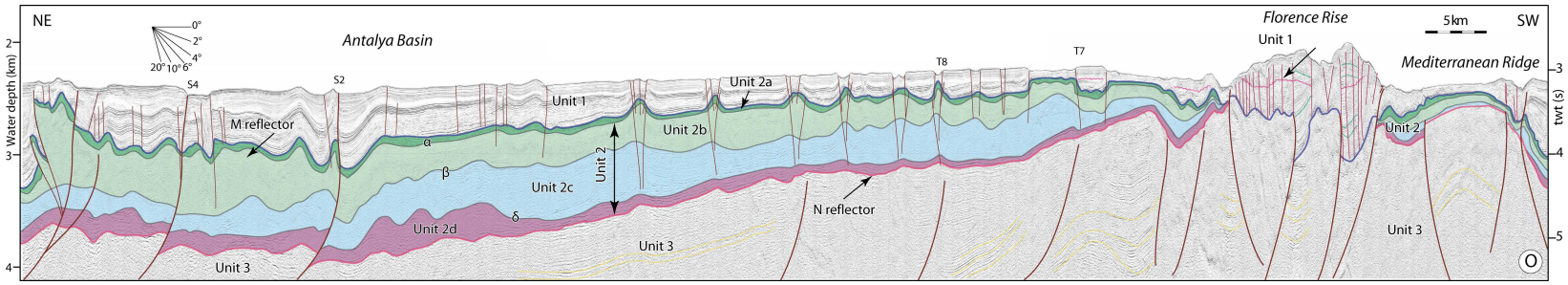

Figure 4.28: High-resolution multi-channel seismic reflection profile O showing the internal architecture of Unit 2 associated with the deposition during the Messinian Salinity Crisis. Note that the prominent M- and N-reflectors define the top and base of Unit 2, respectively and that less prominent reflectors α, β and δ define the bounding surfaces of the sub-units 2a–2d. Location is shown in Figure 4.1. EMED10 (fix 1814-1904)

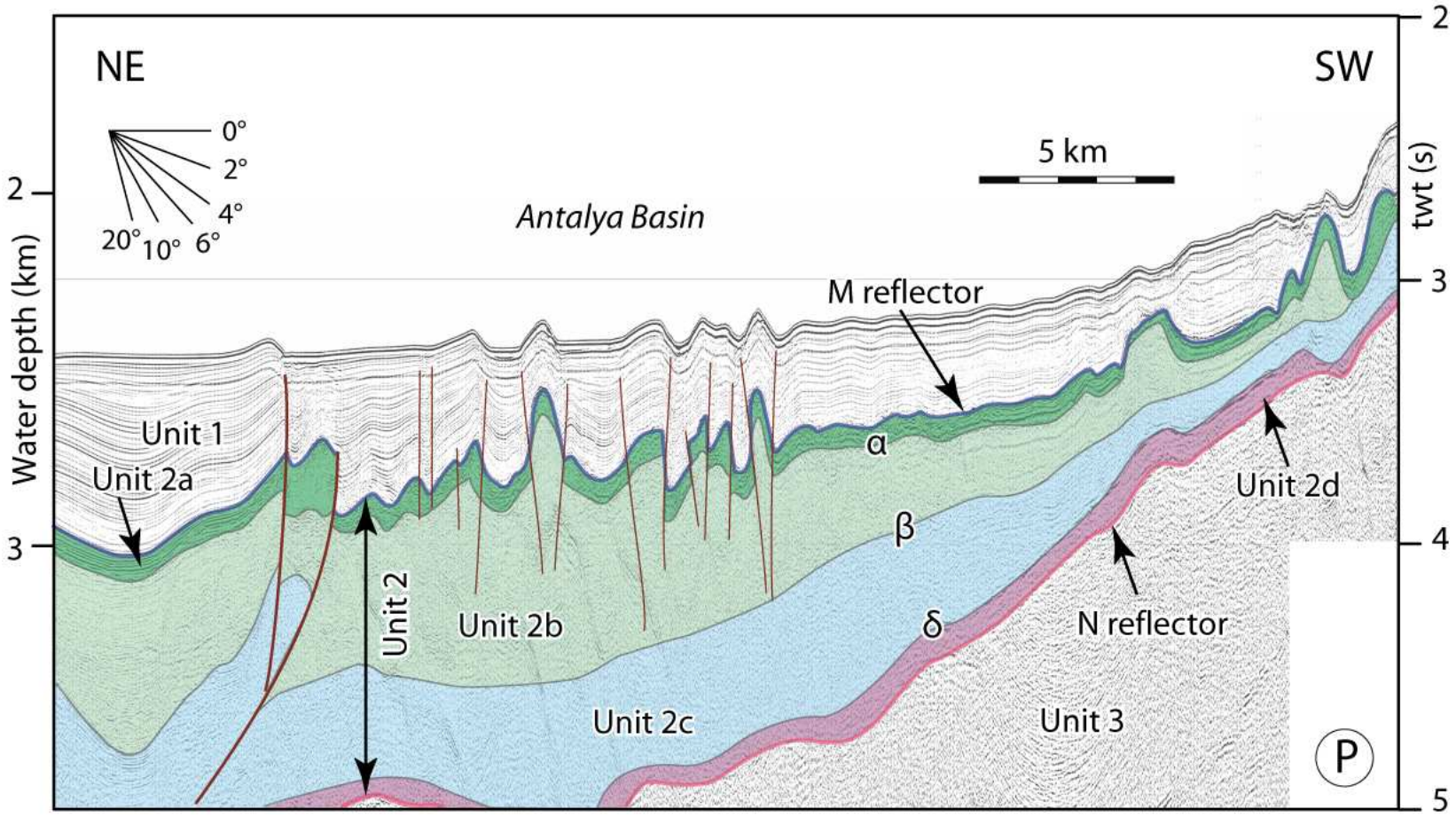

Figure 4.29: High-resolution multi-channel seismic reflection profile P showing the internal architecture of Unit 2 associated with the deposition during the Messinian Salinity Crisis. Note that the prominent M- and N-reflectors define the top and base of Unit 2, respectively and that less prominent reflectors α, β and δ define the bounding surfaces of the sub-units 2a–2d. Further note that sub-units 2b and 2c dramatically thin toward the south where they eventually pinch-out. Location is shown in Figure 4.1. EMED10 (fix 1278-1302)

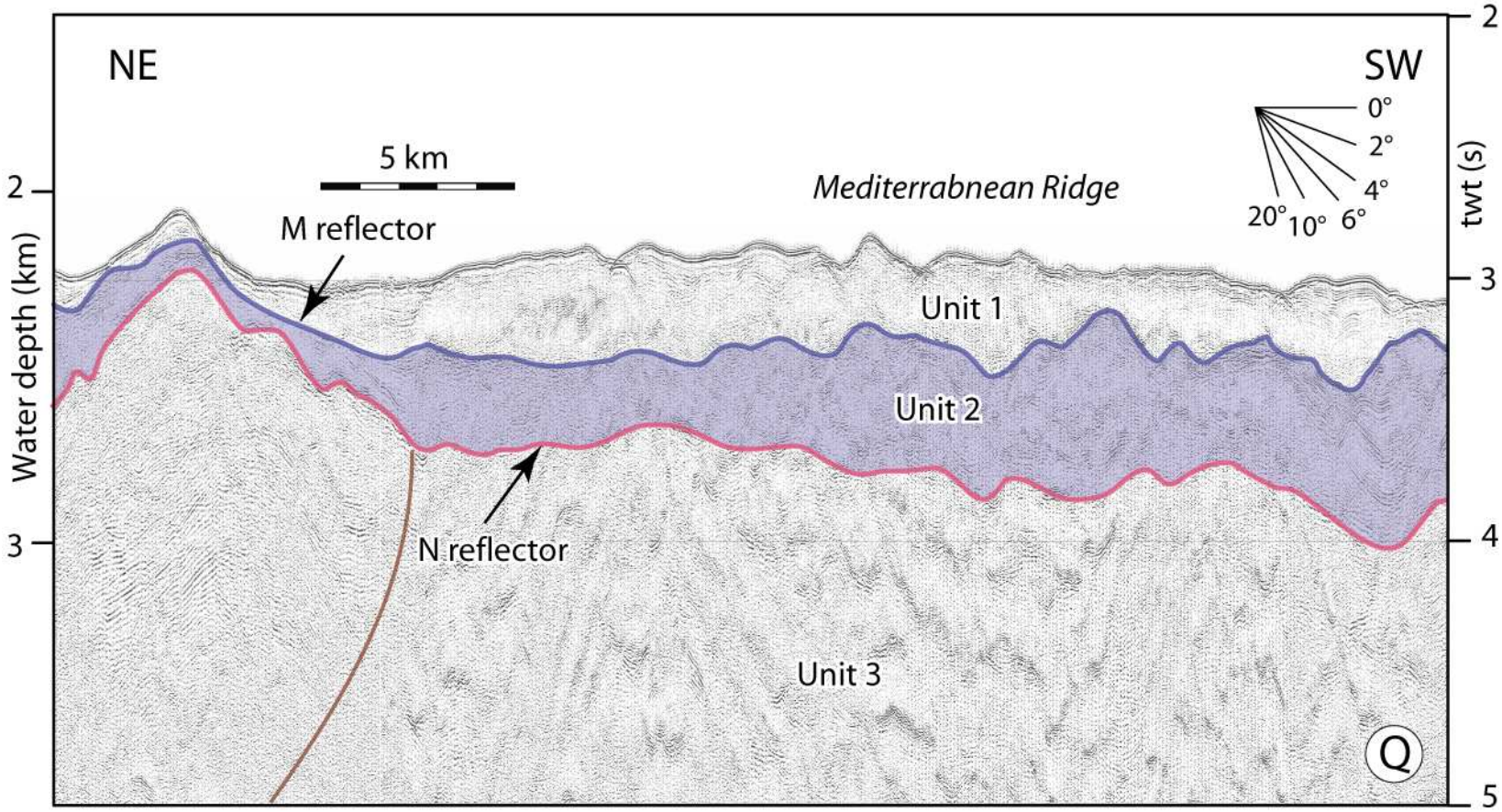

Figure 4.30: High-resolution multi-channel seismic reflection profile Q showing the internal architecture of Unit 2 across the Mediterranean Ridge. Note that reflectors α, β and δ which define the bounding surfaces of the sub-units 2a–2d cannot be readily identified in this region. Location is shown in Figure 4.1. EMED 10 (fix 1444-1470)

4.6.3 Sub-unit 2a (Upper Unit)

Sub-unit 2a constitutes the youngest and uppermost portion of the evaporite successions associated with the Messinian Salinity Crisis (Table 4.1, Figs. 4.13, 4.16, 4.15). Sub-unit 2a, where present, immediately underlies the M-reflector which generally forms a prominent reflection with a strong erosional character (e.g., Fig. 4.13). In most regions, the M-reflector and sub-unit 2a are harmonically folded and sharply segmented across adjacent synclines and anticlines. The boundary between sub-units 2a and 2b is delineated by the α-reflector, which often shows an erosional character across the southern Antalya Basin (Fig. 4.18). Where sub-unit 2a is absent, the α-reflector merges with the M-reflector often creating an angular discordance between sub-unit 2b and the overlying Unit 1 reflections.

Sub-unit 2a exhibits a strong seismic expression with good lateral continuity, and high amplitude parallel reflectors with locally internal unconformities and/or chaotic facies changes. In the deeper part of the eastern Mediterranean this sub-unit was deposited conformable above the mobile sub-unit 2b and below the uppermost Messinian-Quaternary Unit 1; however it pinches out at the Antalya Basin margin slope above the N-reflector (Fig. 4.20). The dense grid of seismic reflection profiles showed that sub-unit 2a increases markedly in thickness towards the Antalya Basin. It is thickest ($\sim$250–300 ms) across the central portion of the deep Antalya Basin and the succession includes occasionally local unconformities, where the reflectors of the sub-unit 2a onlap the α-reflector (e.g., Fig. 4.14). The acoustic character of sub-unit 2a shows sharp changes around the Florence Rise with less continuous irregular, strong and high amplitude reflectors (Figs. 4.27, 4.28).

Using the interval velocities of 3500–4000 m s^{-1}, sub-unit 2a is correlated with Unit V (Sub-unit Vd) and the upper part of Unit VI (sub-unit VIa) recovered in the DSDP Sites 375 and 376. This correlation suggests that the lower part of sub-unit 2a corresponds to six to seven gypsum horizons interbedded with green dolomitic marlstone cored at Sites 375 and 376. Correlations with bore hole data further suggest that, the clear boundary between the strongly reflective sub-unit 2a and the over-

lying Unit 1 (as defined by the M-reflector) must arise from the strong acoustic impedance contrast between the marls of Unit 1 with a significant amount of marine microfossils (such as oligotypic planktonic foraminifers and cysts of marine planktonic algae) and the mainly dolomitic marls and evaporites of the sub-unit 2a. The presence of these fossils suggests the occasional influx of marine waters into this predominantly brackish *Lago Mare* environment during the Messinian–Pliocene transition (Orszag-Sperber et al., 2000; Rouchy et al., 2001). Sub-unit 2a is also correlated with Upper Gypsum Unit of the marginal evaporites of Lapatza and Kalovasos formations of Cyprus Island (Gass, 1960; Orzsag-Sperber et al. 2009; Lofi et al., 2011a; Manzi et al., 2014; Roveri et al., 2014a,b) and the Upper Gypsum Unit in the Polemi and Pissouri basins (Manzi et al., 2014).

4.6.4 Time-Thickness of Unit 2 (Messinian Evaporites)

The isopach map of the Messinian evaporites of Unit 2 shows the presence of a very prominent Messinian depocentre which was nestled between the northern foothills of the Florence Rise and the southern continental margin of the Antalya Basin (Fig. 4.31). This depocentre was broadly oriented in a northwest southeast direction, and was bounded by the Amanos-Kormakiti zone in the east and the Kemer Peninsula in the west. Thickest sediments exceeding 2000 ms occur across the southern Antalya Basin. The internal architecture of the Messinian depocentre is characterized by a series of northwest-southeast trending, tear-drop shaped sub-basins, containing 800–1600 ms thick Unit 2 successions. Previous studies suggested that these narrow basins developed as prominent piggy-back basins associated with a family of northwest-southeast-striking and predominantly southwest-verging thrust culminations (Işler et al., 2005; Hall et al., 2014a). Throughout the Antalya Basin all four sub-units of Unit 2 are well developed (e.g., Güneş et al., 2014, 2015). Toward the south and southwest, Unit 2 shows notable thinning by convergence of internal reflectors, as well as progressive onlap of sub-units 2a, 2b, 2c and 2d on the α–, β–, δ– and N–reflectors, respectively.

Examination of the sedimentary architecture of the uppermost Messinian–Quaternary succes-

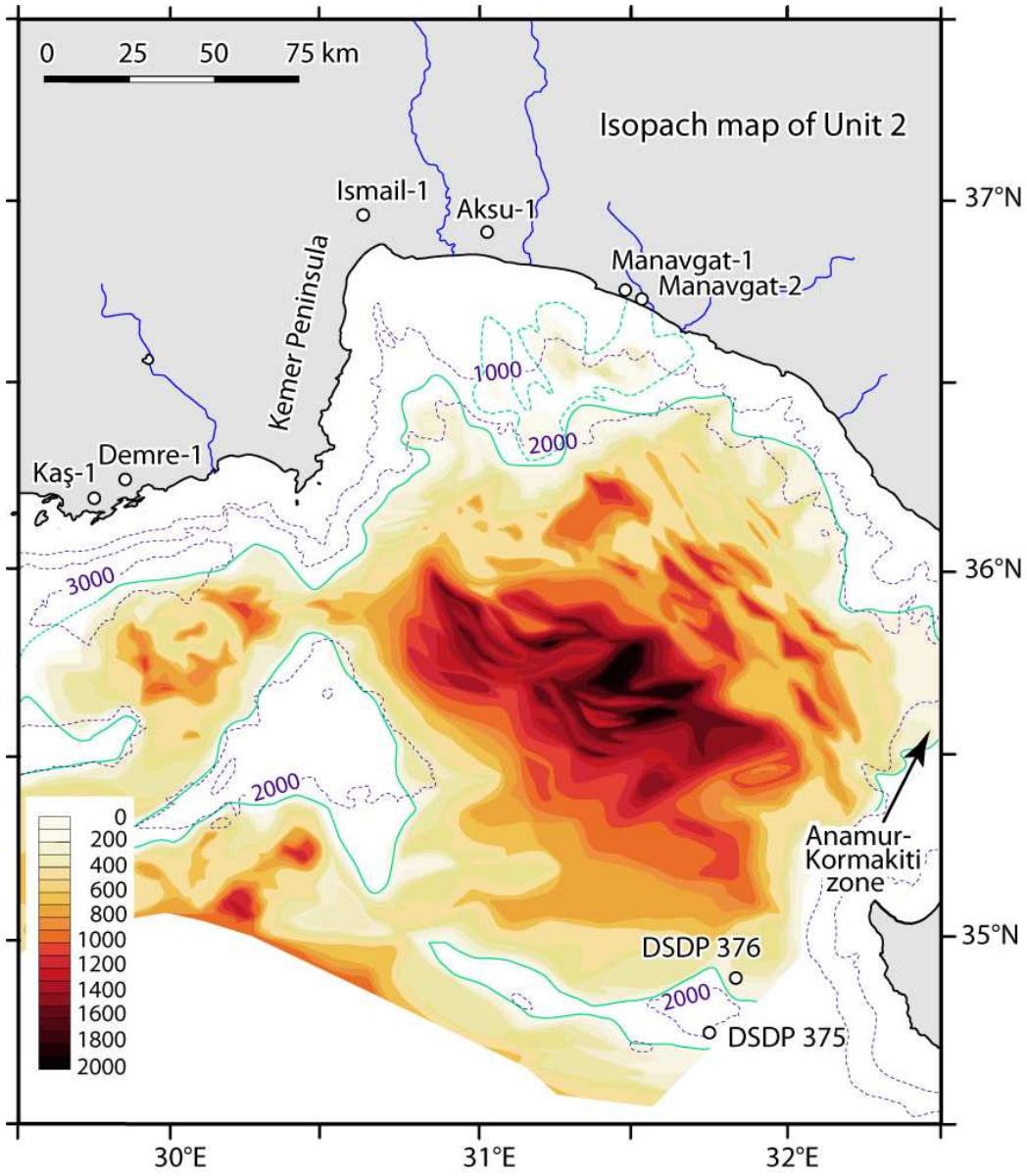

Figure 4.31: Isochron map of the Messinian successions of Unit 2 (in millisecond two-way time= twt) in Antalya Basin, Florence and environs. Isobaths contours 1000 m, 2000 m and 3000 m are taken from the International Bathymetric Charts of the Mediterranean (IOC, 1981). Note that the remarkable coincidence between the zero isobaths of Unit 2 and the 2000m isobath across the Antalya Basin and the Anaximander Mountains, and to a lesser extend across the Florence Rise. This relationship is not observed across the Finike Basin.

sions clearly demonstrate that the elongated tear-drop shaped sub-basins are predominantly developed during the Pliocene–Quaternary associated with the halokinetic movement of the seismic stratigraphic sub-units 2b and 2c. The zero line of Unit 2 is clearly mapped across the study area (Fig. 4.31). Comparison between the isobath and isochron contours show that there is a modest correlation between the 2000 m isobath and the 0 ms isopach across the study area. This correlation is best observed along the northern and western segments of the Antalya Basin, but is also observed along the northern foothills of the Florence Rise and the Anaxagoras Mountain (Fig. 4.31). Variations are however significant: for example in the Finike Basin the 0 ms isopach contour cuts the 3000 m isobath (Fig. 4.31; also see Aksu et al., 2014c).

The present-day zero edge of Unit 2 in the study area may be a function of (a) the original depositional edge of the evaporite basin, and/or (b) the position of the zero thickness of the evaporite succession developed as the result of evacuation of salt and the associated weld development, and/or (c) the margin where the evaporites are completely removed by erosion, and/or (d) the original shallower depositional edge of the evaporite succession is brought down to deeper levels by regional basin subsidence. The zero edge of Unit 2 observed along the northern, western and southern margins of the Antalya Basin is believed to be the result of the original depositional edge of the Messinian evaporite basin, modified by the evacuation of the evaporites from the mid-slope regions and migration to lower slope–abyssal depths where halokinetic structures developed during the Pliocene–Quaternary (Işler et al., 2005). These welds are commonly observed immediately landward of the salt roller and pillows along the continental margin of the Antalya Basin (e.g., Fig. 4.20). The present-day zero edge in the Antalya Basin must have also been influenced by the regional basin subsidence associated with the loading of the thick Pliocene–Quaternary successions. This is further discussed in Chapter 6.

Messinian evaporites of Unit 2 are largely absent across the continental shelf and continental slope, except for very thin pockets of Unit 2 preserved within the paleotopographic lows below the M-

reflector. Messinian evaporites are also absent or very thin across the northwest-southeast trending crestal zone of the Florence Rise as well as the bulk of the Anaximenes and Anaxagoras Mountains (Fig. 4.31). The correlation observed between the 2000 m isobath and the 0 ms isopach is not readily seen across the Finike Basin, where the 0 ms isochron is closer in its position to the 3000 m isobath, which is interpreted as the result of dramatic subsidence observed across the Finike Basin (e.g., Aksu et al., 2009; 2014c). This is further discussed in Chapter 6. Southward of the Florence Rise and the Anaxagoras and Anaximenes Mountains, the Messinian evaporites of Unit 2 thicken into the Mediterranean Ridge area (Fig. 4.31). However, the available data in this study does not allow a detailed mapping in this region.

4.7 Summary

The new seismic reflection data documented that the Messinian evaporite succession of Unit 2 is widespread across the Antalya Basin and the Florence Rise regions of the eastern Mediterranean Sea. The very thick occurrence of Unit 2 in these areas exceeding 2000 ms thickness ($\sim$ 4–5 km) suggested that this region must have been a primary evaporite basin during the Messinian. But maybe more importantly, the new data clearly show for the first time that there are four distinct Messinian evaporite sub-units (i.e., 2a–2d) which are separated by regionally traceable reflectors (i.e., α, β and δ). Acoustically similar sub-units have been previously described from the western Mediterranean basins (e.g., Lofi et al., 2011a, b), but were never observed across the more extensively studied Levantine and Herodotus basins of the eastern Mediterranean. The documentation that the Messinian sub-units also occur across the Antalya Basin and the Florence Rise regions of the eastern Mediterranean Sea suggested that there are greater sedimentary and seismic stratigraphic similarities between the western and eastern Mediterranean basins, implying a common and possibly coeval development of Messinian Salinity Crisis along the entire Mediterranean region (Fig. 4.32).

The data presented in this Chapter document that the successions associated with the Messinian

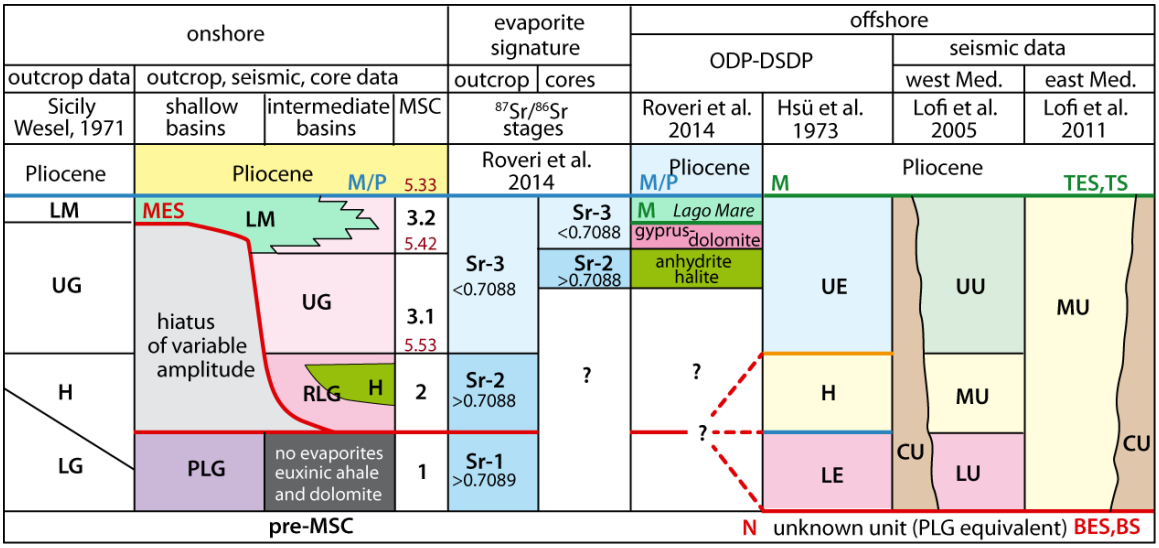

Figure 4.32: Synthesis of nomenclature assigned in the literature to onshore and offshore Messinian stratigraphic units in western Mediterranean region (adopted from Roveri et al., 2014b). Onshore units: LG, Lower Gypsum; PLG, Primary Lower Gypsum; H, halite; RLG, Resedimented Lower Gypsum; UG, Upper Gypsum; LM, *Lago Mare*; MES, Messinian erosional surface. M/P, Miocene–Pliocene Boundary. MSC stages: 1, 2, 3.1, 3.2. Strontium Isotope stages: Sr-1, Sr-2, Sr-3. Offshore units: LE, Lower Evaporites=LU, Lower Unit; H, Messinian Salt= MU, Mobile Unit; UE, Upper Evaporites= UU, Upper unit; CU, Complex Unit. Offshore surfaces: MES, marginal erosional surface; horizon N=BES, basal erosional surface/BS, basal surface, base of Messinian evaporites; horizon M=TES, Top erosional surface/TS, Top Surface: top of Messinian evaporites. Table 4.1 The Messinian Salinity Crisis seismic markers have been recognized over the Antalya Basin and Florence Rise area offshore domain and their correlations with Messinian Salinity Crisis Seismic Atlas markers.

Salinity Crisis across the Antalya Basin and Florence Rise can be evaluated within three distinct depositional stages, similar to the models presented across the western Mediterranean (Roveri et al., 2014a–c): "Resedimented Lower Evaporites", "Mobile Units 1 and 2" and "Upper Evaporites", terminated by the deposition of the *Lago Mare* facies (Fig. 4.32).

The diachroneous deposition model introduced a three-stage desiccation of the western Mediterranean deep basins (Fig. 4.32). Stage 1 (5.97–5.60 Ma; Manzi et al., 2014) involving minor sea-level drawdown with early evaporite precipitation. The onshore–offshore correlations across the shallow marginal basins suggested that this stage is probably marked by the deposition of the "Primary Lower Gypsum", whereas in the deeper basins only organic-rich shale and carbonate deposition took place (de Lange and Krijgsman 2010; Lugli et al. 2010, Roveri et al., 2008b). During Stage 2 (5.60–5.53 Ma, Roveri et al., 2014a–c), the shallow-water peri-Mediterranean areas were exposed to subaerial erosion and evaporite deposition moved to the deeper basins with the widespread deposition of primary halite and clastic gypsum-carbonate deposits. These clastic evaporites are referred to as the "Lower Evaporites" (Roveri et al., 2008a, 2014a), and were derived from the resedimentation of the primary lower gypsum. The second stage involved a combination of base-level drop, tectonic uplift and variation in the sedimentation rate of evaporites and records the peak of the Messinian Salinity Crisis (Fig. 4.32). Stage 3 (5.53–5.33 Ma; Hilgen et al., 2007; Manzi et al., 2009) included the deposition of the Upper Evaporites in both shallow and deep basin settings. It is characterized by gypsum and marl deposits of the *Lago Mare* facies, which represent sedimentation in a brackish to fresh water environment (Gignoux, 1950; Ruggieri, 1962; Cita and Colombo, 1979; Bertini et al., 1995; Orszag-Sperber et al., 2006). This study clearly shows that the Messinian evaporites in the Florence Rise and the Antalya Basin include the four seismic stratigraphic subunits identified in the western Mediterranean region. From this perspective alone, the data in this study do not fully agree with Roveri et al. (2014a–c), which is fully discussed in Chapter 7.

The critical question here is whether or not the events that took place across the western Mediter-

ranean basins occurred in synchroneity across the eastern Mediterranean basins. The answer to this question lies across the gateways that connect the eastern and western Mediterranean regions to the global ocean where saline waters for the development of thick evaporites deposited across the Mediterranean basins originated. The balanced tectonic uplift and erosion model of Garcia-Castellanos and Villaseñor (2011) eloquently explains how the competing tectonics and erosion across the Betic and Rif gateways provided the much needed trickling input of saline water into the evaporative western Mediterranean basins. However, the Sicilian sill must have been subaerially exposed when the western Mediterranean basins were experiencing evaporite deposition, thus cutting off the saline water influx into the eastern Mediterranean. Thus, unless there is an additional gateway that provided the same "trickling saline water input" into the eastern Mediterranean basins at exactly the same time as the competing tectonic uplift and erosion across the Betic and Rif gateways, the chronology of the evaporite deposition across the eastern Mediterranean basins cannot be synchronous with that across the western Mediterranean basins. The only such possible gateway across the eastern Mediterranean region is the Suez connection to the Red Sea. Although Popov et al. (2004, 2006) suggested that by the time of the onset of the Messinian Salinity Crisis the connection of the eastern Mediterranean Sea to the Red Sea was severed, detailed sedimentological, stratigraphic and regional tectonic studies comparable to the Betic and Rif gateways of the Gibraltar region are missing across the Suez region. This statement primarily applies to the Mobile Units 1 and 2 (i.e., seismic stratigraphic sub-units 2c–2b, because these are the predominantly halite units. The development of the lower sub-unit 2d may well be a synchronous event across the entire Mediterranean region, because the underlying cause of the regional desiccation of the Mediterranean is the closure of the Betic and Rif gateways. Similarly, the exit from the Messinian Salinity Crisis was likely to be a quasi–synchronous event. These are further discussed in Chapter 7.

The other, but more serious shortcoming of the present state of knowledge of the eastern Mediterranean region is the lack of good chronological control on the Messinian evaporite sub-units 2a–2d

from the Antalya Basin and the northern foothills of the Florence Rise. Thus, unless new borehole data and geochemical and biostratigraphic data exit from these regions, the correlations between the eastern and western Mediterranean basins can only be regarded as tentative. The east-west correlation and the place of the eastern Mediterranean within the broader Messinian Salinity Crisis is further discussed in Chapter 7.

Chapter 5

Seismic Structural Interpretation and Deformation History of the Western Cyprus Arc

Introduction

The study area is situated along the western segment of the Cyprus Arc in the eastern Mediterranean which defines the boundary between the African Plate in the south and southwest and the Aegean-Anatolian Microplate in the north and northeast (Fig. 5.1). Structurally, it defines a convergence zone, and is characterized by a broad northwest-southeast trending accretionary prism delineated by the Florence Rise, a poorly defined trench north of the Mediterranean Ridge, and a prominent bathymetric ridge at the southeastern portion of the Florence Rise (Ivanov et al., 1992; Robertson 1998b). The Antalya Basin is situated to the north and northeast of the Florence Rise. The entire region is situated in a forearc setting, with the arc being located in central Anatolia (Fig. 5.1; Ben Avraham et al., 1995; Robertson, 1998). Previous studies strongly suggested that the subduction has ceased and that continent-to-continent collision is incipient (Sage and Letouzey., 1990; Robertson,

1998a; McClusky et al., 2000; Woodside et al., 2002).

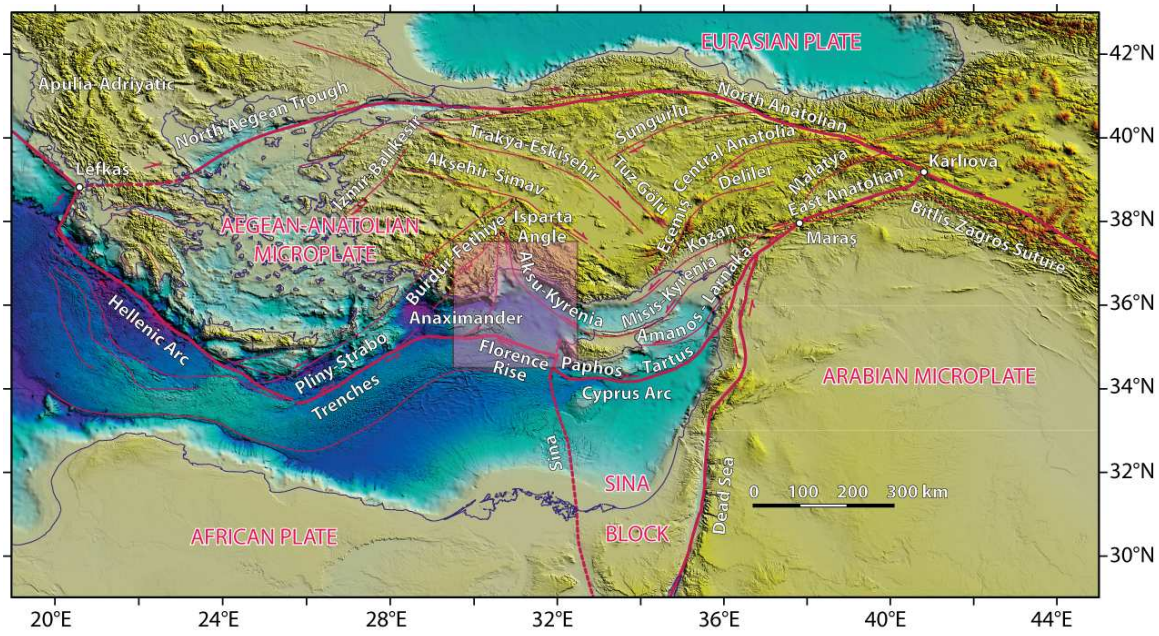

Figure 5.1: Detailed topography, bathymetry and simplified tectonic map of the eastern Mediterranean showing: (1) the Florence Rise and Antalya Basin and their relationship with the major tectonic elements in the region, (2) the boundary between the African Plate and the Aegean–Anatolian Microplate, as defined by the position of the hard boundary of the overriding lithosphere. The topography and bathymetry are compiled fromGeoMapApp (Ryan et al., 2009), the coastline and the selected isobaths contours are from the Intergovernmental Oceanographic Commission (1981), except for the Anaximander and environs: these contours are from the ANAXIPROBE 95 multibeam data.

The most important unresolved scientific issue of the northeastern sector of the eastern Mediterranean was the delineation of the Miocene–Recent morpho-tectonic architecture and the structural framework of the Antalya Basin and the Florence Rise, so that the role of these crustal-scale structures can be understood within the Miocene–Recent tectonic evolution of the greater Cyprus Arc. Until now, these areas were only imaged using very sparse very low resolution single channel seismic reflection profiles (e.g., Zitter et al., 2003). This Chapter fills this void in the literature by providing

a set of very detailed tectonic and paleogeographic maps that were compiled using high-resolution multichannel seismic reflection profiles processed and interpreted by the author. Finally, although the Messinian sedimentary successions are one of the most studied examples of salt basins understanding of the Messinian sedimentation requires a fundamental understanding of the tectonic history of the entire eastern Mediterranean. The regional maps and the new data from the Antalya Basin and Florence Rise provides this much-needed framework. Within this backdrop, the descriptions of the structural elements and mapping in the study area will be made in three distinct temporal domains: (i) pre-Messinian Miocene (and older), (ii) Messinian and (iii) uppermost Messinian–Quaternary. These descriptions will further include correlations with the seafloor morphology, where appropriate.

5.1 Seafloor Morphology

In regions dominated by active tectonism the morphology of the seabed reflects the intensity and style of the ongoing deformation. This is also true for the eastern Mediterranean region (Figs. 5.1, 5.2). There are two types of bathymetric data which are available for the eastern Mediterranean Sea. High-resolution multibeam bathymetry mosaics with $\sim$100 m spatial resolution are available across the Rhodes, Finike and Herodotus basins, the Anaximander Mountains, Cyprus Arc, the Mediterranean Ridge, as well as the southernmost portion of the Antalya Basin. However, only the International Bathymetric Charts of the Mediterranean (IBCM) compilations of spot soundings contoured at 200 m intervals are available for the Antalya and Cilicia basins (IOC, 1981).

The very low spatial resolution of the IBCM data sets does not allow detailed morphologic interpretation to be drawn from the bathymetric data. These data show that the deep Antalya Basin has a water depth exceeding 2400 m. The continental shelf is 5-10 km wide. The shelf break occurs at around 200 m, with steep slopes leading to the abyssal depth in central Antalya Basin. The slope face is dissected by numerous submarine canyons leading submarine fans (Işler et al., 2005, Hall et

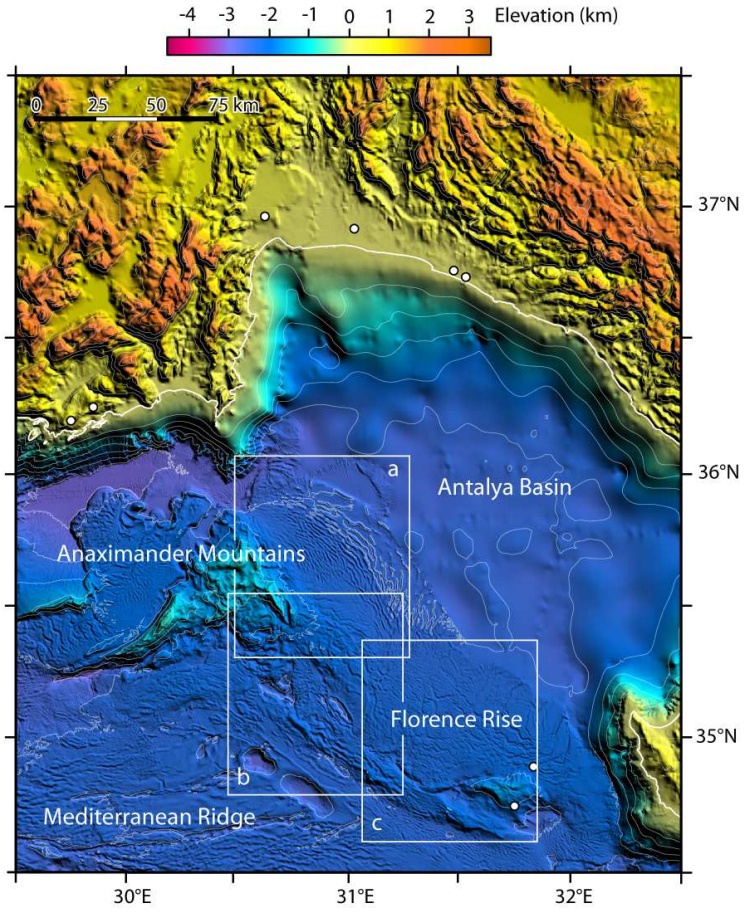

Figure 5.2: Bathymetry and topography of the study area. The topography is compiled using GeoMapApp (Ryan et al., 2009), and shaded using Caris Base Editor (4.1). The multibeam bathymetry are from the 100 M–resolution ANAXIPROBE 95 data (Woodside, 1995) for the Anaximander Mountains and Rhodes Basin and the 500 M–resolution EMODnet (European Marine Observation and Data Network, Portal for Bathymetry, http://www.emodnet-hydrography.eu/) data for the southern Antalya Basin and Florence Rise. The bathymetry of the Turkish continental shelf and the Antalya Basin is from the International Bathymetric Charts of the Mediterranean (IOC, 1981). Isobaths contours (thin white lines) are in meters, calculated using the multibeam data and Caris Base Editor (4.1), and taken from the IOC (1981) data where multibeam data are absent. White circles = exploration wells (A–1 = Aksu–1, D–1 = Demre–1, I–1 = Ismail–1, K–1 = Kaş– 1, M–1 = Manavgat–1, M–2 = Manavgat–2) in the onland Aksu, Köprüçay and Manavgat basins and DSDP boreholes (Sites 375–376) in the Florence Rise.

al., 2014a).

The multibeam mosaic of the eastern Mediterranean shows the presence of two prominent arcuate structures: the Hellenic Arc and its northeast continuation the Pliny-Strabo Trenches in the west and the Cyprus Arc and its northwestern segment the Florence Rise in the east (Figs. 5.1, 5.2). These two prominent arcs meet at a complicated junction, presently occupied by the Anaximander Mountains.

The Anaximander Mountains emerge as three prominent hills: (a) the Anaximander Mountain (*sensu stricto*) is an open V-shaped narrow and arcuate hill with its crest at ∼1100 m depth, (b) the Anaximenes Mountain is a northeast-southwest trending broadly arcuate hill with its crest at ∼750 m depth, and (c) the Anaxagoras Mountain is a mainly northwest-southeast trending broad structure with several prominent peaks at ∼1200–950 m elevations (Fig. 5.2). The Anaxagoras Mountain defines the northwestern edge of the Florence Rise. It is an approximately 25 km wide structure which includes a narrow (6-7 km) but notably shallower northeast segment and a broader and deeper southwestern segment. Traced toward the southeast, the Anaxagoras Mountain loses its morphological expression as a hill and merges with the arcuate Florence Rise (Fig. 5.2).

Along the northwestern segment of the Cyprus Arc, there are several northwest-southeast trending internally-parallel structures, including the Mediterranean Ridge, the Florence Rise and the deep trough situated between these two structures. The Florence Rise emerges as a prominent regional bathymetric high in the eastern Mediterranean Sea. The core of the Florence Rise is a broadly west-northwest–east-southeast oriented bathymetric ridge which stands ∼500–1000 m above the adjacent seafloor situated at the southeast portion of the Cyprus Arc (Fig. 5.2). It is a tear-drop shape 35 km × 15 km structure.

Across the Florence Rise, where detailed multibeam bathymetry exists, several distinctive morphological regions are observed, including (i) a corrugated seafloor across the southwestern Antalya Basin, extending onto the foothills of the Anaxagoras Mountain, (ii) a broad zone of seafloor that exhibits anastomosing canal-like depressions, (iii) northwest-southeast trending broadly elliptical deep

depressions, and (iv) small-scale ridges and runnels (Fig. 5.2).

5.1.1 Corrugated seafloor morphology

The corrugated seafloor across the southwestern Antalya basin is characterized by numerous northwest-southeast trending ridges that are 50 to 100 m elevated from the adjacent depressions. They form quasi linear features that extend 5–15 km, with wavelengths of 1–2 km. The ridges commonly merge to form Y–shaped morphologies (Fig. 5.2). Toward the northwest this zone of corrugated seafloor morphology becomes progressively less prominent, disappearing near the Finike Basin. Toward the southeast the individual ridges in the zone gradually assume a broadly north-south orientation, rendering the zone to appear as a northeast convex seafloor morphology. There is a faint boundary where the ridges and their intervening depressions transition to a seafloor exhibiting a blocky appearance with canal-like depressions forming loosely anastomosing seafloor morphology (Fig. 5.2). The seismic reflection profiles (both previous studies and this study) show that this region of corrugated seafloor morphology extends considerable northward into the Antalya Basin where there is presently no multibeam data.

5.1.2 Anastomosing canal-like depressions

The southeastern portion of the Florence Rise is characterized by a relatively smooth seafloor that appears dissected by a network of canal-like seafloor depressions that stand 10–70 m below the adjacent seafloor (Fig. 5.2). These depressions are approximately 2-5 km apart, but often appear to merge and/or diverge to form a broadly anastomosing appearance. In the southeastern segment of the Florence Rise, the canal-like depressions trend in a northwest-southeast orientation, whereas in the central segment of the rise, they are oriented in a broadly north-south direction (Fig. 5.2).

5.1.3 Elliptical deep depressions morphology

There are several northwest-southeast oriented elliptical depressions situated immediately southwest of the Florence Rise (Fig. 5.2). They are 10–20 km long 5–7 km wide and are 400–600 m deeper than the adjacent seafloor.

5.1.4 Small-scale ridges and troughs

Immediately southeast of the core of the Florence Rise there is a narrow 10–15 km wide zone characterized by a network of small amplitude corrugations where the ridges and the intervening troughs that show little lateral continuity, giving the appearance of a weakly wrinkled seafloor. These ridges and troughs are 1–3 km long with wavelengths of 0.5–1 km. The ridges are only 10–40 m above the adjacent seafloor.

5.2 Tectonic Framework

The following description of the structural architecture and regional tectonic framework of the Antalya Basin and Florence Rise is done primarily using the deeper penetration ($\sim$9 s sub-seafloor), lower resolution industry multi-channel seismic reflection profiles, supplemented by the notably shallower penetration ($\sim$3-4 s sub-seafloor), but high-resolution multi-channel seismic reflection profiles, collected by Memorial University of Newfoundland (§ Chapter 2). The structural geological interpretation of the data is separated into three time domains: (i) pre-Messinian Miocene, (ii) Messinian and (iii) uppermost Messinian–Quaternary. It is important to note that only the most prominent crustal–scale thrusts are indicated in the industry seismic profiles, whereas all faults and associated structures are shown in the high-resolution profiles.

5.2.1 pre-Messinian Miocene

The pre-Messinian Miocene structural architecture of the Antalya Basin and its southwestern extension into the Florence Rise is characterized by a very prominent broadly northwest-southeast striking and largely southwest verging fold thrust belt, with occasional northeast verging back-thrusts (Figs. 5.3–5.8). This belt extends from the southwestern foothills of the Florence Rise across the entire Antalya Basin into the eastern limb of the onland Isparta Angle, delineating a 200–250 km wide deformation zone presently located north and northeast of the greater Cyprus Arc (Figs. 5.1, 5.3).

Several previous studies have been carried out in the Antalya Basin, mainly localized on small regions (e.g., Işler et al., 2005, King, 2014, Hall et al., 2014), or as more regional studies in the adjacent areas, but extending into the Antalya Basin (e.g., Barnes, 2015, Çınar, 2015). However, none of these studies extended into the southern and southwestern Antalya Basin, but as importantly, none of these studies delineated the regional tectonic and kinematic evolution of the Antalya Basin and Florence Rise in a holistic manner. In order to provide a holistic and regionally extensive tectonic interpretation, the entire Antalya Basin including the previously extensively studied northern and northwestern segment have been included in this study. All seismic data from the northern and northeastern portion of the Antalya Basin have been re-interpreted and integrated, particularly in the light of the new deep penetration Turkish Petroleum Corporation seismic reflection profiles (e.g., Figs. 5.4–5.8) which were not available for the previous studies. However, all previous studies in the region are duly acknowledged and referenced in the following sections, where appropriate.

In the trailing segment of the fold-thrust belt in northern and northeastern portion of the Antalya Basin, the belt consists of several large thrust panels, delineated by major thrust culminations (Figs. 5.3, 5.4, 5.9, 5.10). The leading thrust (T3) of the fold-thrust belt is characterized by a huge thrust culmination delineated by the present-day continental slope (e.g., Figs. 5.4, 5.9). Several smaller thrusts splay-off thrust T3 (e.g., Figs. 5.9, 5.10). The thrusts within the belt have a northeast-

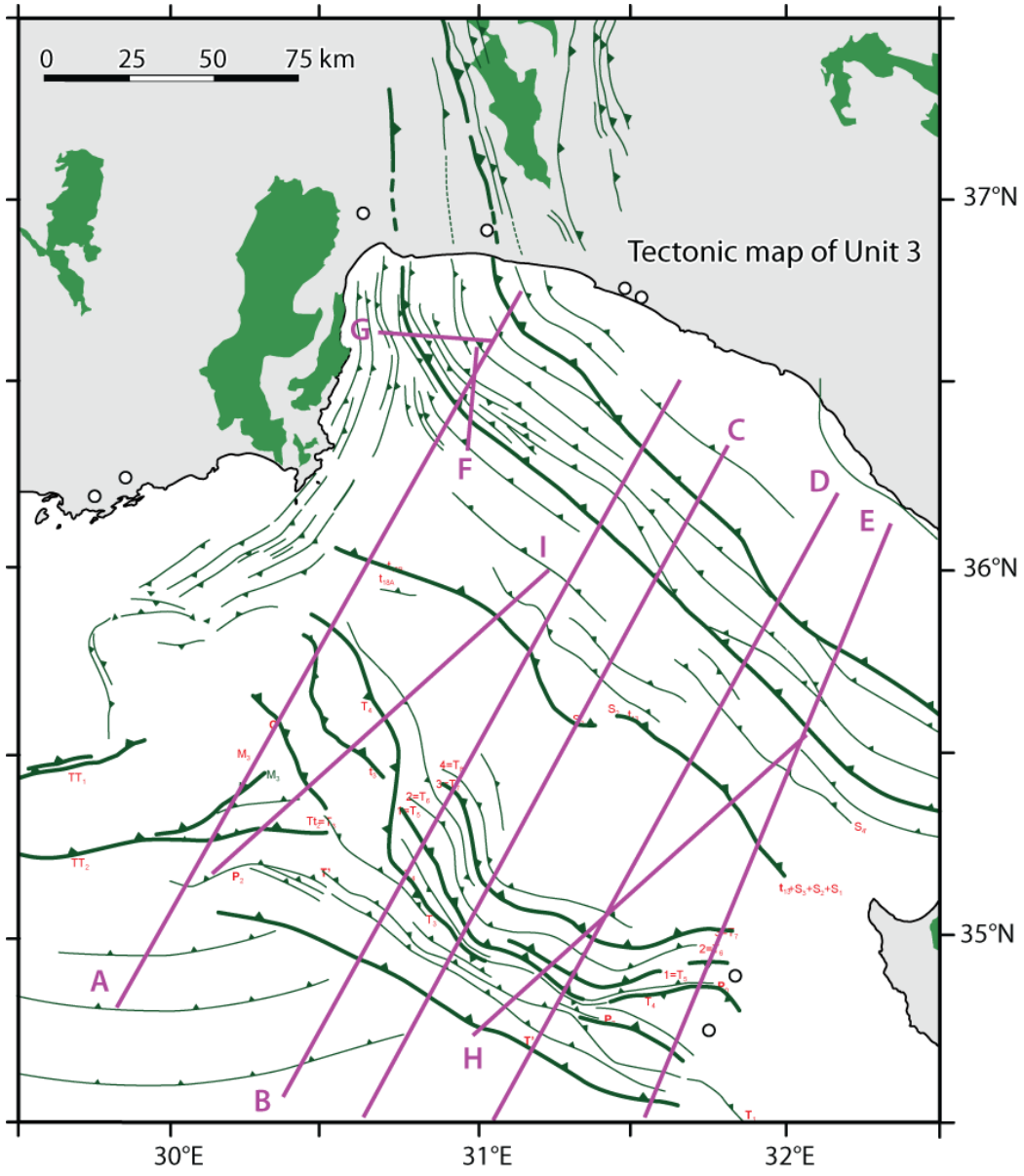

Figure 5.3: pre-Messinian Miocene tectonic map of the Antalya Basin and Florence Rise showing the distribution of the major fold-thrust belt. Filled triangles are placed on the hanging wall. Solid line segments are seismic reflection profiles illustrated in Figures 5.4–5.12. Thrust labels correspond to those illustrated in these seismic reflection profiles. Light purple fill = no multi-channel seismic reflection profile. White circles = exploration wells and DSDP boreholes.

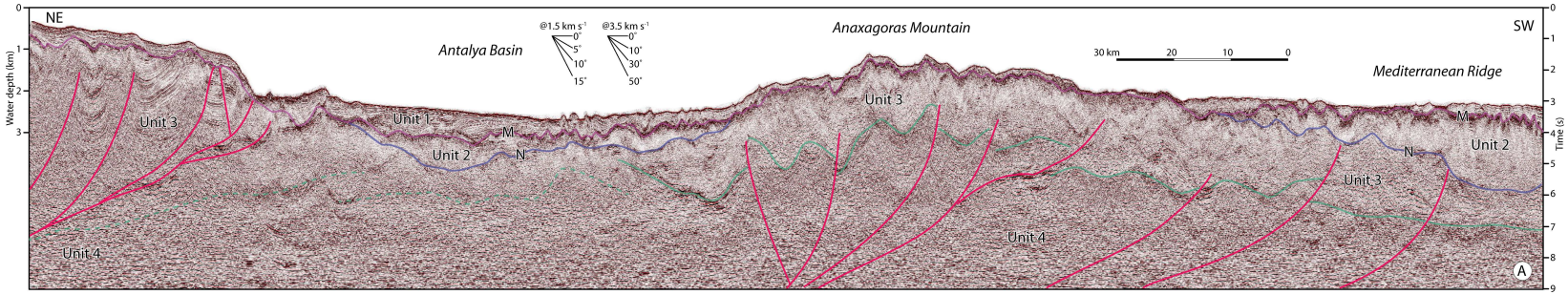

Figure 5.4: Industry multi-channel seismic reflection profile A showing the structural architecture and tectonic framework of the western Antalya Basin and the Anaxagoras Mountain. Units 1–4 are described in Chapter 4. The profile is kindly provided by the Turkish Petroleum Corporation. Location is shown in Figure 5.3. TPAK071-7 (sp.300-19100)

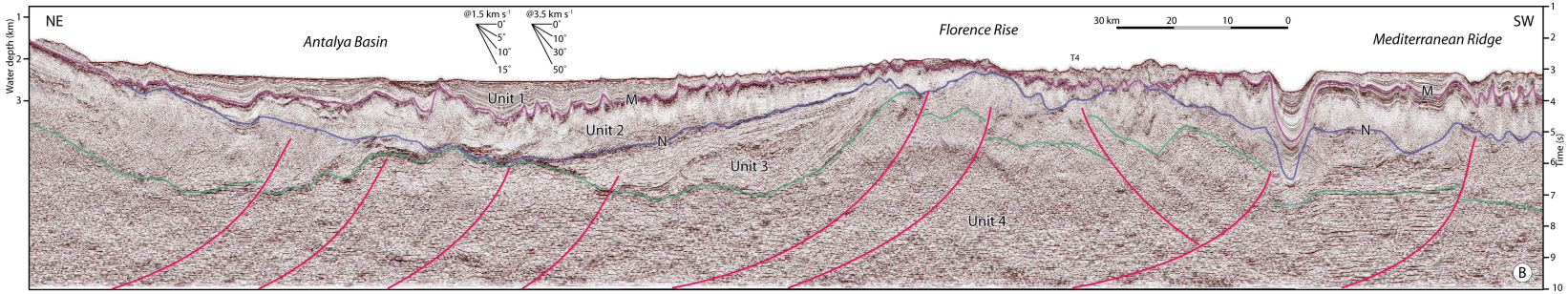

Figure 5.5: Industry multi-channel seismic reflection profile B showing the structural architecture and tectonic framework of the western Antalya Basin and the northwestern segment of the Florence Rise. Units 1–4 are described in Chapter 4. The profile is kindly provided by the Turkish Petroleum Corporation. Location is shown in Figure 5.3. TPAK071-7 (sp. 670-19800)

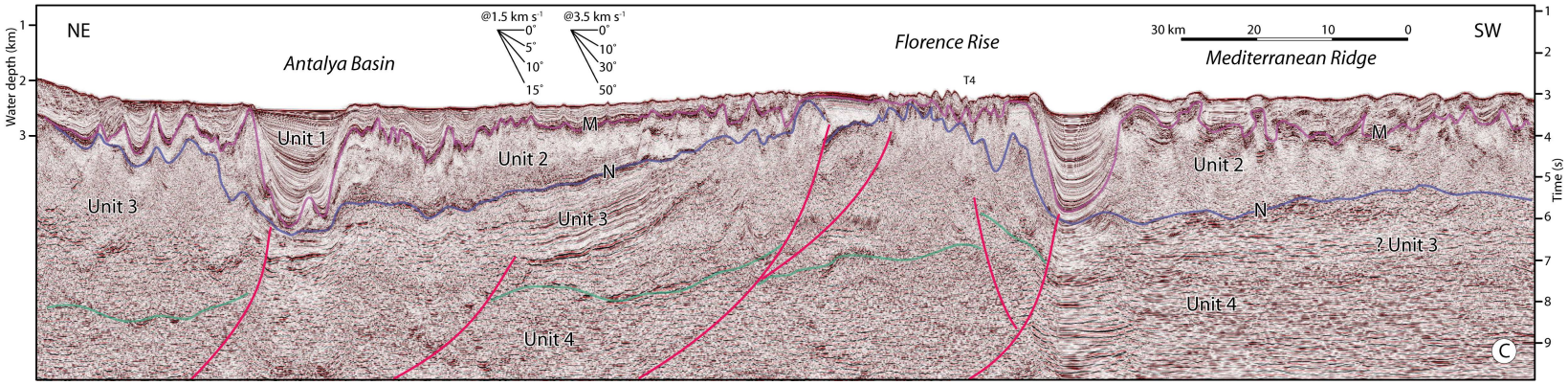

Figure 5.6: Industry multi-channel seismic reflection profile C showing the structural architecture and tectonic framework of the central Antalya Basin and the Florence Rise. Units 1–4 are described in Chapter 4. The profile is kindly provided by the Turkish Petroleum Corporation. Location is shown in Figure 5.3. TPAK071-5 (sp.6700-24900)

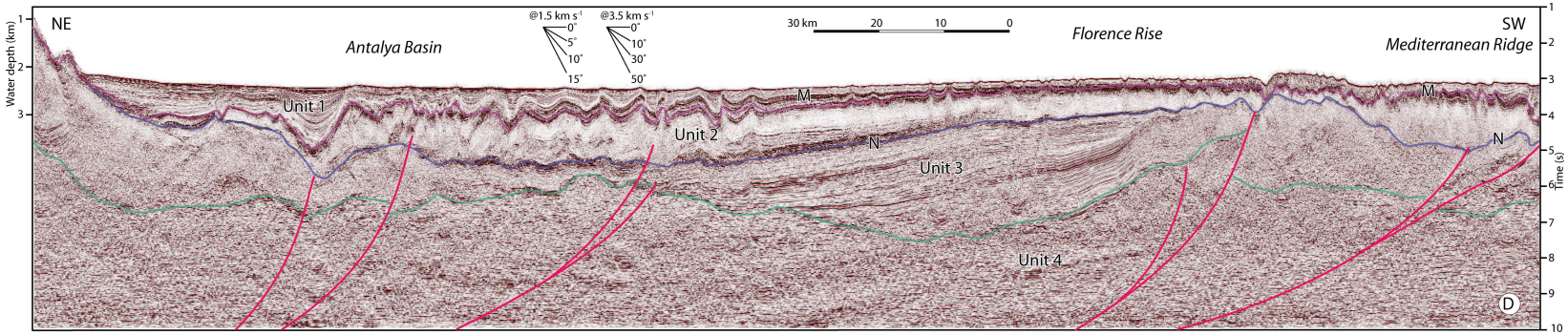

Figure 5.7: Industry multi-channel seismic reflection profile D showing the structural architecture and tectonic framework of the eastern Antalya Basin and the southeastern segment of the Florence Rise. Units 1–4 are described in Chapter 4. The profile is kindly provided by the Turkish Petroleum Corporation. Location is shown in Figure 5.3. TPAK071-6 (sp.720-17500)

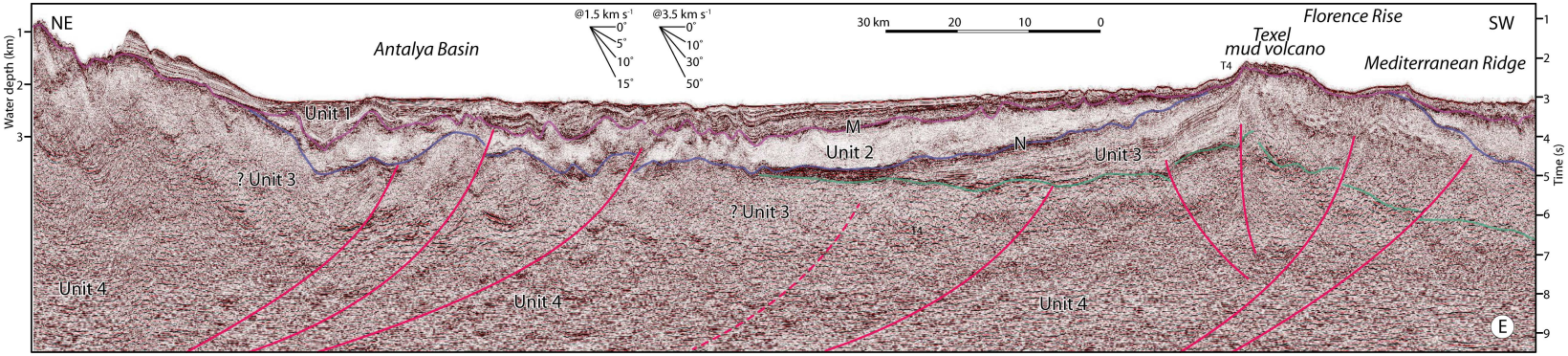

Figure 5.8: Industry multi-channel seismic reflection profile E showing the structural architecture and tectonic framework of the eastern Antalya Basin and the southeastern segment of the Florence Rise. Units 1–4 are described in Chapter 4. The profile is kindly provided by the Turkish Petroleum Corporation. Location is shown in Figure 5.3. TPAK071-7 (sp.5600-20800)

southwest strike, and predominantly southwest vergence. However, a prominent similarly striking but northeast-verging backthrust is also clearly visible in the seismic reflection profiles. This backthrust is also identified in previous studies (e.g., King, 2014; Hall et al., 2014a). Toward the northwest, the fold-thrust belt progressively swing and assume a north-south strike, and trend toward the present-day coastline of the Antalya Bay (Fig. 5.3; King, 2014; Hall et al., 2014a; Barnes, 2015). Several industry seismic reflection profiles in this region clearly show that the fold-thrust belt readily extends toward the onland Antalya Basin, linking with the thrust panels of the Aksu Fault zone. Thus, this fold thrust belt forms a prominent crustal-scale structural element in the eastern Mediterranean extending from the Kyrenia Range of northern Cyprus to the Aksu fault zones of south-central Turkey. It is referred to as the Aksu-Kyrenia Fault zone.

Except for a few smaller thrusts that splay-off from T3, the individual thrusts of the fold-thrust belt have their tip points within the uppermost segment of the pre-Messinian Miocene succession of Unit 3. These thrusts never cut the N-reflector when the evaporite succession of Unit 2 is present, or the M-reflector, where the evaporites are absent. Growth strata observed on the backlimb of the thrusts and the deformation associated with the frontal basins strongly suggest that these structures are pre-Messinian Miocene in age. In industry seismic reflection profiles the thrusts display listric trajectories and sole deep within Unit 4 at 8–9 s twt. This internal seismic stratigraphic architecture suggests that the trailing segment of the fold-thrust belt constitutes a crustal-scale imbricate system. There are 2–3 splays that rise from thrust T3 extending into and structuring Units 2 and 1: these are further described later (see § 5.2.2 and 5.2.3).

This portion of the fold-thrust belt is also identified in previous studies (e.g., King, 2014; Hall et al., 2014a). These authors referred the trailing segment of the fold-thrust belt as the leading thrust panels of the Western Taurus Mountains (Hall et al., 2014a).

Across the southeastern Antalya Basin, immediately west of the Kyrenia Range the fold-thrust belt is defined by 3–4 large thrust culminations (Figs. 5.3, 5.7, 5.8). These thrusts have northwest-

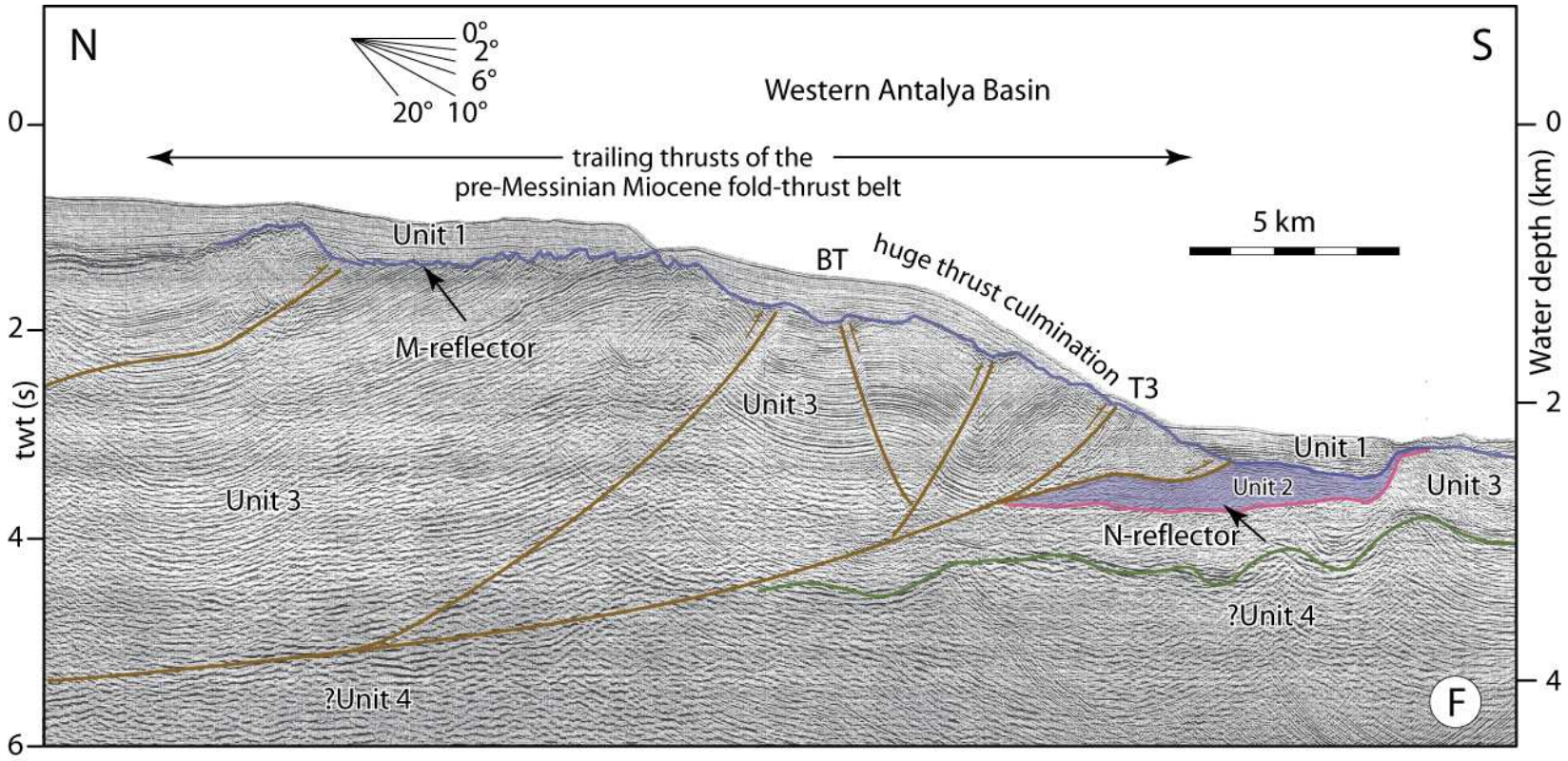

Figure 5.9: Industry multichannel seismic reflection profile F showing the pre-Messinian Miocene structural architecture of the western Antalya Basin. Note that the leading thrust of the fold thrust belt delineates the base of slope in western Antalya Basin, and that the slope face is the forelimb of a huge thrust culmination. The profile is kindly provided by the Turkish Petroleum Corporation. Location is shown in Figure 5.3. TPAO-10 (sp.440-1546)

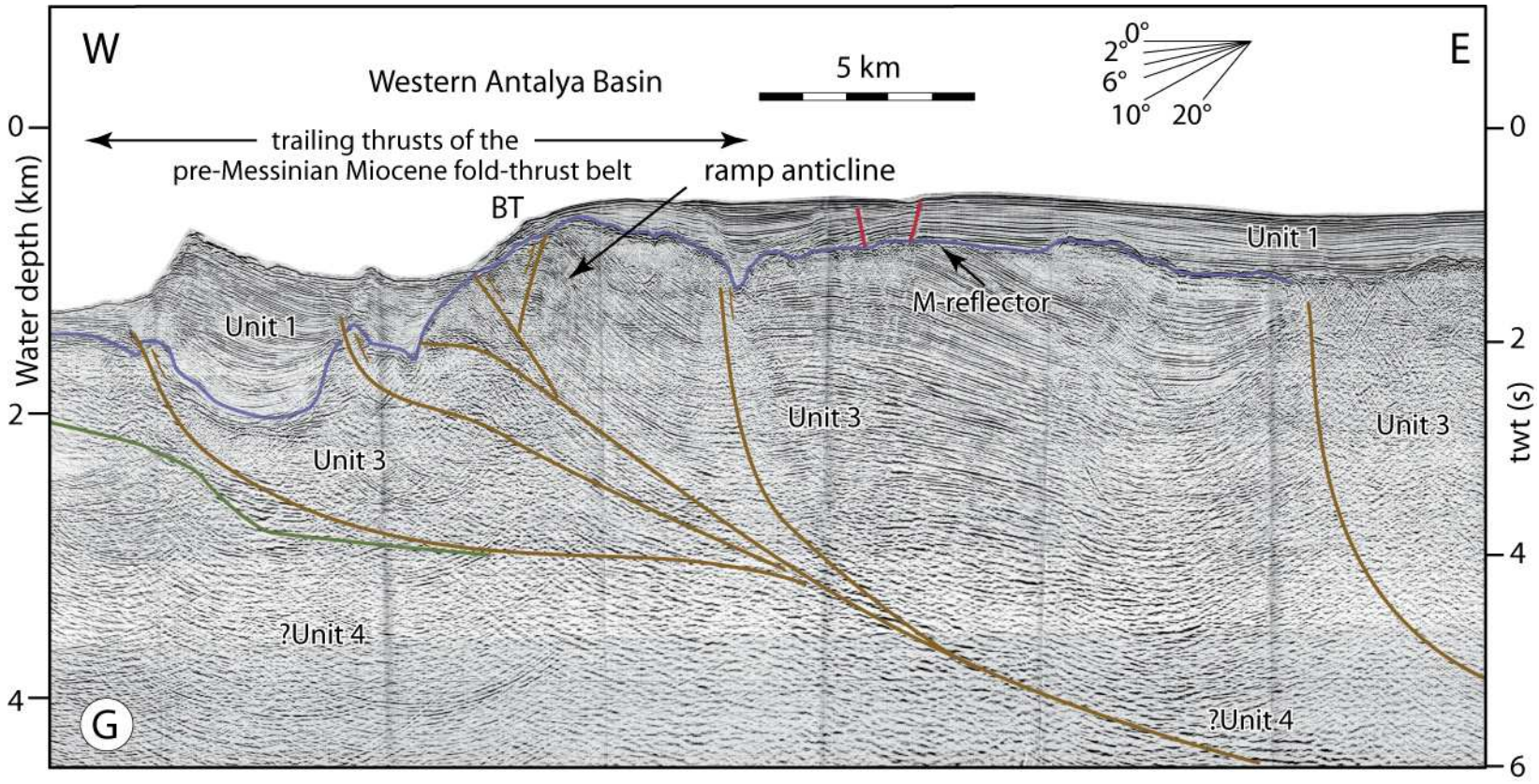

Figure 5.10: Industry multichannel seismic reflection profile G showing the Miocene structural architecture of the western Antalya Basin. Note the presence of a prominent ramp anticline delineated by the M-reflector. Profile is kindly provided by the Turkish Petroleum Corporation. Location is shown in Figure 5.3. TPAO-03 (sp.1280-2398)

southeast strike and invariably verge toward the southwest. Unlike the thrusts across the northwestern portion of the Antalya Basin, these thrusts often cut the N-reflector extending into the evaporite succession of Unit 2. However, none of the thrusts cut the M-reflector. Previous studies in the southeastern portion of the Antalya Basin have documented that these thrust culmination are the western marine extensions of the onland Orga, Kythria, Ovgos and Mesaoria thrusts which define the core of the Kyrenia Range of northern Cyprus (Işler et al., 2005; Calon et al., 2005a,b). These major thrust culminations extend from the Kyrenia Range toward the northwest where several smaller splays are developed.

The southern portion of the Antalya Basin is a tectonically quite zone for the pre-Messinian Miocene successions of Units 3 and 4, characterized by 2–4 northwest-southeast striking and southwest verging thrusts in this region (Figs. 5.3, 5.11, 5.12). These thrusts rise from Units 3 and 4 with listric trajectories and often tip below the N-reflector, such as thrusts T7 and T8 (Figs. 5.7, 5.8, 5.11). However, toward the north nearly all thrusts cut the N- and M-reflectors and extend into the uppermost Messinian–Quaternary succession of Unit 1 (e.g., thrusts S2, S4; Fig. 5.11).

The Florence Rise and its northwestern extension into the Anaxagoras Mountain is a complexly-faulted tectonic domain with several curvilinear faults consisting of broadly northwest-southeast striking and predominantly southwest verging thrusts with occasional similarly striking but northeast verging back thrusts (Fig. 5.3). This zone appears to further extend toward the southeast, possibly linking with the central segment of the Cyprus Arc (Fig. 5.1).

The structural architecture of the Florence Rise and the Anaxagoras Mountain is best imaged in the industry seismic reflection profiles (e.g., Figs. 5.4–5.8). These profiles show the presence of a very prominent crustal-scale fold-thrust belt across this region, characterized by 3–4 large thrust panels cored by southwest-verging thrusts. These thrusts rise from 9-10 seconds depth and extend with listric trajectories into the upper portion of the pre-Messinian Miocene Unit 3 (Figs. 5.4–5.8). Most of the thrusts show tip points below the N-reflector; however, a few thrusts cut the N- and M-

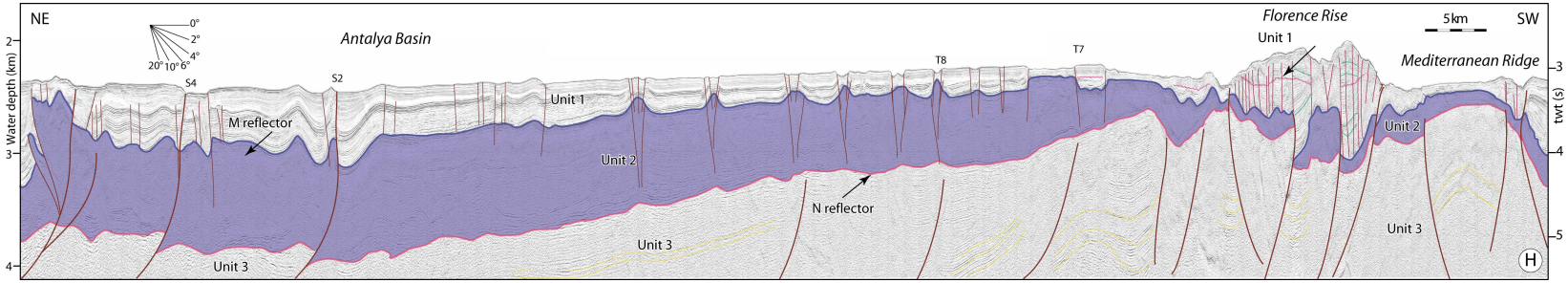

Figure 5.11: High-resolution multi-channel seismic reflection profile H showing the architecture of the southeastern Antalya Basin and eastern Florence Rise. Location is shown in Figure 5.3. EMED10 (fix 1814-1904)

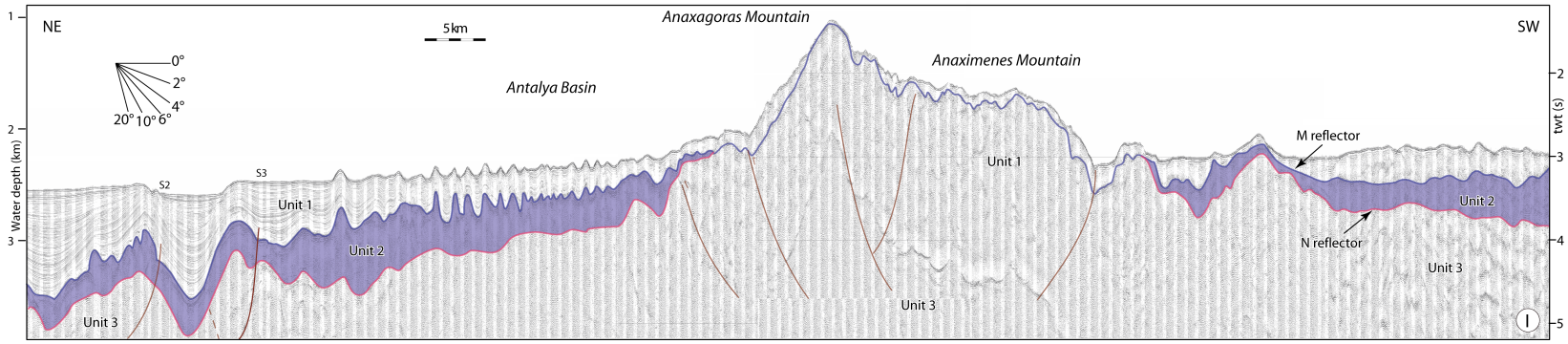

Figure 5.12: High-resolution multi-channel seismic reflection profile I showing the architecture of the southwestern Antalya Basin and the Anaxagoras and Anaximenes Mountain. Location is shown in Figure 5.3. EMED10 (fix 1451-1536)

reflectors and extend into the uppermost Messinian–Quaternary successions of Unit 1. These thrusts are believed to have been re-activated during the uppermost Messinian–Quaternary (explained later). A few northeast-verging back thrusts are also imaged, such as thrust T4 (Fig. 5.5, 5.6, 5.8). The high-resolution multi-channel seismic reflection profiles show that in addition to these crustal-scale thrusts, there are smaller thrusts which splay off from these prominent thrusts (e.g., Figs. 5.11, 5.12).

The linkage between the Florence Rise and its continuation into the Anaxagoras Mountain with the Anaximander Mountains (*sensu lato*) is complex. There are several previous works in this region (e.g., Aksu et al., 2009; Barnes, 2014). These previous studies documented the presence of two crustal-scale thrust culminations which carry the Anaximander and Anaximenes mountains (Fig. 5.3). Thrust TT2 delineates the southern margin of the Anaximenes Mountain and is a deeply rooted crustal-scale structure running essentially parallel to the thrust TT1. In turn, thrust TT1 defines the southern margin of the Anaximander Mountain, and is another deeply-rooted crustal-scale structure (Aksu et al., 2009; Barnes, 2014). These authors speculated that the thrust TT2 links with the thrust TT1 at depth, and forms a crustal-scale N-dipping, S-verging, thick-skinned linked imbricate thrust system. Aksu et al. (2009) also showed that traced toward the northeast, the orientation of the map trace of the TT2 thrust shows a progressive rotation from an E–W trend to a predominantly NE–SW trend. These authors speculated that this swing in the trend of the TT2 thrust represents a 35–40° counterclockwise rotation of the eastern segment of the Anaximenes block sometime during the uppermost Messinian–Quaternary. Previous studies also noted that the large thrust culminations that define the northeastern and southwestern margins of the Anaxagoras Mountain and the Florence Rise display similar vergence, and that these two thrusts are nearly parallel to one another (Fig. 5.3, Aksu et al., 2009; Barnes, 2014). These authors speculate that these two thrusts must merge at depth, forming a crustal-scale northeast-dipping, southwest-verging, thick-skinned linked imbricate thrust system.

The data described above, including the linkage of the Florence Rise with the Anaximander

Mountains (*sensu lato*) clearly document that during the pre-Messinian Miocene, there was a broadly north-south or northwest-southeast oriented contractional belt extending approximately 250 km in front of the subduction zone in the eastern Mediterranean. This belt was characterized by numerous large culminations cored by predominantly southwest-verging thrusts. The deformation across the contractional belt was concentrated into two distinct zones: (a) the leading portion of the belt across the Florence Rise and Anaxagoras Mountain is delineated by 3–4 southwest-verging thrusts with 1–2 back thrusts and (b) the trailing portion of the belt across the inner Antalya Basin is delineated by 6–9 southwest-verging thrusts with at least 1 back thrust. The zone between the leading and the trailing portions of the fold-thrust belt across the southern Antalya Basin was relatively free of structuring. The thrust trajectories extending to 9–10 s depths imaged in the industry seismic reflection profiles clearly document that this 200–250 km wide fold-thrust belt must represent a crustal-scale deformation zone across the eastern Mediterranean.

5.2.2 Messinian

The identification and mapping of the strictly Messinian faults were challenging because of the masking effect of the evaporites. This means that the low competence of the evaporites cause detachment of structures in the Messinian, but as importantly the post-Messinian halokinetic deformation associated with the loading of the uppermost Messinian–Quaternary successions of Unit 1. Faults are identified as "Messinian" if they met one or all of the following criteria: (a) thrusts and their trajectories are clearly imaged in the seismic reflection profiles, creating well defined ramp anticlines within Unit 2, (b) there is clear evidence of growth strata development within Unit 2 on the backlimb of an asymmetric fold (i.e., thrust culmination), and (c) there is clear evidence of structuring by a deeply-seated blind thrusts at the N-reflector and possibly M-reflector levels where structuring does not continue into the uppermost Messinian–Quaternary succession of Unit 1. However, the absence of Unit 2 across large stretches of the northern sector of the Antalya Basin shallower than the

present-day 2000 m isobaths creates uncertainties in the determination of tectonic activity during the Messinian. In these areas, the only circumstantial evidence that can be used for fault activity may be associated with the harmonic structuring of the M-reflector with the underlying pre-Messinian Miocene successions (e.g., Fig. 5.13). For example, in Figure 5.13, there are four thrusts identified within Unit 3 (N2–N5). The only thrust that remained active during the Messinian is N5, which also shows a well-developed ramp anticline and the M-reflector is harmonically folded relative to Unit 3.

The Messinian structural architecture of the Antalya Basin and its southwestern extension into the Florence Rise is characterized by several prominent broadly northwest-southeast striking and predominantly southwest verging fold thrusts, with occasional northeast verging back-thrusts (Figs. 5.11, 5.12, 5.14). Comparison between the pre-Messinian Miocene and Messinian tectonic maps reveals that a number of prominent thrusts remained active during the Messinian (Figs. 5.3, 5.20). For example, seismic reflection profiles along the eastern portion of the Antalya Basin shows the presence of 3–4 large thrusts that clearly cut the N-reflector extending into Unit 2, then further cut the M-reflector extending to the depositional surface where they create distinct seafloor inflections (e.g., S2, S4, S5; Figs. 5.15, 5.16). These thrusts created ramp anticlines within Unit 2, and the distinctive reflectors within the unit show footwall and hanging wall cutoffs, indicating that the thrusts were active during the deposition of Unit 2.

However, numerous thrusts which were active during the pre-Messinian Miocene became inactive during the Messinian, as indicated by the tip points of these thrusts being located below the un-structured N-reflector. For example, thrusts N1–N5 are clearly imaged in the pre-Messinian Miocene successions of Unit 3, where several reverberatory reflectors can be highlighted delineating large ramp anticlines (Figs. 5.13, 5.17, 5.18). All these thrusts show tip points within the uppermost portion of Unit 3, but they do not affect the overlying N-reflector and Unit 2, indicating that the thrust activity must have ceased prior to the development of the unconformity represented by the

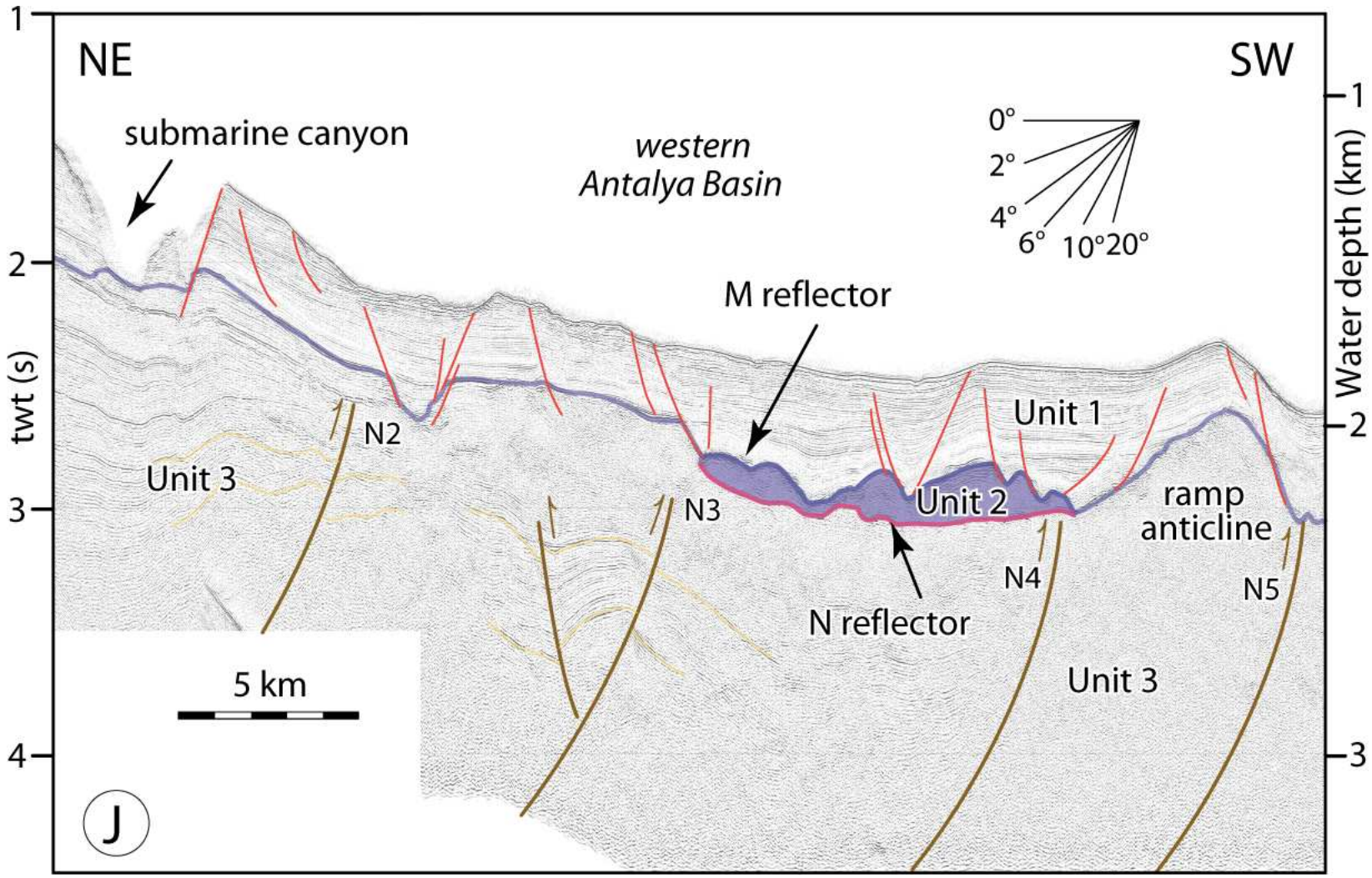

Figure 5.13: High-resolution multi-channel seismic reflection profile J showing the architecture of the northwestern Antalya Basin slope. Note that thrust faults N2–N4 ceased their activity prior to the development of the unconformity delineated by the M-reflector, but also note that thrust N5 remained active during the latest Messinian and early Pliocene as indicated by the development of the prominent ramp anticline across this thrust (see text for explanation). Location is shown in Figure 5.13. EMED92 (fix 2119-2141)

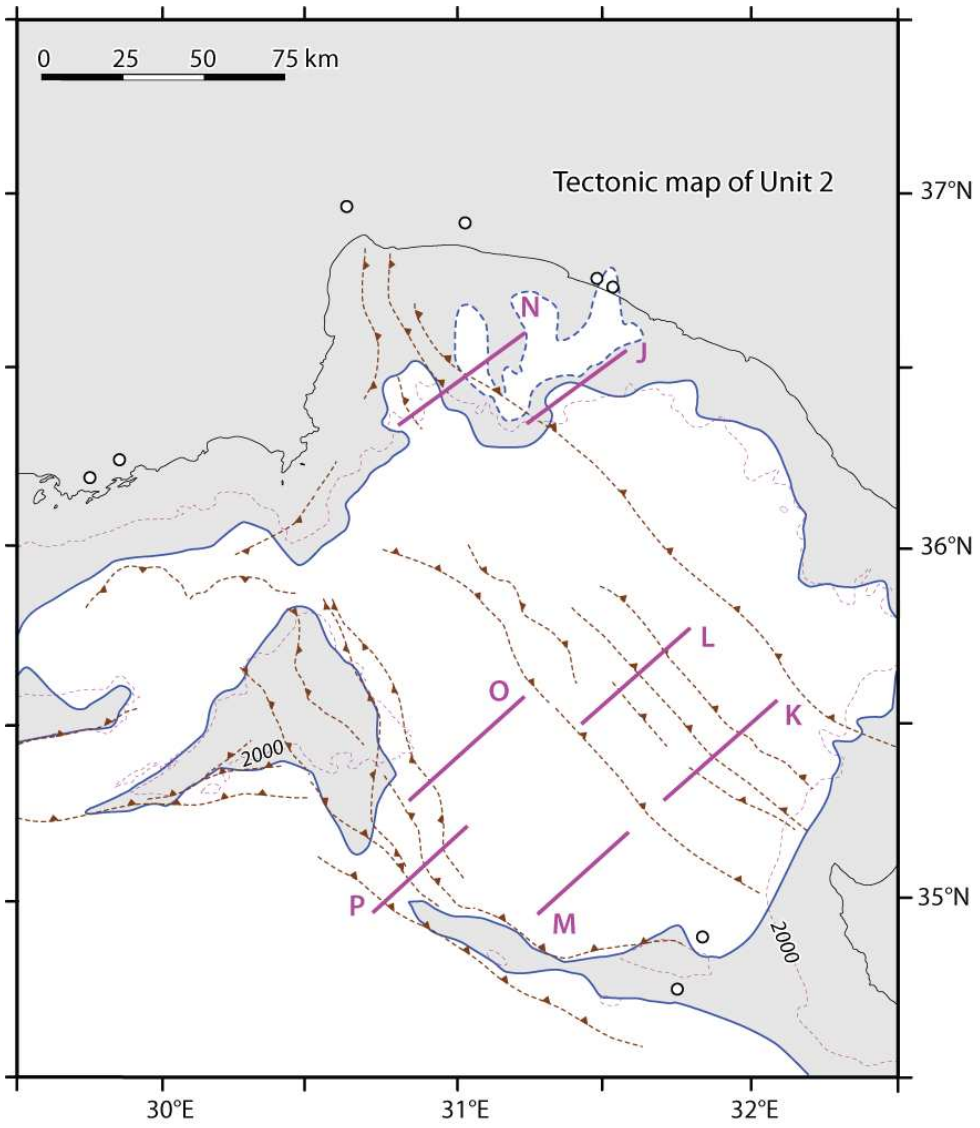

Figure 5.14: Messinian tectonic map of the Antalya Basin and Florence Rise showing the distribution of the major thrusts. Filled triangles are placed on the hanging wall. Solid blue lines are the zero ms isopach contour of Unit 2 (see Fig. 4.31), and represent the approximate position of the Messinian coastline, with the gray fill representing regions that are exposed subaerially during the Messinian Salinity Crisis. Present-day coastline and present-day 1000 m and 2000 m isobaths contours are also shown with thin black lines and thin dashed blue lines, respectively. Purple line segments are seismic reflection profiles illustrated in Figures 5.13–5.19. Thrust labels correspond to those illustrated in these seismic reflection profiles. White circles = exploration and DSDP boreholes.

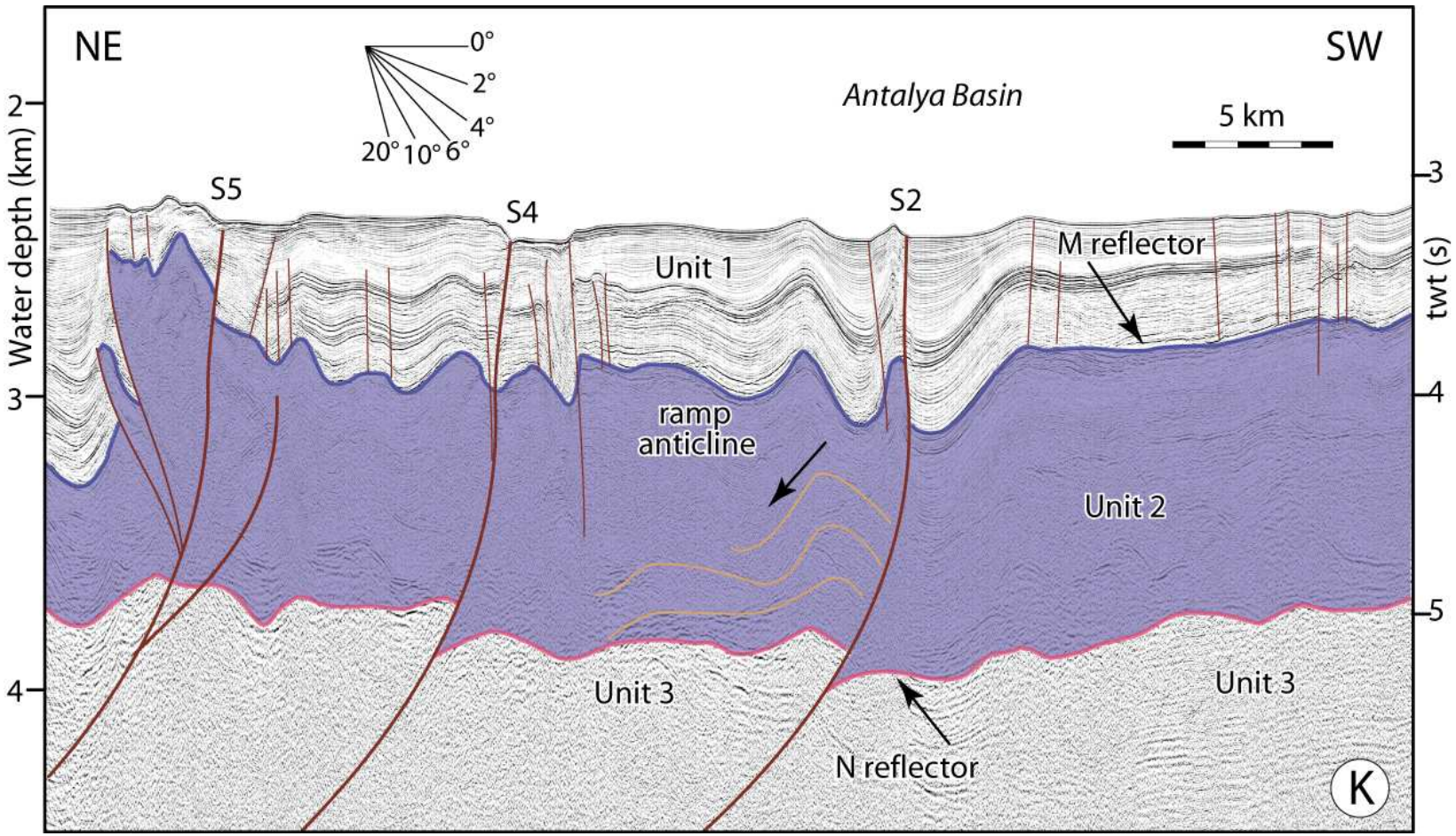

Figure 5.15: High-resolution multi-channel seismic reflection profile K showing the thrust faults that remained active during the Messinian in the south-eastern sector of the Antalya Basin (see text for explanation). Location is shown in Figure 5.13. EMED10 (fix 1814-1846)

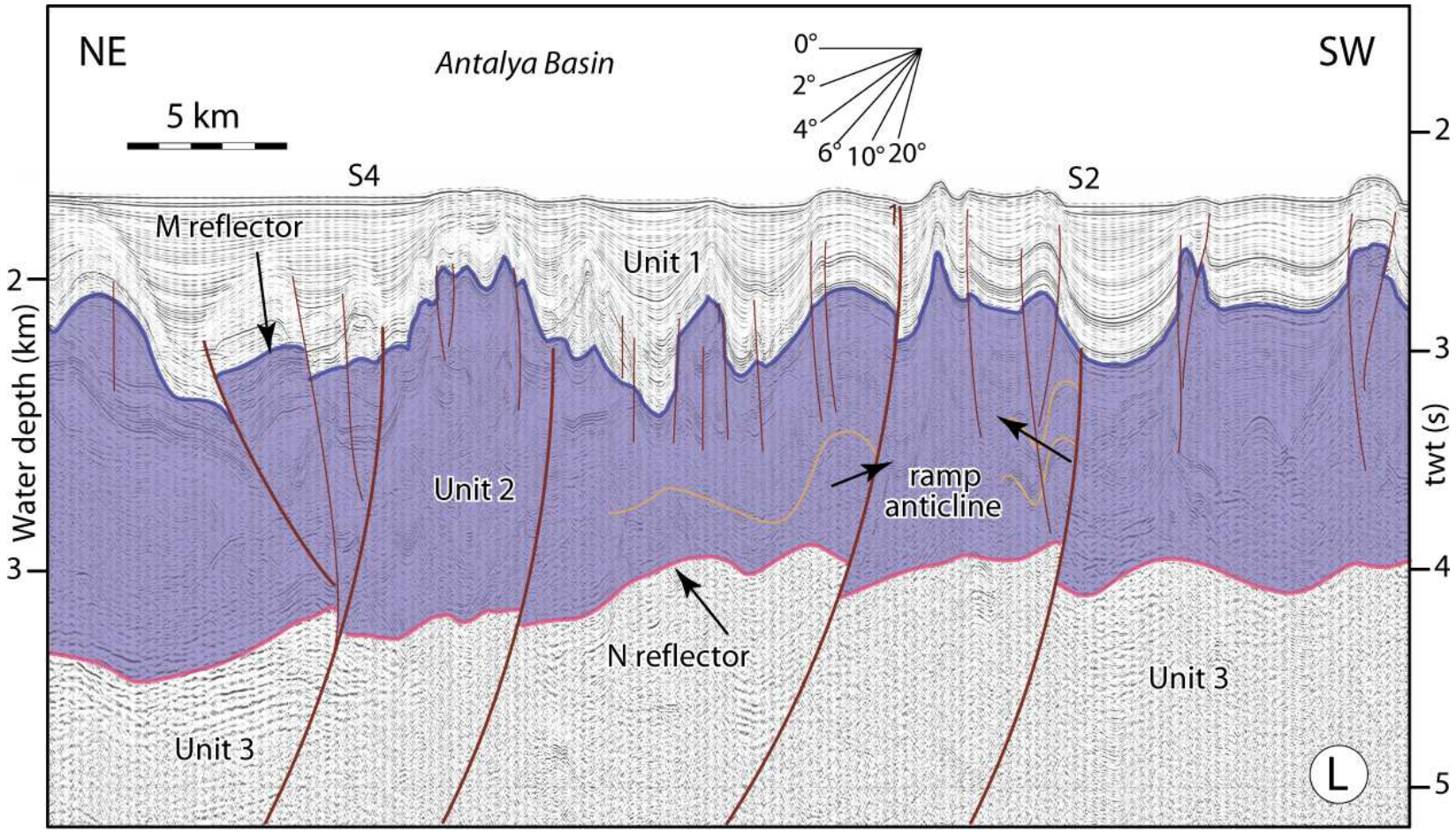

Figure 5.16: High-resolution multi-channel seismic reflection profile L showing the thrust faults that remained active during the Messinian in the south-eastern sector of the Antalya Basin (see text for explanation). Location is shown in Figure 5.13. EMED10 (fix 1575-1604)

N-reflector.

The tectonic architecture described above strongly suggests that the north-south and/or northwest-southeast convergence that was predominant during the pre-Messinian Miocene across the Antalya Basin and the Florence Rise notably waned during the Messinian. A similar conclusion was also noted by numerous previous workers across the eastern Mediterranean, from the Latakia, Cyprus and Mesaoria basins (Hall et al., 2005a,b; Calon et al., 2005a,b), the Iskenderun, Adana and Cilicia basins (Aksu et al., 2005a,b; Burton-Ferguson et al., 2005; Aksu et al., 2014b,c; Walsh-Kennedy et al., 2014), the Finike and Rhodes basins and the Anaximander Mountains (Aksu et al., 2009, 2014a; Hall et al., 2009, 2014b), as well as the northern sector of the Antalya Basin (Işler et al., 2005; Hall et al., 2014a). The progressive waning of the tectonic activity toward the upper Miocene and the relatively quite tectonism during the Messinian will be evaluated later in Chapter 6.

5.2.3 Uppermost Messinian–Quaternary

The tectonic framework of the uppermost Messinian–Quaternary successions of Unit 1 is notably more complex than that of the Messinian successions of Unit 2 and the pre-Messinian Miocene successions of Unit 3 (Fig. 5.20). There are five broadly northwest-southeast trending morpho-tectonic domains in the uppermost Messinian–Quaternary successions of Unit 1, each delineated by a distinctive seafloor morphology (Figs. 5.2, 5.20): (a) a domain in inner and western Antalya Basin dominated extensional faults, (b) a domain immediately south of the extensional faults, characterized by contractional structures, (c) a halokinetic domain in southwestern Antalya Basin north of the foothills of the Anaxagoras Mountain, (d) a domain across the crestal portion of the Florence Rise dominated by inversion structures, and (e) a domain across the northeastern and southwestern margins of the Florence Rise characterized by positive flower structures. Thus, the uppermost Messinian–Quaternary tectonic architecture will be described under these sub-headings, followed by a holistic summary at the end of the Chapter.

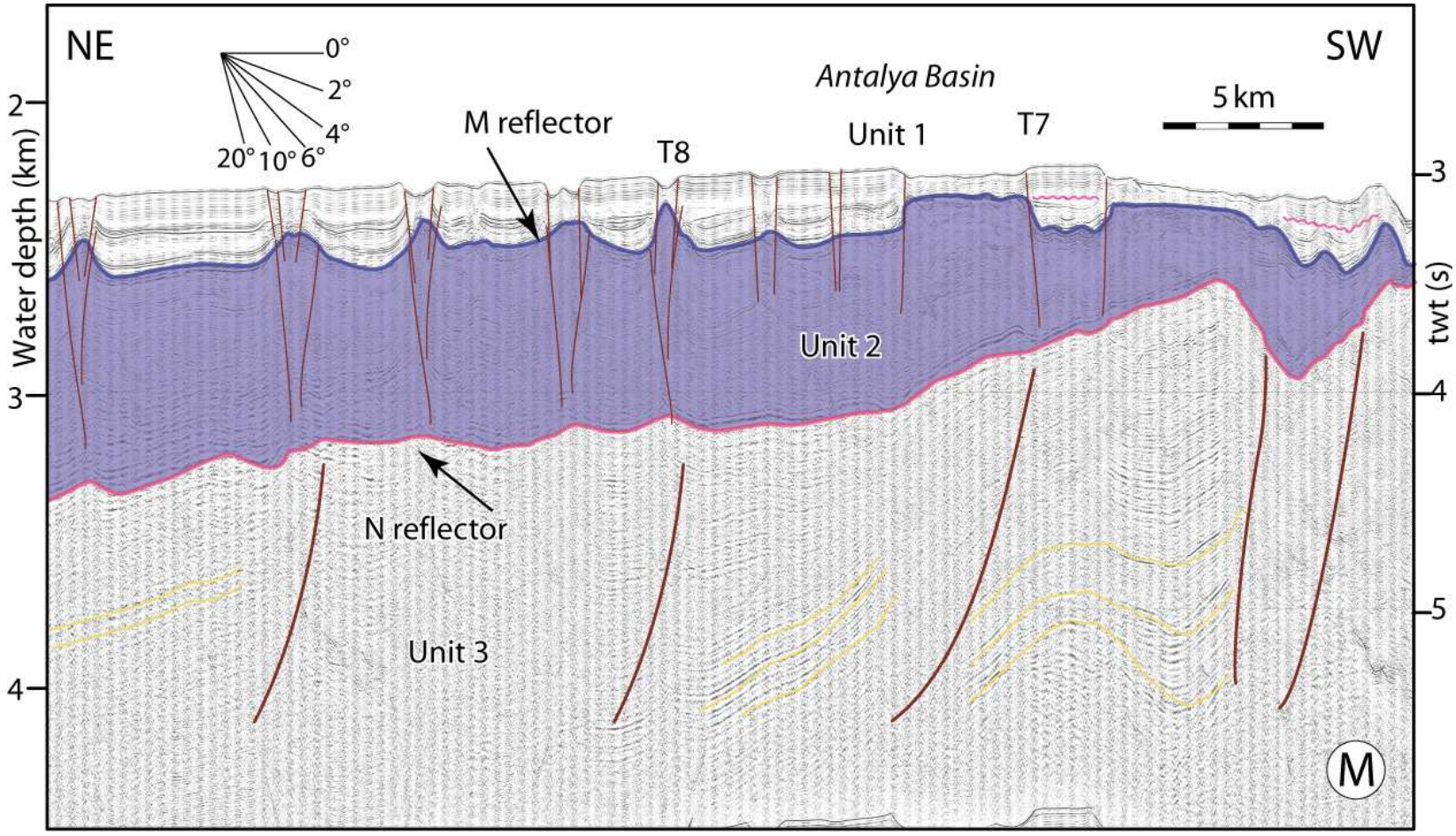

Figure 5.17: High-resolution multi-channel seismic reflection profile M showing architecture of the southern Antalya Basin, where numerous thrust faults ceased their active prior to the development of the unconformity delineated by the M-reflector. Note that the reflectors within the pre-Messinian Miocene succession of Unit 3 are disharmoniously structured relative to the M-reflector and the overlying Messinian successions of Unit 2. Location is shown in Figure 5.13. EMED10 (fix 1855-1885)

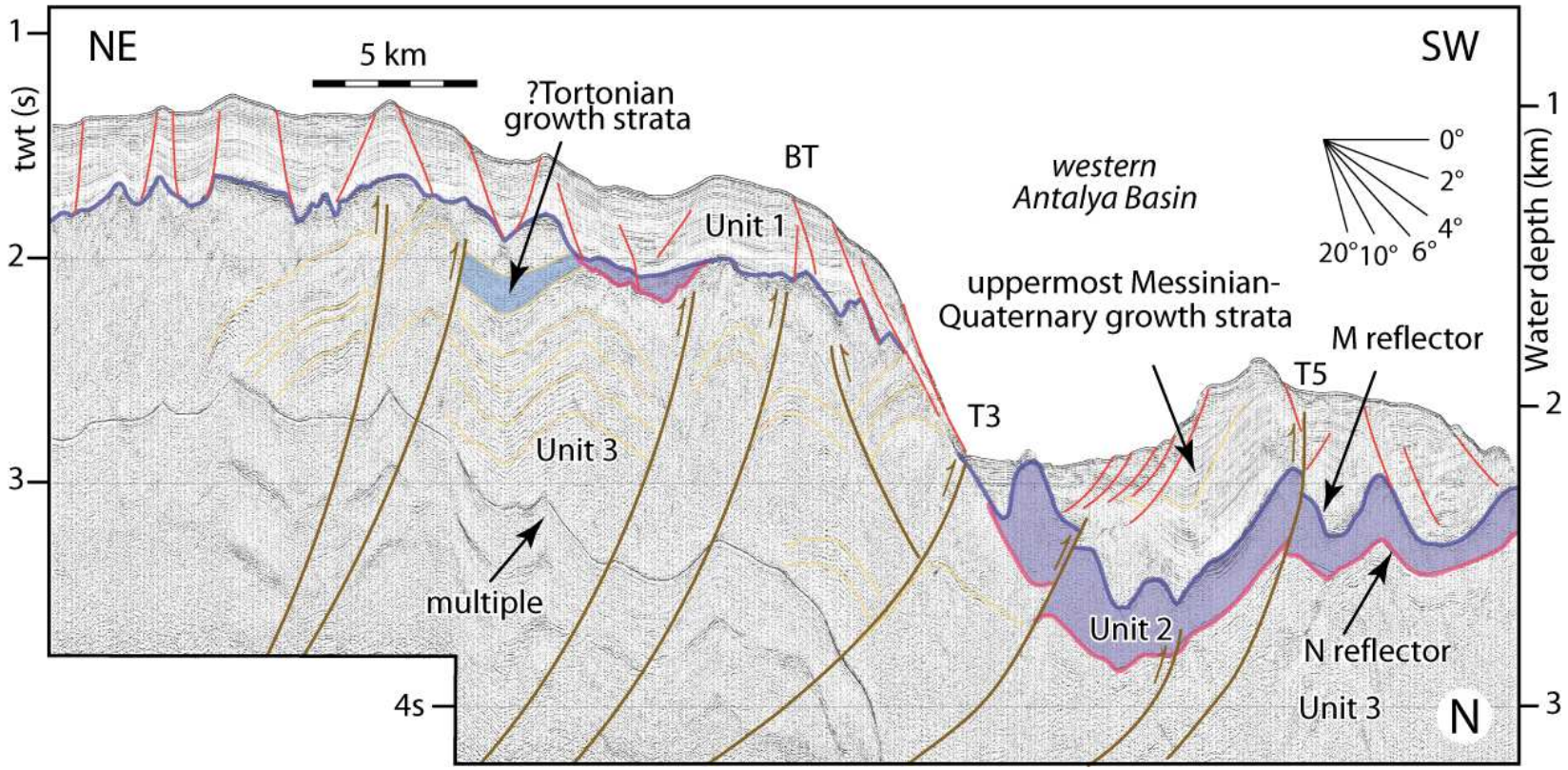

Figure 5.18: High-resolution multi-channel seismic reflection profile N showing architecture of the southern Antalya Basin, where numerous thrust faults ceased their active prior to the development of the unconformity delineated by the M-reflector. Note that the reflectors within the pre-Messinian Miocene succession of Unit 3 are disharmoniously structured relative to the M-reflector and the overlying Messinian successions of Unit 2. Location is shown in Figure 5.13. EMED01 (fix 1166-1198)

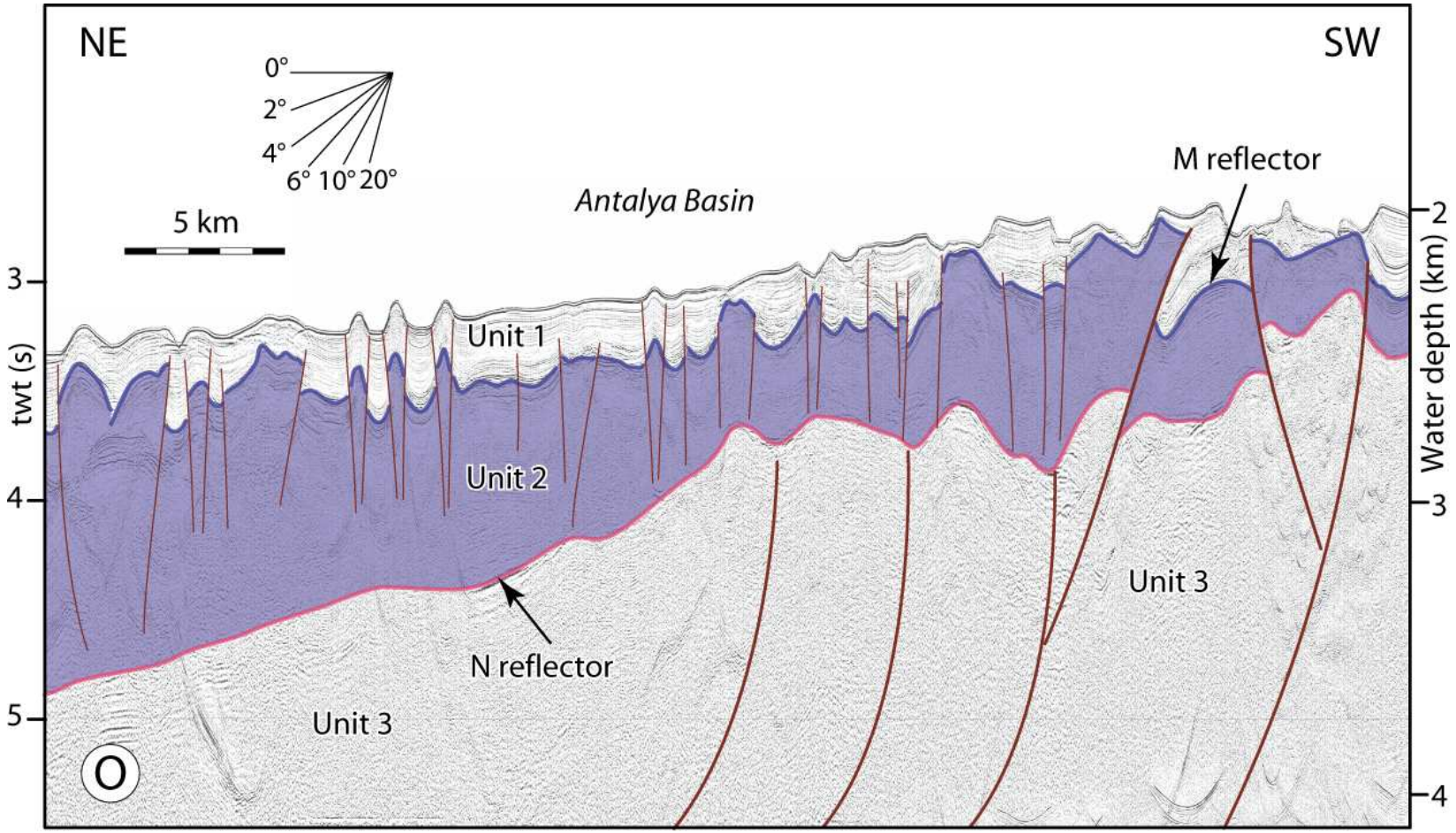

Figure 5.19: High-resolution multi-channel seismic reflection profile O showing architecture of the southern Antalya Basin, where numerous thrust faults ceased their active prior to the development of the unconformity delineated by the M-reflector. Note that the reflectors within the pre-Messinian Miocene succession of Unit 3 are disharmoniously structured relative to the M-reflector and the overlying Messinian successions of Unit 2. Location is shown in Figure 5.13. EMED10 (fix 1716-1748)

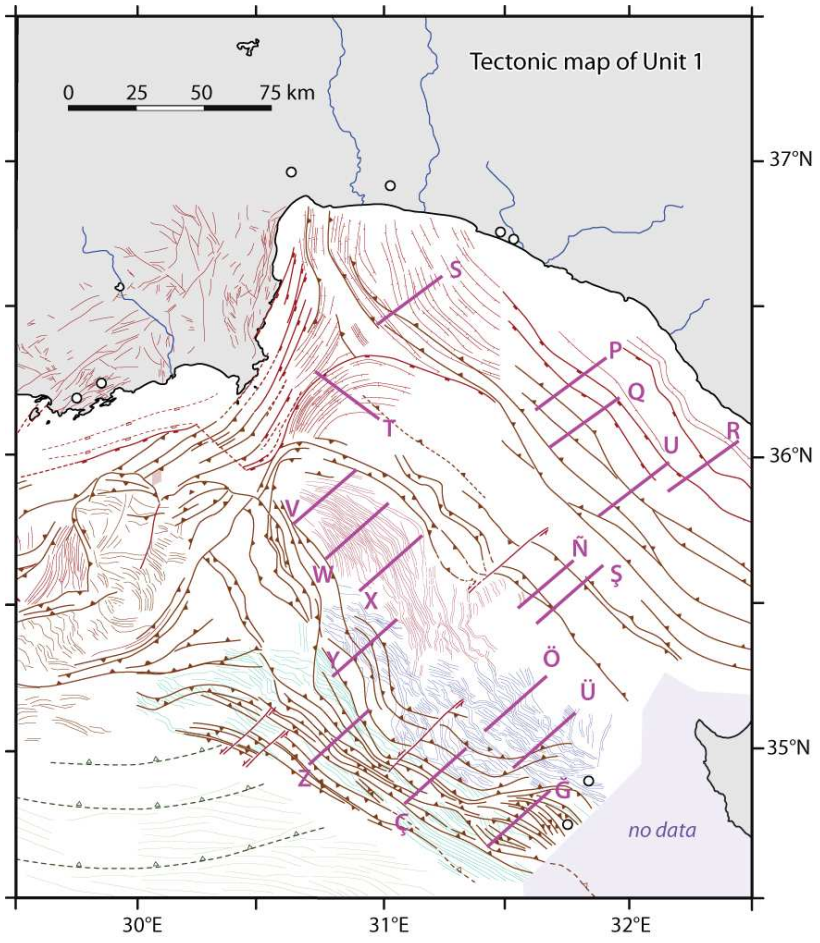

Figure 5.20: uppermost Messinian–Quaternary tectonic map of the Antalya Basin and Florence Rise showing the distribution of the major structures. Filled triangles are placed on the hanging walls of thrusts, while filled rectangles and small ticks are placed on the hanging walls of normal faults. Thin red lines are seafloor expressions of salt cored folds, thin aquamarine lines are the seafloor expressions of the inversion structures, thin blue lines are the seafloor expressions of the positive flower structures. Purple line segments are seismic reflection profiles illustrated in Figures 5.21–5.26, 5.28–5.30, 5.32–5.34, 5.36–5.41. Fault labels correspond to those illustrated in these seismic reflection profiles. White circles = exploration and DSDP boreholes. Black circles from A to E = Locations of the upper-most Messinian–Quaternary structural domains (see § 5.2.3 in the text). Structures of the Anaximander and Anaximenes mountains, the Sırrı Erinç Plateau, the Finike Basin and the northwestern sector of the Antalya Basin are from Barnes (2015), Aksu et al. (2009, 2014) and Hall et al. (2014a).

(A) Extensional domain

Across the northern and northeastern sectors of the Antalya Basin, the uppermost Messinian–Quaternary tectonic framework is characterized by a prominent family of broadly northwest-southeast striking and northeast- and southwest-dipping faults that display extensional separations (Fig. 5.20). Toward the northwest, these faults progressively swing to assume a mainly north-south strike. In eastern Antalya Basin, these faults display listric trajectories and sole in the evaporite successions of Unit 2 or extend into the pre-Messinian Miocene successions of Unit 3 (Figs. 5.21, 5.22). Prominent uppermost Messinian–Quaternary growth strata wedges developed on the hanging walls of the faults suggest that faulting occurred during sedimentation. Tip points of these faults are either within the uppermost portion of Unit 1 (e.g., Fig. 5.21) or occur on the seafloor, where they create prominent steps on the depositional surface (e.g., Fig. 5.22). High-resolution seismic reflection profiles also show the presence of several smaller extensional faults some forming near bedding-parallel detachments associated with prominent surface inflections fans, interpreted as slides, yet others are steeper and planar faults associated with halokinetic movements (Figs. 5.21, 5.22). These faults are also noted and mapped by previous workers in the area (e.g., Işler et al., 2005; King, 2014; Hall et al., 2014a).

Several faults in the upper portion of the continental slope show footwall–hanging wall geometries that are counter-intuitive with regards to normal faults (e.g., Fig. 5.23). In syn-sedimentary normal faulting the sediment thickness on the footwall is invariably thinner than that in the hanging wall, while post-sedimentary faulting shows no discernible thickness variations across the fault. However, in this example, the footwall block hosts thicker sedimentary accumulation than the hanging wall block (Fig. 5.23). This geometry strongly suggests that there exist strike slip displacements across these faults and that the footwall (or the hanging wall) is laterally transported to the site. Thus these faults are best described as having oblique slip. The possible strike slip component of these faults was also previously noted by Işler et al. (2005). Careful mapping of these faults with oblique

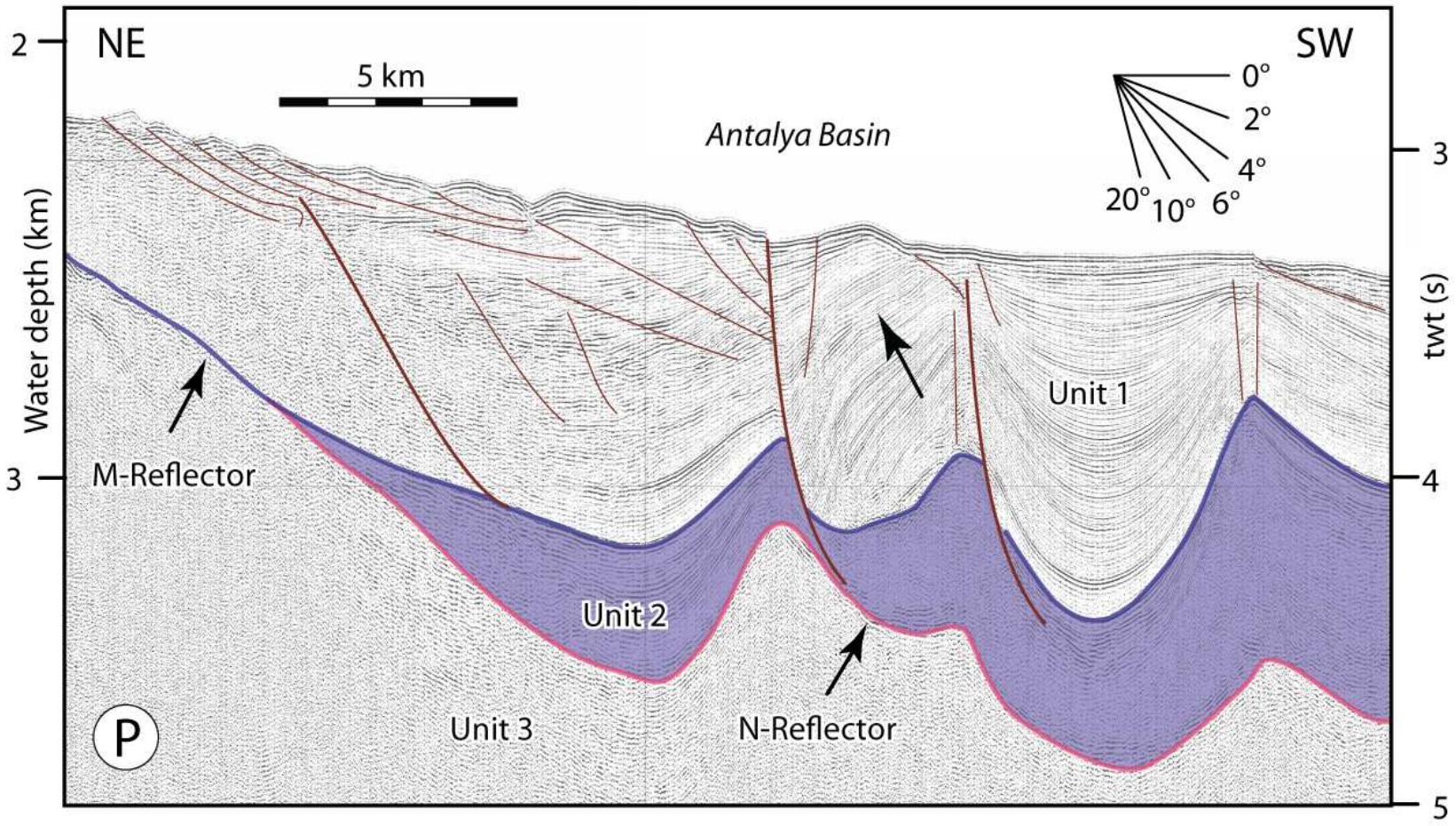

Figure 5.21: High-resolution multi-channel seismic reflection profile P showing the architecture of the northeastern Antalya Basin. Note the prominent listric extensional faults that developed within the uppermost Messinian–Quaternary successions of Unit 1. Further note the near bedding parallel detachments associated with surface slides. Location is shown in Figure 5.20. EMED01 (fix 490-510)

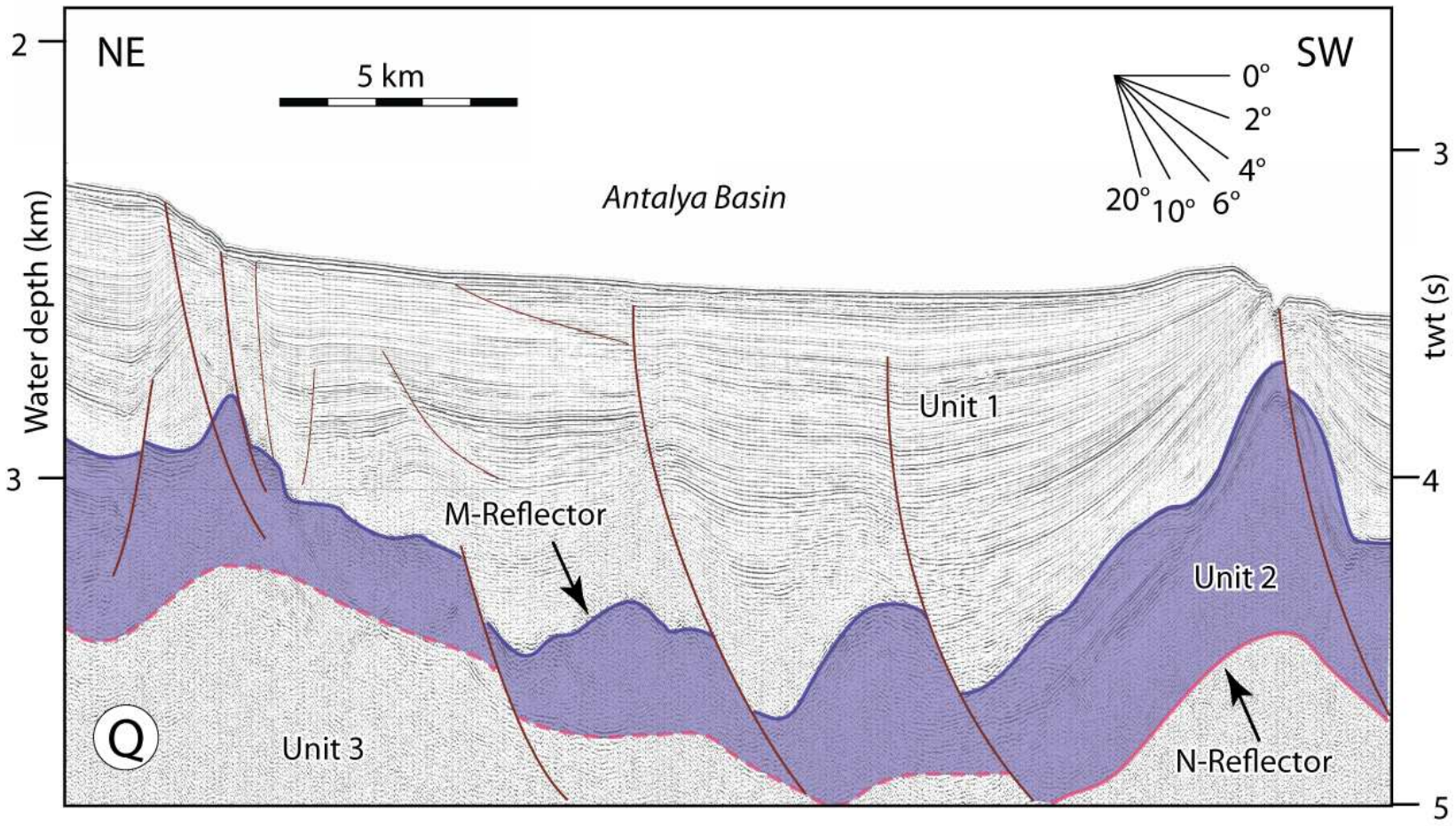

Figure 5.22: High-resolution multi-channel seismic reflection profile Q showing the architecture of the northeastern Antalya Basin. Note the prominent listric extensional faults that developed within the uppermost Messinian–Quaternary successions of Unit 1. Further note the near bedding parallel detachments associated with surface slides. Location is shown in Figure 5.20. Location is shown in Figure 5.13. EMED01 (fix 542-562)

slip shows that they are largely confined to the shallower northeastern sector of the Antalya Basin and that they are readily traced toward the land, possibly linking with the dextral strike slip Kırkkavak Fault and the dextral Aksu Fault zone (further discussed in Chapter 6).

Farther northwest, south and southwest of the oblique faults, the tectonic framework of the northwestern sector of the Antalya Basin is delineated by two prominent extensional fault systems (Fig. 5.20). In the east there is a prominent arcuate zone trending from northwest-southeast to mainly north-south which is characterized by numerous extensional faults that show southwest and northeast dips (e.g., Figs. 5.18, 5.24). The fault trajectories are often listric extending from the M-reflector to the depositional surface, where the faults create distinct steps. In cross sectional view, they resemble horst and graben (Fig. 5.18, 5.24). Many faults in this fan do not cut the M-reflector, but a few extend into the uppermost portion of the underlying Unit 3. This fault fan is also mapped by previous workers, including King (2014), Hall et al. (2014a), and Barnes (2015). Although all profiles are re-interpreted by the author, the fault traces in this area are taken from Barnes (2015) and Hall et al. (2014a).

A second prominent extensional fault system occurs across the western sector of the Antalya Basin (Fig. 5.25). This area is extensively studied by previous workers (e.g., Çınar 2014; King, 2014; Hall et al., 2014a; Barnes, 2015). The extensional fault system has two distinct fans: an inner shelf-edge fan is delineated by steeper and planar extensional faults that are developed along the western Antalya continental margin and a second outer fan which is characterized by listric extensional faults that occur within the deeper portion of the western Antalya Basin (Figs. 5.20, 5.25). The inner fan has a north-northeast – south-southwest strike, paralleling the Kemer Peninsula. Many of the faults extend into the coastline and define steep scarps onland (e.g., Çınar 2014; King, 2014; Hall et al., 2014a; Barnes, 2015). The outer fan has a distinctly northwest-convex arcuate shape. The master faults that control this convex shape can be readily mapped in the dense grid of seismic reflection profiles. Southeast of the master faults, the deep water region of the northwest Antalya Basin is

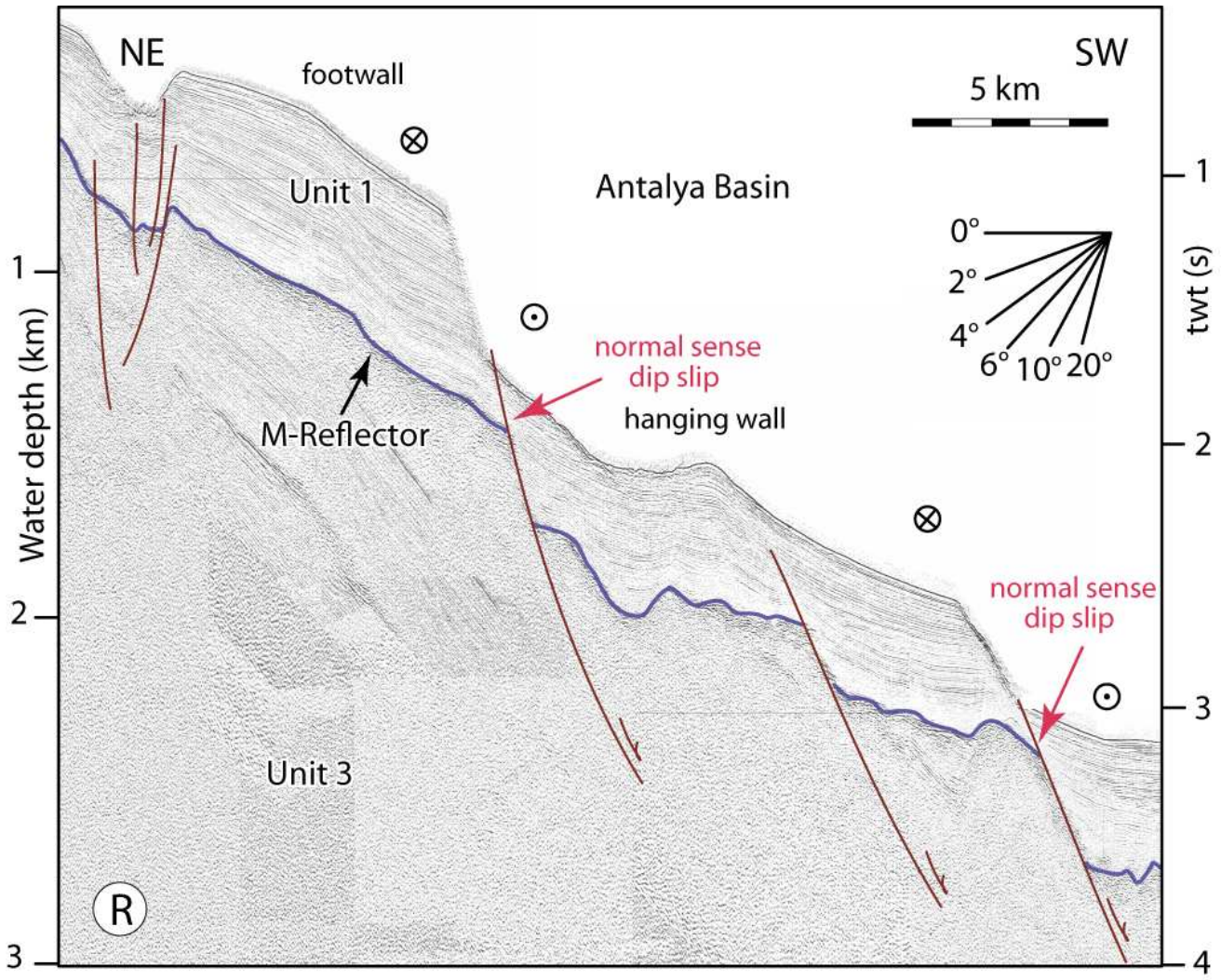

Figure 5.23: High-resolution multi-channel seismic reflection profile R showing the footwall and hanging wall geometries across several faults that cut the entire uppermost Messinian–Quaternary successions of Unit 1 across the upper slope region in northeastern Antalya Basin. Note that the sediments are thicker in the footwall block than they are in their hanging wall counterparts, suggesting the presence of strike slip component in these faults. The dextral sense for the strike slip is based on correlation of these faults with the onland Kırkkavak Fault and the Aksu Fault zone (§ Chapter 6). Location is shown in Figure 5.20. EMED01 (fix 1778-1798)

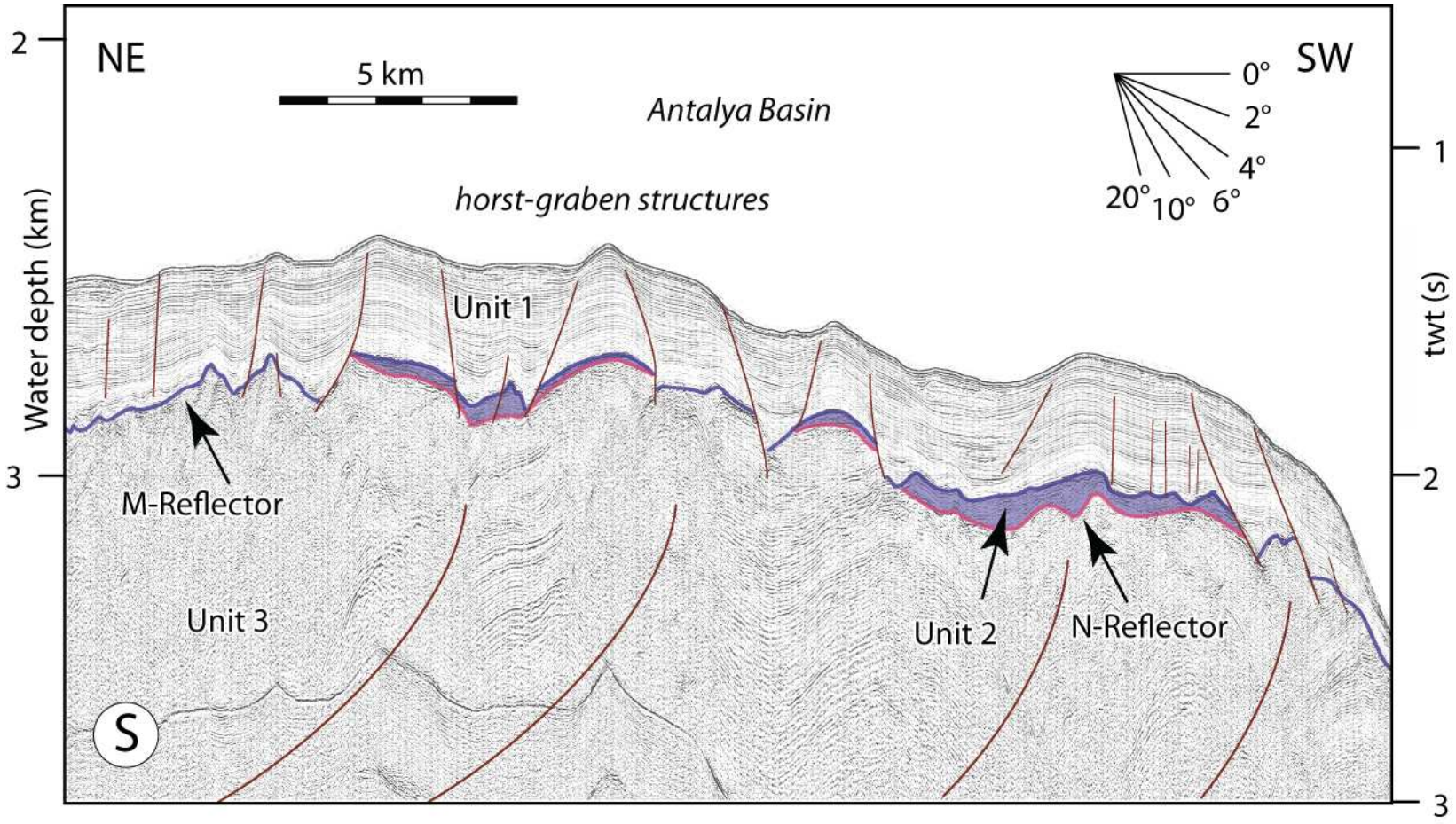

Figure 5.24: High-resolution multi-channel seismic reflection profile S showing architecture of the northwestern sector of the Antalya Basin. Note that numerous thrust faults ceased their active prior to the development of the unconformity delineated by the M-reflector. Further note that the reflectors within the pre-Messinian Miocene succession of Unit 3 are disharmoniously structured relative to the M-reflector and the overlying Messinian successions of Unit 2 and the uppermost Messinian–Quaternary successions of Unit 1. Location is shown in Figure 5.20. EMED92 (fix 1178-1198)

dominated by superficial extensional faults that often create bedding parallel detachments and/or faulting associated with halokinetic movements (e.g., Fig. 5.25).

(B) Contractional domain

The contractional domain is situated immediately southwest of the extensional domain and define a 25–50 km wide zone dominated by 6–9 prominent thrusts (Fig. 5.20). Their tip points may lie in the Messinian but the overlying ramp-antiforms deform the Pliocene-Quaternary succession, this confirms their young age. In the northern portion of the domain the thrusts have northwest-southeast strike and are invariably southwest verging (Figs. 5.20, 5.26). These thrusts can be readily mapped toward the northwest, where they progressively assume a north-south strike, similar to their pre-Messinian Miocene and Messinian counterparts. In this area, a prominent thrusts splays from the main thrust and extends westward into the extensional domain (Figs. 5.10, 5.20). However, in the southern portion of the domain, there are also 2–3 northeast verging thrusts. This domain, including the southern portion where oppositely-verging thrusts exist, has been identified in previous studies (e.g., Işler, 2003; Işler et al., 2005). These authors interpreted the domain as a transpressional zone between the extensional domain in the north and the Florence Rise in the south.

Compressional faults also occur across the westernmost portion of central Antalya Basin, immediately southeast of the Kemer Peninsula (Fig. 5.20; Çınar 2014; Aksu et al., 2014a). In this area, the uppermost Messinian–Quaternary structural architecture is characterised by 4–5 northeast-southwest striking and invariably northwest verging thrusts. These thrusts have tip points within the lower portion of Unit 1 (Çınar 2014; Aksu et al., 2014a).

(C) Halokinetic domain – salt cored folds

A prominent zone characterized by upright anticlines and their intervening synclines occur across the southwestern portion of the Antalya Basin, over the northeastern foothills of the Anaxagoras

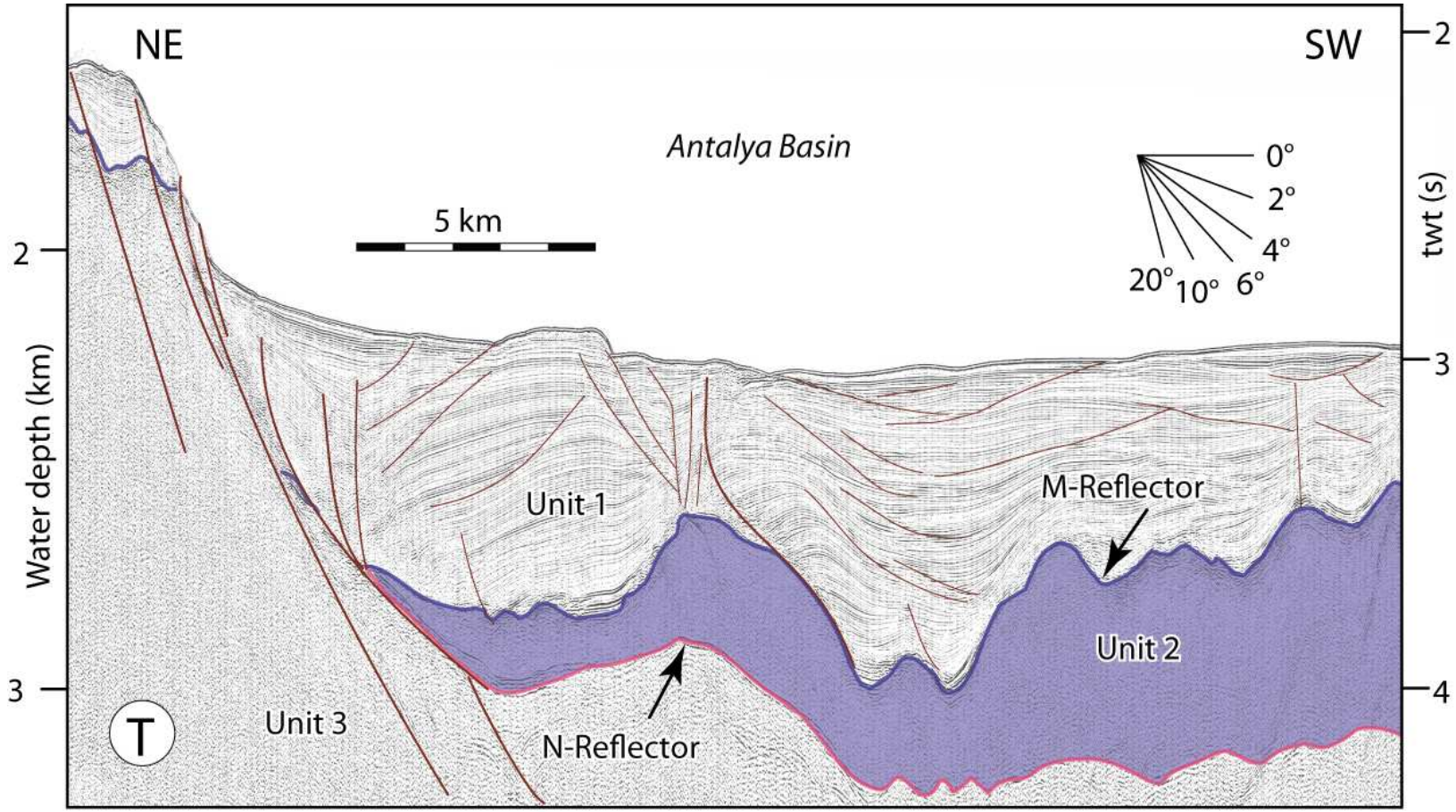

Figure 5.25: High-resolution multi-channel seismic reflection profile T showing architecture of the western sector of the Antalya Basin. Note that several listric normal faults define the tectonic architecture of the uppermost Messinian–Quaternary successions of Unit 1. Also note that numerous near bedding parallel detachments occur within Unit 1. Location is shown in Figure 5.20. EMED01 (fix 961-981)

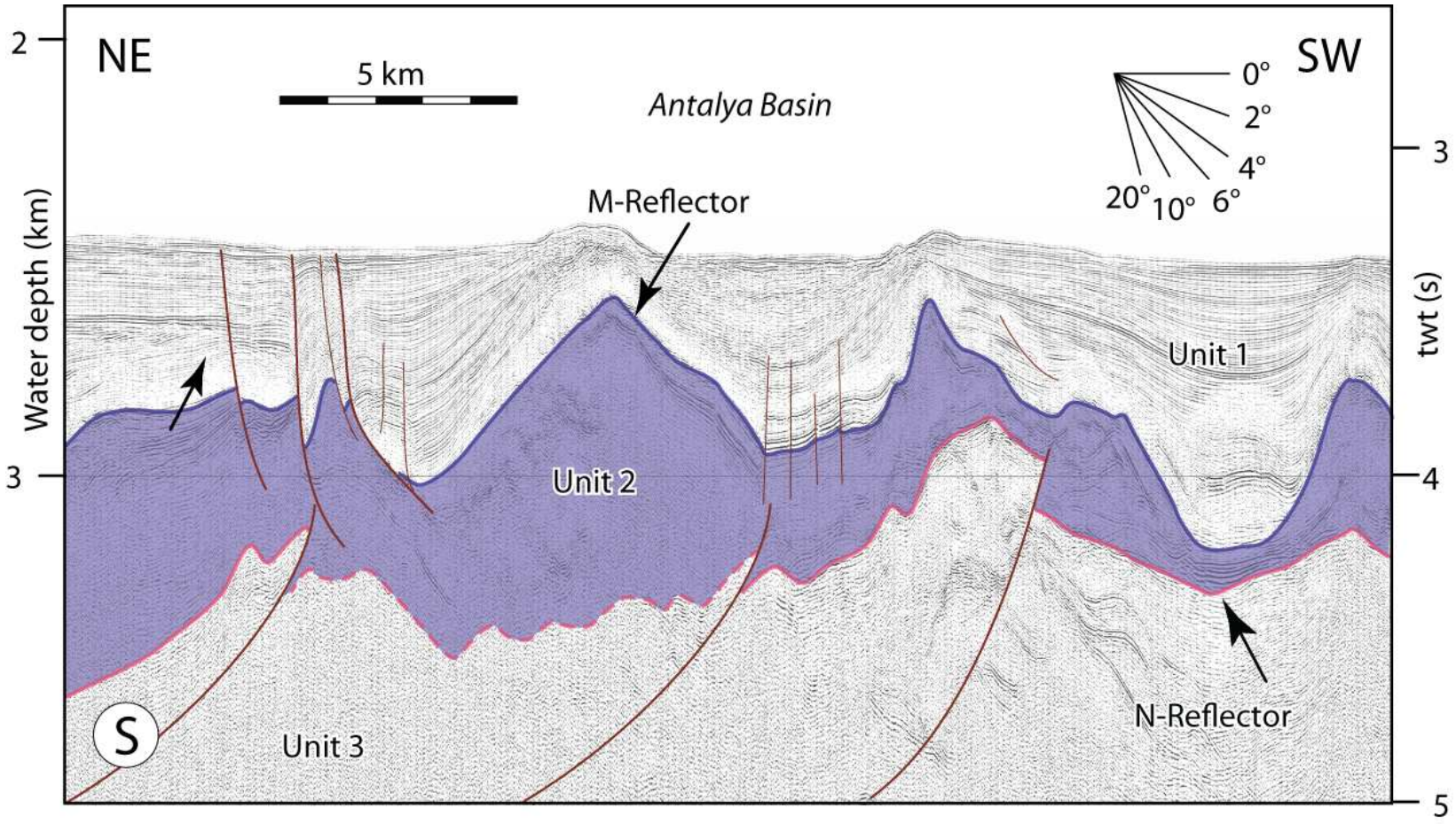

Figure 5.26: High-resolution multi-channel seismic reflection profile U showing architecture of the eastern sector of the Antalya Basin. Note that numerous thrust faults ceased their active prior to the development of the unconformity delineated by the M-reflector. Further note that the reflectors within the pre-Messinian Miocene succession of Unit 3 are disharmoniously structured relative to the M-reflector and the overlying Messinian successions of Unit 2 and the uppermost Messinian–Quaternary successions of Unit 1. Location is shown in Figure 5.20. EMED01 (fix 686-706)

Mountain (Fig. 5.20). In this area the seafloor is notably corrugated and includes several broadly northwest-southeast trending curvilinear ridges and troughs which exhibit moderate lateral continuity (Figs. 5.2, 5.27). Comparison between the multibeam mosaic and the high-resolution seismic reflection profiles shows that this seafloor morphology is the expression of the positive flower structures created by notably high-angle bi-vergent thrust faults that developed within the uppermost portion of the evaporite successions of Unit 2 and the entire uppermost Messinian–Quaternary successions of Unit 1 (Figs. 5.28–5.30). The M-reflector can be readily traced across the anticlines and synclines, which reveals that the core of the anticlines are penetrated by the evaporites. Similar structures in the eastern Mediterranean region have been named as "salt cored folds" (e.g., Aksu et al., 2005a,b, 2009, 2014a; Hall et al., 2005a,b).

(D) Prominent shear zone – basin inversions

This domain occurs along the crestal region of the Florence Rise and it is topographically notably elevated from the adjacent seafloor of the Antalya Basin in the north and the northern foothills of the Mediterranean Ridge in the south (Fig. 5.2). The detailed multibeam mosaic across the western segment of this zone shows a complex seafloor morphology, with prominent northwest-southeast elongated hills and similarly elongated depressions overprinted on the generally northwest-southeast trending seafloor lineations (Fig. 5.31). High-resolution seismic reflection profiles further illustrate this complexity (Figs. 5.32, 5.33). One of the most important features of the uppermost Messinian–Quaternary successions is the reciprocal relationship that the M-reflector exhibits with the seafloor: in regions where the M-reflector goes down, the seafloor goes up, and in regions where the M-reflector goes up, the seafloor goes down. This is further highlighted by the presence of a local mid-Unit 1 unconformity, which was never observed elsewhere in the Antalya Basin. When examined carefully it becomes apparent that Unit 1 reflectors below the local unconformity exhibit a concave upwards pattern, whereas in many instances those above the local unconformity exhibit

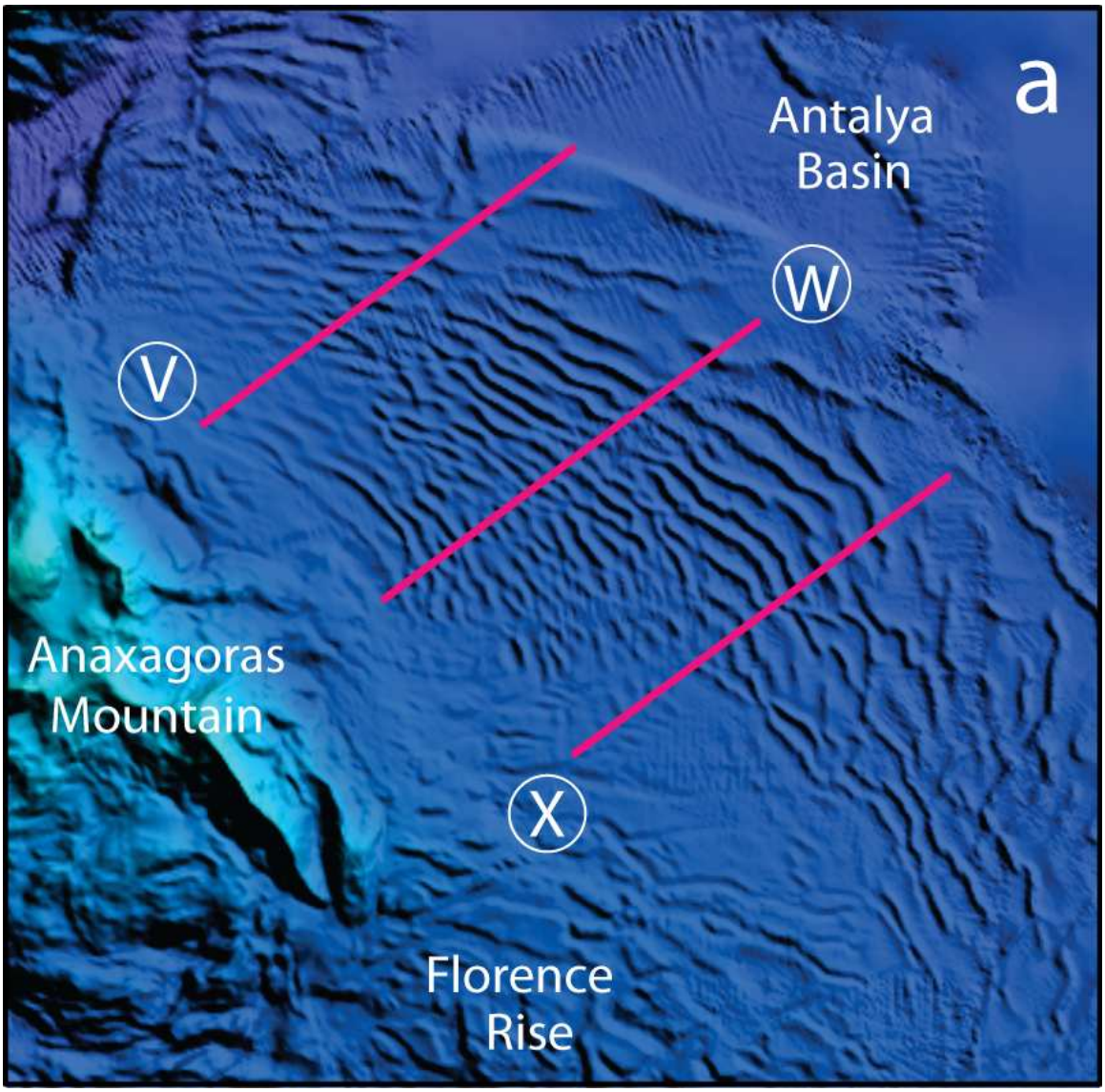

Figure 5.27: Multibeam bathymetry of the northwestern segment of the Florence Rise near the junction with the Anaxagoras Mountain. The multibeam bathymetry are from the 100 M–resolution ANAXIPROBE 95 data (Woodside, 1995) for the Anaximander Mountains and Rhodes Basin and the 500 M–resolution EMODnet (European Marine Observation and Data Network, Portal for Bathymetry, http://www.emodnet-hydrography.eu/) data for the southern Antalya Basin and Florence Rise. Location is shown in Figure 5.2.

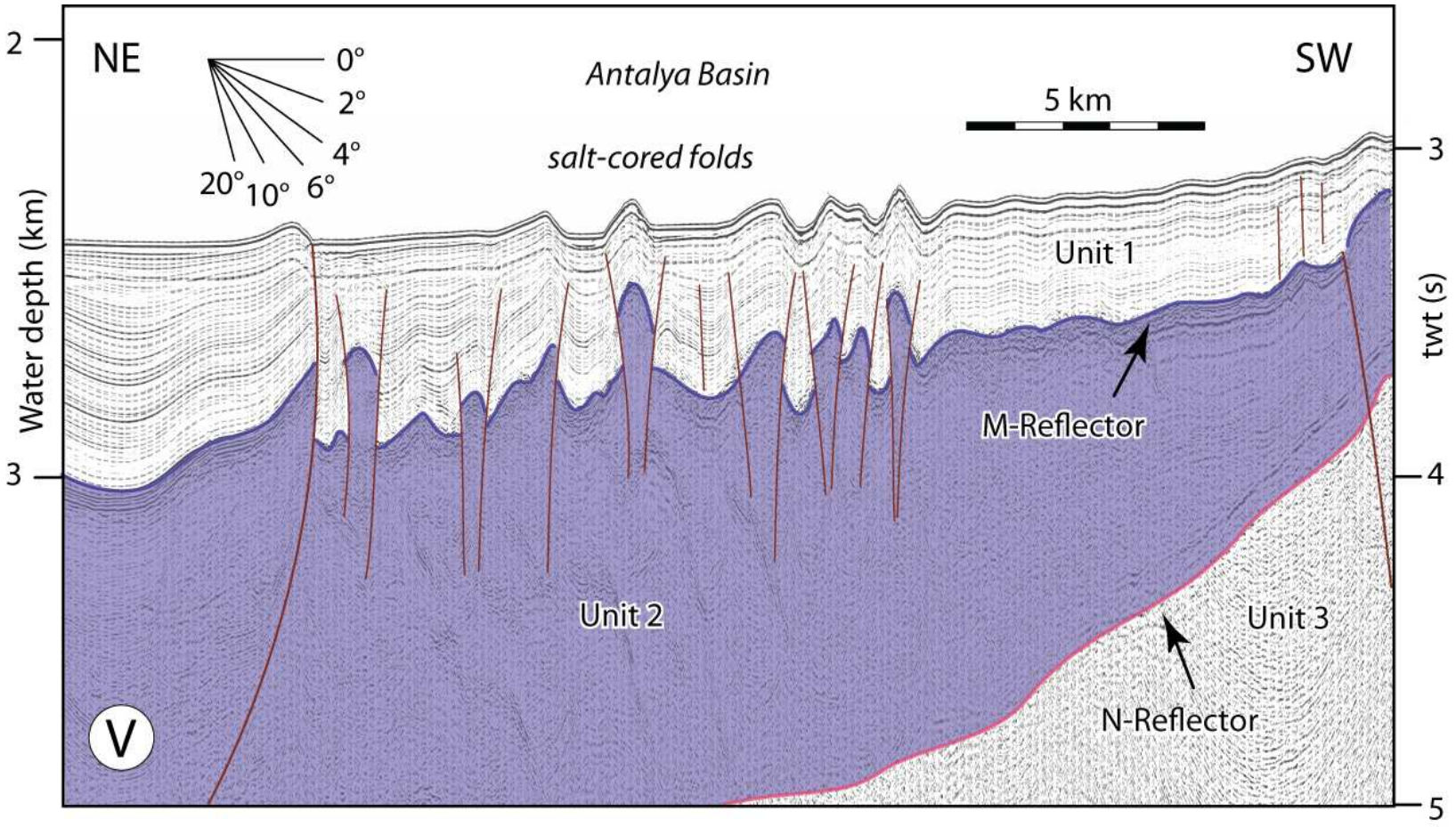

Figure 5.28: High-resolution multi-channel seismic reflection profile V showing architecture of the southwestern sector of the Antalya Basin. Note the occurrence of a thick Messinian evaporite succession (i.e., Unit 2) and the development of several upright anticlines and their intervening synclines within the uppermost Messinian–Quaternary successions of Unit 1. Further note that these anticline syncline pair are bounded by oppositely-verging thrust faults. Location is shown in Figure 5.20. EMED10 (fix 1282-1302)

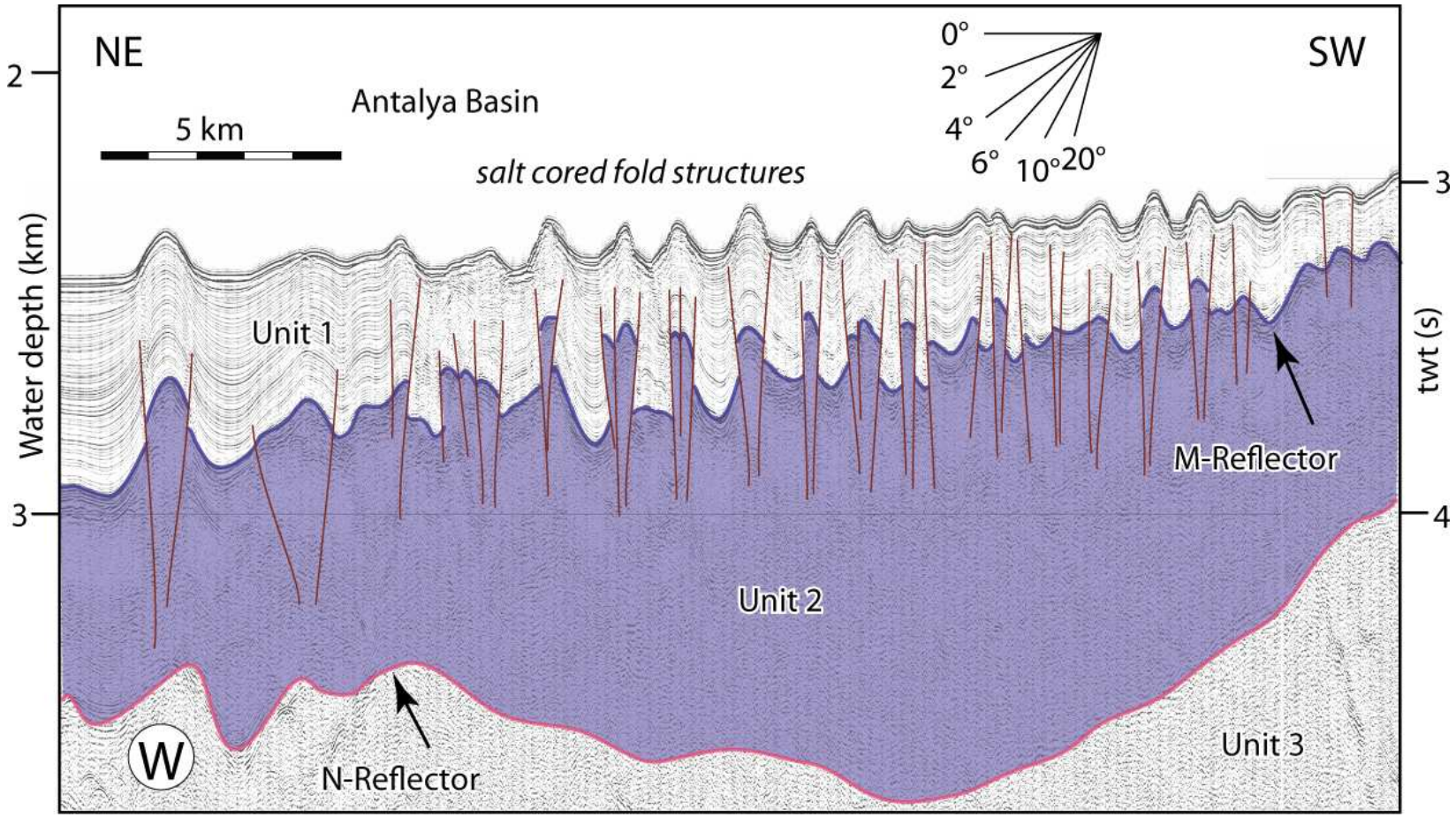

Figure 5.29: High-resolution multi-channel seismic reflection profile W showing architecture of the southwestern sector of the Antalya Basin. Note the occurrence of a thick Messinian evaporite succession (i.e., Unit 2) and the development of numerous upright anticlines and their intervening synclines within the uppermost Messinian–Quaternary successions of Unit 1. Further note that these anticline syncline pair are bounded by oppositely-verging thrust faults. Location is shown in Figure 5.20. EMED10 (fix 1501-1521)

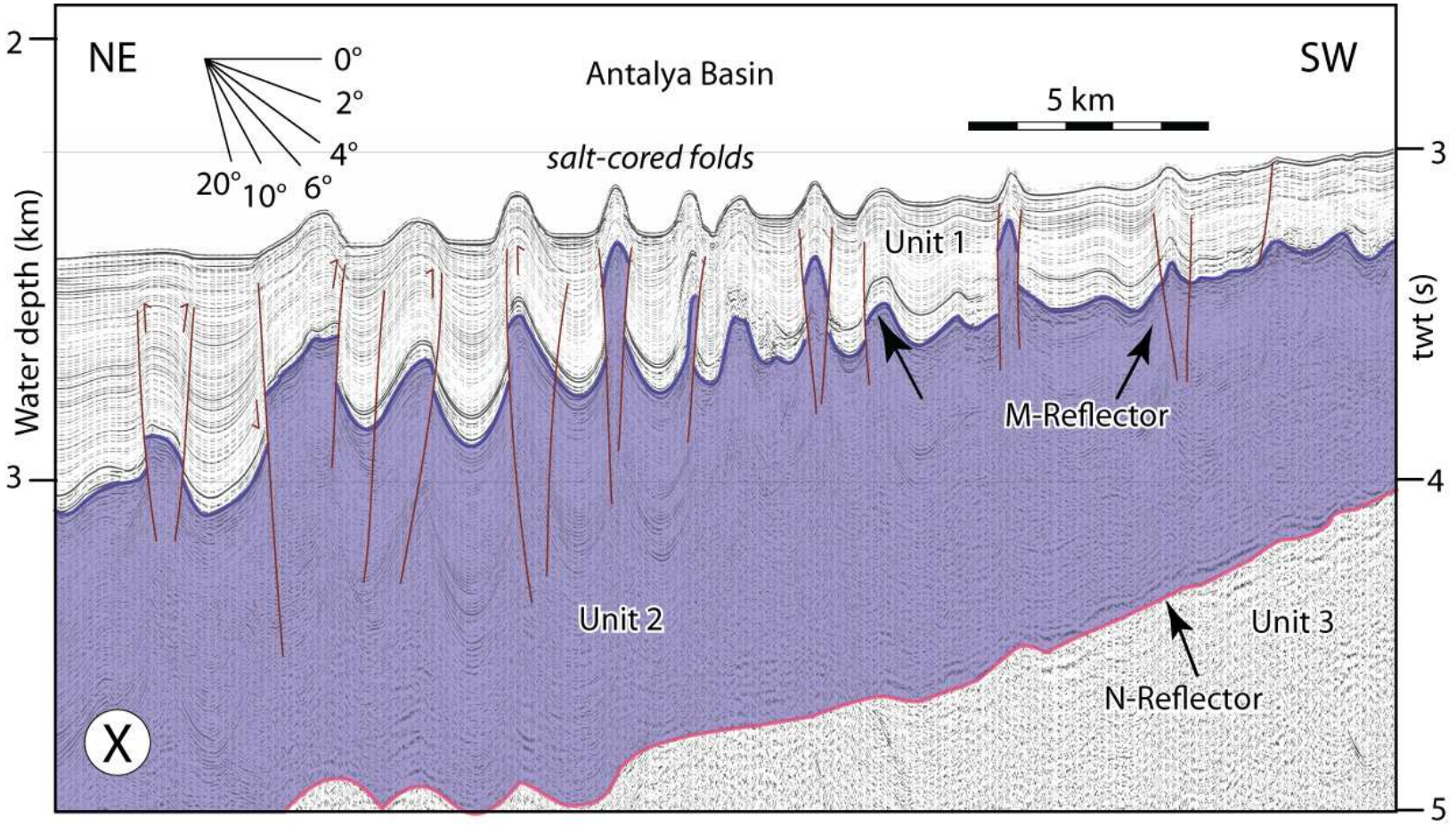

Figure 5.30: High-resolution multi-channel seismic reflection profile X showing architecture of the southwestern sector of the Antalya Basin. Note the occurrence of a thick Messinian evaporite succession (i.e., Unit 2) and the development of several upright anticlines and their intervening synclines within the uppermost Messinian–Quaternary successions of Unit 1. Further note that these anticline syncline pair are bounded by oppositely-verging thrust faults. Location is shown in Figure 5.20. EMED10 (fix 1355-1375)

a convex upwards pattern (Figs. 5.33, 5.34). A nearly identical seismic stratigraphic architecture was described from the Outer Latakia Basin to the east of Cyprus, where the reciprocity of the M-reflector and the seafloor as well as the development of the mid-Unit 1 unconformity were explained by a phase of basin inversion during the middle portion of the Pliocene–Quaternary (Hall et al., 2005a).

Another very notable feature of the central segment of the Florence Rise is the presence of a very prominent positive flower structure (Figs. 5.33, 5.34). The structure is bounded by 1–2 northwest-southeast striking and southwest verging thrust faults, complemented by 1–2 similarly striking but northeast verging thrust faults. Within the central portion of the structure the uppermost Messinian–Quaternary successions of Unit 1 range between 900 ms and 1400 ms, yet the crestal region of the structure stands 300–500 ms above the adjacent seafloor (Figs. 5.33, 5.34). Similar to the geometry described above, Unit 1 exhibits a concave architecture below the mid-Unit 1 unconformity, but a convex architecture above the local unconformity. This geometry clearly documents that there was an uppermost Messinian–Quaternary basin in the general region of the present-day crest of the Florence Rise, but this basin became dramatically inverted sometime during the Quaternary.

Across the northern foothills of the Florence Rise, the seafloor exhibits a "cracked" appearance with notably sinuous and predominantly northwest-southeast trending troughs merge and diverge, similar to an anastomosing pattern (Fig. 5.35). In high-resolution seismic reflection profiles the irregular ridges and troughs appear to be bounded by vertical discontinuities (Figs. 5.36, 5.37). The reciprocal relationship between the seafloor and the M-reflector observed in the large inversion structures are similarly observed in these smaller structures. The uppermost Messinian–Quaternary successions of Unit 1 also exhibit the mid-Unit 1 unconformity. On the basis of the similarities of their internal architecture with the previously described inversion structures, these are interpreted to develop as the inversion-related deformation (e.g., Hall et al., 2005a). However, the seismic architecture of some of these inversion structures also resemble the fluid escape structures, the associated mud

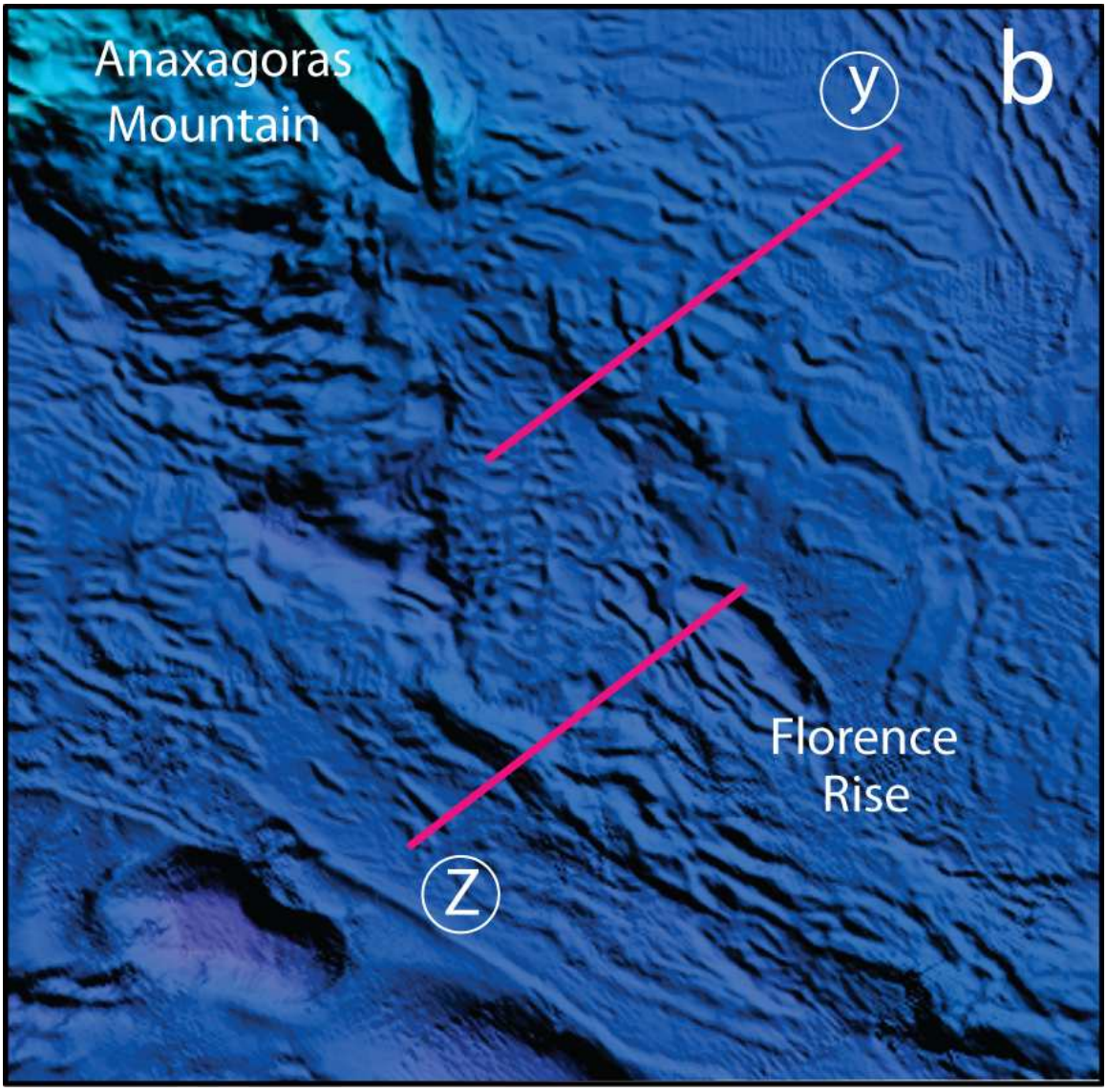

Figure 5.31: Multibeam bathymetry of the central segment of the Florence Rise. The multibeam bathymetry are from the 100 M–resolution ANAXIPROBE 95 data (Woodside, 1995) for the Anaximander Mountains and Rhodes Basin and the 500 M–resolution EMODnet (European Marine Observation and Data Network, Portal for Bathymetry, http://www.emodnet-hydrography.eu/) data for the southern Antalya Basin and Florence Rise. Location is shown in Figure 5.2.

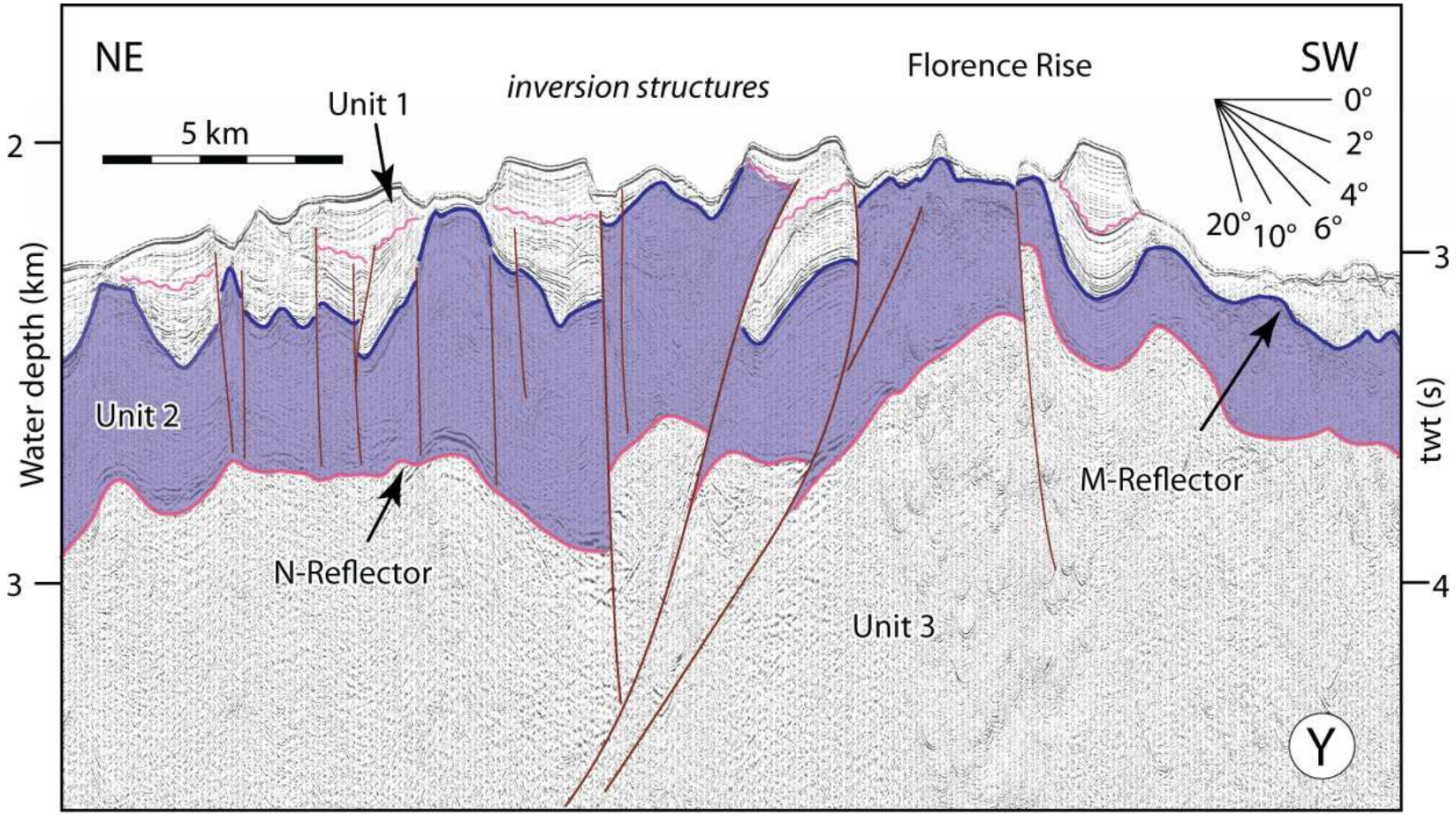

Figure 5.32: High-resolution multi-channel seismic reflection profile Y showing the complexly faulted and folded structural architecture of the western sector of the Florence Rise. Note the occurrence of a mid-Unit 1 unconformity. Further note the occurrence of a centrally located deeply seated positive flower structure. Location is shown in Figure 5.20. EMED10 (fix 1713-1733)

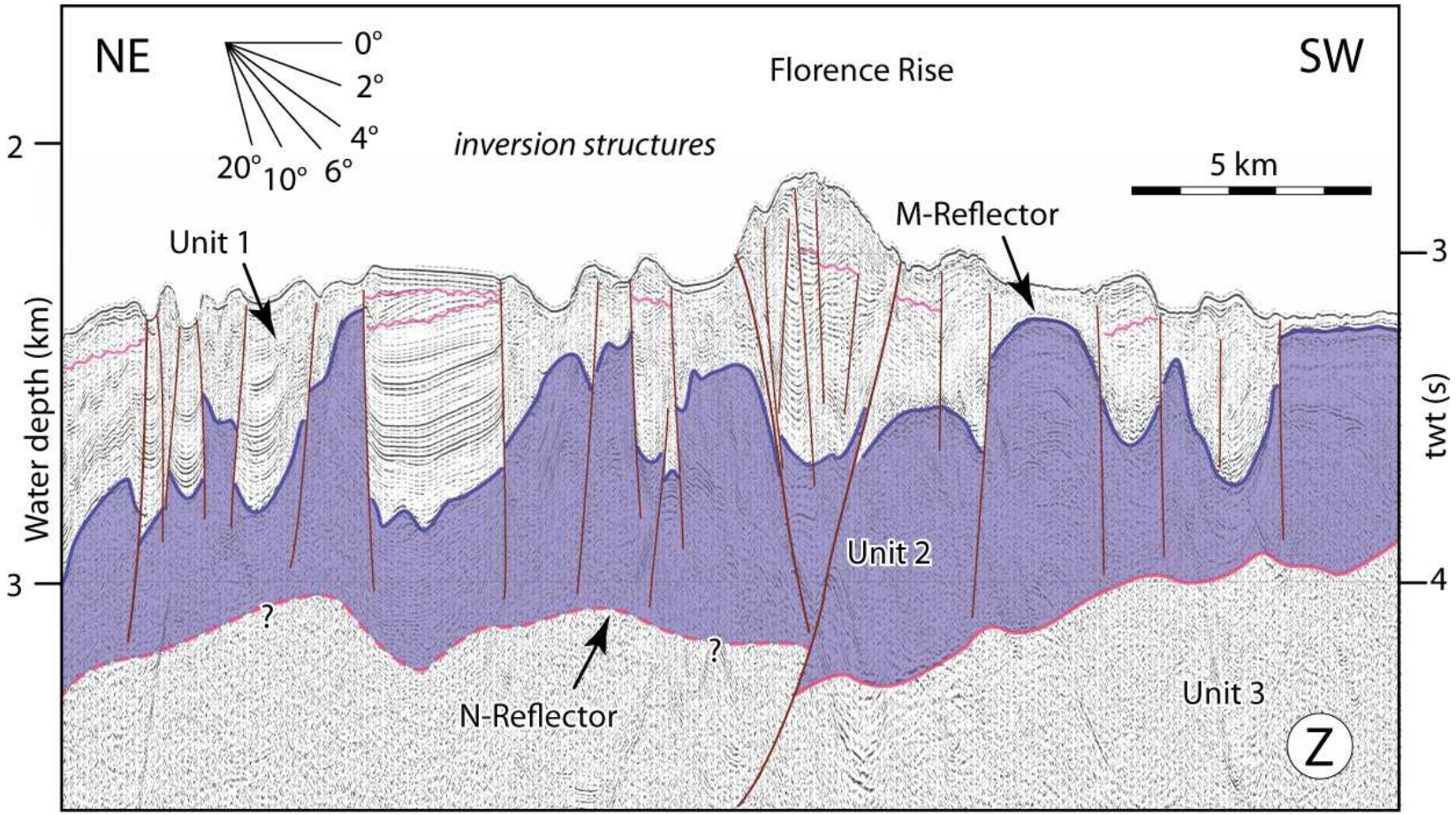

Figure 5.33: High-resolution multi-channel seismic reflection profile Z showing the complexly faulted and folded structural architecture of the western sector of the Florence Rise. Note the occurrence of a mid-Unit 1 unconformity. Further note the occurrence of a centrally located deeply seated positive flower structure. Location is shown in Figure 5.20. EMED10 (fix 1642-1662)

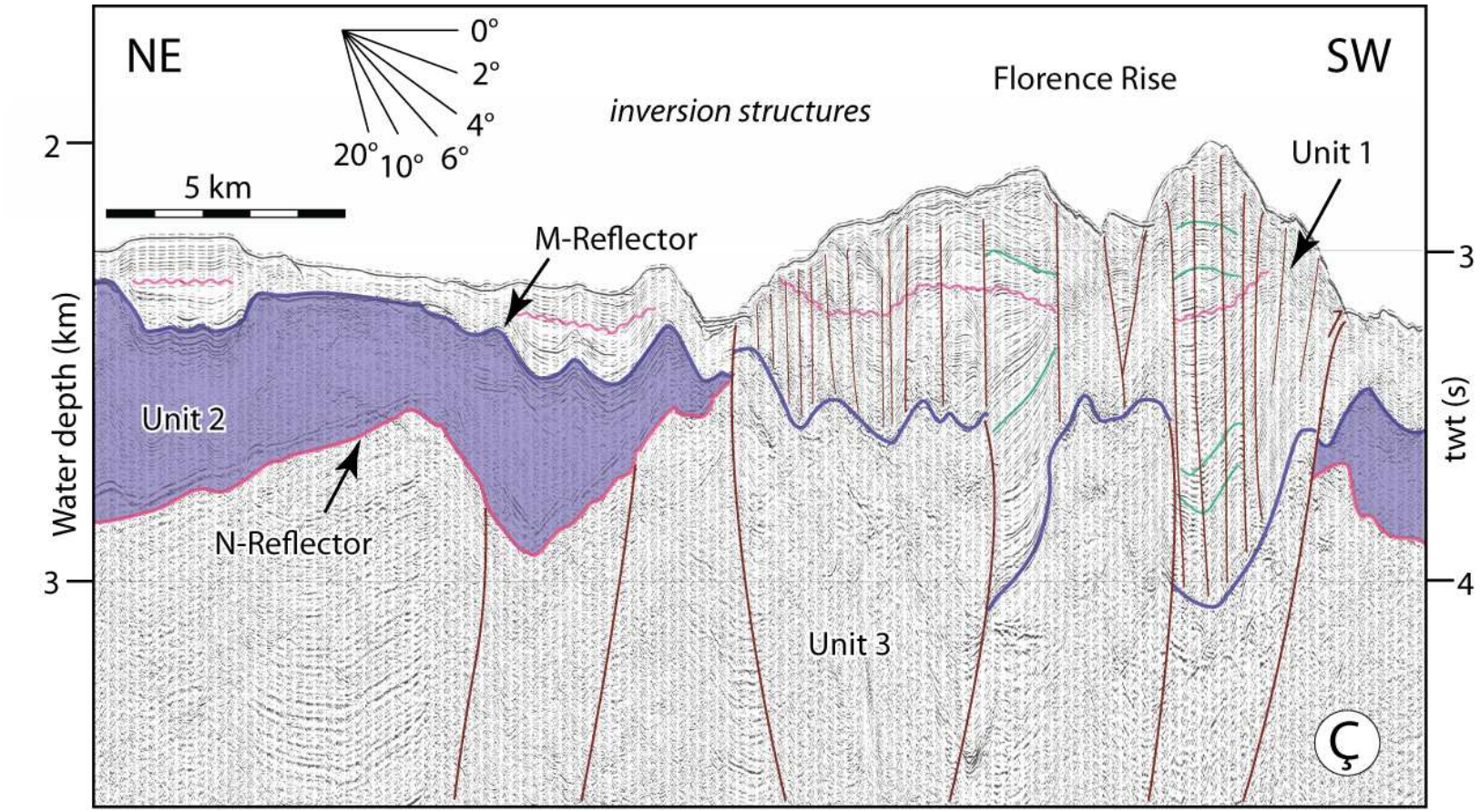

Figure 5.34: High-resolution multi-channel seismic reflection profile Ç showing the complexly faulted and folded structural architecture of the western sector of the Florence Rise. Note the occurrence of a mid-Unit 1 unconformity. Further note the occurrence of a centrally located deeply seated positive flower structure. Location is shown in Figure 5.20. EMED10 (fix 1875-1895)

diapirism and salt dissolution-related structures (see Mascle et al. 2014 for a review). These studies documented that fluid escape structures are often represented by notably narrow near vertical acoustically transparent zones in seismic reflection profiles (Hübscher and Dümmong, 2011; Mascle et al., 2014). This acoustic character is similar to what is observed in some structures across the Florence Rise (Figs. 5.37, 5.38). In the multibeam mosaic images of the seafloor the fluid escape vents are almost always represented by circular to near circular seafloor morphologies (Loncke et al., 2004), even so when the venting occurs along discrete faults (e.g., Flood et al., 2009). However, there are also incidences where circular structures are replaced by near linear seafloor expressions (Lofi et al., 2011b). The strong acoustic similarities between the previously-reported fluid escape structures and the associated mud venting and diapirism (Woodside et al., 2002) and those imaged in the seismic reflection profiles from the Florence Rise sector of the study area (e.g., Figs. 5.37, 5.38) suggest that some of the inversion-related structures may also involve varying amounts of fluid escape and mud diapirism. Fluids are present in underconsolidated sediments beneath and within Unit 2, arising from the conversion of gypsum to anhydrite and/or as an expulsion product of the intercalated siliciclastics during the early diagenesis. These fluids escape from beneath and within mobile Unit 2 and create mud volcanoes or dissolution craters. For example, the prominent diapir-like structures imaged in the seismic reflection profiles are developed within the lower sub-units 2d and 2c of the Messinian evaporite successions (Fig. 5.38). The notably acoustically stratified seismic facies define the core of these diapirs. However, beneath these structures the N-reflector is nearly flat and is disharmoniously folded relative to the core of the diapirs, suggesting that the siliciclastic-rich evaporites of the lower two sub-units became mobilized during the uppermost Messinian–Quaternary.

Across the southeastern sector of the Florence Rise a major mud volcano is identified in previous studies (Woodside et al., 2002). This structure, known as Texel mud volcano and it feeder channel across the pre-Messinian Miocene successions of Unit 3 are clearly imaged in the industry seismic reflection profiles (Fig. 5.8). However, high-resolution multichannel seismic reflection profiles fur-

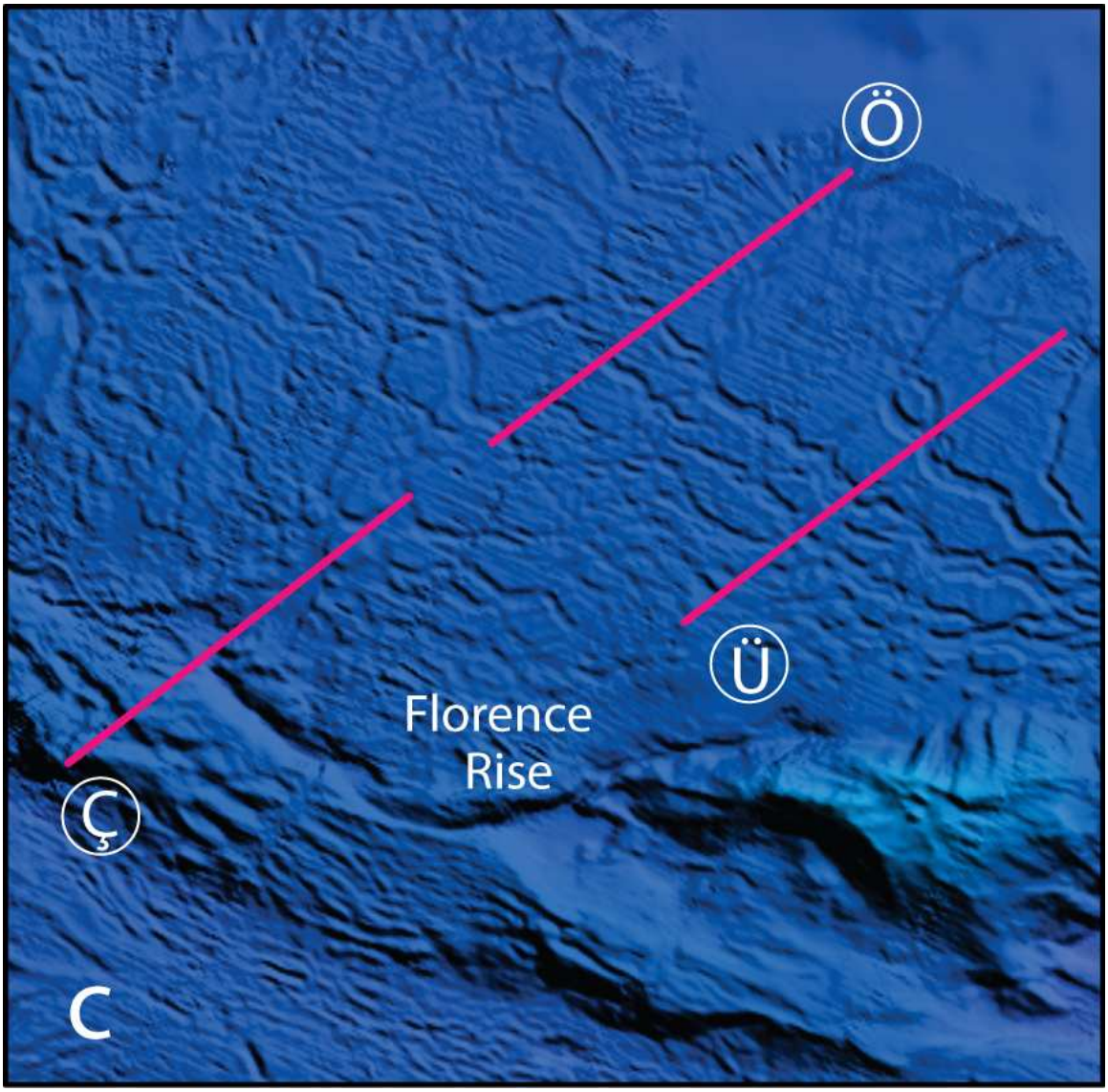

Figure 5.35: Multibeam bathymetry of the eastern segment of the Florence Rise. The multibeam bathymetry are from the 100 M–resolution ANAXIPROBE 95 data (Woodside, 1995) for the Anaximander Mountains and Rhodes Basin and the 500 M–resolution EMODnet (European Marine Observation and Data Network, Portal for Bathymetry, http://www.emodnet-hydrography.eu/) data for the southern Antalya Basin and Florence Rise. Location is shown in Figure 5.2.

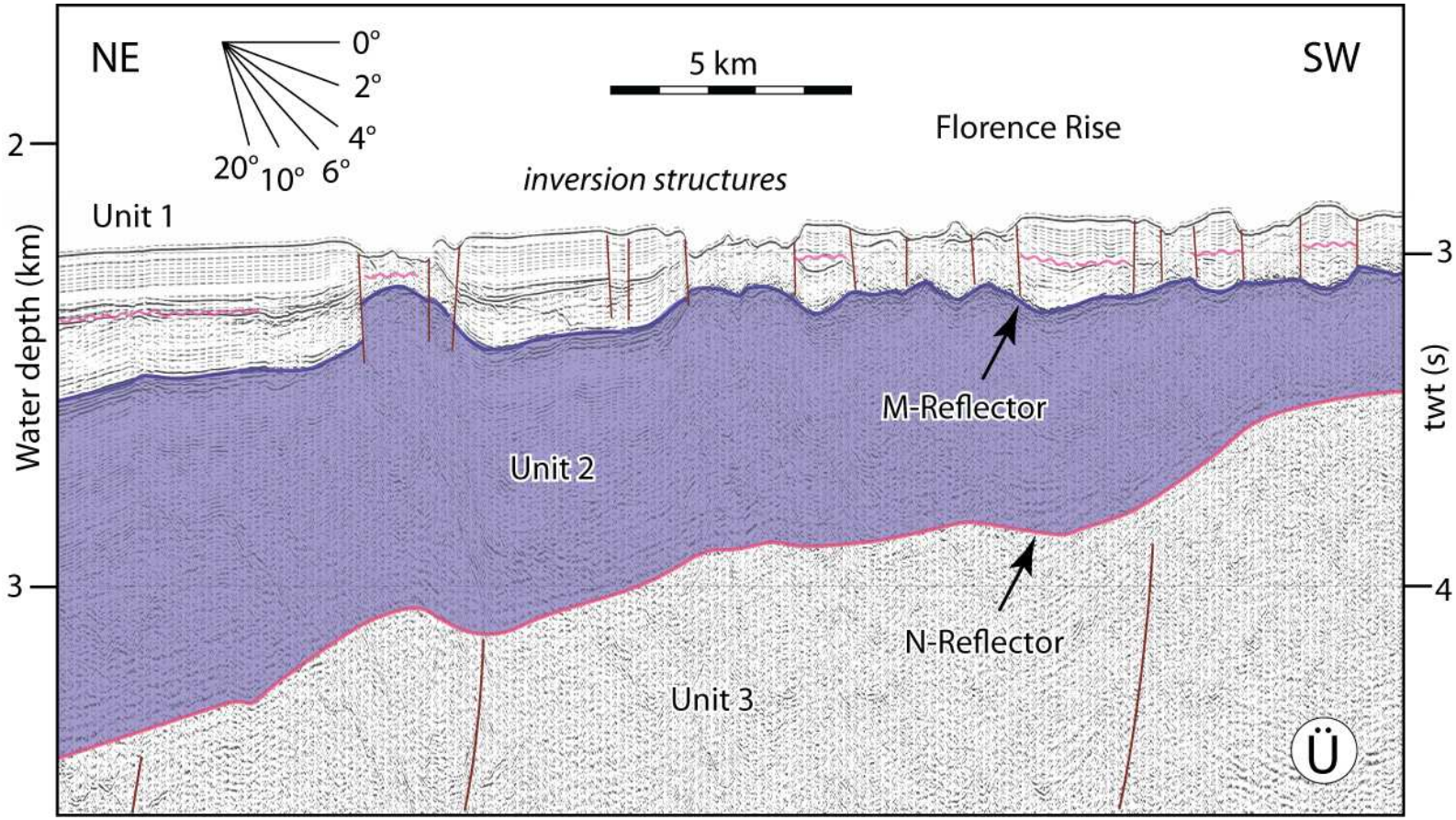

Figure 5.36: High-resolution multi-channel seismic reflection profile Ü showing the development of small-scale inversion structures along the northern foothills of the Florence Rise. Note the occurrence of a mid-Unit 1 unconformity. Location is shown in Figure 5.20. EMED10 (fix 2122-2142)

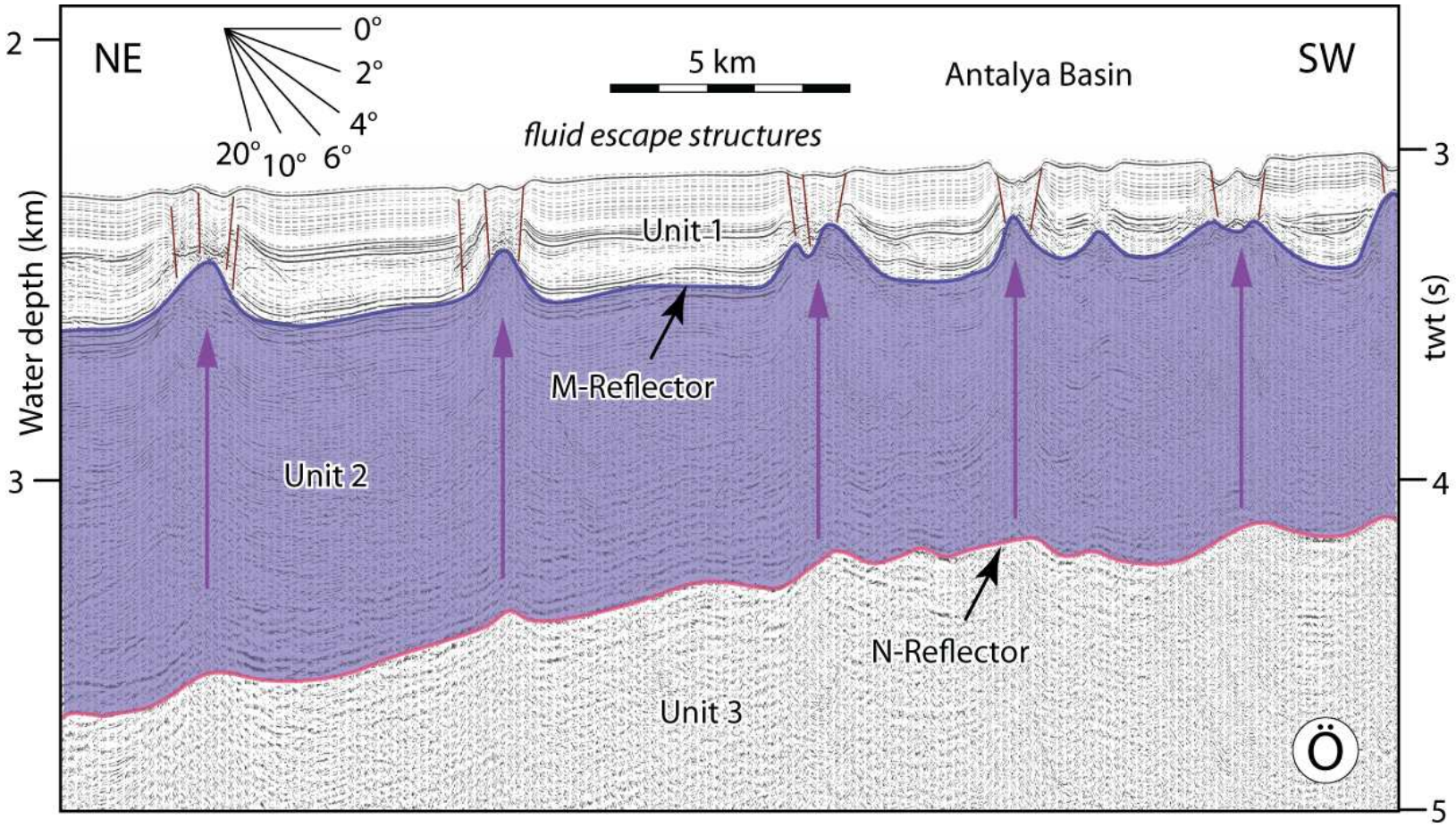

Figure 5.37: High-resolution multi-channel seismic reflection profile Ö showing the development of small-scale inversion structures along the northern foothills of the Florence Rise. Note the occurrence of a mid-Unit 1 unconformity. Location is shown in Figure 5.20. EMED10 (fix 1849-1869)

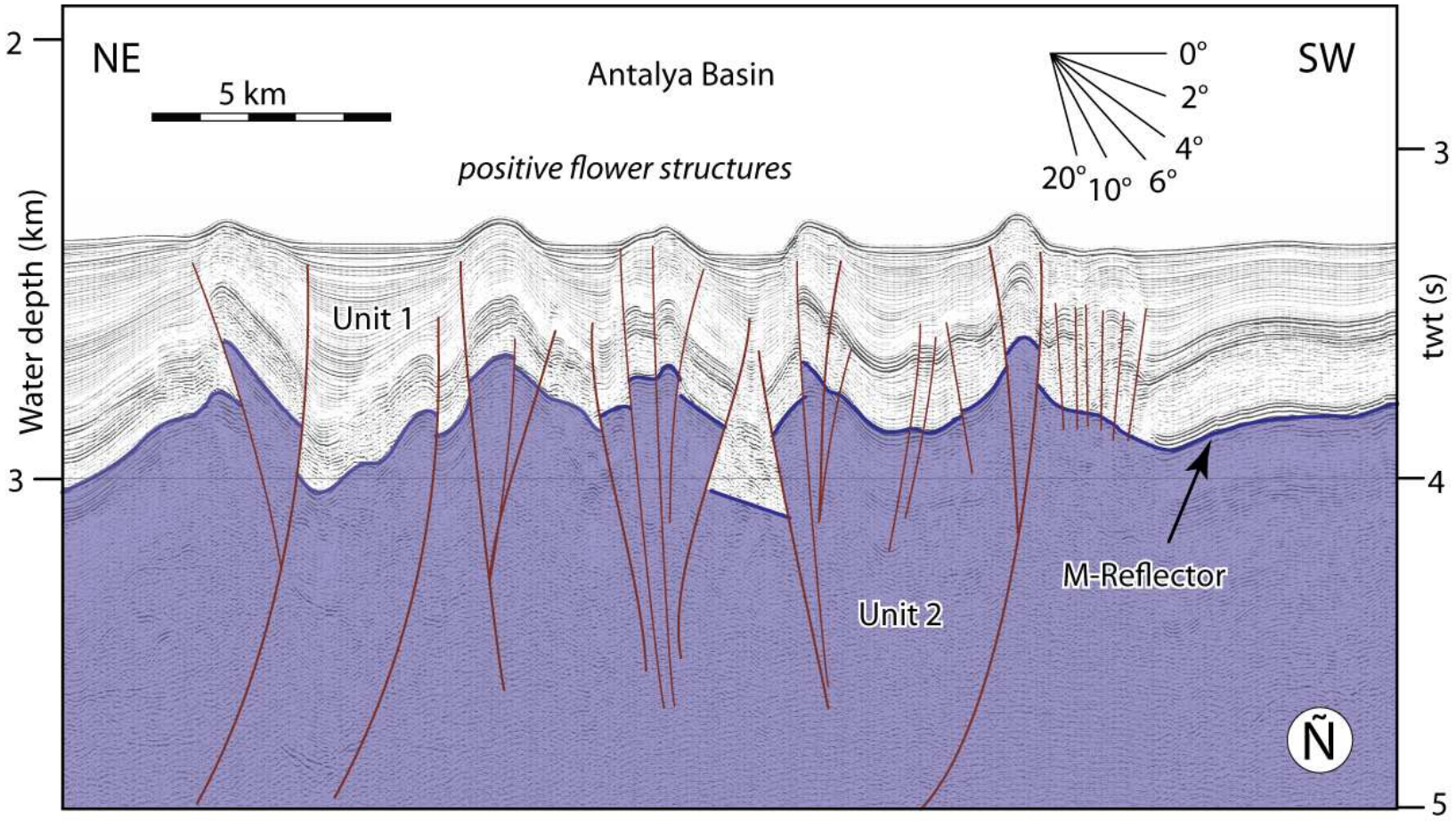

Figure 5.38: High-resolution multi-channel seismic reflection profile Ñ showing the development of small-scale inversion structures along the northern foothills of the Florence Rise. Note the occurrence of a mid-Unit 1 unconformity. Location is shown in Figure 5.20. EMED07 (fix 636-656)

ther illustrate that the core of this structure is also extensively cut by several bi-vergent thrust faults (Figs. 5.20, 5.39).

(E) Positive flower structures

Farther to the north, across the southernmost Antalya Basin seismic reflection profiles display some of the most spectacular examples of positive flower structures (Figs. 5.39, 5.40). Here, a bundle of strong and laterally continuous mid-Unit 1 reflectors allow the clear delineation of footwall and hanging wall cutoffs. The seismic data reveal the presence of at least two oppositely-verging thrusts that rise from a common stem, associated with several smaller thrusts. The tip points of these thrusts lie immediately below the depositional base, but the faults clearly affect the seafloor (Figs. 5.40, 5.41). Some of the faults that bound the positive flower structures have listric trajectories and sole deep within the Messinian successions of Unit 2, suggesting that these structures must have developed by the reactivation of the pre-existing Messinian and/or pre-Messinian Miocene structures. Growth strata observed in the upper portion of the uppermost Messinian–Quaternary successions of Unit 1 suggest that these structures developed during the Pliocene–Quaternary. Unfortunately there is no multibeam image in this portion of the Antalya Basin, therefore the seafloor expression of the troughs and ridges created by these positive flower structures cannot be accurately mapped.

The positive flower structures resemble in their internal architecture and seafloor geometries to the salt cored fold belt described above. The evaporite successions of Unit 2 have also penetrated into the core of the positive flower structures; however, they remained low within the structures, unlike the salt cored fold belt where the evaporites penetrated quite high within the core of the structures.

5.2.4 Summary

The most important unresolved scientific issue of the northeastern sector of the eastern Mediterranean is the adequate delineation of the morpho-tectonic architecture and the structural framework

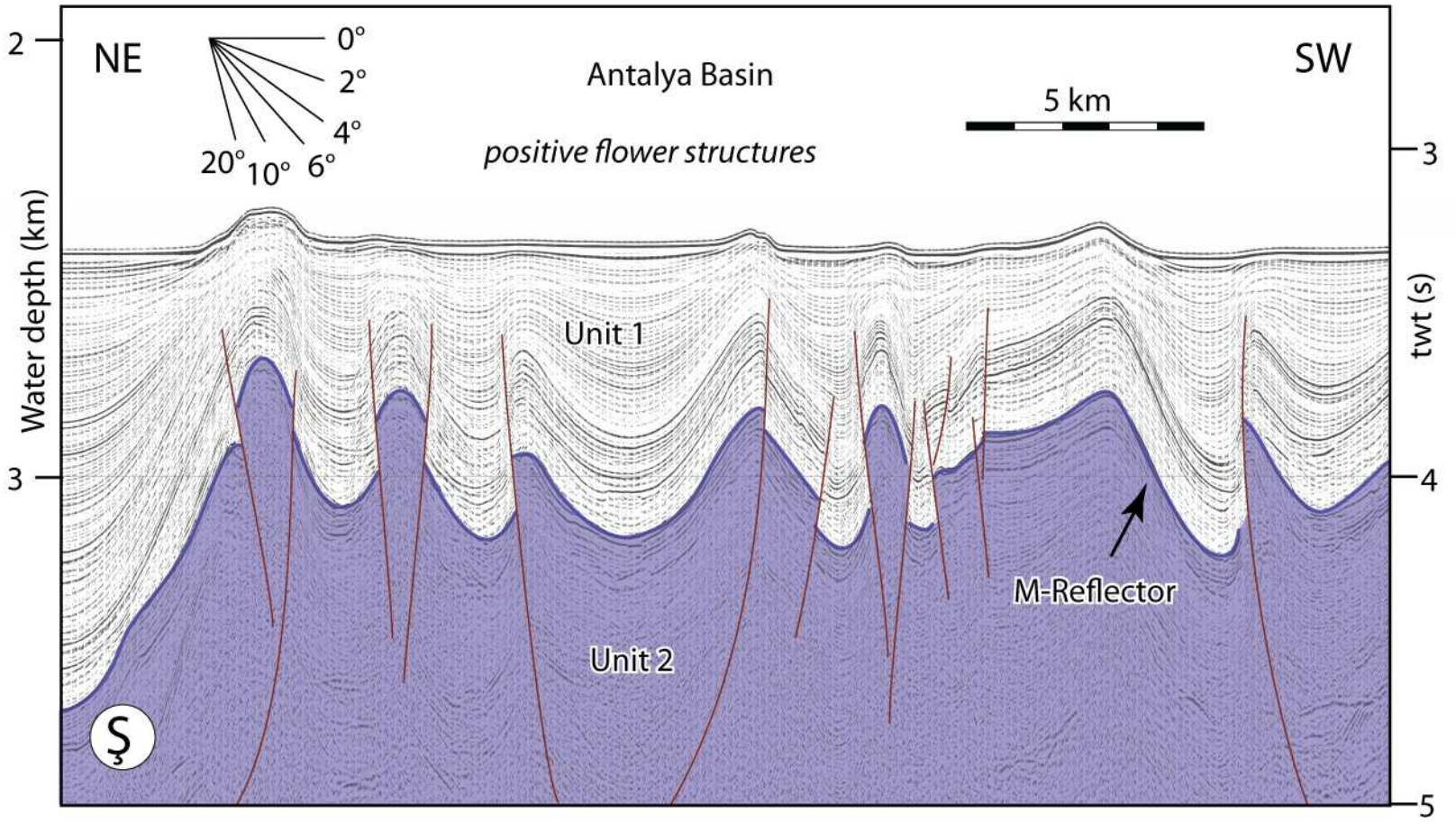

Figure 5.39: High-resolution multi-channel seismic reflection profile Ş showing the development of positive flower structures along the northern foothills of the Florence Rise. Note the highly reflective and laterally continuous bundle which allows the delineation of footwall and hanging wall cutoffs. Location is shown in Figure 5.20. EMED10 (fix 1976-1996)

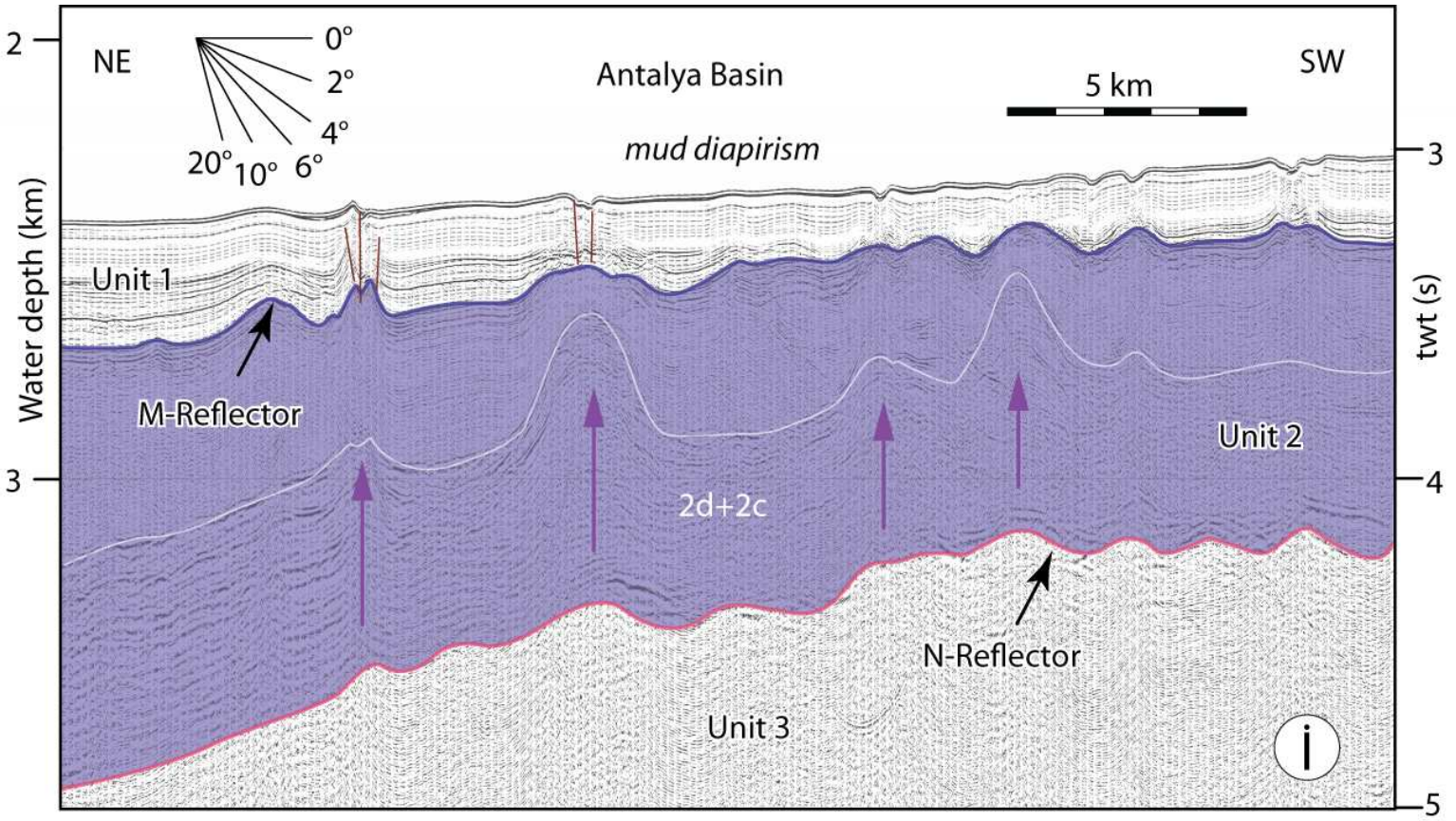

Figure 5.40: High-resolution multi-channel seismic reflection profile İ showing the development of positive flower structures along the northern foothills of the Florence Rise. Note the highly reflective and laterally continuous bundle which allows the delineation of footwall and hanging wall cutoffs. Location is shown in Figure 5.20. EMED10 (fix 1949-1969)

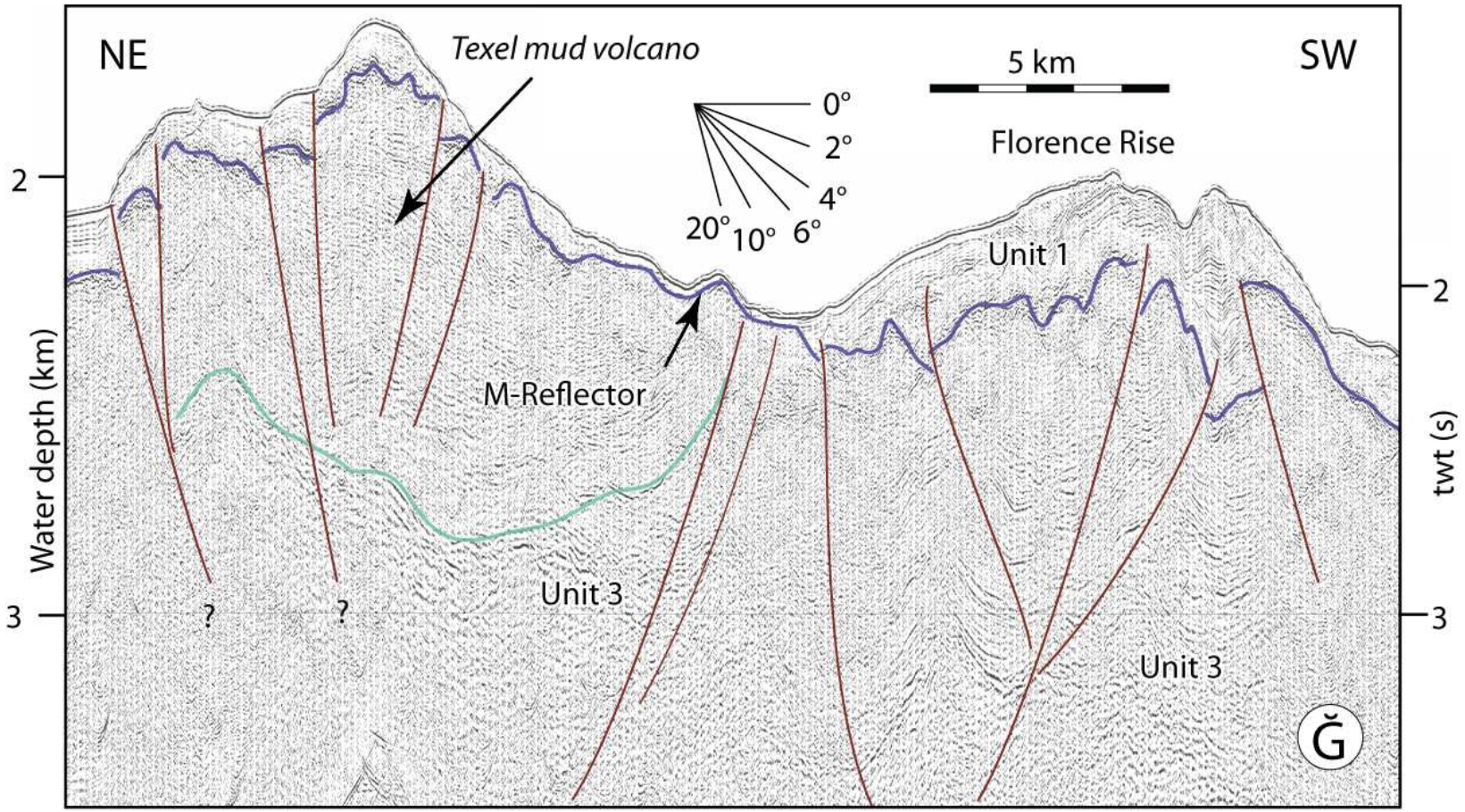

Figure 5.41: High-resolution multi-channel seismic reflection profile Ğ showing the Texel mud volcano and the development of positive flower structures along the Florence Rise. Location is shown in Figure 5.20. EMED10 (fix 2056-2076)

of the Antalya Basin and the Florence Rise, so that the role of these crustal-scale structures can be understood within the Miocene–Recent tectonic evolution of the greater Cyprus Arc. There are several specific questions in this area, for example, (i) is subduction still taking place across the Florence Rise segment of the Cyprus Arc? (ii) how is the collision between the Eratosthenes Seamount and the Island of Cyprus reflected in the structural architecture of the Florence Rise? (iii) how is the kinematic switch from a pervasive collision between the African and Eurasian plates in the Miocene to the escape tectonics and block rotations in the Pliocene-Quaternary reflected in the architecture of the Pliocene–Quaternary successions across the Florence Rise and Antalya Basin? (iv) how are the Florence Rise structures linked with the Hellenic Arc across the Anaximander Mountains in the northwest? These critical questions are addressed in this chapter where very detailed descriptions of the Miocene and Pliocene–Quaternary structures as well as the detailed seismic stratigraphic architecture of these deposits have been made. For example, , this study documented that the Miocene successions exhibit contractional deformation in the entire area studied, but that the amplitude of strain and its character is clearly spatially partitioned during the Pliocene–Quaternary into discrete morpho-tectonic domains across the Florence Rise and Antalya Basin. This study unequivocally documented the tectonic linkages between the Anaxagoras Mountain and the Florence Rise indicating that Anaxagoras has been deformed like Florence Rise but is more intensely strained and confirmed that the Anaximander Mountains define a critical junction between the greater Cyprus Arc in the east and the Hellenic Arc in the west, by terminating the contractional WNW-ESE structures of the Florence Rise against the NE-SW structures associated with the margins of the STEP zone separating the Cyprus Arc from the Hellenic Arc. The full discussion of these structures and their regional significance is made in Chapter 6.

Chapter 6

Tectonic and Kinematic Evolution – Discussion

This Chapter provides a regional tectonic synthesis. All previous work on the Miocene–Recent tectonic evolution of the eastern Mediterranean was done in small isolated regions, which provided a "postage stamp-like" maps and the associated local evolutionary history within the backdrop of a very complex incipient orogenesis that is occurring across the eastern Mediterranean. It is clear that the complete tectonic picture could only be presented if the entire eastern Mediterranean is examined in a set of regional maps. This thesis (in this Chapter) presents for the first time several critical tectonic maps which are compiled using authors mapping as well as data and maps from previous studies that encompass the entire eastern Mediterranean region. These maps in turn, allowed a holistic tectonic interpretation and discussion to be made in three time intervals: pre-Messinian Miocene, Messinian and Pliocene–Quaternary. Results from these compiled mapping and interpretation suggest that there was a single large basin across the eastern Mediterranean during the Early–Middle Miocene. This ancestral early Miocene basin was split into several depocenters by the development of prominent three fold-thrust belts which delineate a 300–350 km wide deformation zone extending from the

Central Taurus Mountains to the African–Eurasian plate boundary during the Late Miocene. Most specifically the third arcuate fold-thrust belt of this deformation zone extends from the Baër Bassit region of western Syria, across the Cyprus Arc, linking with the Florence Rise. This fold-thrust belt may further extend into the Antalya Complex of southwestern Turkey, or link with the Anaximander Mountains. This is the important contribution of this thesis.

Introduction

The eastern Mediterranean includes the last vestiges of the southern branch of the once very prominent Neo-Tethys Ocean that existed between Africa and Eurasia. The sustained consumption of the Neo-Tethys oceanic lithosphere beneath the Eurasian Plate since the Eocene and the collision and accretion of various continental fragments and terranes, such as the Mamonia Complex, the Hecateus Ridge, and the Eratosthenes Seamount rendered the present-day oblique collisional geometry observed in the eastern Mediterranean Region. The present-day boundary between the African Plate and the overriding Aegean-Anatolian Microplate can be drawn based on the position of the edge of the overriding lithosphere or based on the position associated with the deformation over the downgoing lithosphere (Fig. 6.1). However, regardless of how one defines the plate boundary, the region south of it clearly represent the passive margin successions developed over the continental edges of the African Plate. The successions that are developed north of the boundary between the African Plate and the Aegean-Anatolian Microplate show the typical predominantly contractional deformation associated with a collisional margin. In this context, Figure 6.1b is a better representation of the limit of contractional deformation. The volcanic arc associated with the Cyprus Arc lies within central Anatolia, whereas that associated with the Hellenic Arc is situated in central Aegean Sea (Fig. 6.1). Therefore, the region between the volcanic arc(s) and the southern plate boundary of the Aegean-Anatolian Microplate is best described as the forearc region of the evolving orogen.

Any attempt to evaluate the detailed Miocene structural evolution of the eastern Mediterranean

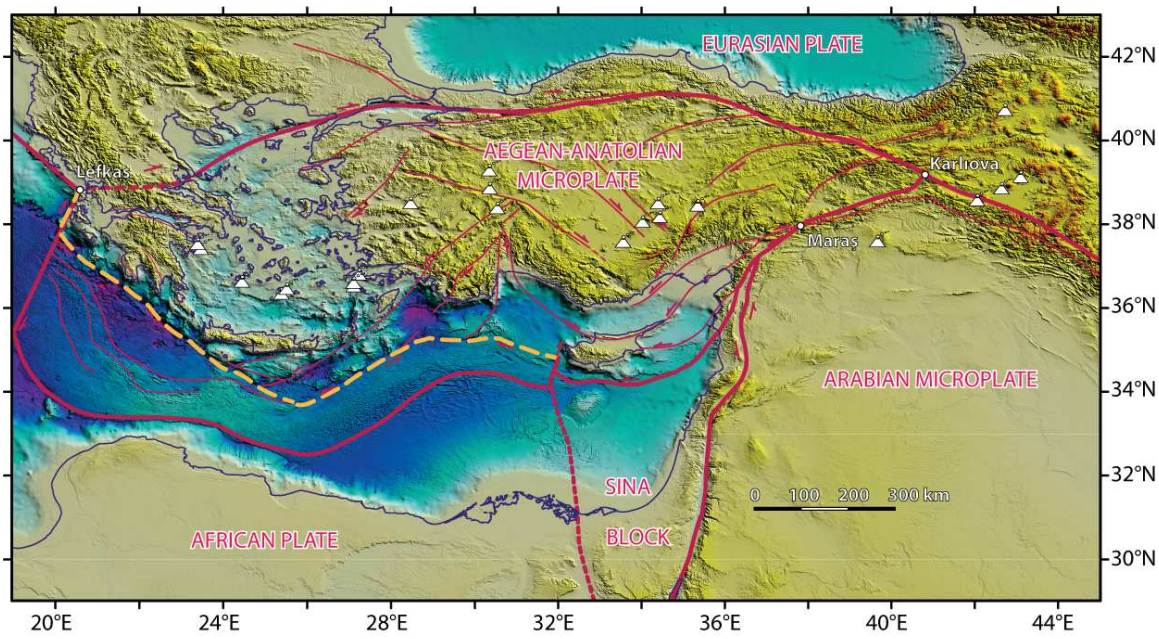

Figure 6.1: Simplified tectonic map of the eastern Mediterranean region showing the prominent fault zones (thin red lines), plate boundaries and the triple junctions (small white circles). Across the southwestern portion of the Aegean-Anatolian Microplate the thick gold dashed line shows the position of the plate boundary based on the location of the hard overriding lithosphere (from Aksu et al., 2009), whereas the thick red line shows the plate boundary defined by the deformation above the down-going African lithospheric slab. Note the considerable southward shift of the plate boundary south of Hellenic Arc. The topography is compiled using GeoMapApp (Ryan et al., 2009), and shaded using Global Mapper. The multibeam bathymetry from the high-resolution EMODnet (European Marine Observation and Data Network, Portal for Bathymetry, http://www.emodnet-hydrography.eu/). The coastline is taken from the International Bathymetric Charts of the Mediterranean (IOC, 1981). Pink inset = study area, half arrows = transform/strike-slip faults (modified from Aksu et al., 2009).

region requires the compilation and evaluation of the detailed pre-latest Messinian Miocene field studies and data from several critical regions, such the Bitlis–Zagros suture, the Kyrenia Mountains, the Mamonia Complex and southern Taurus Mountains onland, and the Adana, Cilicia, Latakia, Iskenderun and Cyprus basins in the marine areas. In addition, palinspastic restorations are needed across several, if not all these areas so that the Miocene geometry of the collisional margin can be delineated. These are clearly beyond the scope of this present study. Therefore, the following discussion is mainly focused on the evolution of the eastern Mediterranean region since the latest Miocene. However, a synoptic discussion of the pre-Messinian Miocene and Messinian is also presented.

6.1 Pre-Messinian Miocene structural evolution of eastern Mediterranean

The pre-Messinian Miocene structural architecture of the eastern Mediterranean region is controlled by the pervasive convergence between the African and Eurasian plates, associated with the closure of the Neotethys Ocean. Various previous studies documented the development of a large, broadly east–west-oriented foredeep in front of the evolving arcuate Tauride fold–thrust belt in the eastern Mediterranean (Williams et al., 1995, Aksu et al., 2009, Hall et al., 2009). For example, remarkable depositional similarities of the marine Aquitanian–Tortonian successions in the onland Mut and Adana basins (Eriş et al., 2005; Şafak et al., 2005), Aksu, Köprüçay and Manavgat basins (Poisson et al., 2003a,b; Deynoux et al., 2005; Karabıyıkoğlu et al., 2005), the Mesaoria Basin of central Cyprus (Robertson and Woodcock, 1986), the Misis Mountains of southern Turkey (Gökçen et al., 1988) and the Kyrenia Range (Calon et al., 2005a,b), the Aksu Thrust (Poisson et al., 2003a,b), as well as the marine Cilicia, Iskenderun, Antalya and Finike basins (Figs. 1.1, 1.4; Uffenorde et al., 1990; Aksu et al., 2005a,b, 2009, 2014c; Işler et al., 2005) strongly suggest that there was a single large basin across the eastern Mediterranean during the Early–Middle Miocene. This large ancestral

foredeep basin probably extended from the Karsantı and Maraş basins in the east (Calon et al., 2005a; Hall et al., 2005a; Ilgar and Nemec, 2005; Satur et al., 2005; Hüsing et al., 2009) into the Antalya and Kasaba basins in the west (Işler et al., 2005; Çiner et al., 2008). The region south of the foredeep must have been situated over the northern fringes of the African Plate. This is clearly visible on the pre-Messinian Miocene tectonic map of the eastern Mediterranean, where the style of tectonism is markedly different from that seen across the forearc region (Figs. 6.2, 6.3). While the present-day Nile cone is characterized by two sets of extensional faults that cut one another in an orthogonal fashion (e.g., Abd-Allah et al., 2012), the forearc region is characterized by several internally parallel fold-thrust belts (Figs. 6.2, 6.3). For example, a prominent fold-thrust belt extends from the Misis Mountains of southern Turkey across the Cilicia-Latakia basins into the Kyrenia Range of northern Cyprus. This broad predominantly mid- to late-Miocene structure is known as the Misis-Kyrenia fold-thrust belt (Calon et al., 2005a, Hall et al., 2005a). This belt farther extends into the Antalya Basin and then linking the Aksu thrust, located within the apex of the Isparta Angle (Poisson et al., 2003a,b, Calon et al., 2005b, Işler et al., 2005, Hall et al., 2014a), delineating a >700 km long arcuate fold-thrust belt, referred to as the Misis–Kyrenia–Aksu fold-thrust belt (Figs. 6.2, 6.3). Similarly, a prominent fold-thrust belt occurs across the Amanos Mountains of southern Turkey where it carries the Hatay–Kızıldağ ophiolites. The belt extends across the Latakia Basin and links with the Yerasa fold-thrust belt of southern Cyprus, which carries the Troodos ophiolites, including the Paralimni mélange (Calon et al., 2005a,b, Hall et al., 2005a,b). This belt further extends into the southern Antalya Basin and links with the Antalya Complex of southwestern Turkey (Figs. 6.2, 6.3). This >700 km long structure is informally referred to as the Kızıldağ Troodos–Antalya fold-thrust belt, which runs remarkably parallel to the Misis–Kyrenia–Aksu fold-thrust belt. A third arcuate fold-thrust belt extends from the Baër Bassit region of western Syria, across the Cyprus Arc, linking with the Florence Rise (Figs. 6.2, 6.3). This fold-thrust belt may further extend into the Antalya Complex of southwestern Turkey, or link with the Anaximander Mountains.

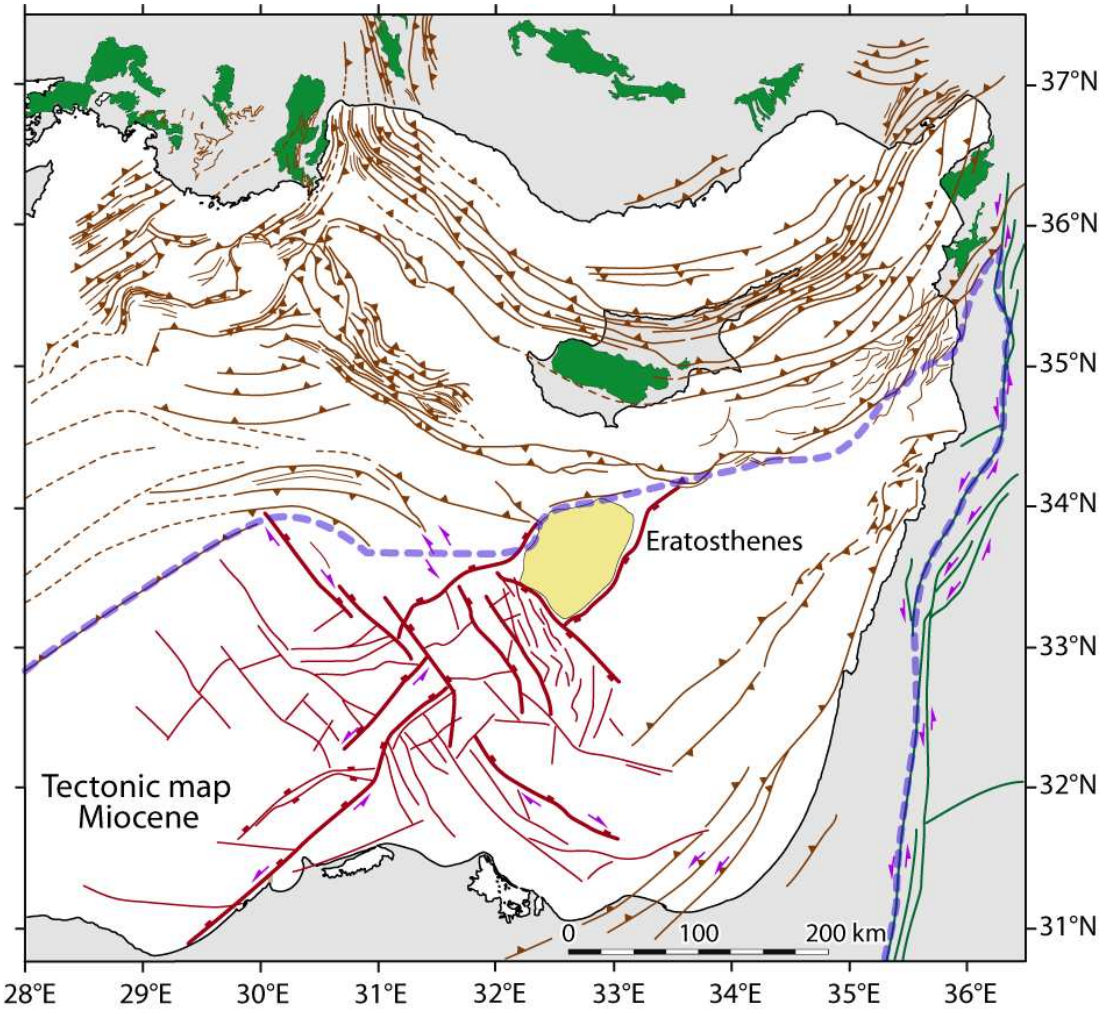

Figure 6.2: Pre-Messinian Miocene tectonic map of the eastern Mediterranean. Map is compiled by Aksu using data from (a) Florence Rise (Güneş, this thesis); (b) Rhodes and Finike basins, Anaximander Mountains (Hall et al., 2009, Aksu et al., 2009, Cranshaw, 2010, Barnes, 2015), (c) Adana, Cilicia, Latakia, Iskenderun basins (Aksu et al., 2005, 2014a,b, Hall et al., 2005a,b, Walsh-Kennedy et al., 2014), (d) offshore Israel, offshore Lebanon, Levantine Basin (Carton et al., 2009, Gvirtzman et al., 2010), (e) Eratosthenes Seamount, Herodotus Basin (Montadert et al., 2010, Skiple et al., 2012), (f) offshore Syria (Bowmann 2011), and (g) Nile delta (Mascle et al., 2000, Abd-Allah et al., 2012). The coastline is from the International Bathymetric Charts of the Mediterranean (IOC, 1981). Brown lines = thrust faults with triangle ticks on hanging wall, red lines = normal faults with rectangular ticks on hanging wall, green lines = strike slip faults with purple half arrows showing slip direction, green fill = ophiolites.

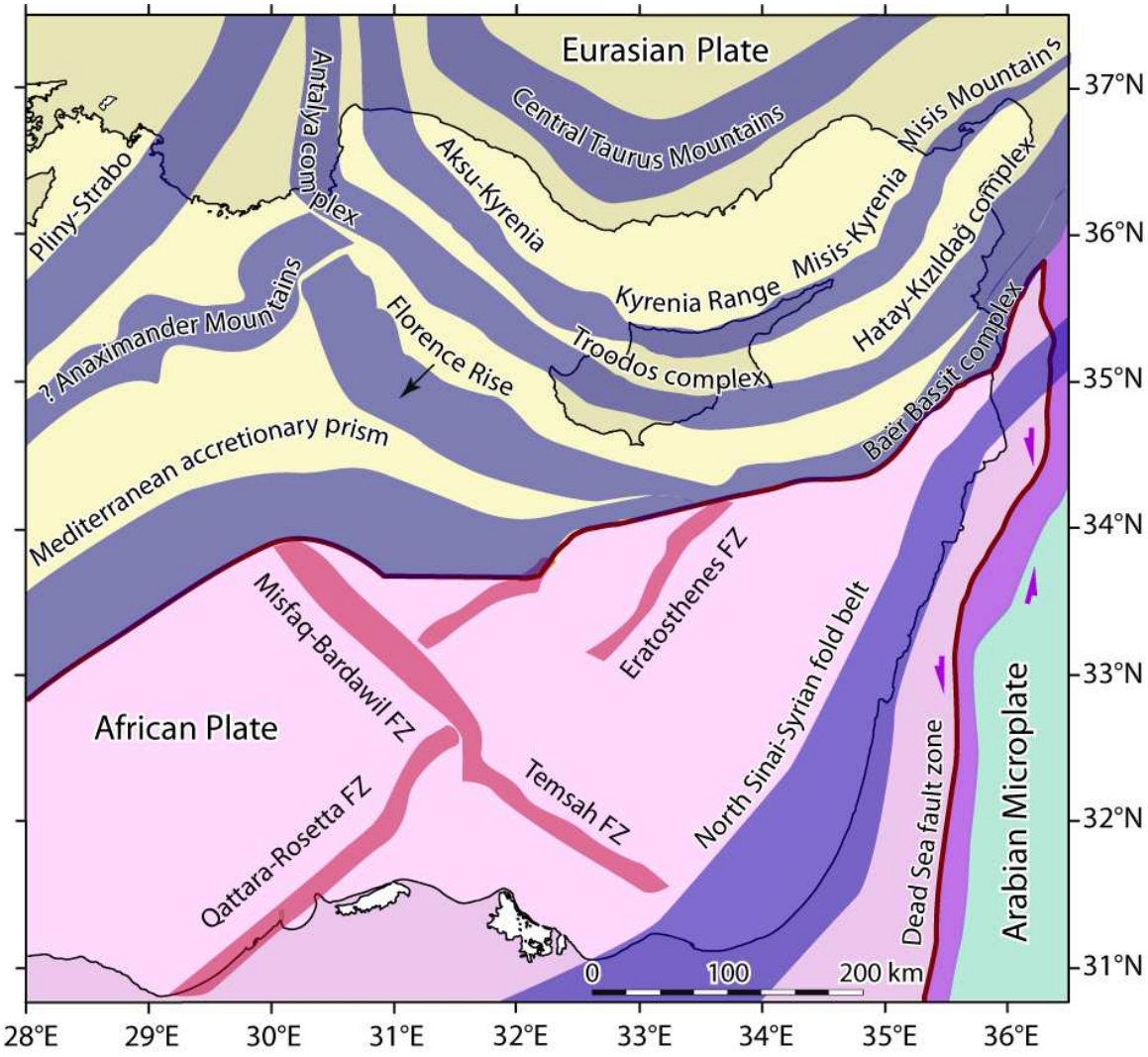

Figure 6.3: Pre-Messinian Miocene map of the eastern Mediterranean showing the African Plate and the Arabian and Aegean-Anatolian microplates, simplified from Figure 6.2. Various fault zones are drawn: purple= strike-slip, blue= contractional, red= extensional with strike slip component. The coastline is from the International Bathymetric Charts of the Mediterranean (IOC, 1981).

The three prominent fold-thrust belts delineate a 300–350 km wide deformation zone extending from the Central Taurus Mountains to the African–Eurasian plate boundary. The ancestral early Miocene basin was split into several depocenters by the development of fold-thrust belts during the Late Miocene.

6.2 Messinian structural evolution of eastern Mediterranean

During the Messinian, the pervasive contractional tectonic activity notably diminished across the entire forearc portion of the eastern Mediterranean (Fig. 6.4; Aksu et al., 2005a,b, 2009, 2014a–c, Hall et al., 2005a,b, 2009, 2014a,b, Calon et al., 2005a,b). The present study also documented a marked decrease in tectonic activity during the deposition of the Messinian successions of Unit 2 (§ Chapter 5). The sparse data compiled from the northern margin of the African Plate show that there was little change in the style and intensity of the tectonic activity across the passive continental margin succession of the present-day Nile cone and the Levantine Basin (Fig. 6.4). The marked slowdown of the intensity of tectonism is ascribed to the incipient collision of the Arabian Microplate with the Eurasian Plate during the Late Miocene. The subsequent full-scale collision and suturing of the Arabian Microplate with the south-central portion of the Eurasian Plate initiated the development of the new Aegean-Anatolian Microplate, and its west-directed escape during the Pliocene–Quaternary.

6.3 Latest Messinian–Recent structural architecture of the eastern Mediterranean

6.3.1 Southern forearc region – Aegean–Anatolian Microplate

A compilation of tectonic elements across the eastern Mediterranean region shows that the southern sector of the eastern Mediterranean including the Nile delta has a distinctly different tectonic

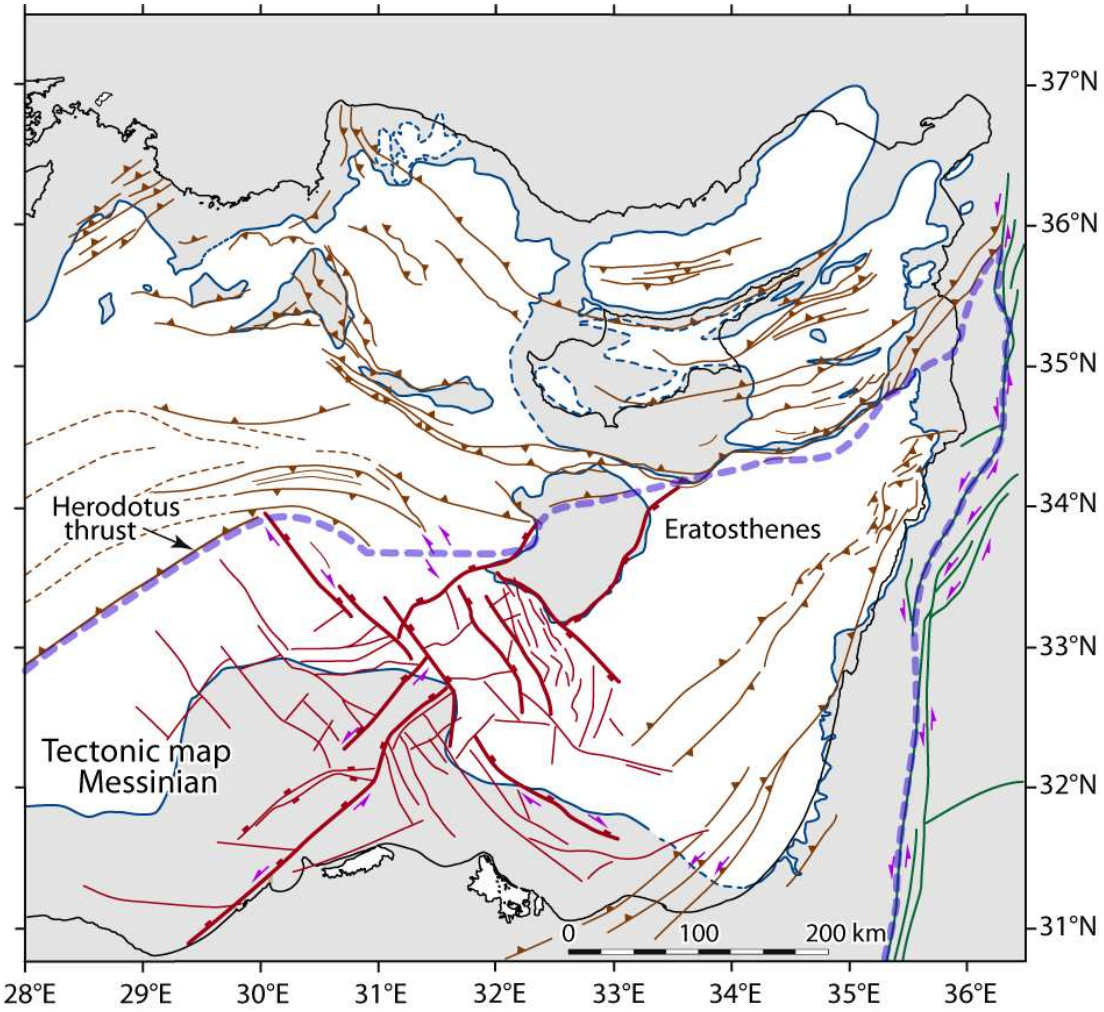

Figure 6.4: Messinian tectonic map of the eastern Mediterranean. Map is compiled by Aksu using data from (a) Florence Rise (Güneş, this thesis); (b) Rhodes and Finike basins, Anaximander Mountains (Hall et al., 2009, Aksu et al., 2009, Cranshaw, 2010, Barnes, 2015), (c) Adana, Cilicia, Latakia, Iskenderun basins (Aksu et al., 2005, 2014a,b, Hall et al., 2005a,b, Walsh-Kennedy et al., 2014), (d) offshore Israel, offshore Lebanon, Levantine Basin (Carton et al., 2009, Gvirtzman et al., 2010), (e) Eratosthenes Seamount, Herodotus Basin (Montadert et al., 2010, Skiple et al., 2012), (f) offshore Syria (Bowmann 2011), and (g) Nile delta (Mascle et al., 2000, Abd-Allah et al., 2012). The coastline is from the International Bathymetric Charts of the Mediterranean (IOC, 1981). Brown lines = thrust faults with triangle ticks on hanging wall, red lines = normal faults with rectangular ticks on hanging wall, green lines = strike slip faults with purple half arrows showing slip direction.

architecture, dominated by large oblique faults with both normal and strike slip components, from that of the northern sector where the tectonic architecture is largely dominated by prominent thrusts with some strike slip components (Fig. 6.5). A prominent broadly northeast-southwest striking and southeast-verging thrust (informally referred to as the Herodotus thrust) delineates the boundary between the southern and northern sectors, defining the southern margin of the Herodotus Basin and extending to the Eratosthenes Seamount (Montadert et al., 2010, Skiple et al., 2012). Farther east-northeast the Herodotus thrust appears to merge with the eastern segment Cyprus Arc, which notably curves toward the northeast (Fig. 6.5). To the east, the Dead Sea Fault zone emerges as a prominent structural element, consisting of several fault segments all of which invariably exhibit sinistral strike slip (Fig. 6.5; Gomez et al., 2007, Ferry et al., 2011, Karabacak and Altunel, 2013). Thus, solely based on the upper crustal deformation, the boundary between the Aegean-Anatolian Microplate and the African plate is delineated by the Herodotus fault zone and the eastern sector of the Cyprus Arc, (or the Tartus–Baër Bassit fault zone), whereas the boundary between the Arabian Microplate and the African Plate is delineated by the Dead Sea Fault zone (Fig. 6.6).

The forearc region of the Cyprus Arc is characterized by a series of internally parallel concave to the south arcuate fault zones (Figs. 6.5, 6.6). From north to south these are: (a) the Kozan–Anamur-Silifke–Kırkkavak fault zone, (b) Misis–Kyrenia–Aksu fault zone, (c) the Anamos–Larnaka–Troodos–Antalya fault zone, (d) Tartus–Baër Bassit–Florence Rise–Anaxagoras fault zone and (e) the Herodotus fault zone. The forearc region of the Hellenic Arc resides outside the study area, with the exception of the northeastern segment of the arc, where two broadly parallel zones occur: (f) Pliny-Strabo-Burdur-Fethiye fault zone and (g) Sırrı Erinç shear zone. The seafloor morphology map clearly shows the belts, particularly in regions where detailed multibeam bathymetry exits (Fig. 6.7). These zones, briefly described below, delineate the deformation associated with the greater Cyprus Arc and the northeastern segment of the Hellenic Arc, which extends northward more than 250–350 km from the boundary between the Aegean-Anatolian Microplate and the African Plate (Fig. 6.6).

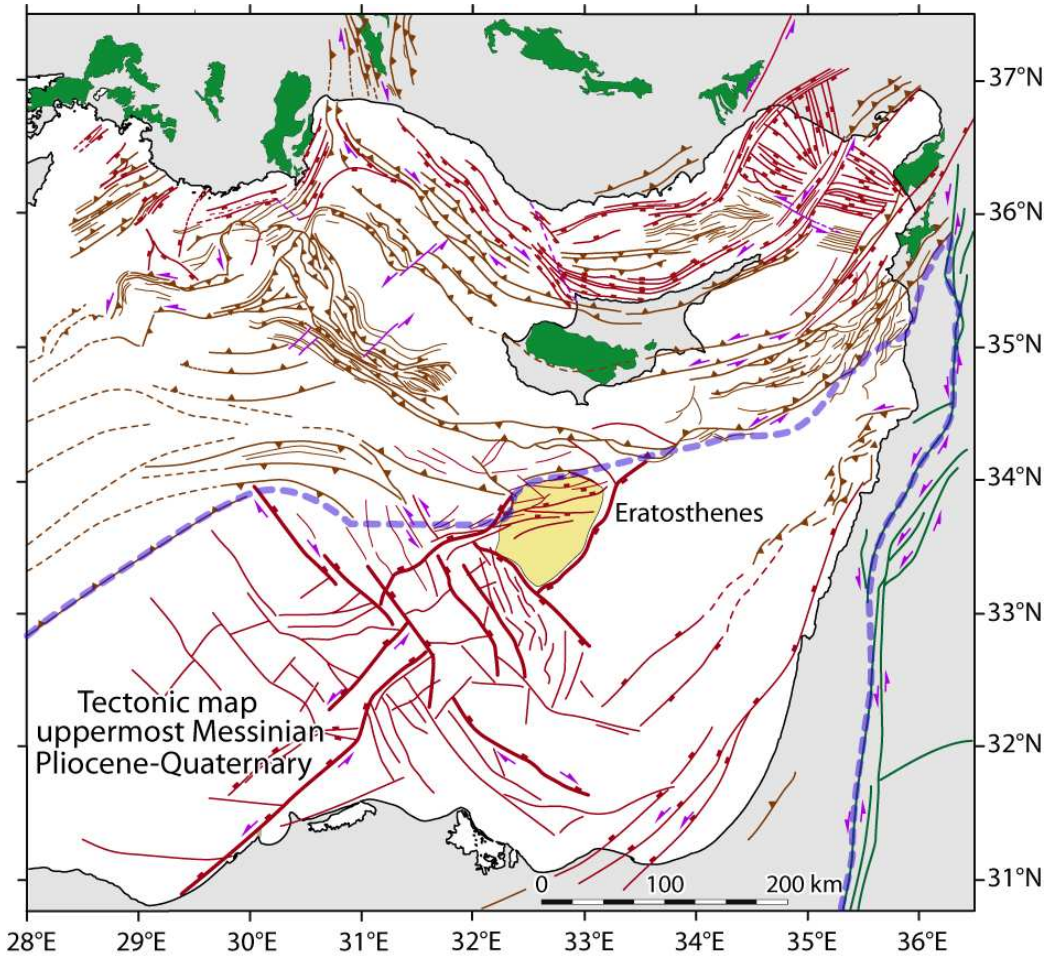

Figure 6.5: Uppermost Messinian–Recent tectonic map of the eastern Mediterranean. Map is compiled by Aksu using data from (a) Florence Rise (Güneş, this thesis); (b) Rhodes and Finike basins, Anaximander Mountains (Hall et al., 2009, Aksu et al., 2009, Cranshaw, 2010, Barnes, 2015), (c) Adana, Cilicia, Latakia, Iskenderun basins (Aksu et al., 2005, 2014a,b, Hall et al., 2005a,b, Walsh-Kennedy et al., 2014), (d) offshore Israel, offshore Lebanon, Levantine Basin (Carton et al., 2009, Gvirtzman et al., 2010, Gardosh et al., 2008b), (e) Eratosthenes Seamount, Herodotus Basin (Montadert et al., 2010, Skiple et al., 2012), (f) offshore Syria (Bowmann 2011), and (g) Nile delta (Mascle et al., 2000, Abd-Allah et al., 2012). The coastline is from the International Bathymetric Charts of the Mediterranean (IOC, 1981). Brown lines = thrust faults with triangle ticks on hanging wall, red lines = normal faults with rectangular ticks on hanging wall, green lines = strike slip faults with purple half arrows showing slip direction, green fill = ophiolites. This figure is also shown as a foldout in Appendix 1.

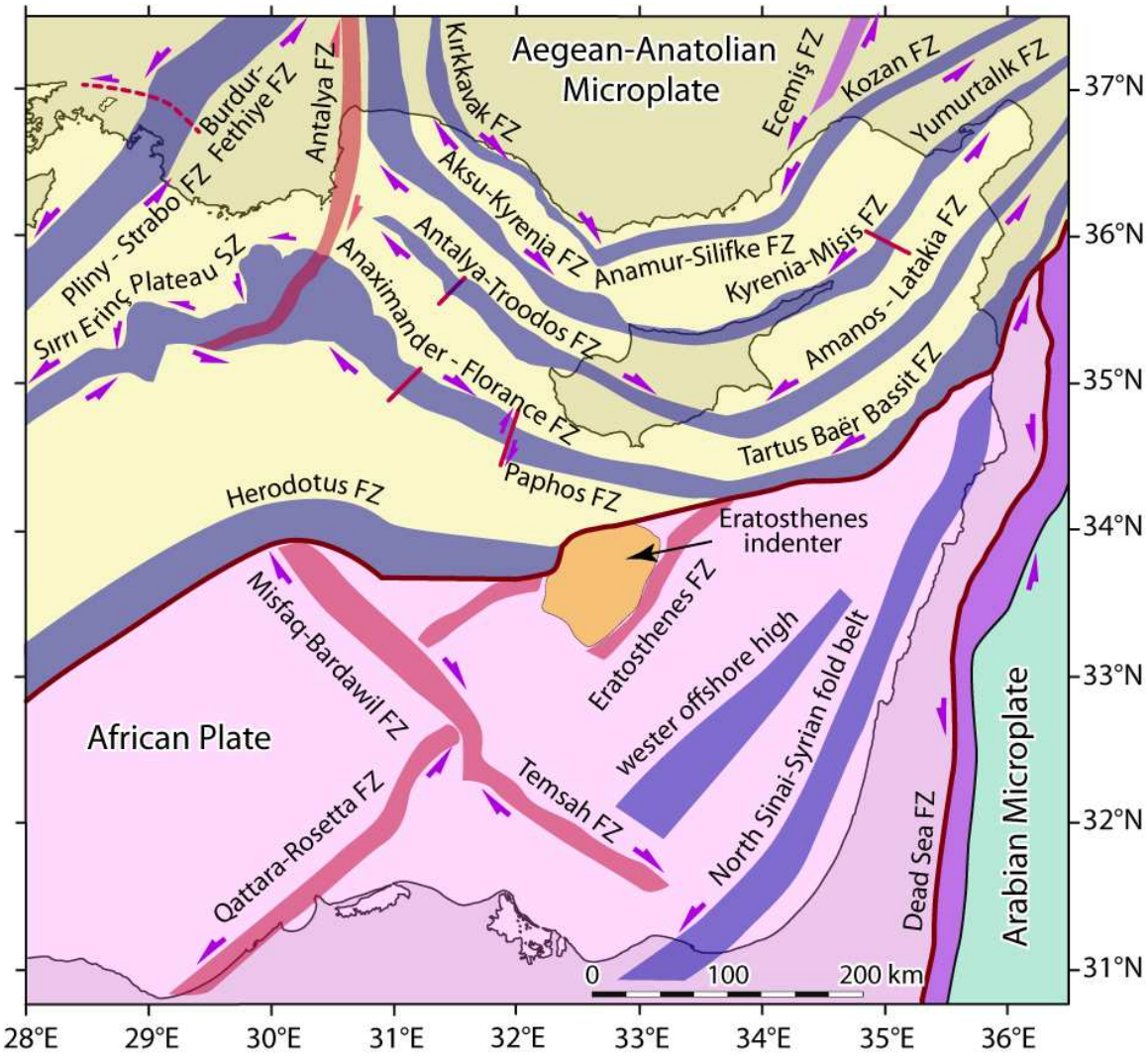

Figure 6.6: Uppermost Messinian–Recent tectonic map of the eastern Mediterranean. Map showing the African Plate and the Arabian and Aegean-Anatolian microplates, simplified from Figure 6.5. Various fault zones are drawn: purple= strike-slip, blue= contractional with strike slip component, red= extensional with strike slip component. The coastline is from the International Bathymetric Charts of the Mediterranean (IOC, 1981).

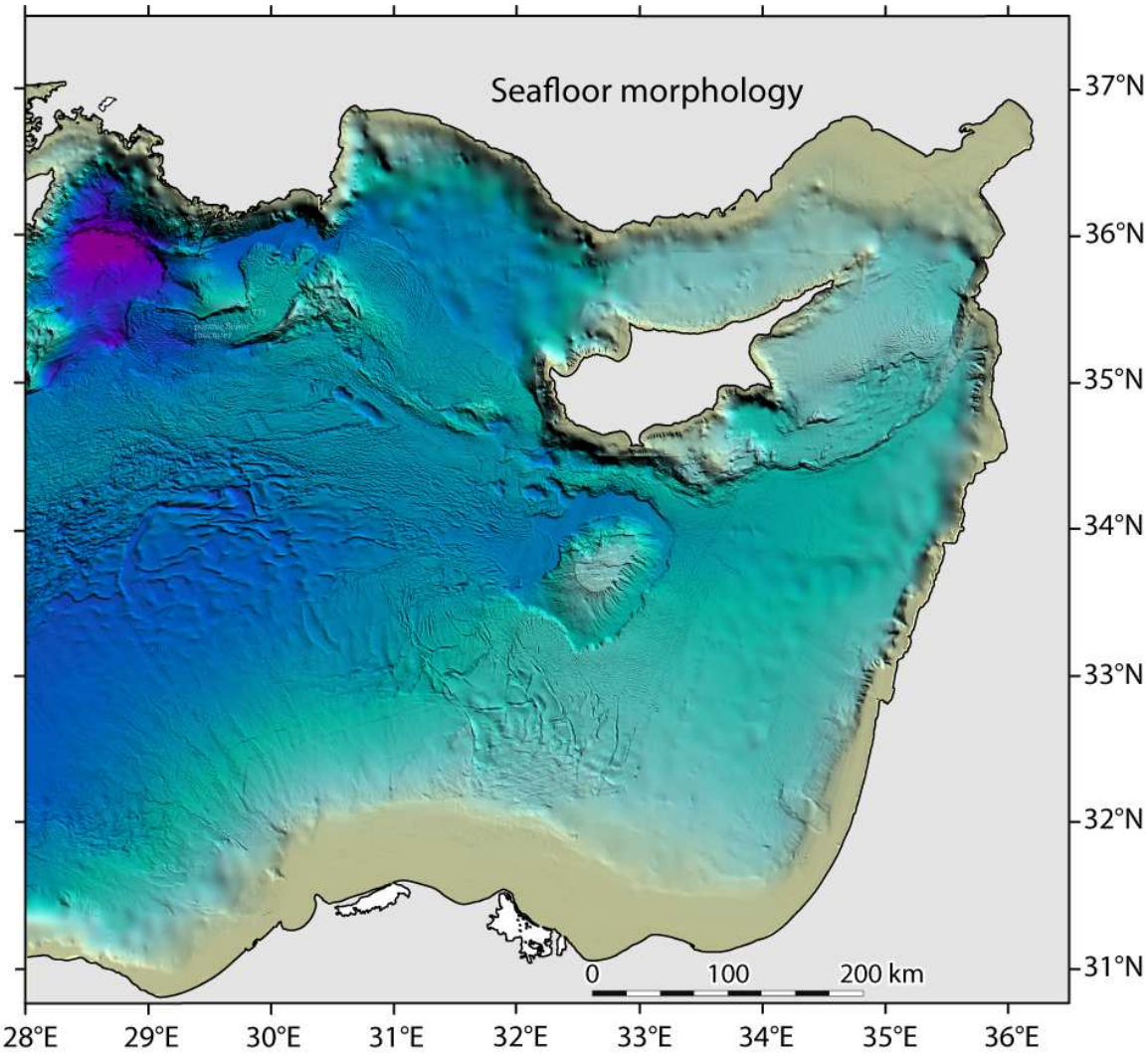

Figure 6.7: Map of the eastern Mediterranean showing the morphology of the seafloor. The multi-beam bathymetry is superimposed on the International Bathymetric Charts of the Mediterranean (from the high-resolution EMODnet, European Marine Observation and Data Network, Portal for Bathymetry, http://www.emodnet-hydrography.eu/). The coastline is taken from the International Bathymetric Charts of the Mediterranean (IOC, 1981).

(a) Kozan–Anamur-Silifke–Kırkkavak fault zone

The Kozan–Anamur-Silifke–Kırkkavak fault zone is composed of several discrete segments: the Kozan fault zone in the east, the Kırkkavak fault zone in the west and the Silifke fault zone that connects these two systems across the northern margin of the Outer Cilicia Basin (Fig. 6.6). The Kozan fault zone has been extensively studied in the onland portion of the zone across the northwestern Adana Basin (e.g., Burton-Ferguson et al., 2005) as well as the marine portion across the northwestern Cilicia Basin (e.g., Aksu et al., 2005, 2014a,b, Walsh-Kennedy et al., 2014). In these regions the Kozan fault zone defines a ∼300 km long and 15–20 km-wide "lazy-S" shaped structure along the southeastern fringes of the Taurus Mountain and along the northwestern margins of the Cilicia and Adana basins (Fig. 6.5). The zone is described as an arcuate structure consisting of several east-northeast–west-southwest and north-northeast south-southwest striking, closely-spaced relatively high-angle oblique faults with both normal dip slip and sinistral strike slip. In the marine Cilicia Basin the zone consists of several relatively high-angle faults which exhibit small normal-sense dip separations on the M-reflector and have tip points situated mainly in the lower and middle portion of the Pliocene–Quaternary successions (Aksu et al., 2005, 2014a,b, Walsh-Kennedy et al., 2014). In the onland Adana Basin the Kozan fault zone is defined by northeast-striking and southeast dipping extensional faults which occur along the western and northwestern margin of the basin (Burton-Ferguson et al., 2005). These faults cut down with relatively steep dip into the ∼700 ms thick Tortonian and older Miocene successions.

The Anamur-Silifke fault zone is developed along the northern margin of the Outer Cilicia Basin (Aksu et al., 2005, 2014b). The structural architecture of this region is delineated by a prominent 20–25 km wide zone of faults which show significant normal-sense dip separations (Fig. 6.5). Across the Outer Cilicia Basin, this fault system has an east–west strike, but traced toward the Inner Cilicia Basin, the fault zone progressively swings to assume a northeast–southwest strike, linking with the Kozan fault zone (Aksu et al., 2014b). In the Outer Cilicia Basin the Anamur-Silifke fault zone is

characterized by several relatively steeply dipping faults which show their main expression across the M-reflector where they create 25–150 ms offsets with normal-sense dip separations. These faults also cut the lower portion of the Pliocene–Quaternary succession of Unit 1, and extend into the pre-Messinian Miocene successions of Unit 3. In the deeper water regions in the Outer Cilicia Basin, the faults commonly extend into the middle portion of the Pliocene–Quaternary succession where they create small horst–graben structures. Aksu et al. (2014b) documented during the Late Pliocene, the Kozan fault zone propagated toward the southwest creating a restraining bend in the Cilicia Basin, and a new east–west oriented strike-slip fault (i.e., Anamur-Silifke Fault) in the Outer Cilicia Basin (Figs. 6.5, 6.6).

The Kırkkavak fault zone is originally described onland by Dumond and Kerey (1975), as a major Pliocene-Quaternary lineament east of the onland Aksu Thrust (Fig. 6.5). It is described as a broadly north-south striking dextral slip system with a predominantly east-verging reverse component (Yağmurlu et al., 1997, Piper et al., 2006, Monod et al., 2006, Toprak et al., 2009, Meijers et al., 2010). The Kırkkavak fault zone can be readily traced southward, but becomes buried before reaching the present-day shoreline (Fig. 6.5). Çiner et al. (2008) document that the Kırkkavak fault zone has been reactivated during the Pliocene–Quaternary as a prominent dextral strike slip fault. The Pliocene–Quaternary structural architecture of the northern and northeastern portions of the marine Antalya Basin is characterized by a prominent family of broadly arcuate northwest-southeast striking and predominantly southwest dipping extensional faults (Fig. 6.5; Işler et al., 2005; Hall et al., 2014b). These faults define a prominent zone that extends toward the shoreline with a remarkably similar orientation to the onland Kırkkavak fault zone (Hall et al., 2014a). Işler et al. (2005) first mapped these extensional faults, and also documented that these faults exhibit an important strike slip component. These authors suggested that this extensional fan developed on the trailing portion of the thrusts that are correlated with the Aksu fault zone (also discussed later). The position and orientation of these faults immediately southeast of the onland Kırkkavak fault zone provide a

more compelling correlation with the onland Kırkkavak fault zone, which then extends toward the southeast and possibly linking with the Amanos-Silifke fault zone.

(b) Misis–Kyrenia–Aksu fault zone

Three prominent, northeast-southwest striking and southeast verging internally parallel thrust faults delineated the onland Misis Mountains: the Misis, Aslantaş and Yumurtalık faults (Figs. 6.5, 6.6; Kelling et al., 1987, Kozlu, 1987, Karig and Kozlu, 1990). These thrusts, which are often collectively referred to as the Misis fold-thrust belt, developed during the middle-late Miocene and delineated a fold-thrust belt extending from the Kyrenia Range of northern Cyprus toward the Misis Mountains of southern Turkey. During the Pliocene–Quaternary the leading thrust panels of the fold-thrust belt became reactivated as a sinistral strike slip system as part of the horse-tail-like splays from the East Anatolian Fault zone (Kelling et al., 1987, Kozlu, 1987, Karig and Kozlu, 1990). The Yumurtalık fault defines the northwestern margin of the marine Iskenderun Basin.

A prominent arcuate 3–8 km wide bathymetric high, extending from the southern tip of the Misis Mountains to the northeastern tip of the Kyrenia Range separates the marine Cilicia and Latakia basins (Figs. 6.5, 6.6; Aksu et al., 2005a, Hall et al., 2005a, Calon et al., 2005a,b). This bathymetric high is developed near the crest of a 30–40 km wide pre-Messinian basement high, interpreted as the erosional remnant of a late Miocene (Tortonian), southeast-verging fold–thrust belt (Aksu et al., 2005a, Hall et al., 2005a, Calon et al., 2005a). The narrow bathymetric high is the expression of the basin bounding fault system developed during the Pliocene–Recent, and is referred to as the Misis–Kyrenia central horst block, developed as the result of northeast-southwest trending and northwest and southeast dipping faults across the structure (Aksu et al., 2005a, Hall et al., 2005a). The architecture of the middle–late Miocene strata in the Inner Cilicia and Adana basins (Aksu et al., 2005a, Burton-Ferguson et al., 2005), shows that the fold–thrust activity initiated in the Serravallian–Tortonian for the Misis segment belt. Thick wedges of Tortonian fluvio-deltaic strata represent

the unconformable fill of a piggy-back basin that evolved on the western backlimb of the thrust culmination, whereas Tortonian strata are involved in the thrust structures along the eastern front of the culmination (Kelling et al., 1987; Hall et al., 2005). In the Inner Cilicia Basin, the dramatic thickening of the Tortonian wedge toward the west suggests that the Miocene depocentre originated as a foredeep in front of the Tauride culmination. The Misis–Kyrenia culmination evolved into an emergent structure during the Tortonian to Messinian interval (Calon et al., 2005a,b). This is indicated in the Misis segment by the predominantly terrestrial lithofacies of the Tortonian succession and the erosional truncation of fold structures in the sub-Tortonian strata within the culmination. Messinian evaporites were deposited in two parallel trending depocentres (Cilicia and Latakia basins) separated by the eroding crest of the culmination, which clearly defined a latest Miocene paleohigh.

The Kyrenia fold/thrust belt defines the core of the Kyrenia Range in northern Cyprus. It is interpreted as a S-verging linked thrust system in the form of a trailing imbricate fan with largest displacements concentrated in the northern portion of the fold-thrust belt (Calon et al., 2005a,b). The fan is deeply rooted in the early-mid Tertiary units of the northern and central zones and its sole may penetrate the ophiolitic basement beneath the northern zone as indicated by the occurrence of small serpentinite slivers in thrust sheets exposed on the Karpas Peninsula. Toward the foreland the sole thrust of the fan has climbed to the base of the Miocene successions and the front of the fan is formed by detached fold/thrust structures restricted to the Miocene succession in the Outer Latakia Basin. The present-day structural framework of the Kyrenia Range is characterized by an imbricate fold–thrust system consisting of four major thrust panels: the northernmost Orga thrust, the central Kythrea and Ovgos thrusts and the southern Mesaoria thrust (e.g., Calon et al., 2005b). The Orga Fault defines a major north-dipping, south-verging fold–thrust structure that forms the spine of the Kyrenia Range, while the Kythrea and Ovgos Faults also define south-verging imbricate fold–thrust systems and form the central zone of the Kyrenia Range (Fig. 6.5). The Mesaoria Fault is interpreted by Calon et al. (2005b) as the leading splay of this imbricate fan system. These four

prominent thrust culminations and three major synclines that occur across the Kyrenia Range have been correlated with the structures across the Latakia Basin (Calon et al., 2005a) and the Antalya Basin (Calon et al., 2005b). For example, the Mirtou-Vasili and Aspromouti-Tricomo synclines are readily traced across the Kyrenia Range by Calon et al. (2014b) as large piggy-back basins carried on the back of the Kythrea and Ovgos thrusts, respectively. In the northwestern Latakia Basin, these synclines are correlated with the large synclines developed along the leading thrust panels of the Misis-Kyrenia fold-thrust belt above prominent thrusts which are linked with the onland Kythrea and Ovgos thrusts (Calon et al., 2014a,b). Similarly, in the east, the Mesaoria Basin is delineated as also a piggy-back basin carried on the backlimb of the Mesaoria Fault and its eastern extension into the outer Latakia Basin. The Mesaoria Basin is thus correlated with central axis of the Outer Latakia Basin. In the easternmost Antalya Basin, the prominent thrust Tα+β is delineated as the western continuation of the Mesaoria Fault (Calon et al., 2005a,b).

The Kormakiti Ridge defines the northwestern onland termination of the Kyrenia Range: however, the ridge farther continues as a prominent submarine structure into the Antalya Basin (Işler et al., 2005; Calon et al., 2005b). Işler et al. (2005) showed that the structural architecture of the inner portion of the Antalya Basin is characterized by three prominent broadly northwest-southeast striking and southwest verging thrusts (Fig. 6.5). Several smaller parasitic thrusts associated with each major thrust define three internally parallel fault zones (Fig. 6.6). The three large thrust sheets (labeled as T1, T2 and T3 by Işler et al., 2005) can be readily traced towards the eastern Antalya Basin. Işler et al. (2005) used the similarities in the strike and stratigraphic architecture of the thrusts mapped within the Antalya Basin and those described across the western Kyrenia Range and its immediate extension into the easternmost Antalya Basin to correlate the three northernmost prominent thrust panels of the imbricate fold–thrust system in the Antalya Basin, T1, T2 and T3 with the Orga, Kythrea and Ovgos faults of Cyprus, respectively (Figs. 6.5, 6.6).

Across the northwestern sector of the Antalya Basin, Hall et al. (2014a) mapped a prominent

arcuate northwest-southeast striking and predominantly southwest verging imbricate fold-thrust belt. They showed that the belt progressively swings and assumes a north-south trend, becoming aligned with the structures mapped onland which define the eastern limb of the Isparta Angle (e.g., Poisson et al., 2003a,b). Specifically, the prominent thrusts T1–T3 collectively link with the Aksu thrust zone within the Isparta Angle (Hall et al., 2014a). Several studies suggested that the onland Aksu fault zone is a dextral strike-slip system which has overprinted, during the Pliocene–Quaternary, the large Miocene re-activated thrusts (Barka and Reilinger, 1997; Yağmurlu et al., 1997; Poisson et al., 2003a,b, 2011; Piper et al., 2006; Çiner et al., 2008; Toprak et al., 2009). These studies imply that the offshore continuations of these re-activated thrusts must also have a dextral sense of slip.

(c) Anamos–Larnaka–Troodos–South Antalya fault zone

The Amanos–Larnaka fault zone constitutes the arcuate southeastern margin of the Iskenderun–Latakia–Mesaoria Basin Complex (Figs. 6.5, 6.6). The lineament exhibits prominent terrestrial relief in both the Amanos and Troodos Mountains. In the marine Latakia Basin, the lineament can be traced as an arcuate belt extending from the westernmost promontories of the Amanos Mountains southwest toward eastern Cyprus. The Amanos–Larnaka fault zone represents one of two prominent late Cretaceous–Miocene fold-thrust belts (the other is Tartus–Baër Bassit fault zone, discussed below) which are responsible for the emplacement of the ophiolitic bodies in the eastern Mediterranean (Dilek and Moores, 1990). The lineament depicts the leading edge of the thrust system which carries the Hatay and Kızıldağ ophiolite complexes and their Paleozoic–Mesozoic basement in the Amanos Mountains and at least in part the Troodos ophiolite complex in Cyprus (Pişkin et al., 1984; Dean et al., 1986; Gass et al., 1994).

The Amanos fault zone is a prominent north-northeast–south-southwest to northeast–southwest striking transcurrent fault, which delineates the eastern margin of the Amanos Mountains of south-central Turkey (Figs. 6.5, 6.6, Perinçek et al., 1987; Perinçek and Eren, 1990). This fault zone is

one of the main strands of the East Anatolian Fault zone and links the latter with the Dead Sea Fault zone (Perinçek et al., 1987). The Asi Graben (Fig. 6.5) is situated between the Amanos fault zone in the west and the western strand of the Dead Sea Transform Fault in the east (Günay, 1984). In the north, the Asi Graben is a 15–25 km-wide north-northeast–south-southwest trending structure which is bounded on each side by several high-angle normal faults (Dean et al., 1986). In the south the graben trends in a northeast–southwest direction and extends toward the Mediterranean shoreline. In this region the graben is $\sim$5 km-wide and controls the course of the Asi River.

The structural architecture of the marine Latakia Basin is characterized by a prominent northeast-southwest trending and southeast-verging thrust culmination (Figs. 6.5, 6.6; Hall et al., 2005a). Toward the southwest this thrust culmination progressively swings to assume a broadly east-west trend and south vergence. This basement-cored (possibly ophiolite) structure can be readily traced as an arcuate belt from the Asi Graben to the Larnaka region of eastern Cyprus, and is referred to as the Amanos–Larnaka fault zone (Figs. 6.5, 6.6). In the marine areas, there are several northeast–southwest striking, and east-dipping faults with normal-sense dip-slip immediately seaward of the Asi Graben (Hall et al., 2005a). These authors showed that the east–dipping forelimb of the ophiolite-cored basement culmination is transected by a prominent, 1–3 km-wide relatively high-angle extensional fault zone, which extends towards the northeast linking with the northeast–southwest striking, and east-dipping faults.

In southeast Cyprus the Amanos–Larnaka fault zone is defined by a culmination of the Paralimni Mélange at Cape Greco (Follows and Robertson, 1990), the small inlier of the Troodos ophiolite complex near Athienou (Gass, 1960) and the Miocene fold-thrust belt of the Larnaka region (Figs. 6.5, 6.6; Bagnall, 1960). To the west, the fault zone is expressed by the large culmination of the main Troodos ophiolite complex bounded on its southern margin by the Yerasa fold-thrust belt (Gass et al., 1994). The Amanos–Larnaka fault zone probably further extends westward into the region of the Troodos–Mamonia suture zone assemblage (Swarbrick, 1993).

In southern Antalya Basin, this thesis study documented the presence of a prominent northwest-southeast striking, southwest verging prominent thrust, informally referred to as the South Antalya fault (Figs. 6.5, 6.6). This zone extends across the entire width of the southern Antalya Basin aligning in its southeastern segment with the Troodos culmination. It is suggested that the Amanos–Larnaka–Troodos fault zone farther extends toward the northwest linking with the South Antalya fault zone. In keeping with the western segments of the previously described fault zones, it is suggested that the South Antalya fault zone must also have a dextral strike slip component.

(d) Tartus–Baër Bassit–Florence Rise–Anaxagoras fault zone

The greater Cyprus Arc includes the Anaxagoras Mountain and its southeast continuation (the Florence Rise) in the west and the Latakia and Tartus ridges in the east with the narrow zone linking the eastern and western segments of the arc representing the incipient collision between the Eratosthenes Seamount and the Island of Cyprus (Figs. 6.5, 6.6). The Cyprus Arc farther continues into the Baër Bassit complex of western Syria, which represents the other Late Cretaceous to Miocene fold-thrust belts which is responsible for the emplacements of the ophiolitic bodies in the eastern Mediterranean (Dilek and Moores, 1990). The structural framework of the ophiolitic complex is delineated by a series of northeast–southwest-trending northwest-dipping ramp anticlines carried by large crustal-scale thrust faults which sole in the metamorphic basement (Kazmin and Kulakov, 1968, Al Riyami et al., 2000, 2002). The eastern flank of the leading thrust culmination of the imbricate stack is overprinted by the northeast-trending Nahr el Kebir graben that formed during the Pliocene–Quaternary. Further to the northeast, the Nahr el Kebir graben links with the sinistral Dead Sea Fault zone (Kazmin and Kulakov, 1968). The large thrust culminations of the Baër Bassit complex can be readily traced toward the southwest into the northeastern segment of the Tartus Ridge (Figs. 6.5, 6.6). The leading thrust of the ophiolitic complex is correlated with the large Miocene ramp anticline imaged across the Tartus Ridge (Hall et al., 2005b). This correlation suggests that the

Tartus Ridge is probably cored by ophiolitic basement. A similar ophiolitic basement culmination is also inferred for the core of the Amanos–Larnaka culmination further to the north, as described above (Hall et al., 2005a).

The Tartus Ridge is a large bathymetric high that links the Latakia Ridge to the Baër Bassit ophiolitic basement high in northwestern Syria. The southwestern segment of the ridge is clearly imaged in the MUN seismic reflection profiles as a single, very broad and flat-crested structure (Hall et al., 2005b). Further to the northeast, the northwestern edge of the structure is developed into a graben with moderately thick Pliocene–Quaternary strata cut by several normal faults. The structural architecture of the Tartus Ridge is characterized by a series of northeast-southwest striking and both southeast and northwest verging large thrusts developed within the pre-Messinian Miocene and older successions (Figs. 6.5, 6.6). Hall et al. (2005b) interpreted the Tartus Ridge as a broad transpressive pop-up, bounded by oppositely verging backthrust and forethrust situated at the footwall cutoffs of the M-reflector.

Toward the southwest, the Tartus Ridge transitions into the Latakia Ridge, which is a prominent northeast trending narrow structure, linking the southern sector of the Hecateus Ridge with the Latakia region of the northern Levantine coast (Figs. 6.5, 6.6). Farther west, the ridge emerges gradually from the lower slope of the Hecataeus Rise. The Latakia Ridge has a distinct morphological expression on the seabed. The ridge is interpreted as a positive flower structure that developed by reactivation of the southeast-verging thrust ramp anticline cored by a blind thrust (Hall et al., 2005b).

Farther to the west and northwest, the Florence Rise and its continuation into the Anaxagoras Mountain defines the western sector of the greater Cyprus Arc. This study documented that the Florence Rise represents a prominent pre-Messinian Miocene and older fold-thrust belt, which was characterized by several northwest-southeast striking and predominantly southwest verging large thrust culminations (Figs. 6.5, 6.6; § Chapter 5). During the latest Miocene–Quaternary this fold-thrust belt experienced transpressional deformation when several northeast verging thrusts developed. The

resultant large scale basin inversion across the Florence Rise (*sensu stricto*) and the numerous pop-up structures that are developed across the regional structure suggest that the region is transected by a wrench (§ Chapter 5). This interpretation is consistent with previous studies which also suggested the development of a dextral wrench across the Florence Rise (Zitter et al., 2003; Sellier et al., 2013a,b).

(e) Herodotus fault zone

There is very little published from this region of the eastern Mediterranean Sea. Sparsely-spaced industry multichannel profiles show that this zone extends from the leading thrusts of the Florence Rise toward the south and includes the Mediterranean Ridge (Figs. 6.5, 6.6). The Herodotus fault zone is characterized by 3–7 large northeast-southwest striking and mainly northwest verging thrusts which are located immediately northwest of the orthogonal extensional oblique faults of the Nile delta. The southeastern boundary of the zone is delineated by two prominent northeast-southwest striking but southeast verging large thrusts (Kopf et al., 2003). The zone defines a 25–60 km wide arcuate belt that delineates the boundary (based on the upper crustal deformation on the down-going slab) between the African Plate in the south and the Aegean–Anatolian Microplate in the north.

Summary of fault zones associated with the Cyprus Arc

- The Kozan–Anamur-Silifke–Kırkkavak fault zone forms a arcuate structure immediately south of the similarly trending central Taurus Mountains of southern Turkey (Fig. 6.6). It is a relatively young structure developed during the Pliocene–Quaternary as a sinistral strike slip along the Kozan and possibly the Anamur-Silifke sectors of the fault zone, but farther continues toward the northwest as a dextral strike slip along the northeastern Antalya Basin linking with the onland Kırkkavak fault zone.

- The Misis–Kyrenia–Aksu fault zone defines a prominent orocline that extends the entire width

of the orogen from the Misis Mountains of southern Turkey to the Kyrenia Range of northern Cyprus to the eastern limb of the Isparta Angle, paralleling the Kozan–Anamur-Silifke–Kırkkavak fault zone (Fig. 6.6). The Misis–Kyrenia–Aksu fault zone represents a major fold-thrust belt which is reactivated during the Pliocene–Quaternary as a sinistral strike slip along the Misis–Kyrenia segment, but a dextral strike slip along the Aksu–Kyrenia segment, while the Kyrenia segment remaining contractional.

- Similarly, the Amanos-Larnaka-Troodos-Antalya Fault zone also defines a prominent orocline linking the Amanos Mountains of south-central Turkey to the Troodos mountains of Cyprus via the Amanos-Larnaka-Troodos culmination, then extending farther northwest linking with the Antalya fault zone. The eastern segment of this fault zone also exhibits sinistral strike slip, and the western segment is suggested to display dextral strike slip in keeping with the Kozan–Anamur-Silifke–Kırkkavak, Misis–Kyrenia–Aksu and the Tartus–Baër Bassit–Florence Rise–Anaxagoras fault zones.

- The Tartus–Baër Bassit–Florence Rise–Anaxagoras fault zone defines a prominent arcuate orocline across the eastern Mediterranean, similar to the above described three oroclines. It developed as a major fold-thrust belt, which later became overprinted by strike-slip activity during the Pliocene–Quaternary. Similar to the above-described fault zones, the eastern and western segments of the Tartus–Baër Bassit–Florence Rise–Anaxagoras fault zone show sinistral and dextral strike slip, respectively. The Tartus–Baër Bassit–Florence Rise–Anaxagoras fault zone further delineates the hard boundary (based on the overriding slab) between the African Plate in the south and the Aegean–Anatolian Microplate in the north.

- The Herodotus fault zone is a northeast–southwest trending structure terminating along the western margin of the Eratosthenes Seamount. It represents the Mediterranean Ridge.

The above literature review and summary clearly show that (a) the forearc region across the eastern Mediterranean includes 4–5 prominent fault zones, indicating that the deformation associated with the African Plate and Aegean–Anatolian Microplate convergence is distributed across a 250–350 km zone (if the present-day Central Taurus Mountains are also included), (b) the fault zones are all developed during the Pliocene–Quaternary over the prominent pre-existing Miocene fold-thrust belt across the region, and (c) the fault zones all display strike slip in addition to contraction (and to a lesser extent extension), with the eastern segments of the fault zones invariably showing sinistral strike slip, whereas the western segments showing dextral strike slip. The fact that the eastern and western segments of the fault zones respectively have sinistral and dextral strike slip poses a major kinematic conundrum: any kinematic model dealing with the tectonic evolution of the eastern Mediterranean must account for the south-directed extrusion of the central Anatolia, while explaining the west-directed tectonic escape of the Aegean-Anatolian Microplate.

(f) Pliny–Strabo–Burdur–Fethiye fault zone

The Burdur–Fethiye fault zone is a 75–90 km wide northeast-southwest trending structure across southwestern Turkey (Figs. 6.2, 6.3). It cuts through the eastern area of the Lycian nappes close to their boundary with the Beydağları para-autochthon to the east (Şenel, 1997a,1997b; Şenel and Bölükbaşı, 1997). The fault zone lies along the boundary between the Aegean extensional domain and more stable central Anatolia (Barka and Reilinger, 1997; Dumont et al., 1979). The fault zone includes many short segment near-vertical northeast–southwest striking faults, showing normal offsets, with some showing dextral strike-slip such as those seen in the Çameli Basin (Alçiçek et al., 2006). Elitez et al. (2015) showed that there is differential motion across the Burdur–Fethiye fault zone. For example, these authors documented that close to the Turkish coast, the GPS vectors directed to the southwest vary from 25 mm yr^{-1} on the northwest side of the zone to 13 mm yr^{-1} on the southeast side of the zone. They argued that the simplest interpretation of this differential

motion is that there is a left lateral displacement of 12 mm yr $^{-1}$ across the fault zone. Elitez et al. (2015) showed that farther to the northeast, the differential motion across the Burdur–Fethiye fault zone is 7 mm yr^{-1}, which supports the left lateral displacement decreasing to the northeast. These authors further indicated that the northeast decrease of the displacement is be expected of a break in the down-going slab of the African plate as it propagates into the upper Aegean–Anatolian Microplate. They noted that such motion, if continued over 5 Ma, would give an overall displacement of a few tens of kilometres, distributed over the 75–90 km width of Burdur–Fethiye fault zone. Finally they concluded that the strain, distributed over many faults, would only result in small offsets across individual faults, particularly those seen in younger Quaternary strata.

The pre-Messinian Miocene structural architecture of the Rhodes Basin demonstrates the basin-wide presence of a prominent northeast–southwest striking and invariably southeast verging fold–thrust belt (Figs. 6.5, 6.6, Hall et al., 2009, 2014b). The fold-belt is composed of 6–7 thrust panels, which are $\sim$3–7 km apart from one another, delineated by asymmetric anticline–syncline pairs, where the anticlines exhibit long, gently northwest-dipping back limbs and shorter and more steeply southeast-dipping forelimbs, suggesting that these structures define southeast-verging fold system (Hall et al., 2009, 2014b). Internally, the core of the ridges are characterized by strongly reflective, generally gently folded reflectors of Unit 3. Hall et al. (2014b) documented that this fold–thrust belt conspicuously extends from the southwestern segment of the Rhodes Basin immediately northeast of the Pliny–Strabo Trenches toward the Burdur–Fethiye Fault Zone. Hall et al. (2014b) also demonstrated that the architecture of the Pliocene-Quaternary successions in the Rhodes Basin is characterized by a series of northeast–southwest trending ridges and their intervening basins, where Miocene thrust culminations also define Pliocene–Quaternary thrust culminations. These authors used the coincidence of the Miocene and Pliocene–Quaternary fold–thrust structures to suggest that older thrusts became re-activated during the Pliocene-Quaternary.

(g) Sırrı Erinç shear zone

The Sırrı Erinç Plateau defines a concave-to-the-north zone between the Anaximenes/Anaxagoras Mountains in the southeast and the Finike Basin and the Anaximander Mountain (*sensu stricto*) in the north and northwest (Figs. 6.5, 6.6, Appendix 1, Aksu et al., 2009, Barnes 2015). The zone is bounded in its north and northeast by a prominent broadly east-west striking, but curvilinear north-verging thrust that separates the Finike Basin to the north (Figs. 6.5, 6.6, Appendix 1, Aksu et al., 2009, 2014c, Barnes, 2015). This thrust (TT0) links with a north-south striking and west-verging thrust (R1) that defines the northwestern margin of the Sırrı Erinç Plateau (Figs. 6.5, 6.6, Appendix 1). To the west, the north-south striking thrust (R1) in turn links with the broadly east-west striking and south verging thrust (TT1) that bounds the southern margin of the Anaximander Mountain (Aksu et al., 2009, Barnes, 2015). This thrust (TT1) extends into the southern Rhodes Basin, where it links with another north-south striking west verging thrust (R2), which delineated the western margin of the Sırrı Erinç Plateau in southern Rhodes Basin (Figs. 6.5, 6.6, Appendix 1, Hall et al., 2009, Barnes, 2015). Thus, the northern margin of the Sırrı Erinç Plateau is composed of two east-west striking (TT0, TT1) and two north-south striking (R1, R2) major thrusts (Figs. 6.5, 6.6, Appendix 1). The southern margin of the Sırrı Erinç Plateau follows a similar trend to its northern margin. In the east an arcuate zone delineated by a broadly northeast-southwest striking and northwest verging thrust separates the Sırrı Erinç Plateau from the Anaxagoras and Anaximenes Mountains (Figs. 6.5, 6.6, Appendix 1, Aksu et al., 2009, Barnes 2015). Toward the west, this thrust gradually merges with an east-west striking and south verging thrust (TT2) that defines the southern margin of the Anaximenes Mountain. Farther to the west a broadly north-south striking and west verging thrust (R3) links with thrust TT2 (Figs. 6.5, 6.6, Appendix 1, Barnes 2015).

Thus, the zone that defines the Sırrı Erinç Plateau is 50 km wide in the northeast but notably narrows to $\sim$25 km in the west. The surface morphology of the Sırrı Erinç Plateau is characterized by numerous lazy-S shaped lineations which render an irregularly-corrugated seafloor appearance.

In the northern portion of the plateau immediately south of the Finike Basin, these corrugations are west-northwest–east-southeast and/or northwest-southeast orientation; whereas in the western portion of the plateau, the corrugations are notably north-northwest–south-southeast oriented (Barnes, 2015). The Sırrı Erinç Plateau is interpreted as a 25–50 km wide complex sinistral shear zone (Figs. 6.5, 6.6, Aksu et al., 2009, Hall et al., 2009, Barnes 2015).

Summary of fault zones associated with the northeast segment of Hellenic Arc

- The Pliny–Strabo–Burdur–Fethiye fault zone is a 75–90 km zone that extends from the Pliny-Strabo Trenches toward the northeast delineating the western limb of the Isparta Angle (Figs. 6.5, 6.6). This zone is characterized by several prominent thrusts across the deep Rhodes Basin, but transitions into a swarm of high-angle extensional faults across the northern shelf region of the Rhodes Basin as well as across southwestern Turkey: in all regions it exhibits sinistral strike slip.

- The Sırrı Erinç shear zone defines an arcuate north-facing concave up zone between the Anaximenes/Anaxagoras Mountains in the southeast and the Finike Basin and the Anaximander Mountain (*sensu stricto*) in the north and northwest (Figs. 6.5, 6.6). It is bounded both on its northern and southern margin by two east-west striking thrusts which are linked with two north-south striking thrusts (Figs. 6.5, 6.6). The zone is interpreted as a sinistral shear zone at the critical junction between the Hellenic and Cyprus arcs.

6.3.2 Northern passive continental margin – African Plate

(a) Offshore Nile delta

The Pliocene–Quaternary tectonic architecture of the northern margin of the African Plate immediately south of the boundary between the African Plate and the Aegean–Anatolian Microplate has a dramatically different character from that of the forearc region described above (Figs. 6.5, 6.6).

This region is characterized by two prominent sets of oblique faults with notable dip-slip components that transect one another in an orthogonal fashion (Harrison et al., 2004, Abd-Allah et al., 2012, Othman et al., 2014). One set displays northwest-southeast strike, predominantly northeast dips and invariably dextral strike slip (e.g., the Temsah and Misfaq-Bardawil trend), while the other set exhibits northeast-southwest strike, predominantly northwest dips and invariably sinistral strike slip (e.g., the Qattara-Rosetta trend). These faults show a complicated intersection pattern south and southeast of the large Messinian evaporite structures developed within the Herodotus Basin (Abdel Aal et al., 2000, 2001, Abd-Allah et al., 2012, Othman et al., 2014). The onshore portion of the Nile delta is affected by several east–west striking and both north- and south-dipping extensional fault that show predominantly dextral strike-slip components (e.g., Abd-Allah et al., 2012). These faults are also observed in the nearshore region north of the Nile coastline; however they are absent further northward in the region of the orthogonally intersecting oblique faults.

The orthogonally intersecting faults cut the entire Pliocene–Quaternary successions, extending to the seafloor where they create very prominent morphologies (Fig. 6.7). For example, detailed multibeam images by the Prismed II survey revealed the presence of an intricate network of quasi-linear seafloor depressions running tens to hundreds of kilometers in the direction of N145°E, which are flanked by small and discontinuous ridges (Fig. 6.7, Mascle et al., 2000). These features are clearly identified on seismic reflection lines, as large normal-slip master fault zones with vertical offsets on the order of 1.5 s twt (Mascle et al., 2000). These authors identified secondary but well marked seafloor depressions trending N160°E which appear closely associated with the main faults. Mascle et al. (2000) interpret these seafloor lineations and the underlying faults as R Riedel-type fractures. At lat 33°N, long 32°E, the central master fault is interrupted by a depression that displays the characteristics of a releasing overstep along a N145°E transcurrent trend (Fig. 6.7). Within the central and southern portions of the Nile delta series of minor ridges and troughs are identified whose axial trends vary between N15°E and N90°E, where the depressions display the character of typical

sigmoidal tension gashes (Mascle et al., 2000). These authors suggested that the N145°E normal-slip master faults have a horizontal strike-slip component and may thus be interpreted as transcurrent transtensive type faults.

(b) Levantine margin

The Levantine margin is one of the least tectonically active regions of the eastern Mediterranean. Here the Pliocene–Quaternary successions are generally undisturbed, except for 2–3 large north-northeast–south-southwest striking and invariably west-northwest dipping listric normal faults across the basin margin which show notable growth and roll-over (Figs. 6.5, 6.6; Khair and Tsokas, 1999, Gardosh et al. 2008a,b, Carton et al., 2009, Gvirtzman et al., 2010, Skiple et al., 2012). These authors also indicated that this fault system must have a sinistral strike slip component. Neev and Hall (1982) suggested that the north-northeast–south-southwest trend (particularly also observed in the Miocene and older strata) is part of a major system of *en échelon* left-lateral megashears that dominated the region since the Precambrian.

6.3.3 Paleomagnetic data and block rotations

A recent MSc thesis at Memorial University of Newfoundland provided an excellent review of the paleomagnetic data and the associated block rotations across central and western Turkey (Barnes, 2015). The summary figure in this study is shown here because it provides a comprehensive insight to the Miocene to Recent block movements and rotations (Fig. 6.8). Barnes (2015) correctly stated that "...the tectonic evolution of the northwestern portion of the eastern Mediterranean cannot be viewed in isolation and that it must be integrated with the tectonic evolution of the southwestern Turkish mainland...". She carried out a thorough evaluation of the onland paleommagnetic studies where block rotations are delineated (Kissel and Poisson, 1986; Sen and Valet, 1986; Kissel et al. 1987, 1989, 1993, 2003; Duermeijer et al., 1989; Tatar et al., 2002; Gürsoy et al., 1989, 2003;

Kondopoulou et al., 1993; Piper et al., 2010; van Hinsbergen et al., 2007, 2010a,b,c; Meijers et al. 2011).

Van Hinsbergen et al. (2007) showed that from 3.8 to 3.6 Ma, Rhodes experienced 9±6° counterclockwise vertical axis rotation, which was followed from 2.5 to 1.8 Ma by southeast tilting and 500–600 m of subsidence of the southeastern coast, leaving the rest of the island above sea level. These authors further documented that between 1.5 and 1.1 Ma, the Island of Rhodes tilted to the northwest and the southeastern coast re-emerged above sea level, which was followed by a tectonic phase of 17±6° counterclockwise rotation post 0.8 Ma. These data show that, the oldest (∼4.2–3.8 Ma) successions on the island experienced ∼26±6° counterclockwise rotation (Fig. 6.8). The northwest tilting of the Island of Rhodes was also reported by Kontogianni et al. (2002), where the tilting was ascribed to a prominent northeast-southwest striking thrust fault imaged in the northwestern margin of the deep Rhodes Basin in a seismic reflection profile illustrated by Woodside et al. (2000). Van Hinsbergen et al (2007) also argued that the vertical motions observed on the Island of Rhodes must have occurred along normal faults and a well-constrained thrust fault offshore, illustrated along the eastern margin of the island by Woodside et al. (2000).

Along the eastern portion of the Island of Crete, Duermeijer et al. (1998) reported consistent counterclockwise rotations in the late Miocene-Pleistocene successions and concluded that the observed rotation pattern resulted from the left-lateral strike-slip deformation associated with southwestward wrenching along the Pliny and Strabo Trenches (Fig. 6.8). To the north, Sen and Valet (1986) reported a small counterclockwise rotation (6±4°) from the Island of Samos since the middle Miocene.

Paleomagnetic data showed that the southwestern Turkey (i.e., Beydağları region) underwent no rotation between the Late Cretaceous and Late Burdigalian, but experienced an ∼20° counterclockwise rotation between 16 and 5 Ma (Fig. 6.8, van Hinsbergen et al., 2010a). Paleomagnetic data from the Pliocene sediments within the apex of the Isparta Angle showed that this region had no sig-

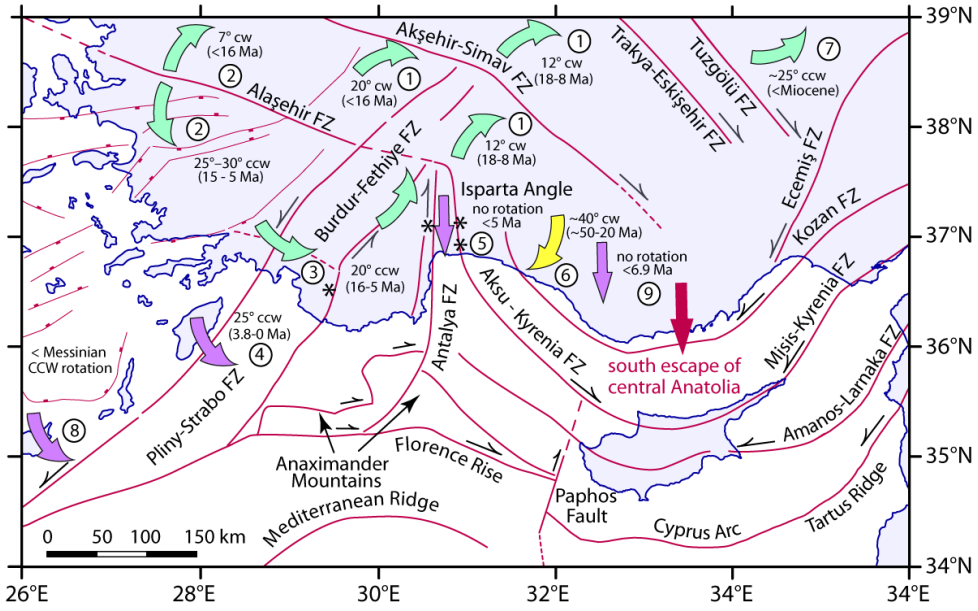

Figure 6.8: Map of the eastern Mediterranean showing the major tectonic elements and the block rotations delineated using paleomagnetic studies (adopted from Barnes, 2015). yellow arrow= pre-Miocene; aqua= Miocene, purple= Pliocene-Quaternary rotations. Paleomagnetic data from: 1= Gürsoy et al. (2003), 2= van Hinsbergen et al. (2010b,c), 3= van Hinsbergen et al. (2010a), 4= van Hinsbergen et al. (2007), 5= Kissel and Poisson (1986), 6= Kissel et al. (1993), 7= Tatar et al. (2002), 8= Duermeijer et al. (1998), 9= Piper et al. (2010). Tectonic data from: Akşehir-Simav Fault Zone (FZ)= Koçyiğit and Özacar (2003), Gürsoy et al. (2003); Aksu-Kyrenia FZ= Işler et al. (2005), Hall et al. (2014b), Barnes (2015); Alaşehir FZ= Francalanci et al. (2000), van Hinsbergen et al. (2010b,c); Amanos-Larnaka FZ= Hall et al. (2005b); Anaximander Mountains= Aksu et al. (2009), Barnes (2015); Antalya FZ= Savaşçın et al. (1995), Glover and Robertson (1998a,b), Francalanci et al. (2000), Hall et al. (2014a), Barnes (2015); Cyprus Arc= Welford et al. (2015), Hall et al. (2005b); Ecemiş FZ= Aksu et al. (2005a, 2014b,c); Kozan FZ= Aksu et al. (2005a, 2014b,c); Mediterranean Ridge= Kopf et al. (2003); Misis-Kyrenia FZ= Aksu et al. (2005a, 2014b,c); Paphos FZ= Papadimitriou and Karakostas (2006); Pliny-Strabo FZ= Hall et al. (2014b), Barnes (2015); Tartus Ridge= Hall et al. 2005b; Trakya-Eskişehir FZ= Bozkurt (2001), Yaltırak (2002); Tuzgölü FZ= Gürsoy et al. (1998, 2003). Red arrow is the postulated south-directed extrusion of the Central Anatolian Block along the dextral Aksu-Kyrenia, Akşehir-Simav, Trakya-Eskişehir, Tuzgölü Fault Zones and the sinistral Misis-Kyrenia, Kozan and Ecemiş Fault Zones.

nificant rotation since the Pliocene (Kissel and Poisson, 1986). These data strongly suggest that the middle to late Miocene rotation of the Beydağları region must have taken place prior to deposition of the non-rotated Pliocene sediments within the core of the Isparta Angle (van Hinsbergen et al., 2010a).

Kissel et al. (2003) published paleomagnetic data which showed that the central Anatolian block experienced a $\sim$25° counterclockwise rotation during the Miocene (Fig. 6.8). These data suggest the possibility that the 20° counterclockwise rotation of the Beydağları region may be related to the 25° counterclockwise rotation of the Anatolian block. However, van Hinsbergen (2010a) indicated that the Beydağları region forms the eastern limb of the Aegean orocline (Fig. 6.1, 6.5), and that it rotated within the same time span of 16-5 Ma, in synchroneity with the western limb, and that it must have been rotating independent of the central Anatolian block (van Hinsbergen et al. 2005). Furthermore, van Hinsbergen et al. (2010a) suggested the rotation of the block that hosts the Beydağları was probably bounded in the south at the boundary between the Africa Plate and the Aegean-Anatolian Microplate and that in the east the Aksu thrust and the Kırkkavak dextral strike-slip fault must have together partitioned the dextral transpression induced by the rotation of the Beydağları block. However, Barnes (2015) pointed out that, because the northeastern portion of the Beydağları region experienced an approximately 20° counterclockwise rotation 16-5 Ma (van Hinsbergen et al., 2010a), while the Afyon region immediately northeast of the Isparta Angle experienced a mean clockwise rotation of $\sim$12° during 18-8 Ma (Gürsoy et al., 2003), there must exist a fundamental boundary between the Beydağları block and the eastern limb of the Isparta Angle (Figs. 6.8, 6.9). Barnes (2015) argued that this fundamental boundary must be located at or west of the eastern limb of the Isparta Angle, thus can be at the Aksu Thrust and the Kırkkavak dextral strike-slip fault as suggested by van Hinsbergen et al. (2010a). She indicated that if this boundary is correctly placed at the Aksu Thrust and the Kırkkavak dextral strike-slip fault, this geometry requires that the eastern boundaries of the counterclockwise-rotating block must include the Aksu-Kyrenia Fault Zone, the Paphos Fault and

the Florence Rise (Fig. 6.5). Barnes (2015) further argued that the identification and mapping of the Antalya fault zone as a dextral strike slip along the western sector of the Antalya Basin (Hall et al., 2014a, Barnes, 2015) provides an alternative eastern boundary for the Beydağları block. She indicated that regardless of where the boundary of the counterclockwise rotating Beydağları block was (i.e., Aksu Thrust–Kırkkavak dextral strike-slip fault versus the Antalya Fault Zone) it must have extended southwest linking with the Miocene Hellenic Arc (Fig. 6.5), which requires that it must have had a dextral slip component during the Miocene. This region presently forms the Pliny-Strabo Trenches and exhibits a sinistral strike slip regime.

The paleomagnetic data presented in van Hinsbergen et al. (2010a) show that the Lycian Nappes were emplaced prior to the rotation of the Beydağları and the fundamental thrusts situated between these units did not form the boundary for the rotation, suggesting that the Beydağları region and the Lycian Nappes formed a cohesive unit during the Miocene. The $\sim 20^{\circ}$ rotation of the Lycian Nappes and Beydağları between 16 and 5 Ma, occurred contemporaneously with the exhumation of the central Menderes Massif along prominent extensional detachments: following the latest Oligocene to early Miocene exhumation of the northern and southern Menderes massifs (van Hinsbergen et al., 2010c). The lower Miocene volcanics in the region from Lesbos to Uşak revealed that exhumation of the central Menderes Massif was associated with a vertical axis rotation difference between the northern and southern Menderes massifs of $\sim 25^{\circ}$–30° (van Hinsbergen et al., 2010c). These authors noted the divergence of the rotations along a northwest-southeast line extending from the apex of the Isparta Angle toward the southern shores of the Island of Lesbos, and suggested that the northwest-southeast striking prominent Alaşehir fault that bound the Alaşehir and the eastern segment of the Büyük Menderes graben may delineate the northern boundary of the $\sim 20^{\circ}$ rotation in the Lycian Nappes and Beydağları block during the middle-late Miocene (Figs. 6.8, 6.9).

Barnes (2015) indicated that the evaluation of the paleomagnetic data clearly suggests that the core of the Aegean-Anatolian Microplate is fragmenting along a group of northwest-southeast ori-

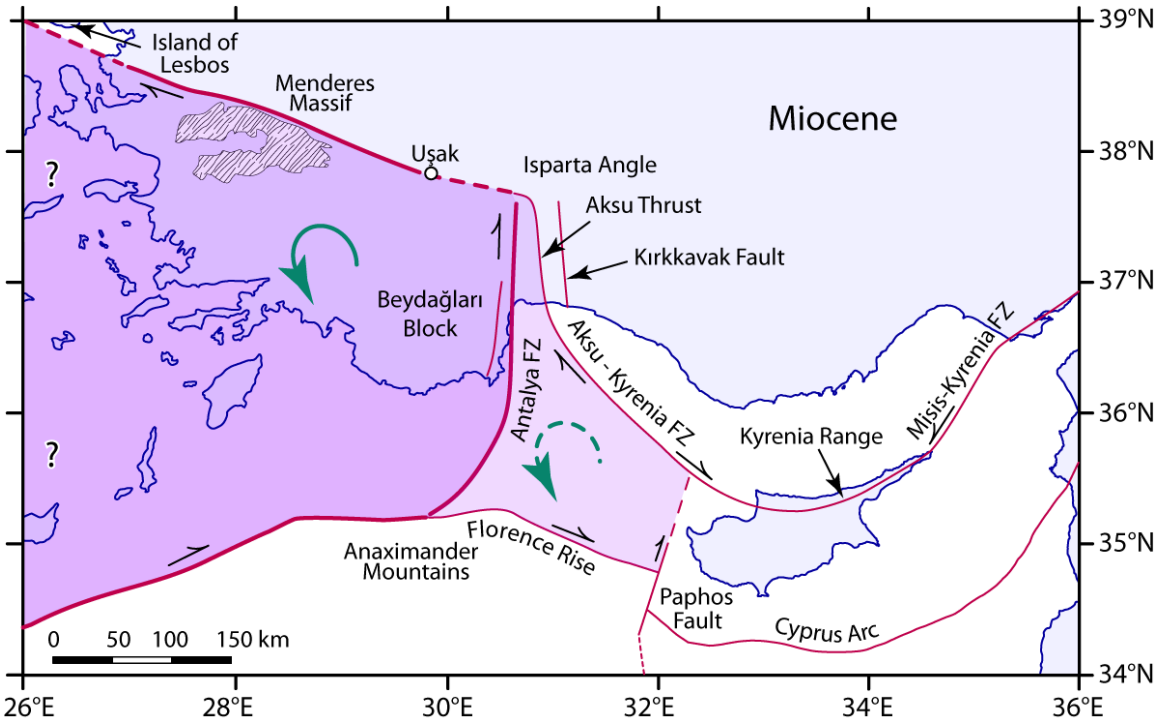

Figure 6.9: Map of the eastern Mediterranean showing the probable boundaries of late Miocene block rotation including the Beydağları region and the Lycian Nappes (adopted from Barnes, 2015). Appendix 1 Uppermost Messinian–Recent tectonic map of the eastern Mediterranean. Map is compiled by Aksu using data from (a) Florence Rise (Güneş, this thesis); (b) Rhodes and Finike basins, Anaximander Mountains (Hall et al., 2009, Aksu et al., 2009, Cranshaw, 2010, Barnes, 2015), (c) Adana, Cilicia, Latakia, Iskenderun basins (Aksu et al., 2005, 2014a,b, Hall et al., 2005a,b, Walsh-Kennedy et al., 2014), (d) offshore Israel, offshore Lebanon, Levantine Basin (Carton et al., 2009, Gvirtzman et al., 2010, Gardosh et al., 2008b), (e) Eratosthenes Seamount, Herodotus Basin (Montadert et al., 2010, Skiple et al., 2012), (f) offshore Syria (Bowmann 2011), and (g) Nile delta (Mascle et al., 2000, Abd-Allah et al., 2012). The coastline is from the International Bathymetric Charts of the Mediterranean (IOC, 1981). Brown lines = thrust faults with triangle ticks on hanging wall, red lines = normal faults with rectangular ticks on hanging wall, green lines = strike slip faults with purple half arrows showing slip direction, green fill = ophiolites. This figure is also shown in Figure 6.5.

ented dextral strike-slip fault zones (Aksu-Kyrenia, Akşehir-Simav, Trakya-Eskişehir, Tuzgölü Fault zones) in the west that are complemented by another group of northeast-southwest oriented sinistral strike-slip fault zones (Misis-Kyrenia, Kozan and Ecemiş Fault zones) in the east. She pointed out that these oppositely oriented strike-slip fault zones require the broadly south-directed extrusion of the Central Anatolian Block toward a zone of regional convergence along the Kyrenia Range of northern Cyprus (Fig. 6.8). Barnes (2015) noted a first order similarity between the postulated south-directed extrusion of the Central Anatolian Block and the south-directed migration of the Aegean sector of the Aegean-Anatolian Microplate toward the Hellenic Arc and pointed out that the western and eastern segments of the Hellenic Arc similarly show a 25° clockwise rotation in the Pliocene-Quaternary and a 30° counterclockwise rotation in the middle-late Miocene, respectively (e.g., Kissel and Laj, 1988). Here, the westerly moving Aegean-Anatolian Microplate is colliding with the Apulia–Adriatic platform (Underhill, 1989), and was forced to progressively rotate counterclockwise toward the free face along the Hellenic Arc (Mann, 1997). The pulling of the subducting African Plate beneath the Hellenic Arc associated with trench suction due to roll-back of the Hellenic arc is mainly responsible for the south-directed migration of the Aegean sector of the Aegean-Anatolian Microplate (Ganas and Parsons, 2009; Rontogianni et al., 2011). Barnes argued that this first order similarity between the south-directed migrations between the Aegean and Central Anatolian sectors of the Aegean-Anatolian Microplate poses the question whether the processes associated with the postulated south-directed extrusion of the Central Anatolian Block are related to the roll back of the subducting slab beneath the Cyprus Arc during the Pliocene-Quaternary.

6.4 Latest Messinian–Recent tectonic evolution of the eastern Mediterranean

Many previous studies on the tectonic and kinematic evolution of the eastern Mediterranean documented the occurrence of a dramatic change in the style of deformation from the Late Miocene into the Pliocene (e.g., Hall et al., 2005a,b, 2009, 2014a,b, Calon et al., 2005a,b, Aksu et al., 2005a,b, 2009, 2014a–c). These studies stressed the tectonic quiescence during the Messinian as a signal for the switch in the regional tectonic regime. The primary cause of this tectonic switch is related to the collision and subsequent suturing of the Arabian Microplate with the Eurasian Plate (Şengör and Yılmaz, 1981, Dewey et al., 1986, Toksöz et al., 2007). In fact, this collision is responsible for the development of the Aegean-Anatolian Microplate, as it forced a large continental fragment along the southern margin of the Eurasian Plate to start a west-directed tectonic escape (e.g., Şengör et al., 1985, Mann, 1997). Thus, the west-directed tectonic escape of the Aegean-Anatolian Microplate during the Pliocene, in turn, resulted in the partitioning of strain across the southern boundary between the African Plate and the Aegean-Anatolian Microplate.

The summary of structures presented in this chapter clearly show that there is a very wide zone of deformation extending from the southern fringes of the Mediterranean Ridge across the entire forearc region into Taurus Mountains of southern Turkey. The specific study area is only a small region within this broad evolving orogen. The discussion on the uppermost Messinian–Recent (i.e., Unit 1) temporal evolution of the orogen requires the establishment of a tight chronostratigraphic framework (§ Chapter 3). As shown in Chapter 3, the chronology of the seismic stratigraphic units only allows a first order timeframe. Therefore, the following discussion will be presented under the following headings: (a) lower Unit 1, (b) middle Unit 1 and (c) late Unit 1.

(a) Lower Unit 1 (early portion of uppermost Messinian–Recent)

The prominent southerly-verging thrusts that dominated the pre-Messinian Miocene and the Messinian are largely confined to successions developed below the M-reflector. Only a limited number of large thrusts remained active during the early uppermost Messinian–Recent, such as those described in the deep Rhodes Basin (Hall et al., 2009, 2014b), Anaximander Mountains (Aksu et al., 2009, 2014c), the west-central Antalya Basin (Işler et al., 2005, Hall et al., 2014a) and the Florence Rise (this study). Many prominent fault zones became reactivated as transtensional and transpressional systems. For example, during the Pliocene–Quaternary the Misis–Kyrenia sector of the Misis–Kyrenia–Aksu fault zone is developed as a prominent horst, with notable sinistral strike-slip (Calon et al., 2005a, Aksu et al., 2005a, Hall et al., 2005a). Similarly the Amanos–Larnaka sector of the Amanos–Larnaka–Troodos–South Antalya fault zone is reactivated as a prominent graben in the northeast which linked with a complicated extensional fault zone that is developed over the southeast-verging large thrust panels (Hall et al. 2005a,b). Previous studies documented the linkages of the northeastern sectors of the prominent fault zones with the East Anatolian Fault zone which developed as a response to the collision of the Arabian Microplate with Eurasia, and the development and west directed escape of the Anatolian sector of the Aegean–Anatolian Microplate. In fact, a horse-tail like faults, all with notable sinistral strike slip spay off from the main branch of the East Anatolian fault zone, extending toward the southwest.

The western sectors of the prominent zones also became reactivated during the early uppermost Messinian–Pliocene. For example, the Aksu thrust became reactivated during the Pliocene, exhibiting compression and dextral strike slip (Poisson et al., 2003a,b, 2011). Similarly, the Kırkkavak fault zone also became reactivated during the Pliocene as a prominent thrust again with dextral strike slip (Dumond and Kerey, 1975; Çiner et al., 2008). Finally, this study documented that the Florence Rise became reactivated as a broad fold-thrust belt during the early uppermost Miocene–Pliocene (§ Chapter 5). Previous studies suggested that the Florence Rise developed as a dextral wrench dur-

ing the Pliocene–Quaternary (Zitter et al., 2003; Sellier et al., 2013a,b): however, this study clearly documented that the timing of this wrench development is during the middle uppermost Messinian–Recent, as further discussed below.

(b) Middle Unit 1 (middle portion of uppermost Messinian–Recent)

During the deposition of the middle Unit 1 (i.e., the middle portion of the uppermost Messinian–Recent) there was a major tectonic upheaval across the southern portion of the forearc region. Across the Florence Rise and the southern sector of the Antalya Basin, this interval is marked by a conspicuous unconformity, which toward the deeper Antalya Basin becomes conformable within the strongly stratified Unit 1 successions (§ Chapter 5). This unconformity, labeled as the γ-reflector, is best imaged across the crestal region of the Florence Rise, where a former basin that accumulated a thick succession of lower Unit 1 strata (i.e., the lower portion of the uppermost Miocene–Recent) became inverted during the deposition of the middle portion of Unit 1. A similar unconformity and the associated basin inversion is also mapped across the Amanos–Larnaka Ridge in Latakia Basin (Hall et al., 2005a, Calon et al., 2005a). Farther west across the northern foothills of the Anaximander Mountain (*sensu stricto*) the prominent mid-Unit 1 unconformity, also represented by the γ-reflector is delineated and mapped (Aksu et al., 2009, Cranshaw, 2010). Recent re-evaluation of the previously collected seismic reflection profiles clearly show that the γ-reflector can be readily traced and mapped as a prominent unconformity across the southern margin of the Rhodes Basin (Aksu, personal communication, May-June, 2016). Across the Anaximander Mountain and southern Rhodes Basin, the γ-reflector separates a isopachous lower Unit 1 from the upper Unit 1 which show remarkable growth over the γ-reflector. This geometry is interpreted as the onset of the reactivation of the forethrust that carries the Anaximander Mountain (e.g., Aksu et al., 2009), while the Rhodes Basin experienced a dramatic subsidence during the middle uppermost Messinian–Recent interval (Aksu et al., in prep).

This tectonically active interval is believed to be the result of the docking and incipient collision of the Eratosthenes Seamount with the Island of Cyprus (e.g., Robertson et al., 1995, Kempler 1998, Galindo-Zaldívar et al., 2001). The Kyrenia Range and the Mesaoria Basin (Cyprus) also became emergent during the Pliocene–Quaternary, where the uplift was accelerated by the docking of the Eratosthenes (Calon et al., 2005a,b).

(c) Upper Unit 1 (upper portion of uppermost Messinian–Recent)

This interval is marked by a dramatic collapse of the Rhodes and Finike basins in the west (Hall et al., 2009, 2014b, Aksu et al., 2009, 2014c), and continued subsidence of the Cilicia, Latakia and Cyprus basins in the east (Walsh-Kennedy et al., 2014, Hall et al., 2005a,b). The morphological expression of the major fault zones became prominent as these structures further developed, such as the development of a major wrench and inversion of the Florence Rise (this study), uplift of the Anaximander Mountains south of the Rhodes and Finike basins (Aksu et al., 2009, Barnes, 2015), the development of the prominent horst block across the Misis–Kyrenia fold-thrust belt (Aksu et al., 2005a, 2014a,b, Hall et al., 2005a, Walsh-Kennedy et al., 2014), as well as the accelerated growth of the Latakia and Tartus ridges along the eastern sector of the Cyprus Arc (Hall et al., 2005b).

A very prominent feature of the eastern Mediterranean today is the Eratosthenes Seamount and the way in which it shaped the evolving orogen (Figs. 6.5, 6.6). It appears as an indentor in the region, clearly visible both in the present-day seafloor morphology of the eastern Mediterranean (Fig. 6.7) as well as the regional curvatures of the major fault zones, particularly those which occupy the southern margin of the orogen.

The docking of the Eratosthenes Seamount is also clearly affecting the style of deformation across the passive margin successions, immediately south of the African Plate – Aegean–Anatolian Microplate boundary (Figs. 6.5, 6.6). For example, Mascle et al. (2000) noted that the Gulf of Suez also exhibits a N145°E trend (Garfunkel and Bartov, 1977; Colletta et al., 1988), and speculated that

the predominantly northwest-southeast trending fault belt probably extends toward the Gulf of Suez rift system, linked by north-trending structural relays. Rifting of the Red Sea is still active with a minor possibly sinistral transcurrent component across the Gulf of Suez (Joffe and Garfunkel, 1987). Mascle et al. (2000) used the fault data across the Nile core to suggest the incipient development of a new microplate, referred to as the Levantine-Sinai Microplate. These authors further suggested that if this interpretation is correct, the Levantine-Sinai Microplate is probably a piece of the African craton, broken and progressively disconnected from the African Plate in response to the collision between Eratosthenes Seamount and Cyprus.

Yet other research suggested that the predominantly northeast-southwest trending set of faults across the present-day Nile cone represent a trans-African *en échelon* sinistral megashear system, referred to as the Pelusium megashear (e.g., Neev 1973, Neev and Friedman 1978, and Neev et al., 1982). These authors view the Qattara-Rosetta and the Eratosthenes fault zones as part of this system.

6.5 Summary and future work

The eastern Mediterranean offers one of the best constrained environments in which to study (a) the active processes of oceanic closure, microplate and continental collision, with concomitant mountain building, and (b) the tectonic and sedimentary evolution of basins near the edge of active orogenic settings with complicated microplate configurations, and (c) the geodynamics of the mainly extensional and transtensional deformation along the northeastern passive margin of the African Plate and the predominantly contractional deformation across the collisional margin between the Aegean-Anatolian Microplate.

The interpretation and mapping of the tightly-spaced high-resolution multichannel seismic reflection profiles clearly improved our understanding of the Late Miocene–Recent tectonic and kinematic evolution of the Antalya Basin and Florence Rise and it is relationship with Cyprus-Eratosthenes

collision zone, along the plate boundary between the African Plate and the overriding Aegean-Anatolian Microplate. However, one major scientific revelation of this study is the realization that the upper crustal deformation can only be critically evaluated if they can be tangibly linked to the deeper slab-scale lower crustal and upper mantle structures. Several recent publications stressed this and hypothesized that the style and orientation of the upper crustal structures mapped in the upper 3-5 seconds (∼5-20 km) in seismic reflection profiles must be the upper crustal strain-response to the processes that are occurring deep within the lower crust and uppermost mantle, including subduction and detachment and/or tear of slabs (Hall et al., 2014a,b, Aksu et al., 2014c, Elitez et al., 2015). However, neither direct linkages of structures nor the correlations between upper crustal tectonic domains and lower crustal elements could be established, rendering the strain transferred across the crust purely speculative. Thus, there are still major challenges associated with the linkages between the upper crustal deformation (such as shown in various regional tectonic maps in this study) and the fundamental uppermost mantle and lower crustal structural elements (such as tomographically shown lithospheric tears, break-offs and large scale mantle upwelling) that drive this shallow crustal deformation. What is needed to fill this gap?

- The acquisition of a grid of regional deep reflection data that image the uppermost ∼100–150 km of the crust is the most critical first step in filling this data gap.

  These new data will assist in the delineation of potential linkages between (a) the Cyprus Arc and the crustal scale structures associated with the continental fragments of Hecateus Ridge, and the Eratosthenes Seamount and the Paphos Fault Zone, (b) the subduction beneath the Cyprus Arc and the prominent internally parallel upper crustal structures such as the Kozan–Anamur–Silifke–Kırkkavak, Kyrenia–Misis–Aksu, Amanos–Larnaka–Troodos–Antalya, Latakia Ridge–Tartus Ridge–Baër Bassit fault zones, as well as the Central Taurus Mountains, (c) the subduction beneath the Cyprus Arc and the upper crustal structures across the accretionary prism delineated by the Mediterranean Ridge, Florence Rise and the possibly the

Anaxagoras Mountain, and the eastern marine extension of the Isparta Angle.

- The second important need is to better evaluate the eastern Mediterranean plate kinematics in a quantitative manner using 2D/3D balanced cross-section constructions based on the fault maps created during the earlier studies and use of finite element model(s) incorporating plate motion boundary conditions, fault constraints and space geodetic velocities.

  These new data will allow the better understanding of (a) the accommodation of the 20° counterclockwise rotation of the Beydağları block (van Hinsbergen et al., 2010a) in the marine areas, (b) the accommodation of extensional deformation, particularly seen across the Adana, Cilicia, Latakia and inner Antalya basins, within a regionally contractional setting across the broad collisional zone between the Aegean–Anatolian Microplate and the African Plate, and (c) the postulated south-directed migration of the central Anatolian block within the context of west-directed escape of the Aegean–Anatolian Microplate.

Chapter 7

Messinian Salinity Crisis – Discussion

Introduction

The Messinian evolution and history of the Mediterranean is one of the most extensively studied topics across Europe, but also globally. There are numerous hypotheses for the development of the Messinian Salinity Crisis, although there exists a general agreement that it developed as the result of a complex combination of tectonic and glacio-eustatic processes which progressively restricted and finally isolated the Mediterranean Sea from the open ocean (e.g., Wijermars, 1988; Hodell et al., 1994, Butler et al., 1995, Clauzon et al., 1996). There is also considerable disagreement on the timing and duration of the Messinian Salinity Crisis. For example, some authors suggest synchroneity of evaporite deposition across the eastern and western Mediterranean regions (e.g., Hsü et al., 1973), others suggested a two-step event where the deposition of evaporites initially started across the marginal basins and subsequently developed within the deep basins (e.g., Clauzon et al., 1996), yet others suggested a completely diachronous evolution of the evaporites across the eastern and western Mediterranean basins (e.g., Butler et al., 1995). Equally large controversies exist over

the cause, and the effects, of the isolation of the Mediterranean: for example some authors argued that a large glacio-eustatic sea-level drop, related to expanding polar ice volume was the cause of the onset of the Messinian Salinity Crisis (Hodell et al., 1994), but others advocated that the orogenic uplift accompanied by gravity-driven sliding of large nappe complexes across the Gibraltar Arc was the primary mechanism responsible for the isolation of the Mediterranean Sea from the global ocean (Wijermars, 1988).

7.1 Messinian Salinity Crisis deposits

The presence of evaporites, not only halite, but also gypsum, anhydrite, and dolomite, in the Mediterranean was proven by DSDP drilling (Shipboard Scientific Party, 1978). Combining the drilling results with evidence furnished by geophysical records, the existence of an extensive evaporite unit of Upper Miocene age has been previously established by Hsü et al. (1973). The distribution and thickness of evaporites follow a close relationship with basin configuration that is in turn defined by local and regional tectonic processes, including uplift and subsidence which control the sedimentary processes of deposition and erosion. At the peak of the Messinian Salinity Crisis, the drawdown gave a new configuration to the greater Mediterranean basin, creating a series of morphological and sedimentological changes. As a result, evaporites of variable thickness and lateral extent were deposited during the Messinian. Up to 3.5 km-thick evaporite successions were deposited within the deep central basins (Hsü et al., 1973; Cita, 1973; Ryan, 1978; Garfunkel and Almagor, 1987). But, the Messinian evaporite successions are not solely composed of evaporite minerals, but also include variable proportions of terrigenous siliciclastic debris (e.g., Roveri et al., 2014a–c, Manzi et al., 2014). This deposition coincided with intense subaerial erosion of the basin margins and subsequent deposition of these siliciclastic materials in the deep central basins (Hsü et al., 1978; Ryan and Cita, 1978; Barber, 1981; Savoye and Piper, 1991; Druckman et al., 1995; Lofi et al., 2005; Ryan, 2009; Bache et al., 2009).

Although many previous studies showed the evaporite thicknesses in small local regions, none of the previous studies has shown a detailed Messinian evaporite thickness map across the entire eastern Mediterranean. Here, the evaporite thicknesses determined using the seismic data from the Antalya Basin and Florence Rise are combined with the result of the previous studies around the eastern Mediterranean and a regional isopach map is presented, which illustrates the distribution and thickness variations of the Messinian evaporites across the entire eastern Mediterranean region (Fig. 7.1). This map also forms the basis for discussion on the regional implications of the Messinian Salinity Crisis in the eastern Mediterranean, allowing comparisons to be made of the Messinian Salinity Crisis deposits between different eastern Mediterranean basins, including the Antalya, Cilicia, Latakia, Levantine and Herodotus basins as well as the area around the Nile cone.

Roveri et al. (2014a–c) classified the Messinian depositional environment into three categories: shallow-water (0–200 m), intermediate-water (300–1000 m) and deep water (>1000 m) environments. These authors suggested that the shallow and intermediate water regions are marginal/peripheral basins, which are presently situated onshore, while the deep basins and some intermediate basins are presently located in the offshore: however, all these environments were physically disconnected from one another during the deposition of the evaporites across the Mediterranean (Roveri et al., 2014a–c). In this regional basin configuration, the Messinian evaporite successions are generally thicker in the deep-central basins and thinner across the marginal basins. In the seismic reflection profiles collected from the deep-central and intermediate basins, a strong reflector that marks the top of the evaporites is identified as the M-reflector (Ryan et al., 1973). This surface corresponds to the unconformity at the top of the Messinian evaporites and it separates: (a) the Messinian evaporites from the overlying uppermost Messinian–Quaternary successions where Messinian is present, and (b) the pre-Messinian Miocene and/or older successions from the uppermost Messinian-Quaternary deposits where the Messinian evaporites are absent. The M-reflector marks the subaerial erosion during the drawdown as well as the ravinement associated with the post-Messinian sea-level rise. In

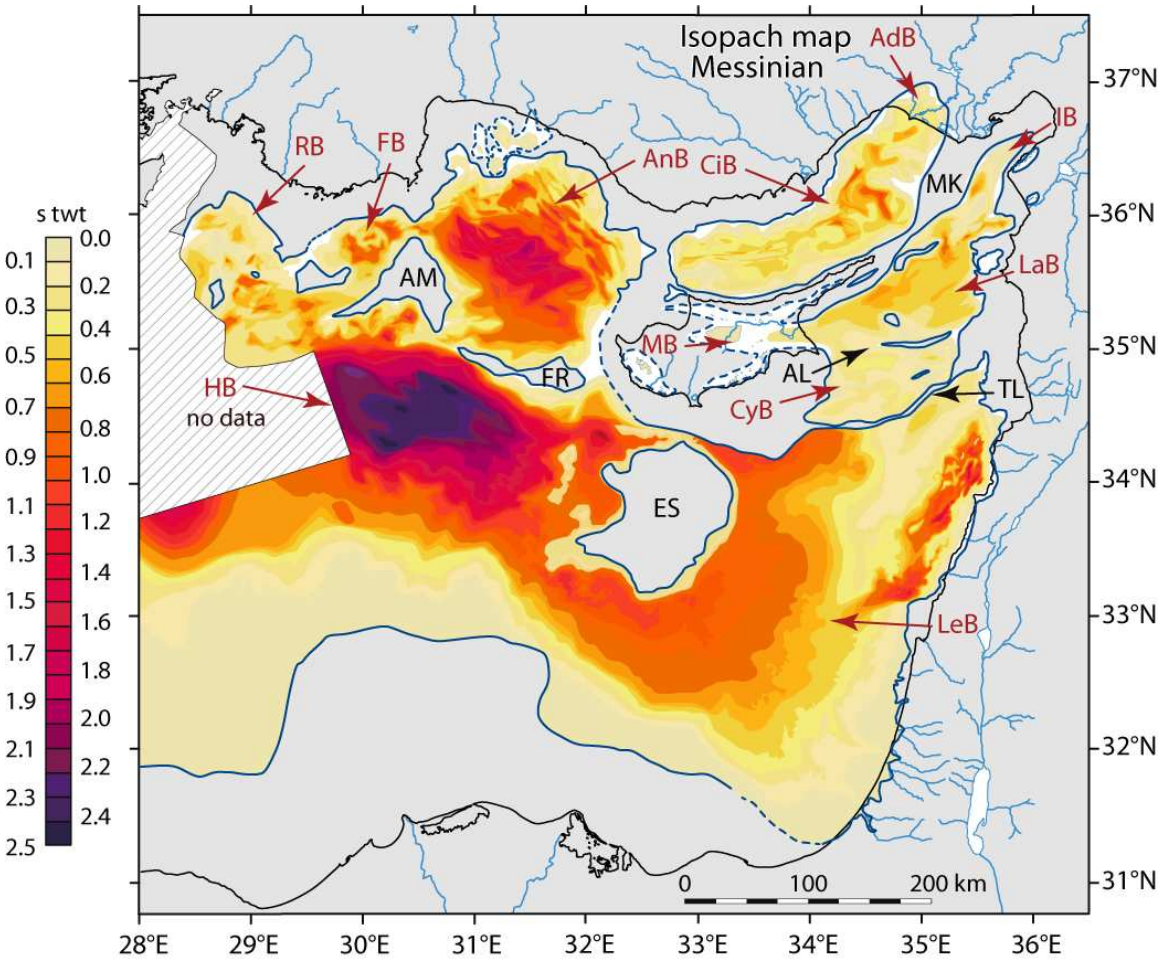

Figure 7.1: Isopach map of the Messinian evaporites across the eastern Mediterranean. Map is compiled by Aksu using data from (a) Florence Rise (Güneş, this thesis); (b) Rhodes and Finike basins, Anaximander Mountains (Barnes, 2015), (c) Adana, Cilicia, Latakia, Iskenderun basins (Aksu unpublished data), (d) offshore Israel, offshore Lebanon, Levantine Basin, (Carton et al., 2009, Gvirtzman et al., 2010) (e) Eratosthenes Seamount, Herodotus Basin (Montadert et al., 2010a,b), (f) offshore Syria (Bowmann, 2011), (g) Nile delta (Loncke et al., 2006). The coastline is from the International Bathymetric Charts of the Mediterranean (IOC, 1981). 1 s twt is equivalent to about 2000 m of Messinian sediment thickness, depending on the lithologies present.

the seismic reflection profiles the M-reflector is marked by a notable unconformity, often delineated by erosional truncation below and progressive onlap above (§ Chapters 3, 5). Another strong reflector defines the base of the Messinian evaporites: this is referred to as the N-reflector along the deep and intermediate sub-basins of the entire Mediterranean basin. Across the shallow-water marginal basins the M- and N-reflectors merge defining a major erosional surface (e.g., Vidal et al., 2000). In many studies across the Mediterranean, the top surface of the Messinian evaporites is indicated as MES (or Messinian erosional surface/marginal erosional surface), TES (or top erosional surface) and/or TS (or top surface), whereas the basal surface is indicated as BES (or basal erosional surface) and BS (basal surface) (Lofi at al., 2005, 2010; Maillard et al., 2006; CIESM, 2008; Roveri et al., 2014a-c). The marine high-resolution multi-channel seismic reflection profiles do not allow the differentiation of these specific terms, although this terminology is also carried into the marine realm by many studies (Lofi at al., 2005, 2010; Maillard et al., 2006; CIESM, 2008; Roveri et al., 2014a-c), where the descriptive term of a reflector became an interpreted term. In this study, the top unit surfaces, including MES, TES and TS are collectively indicated by the M-reflector, whereas the base unit surfaces, such as BES and BS are indicated by the N-reflector (also see Chapters 3, 4).

Thus the isopach map of the Messinian evaporite successions represents thicknesses between the M- and N-reflectors.

7.1.1 Distribution of the Messinian Salinity Crisis deposits

During the Messinian Salinity Crisis, a variably thick succession of Messinian evaporites was deposited across the eastern Mediterranean. Because of the limited resolution of seismic interval velocities in our studies, thicknesses are quoted in two-way reflection interval times (twt). 1 s twt is equivalent to about 2000 m of Messinian sediment, varying with the lithological content. Thickness ranges from 100–900 ms along the shallow marginal basins, such as Adana, Cilicia, Latakia, Iskenderun and Mesaoria basins to >1500–2000 ms in the deep central basins, such as the Antalya,

Levantine and Herodotus basins (Fig. 7.1). Well data along the easternmost sector of the eastern Mediterranean show the ubiquitous occurrences of the Messinian evaporites along the coastal and nearshore zones (Figs. 7.2–7.4). For example, the south–north cross section across western Israel shows that in the present-day onland and nearshore wells, such as the Afiq 1, Nahal Oz 1, God 1, Hof Ashdod 1A, Natanya 1, Kanusa 1, Qishom Yam 1, the Messinian successions are characterized by gypsum and chemically-precipitated carbonates, giving way to halite immediately offshore, such as Hanna 1 and Hof Ashdod 1 wells (Fig. 7.2; Gardosh et al., 2008a,b). Farther to the north and along Lebanon, Syria and the Iskenderun Basin, a similar situation is observed, where anhydrite and limestone dominate the Messinian successions in the present-day onshore boreholes Latakia 1, Latakia 2 and Fidio 1, as well as the onshore Iskenderun–Arsuz and Hatay–Samandağ basins in southern Turkey (Fig. 7.3; Bowmann, 2011, Tekin et al., 2010). However, the anhydrite–carbonate lithologies are replaced by halite in the marine Iskenderun Basin wells Iskenderun 1 and Gülcihan 1, but reverting back to anhydrite in the shallower water Payas 1 well (Fig. 7.3, Uffenorde et al., 1990). Messinian sediments rapidly thin toward the northeast, eventually pinching out in the onland Osmaniye–Bahçe Basin (Fig. 7.3). Along the northeastern sector of the eastern Mediterranean, the wells in the southern portion of the onland Adana Basin (e.g., T191 and Kuranşa 2 wells) and the offshore Cilicia Basin (e.g., Seyhan 1 and Karataş 1 wells) clearly show that the Messinian successions in these basins are characterized by halite (Fig. 7.4, Turkish Petroleum Corporation unpublished data, Cipollari et al., 2013, Ilgar et al., 2013). The halite–anhydrite transition is clearly observed in T191 and Arapali wells (Fig. 7.4). Finally, a cross section across western Cyprus (Fig. 7.4) shows that in the Xeri well and the Polemi Basin there is a well developed Messinian succession, dominated by anhydrite and chemical limestone precipitate (Manzi et al., 2014). The cross section can be readily extended west into the DSDP Site 375 over the crestal region of Florence Rise, where a thin succession of anhydrite and halite represent the Messinian evaporites (Fig. 7.4, Shipboard Scientific Party, 1978).

The three cross sections described above (i.e., Figs. 7.2–7.4) and the associated review of the

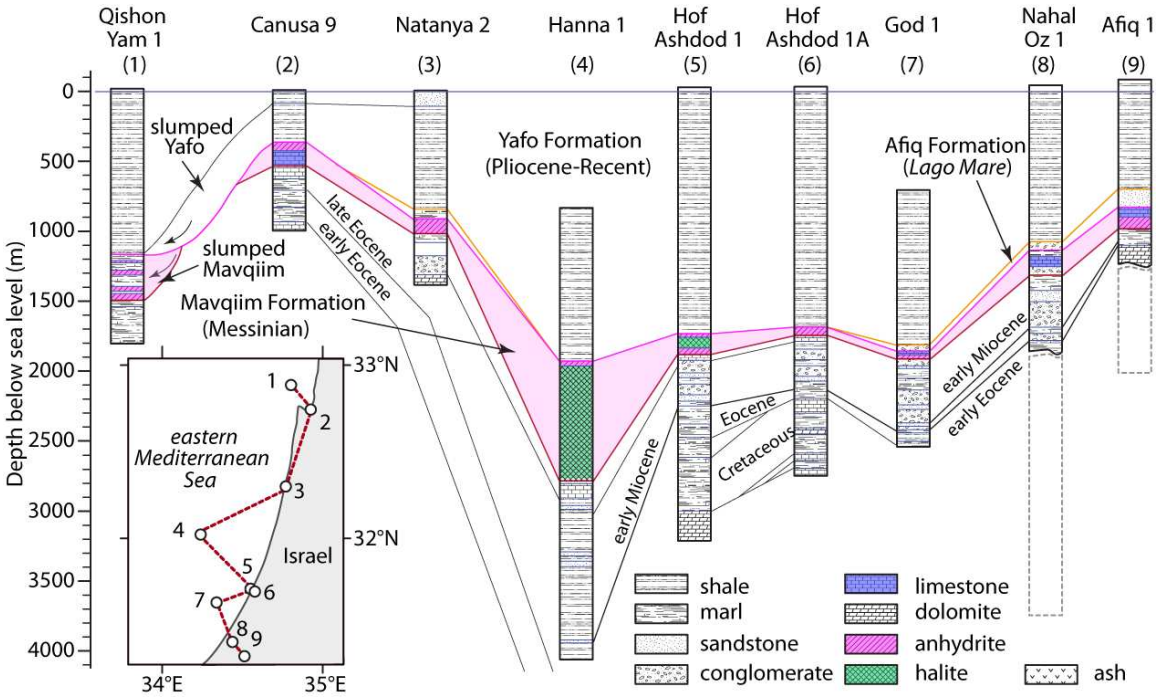

Figure 7.2: Cross section across the coastal and marine sectors of western Israel showing the distribution of the Messinian evaporite successions. Note that Yafo, Afiq and Mavqiim formations represent the Pliocene–Recent, uppermost Messinian *Lago Mare* and the Messinian successions. Inset shows the locations of the wells (filled circles). Compiled and redrawn from Gardosh et al. (2008a,b).

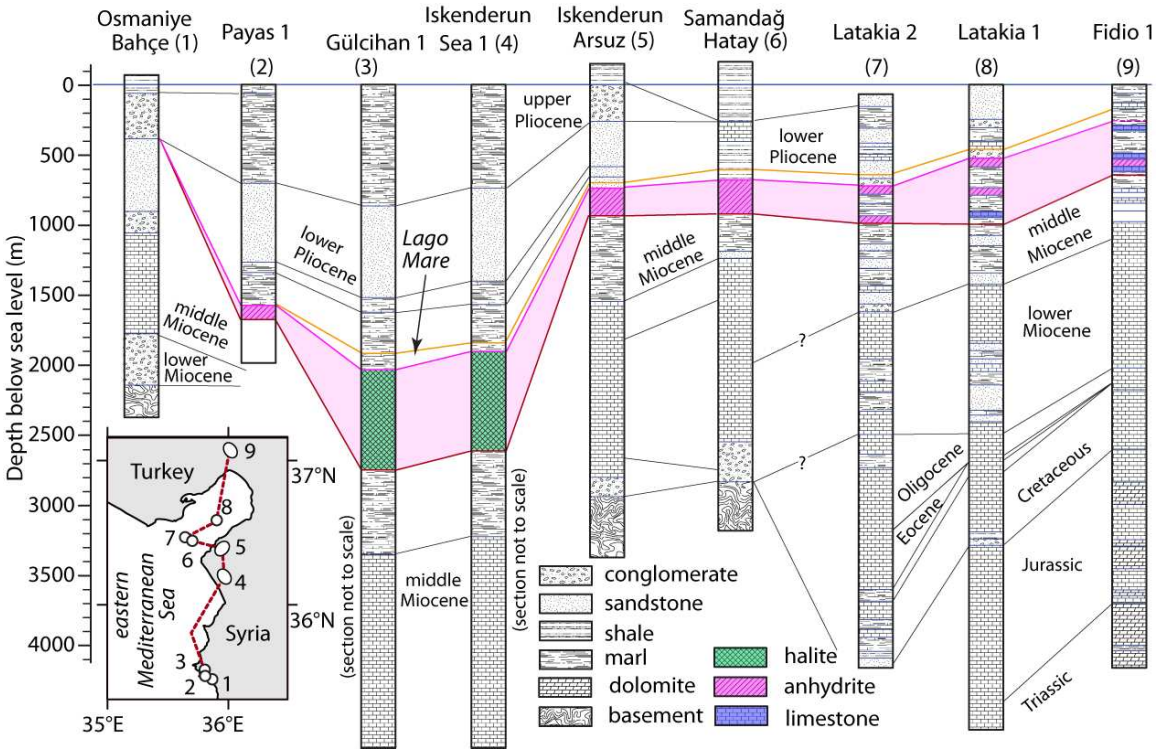

Figure 7.3: Cross section across the coastal and marine sectors of western Syria and southwest Turkey showing the distribution of the Messinian evaporite successions. Compiled and redrawn from Bowmann (2011) = Latakia 1 and 2 and Fidio 1; Tekin et al (2010) = Samandağ–Hatay, Iskenderun–Arsuz and Osmaniye–Bahçe sub-basins; Uffenorde et al (1990). Inset shows the locations of the wells (filled circles) and measured sections (filled ellipses).

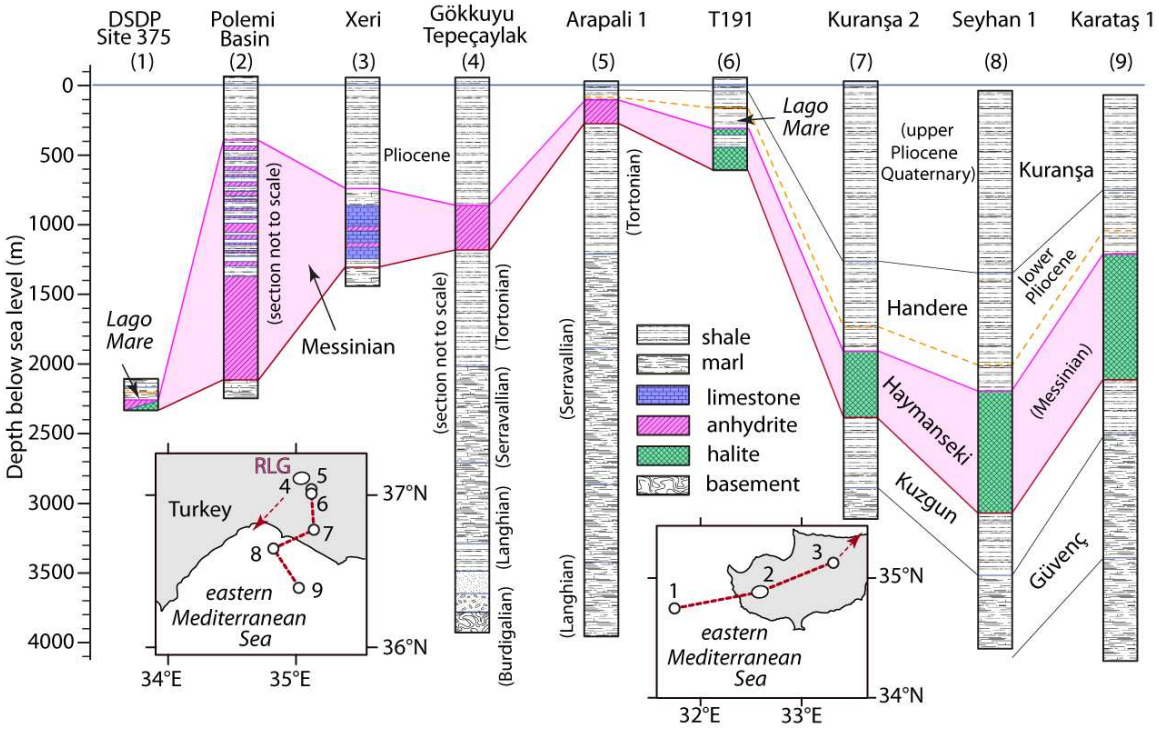

Figure 7.4: Cross section across the coastal and marine sectors of western Syria and southwest Turkey showing the distribution of the Messinian evaporite successions. Compiled and redrawn from data kindly provided by the Turkish Petroleum Corporation (Karataş, Kuranşa, Seyhan and Arapali wells), Cipollari et al. (2013) = T191 well, Ilgar et al (2013) = Gökkuyu Tepeçaylak measured sections, Manzi et al. (2014) = Xeri well and Polemi Basin measured section and Shipboard Scientific Party (1978) for DSDP Leg XLII, Site 375. Inset shows the locations of the wells (filled circles) and measured sections (filled ellipses).

existing literature (e.g., Shipboard Scientific Party, 1978, Gardosh et al., 2008a,b, Bowmann, 2011, Tekin et al., 2010, Cipollari et al., 2013, Ilgar et al., 2013, Manzi et al., 2014) clearly documented that the intermediate and marginal basins across the eastern and northeastern Mediterranean experienced evaporative sedimentation during the Messinian Salinity Crisis. The Messinian isopach map reveals three important trends (Fig. 7.1): (a) during the Messinian the eastern Mediterranean was partitioned into several discrete basins, which were separated from one another by prominent ridges, (b) in these basins dramatically different thicknesses of Messinian successions were deposited, and (c) associated with the drawdown, rivers entering into the eastern Mediterranean deeply incised their canyons. These issues are further discussed below.

Several discrete basins

During the Late Miocene, the eastern Mediterranean included 1–2 large ancestral basins. The protracted subduction of the African Plate beneath the Eurasian Plate and the associated tectonic activity partitioned these ancestral basins into several distinct depocentres which were separated from one another by prominent ridges (§ Chapters 5, 6). The sea level drawdown during the Messinian Salinity Crisis simply accentuated the evolving morphological framework of the eastern Mediterranean. The zero line of the Messinian isopach map predominantly represents the depositional edge of the evaporites in these depocentres (Fig. 7.1). For example, the Adana–Cilicia basin complex developed between the evolving Taurus Mountains of southern Turkey and the Kyrenia Range of northern Cyprus (Fig. 7.1). This basin complex was separated from the Antalya Basin by the broadly north-south trending Anamur–Kormakiti Ridge and from the Iskenderun–Latakia–Mesaoria basin complex by the northeast-southwest trending arcuate Misis–Kyrenia Ridge. The smaller and less conspicuous Amanos–Larnaka Ridge and its prominent western continuation into the Troodos Mountains separated the Iskenderun–Latakia–Mesaoria basin complex in the north from the Cyprus Basin in the south (Fig. 7.1). The Cyprus Basin in turn, was separated from the Levantine Basin in the south by

the prominent Tartus–Latakia Ridge of the eastern Cyprus Arc. In the west, the Florence Rise and its northwestern continuation into the Anaxagoras Mountain separated the two prominent Messinian depocentres, the Antalya Basin in the north and the Herodotus Basin in the south. The Eratosthenes Seamount also largely partitioned the Levantine and Herodotus basins (Fig. 7.1).

Variable Messinian evaporite thicknesses

The Messinian evaporite successions show dramatic thickness variations across the eastern Mediterranean, ranging from $<$100 ms along marginal basins to $>$2400 ms (Fig. 7.1). For example Messinian successions are very thick within the Herodotus Basin, where central thicknesses exceed 2400 ms, and deposits define broadly east–west trending cylindrical bodies (Fig. 7.1). The Messinian evaporites are also notably thick in the Antalya Basin, where central thicknesses range between 1500 ms and 2000 ms (Fig. 7.1). In both Herodotus and Antalya basins, Messinian evaporites become thicker toward the deep central regions of the ancestral basins, but become notably thin toward the continental margins. The Eratosthenes Seamount partitions the Levantine Basin to the east, where Messinian deposits range in thickness from $<$100 ms to $>$1200 ms (Fig. 7.1). A broadly north-northeast–south-southwest trending trough with thick Messinian successions is clearly visible across offshore Lebanon.

Across the northern sector of the eastern Mediterranean, the Messinian evaporite successions are notably thinner (i.e., $<$900 ms) across the present-day marginal and intermediate-depth basins, such as the Adana–Cilicia and Iskenderun–Latakia–Mesaoria basin complexes (Fig. 7.1). In these basin complexes a 700–900 ms thick northwest-southeast trending salt wall developed as the result of gravitational gliding of the thick Pliocene–Quaternary delta lobes over the Messinian salt lake (Fig. 7.1, Bridge et al., 2005). Messinian evaporite successions are also thin across the present-day very deep Rhodes and Finike basins, as well as the Sırrı Erinç Plateau, ranging between $<$100 ms and $\sim$700 ms (Barnes, 2015, Fig. 7.1).

These dramatic thickness variations can be interpreted as the result of the interplay between the sea level variations during the Messinian and the morphology of the basins, which is a function of the ensuing tectonic activity associated with the convergence between the African and Eurasian plates. The sedimentation during the Messinian Salinity Crisis was characterized by two critical and competing modes: (a) evaporative sedimentation leading to the deposition of carbonates, gypsum and halite and (b) siliciclastic sedimentation associated with the rivers entering into the eastern Mediterranean. Today, there is one very large river (Nile), several intermediate rivers (Seyhan, Ceyhan, Asi, Göksu, Aksu, Köprü, Manavgat, Nahal Besor), and several smaller rivers (Dalaman, Eşen(çay), Tarsus, Nahr er Kebir, Litani, Kishon, Yarkon) that provide siliciclastic input into the eastern Mediterranean (Figs. 7.5, 7.6).

There is no direct information on the water and sediment discharge rates of these rivers during the Messinian. The overall water discharge from the drainage basin depends on the relationship between precipitation and water storage factors across the drainage basin (Milliman and Farnsworth, 2011), and can be summarised as follows: drainage basin discharge = precipitation – evapo-transpiration $\pm$ changes in storage. Other factors affecting river discharge include the rock type(s) across the drainage basin, relief of the drainage basin, and climate and rainfall. Some basic assumptions can be made here: (a) the Messinian climate of the eastern Mediterranean was relatively similar to the arid and evaporative climate that prevails across the region today (e.g., Blanc, 2000), (b) thus, the Messinian water and sediment discharge rates must have been comparable to those seen today, (c) the rock types across the drainage basins of the eastern Mediterranean rivers are the same, (d) but the relief must have been dramatically different across the drainage basins during the Messinian – this is further discussed later in river incision. Sediment discharge of a river is a log-linear function of basin area and maximum elevation of the river basin with climate and runoff being of secondary importance (Milliman and Syvitski, 1992). The above discussion suggests that the present-day water discharge rates of the rivers entering the eastern Mediterranean can be used as a proxy for the Messinian

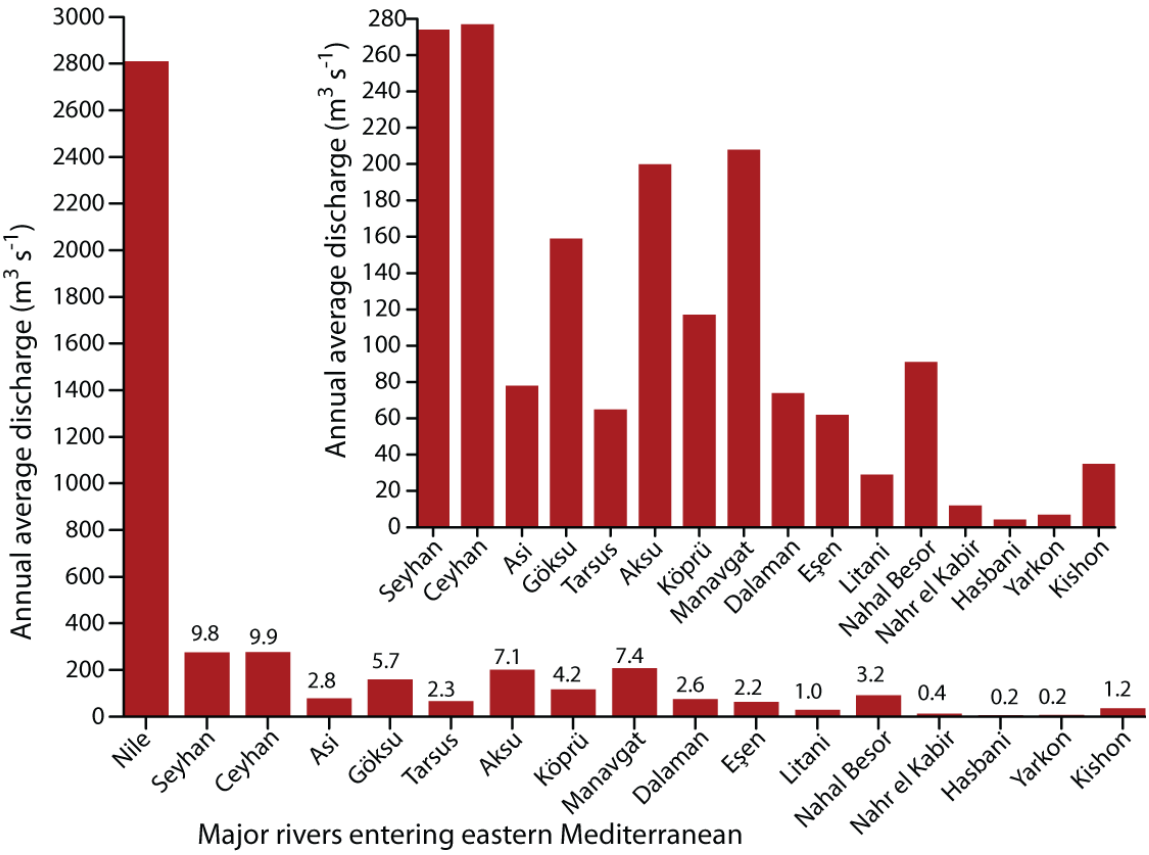

Figure 7.5: Histogram showing the average annual water discharges of rivers entering the eastern Mediterranean Sea (data from EIE, 1984; Amery, 1993;, Brigden and Stringer, 2001; Nilsson et al., 2005; Wohl, 2007; Crouvi et al., 2015). Note the overwhelming dominance of the Nile River. Numbers above bars represent the percentage contribution of the water input relative to the Nile River.

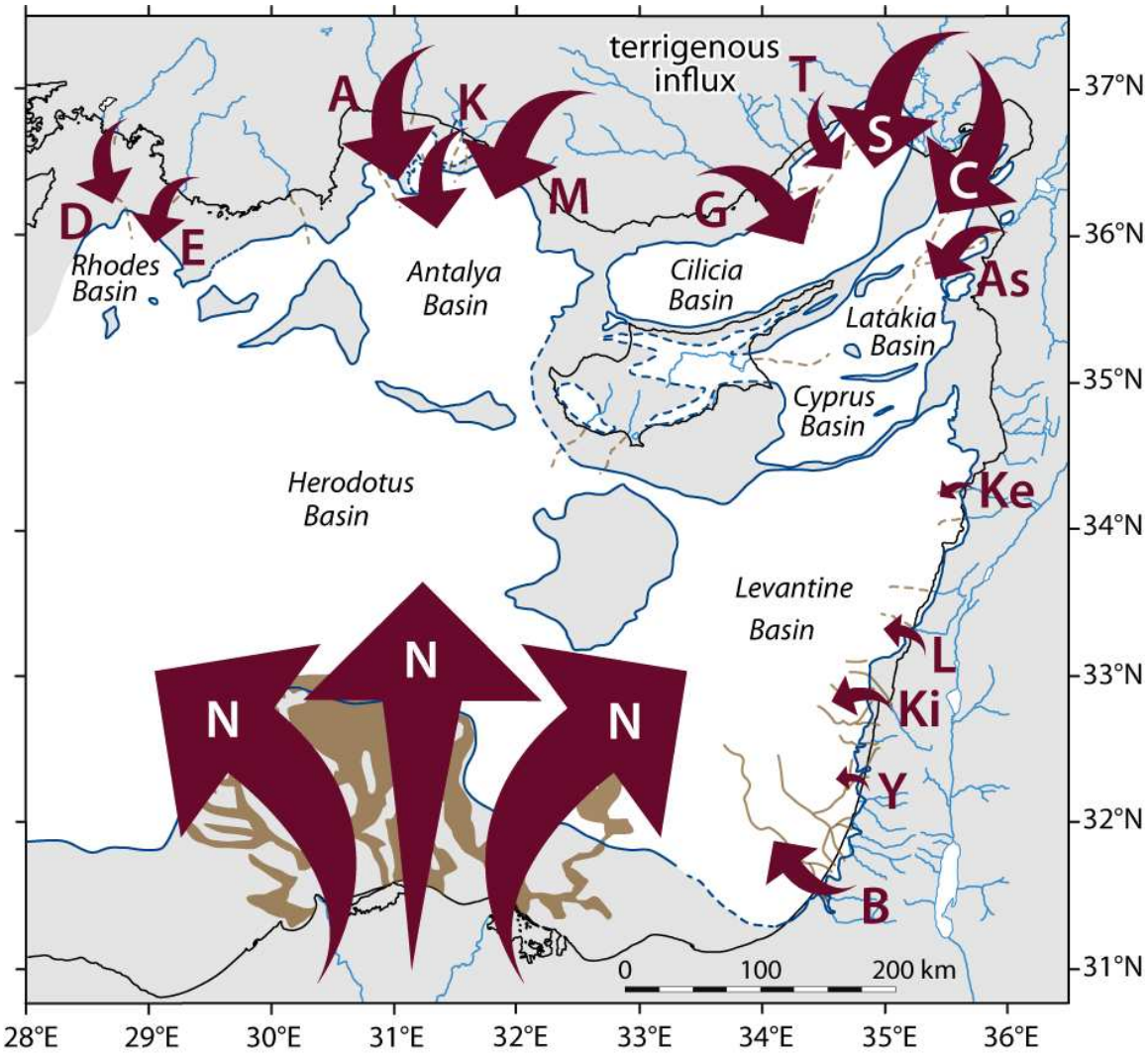

Figure 7.6: Potential detrital siliciclastic source input into the eastern Mediterranean. The arrows are proportional to the percentages of river discharges presented in Figure 7.5. Rivers: A= Aksu, As=Asi, B= Nahal Besar, C= Ceyhan, D= Dalaman, E= Eşen(çay), G= Göksu, K= Köprü(çay), Ke= Nahr el Kabir, Ki= Kishon (Qishon), L= Litani, M= Manavgat, N= Nile, S= Seyhan, T= Tarsus, Y= Yarkon. The Messinian canyons across the Nile River from Aal et al. (2000, 2001). Messinian coastline from Figure 7.1. Also shown are the present-day coastline (from IOC, 1981) and rivers.

conditions, with the exception of the river gradient and the subsequent incision discussed below.

River incision

The southern continental margin of the eastern Mediterranean is dissected by a very prominent system of anastomosing and deep canyons that were cut during the Messinian Salinity Crisis (Fig. 7.7, Aal et al., 2000, 2001). The eastern continental margin was also dissected by numerous smaller canyons (e.g., the Afiq Canyon, Gardosh et al., 2008a,b). These canyons must have supplied considerable quantities of siliciclastic material into the basinal settings during the onset of the Messinian Salinity Crisis, as the base level dropped dramatically from what is $\sim$20 m above present sea level (Lisiecki and Raymo, 2005) to a low of 1500 m to 2250 m below present-sea level during the Messinian (Gargani and Rigollet, 2007; also § Chapter 4). How much sediment has been excavated from the Nile canyon during the Messinian? Said (1993) shows that the Messinian incision of the Nile River channel reached a depth of -170 m in Aswan, -800 m in Assuit and $>$-2500 m immediately north of Cairo, $\sim$900 km, 500 km and 150 km south of the coast, respectively (Fig. 7.8). Similar deep Messinian channels occur across the continental margins of Israel, Libya and Syria (Griffin, 2002). A back-of-the-envelope calculation can be made of the volume of sediment that has been excavated from the Nile gorge during the Messinian, provided that we can also determine the width and shape of the gorge. The geological cross section published by Chumakov (1967) based on boreholes drilled during the construction of the Aswan Dam shows a deep V-shaped gorge excavated in granite. This gorge is $\sim$350–500 m wide at the surface. The width of the Nile north of Aswan is $\sim$2.8 km on average (Said, 1993, Catterall et al., 2010). Assuming that the Nile gorge is (a) V-shaped, (b) has an average width of 1500 m between Aswan and Assuit and 2500 m between Assuit and the Mediterranean shore, (c) has an average depth of $\sim$500 m between Aswan and Assuit and 1650 m between Assuit and Cairo, and (d) the distance between Aswan and Assuit is 390 km and that between Assuit and the Mediterranean shore is 500 km, two triangular prisms can be constructed so that the volume

of the gorge can be estimated. These calculations suggest that a total of $\sim$1146 km^3 of sediments were excavated from the Nile gorge during the Messinian Salinity Crisis. Previous studies show that the Nile delta is emplaced on a passive margin covering an area of $\sim$100,000 km^2, with the delta development staring during the latest Miocene, at the end of the Messinian salinity crisis (Salem, 1976; Ross and Uchupi, 1977; Ryan and Cita, 1978; Loncke et al., 2006), and reaching its maximum thickness of 9 km during the Pliocene–Quaternary (Aal et al., 2001, Mascle et al., 2003). Therefore, it is clear that the eroded material from the excavated gorge did not become part of the Nile delta development, but was directly supplied directly into the deep Mediterranean Messinian basin, which is sometime referred to as the Lake Cyrenaica (Griffin, 2002).

So, what would the areal extent of a lobe of eroded siliciclastic material look like and how would that compare with the isopach map of the Messinian evaporite successions? Assuming that the average compaction of the Messinian sediments imaged in the seismic reflection profiles is 50‰, the total volume of excavated material would be $\sim$1719 km^3. A back-of-the-envelope calculation can be made to determine the surface area that the excavated material would occupy immediately north of the deeply incised Nile canyons across the southern Mediterranean (Fig. 7.7). This exercise, which does not include the sediment load otherwise carried from the drainage basin, suggest that the Messinian evaporite successions across the Herodotus Basin must also contain considerable quantities of siliciclastic material. Because the gorge incision and the associated excavation of the material did not occur "geologically instantaneously" it is believed that the siliciclastic material initially formed a prominent layer across the eastern Mediterranean immediately above the N-reflector, but subsequently became interbedded with the evaporite sediments. Fuchs et al. (2014) used optically stimulated luminescence dating of fluvial terraces across the rivers of the Pamir Mountains to determine fluvial incision rates. The eastern Mediterranean rivers probably had similar river profiles to the present-day Pamir Mountains during Messinian. Average river incision rates ranging from 4–5 mm yr^{-1} to 6–7 mm yr^{-1} have been calculated for river incision during the last 26 ka (Fuchs

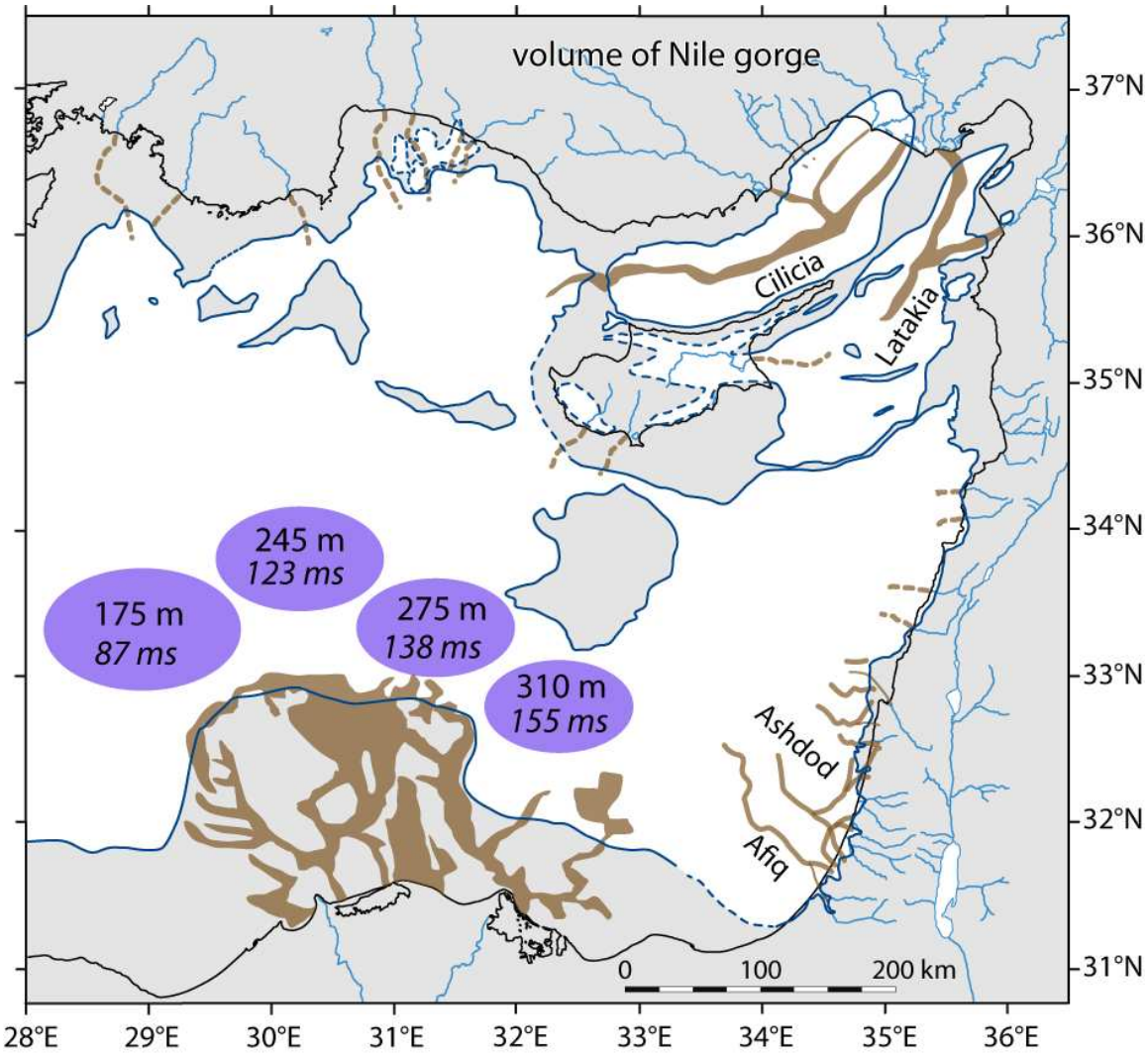

Figure 7.7: Map showing the Messinian basin configuration and surface area that the ∼1146 km^3 of material excavated from the Nile gorge would occupy across the Herodotus Basin (converted into ms using a 50% decompaction factor and a 4000 m s^{-1} seismic velocity, explained in text). The numbers in the ellipses are the thickness of the siliciclastics that would account the excavated material from the Nile gorge to various surface areas. The Messinian coastline is from Figure 7.1, the Messinian canyons across the Nile delta are from Aal et al. (2000, 2001); the Messinian canyons across the Cilicia and Latakia basin are from Aksu (unpublished data) the present-day coastline is from the International Bathymetric Charts of the Mediterranean (IOC, 1981).

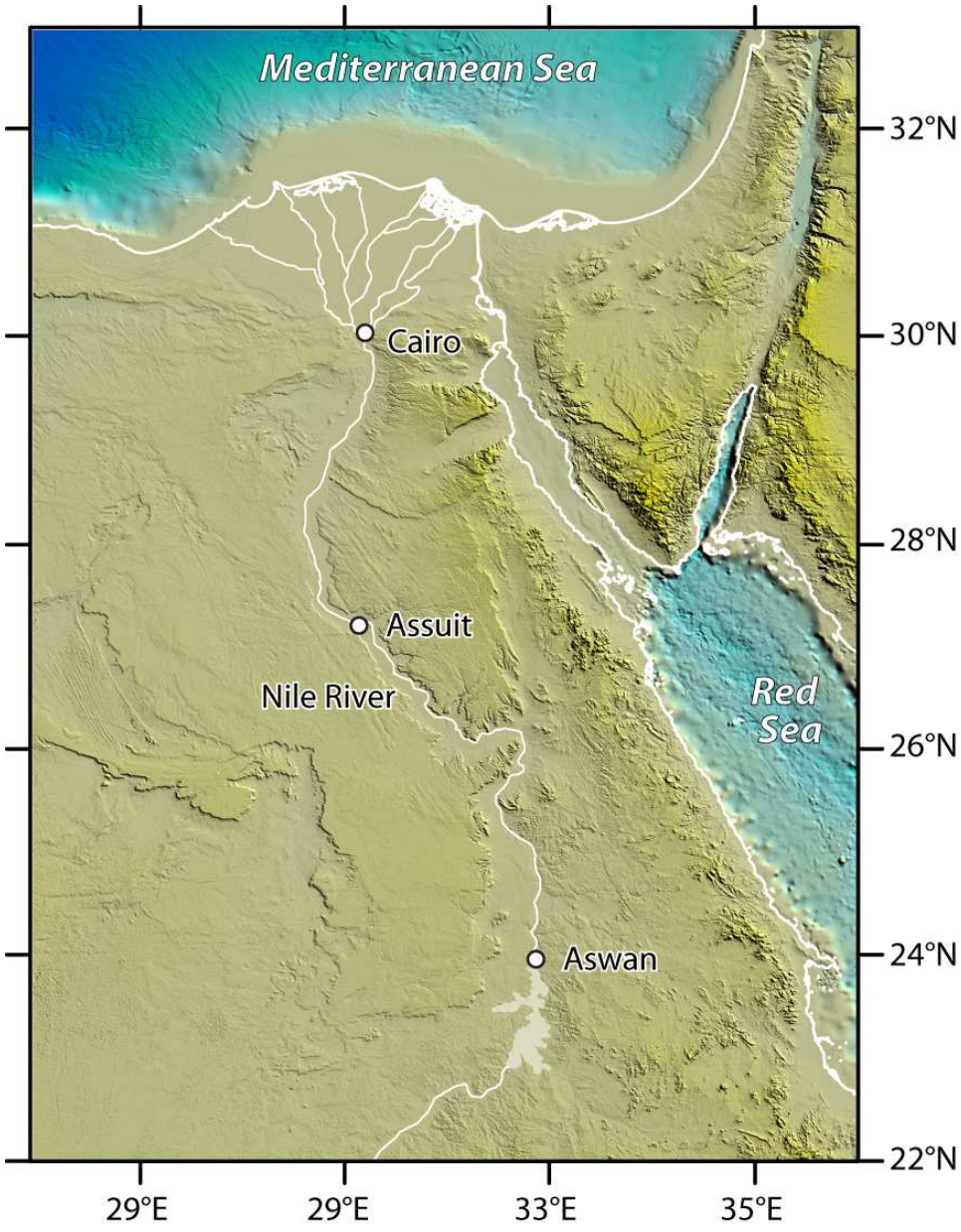

Figure 7.8: Map showing the lower course of Nile River, and the place names such as the Aswan, Assui and Cairo mentioned in text. The topography is compiled using GeoMapApp (Ryan et al., 2009), and shaded using Global Mapper. The multibeam bathymetry from the high-resolution EMODnet (European Marine Observation and Data Network, Portal for Bathymetry, http://www.emodnet-hydrography.eu/). The coastline (www.ngdc.noaa.gov/mgg/dat/geodas/coastlines/LittleEndian/coast41.zip) is extracted using GEODAS Version 4.1.

et al., 2014). At these incision rates, the gorge depth of -2500 m along the present-day coastline of the Nile delta (Said, 1993) would require 350 ka – 500 ka for the excavation of the Nile gorge, further suggesting that the excavation of the Nile gorge occurred during a prolonged period during the Messinian.

Dramatic river incision across the eastern Mediterranean was not unique to the Nile River, as many smaller rivers also incised their river valleys. A highly developed submarine canyon and channel system occurs across the southeastern continental margin of the eastern Mediterranean (Fig. 7.7, Gardosh et al., 2008a,b). For example, the Afiq and Ashdod canyons are deeply incised: the depth of the Afiq Canyon is up to 1500 m onshore (Druckman et al., 1995) and several hundred metres offshore. The Ashdod Canyon cuts a 700 m-deep gorge into Mesozoic strata some 40 km offshore. The incisions in the smaller canyon to the north of the Ashdod canyon are limited to the upper slope (Fig. 7.7, Gardosh et al., 2008a,b). Although no incision data is available from the Afiq and Ashdod canyons, smaller quantities (compared to the Nile) of siliciclastic sediments must have also been supplied into the Levantine Basin from the continental margins of Israel, Lebanon and Syria. There are also several medium-size rivers that enter the northeastern Mediterranean Sea, feeding large delta successions into the intermediate-depth Cilicia and Latakia Basins (Figs. 7.5, 7.6). Previous studies in these areas did not identify canyons incised into the pre-Messinian successions (e.g., Aksu et al., 2005a,b, 2014a,b, Hall et al., 2005a). However, re-evaluation of the seismic reflection profiles delineated a major canyon that extends from the mouths of the Seyhan, Tarsus and Göksu rivers across the Outer Cilicia Basin, crossing the Anamur–Kormakiti Ridge and entering into the eastern Antalya Basin (Fig. 7.7, Aksu personal communication, July 2016). Similarly, another prominent canyon extends from the mouths of the Ceyhan and Asi rivers and enters into the Inner Latakia Basin (Fig. 7.7, Aksu personal communication, July 2016). These two prominent canyons must also have supplied siliciclastic material mainly to the intermediate-depth Cilicia and Latakia basins, but also to the deeper Antalya Basin in the west and the Cyprus Basin in the east. The absence of any pre-M-

reflector delta deposits across the Cilicia Basin also support this contention: otherwise the Seyhan, Tarsus and Göksu rivers and possibly the Ceyhan River would have constructed a large delta across these areas. Messinian channels/gorges are readily identified travelling extreme distances across the Mediterranean (e.g., the Rhône, Po and Nile rivers, Lofi et al., 2011b)

The above discussion highlights the fact that the Messinian evaporite successions also include variable proportions of continentally derived siliciclastic debris. In the next section, the stratigraphy and compositional makeup of the deposits associated with the Messinian Salinity Crisis across the eastern Mediterranean will be evaluated.

7.1.2 Internal seismic stratigraphy of the Messinian evaporites

Previous studies across the eastern Mediterranean indicated that the Messinian evaporite successions define an acoustically transparent unit in multichannel seismic reflection profiles (e.g., Aal et al., 2000, Aksu et al., 2005a,b, Hall et al., 2005a,b, Bridge et al., 2005, Işler et al., 2005, Hawie et al., 2013). For example, the seismic profile across the eastern fringes of the present-day deep sea fan of the Nile shows the presence of a thick Messinian succession (Figs. 7.9, 7.10). However, internally the evaporite succession exhibits an acoustically chaotic but transparent character with no coherent and laterally continuous reflections (Fig. 7.9). It is clear that the Messinian succession here includes some salt, because it is mobilized to form rollers beneath the footwall of several listric normal faults developed on the proximal portion of the deep sea fan. So the chaotic appearance may be partially due to salt mobilization. But furthermore, the region is proximal to the Nile River which is the most important siliciclastic supply to the eastern Mediterranean Sea today, and also was during the Messinian (e.g., Aal et al., 2000). On the basis of this chaotic and transparent acoustic character, many studies argued that the eastern Mediterranean region, particularly the deep basins lack the 4-unit divisions of the Messinian evaporite successions observed across the western Mediterranean (e.g., CIESM, 2008, Lofi et al., 2011a, b; Roveri et al. 2014a). In the following section, the previously pub-

lished seismic reflection profiles from the southeastern sector of the eastern Mediterranean as well as the high-resolution seismic multichannel reflection profiles from the Cilicia, Latakia and Cyrus basins are re-interpreted to show that the 4-unit division of the Messinian evaporite successions is indeed present across the entire eastern Mediterranean.

Recent studies indicated that the 1500 m-thick Messinian successions across the Levantine Basin show six seismic stratigraphic units (Fig. 7.11, Bertoni and Cartwright, 2005; 2006; Hübscher et al., 2007; Hübscher and Netzeband, 2007; Dümmong and Hübscher, 2011). Seismic profiles crossing the Levantine Basin from Cyprus to the eastern fringes of the Nile deep sea fan and from the Israeli shelf to the Eratosthenes Seamount further suggested that most of these units occur in a basin-wide fashion across these areas (Netzeband et al., 2006). Four of these units are seismically transparent and presumably consist of halite (Fig. 7.11, Bertoni and Cartwright, 2007, Hübscher and Netzeband, 2007). The occurrence of two reflective intervals was related to the presence of interbedded siliciclastics and/or variations within evaporite facies (Garfunkel, 1984; Gradmann et al., 2005). Similarly, across the southeastern Levantine Basin west of Israel Gradmann et al. (2005) and Netzeband et al. (2006) proposed that Messinian layer in deep water has been shown to consist of a stack of five transparent layers bounded by internal reflectors, which can be interpreted either to represent changes of evaporite facies or to mark the presence of intercalated clastic sediments. The acoustic character and stratigraphy of the Messinian evaporite successions imaged across the Levantine Basin is remarkably similar to that imaged in this study across the southern Antalya Basin (e.g., Fig. 7.12). For example, in both regions there is (a) a relatively thin succession characterized by strong laterally continuous reflections immediately above the N-reflector, and (b) an equally strong and laterally continuous reflection interval immediately below the M-reflector (cf., Fig. 7.11 and Fig. 7.12). These two sub-units are identified as 2d and 2a, respectively. Similarly in both areas, there are two predominantly acoustically transparent sub-units between sub-units 2a and 2d, with the lower sub-unit showing notably higher reflectivity and lateral continuity of reflectors (cf., Fig. 7.11 and Fig. 7.12).

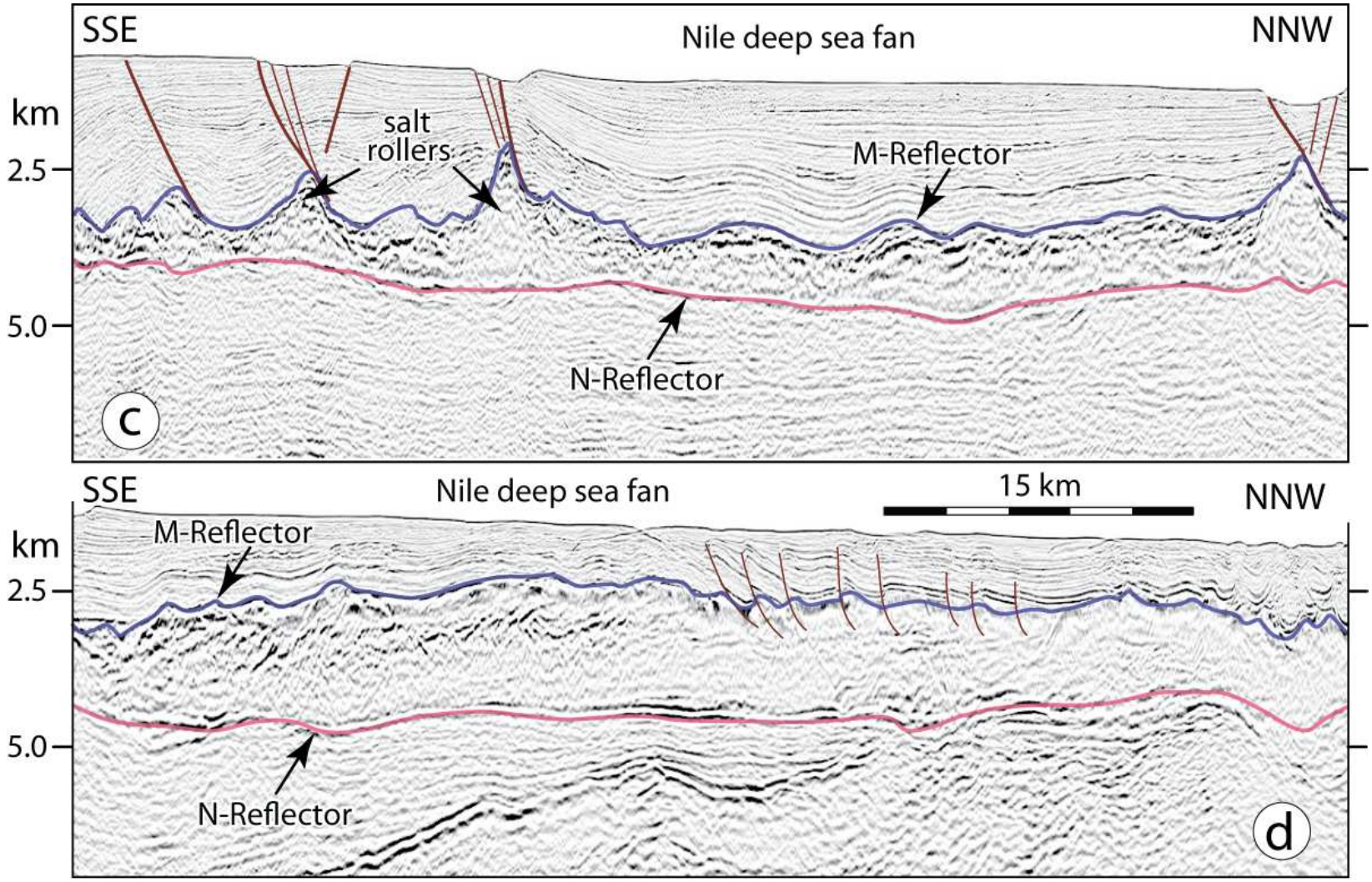

Figure 7.9: Depth-converted multichannel seismic reflection profile across the Nile deep sea fan showing the acoustically transparent and chaotic appearance of the Messinian evaporite successions (profile from Loncke et al., 2010). Location is shown in Figure 7.10.

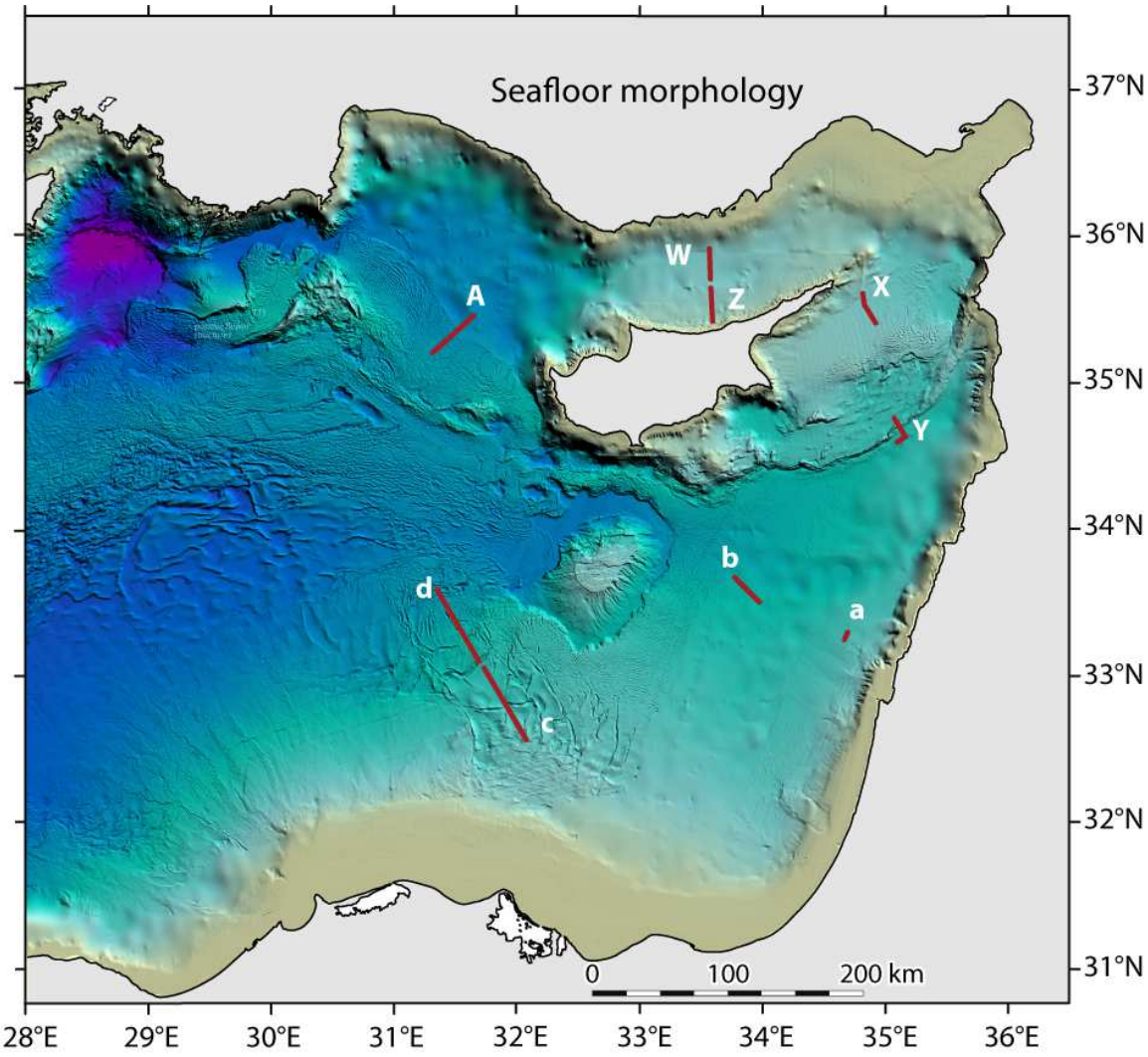

Figure 7.10: Morphological map of the eastern Mediterranean showing the locations of the seismic profiles illustrated in this chapter. The multibeam bathymetry is superimposed on the International Bathymetric Charts of the Mediterranean (from the high-resolution EMODnet, European Marine Observation and Data Network, Portal for Bathymetry, http://www.emodnet-hydrography.eu/). The coastline is taken from the International Bathymetric Charts of the Mediterranean (IOC, 1981).

These are identified as sub-units 2b and 2c. The reflectors separating sub-units 2a – 2b, 2b – 2c and 2c – 2d are identified as α-, β-, and δ-reflectors (Fig. 7.11, Fig. 7.12). The above discussion shows that except for the deep sea fan regions of the Nile delta, the 4-unit divisions of the Messinian evaporite successions observed across the western Mediterranean (e.g., CIESM, 2008; Lofi et al., 2011a, b; Roveri et al. 2014a) is also present across the Levantine Basin.

Messinian evaporite successions are also identified across the Cyprus, Latakia and Cilicia basins (e.g., Hall et al., 2005a,b; Aksu et al., 2005a,b, 2014a,b; Bridge et al., 2005). These studies delineated the top and base of the Messinian evaporite successions (also identified as Unit 2 in these studies), and indicated that there are notable high-amplitude and often laterally continuous reflectors within Unit 2. However these studies did not further subdivide the succession into sub-units. In this study, several critical profiles published in these studies (i.e., Hall et al., 2005a,b; Aksu et al., 2005a,b; 2014a,b; Bridge et al., 2005) are re-interpreted. For example, Figure 7.13 shows the Messinian evaporite successions in a profile extending from the northernmost portion of the Levantine Basin across the Cyprus Arc into the Cyprus Basin. Similarly Figure 7.14 shows the architecture and internal acoustic character of the Messinian evaporite successions across the northern portion of the Latakia Basin, immediately southeast of the Misis-Kyrenia fold-thrust belt (Calon et al., 2005a; Hall et al., 2005a). Finally, Figures 7.15 and 7.16 illustrate the architecture of the Messinian successions across the outer portion of the Cilicia Basin. Comparisons between the high-resolution seismic reflection profiles from the Antalya Basin and those from the northern Levantine, Cyprus, Cilicia and Latakia basins (Figs. 7.11–7.16) clearly show that there are remarkable similarities in the stratigraphic architecture and internal acoustic makeup of the Messinian evaporite successions between these regions, which in turn suggests similarities in the sedimentary processes and Messinian basin evolution.

Across the Nile delta the Messinian successions show notable lateral facies changes from low frequency, high amplitude, low continuity reflections, which are interpreted as siliciclastic sediment to an acoustically transparent seismic facies, interpreted as massive halite (e.g., Aal et al., 2000).

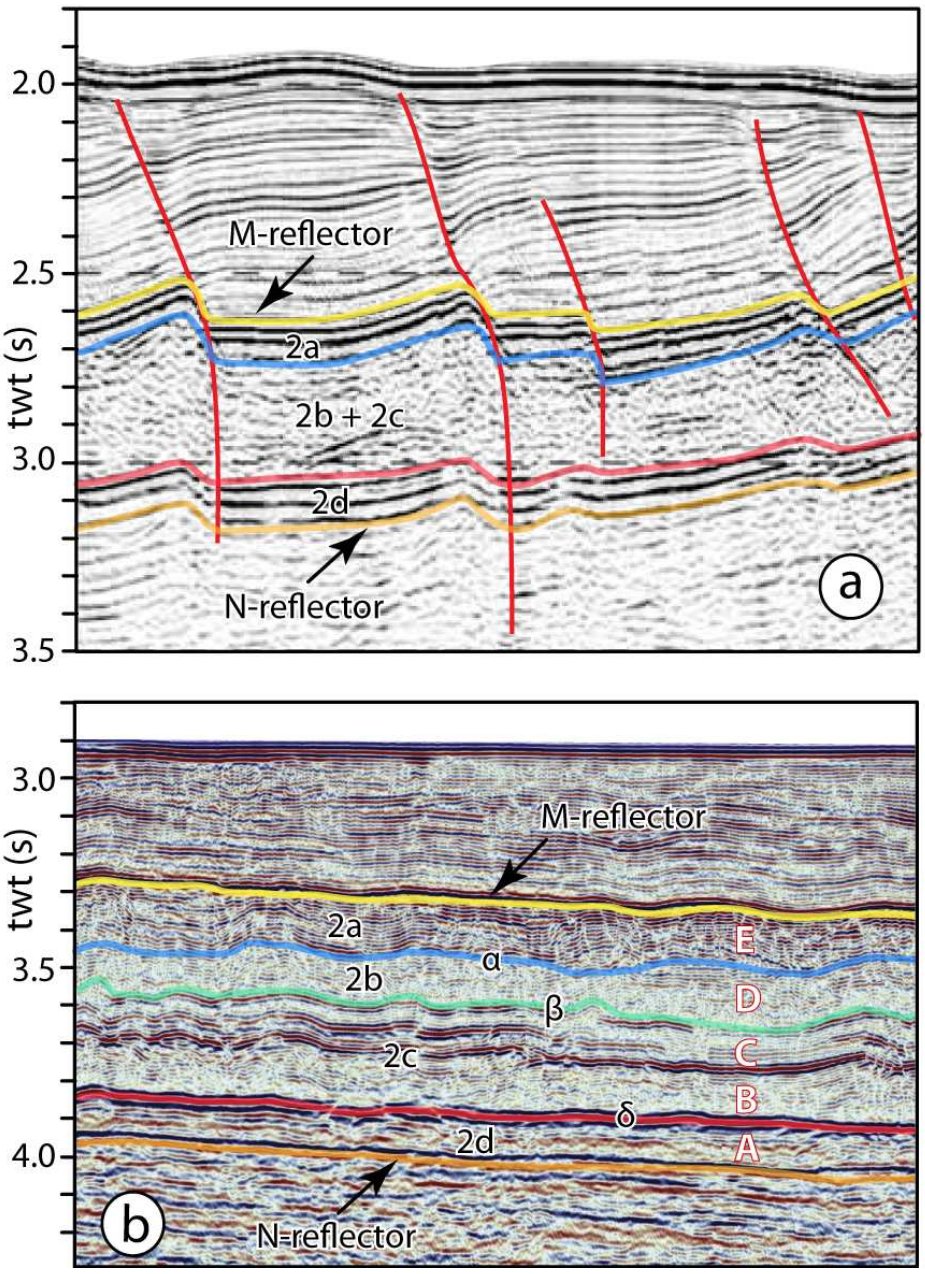

Figure 7.11: Multi-channel seismic reflection profiles from the Levantine Basin showing the internal architecture of the Messinian evaporite successions (profile a and b are from Carton et al., 2009 and Gorini et al., 2015). 2a–2d = Messinian Sub-units identified in this study, A–E in b = Messinian units identified in Gorini et al. (2015). Locations are shown in Figure 7.10.

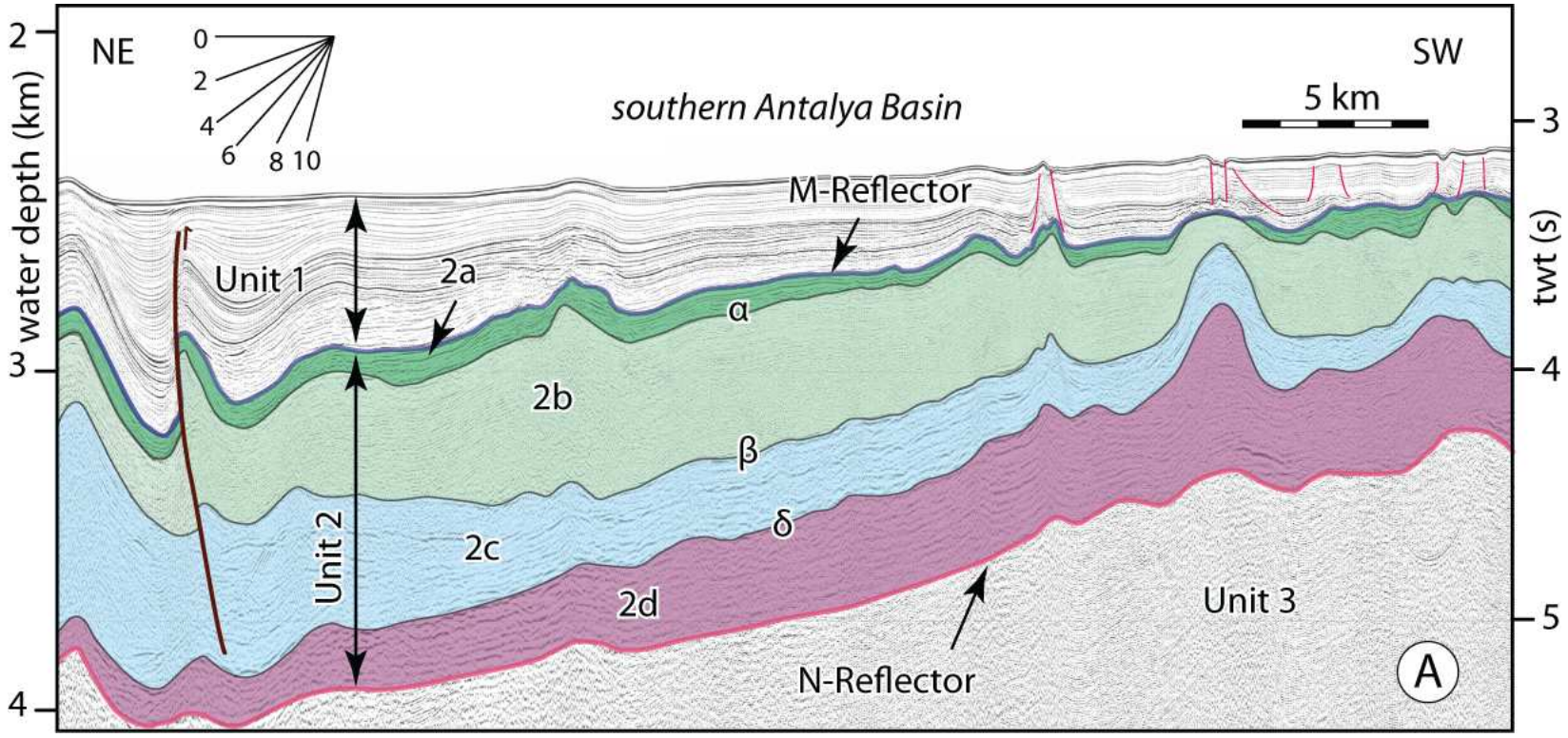

Figure 7.12: High-resolution multi-channel seismic reflection profile A showing the internal architecture of Unit 2 across the southern Antalya Basin. Note the similarities of the acoustic character of sub-units 2a–2d with those illustrated in Figure 7.11. Location is shown in Figure 7.10. This figure is same as Figure 4.13 (§ Chapter 4). EMED10 (fix 1953-1978)

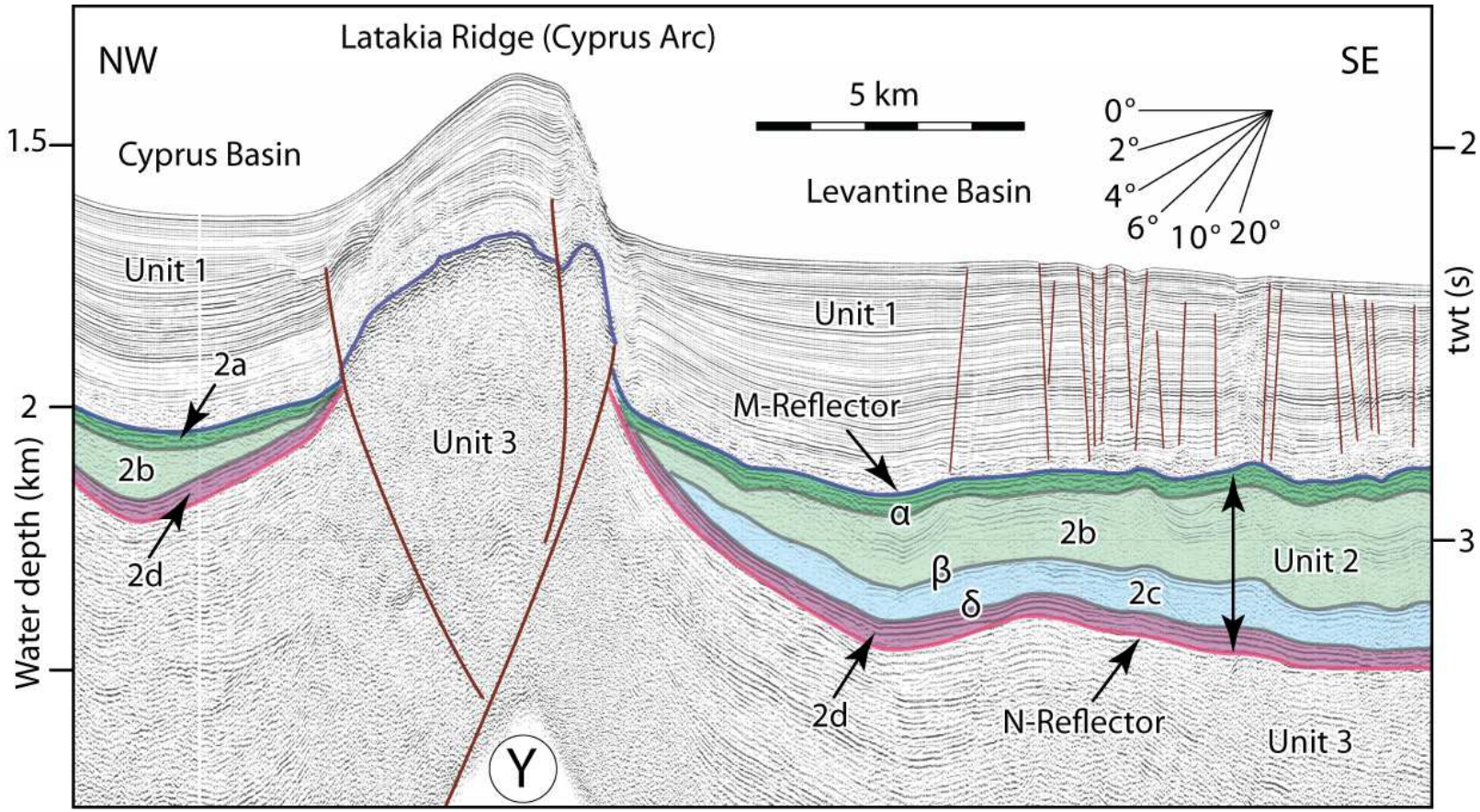

Figure 7.13: High-resolution multi-channel seismic reflection profile Y showing the internal architecture of the Messinian evaporite successions across the northernmost Levantine and Cyprus basins (portion of figure 6 of Hall et al., 2005b). Note the similarities of the acoustic character of sub-units 2a–2d with those illustrated in Figure 7.11. Location is shown in Figure 7.10. EMED92 (fix 823-840)

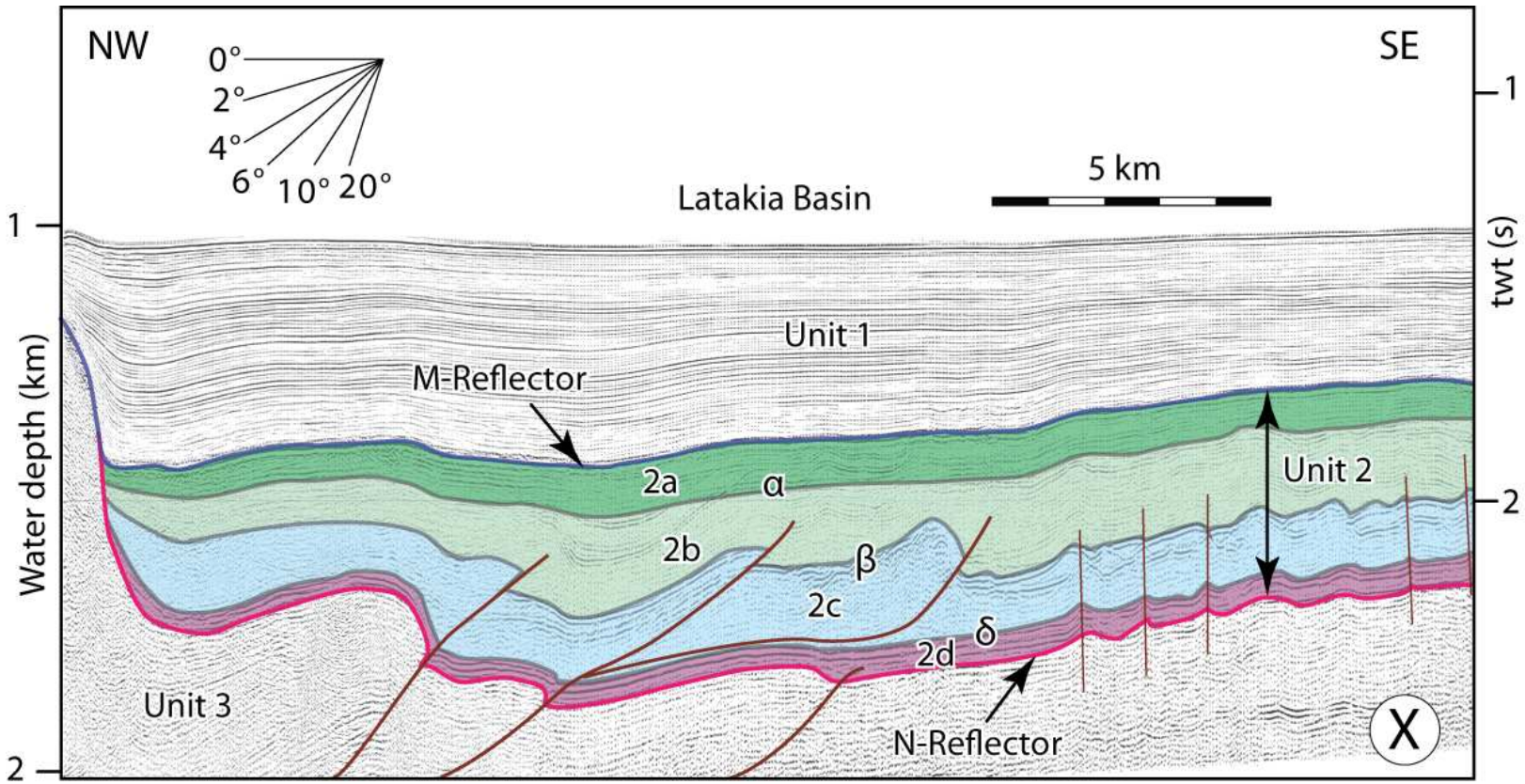

Figure 7.14: High-resolution multi-channel seismic reflection profile X showing the internal architecture of the Messinian evaporite successions across the Latakia Basin (portion of figure 6 of Calon et al., 2005b). Note the similarities of the acoustic character of sub-units 2a–2d with those illustrated in Figure 7.11. Location is shown in Figure 7.10. EMED92 (fix 616-632)

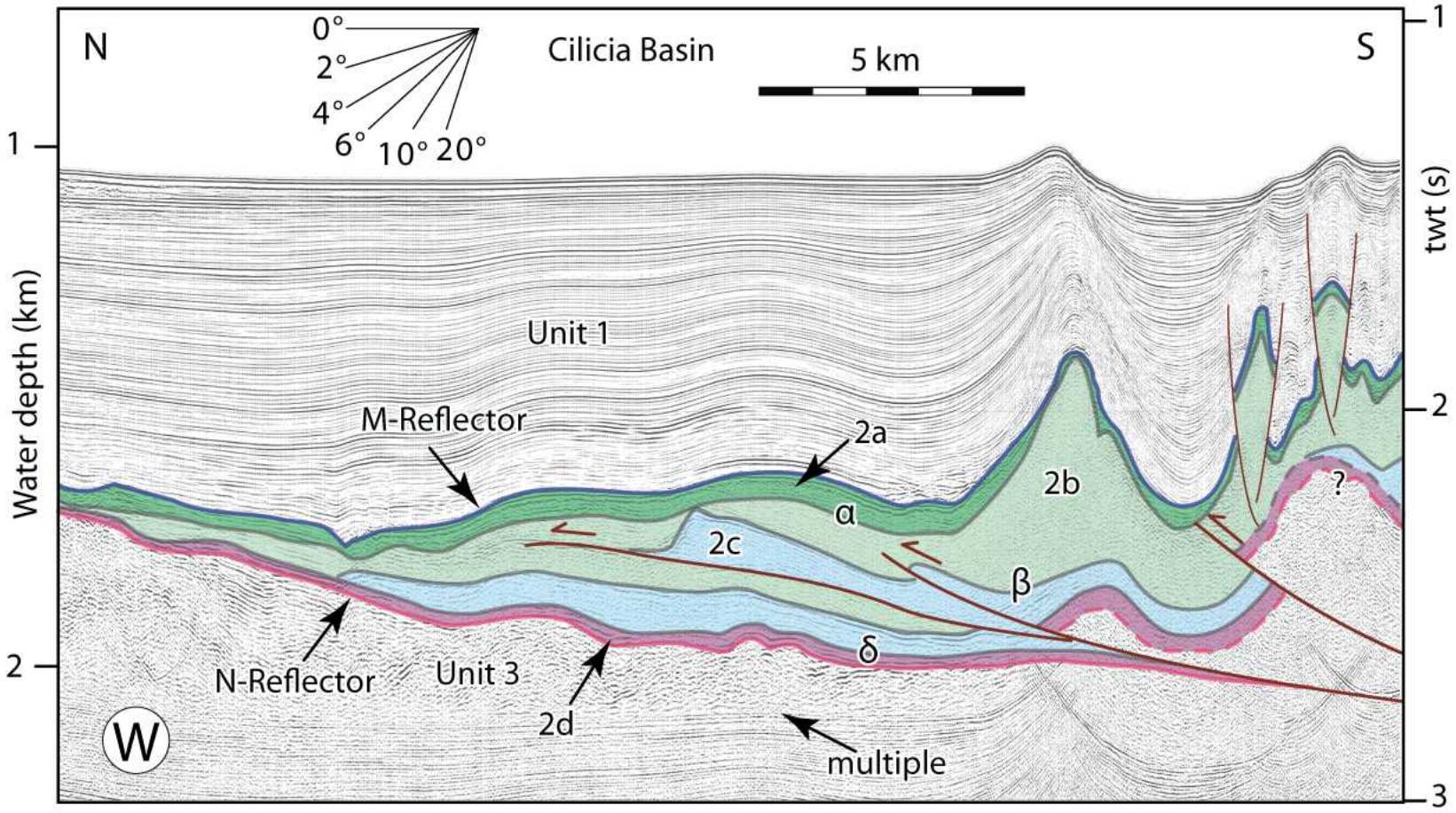

Figure 7.15: High-resolution multi-channel seismic reflection profile W showing the internal architecture of the Messinian evaporite successions across the northern portion of the outer Cilicia Basin (portion of figure 4 of Aksu et al., 2005a). Note the similarities of the acoustic character of sub-units 2a–2d with those illustrated in Figure 7.11. Also note that the N-reflector is interpreted to be lower than that suggested by Aksu et al. (2005). Location is shown in Figure 7.10. EMED92 (fix 1261-1275)

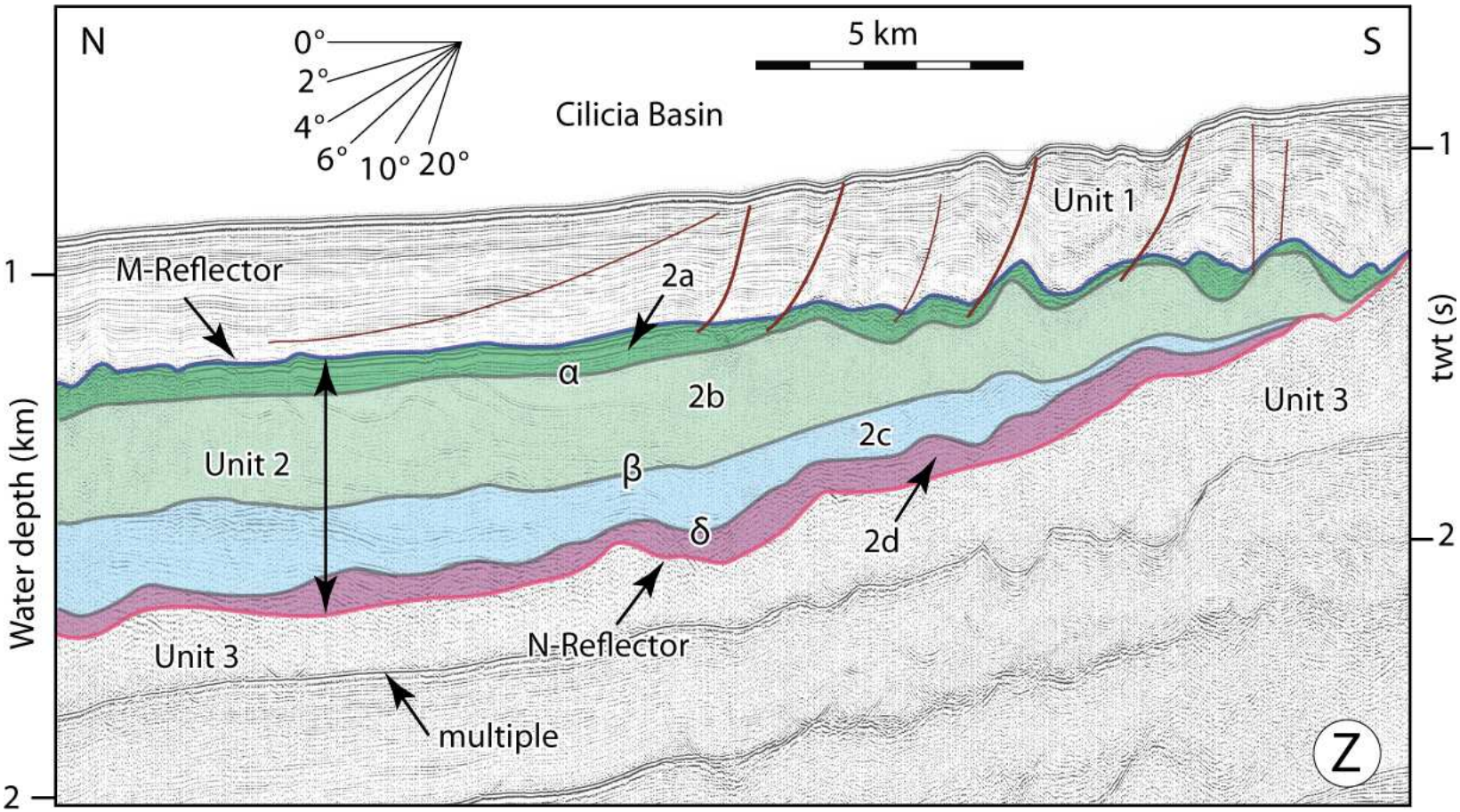

Figure 7.16: High-resolution multi-channel seismic reflection profile Z showing the internal architecture of the Messinian evaporite successions across the southern portion of the outer Cilicia Basin (portion of figure 4 of Aksu et al., 2005a). Note the similarities of the acoustic character of sub-units 2a–2d with those illustrated in Figure 7.11. Location is shown in Figure 7.10. EMED92 (fix 1279-1294)

This lateral seismic facies change is also clearly visible in the Levantine Basin (Gorini et al., 2015) as well as the Antalya and Herodotus basins and the Nile delta. During the onset of the Messinian Salinity Crisis, predominantly siliciclastic sediments eroded from the continental margins and the excavation of the river canyons accumulated in restricted hypersaline Messinian basins. In both, the northern sector (e.g., Antalya, Cilicia, Cyprus, Finike, Iskenderun, Latakia, and Rhodes basins) and southern sectors (e.g., Levantine and Herodotus basins, the Nile delta) of the eastern Mediterranean, Messinian siliciclastics were eroded from the shelf margins and re-deposited in the deep basins as the sea level dramatically dropped associated with the evaporative drawdown. These siliciclastic sediments show an intercalated architecture with evaporite deposits (Gorini et al., 2015) and therefore fully belong to the Messinian Salinity Crisis event. The above discussion and the back-of-the-envelope calculation clearly demonstrated the reason why these siliciclastics are better represented across the Levantine and Herodotus basins: the predominance of the sediment supply by the Nile River, particularly during the initial incision of its gorge when Nile River was forced to readjust to the dramatically falling base level.

Sub-unit 2d (Lower Evaporites /Lower Unit of MSC)

In the deep settings of the Antalya Basin, lower evaporites (sub-unit 2d) of the Messinian corresponds to a highly reflective series of probably detrital sediments deposited by gravity-driven slumps, slides and associated debris flow deposits and the re-deposition of the shallow-water Primary Lower Gypsum during the first stage of sea-level fall. These are known as the Resedimented Lower Gypsum. In shallower settings, the lower evaporites of Messinian Salinity Crisis are commonly related to the presence of incomplete Primary Lower Gypsum (PLG) successions that prevent a precise tuning of the first local gypsum bed. This lower evaporitic succession with primary evaporites precipitation only in marginal basins corresponds to initial stage of the Messinian Salinity Crisis (Roveri et al., 2008a,b, 2015; Manzi et al., 2014). The base of this evaporitic succession defines the onset/base of

the Messinian Salinity Crisis in marginal settings. According to Riding et al. (1998), based on the sedimentary record across the Betic Gateway, evaporite precipitation started in the early Messinian in onshore basins, then moved to the Mediterranean deep basin in the mid-Messinian when it was desiccated, and ended in onshore basins in the late Messinian during its re-flooding.

Manzi et al. (2014) suggested that the base of the unit usually referred to the 'Lower Evaporites' in Cyprus does not actually correspond to the onset of the Messinian salinity crisis. If this is the case in Cyprus, sub-unit 2d in the deep Mediterranean basins (e.g., Antalya Basin) may also not be the time correlative succession of the primary lower evaporites found along the marginal basins across the eastern Mediterranean. Sub-unit 2d correlated with Messinian Salinity Crisis Lower Unit (LU) which is clearly identified on seismic profiles in the deep western Mediterranean basins (e.g., Provençal Basin, Gulf of Lions, Algerian Margin; Lofi et al., 2011b). However, in the eastern Mediterranean previous studies from the Levantine and Herodotus basins and the Nile delta mentioned that these sub-salt Messinian sediments are either missing or were not clearly identified (Loncke et al., 2006, Dümmong and Hübscher, 2010, Reiche, 2015). Hence, Dümmong and Hübscher (2010) and Reiche (2015) proposed that the onset of the Messinian Salinity Crisis in the deep basins corresponds to the base of salt/mobile layer. However, it is very important to precisely define the stratigraphic location of the lowermost predominantly siliciclastic Messinian deposits so that the onset of the Messinian Salinity Crisis in the entire Mediterranean can be accurately delineated. Results of this study and stratigraphic correlations with other eastern Mediterranean sub-basins show that the acoustically transparent layer (inferred to be halite) cannot be the base of the Messinian Salinity Crisis. This is particularly true in regions where large quantities of siliciclastic point-source sediment is present, such as the regions adjacent to large rivers such as Nile, as well as moderate-size rivers such as Aksu, Asi, Manavgat, Ceyhan, Seyhan (Fig. 7.6). Hence the onset of the Messinian Salinity Crisis event must be located at the base of these high frequency reflections, largely corresponding to the Messinian siliciclastics within the lower portion the Messinian Salinity Crisis

successions. These mainly terrestrially-derived sediments must also include variable proportions of Resedimented Lower Gypsum. The latter was originally deposited across nearshore regions during the early evaporative drawdown, but subsequently exposed to gravity-driven mass wasting processes, such as seen in the Qishon Yam 1 well across southeastern Mediterranean continental margin (i.e., slumped Mavqiim Formation sediments, Fig. 7.2).

Sub-unit 2b and 2c -Mobile Unit (MU)

The mobile succession is up to 1500 ms (twt) thick and includes subunits 2b and 2c. Sub-unit 2b shows a reflection-free seismic facies, whereas sub-unit 2c exhibits reflection-free seismic facies with several internal reflections in Antalya Basin and its environs (§ Chapters 3, 4). Within 2c there are high amplitude reflectors with limited lateral continuity, suggesting the presence of layers with distinctive acoustic impedance contrast within a thick package of uniform density (i.e., no significant reflections). Previous studies were vague on the nature of these high amplitude reflectors within the mobile unit (e.g., Lofi et al., 2011a, b). However, interval velocities in the seismic reflection profiles provided much needed information regarding the composition of the high amplitude relatively good continuity reflector. In the southern Antalya Basin, the interval velocities within sub-unit 2c range from 3500 m s^{-1} to 4000 m s^{-1} across the high-amplitude reflector zones, which suggest considerable presence of siliciclastic material in a predominantly evaporite-dominated succession with velocities of 4200–4800 m s^{-1} (§ Chapter 4). This velocity profile strongly suggests that sub-unit 2c must be composed predominantly of massive halite interbedded with anhydrite, Mg and K salts, as well as siliciclastic sediments. The siliciclastic sediments were probably supplied through the erosion of the subaerially exposed continental margin. In the eastern Mediterranean the presence of halite has been recognized by boreholes in the Cyprus Mesaoria Basin (Gass, 1960; Robertson et al., 1995) and Florence Rise (Ref), whereas in the Antalya (this study), Larnaca-Latakia, Herodotus and Levantine basins (Robertson et al., 1995; Maillard et al., 2010) the presence of halite has been

inferred from seismic profiles.

Across the Antalya Basin, the existence of two sub-units (i.e., 2b and 2c) suggests vertical compositional changes within the mobile evaporite facies with intercalated siliciclastics and trapped fluids (Fig. 5.37, § Chapter 5). Very similar facies changes are also suggested for the mobile successions in the Levantine Basin (e.g., Loncke et al., 2004; Gradmann et al., 2005; Netzeband et al., 2006b; Hüsbscher et al., 2008). In the deep Antalya Basin the mobile evaporite sub-units 2b and 2c are generally overlain by the upper evaporites of sub-unit 2a, which are in turn overlain by the *Lago Mare* facies. Elsewhere in the eastern Mediterranean, the mobile evaporite sediments are directly overlain by the Pliocene–Quaternary successions although, some seismic units resembling upper evaporites (UU=Sub-unit 2a) and lower evaporites (LU=Sub-unit 2d) are also observed locally in the Nile delta area (Reiche, 2015; Maillard et al., 2012).

As also discussed earlier, the comparison and correlations with the previous studies showed that the 4-unit divisions of the Messinian evaporite successions observed across the western Mediterranean including the lower evaporites (sub-unit 2d), mobile unit (sub-units 2b and 2c) and upper evaporites (sub-unit 2a) are correlative with the Messinian succession observed across the eastern Mediterranean except for the Nile deep sea fan area. The mobile package in most of the western Mediterranean basins is clearly bounded above and below by two other Messinian Salinity Crisis units: UU and LU, respectively. It is important to note that the mobile unit in the western Mediterranean is much thinner (<500 ms, Lofi et al., 2011b and references herein) than that observed in the eastern Mediterranean.

Sub-unit 2a-Upper evaporites (Upper Unit, UU)

The Upper Unit is the youngest succession in the Messinian trilogy, corresponding to the last stage of the Messinian Salinity Crisis (CIESM, 2008; Roveri et al., 2008a,b; Manzi et al., 2014). It is characterized by periodic salinity changes that occurred throughout the Mediterranean basin (east

and west), and is recorded by alternating evaporites and clastic deposits containing brackish to fresh water faunas (Hsü et al., 1973; CIESM, 2008). The upper evaporites of the Messinian Salinity Crisis have been observed both in marginal and deep basins in the western and eastern Mediterranean (Lofi et al., 2011b; Manzi et al., 2014).

In the Antalya Basin, sub-unit 2a is identified by a group of parallel and relatively continuous reflections of relatively high amplitude which correspond to six to seven gypsum horizons interbedded with green dolomitic marlstone cored at the DSDP Sites 375 and 376 (Shipboard Scientific Party, 1978). In this study the M-reflector has been located between the upper evaporites (sub-unit 2a) and the *Lago Mare* facies (lower sub-unit 1c) which is characterized by brackish water environments (§ Chapters 3, 4). Such deposits are usually considered to have preceded marine re-flooding of the Mediterranean (Cita and Colombo, 1979), but recent researches suggested that the upper evaporites may have coexisted with the *Lago Mare* facies (Clauzon et al., 2005; Popescu et al., 2009). In the deep Antalya Basin, the upper evaporite sub-unit 2a has a lateral continuity and near uniform thickness, and is often faulted associated with the post-Messinian salt tectonics. In more proximal areas, sub-unit 2a pinches out and/or onlaps the continental margin (further discussed below § Section 7.1.3).

Previous studies show thick and widespread upper evaporite sequences in the deep western Mediterranean basins, but indicated that this is not the case for the eastern Mediterranean deep basins (Ryan 1978; Bertoni and Cartwright, 2007a; CISEM 2008; Lofi et al., 2011b). However, high-resolution multi-channel seismic data and velocity analysis results used in this study support the existence of an upper evaporite sub-unit across the deep basinal portion of the eastern Mediterranean. The upper evaporite sub-unit exhibits notable variability in its acoustic character, suggesting variable siliciclastic input from the landmass surrounding the eastern Mediterranean. For example, large quantities of siliciclastic debris must have been transported into the Antalya Basin via the Aksu, Köprü and Manavgat rivers and possibly (and periodically) the Seyhan, Tarsus, Göksu rivers through

the deep canyon that transect the outer Cilicia Basin (Fig. 7.6, Akay et al., 1985; Poisson et al., 2011). However, much less siliciclastic sediment arrived into the intermediate-depth Polemi Basin in Cyprus. Conversely, the intermediate-depth Adana–Cilicia and Iskenderun–Latakia–Mesaoria basin complexes must have received very large quantities of siliciclastic material via the Seyhan, Tarsus, Göksu rivers in the west and the Ceyhan and Asi rivers in the east (Fig. 7.6). In the Levantine and Herodotus basins, enormous quantities of siliciclastic input by the Nile River must have overwhelmed the evaporative sedimentation in the region immediately north of the river mouth, thus the apparent absence of sub-unit 2a in these proximal regions, but well developed sub-unit 2a in distal regions. It is also important to note that, while the Messinian was generally a tectonic quite interval, the Central Taurus and Misis mountains of central Turkey as well as the Kyrenia Range of northern Cyprus were evolving, thus possibly providing additional sedimentary load to the rivers draining Anatolia.

The results from this dissertation document that the Messinian evaporite successions (i.e., Unit 2) across the deep eastern Mediterranean basins show remarkable similarities with their counterparts across the deep western Mediterranean basins. These acoustic similarities strongly suggest similarities in the basin evolution and sedimentary processes, but not necessarily the timing of these events, as further discussed later.

7.1.3 Zero ms isopach of Messinian evaporites

The edge of the Messinian evaporite succession can be readily delineated across the eastern Mediterranean (i.e., the zero ms isopach contour, Fig. 7.1). The zero ms isopach contour can be interpreted as denoting (a) the depositional edge of the Messinian evaporites in the eastern Mediterranean and/or (b) the final area of salt withdrawal associated with the weld development along continental margins, and/or (c) considerable unidirectional Pliocene–Quaternary loading and major salt evacuation. All the above appear to have developed across the eastern Mediterranean.

Weld development and downslope salt migration

It is possible that the depositional edge of the Messinian evaporites was higher on the slope and either during the loading of the Pliocene–Quaternary sediments or associated with gravitational downslope migration, the evaporites assumed a deeper level along the basin edge. For example, Hall et al. (2014) proposed two lines of evidence to argue that the depositional edge of the Messinian evaporite succession may have been much higher along the slope: (1) the widespread occurrence of evaporite deposits in the Cilicia and Adana basins in the eastern Mediterranean suggests that the sea level must have risen considerably sometime during the Messinian to allow evaporite deposition within these basins which are situated 1500 m–2000 m above the present-day floor of the Antalya Basin, and (2) onland studies clearly show that the Gebiz Formation in the Aksu, Köprüçay and Manavgat basins include anhydritic and gypsiferous intervals, suggesting that these now onland basins must have been inundated and were receiving evaporitic deposition during the Messinian (Akay and Uysal, 1985; Akay et al., 1985). The occurrence of evaporites in the Cilicia and Adana basins as well as in the Aksu, Köprü(çay) and Manavgat basins argues that evaporite deposits must have developed higher along the slope and/or the surrounding continental shelves of the Antalya Basin during the Messinian. These possibly thinner evaporite deposits may have migrated downslope during the Pliocene–Quaternary mobilization of Unit 2 (Bridge et al., 2005; Işler et al., 2005), thus creating weld surfaces along much of the present-day continental slope. Thus, the 0 ms isopach contour not only shows the present-day edge of the evaporites, but also suggests that the bulk of the evaporite deposition has taken place in the deeper parts of the Antalya Basin.

Wholesale evacuation of salt

During the Messinian Salinity Crisis large quantities of evaporites were also deposited across the Herodotus Basin, extending southward into the area now occupied by the Nile delta (Ryan and Hsü, 1973, Sage and Letouzey, 1990). Loading of the ductile evaporitic layers by the thick Pliocene–

Quaternary prograded delta successions from the south triggered the gravity-driven salt tectonics that continue to the present-day in most of these areas (Ross and Uchupi, 1977, Sage and Letouzey, 1990, Kempler et al.,1996, Gaullier et al., 2000, Loncke and Mascle, 2004, Loncke et al., 2006). Thus, the distribution and thickness patterns of the Messinian successions observed today across the Nile delta were highly affected by the salt tectonics which caused the northward spreading and/or gliding of both the salt layer and its overburden (Loncke et al., 2006). During the Pliocene–Quaternary rapid delta progradation must have resulted in the evacuation of the Messinian evaporite successions from the Nile delta region, causing the southern limit of thick salt migrating northward through time (Loncke et al., 2006). Today, the thickness of the Messinian evaporite succession is very thin in the proximal area and it is $\sim$3 km near the base of the slope, where the sediment overburden is negligible. Loncke et al. (2006) suggested that this pattern results from two fundamental processes: (a) proximal sedimentary loading has induced some amount of seaward salt migration and distal inflation and (b) as the thick depocentres were translated seaward, the salt layer and its thin overburden located downslope (from the depocentre) were pushed forward, bulldozed, and thickened. Across the Herodotus Basin, the Pliocene–Quaternary sediment thickness is $\sim$2.5 km, whereas salt reaches thicknesses of up to 3 km toward the abyssal plain and 1 km toward the Eratosthenes Seamount (Loncke et al., 2006).

The deep sea fan region of the Nile delta is divided into the eastern, central and western provinces, with each province exhibiting notable geological patterns in (a) the subsalt tectonic architecture, including active or dormant basement faults, (b) the dip and 3D geometry of the base salt, (c) the estimated salt thickness when thin-skinned salt tectonics began, and (d) the presence of a Messinian relief devoid of Messinian salt (Loncke et al., 2006). In the western province, the Messinian sedimentation was lower than that in the central and eastern provinces. There is even evidence that no salt was ever deposited in an area located about 100 km from the southern salt pinch-out (Loncke et al., 2006). Montadert et al. (2014) suggested that during this period, most of the sediments that

were delivered by the Nile River were diverted westward by the prominent Eratosthenes continental block. In the central and western provinces, thickness variations of the Messinian successions follow similar trends which are associated with higher sediment supply: very thin in the south – thickening toward the north, although with some variation occurs across salt rollers in listric growth faults (Loncke et al., 2006).

Seismic data interpretations from the previous studies (Montadert et al., 2010a,b, 2014; Tari et al., 2012; Aksu unpublished data) show that the Herodotus Basin has the thickest Messinian evaporite succession in the eastern Mediterranean area. Figure 7.1 shows that both the pinch-out of the salt around the Eratosthenes Seamount, and the great thickness of evaporites across the Herodotus Basin, reaching up to 2.5 s, are due to the flexure of the eastern Cyprus Arc. In the easternmost regions of the Herodotus Basin and the south of the Eratosthenes Seamount the mobile Messinian evaporite succession is $\sim$1.4 s thick, but $\sim$0.8 s thick east of the seamount. South and west of the seamount, Loncke et al. (2006) proposed that loading of the salt layer and seaward gravity spreading of the prograding sediments contributed to inflating of the distal salt layer, which encroaches onto the base of the seamount. Therefore, Gaullier et al. (2000) suggested that the present-day limit of this partly allochthonous salt mass lies higher and farther north than the initial depositional limit of the autochthonous unit. Near the bathymetric scarp, local thickening of the Messinian succession layer (up to 2000 ms-thick) is visible (Fig. 7.1). Loncke et al. (2006) also proposed that this thickening might be explained by stacked up salt in nappes and overthrust salt.

The appearance of the Messinian evaporite succession pinchout both on the northern and southern flanks of the Florence Rise and its characteristic erosional unconformity at the top of the rise tell us that the Florence Rise was already a positice structure during the Messinian Salinity Crisis and separates two main salt-bearing basins: the Antalya basin to the north and the Herodotus Basin with distal tip of the Nile deep sea fan to the south (Montadert et al., 2010a,b).

7.2 Role of the Sicily gateway during the Messinian Salinity Crisis

The chronology of the events associated with the Messinian Salinity Crisis is intrinsically linked with the tectonic evolution of the western and central Mediterranean regions. This linkage has two important components: (a) the evolution of the Betic and Rif gateways across the westernmost Mediterranean which controlled the saline water influx into the Mediterranean during the Messinian Salinity Crisis, and (b) the evolution of the Sicily gateway in the central Mediterranean which controlled the saline water influx into the eastern Mediterranean, again during the Messinian Salinity Crisis. The present-day depth of the Sicily sill is -430 m (Blanc, 2000). This depth suggest that in order for the Sicily gateway to provide saline water influx into the eastern Mediterranean, the water level must have risen to the breach depth of the sill, which would have probably terminated the deposition of the evaporites across the western Mediterranean. The Messinian evaporite successions comprise a total volume of about 10^6 km^3, and reach thicknesses of up to 1500 m and 3500 m in the western and eastern Mediterranean deep basins, respectively, while thinner evaporite successions were deposited in the marginal basins (Hsü et al., 1977). The present-day volume of the entire Mediterranean, if completely evaporated is not sufficient to create the thickness of the Messinian evaporites observed across the Mediterranean region (e.g., Işler et al., 2005). Modelling done by Blanc (2000) clearly demonstrated that the total quantity of the North Atlantic Surface Water that must have passed through the Betic and Rif straits during the Messinian Salinity Crisis must have been between 75–100 times the present-day volume of the Mediterranean Sea. This volume of saline water was needed to account for the great thicknesses of evaporites deposited across the Mediterranean during the Messinian Salinity Crisis. Therefore, in order to account for the massive thicknesses of evaporites in the Herodotus and Antalya basins and to a lesser extent the Levantine, Cilicia and Latakia basins in the eastern Mediterranean, the Sicily gateway must have been leaky during the deposition of the lower and upper mobile units. The immediate ramification of this statement is this: “the lower and upper mobile units found across the western and eastern Mediterranean basins cannot have been deposited synchronously in

the eastern and western basins" (Blanc, 2000). If this statement is true, then any model proposed for the evolution of the lower and upper mobile units in the eastern Mediterranean must further account for a protracted period (or periods) when the Sicily sill must have remained within a "goldilocks" zone which allowed just the right amount of saline water into the eastern Mediterranean region so that evaporites were deposited there but not across the western Mediterranean region because the sea level was at the breach-level of the Sicilian sill. A similar scenario was proposed for the Gibraltar region where an intricate balance between erosion and uplift maintained the right amounts of saline water influx into the western Mediterranean across the Betic and Rif gateways (Garcia-Castellanos et al., 2009; Garcia-Castellanos and Villaseñor, 2011). Was there a similar set of processes across the Sicily gateway at some interval during the Messinian Salinity Crisis? These are further discussed below.

7.2.1 Plate tectonics of the Betic, Rif and Sicily gateways

The plate tectonic evolution of the western Mediterranean involved a protracted history of subduction rollback and the associated wide-spread extension across the regions on the overriding plate, including the development of the Ligurian Sea, Gulf of Lion and Valencia Trough, and eventually the Alboran Sea (§ Chapter 1, Rosenbaum et al., 2002). Similarly, the plate tectonic evolution of the central Mediterranean also involved subduction beneath the Calabrian Arc and the rollback of the Ionian lithosphere associated with opening of the Tyrrhenian Sea as a back-arc basin (§ Chapter 1, Malinverno and Ryan, 1986; Mattei et al., 2007; Cifelli et al., 2007). In both regions, lithospheric slab detachment has been suggested as the most likely cause for the protracted uplift across the Gibraltar Arc in the west (e.g., Garcia-Castellanos and Villaseñor, 2011) and the Calabrian Arc in the east (e.g., Chiarabba et al., 2008). Both regions have considerable importance for the development of the Messinian Salinity Crisis: the evolution of the Gibraltar Arc controlled the depths of the Betic and Rif gateways, whereas the evolution of the Calabrian Arc controlled the depth of the Sicily

Gateway (Fig. 7.17, Blanc, 2000).

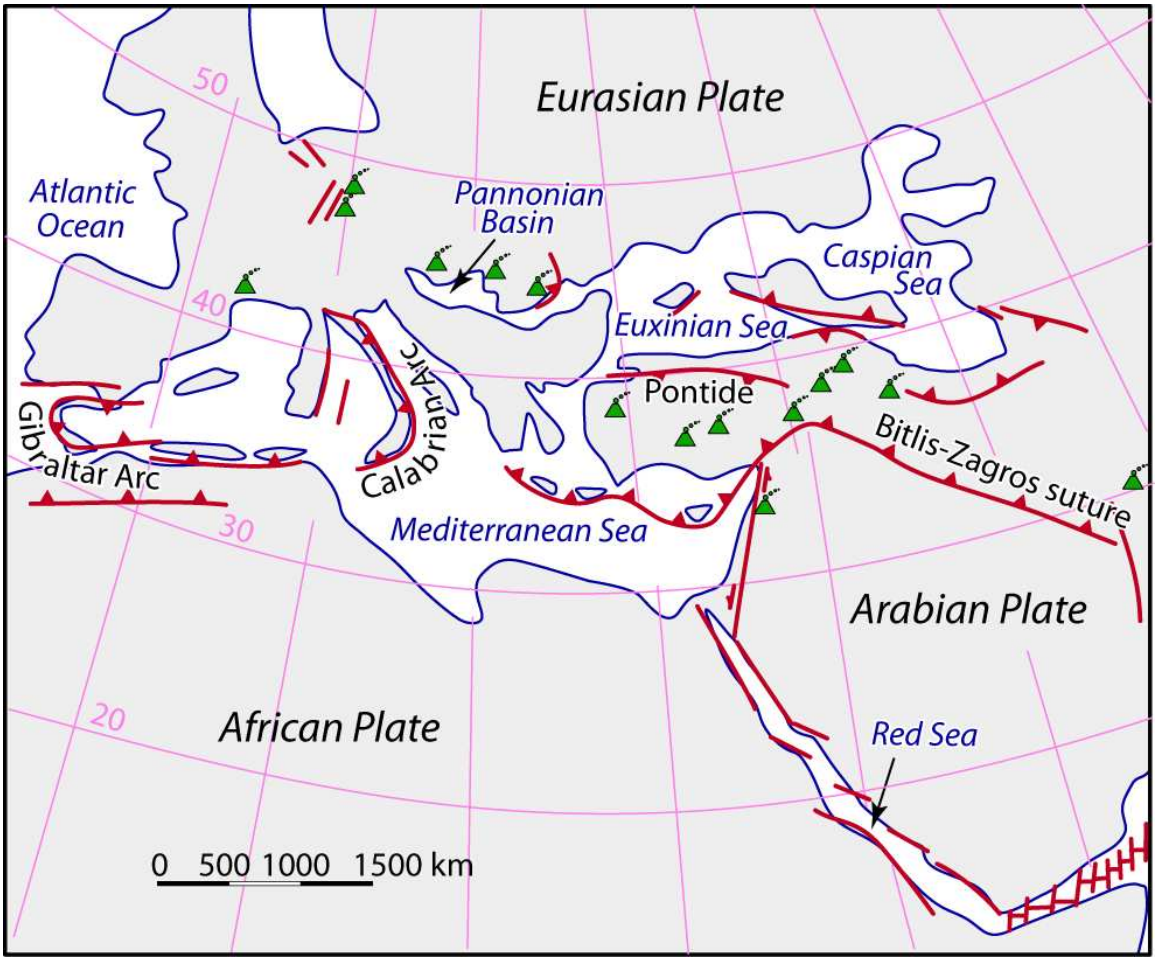

Figure 7.17: Paleogeography of the Mediterranean and environs during the Messinian (adopted from Popov et al., 2004). Note that the only watermass communication between the Mediterranean and the world ocean occur across the Gibraltar Arc region (i.e., the Betic and Rif gateways).

The evolution of the distinctive sedimentary successions associated with the Messinian Salinity Crisis has several unique features and requirements. These unique features are: (a) the Betic and Rif gateways formed the only water-mass communication between the Mediterranean and the Atlantic Ocean during the Messinian (Fig. 7.17, Garcia-Castellanos and Villaseñor 2011), (b) enor-

mous quantities of evaporites precipitated during the Messinian Salinity Crisis, which requires the evaporation of 75–100 times the volume of the Mediterranean (Blanc, 2000), (c) a 4-unit stratigraphy (including sub-units 2a–2d) developed across the western and eastern Mediterranean region (Roveri et al., 2014a,b, this study), (d) largest rivers flowing into the nearly-desiccated Mediterranean excavated deep gorges exceeding ∼2,500 m in Nile delta (Barber 1981) and ∼1,000 m at the mouth of the Rhône River (Clauzon, 1978, 1982), (e) the duration of the two main phases of evaporite deposition (i.e., sub-units 2c and 2b) have been estimated at 360 and 270 kyr, respectively, on the basis of the assumption that the 14 to 17 cycles observed in the gypsum deposited in sub-unit 2c are due to Milankovitch precessional cycles of insolation (van der Laan et al., 2005, 2006), and (f) strontium isotope data indicate that the deposition of sub-unit 2c took place in a restricted Mediterranean with reduced connectivity with the Atlantic, whereas that of sub-unit 2b occurred in predominantly continental waters with little or no connection to the ocean (Flecker and Elam, 2006).

The unique requirements for the evolution of the distinctive sedimentary successions associated with the Messinian Salinity Crisis are: (a) a geologically feasible mechanism is needed for the closure of the Betic and Rif gateways, (b) the evaporation of 75–100 times the volume of the Mediterranean to account for the volume of evaporites deposited across the Mediterranean Sea dictates that the Betic and Rif gateways must have been very shallow, but leaky, (c) the development of evaporites across the eastern Mediterranean and the strontium isotopic data require a geologically feasible mechanism for the closure of the Sicily Gateway, (d) the development of massive quantities of evaporites across the eastern Mediterranean dictates that the Sicily Gateway must have been very shallow, but leaky, and (e) the development of massive gypsum deposits at the basin margins indicating minor sea-level drawdown, and the massive salt deposits across the deep basins requiring kilometre-scale sea-level drawdown clearly document that multiple phases of filling and drawdown must have taken place, requiring an eloquent mechanism for these large-scale sea-level oscillations.

7.2.2 Depositional model

Any model that satisfies the above requirements must also take into account the morphological changes that have taken place across the deep central Mediterranean basins since the Messinian. Previous studies suggested that the Messinian morphology of the Mediterranean basins was similar to that observed today (e.g., Blanc, 2000). To confirm this, an east-west trending cross section is constructed across the present-day Mediterranean, extending from the Gibraltar Strait across the Alboran, Algerian and Baleric basins to the Sicily Strait, and then farther extending across the Ionian, Herodotus and Levantine basins (Fig. 7.18). This cross section formed the basis of a second cross section where the thicknesses of the Messinian and Pliocene–Quaternary sediments are shown (Fig. 7.19a). Finally, the approximate positions of the seafloor for the period immediately after the onset of the Messinian Salinity Crisis and that immediately after the Zanclean flooding are calculated by subtracting subsidence and compaction from the positions of the N- and M-reflectors (Fig. 7.19b). This exercise clearly illustrated the first order similarities, but also the dissimilarities between the cross-sectional morphology between the early Messinian, Zanclean and present-day seafloor.

One of the very critical findings of this study is the requirement that the two major Messinian evaporite mobile sub-units (i.e., 2c and 2d) must have developed first across the eastern Mediterranean. This may have taken place as (a) sub-unit by sub-unit, that is sub-unit 2c deposited in the east first and then followed by sub-unit 2c deposition in the west, then sub-unit 2b deposition in the east, the followed by sub-unit 2b deposition in the west, or (b) as sub-units 2c+2b were deposited in the east, followed by sub-units 2c+2b deposition in the west. Regardless whether the former of the latter is correct, the most critical region for the evaporite deposition across the eastern Mediterranean is the Sicily Gateway, because as already discussed earlier the only source for the saline water for the eastern Mediterranean evaporites was the Atlantic Ocean, and many volumes of present-day Mediterranean were need to form the observed thicknesses of evaporites across the deep eastern Mediterranean basins. But, what kind of a process kept the Sicily Gateway at a most critical water

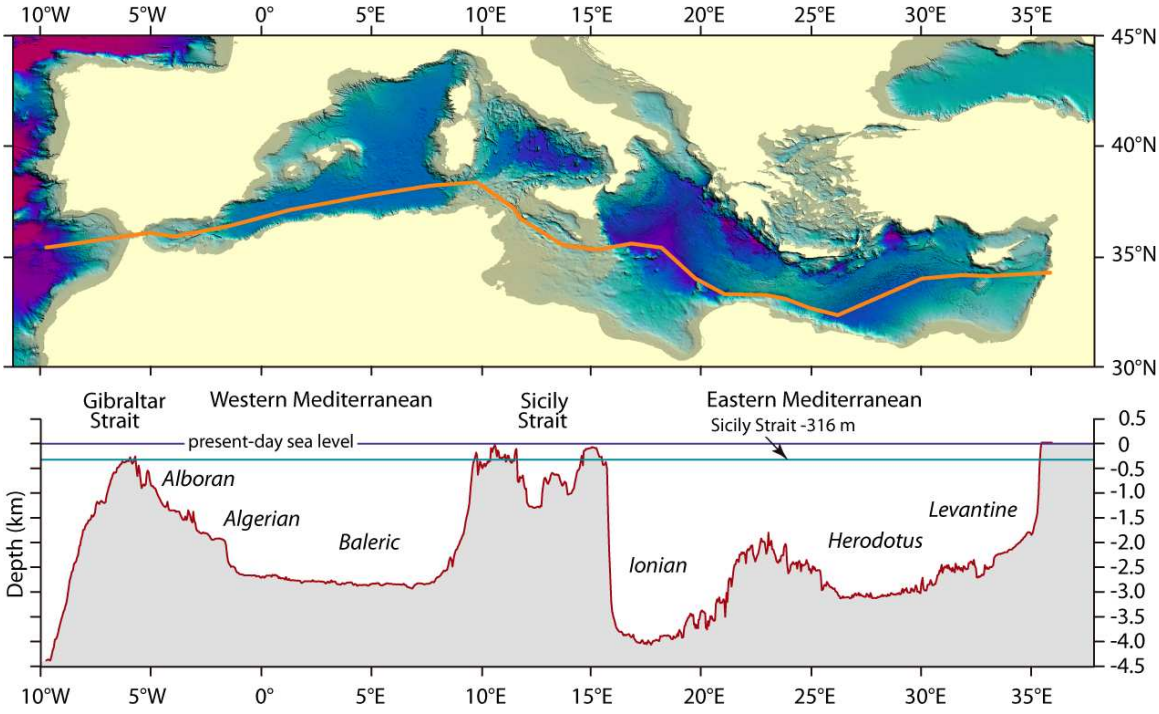

Figure 7.18: Shaded relief map of the Mediterranean Sea, where the high-resolution EMODnet (European Marine Observation and Data Network, Portal for Bathymetry, http://www.emodnet-hydrography.eu/) data are gridded and contoured using Global Mapper. The bathymetric profile is also created using Global Mapper. Note that the Strait of Sicily defines a prominent bathymetric feature separating the eastern and western Mediterranean seas.

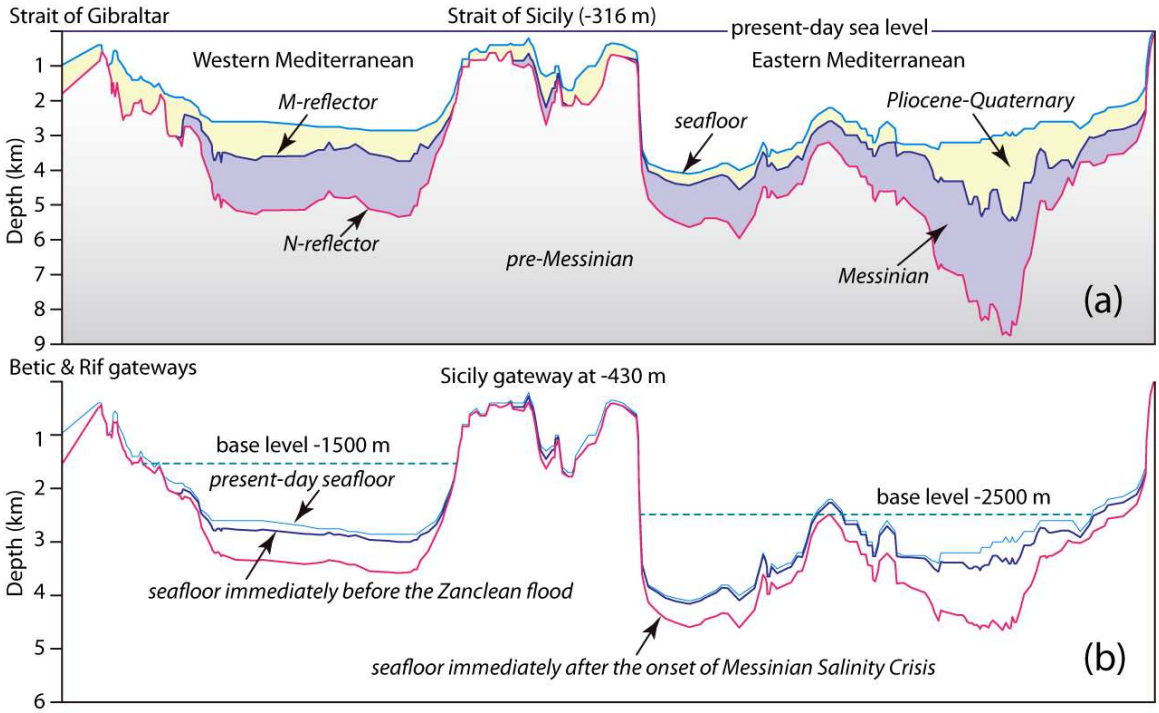

Figure 7.19: **(a)** East-West cross sections across the Mediterranean Sea, showing the present-day seafloor (taken from Figure 7.16) and the positions of the M- and N-reflectors. The position of the M-reflector is calculated using the thickness of the Pliocene–Quaternary sediments (IOC, 1993), whereas that of the N-reflector is calculated using the IOC (1993) data for the western and central Mediterranean and the seismic data used in this study for the eastern Mediterranean. **(b)** The approximate position of the seafloor for the period immediately after the onset of the Messinian Salinity Crisis and that immediately after the Zanclean flooding are calculated by subtracting subsidence and compaction from the positions of the N-and M-reflectors. Subsidence t (km) for an x (km) thickness of sediment with specific gravity of 2.0 g cm^{-3} is calculated using the equation [$t = x/2.3$]. Average compaction is taken as 40% for the Pliocene–Quaternary siliciclastic successions (Allen and Allen 2005) and 20% for the Messinian evaporite successions (Warren 2010). Base levels for the western and eastern Mediterranean seas are from Blanc (2000). Location is shown in Figure 7.16.

depth which allowed the just the right amount of saline water inflow into the eastern Mediterranean for evaporative drawdown, but never high enough to fill the eastern Mediterranean to the breach depth of the Sicily Gateway? The immense literature that exists on the Messinian Salinity Crisis is mute about this.

A very similar question can be asked for the Betic and Rif gateways. As discussed before, both the Betic–Rif gateways and the Sicily Gateway experienced protracted uplift during the Messinian as part of the arc rollback and the associated slab tear across the Gibraltar and Calabrian arcs, respectively. Garcia-Castellanos and Villaseñor (2011) proposed a very eloquent model for keeping the Betic and Rif gateways at the most critical water depth which only allowed the right amount of saline water inflow from the Atlantic Ocean into the western Mediterranean for evaporite deposition there, but never filling the western Mediterranean to the breach depth(s) of the Betic and/or Rif gateways (Figs. 7.20b, 7.21). These authors carried out laboratory experiments to show that competition between uplift and erosion results in harmonic coupling between erosion and inflow of Atlantic water into the Mediterranean, and that in the case of the Gibraltar Arc region the tectonic uplift was balanced by erosion caused by inflowing Atlantic water (Figs. 7.20b, 7.21). These experiments and their results provided an alternative mechanism for the cyclicity observed across the lower evaporite unit (i.e., the 14–17 gypsum cycles) across the western Mediterranean (Garcia-Castellanos and Villaseñor, 2011). This model raises the question whether a similar process also occurred across the Calabrian Arc keeping the Sicily Gateway at the critical water depth to allow just the right amount of saline water inflow from the Atlantic Ocean via western Mediterranean (Figs. 7.20a, 7.21). Anything other than a very balanced inflow would either have completely desiccated the eastern Mediterranean or filled it to the breach depth of the Sicily Gateway. The occurrence of evaporites (both halite and gypsum) across the intermediate water depth Adana, Cilicia, Latakia, Iskenderun, Mesaoria basins across the northeastern sector of the eastern Mediterranean suggests that the rates of saline water inflow across the Sicily Gateway and the rate of erosion of the Sicily sill

may not have been perfectly balanced during some intervals across the Messinian. This speculative idea requires further investigating because of the Sicily Gateway is the only source for saline inflow into the eastern Mediterranean, which must also fulfill many critical requirements of the Messinian evaporite deposition across the eastern Mediterranean (see § 7.3 below).

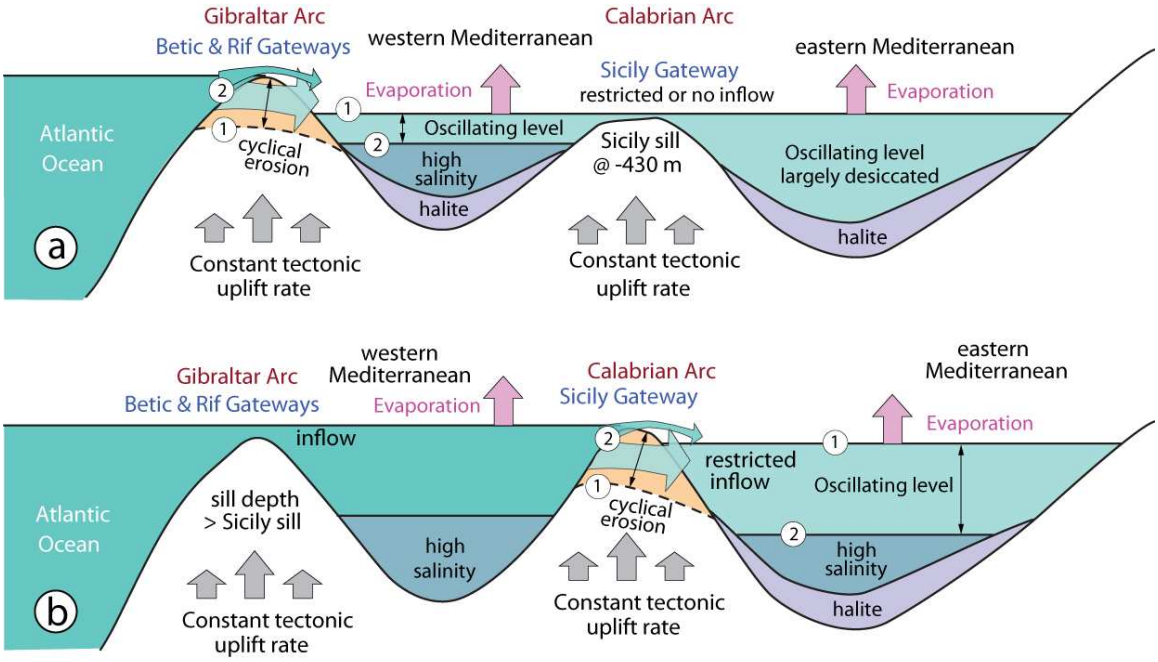

Figure 7.20: **(a)** Schematic east-west cross sections across the Mediterranean showing the possible interplay between the rates of erosion across the Betic and Rif gateways and rates of the uplift across the Gibraltar Arc (modified from Garcia-Castellanos and Villaseñor, 2011). **(b)** Schematic east-west cross section across the Mediterranean showing the proposed interplay between the erosion rates across the Sicily Gateway and the rates of uplift across the Calabrian Arc.

Figures 7.22–7.24 schematically illustrates the evolution of the sub-units 2d through 2a across the Mediterranean Sea. During the Late Miocene the Mediterranean Sea was fully connected to the global ocean and was receiving normal marine sedimentation (Fig. 7.22a). During the early Messinian, the subduction rollback along the Gibraltar Arc (e.g., Rosenbaum et al., 2002) and the

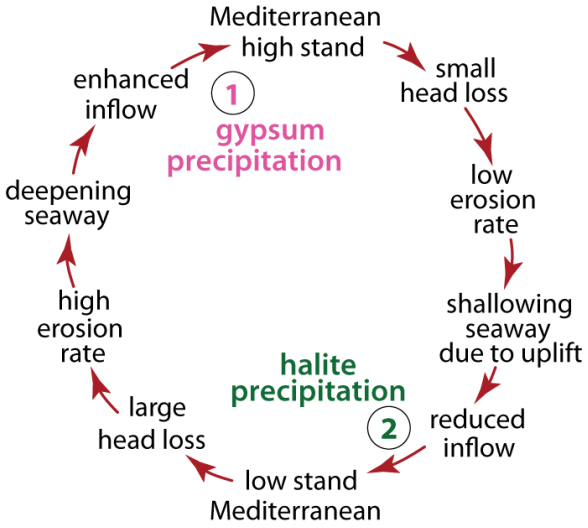

Figure 7.21: Schematic diagram showing the interplay between erosion and uplift leading to the deposition of evaporite minerals (adopted from Garcia-Castellanos and Villaseñor, 2011). Erosion at the sill (whether Betic and Rif or Sicily) is controlled by rock erodibility and water inflow. Head loss= the elevation difference between the Atlantic Ocean and the western Mediterranean or that in the western and eastern Mediterranean.

associated lithospheric slab tear (e.g., Duggen et al., 2003) resulted in the uplift of the Betic and Rif gateways, restricting the watermass exchange between the Mediterranean Sea and the global ocean (Fig. 7.22b, Garcia-Castellanos and Villaseñor, 2011). At this stage, all other waterways formerly connecting the Mediterranean to the Indian Ocean to the south and east were closed (e.g., Popov et al., 2004, 2006). The initial drawdown of 100's of metres resulted in gypsum deposition along the shallow nearshore basins, also known as the Primary Lower Gypsum (Roveri et al, 2008a, b; Manzi et al., 2014). With time, the further drawdown and the onset of incision of river gorges facilitated the transport of the Primary Lower Gypsum downslope into the deeper basins across the eastern and western Mediterranean: these deposits are known as the Resedimented Lower Gypsum (Roveri et al., 2008a, b, Manzi et al., 2014), or sub-unit 2d in this study (Fig. 7.22c). During the later portion of the deposition of sub-unit 2d, the drowdown that resedimented the Primary Lower Gypsum deposits notably restricted the water exchange across the Sicily Gateway. During this time,

the uplift of the Gibraltar Arc also restricted the water exchange between the Atlantic Ocean and the western Mediterranean (Fig. 7.22c).

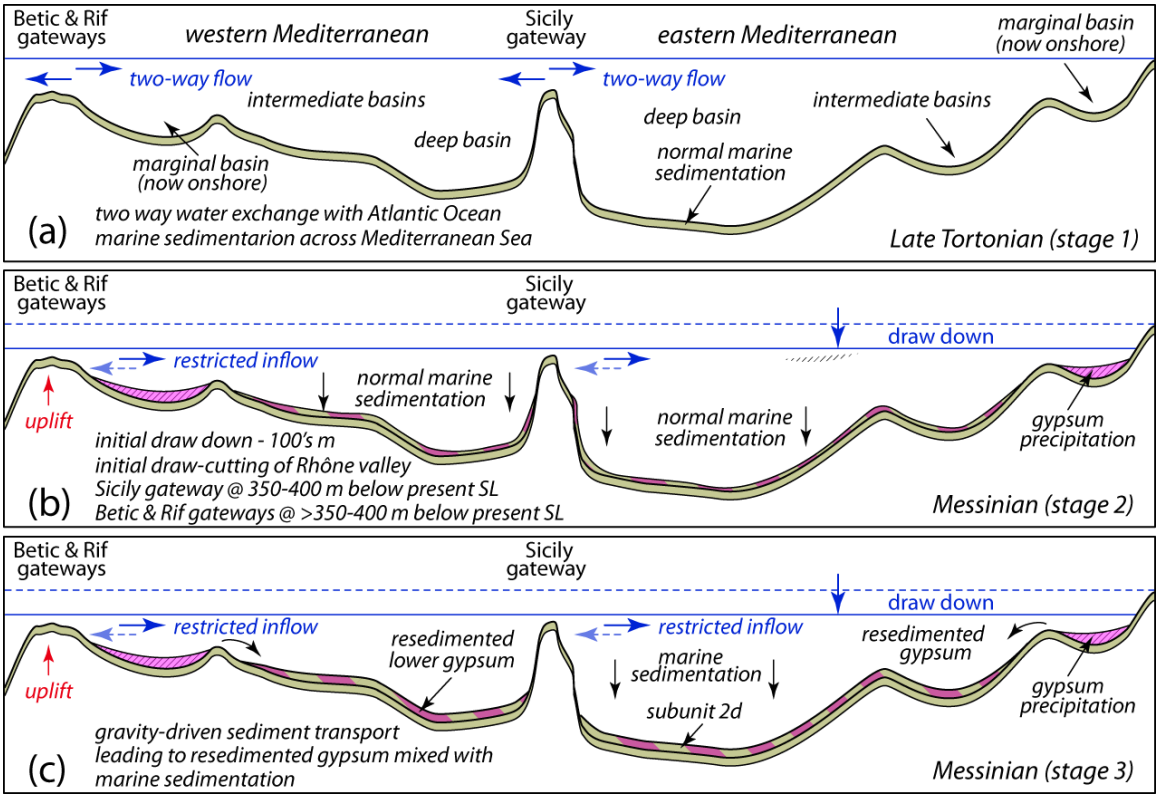

Figure 7.22: Schematic east-west cross sections (base is from Figure 7.18) showing the development of sub-unit 2d, Primary Lower Gypsum, and Resedimented Lower Gypsum across the eastern and western Mediterranean.

The uplift of the Calabrian Arc further restricted the circulation across the Sicily Gateway and the eastern Mediterranean experienced a major drawdown and the associated halite deposition across the intermediate and deep basins (Fig. 7.23d). The presence of enormous quantities of salt across the Herodotus and Antalya basins indicate that the Sicily Gateway provided considerable quantities of saline Atlantic water, possibly via a process of balanced erosion and uplift across the Sicily Gateway, akin to the process proposed for the Betic and Rif gateways by Garcia-Castellanos and Villaseñor

(2011). This process must have taken place for a considerable period, leading to the deposition of sub-units 2c and 2b across the eastern Mediterranean (Fig. 7.23d). Van der Laan et al. (2005, 2006) estimated the duration for the deposition of the mobile units at 270 kyr, on the basis of the assumption that the 14 to 17 cycles observed in the gypsum deposited in sub-unit 2c are due to Milankovitch precessional cycles of insolation. Further uplift of the Calabrian and Gibraltar arcs and the resultant further restriction of the Betic and Rif gateways led to a notable drawdown, which must have isolated the eastern and western Mediterranean, as the Sicily Gateway became subaerial (Fig. 7.23e). The rapid evaporation must have rendered the eastern Mediterranean largely desiccated and possibly erosional, while massive halite sedimentation occurred across the western Mediterranean (Fig. 7.23e). A balance between the rates of uplift and erosion kept the Betic and Rif gateways within the "goldilocks" zone, supplying the needed saltwater into the western Mediterranean.

During the later portion of the Messinian Salinity Crisis, the Mediterranean became completely isolated from the global ocean and probably became largely desiccated and erosional (Fig. 7.23f). The reconnection near the end of the Messinian Salinity Crisis is envisioned to affect the western Mediterranean first, and a thin series of interbedded gypsum and siliciclastic successions were deposited: this is referred to as sub-unit 2a. Further rise led to the deposition of the transgressive brackish water environment with the distinctive *Lago Mare* fauna (Fig. 7.24g). Only after the sea-level reached the breach depth of the Sicily Gateway, did the reflooding of the eastern Mediterranean took place (Fig. 7.24h), where initially the interbedded gypsum and siliciclastics were deposited, which are overlain by the sediments with the *Lago Mare* fauna. The final Zanclean flooding raised the sea level to $\sim$30 m above the present, ending the Messinian Salinity Crisis (Fig. 7.24i).

7.3 Summary and future work

At the opening paragraph of the chapter it is stated that "the Messinian evolution and history of the Mediterranean is one of the most extensively studied topics across Europe, but also globally"

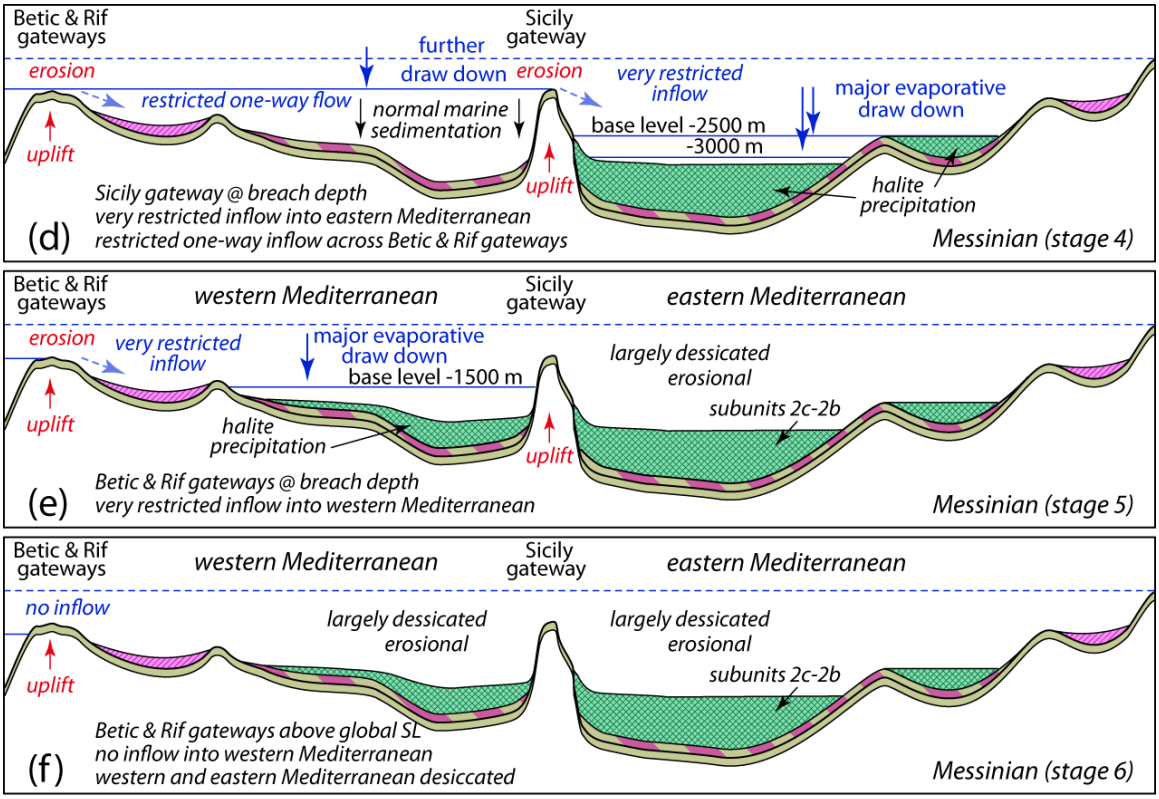

Figure 7.23: Schematic east-west cross sections (base is from Figure 7.18) showing the development of sub-units 2c and 2b, Lower Mobile and Upper Mobile units across the eastern and western Mediterranean.

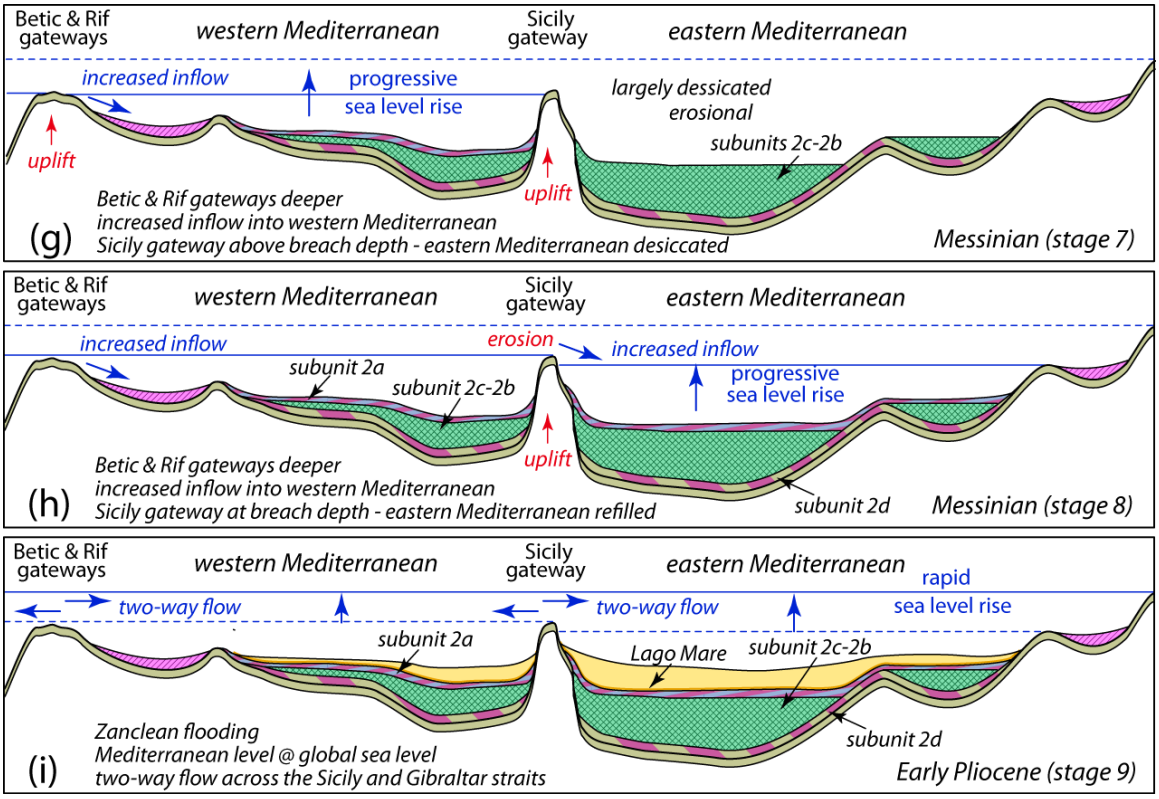

Figure 7.24: Schematic east-west cross sections (base is from Figure 7.18) showing the development of subunit 2a, *Lago Mare* and the Pliocene–Quaternary successions across the eastern and western Mediterranean.

and that some authors suggest synchroneity of evaporite deposition across the marginal and deep Mediterranean regions (e.g., Hsü et al., 1973), others suggested a two-step event where the deposition of evaporites initially started across the marginal basins and subsequently developed within the deep basins (e.g., Clauzon et al., 1996), yet others suggested a completely diachronous evolution of the evaporites across the marginal basins and deep basins of the eastern and western Mediterranean basins (e.g., Butler et al., 1995; Roveri et al., 2014a,b).

My study favours the recent non-synchronous depositional model across the marginal basins and deep basins of the Mediterranean, suggested by Roveri et al. (2008a,b). However, this study does not support the more recent study of an attempt at correlating western and eastern Mediterranean Messinian seismic units has been suggested by Lofi et al., (2010) and Roveri et al. (2014a, b). Their results show that the western Mediterranean Messinian stratigraphy was not similar to the eastern Mediterranean. They suggested that the Messinian Salinity Crisis is largely recorded by a 4-division evaporite stratigraphy in the western Mediterranean and a single salt-bearing seismic unit in the eastern Mediterranean (Fig. 7.25; Roveri et al., 2014a,b).

This study targeted the Antalya Basin and Florence Rise regions of the eastern Mediterranean which were not previously studied in detail, but also incorporated data from areas such as the Adana, Cilicia, Latakia, Cyprus, Rhodes and Finike basins. The results of this study clearly demonstrated the presence of a 4-division Messinian evaporite stratigraphy in the eastern Mediterranean, similar to that observed in the western Mediterranean, suggesting the existence of a similar set of depositional processes across the Mediterranean during the Messinian Salinity Crisis (Figs. 7.25a, 7.26; e.g., CIESM, 2008; Lofi et al., 2011a, b; Roveri et al. 2014a). However, the stratigraphic and depositional similarities of the evaporites between the eastern and western basins do not necessitate synchroneity in their depositional histories. The evidence of enormous quantities of evaporites precipitated in the eastern Mediterranean, and the fact that the only saline water source for the eastern Mediterranean is the Atlantic Ocean via the Sicily sill (a physical barrier between the eastern and

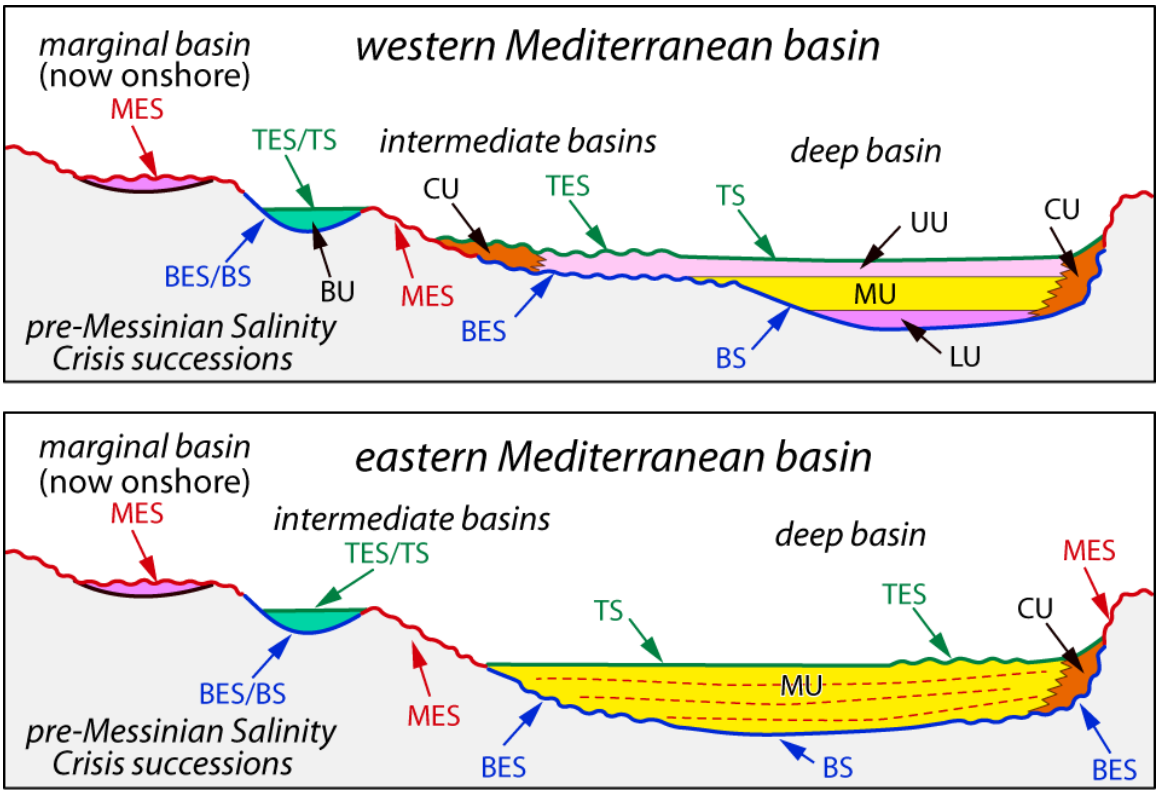

Figure 7.25: Schematic conceptual sketches across the western (a) and eastern (b) Mediterranean basins. (a) Showing that Messinian Salinity Crisis is largely recorded by 4-division evaporite stratigraphy in the western Mediterranean. (b) showing that Messinian Salinity Crisis is recorded by a single salt-bearing seismic unit in eastern Mediterranean (adopted from Roveri et al., 2014a,b). Onshore units: PLG= Primary Lower Gypsum; H= halite; RLG= Resedimented Lower Gypsum; UG= Upper Gypsum; LM= *Lago Mare*; Offshore units: LE= Lower Evaporites; LU= Lower Unit; H= Messinian Salt; MU= Mobile Unit; UE= Upper Evaporites=UU, Upper unit Surfaces: MES= Messinian erosional surface/marginal erosional surface. Base of Messinian evaporites: horizon N = BES, basal erosional surface/BS, basal surface; Top of the Messinian evaporites: horizon M= TES, Top erosional surface/Top Surface.

western Mediterranean), collectively impose several critical environmental conditions. A simple 2-D model is developed which satisfies these conditions (Figs. 7.22, 7.23, 7.24). The model suggests that the eastern and western basin margins experienced a nearly synchronized gypsum deposition associated with the initial drawdown of the Mediterranean level, followed by the resedimentation in the deep basins of the terrigenous and early evaporite deposits as the drawdown intensified. The synchroneity of evaporite deposition across the eastern and western basins broke down as the Sicily Gateway became largely subaerial during a period when the Calabrian Arc area experienced uplift associated with slab break-off: the Sicily sill must have remained within a "goldilocks" zone to allow the right amount of saline water inflow into the eastern Mediterranean so that evaporites (massive halite) could be deposited. During this time, the sea level in western Mediterranean was at the breach-level of the Sicily sill, thus no evaporite deposition took place there. The model suggests that further restriction of the inflow occurred across the Betic and Rif gateways as these regions also largely became subaerial associated with the uplift of the Gibraltar Arc region caused by the lithospheric slab break-off. However, similar to the Sicily Gateway, the Betic and Rif gateways must also have remained within the "goldilocks" zone to allow the right amount of saline water inflow into the western Mediterranean so that massive halite could be deposited. The re-opening of the Betic and Rif gateways reflooded the western Mediterranean first, then the eastern Mediterranean allowing the deposition of a mixed evaporite-siliciclastic unit, followed by the transgressive sediments with a distinctive brackish water *Lago Mare* fauna.

Despite the fact that there is an immense literature on the Mediterranean in general, and the Messinian Salinity Crisis in particular, many ideas associated with this important scientific question unfortunately remain speculative. Introduction of data from previously poorly studied regions of the Mediterranean have brought some clarification, such as the presence or absence of evaporites in certain regions, the details of the internal architecture and stratigraphy of the evaporite successions, but fail to erect a solid chronostratigraphic framework on which to build detailed model that explains

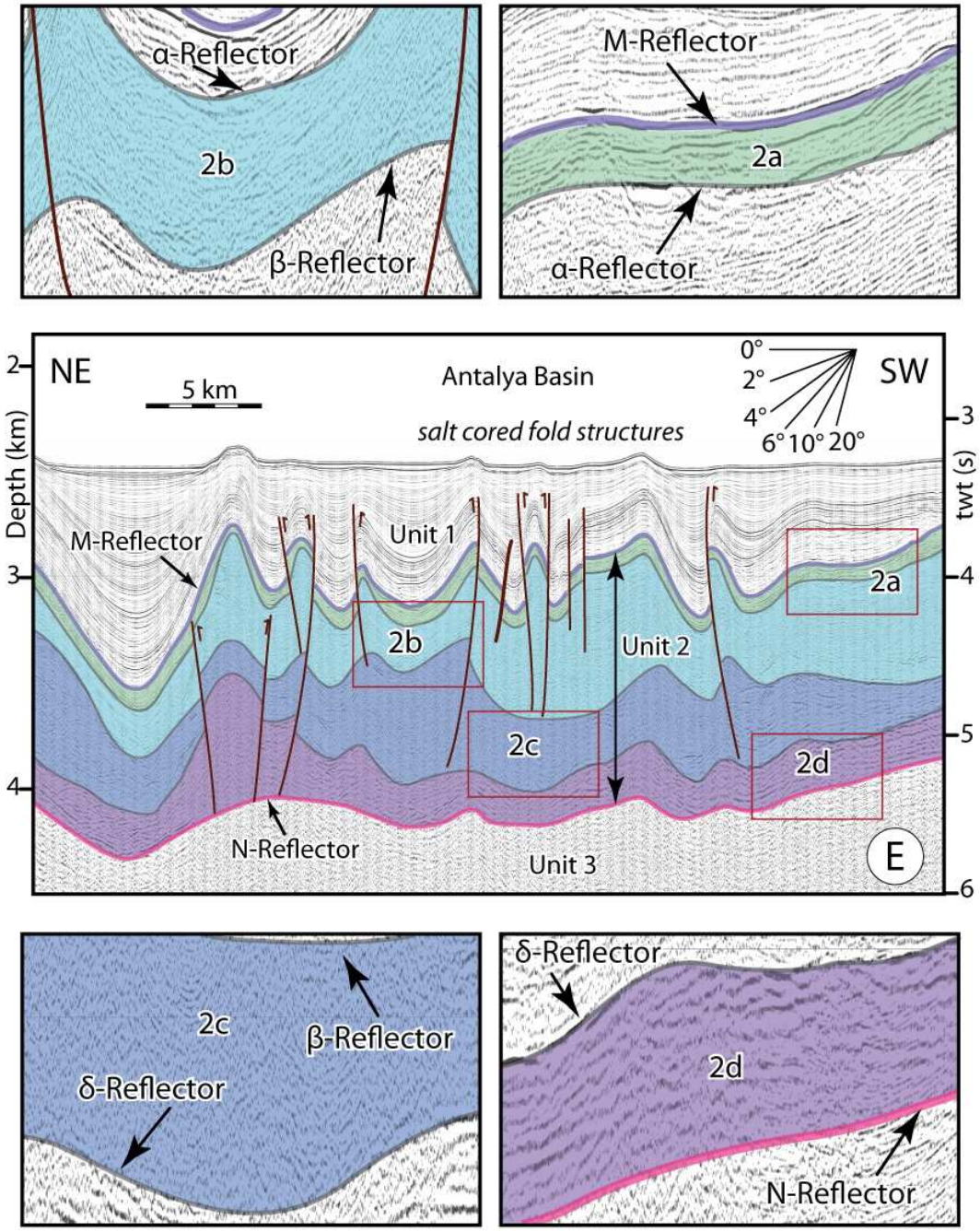

Figure 7.26: High-resolution multi-channel seismic reflection profile D clearly showing the internal architecture of Unit 2 with the presence of a 4-division Messinian evaporite stratigraphy in the eastern Mediterranean, similar to that observed in the western Mediterranean (Fig. 7.25). Location is shown in Figure 4.1. EMED10 (fix 1451-1536)

the temporal and spatial variations of the Messinian evaporite successions. What is needed to do this?

- Several boreholes and continuous cored sections are needed to that recover the entire Messinian evaporite successions from several basins across the eastern and western Mediterranean, where sediments can be accurately dated and the environment of deposition can be delineated using detailed sedimentological, stratigraphic, geochemical and micropaleontological studies.

- Detailed studies across the Suez and Sinai regions to determine whether another connection with the world ocean existed across these areas during the Messinian, because all existing models and thinking assume that the Gibraltar Arc region, specifically the Betic and Rif gateways formed the only water-mass communication between the Mediterranean and the global ocean.

- The Sicily Gateway appears to be a critical region that controlled the water-mass exchange between the eastern and western Mediterranean. The tectonic evolution of this gateway, particularly the protracted uplift of the Calabrian Arc region associated with lithospheric slab breakoff must be viewed in developing models that explain how the Sicily sill remained within a "goldilocks" zone that allowed the right amount of saline water inflow into the eastern Mediterranean so that large quantities of evaporites could be deposited.

Chapter 8

Conclusions

This study targeted the Antalya Basin and Florence Rise regions of the eastern Mediterranean which were not previously studied in detail. My work has provided new seismic data and geological interpretation in the southern Antalya Basin, the Florence Rise and Anaximander mountains enabling me to fill a significant knowledge gap in the Messinian story and so allowing me to come to new conclusion on the Messinian-Recent history of this part of the Mediterranean and it is implications for the regional evolution of the entire Mediterranean Sea. This thesis presented for the first time a detail stratigraphic framework of the study area and described the distribution of the Messinian evaporite successions, which is used to develop a stratigraphic model to better understand the Messinian depositional history of the study area in the content of the entire Mediterranean Sea and also determined the Miocene–Recent structural framework of the study area and delineated the overall style of deformation in the uppermost Messinian–Quaternary successions and explained how and when the deformation formed, and what controls its distribution in the western Cyprus Arc.

The interpretation of a comprehensive set of high-resolution multi-channel seismic reflection profiles, multibeam bathymetry data and the litho- and bio-stratigraphic information from exploration wells across the Antalya Basin and Florence Rise, but also incorporated data from areas such as the Adana, Cilicia, Latakia, Cyprus, Rhodes and Finike basins in the eastern Mediterranean re-

vealed the following specific salient conclusions, which are divided into three categories: (a) general stratigraphy, (b) tectonic framework and (c) Messinian Salinity Crisis.

8.1 General stratigraphy

- Miocene to Recent sedimentary successions across the western Cyprus Arc, including the Florence Rise and the Antalya Basin were characterized using three seismo-stratigraphic units, which are separated from one another by the prominent M- and N-reflectors. These units are: (a) Unit 1 is characterized by acoustically strongly reflective package where reflectors show considerable lateral continuity. It is uppermost Messinian–Quaternary in age and is composed predominantly of siliciclastic sediments; (b) Unit 2 is characterized by an acoustically transparent package with occasional weak reflectors with limited lateral continuity. It is Messinian in age and represents the evaporites and the interbedded siliciclastic successions, and (c) Unit 3 is characterized by a reverberatory seismic package with variable lateral continuity. It represents the undifferentiated pre-Messinian Miocene and older siliciclastic and carbonate successions.

- The uppermost Messinian–Quaternary Unit 1 is divided into three subunits (1a–1c). Subunit 1a is correlated with the Quaternary to late Pliocene of the shallow marine and terrestrial Apolos and Kakkaristra formations in the Mesaoria Basin as well as the as well as the Pleistocene Antalya Tufa and Belkış conglomerate in southwestern Turkey. Subunit 1b is tentatively correlated with the Middle-Upper Pliocene marls of the Athalassa Formation of the Mesaoria Basin and the Alakilise Formation in southwestern Turkey. Subunit 1c corresponds to Early Pliocene – uppermost Messinian. The upper portion of Subunit 1c is correlated with early Pliocene slumped marl successions of lithostratigraphic Unit IV of the DSDP Sites 375 and 376. It is further tentatively correlated with the Nikosia and Mirtou formations of the Mesaoria Basin and Kyrenia Mountains respectively. The lowermost portion of Subunit 1c is tentatively

correlated with the marlstones and interbedded graded sandstones and siltstones of middle to upper Unit V of the DSDP Sites 375-376 (i.e., the sediments with *Lago Mare* fauna).

- The M-reflector corresponds to the bounding erosional surface marking the top of the Messinian evaporite successions, and separating these from the uppermost Messinian sediments with a distinctive *Lago Mare* fauna which form the lowermost portion of Subunit 1c. Although the sediments with the *Lago Mare* fauna are viewed as part of the Messinian Salinity Crisis they occur immediately above the M-reflector. Unlike many studies across the Mediterranean where the top unit surfaces (associated with the Messinian Salinity Crisis) are indicated as MES (or Messinian erosional surface/marginal erosional surface), TES (or top erosional surface) and/or TS (or top surface), and basal surfaces are indicated as BES (or basal erosional surface) and BS (basal surface; Lofi et al., 2005, 2011b; Maillard et al., 2006; CIESM, 2008; Roveri et al., 2014a-c), the marine high-resolution multi-channel seismic reflection profiles do not allow the differentiation of these specific terms, even though this terminology is also carried into the marine realm by many studies (Lofi et al., 2005, 2011b; Maillard et al., 2006; CIESM, 2008; Roveri et al., 2014a-c). In this study, the top unit surfaces, including MES, TES and TS are collectively indicated by the M-reflector, whereas the base unit surfaces, such as BES and BS are indicated by the N-reflector.

8.2 Tectonic and kinematic evolution

- The pre-Messinian Miocene structural architecture of the Antalya Basin and its southwestern extension into the Florence Rise is characterized by a very prominent broadly northwest-southeast striking and largely southwest verging fold thrust belt, with occasional northeast verging back-thrusts. During the Messinian a number of prominent thrusts remained active; however, numerous thrusts which were active during the pre-Messinian Miocene became inac-

tive. During the Pliocene–Quaternary the strain was partitioned into five broadly northwest-southeast trending morpho-tectonic domains, each delineated by a distinctive seafloor morphology: (a) a domain across the inner and western Antalya Basin is dominated by extensional faults, (b) a domain immediately south of the extensional faults, is characterized by contractional structures, (c) a halokinetic zone in southwestern Antalya Basin north of the foothills of the Anaxagoras Mountain is characterized by numerous positive flower structures beneath a corrugated seafloor, (d) a domain across the crestal portion of the Florence Rise is dominated by prominent inversion structures, and (e) a domain across the northeastern and southwestern margins of the Florence Rise characterized by positive flower structures.

- There was an uppermost Messinian–Quaternary basin in the general region of the present-day crest of the Florence Rise, but this basin became dramatically inverted sometime during the Quaternary. Seismic reflection profiles from the Florence Rise sector of the study area suggest that some of the inversion-related structures may also involve varying amounts of fluid escape and mud diapirism. Fluids are present in underconsolidated sediments beneath and within Messinian deposits, arising from the conversion of gypsum to anhydrite and/or as an expulsion product of the intercalated siliciclastics during the early diagenesis. These fluids escape from beneath and within mobile Messinian deposits and create mud volcanoes or dissolution craters.

- In inner and western Antalya Basin northwest-southeast striking extensional faults clearly exhibit strike slip components. These faults can be readily traced toward the land, linking with the dextral strike slip Kırkkavak Fault and the dextral Aksu Fault zone.

- The Texel mud volcano and its feeder channel across the pre-Messinian Miocene successions are clearly imaged in the industry seismic reflection profiles. However, high-resolution multi-channel seismic reflection profiles further illustrate that the core of this structure is also exten-

sively cut by several bi-vergent thrust faults. Some of the faults that bound the positive flower structures have listric trajectories and sole deep within the Messinian successions, suggesting that these structures must have developed by the reactivation of the pre-existing Messinian and/or pre-Messinian Miocene structures. Growth strata observed in the upper portion of the uppermost Messinian–Quaternary successions suggest that these structures developed during the Pliocene–Quaternary.

- The middle portion of Unit 1 (i.e., the middle portion of the uppermost Messinian–Recent) is an interval of major tectonic upheaval across the southern portion of the forearc region. Across the Florence Rise and the southern sector of the Antalya Basin, this interval is marked by a conspicuous unconformity, which toward the deeper Antalya Basin becomes conformable within the strongly stratified Unit 1 successions. This unconformity, labeled as the γ-reflector, is best imaged across the crestal region of the Florence Rise, where a former basin that accumulated a thick succession during the early uppermost Miocene–Recent became inverted during the middle Uppermost Messinian–Recent.

8.3 Sediments associated with the Messinian Salinity Crisis

- In the Antalya Basin and Florence Rise the lowermost portion of sub-unit 1c (i.e., the *Lago Mare*) and the entire Unit 2 represent the deposition associated with the Messinian Salinity Crisis. The very thick development of Unit 2 across the Antalya and Herodotus basins exceeding 2000 ms ($\sim$4–5 km) suggested that these regions must have been primary evaporite basins in the eastern Mediterranean during the Messinian.

- This study documented for the first time that there are four distinct seismic stratigraphic subunits (i.e., 2a–2d) within the Messinian evaporite successions of Unit 2, which are separated from one another by regionally traceable α-, β-, and δ-reflectors. Comparisons between the

high-resolution seismic reflection profiles from the Antalya Basin and those from the northern Levantine, Cyprus, Cilicia, Adana, Latakia, Finike and Rhodes basins clearly show that there are remarkable similarities in the stratigraphic architecture and internal acoustic makeup of the Messinian evaporite successions between these regions, which in turn suggests eastern-Mediterranean-wide similarities in the sedimentary processes and basin evolution. The documentation that the Messinian sub-units also occur across the eastern Mediterranean further suggests that there are greater sedimentary and seismic stratigraphic similarities between the western and eastern Mediterranean basins than previously thought, implying a common basin evolution and sedimentary processes during the Messinian Salinity Crisis along the entire Mediterranean region.

- The edge of the Messinian evaporite succession is delineated across the eastern Mediterranean as the zero ms isopach contour, which may represent: (a) the present-day depositional edge of the evaporites in the eastern Mediterranean suggesting that bulk of the evaporite deposition has taken place in the deeper parts of the Antalya Basin and/or (b) the final area of salt withdrawal associated with the weld development along continental margins, and/or (c) considerable unidirectional Pliocene–Quaternary loading and major salt evacuation.

- The Messinian evaporite successions are very thin and patchy across the continental shelves and slopes, but reaches $\sim$3-5 km across the Herodotus and Antalya basins and to a lesser thicknesses across the Levantine, Cilicia and Latakia basins. The volume of the eastern Mediterranean is clearly insufficient to provide the salt needed for these massive thicknesses, suggesting that the Sicily Gateway must have been leaky during the deposition of the lower and upper mobile units. The immediate ramification of this statement is this: "the lower and upper mobile units found across the western and eastern Mediterranean basins cannot have been deposited in synchroneity", and that any model proposed for the evolution of the lower and upper mobile units in the eastern Mediterranean must account for a protracted period (or periods) when the

Sicily sill must have remained within a "goldilocks" zone, allowing just the right amount of saline water inflow into the eastern Mediterranean so that evaporites were deposited there but not across the western Mediterranean region because the sea level was at the breach-level of the Sicilian sill.

- One of the very critical findings of this study is the requirement that the two major Messinian evaporite mobile sub-units (i.e., 2b and 2c) must have developed first across the eastern Mediterranean. This may have taken place as (a) sub-unit by sub-unit, that is sub-unit 2c deposited in the east first and then followed by sub-unit 2c deposition in the west, then sub-unit 2b deposition in the east, the followed by sub-unit 2b deposition in the west, or (b) as sub-units 2c+2b were deposited in the east, followed by sub-units 2c+2b deposition in the west.

- The chronology of the events associated with the Messinian Salinity Crisis must have been intrinsically linked with the tectonic evolution of the western and central Mediterranean regions. This linkage has two important components: (a) the evolution of the Betic and Rif gateways across the westernmost Mediterranean which controlled the saline water influx into the Mediterranean during the Messinian Salinity Crisis, and (b) the evolution of the Sicily Gateway in central Mediterranean which controlled the saline water influx into the eastern Mediterranean, again during the Messinian Salinity Crisis. The tectonic evolution of the Gibraltar Arc in the west and the Calabrian Arc across the central Mediterranean must have played critical roles in keeping the Betic and Rif gateways and the Sicily Gateway within the "goldilocks" zone.

Bibliography

Aal, A., El Barkooky, A., Gerrits, M., Meyer, H., Schwander, M., Zaki, H., 2000. Tectonic evolution of the Eastern Mediterranean basin and its significance for hydrocarbon prospectivity in the ultra deepwater of the Nile delta. The Leading Edge, 19: 1086–1102.

Aal, A., El Barkooky, A., Marc, G., Hans, J.M., Marcus, S., Hala, Z., 2001. Tectonic evolution of the Eastern Mediterranean basin and its significance for hydrocarbon prospectivity of the Nile Delta Deep Water Area. GeoArabia 6, 363–383.

Abd-Allah, A.M.A., Aal, M.H.A., Ghandour, A., 2012. Structural characteristics and tectonic evolution of the northwestern margin of the Nile Delta, Egypt. Journal of African Earth Sciences, 68, 82–95.

Agard, P.,Omrani, J., Jolivet, L., Mouthereau, F. 2005. Convergence history across Zagros (Iran): constraints from collisional and earlier deformation. International Journal of Earth Sciences, 94, 401–419.

Akay, E. and Uysal, S., 1985. Orta Torosların batısındaki (Antalya) Neojen çökellerinin stratigrafisi, sedimantolojisi ve yapısal jeolojisi. Mineral Research Exploration Institute (MTA), unpublished report, 276 pp.

Akay, E., Uysal, S., Poisson, A., Cravette, J., Müller, C., 1985. Antalya Neojen havzasının stratigrafisi (The stratigraphy of the Neogene Antalya Basin). Bulletin of the Geological Society of

Turkey, 28: 105-119.

Akbulut, A., 1977, Etude Geologique d'une partie du Taurus occidentale au sud d'Eğridir (Turquie): Thesis: Univ.Paris - Sud, Orsay.

Aksu, A.E., Calon, T.J., Piper, D.J.W, Turgut, S, and E.K. Izdar, 1992. Architecture of late orogenic basins in the eastern Mediterranean Sea. Tectonophysics, 210: 191-213.

Aksu, A.E., Calon, T.J., Hall, J., Mansfield, S., Yaşar, D., 2005a. The Cilicia–Adana Basin complex, Eastern Mediterranean: Neogene evolution of an active fore-arc basin in an obliquely convergent margin. Marine Geology, 221, 121–159.

Aksu, A.E., Calon, T.J., Hall, J., Yaşar, D., 2005b. Origin and evolution of the Neogene Iskenderun Basin, northeastern Mediterranean Sea. Marine Geology, 221, 161–187.

Aksu, A.E., Hall, J., Yaltırak, C., 2009. Neogene evolution of the Anaximander Mountains and Finike Basin at the Junction of Hellenic and Cyprus Arcs, Eastern Mediterranean. Marine Geology, 258, 24–47.

Aksu, A.E., Walsh-Kennedy, S., Hall, J., Hiscott, R.N. Yaltırak, C., Akhun, S.D., and G. Çifçi, 2014a. The Pliocene-Quaternary evolution of the Cilicia and Adana Basins, eastern Mediterranean: special reference to the development of the Kozan Fault Zone. Tectonophysics, 622: 22-43.

Aksu, A.E., Calon, T., Hall, J., Kurtboğan, B., Gürçay, S., and G. Çifçi, 2014b. Complex interactions fault fans developed in a strike-slip system: Kozan Fault Zone, Eastern Mediterranean Sea. Marine Geology, 351: 91–107.

Aksu, A.E., Hall, J., Yaltırak, C., Çınar, E., Küçük, M., and G. Çifçi, 2014c. Late Miocene–Recent evolution of the Finike Basin and its linkages with the Beydağları complex and the Anaximander Mountains, eastern Mediterranean. Tectonophysics 635: 59-79.

Aktar, M., Ergin, M., Özalaybey, S., Tapirdamaz, C., Yörük, A., Biçmen, F., 2000. A lower-crustal event in the northeastern Mediterranean: the 1998 Adana Earthquake (Mw = 6.2) and its aftershocks, Geophysical Research Letters, 27, 2361–2364.

Alçiçek, M.C., 2007. Tectonic development of an orogen-top rift recorded by its terrestrial sedimentation pattern: the Neogene Eşen Basin of southwestern Anatolia, Turkey. Sediment. Geol. 200, 117–140.

Alçiçek, M.C., ten Veen, J.H., Özkul, M., 2006. Neotectonic development of the Çameli Basin, southwestern Anatolia, Turkey. In: Robertson, A.H.F., Mountrakis, D. (Eds.), Tectonic Development of the Eastern Mediterranean Region. Geological Society London, Special Publications 260, pp. 591–611.

Al-Lazki, A., Seber,D., Sandvol, E., Türkelli,N., Mohamad, R., Barazangi, M., 2003. Tomographic Pn velocity and anisotropy structure beneath the Anatolian plateau (eastern Turkey) and surrounding regions, Geophys. Res. Lett., 30, doi:10.1029/2003GL017391.

Allen, P.A., Allen, J.R., 2005. Basin Analysis: Principles and Applications, Second Edition, Blackwell Publishing 549 pp.

Allmendinger, R. W., Reilinger, R., Loveless, J. 2007. Strain and rotation rate from GPS in Tibet, Anatolia and the Altiplano. Tectonics, 26, TC3013, doi: 10.1029/2006TC002030.

Al-Riyami, K., Robertson, A.H.F., Xenophontos, C., Danelian, T., Dixon, J.E., 2000. Mesozoic tectonic and sedimentary evolution of the Arabian continental margin in Baer-Bassit (NW Syria). In: Malpas, J., Xenophontus, C., Panayides, A. (Eds.). Proceedings of the 3rd International Conference on the Geology of the Eastern Mediterranean, Nicosia, Cyprus: 61-81.

Al-Riyami, K., Robertson, A.H.F., Dixon, J., Xenophontos, C., 2002. Origin and emplacement of the Late Cretaceous Baer-Bassit ophiolite and its metamorphic sole in NW Syria. Lithos 65,

225-260.

Amery, H.A., 1993. The Litani River of Lebanon. Geographical Review, 83, 929-937.

Anderson, R.Y., Kirkland, D.W. 1980. Dissolution of salt deposits by brine density flow. Geology, 8, 66–69.

Anderson, R.Y., Knapp, R. 1993. An overview of some of the large scale mechanisms of salt dissolution in western Canada. Geophysics, 58(9), 1375–1387.

Angus, D.A.,Wilson, D.C., Sandvol, E., Ni, J.F., 2006. Lithospheric structure of the Arabian and Eurasian collision zone in Eastern Turkey from S-wave receiver functions, Geophys. J. Int., 166(3), 1335–1346.

Argnani, A., 2009. Evolution of the southern Tyrrhenian slab tear and active tectonics along the western edge of the Tyrrhenian subducted slab. In: van Hinsbergen, D.J.J., Edwards, M.A., Govers, R. (eds), Collision and Collapse at the Africa–Arabia–Eurasia Subduction Zone. The Geological Society, London, Special Publications, 311, 193–212.

Arvidsson, R., Ben-Avraham, Z., Eckström, G., Wdowinski, S., 1998. Plate tectonic framework for the October 9, 1996 Cyprus earthquake, Geophysical Research Letters, 25, 2241–2244.

Bache, F., Olivet, J.L., Gorini, C., Rabineau, M., Baztan, J., Aslanian, D. and Suc, J.P., 2009. Messinian erosional and salinity crises: view from the Provence Basin (Gulf of Lions, Western Mediterranean). Earth and Planetary Science Letters, 286(1), pp.139-157.

Bache, F., Popescu, S.M., Rabineau, M., Gorini, C., Suc, J.P., Clauzon, G., Olivet, J.L., Rubino, J.L., Melinte-Dobrinescu, M.C., Estrada, F. and Londeix, L., 2012. A two-step process for the reflooding of the Mediterranean after the Messinian Salinity Crisis. Basin Research, 24(2), pp.125-153.

Barber, P.M., 1981. Messinian subaerial erosion of the proto-Nile delta. Marine Geology, 44, 253–272.

Barka, A., Reilinger, R., 1997. Active tectonics of the eastern Mediterranean region: deduced from GPS, neotectonics and seismicity data. Annali di Geofisika, XL (3), 587-610.

Bagnall, P.S., 1960. The geology and mineral resources of the Pano Lefkara–Larnaca area. Mem.-Geol. Surv. Cypr. 5 (116 pp.)

Barnes, M.C., 2015. Miocene to Recent tectonic and kinematic evolution of the Rhodes, Finike and Antalya basins and the Anaximander mountains, eastern Mediterranean Sea. Unpublished MSc thesis, Memorial University of Newfoundland. 328 pp.

Baroz, F., Bernouilli, D., Biju-Duval, B., Bizon, G., Bizon, J.J., and Letouzey, J., 1978. Correlations of the Neogene formations of the Florence Rise and of northern Cyprus: paleogeographic and structural implications. In Hsü, K., Montadert, L., et al., Init. Repts. DSDP,42: Washington (U.S. Govt. Printing Office), 903–926.

Bassetti, M.A., Jouet, G., Dufois, F., Berné, S., Rabineau, M. and Taviani, M., 2006. Sand bodies at the shelf edge in the Gulf of Lions (Western Mediterranean): deglacial history and modern processes. Marine Geology, 234(1), pp.93-109.

Bellahsen, N., Faccenna, C., Funiciello, F., Daniel, J.-M. & Jolivet, L. 2003. Why did Arabia separate from Africa? Insights from 3-D laboratory experiments. Earth and Planetary Science Letters, 216, 365–381.

Benoit, M.H., Nyblade, A.A., Van Decar, J.C., 2006. Upper mantle P wave speed variations beneath Ethiopia and the origin of the Afar Hotspot, Geology 34: 329–332.

Benkhelil, J., Bayerly, M., Branchoux, S., Courp, T., Gonthier, E., Hübscher, C., Maillard, A.,Tahchi, E., 2005. La branche orientale de l'Arc de Chypre: Aspects morphostructuraux d'une fron-

tière de plaques d'après la campagne BLAC (2003). Comptes Rendus. Geoscience 337 (12), 1075–1083

Benson, R.H., 1973a. An ostracodal view of the Messinian salinity crisis. In: Drooger, C.W. (Ed.), Messinian Events in the Mediterranean. Kon. Ned. Akad. van Wetensch., Geodyn. Sci. Rep., vol. 7, pp. 235–242. Benson, 1973b

Benson, R.H., 1978. The paleoecology of the ostracodes of DSDP Leg 42A. In: Hsü K.J., Montadert, L., et al. (Eds.), Initial Rep. Deep Sea Drill. Proj., vol. 42, I. U.S. Government Printing Office,Washington, pp. 777–788.

Bertoni, C., Cartwright, J.A., 2005. 3D seismic analysis of circular evaporite dissolution structures, Eastern Mediterranean Journal of the Geological Society, London, 162, 909–926.

Bertoni C., Cartwright J., 2006. Controls on the basin-wide architecture of the Messinian evaporites on the Levant margin, Eastern Mediterranean. Sedimentary Geology, 188–189, 93–114.

Bertoni C., Cartwright J., 2007. Major erosion at the end of the Messinian Salinity Crisis: evidence from the Levant Basin, Eastern Mediterranean. Basin Research, 19, 1–18.

Berckhemer, H. 1977. Some aspects of the evolution of marginal seas deduced from observations in the Aegean region. In: MontaderT, L. (ed.) Structural History of the Mediterranean Basins. Technip. Paris, Split, Yugoslavia, 303–313.

Bertini, A., Corradini, D., Suc, J.P., 1995. On Galeacysta etrusca and the connections between the Mediterranean and the Paratethys. Rom. J. Stratigr. 76 (suppl. 7), 141–142 (abstract). Bertoni et al., 2013

Beydoun, Z.R., 1999. Evolution and development of the Levant (Dead Sea Rift) transform system: a historical-chronological review of a structural controversy. In: Mac Niocaill, C. and Ryan,

P.D. (Eds.) Continental Tectonics, Geological Society, London, Special Publications, 164, 239–255.

Bridge, C., Calon, T.J., Hall, J., Aksu, A.E., 2005. Salt tectonics in two convergent margin basins of the Cyprus Arc, northeastern Mediterranean. Marine Geology 221: 223–259.

Brigden, K., Stringer, R., 2001. A critical assessment of the Kishon River Masterplan Report. State of Israel, Ministry of Environment, July 2001, 24 pp.

Biryol, C.B., Beck, S.L., Zandt, G., Arda, Özacar., 2011. Segmented African lithosphere beneath the Anatolian region inferred from teleseismic P-wave tomography. Geophysical Journal International, 184, 1037–1057, doi: 10.1111/j.1365-246X.2010.04910.x

Bizon, G., Biju-Duval B., Letouzey, J., Monod, O., Poisson, A., Özer, B. ve Öztümer, E., 1974, Nouvelles precisious stratigraphiques concernant les bassins tertiaires du sud de la Turquie (Antalya, Mut,, Adana): Rev. I.F.P., 29 (3), 305–325.

Blanc, P.-L., 2000. Of sills and straits: a quantitative assessment of the Messinian Salinity Crisis. Deep-Sea Research, I 47, 1429–1460.

Bowmann, S.A., 2011. Regional seismic interpretation of the hydrocarbon prospectivity of offshore Syria. GeoArabia, 2011, 16 (3), 95–124.

Bozkurt, E., 2001. Neotectonics of Turkey – a synthesis. Geodinamica Acta, 14, 3–30.

Bridge, C., Calon, T.J., Hall, J. and Aksu, A.E., 2005. Salt tectonics in two convergent margin basins of the Cyprus Arc, northeastern Mediterranean. Marine Geology 221: 223-259.

Burton-Ferguson, R., Aksu, A.E., Calon, T.J., and Hall, J., 2005. Seismic stratigraphy and structural evolution of the Adana Basin, Eastern Mediterranean. Marine Geology 221: 189-222.

Busson, 1990 Busson, G., 1990. Le Messinien de la Méditerranée...vingt ans après. Géologie de la France 3–4, 3–58

Butler, R.W.H., Lickorish, W.H., Grasso, M., Pedley, H.M., Ramberti, L., 1995. Tectonics and sequence stratigraphy in Messinian basins, Sicily: constraints on the initiation and termination of the Mediterranean salinity crisis. Geological Society of America Bulletin, 107, 425–439.

Calon, T., Hall, J., Aksu, A.E., 2005a. The Oligocene–Recent evolution of the Mesaoria Basin (Cyprus) and its western marine extension, Eastern Mediterranean. Marine Geology, 221, 95–120.

Calon, T., Aksu, A.E., Hall, J., 2005b. The Neogene evolution of the Outer Latakia Basin and its extension into the Eastern Mesaoria Basin (Cyprus), Eastern Mediterranean. Marine Geology, 221, 61–94.

Carton, H., Singh, S.C., Tapponnier, P., Elias, A., Briais, A., Sursock, A., Jomaa, R., King, G.C.P., Daëron, M, Jacques, E., Barrier, L., 2009. Seismic evidence for Neogene and active shortening offshore of Lebanon (Shalimar cruise), Journal of Geophysical Research, 114, B07407, doi:10.1029/2007JB005391.

Catterall, V., Redfern, J., Gawthorpe, R., Hansen, D., Thomas, M., 2010. Architectural style and quantification of a submarine channel–levee system located in a structurally complex area: offshore Nile delta. Journal of Sedimentary Research, 80, 991–1017.

Chumakov, I.S., 1967. Academy of Science, Geological Institute Transactions, USSR, Moskow, 170, 5

Cartwright, J.A., Jackson, M.P.A., 2008. Initiation of gravitational collapse of an evaporitic basin margin: the Messinian saline giant, Levant Basin, eastern Mediterranean. Geological Society of America Bulletin 120, 399–413.

Cartwright, J., Stewart, S., Clark, J., 2001. Salt dissolution and salt-related deformation of the Forth Approaches Basin, UK North Sea. Marine and Petroleum Geology, 18, 757–778.

Chiarabba, C., De Gori, P., Speranza, F., 2008. The southern Tyrrhenian subduction zone: Deep geometry, magmatism and Plio-Pleistocene evolution. Earth and Planetary Science Letters, 268, 408–423.

CIESM, 2008. The Messinian salinity crisis from mega-deposits to microbiology. In: Briand, F. (Ed.), A consensus report, in 33ème CIESM Workshop Monographs, 33. CIESM, 16, bd de Suisse, MC-98000, Monaco, pp. 1–168.

Cifelli, F., Mattei, M., Rossetti, F., 2007. Tectonic evolution of arcuate mountain belts on top of a retreating subduction slab: the example of the Calabrian Arc. Journal of Geophysical Research, 112, B09101, doi:10.1029/2006JB004848.

Cipollari, P., Cosentino, D. and Gliozzi, E., 1999. Extension-and compression-related basins in central Italy during the Messinian Lago-Mare event. Tectonophysics, 315(1), pp.163-185.

Cipollari, P., Cosentino, D., Radeff, G., Schildgen, T.F., Faranda, C., Grossi, F., Gliozzi, E., Smedile, A., Gennari, R., Darbaş, G., Dudas, F.Ö., Gürbüz, K., Nazik, A., and Echtler, H., 2013. Easternmost Mediterranean evidence of the Zanclean flooding event and subsequent surface uplift: Adana Basin, southern Turkey. Geological Society, London, Special Publications, 372: 473–494, doi:10.1144/SP372.5

Cita, M.B., 1973. Mediterranean evaporite: paleontological arguments for a deep-basin desiccation model. In: Drooger, D.W. (Ed.), Messinian Events in the Mediterranean. North Holland Publishing Company, Amsterdam, London, pp. 206–228.

Cita, M.B., Colombo, L., 1979. Sedimentation in the latest Messinian at Capo Rossello (Sicily). Sedimentology 26, 497–522.

Cita, M.B., Wright, R.C., Ryan, W.B.F. and Longinelli, A., 1978a. Messinian paleoenvironments. In: Initial Reports of the Deep Sea Drilling Project (Eds. K.J. Hsü and L. Montadert), Vol. 42A, pp. 1003–1035. U.S. Government Printing Office, Washington, DC.

Cita, M.B., Ryan, W.B.F. and Kidd, R.B., 1978b. Sedimentation rates in Neogene deep sea sediments from the Mediterranean and geodynamic implications of their changes. In: Initial Reports of the Deep Sea Drilling Project (Eds. K.J. Hsü and L. Montadert), 42A, 991–1002. U.S. Government Printing Office, Washington DC.

Cita, M.B., Santambrogio, S., Melillo, B., Rogate, F., 1990. Messinian paleoenvironments: new evidence from the Tyrrhenian sea (ODP Leg 107). In: Kastens, K.A., Mascle, J., et al. (Eds.), Proceedings Ocean Drilling Program. Scientific Results, 107, pp. 211–227.

Chaumillon, E., Mascle, J., 1997. From foreland to forearc domains: New multichannel seismic reflection survey of the Mediterranean ridge accretionary complex (Eastern Mediterranean). Marine Geology, 138, 237–259.

Çınar, E., 2014. The Miocene to recent tectonic evolution of an active transform fault at the junction of Hellenic and Cyprus arcs, Eastern Mediterranean: the linkage between the western Antalya Basin, Finike Basin and Anaximander Mountains. Unpublished MSc thesis, Memorial University of Newfoundland, 282 pp.

Çiner, A., Karabıyıkoğlu, M., Monod, O., Deynoux, M. and Tuzcu, S., 2008. Late Cenozoic sedimentary evolution of the Anyalya Basin, southern Turkey. Turkish Journal of Earth Sciences, 17: 1-41.

Clauzon, G., 1978. The Messinian Var canyon (Provence, southern France): paleogeographic implications. Marine Geology, 27, 231–246.

Clauzon, G., 1982. Le canyon messinien du Rhône, une preuve décisive du "desiccate deep-basin model" [Hsü, Cita et Ryan, 1973]. Bull. Soc. Géol. Fr., sér. 7, 24, 597–610.

Clauzon, G., Suc, J.P., Gautier, F., Berger, A. and Loutre, M.F., 1996. Alternate interpretation of the Messinian Salinity Crisis: controversy resolved? Geology, 24, 363–366.

Clauzon, G., Suc, J.-P., Popescu, S.-M., Marunt, Eanu, M., Rubino, J.-L., Marinescu, F., Melinte, M.C., 2005. Influence of the Mediterranean sea-level changes over the Dacic Basin (Eastern Paratethys) in the Late Neogene. The Mediterranean Lago Mare facies deciphered. Basin Research 17, 437–462.

Clauzon, G., Suc, J.P., Popescu, S.M., Melinte-Dobrinescu, M.C., Quillévéré, F., Warny, S.A., Fauquette, S., Armijo, R., Meyer, B., Rubino, J.L. and Lericolais, G., 2008. Chronology of the Messinian events and paleogeography of the Mediterranean region s. l. In *CIESM Workshop Monographs* (Vol. 33, pp. 31-37).

Cleintaur, M.R., Knox, G.J. and Ealey, P.J., 1977. The geology of Cyprus and its place in the eastern Mediterranean framework. Geologie em Mijnbouw, 56(1): 66-82.

Cohen, A., 1993. Halite–clay interplay in the Israeli Messinian: Sedimentary Geology, 86, 211–228.

Costa, E., Camerlenghi, A., Polonia, A., Cooper, C., Fabretti, P., Mosconi, A., Murelli, P., Romanelli, M., Sormani, L., Wardell, N., 2004. Modeling deformation and salt tectonics in the eastern Mediterranean Ridge accretionary wedge Geological Society of America Bulletin 116, 7, DOI: 10.1130/B25309.1

Chumakov, I.S. 1967. Pliocene and Pleistocene deposits of the Nile Valley in Nubia and Upper Egypt (in Russian). *Transactions Geol. Inst. Acad. Sci. USSR*, 170, 5–111.

Chumakov, I. 1973. Geological history of the Mediterranean at the end of the Miocene-the beginning of the Pliocene according to new data. In: *Leg 13* (Ed. by W.B.F. Ryan, K.J. Hsü et al.),

Init. Rep. Deep Sea Drill. Proj., 13, 2, 1241–1242.

Crouvi, O., Enzel, Y., Ben-Dor, Y., Amit, R., 2015. Atmospheric Dust, Dust Deposits (Loess) and Soils in the Negev Desert – Guide book prepared for The Batsheva de Rothschild Seminar on Atmospheric Dust, Dust Deposits (Loess) and Soils in Deserts and the Desert Fringe, Jerusalem & Negev, Israel, 14th-19th October 2015, 208 pp.

D'Agostino, N., D'Anastasio, E., Gervasi, A., Guerra, I., Nedimovic, M.R., Seeber, L., Steckler, M., 2011. Forearc extension and slow rollback of the Calabrian Arc from GPS measurements Geophysical Research Letters 38, L17304, doi:10.1029/2011GL048270, 2011

Dean, W.T., Monod, O., Günay, Y., 1986. Lower Paleozoic stratigraphy in the southern and central Amanos Mountains, south central Turkey. Geological Magazine 123, 215– 226.

Decima, A. and Wezel, F.C., 1971. Osservazioni sulle evaporiti Messiniane della Sicilia centromeridionale. Rivista Mineraria Siciliana 130–134, 172–187.1

Decima, A. and Wezel, F.C., 1973. Late Miocene evaporites of the Central Sicilian Basin. In: Initial Reports of the Deep Sea Drilling Project (Eds W.B.F. Ryan and K.J. Hsu), Vol. 13, Part 2, pp. 1234–1240. U.S. Government Printing Office, Wash- ington, DC

De Lange, G.J., Krijgsman, W., 2010. Messinian salinity crisis: a novel unifying shallow gypsum/deep dolomite formation mechanism. Marine Geology 275, 273–277.

Dentith, M., Mudge, S.T., 2014. Geophysics for the Mineral Exploration Geoscientist. Cambridge University Press, Cambridge, 426 pp.

Do Couto, D., Popescu, S.M., Suc, J.P., Melinte-Dobrinescu, M.C., Barhoun, N., Gorini, C., Jolivet, L., Poort, J., Jouannic, G. and Auxietre, J.L., 2014. Lago Mare and the Messinian Salinity Crisis: Evidence from the Alboran Sea (S. Spain). *Marine and Petroleum Geology*, 52, pp.57-76.

Dercourt, J., 1986, Geological evolution of the Tethys belt from the Atlantic to the Pamirs since the Lias, Tectonophysics, 123, 241–315.

Dewey, J.F., Pittman, III, W.C., Ryan, W.B.F., Bonnin, J., 1973. Plate tectonics and the evolution of the Alpine system, Geological Society of America Bulletin, 84, 3137-3180.

Dewey, J.F., Şengör, A.M.C. 1979. Aegean and surrounding regions: Complex multiplate and continuum tectonics in a convergent zone. Geological Society of America Bulletin, 90, 84–92.

Dewey, J.F., Hempton, M.R., Kidd, W.S.F., Şaroğlu, F., Şengör, A. M. C. 1986. Shortening of continental lithosphere: the neotectonics of eastern Anatolia – a young collision zone, In: Coward, M.P. and Ries, A.C. (eds) Collision Tectonics, Geological Society, London, Special Publication, 19, 3–36.

Deynoux, M., Çiner, A., Monod, O., Karabıyıkoğlu, M., Manatschal, G. and Tuzcu, S., 2005. Facies architecture and depositional evolution of alluvial fan to fan-delta complexes in the tectonically active Miocene Köprüçay Basin, Isparta Angle, Turkey. Sedimentary Geology, 173, 315-343.

Dilek, Y., Moores, E.M., 1990. Regional tectonic of the eastern Mediterranean ophiolites. In: Malpas, J., Moores, E.M., Panayiotou, A., Xenophontos, C. (Eds.), Ophiolites, Oceanic Crustal Analogues. Proceedings of the Symposium “Troodos 1987”. The Geological Survey Department, Ministry of Agriculture and Natural Resources, Nicosia, Cyprus, pp. 295–309, 733 pp.

Dilek, Y., E. Sandvol (2009), Seismic structure, crustal architecture and tectonic evolution of the Anatolian-African plate boundary and the Cenozoic orogenic belts in the Eastern Mediterranean region, in Ancient Orogens and Modern Analogues, edited by J. B. Murphy, J. D. Keppie, and A. J. Hynes, Geol. Soc. Spec. Publ., 327, 127–160, doi:10.1144/SP327.8.

Dixon, J.E., Robertson, A.H.F., 1984. The Geological Evolution of the Eastern Mediterranean. Geological Society Special Publication 17, 824 p.

dos Reis, A.T., Gorini, C., Mauffret, A., 2005. Implications of salt-sediment interactions for the architecture of the Gulf of Lions deep-water sedimentary systems–western Mediterranean Sea. Marine and Petroleum Geology, 22 (6–7), 713–746.

Droz, L., R. Kergoat, P. Cochonat, S. Berné, 2001. Recent sedimentary events in the western Gulf of Lions (western Mediterranean). Marine Geology 176: 23-37.

Druckman, Y., Buchbinder, B., Martinotti, G.M., Tov, R.S., Aharon, P., 1995b. The buried Afiq Canyon (eastern Mediterranean, Israel): a case study of a tertiary submarine canyon exposed in late Messinian times. Marine Geology, 123, 167– 185.

Duermeijer, C.E., Krijgsman, W., Langereis, C.G., ten Veen, J.H. 1998. Post early Messinian counter-clockwise rotations on Crete: implications for the late Miocene to Recent kinematics of the southern Hellenic Arc. Tectonophysics, 298: 77–89.

Duggen, S., Hoernle, K., van den Boogard, P., Rüpke l., Morgan, J.P., 2003. Deep roots of the Messinian Salinity Crisis, Nature, 422, 602–606.

Dumont, J.-F., Kerey, E. 1975. Kırkkavak fayı: batı Toroslar ile Köprüçay Baseni sınırında kuzey–güney duğrultu atımlı fay [Kırkkavak fault: A N–S-trending strike-slip fault at the contact between the western Taurides and Köprüçay Basin]. Bulletin of the Geological Society of Turkey 18, 59–62 [in Turkish with English abstract].

Dümmong, S., Hübscher, C., 2010. Levant Basin. In: Lofi, J., Déverchère, J., Gaullier, V., Gillet, H., Gorini, C., Guennoc, P., Loncke, L., Maillard, A., Sage, F., Thinon. I. (Eds), Atlas of the Messinian Salinity Crisis: seismic markers in the Mediterranean and Black seas. Commission for the Geological Map of the world 77, rue Claude-Bernard, 75055 Paris, France, 55, 76 pp.

Dupoux, B., 1983, Etude comparee de la téctonique Neogene des bassins du sud de Chypre et du bassin d'Antalya (Turquie) : Docteur 3ème cycle, Univiverité Paris - Sud, 120 (unpublished), Orsay, France.

EIE, 1984. Elektrik İşleri Etüd İdaresi Genel Müdürlüğü (General Directorate of Electrical Power Resources Survey and Development Administration). 1984 water year discharges, 304 pp.

Elitez, İ., Yaltırak, C., 2014a. Miocene–Quaternary geodynamics of Çameli Basin, Burdur–Fethiye Shear Zone (SW Turkey). Geol. Bull. Turk. 57, 41–67.

Elitez, I., Yaltırak, C., Hall, J., Aksu, A.E., Çifçi, G., 2015. Reply to the comment by M.C. Alçiçek on "The Fethiye–Burdur Fault Zone: A component of upper plate extension of the subduction transform edge propagator fault linking Hellenic and Cyprus Arcs, Eastern Mediterranean" [Tectonophysics, 635, 80–99]. Tectonophysics, 664: 5–13.

Ellion, P. 1983. Étude structurale et sedimentologique du bassin Neogène de Pissouri (Chypre). PhD thesis, University of Paris.

Emeis, K.-C., Robertson, A.H.F., Richter, C., et al., 1996. Proceedings of the Ocean Drilling Program, Initial Reports, 160: College Station, TX (Ocean Drilling Program).

Eriş, K.K., Bassant, P. and Ülgen, U.B., 2005 Tectono-stratigraphic evolution of an Early Miocene incised valley-fill (Derinçay Formation) in the Mut Basin, Southern Turkey. Sedimentary Geology, 173: 151-185.

Faccenna, C., Bellier, O., Martinod, J., Piromallo, C., Regard, V. 2006. Slab detachment beneath eastern Anatolia: A possible cause for the formation of the North Anatolian Fault. Earth and Planetary Science Letters, 242, 85–97.

Fantozzi, P.L., Sgavetti, M., 1998. Tectonic and sedimentary evolution of the eastern Gulf of Aden continental margins: new structural and stratigraphic data from Somalia and Yemen.

In: Purser, B.H., Bosence, D.W.J. (eds), Sedimentation and tectonics of rift basins: Red Sea-Gulf of Aden. Chapman & Hall, London, 56–76.

Fernández-Blanco, D., 2015. Evolution of Orogenic Plateaus at Subduction Zones: Sinking and raising the southern margin of the Central Anatolian Plateau. Ph.D thesis, VU University Amsterdam, 282 pp.

Ferry, M., Meghraoui, M., Karaki, N.A., Al-Taj, M., Khalil, L., 2011. Episodic behavior of the Jordan Valley section of the Dead Sea Fault inferred from a 14-ka-long integrated catalog of large earthquakes. Bulletin of the Seismological Society of America, 101, 39–67.

Finetti, I., Morelli, C., 1973. Geophysical exploration of the Mediterranean Sea, Boll. Geof. Teor. Appl., 60, 263–341.

Flecker, R., Ellam, R.M., 2006. Identifying late Miocene episodes of connection and isolation in the Mediterranean-Paratethyan realm using Sr isotopes. Sedimentary Geology, 188–189, 189–203.

Flecker, R., Robertson, A.H.F., Poisson, A. and Müller, C., 1995. Facies and tectonic significance of two contrasting Miocene basins in south coastal Turkey. Terra Nova, 7(2), pp.221-232.

Flecker, R., Ellam, R.M., Müller, C., Poisson, A., Robertson, A.H.F. and Turner, J., 1998. Application of Sr isotope stratigraphy and sedimentary analysis to the origin and evolution of the Neogene basins in the Isparta Angle, southern Turkey. Tectonophysics, 298: 83-101.

Flood, R.D., Hiscott, R.N. and Aksu, A.E., 2009. Morphology and evolution of a channel system created by saline underflow into the Black Sea. Sedimentology, 56: 807-839.

Follows, E.J., Robertson, A.H.F., 1990. Sedimentology and structural setting of reefal limestones in Cyprus. In: J. Malpas, E.M. Moores, A. Panayiotou, C. Xenophontos (Eds.), Ophiolites, Oceanic Crustal Analogues. Proceedings of the Symposium “Troodos 1987”. Geological

Survey Department, Ministry of Agriculture and Natural Resources, Nicosia, Cyprus, pp. 207–215. 733 pp.

Fortuin, A.R., Krijgsman, W., 2003. The Messinian of the Nijar Basin (SE Spain): sedimentation, depositional environments and paleogeographic evolution. Sedimentary Geology 160, 213–242.

Francalanci, L., Innocenti, F., Manetti, P., Savaşçın, Y., 2000. Neogene alkaline volcanism of the Afyon-Isparta area, Turkey: petrogenesis and geodynamic implications. Mineralogy and Petrology, 70, 285–312.

Fuchs, M.C., Gloaguena, R., Krbetschek, M., Szulca, A., 2014. Rates of river incision across the main tectonic units of the Pamir identified using optically stimulated luminescence dating of fluvial terraces. Geomorphology, doi: 10.1016/j.geomorph.2014.03.027

Ganas, A., Parsons, T., 2009. Three-dimensional model of Hellenic Arc deformation and origin of the Cretan uplift. Journal of Geophysical Research, 114, B06404, doi:10.1029/2008JB005599.

Gans, C.R., Beck, S.L., Zandt, G., Biryol, C.B., and Özacar, A.A. 2009. Detecting the limit of slab break-off in central Turkey: new high-resolution Pn tomography results. Geophysical Journal International, 179, 1566-1572.

Garcia-Castellanos, D., Villaseñor, A., 2011. Messinian salinity crisis regulated by competing tectonics and erosion at the Gibraltar arc. Nature, 480, 359–363, doi:10.1038/nature10651.

Garcia-Castellanos, D., Estrada, F., Jiménez-Munt, I., Gorini, C., Fernàndez, M., Vergés, J., De Vicente, R., 2009. Catastrophic flood of the Mediterranean after the Messinian salinity crisis, Nature, 462, 778–781, doi:10.1038/nature08555.

Gardosh, M., Druckman, Y., Buchbinder, B., Calvo, R., 2008a. The Oligo-Miocene deepwater system of the Levant Basin. Geological Survey of Israel, GSI/33/2008, GII 446/426/08, 73

pp.

Gardosh, M., Druckman, Y., Buchbinder, B., Rybakov, M., 2008b. The Levant Basin offshore Israel: stratigraphy, structure, tectonic evolution and implications for hydrocarbon exploration. Geological Survey of Israel, GSI/4/2008, GII 429/328/08, 118 pp.

Garfunkel, Z., 1984. Large-scale submarine rotational slumps and growth faults in the Eastern Mediterranean. Marine Geology, 55, 305–324.

Garfunkel, Z., Almagor, G., 1987. Active salt dome development in the Levant Basin, southeastern Mediterranean. In: Lerche, I., O'Brien, J.J. (Eds.), Dynamical Geology of Salt and Related Structures. Academic Press, Orlando, FL, pp. 263– 300.

Gargani, J., Rigollet, C., 2007. Mediterranean sea-level variations during Messinian Salinity Crisis. Geophysical Research Letters, 35, L10405.

Garrison, R.E., Schreiber, B.C., Bernoulli, D., Fabricius, F.H., Kidd, R.B., and Mélières, F., 1978. Sedimentary petrology and structures of Messinian evaporitic sediments in the Mediterranean Sea, Leg 42A, Deep SeaDrilling Project. In Hsü, K.J., Montadert, L., et al., Init. Repts. DSDP,42 (Pt. 1): Washington (U.S. Govt. Printing Office), 571–611.

Gass, I.G. 1960. The geology and mineral resources of the Dhali area. Mem. Geol. Surv. Dept. Cyprus 4, 116 pp.

Gass, I.G., MacLeod, C.J., Murton, B.J., Panayiotou, A., Simonian, K.O., Xenophonthos, C., 1994. The geology of the southern Troodos transform fault zone. Memoir, vol. 9. Geological Survey of Cyprus.

Gaullier, V., Y. Mart, G. Bellaiche, B. Vendeville, J.Mascle, T. Zitter, and the second leg "PRISMED II" scientific party, 2000. Salt tectonics in and around the Nile deep-sea fan: Insights from the "PRISMED II" cruise, In: B.C. Vendeville, Y. Mart, J.L. Vigneresse (Eds), Salt, shale, and

igneous diapirs in and around Europe: Geological Society (London) Special Publication 174, 111–129.

Gaullier V., Loncke L., Vendeville B., Déverchère J., Droz L., Obone Zue Obame E.M., Mascle J., 2008. Salt tectonics in the deep Mediterranean: indirect clues for understanding the Messinian salinity crisis (Abstract). *In:* Briand F., Ed., The Messinian salinity crisis from mega-deposits to microbiology – A consensus report. – 33ème CIESM Workshop Monographs, Monaco, 33, 91-96.

Gaullier V., Loncke L., Vendeville B., Déverchère J., Droz L., 2010. Interactions between salt tectonics and deep-seated tectonics. Part I: Examples from the western Mediterranean (Abstract). In: International Conference SEPM –The Geological Society, "*Salt tectonics, sediments and prospectivity*," 20-22 January 2010, London, United Kingdom, 84 p.

Giermann, G., 1966. Gedanken zur Ostmediterraneen Schwelle, Bull. Inst. Oceanogr. Monaco, no. 1362 B.

Giermann, G., 1969. The eastern Mediterranean ridge, Rapp. Comm. int. Mer Medit., 19: 605–607

Gignoux, M., 1950. Géologie stratigraphique, 4th edition, Masson (Ed.), Paris, 735 p

Girdler, R. W., 1990. The Dead Sea transform fault system, Tectonophy-sics, 180 , 1–13, doi:10.1016/0040-1951(90)90367-H.

Gliozzi, E., Cipollari, P., Cosentino, D., 2002. The Messinian Lago-Mare event in central Italy: palaeogeographical reconstruction using geological data and ostracod assemblages. Geo Institute Special Publication, 26, pp. 153–168 (Belgrade).

Gliozzi, E., Ceci, M.E., Grossi, F., Ligios, F., 2007. Paratethyan Ostracod immigrants in Italy during the Late Miocene. Geobios 40, 325–337

Glover, 1995 Glover, C.P. 1995. Plio-Pleistocene sediments and neotectonics of the Isparta Angle, SW Turkey. PhD Thesis, University of Edinburgh.

Glover, C.P., Robertson, A.H.F., 1998a. Role of regional extension and uplift in the Plio-Pleistocene evolution of the Aksu Basin, SW Turkey. Journal of the Geological Society (London), 155: 364–387.

Glover, C.P., Robertson, A.H.F., 1998b. Neotectonic intersection of the Aegean and Cyprus tectonic arcs: extensional and strike-slip faulting in the Isparta Angle, SW Turkey. Tectonophysics, 298: 103–132.Gök, R., Türkelli, N., Sandvol, E., Seber, D., Barazangi, M., 2000. Regional wave propagation in Turkey and surrounding regions, Geophys. Res. Lett., 27, 479–432.

Gökçen, S.L., Kelling, G., Gökçen, N. and Floyd, P.A., 1988. Sedimentology of a late Cenozoic collisional sequence: the Misis Complex, Adana, southern Turkey. Sedimentary Geology 59: 205-235.

Gomez, F., Karam, G., Khawlie, M., McClusky, S., Vernant, P., Reilinger, R., Jaafar, R., Tabet, C., Khair, K., Barazangi, M. 2007. Global Positioning System measurements of strain accumulation and slip transfer through the restraining bend along the Dead Sea fault system in Lebanon. Geophysical Journal International 168, 1021–1028.

Gorini, C., Le Marrec, A., Mauffret, A., 1993. Contribution to the structural and sedimentary history of the Gulf of Lions (Western Mediterranean), from the ECORS profiles, industrial seismic profiles and well data. Bulletin de la Société Géologique de France 164 (3), 353-363.

Govers, R. and Wortel, M.J.R., 2005. Lithosphere tearing at STEP faults: Response to edges of subduction zones. Earth and Planetary Science Letters, 236: 505-523.

Gradmann, S., Hübscher, C., Ben-Avraham, Z., Gajewski, D., Netzeband, G., 2005. Salt tectonics

off northern Israel, Marine and Petroleum Geology, 22, 597–611
doi:10.1016/j.marpetgeo.2005.02.001.

Griffin, D.L., 2002. Aridity and humidity: two aspects of the late Miocene climate of North Africa and the Mediterranean. Palaeogeography, Palaeoclimatology, Palaeoecology, 182, 65–91.

Grossi, F., Cosentino, D., Gliozzi, E., 2008. Late Messinian Lago-Mare ostracods and palaeoenvironments of the central and eastern Mediterranean Basin. Bollettino della Societa Paleontologica Italiana 47, 131–146.

Guerra-Merchán, A., Serrano, F., Garcés, M., Gofas, S.Esu, D., Gliozzi, E. and Grossi, F., 2010. Messinian Lago-Mare deposits near the strait of Gibraltar (Malaga basin, S Spain). *Palaeogeography, Palaeoclimatology, Palaeoecology*, 285(3), pp.264-276.

Gutnic, M., Monod, O., Poisson, A., Dumont, J.F., 1979. Geologie des Taurides Occidentales (Turquie) . Memoires de La Societe Geologique de France, 137, 112.

Günay, Y., 1984. The geology of the Amanos Mountains and the petroleum potential of the Kocasu–Hatay graben (in Turkish). Report No: 1954, Turkish Petroleum Corporation.

Güneş, P., Hall, J., Aksu A.E., and Çifçi, G., 2014. Miocene to Recent Tectonic and Kinematic Evolution of the Florence Rise and It's Linkage with the Anaximander Mountains at the Junction of the Cyprus and Hellenic Arcs, Eastern Mediterranean, AAPG, International Conference & Exhibition, 16 September 2014 Istanbul, Turkey.

Güneş, P., Aksu, A.E., Hall, J., 2015. Seismic Stratigraphic Analysis of tem the Messinian Evaporite Deposits and Their Temporal and Spatial Distribution in tem the Western Cyprus Arc, Northeastern Mediterranean. AGU- Joint Assembly, May 3-7, 2015, Montreal, Canada.

Gürsoy, H., Piper, J.D.A., Tatar, O. And Mesci, L., 1998. Palaeomagnetic study of the Karaman and Karapinar volcanic complexes, central Turkey: neotectonic rotation in the south-central

sector of the Anatolian Block. Tectonophysics, 299: 191-211.

Gürsoy, H., Piper, J.D.A., Tatar, O., 2003. Neotectonic deformation in the western sector of tectonic escape in Anatolia: Palaeomagnetic study of the Afyon region, central Turkey. Tectonophysics, 374, 57–79.

Gvirtzman, Z., Steinberg, J., Bar, O., Buchbinder, B., Zilberman, E., Siman-Tov, R., Calvo, R., Grossowicz, L., Almogi-Labin, A., and Rosensaft, M. 2010. Retreating Late Tertiary shorelines in Israel: implications for the exposure of north Arabia and Levant during Neo-Tethys closure. In: Z. Gvirtzman (Ed.) Gradual uplift and exposure of north Arabia and enhanced sedimentation in the Levant basin during Neo-Tethys closure. Geological Survey of Israel, Report GSI/26/2010, 24 pp.

Harrison, R., Newell, W., Batıhanlı, H., Panayides, I., McGeehin, J., Mahan, S., Özhür, A., Tsiolakis, E., Necdet, M., 2004. Tectonic framework and late Cenozoic tectonic history of the northern part of Cyprus: implications for earthquake hazards and regional tectonics. Journal of Asian Earth Sciences, 23, 191–210.

Hafkenscheid, E.,Wortel, M. J.R., Spakman, W. 2006. Subduction history of the Tethyan region derived from seismic tomography and tectonic reconstructions. Journal Geophysical Research, 111, doi: 10.1029/ 2005JB003791.

Hall, J., Aksu, A.E., Calon, T.J., Yaşar, D., 2005a. Varying tectonic control on basin development at an active Microplate margin: the Iskenderun - Latakia Basin complex, Eastern Mediterranean. Marine Geology, 221, 15–60.

Hall, J., Calon, T.J., Aksu, A.E., Meade, S.R., 2005b. Structural evolution of the Latakia Ridge and Cyprus Basin at the front of the Cyprus Arc, Eastern Mediterranean Sea. Marine Geology, 221, 261–297.

Hall, J., Aksu, A.E., Yaltırak, C., Winsor, J.D., 2009. Structural architecture of the Rhodes Basin: a deep depocentre that evolved since the Pliocene at the junction of Hellenic and Cyprus Arcs, eastern Mediterranean. Marine Geology, 258, 1–23.

Hall, J., Aksu, A.E., King, H., Gogacz, A., Yaltırak, C., Çifçi, G., 2014a. Miocene–Recent evolution of the western Antalya Basin and its linkage with the Isparta Angle, eastern Mediterranean. Marine Geology, 349, 1–23.

Hall, J., Aksu, A.E., Elitez, I., Yaltırak, C., Çifçi, G., 2014b. The Fethiye-Burdur fault zone: upper plate extension of the subduction transform edge propagator fault linking Hellenic and Cyprus arcs, eastern Mediterranean. Tectonophysics 635: 80-99.

Hayward, A.B., 1984. Sedimentation and basin formation related to ophiolite nappe emplacement; Miocene, SW Turkey. Sedimentary Geology, 40, 105–129.

Hessami, K., Koyi, H.A., Talbot, C.J., Tabasi, H., Shabanian, E. 2001. Progressive unconformities within an evolving foreland fold-thrust belt, Zagros Mountains. Journal of the Geological Society, London, 158, 969–981.

Hilgen, F., Kuiper, K., Krijgsman, W., Snel, E., van der Laan, E., 2007. Astronomical tuning as the basis for high resolution chronostratigraphy: the intricate history of the Messinian Salinity Crisis. Stratigraphy 4, 231–238.

Hodell, D.A., Benson, R.H., Kent, D.V., Boersma, A., Rakic-El Bied, K., 1994. Magnetostratigraphic, biostratigraphic, and stable isotope stratigraphy of an upper Miocene drill core from the Salé Briqueterie (northwestern Morocco): a high-resolution chronology for the Messinian stage. Paleoceanography, 9, 835–855.

Hossack, J., 1995. Geometric rules of section balancing for salt structures. In: Jackson, M.P.A., Roberts, D.G., Snelson, S. (Eds.), Salt Tectonics: a Global Perspective, AAPG Memoir, vol.

65, pp. 29–40.

Hsü, K.J., Ryan, W.B.F., Cita, M.B., 1973 Late Miocene desiccation of the Mediterranean. Nature 242, 240–244.

Hsü, K.J., Montadert, L., Bernoulli, D., Cita, M.B., Erickson, A., Garrison, R.E., Kidd, R.B., Mélières, F., Müller, C., Wright, R., 1977. History of the Mediterranean salinity crisis, Nature, 267, 399– 403.

Hsü, K.J., Montadert, L., Bernoulli, D., Cita, M.B., Erickson, A., Garrison, R.E., Kidd, R.B., Mélières, F., Müller, C., Wright, R., 1978. History of the Mediterranean Salinity Crisis. In: K.J. Hsü, L. Montadert, D. Bernoulli, G. Bizon, M.B. Cita, A. Erickson, F. Fabricius, R.E. Garrison, R.B. Kidd, F. Mélières, C. Müller, R.C. Wright, DSDP Volume XLII Part 1, 1053–1078. U.S. Government Printing Office, Washington, DC.

Hübscher, C., Netzeband, G.L., 2007. Evolution of a young salt giant: the example of the Messinian evaporites in the Levantine Basin. In: Wallner, M., Lux, K.-H., Minkley, W., Hardy Jr., H.R. (Eds.), The Mechanical Behaviour of Salt—Understanding of THMC Processes in Salt. Taylor & Francis Group, London, pp. 175–184.

Hübscher C., Dümmong S., 2010. The Levant, Salt and Fluid Dynamics. In: Lofi, J., Déverchère, J., Gaullier, V., Gillet, H., Gorini, C., Guennoc, P., Loncke, L., Maillard, A., Sage, F., Thinon. I. (Eds), Atlas of the Messinian Salinity Crisis: seismic markers in the Mediterranean and Black seas. Published in 2010 by Commission for the Geological Map of the world 77, rue Claude-Bernard, 75055 Paris, France, 58, 76 pp.

Hübscher C., Cartwright J., Cypionka H., De Lange G., Robertson A., Suc J.P., Urai J., 2007. Global look at Salt Giants. EOS 88(16), 177–179.

Hudec, M.R., Jackson, M.P.A., 2002. Structural segmentation, inversion and salt tectonics on a

passive margin: evolution of the inner Kwanza Basin, Angola. Geological Society of America Bulletin, 114(10), 1222–1244.

Hudec, M.R., Jackson, M.P.A., 2007. Terra infirma: understanding salt tectonics. Earth Science Reviews 82 (1–2), 1–28.

Hüsing, S.J., Zachariasse, W-J., Douwe, van Hinsbergen, J.J., Krijgsman, W., Inceöz, M., Harzhauser, M., Mandic, O., Kroh, A., 2009. Oligocene–Miocene basin evolution in SE Anatolia, Turkey: constraints on the closure of the eastern Tethys gateway. In: van Hinsbergen, D.J.J., Edwards, M.A., Govers, R. (eds), Collision and Collapse at the Africa–Arabia–Eurasia Subduction Zone. The Geological Society, London, Special Publications, 311, 107–132. DOI: 10.1144/SP311.4

Iaccarino, S.M., Bossio, A., 1999. Paleoenvironment of uppermost Messinian sequences in the western Mediterranean (sites 974, 975 and 978). In: Zahn, R., Comas, M.C., Klaus, A. (Eds.), Proceedings of the Ocean Drilling Program. Scientific Results, 161. Ocean Drilling Program, College Station, TX, pp. 529–540.

Ilgar, A. and Nemec, W., 2005. Early Miocene lacustrine deposits and sequence stratigraphy of the Ermenek Basin, Central Taurides, Turkey. Sedimentary Geology, 173, 233-275.

Ilgar, A., Nemec, W., Hakyemez, A., Karakuş, E., 2013. Messinian forced regressions in the Adana Basin: a near-coincidence of tectonic and eustatic forcing. Turkish Journal of Earth Sciences, 22: 864–889.

Intergovernmental Oceanographic Commission (IOC), 1981. International Bathymetric Chart of the Mediterranean (Published by the Head Department of Navigation and Oceanography, Russia under the authority of IOC, 10 sheets).

Intergovernmental Oceanographic Commission (IOC), 1993. Thickness of the Plio–Quaternary

sediments (IBCM-PQ), of the International Bathymetric Charts of the Mediterranean Geological and Geophysical series (Published by the Head Department of Navigation and Oceanography, Russia under the authority of IOC, 10 sheets).

Işler, F.I., 2003. Miocene to Recent stratigraphy, structural architecture and tectonic evolution of the Antalya Basin, eastern Mediterranean Sea. Unpublished MSc thesis, Memorial University of Newfoundland. 255 pp.

Işler, F.I., Aksu, A.E., Hall, J., Calon, T.J., Yaşar, D., 2005. Neogene development of the Antalya Basin, Eastern Mediterranean: an active fore-arc basin adjacent to an arc junction. Marine Geology 221, 299–330.

Ivanov, M.K., Limonov, A.F., Woodside, J., 1992. Geological and Geophysical Investigations in the Mediterranean and Black Seas. Initial results of the 'Training through Research Cruise' of RV Gelendzhik in the Eastern Mediterranean and the Black Sea (June-July 1991). UNESCO Reports in Marine Science 56, 208 pp.

Ivanovic, R.F., Valdes, P.J., Flecker, R., Gutjahr, M., 2014. Modelling global-scale climate impacts of the late Miocene Messinian Salinity Crisis. Clim. Past, 10, 607–622.

Jackson, M.P.A., Roberts, D.G., Snelson, S., 1995. Salt Tectonics: a global perspective. American Association of Petroleum Geologists, Memoirs, 65.

Jenyon, M.K. 1983. Seismic response to collapse structures in the Southern North Sea. Marine and Petroleum Geology, 1, 27–36.

Jolivet, L. 2001. A comparison of geodetic and finite strain pattern in the Aegean, geodynamic implications. Earth and Planetary Science Letters, 187, 95–104.

Jolivet, L., Faccenna, C. 2000. Mediterranean extension and the Africa-Eurasia collision. Tectonics, 19, 1094–1106.

Just, J., Hübscher, C., Betzler, C., Lüdmann, T., Reicherter, K., 2011. Erosion of continental margins in the Western Mediterranean due to sea-level stagnancy during the Messinian Salinity Crisis. Geo-Marine Letters 31, 51–64.

Kahle, H.G., Cocard, M., Yannick, P., Geiger, A., Reilinger, R., Barka, A., Veis, G., 2000. GPS-derived strain rate fields within the boundary zones of the Eurasian, African and Arabian plates. J. Geophys. Res. 105, 23353–23370.

Karabacak, V., Altunel, E., 2013. Evolution of the northern Dead Sea Fault Zone in southern Turkey. Journal of Geodynamics, 65, 282– 291.

Karig, D.E., Kozlu, H. 1990. Late Palaeogene–Neogene evolution of the triple junction region near Maraş, south-central Turkey. Journal of the Geological Society, London 147, 1023–1034.

Karabıyıkoğlu, M., Çiner, A., Tuzcu, S., Deynoux, M., 1997. Facies, depositional environments and evolution of a gravity induced submarine fan sedimentation (Miocene) in the Aksu foreland basin, Western Taurids, Turkey. European Union of Geoscientists (EUG 9), vol. 9, Terra Nova, Strasbourg, France, p. 325.

Karabıyıkoğlu, M., Çiner, A., Monod, O., Deynoux, M., Tuzcu, S. and Örçen, S., 2000. Tectonosedimentary evolution of the Miocene Manavgat Basin, western Taurides, Turkey. In E. Bozkurt, J.A. Winchester and J.D.A. Piper (Eds.), Tectonics and Magmatism in Turkey and the Surrounding Area. Geological Society, London, Special Publication 173: 271-294.

Karabıyıkoğlu, M., Tuzcu, S., Çiner, A., Deynoux, M., Örçen, S. and Hakyemez, A., 2005. Facies and environmental setting of the Miocene coral reefs in the late-orogenic fill of the Antalya Basin, western Taurides, Turkey: implications for tectonic control and sea-level changes. Sedimentary Geology, 173, 345-371.

Kastens, K.A., Mascle, J., et al., 1990. Proceedings of the Ocean Drilling Program, Scientific Results, 107: College Station, TX (Ocean Drilling Program). doi:10.2973/odp.proc.sr.107.1990

Kazmin, V.G., Kulakov, V.V., 1968. The geological map of Syria. Scale 1: 50 000 (Sheet Al-Latheqiyeh). Explanatory note. Technoexport, Nedra, Moscow: 124 pp.

Kearey, P. Brooks, M., Hill, I., 2002. An Introduction to Geophysical Exploration. 3rd Edition, Blackwell Science, 281 pp.

Kelling, G., Gökçen, S.L., Floyd, P.A., Gökçen, N., 1987. Neogene tectonics and plate convergence in the eastern Mediterranean: New data from southern Turkey. Geology 15, 425–429.

Kempler, D., 1998. Eratosthenes Seamount: the possible spearhead of incipient continental collision in the eastern Mediterranean. In: Robertson, A.H.F., Emeis, K.-C., Richter, C., Camerlenghi, A. (Eds.), Proceedings of the Ocean Drilling Program, Scientific Results, Vol. 160, pp. 709–721.

Kempler, D., 1994. Structures and kinematics in the northeastern Mediterranean: a study of an irregular plate boundary. Tectonophysics, 234: 19–32.

Kempler, D., and Ben-Avraham, Z. 1987. The tectonic evolution of the Cyprean Arc. Anales Tectonicae, 1, 58-71.

Kempler, D. and Garfunkel, Z., 1994. Structure and kinematics in the northeastern Mediterranean: a study of irregular plate boundary. Tectonophysics 234, 19– 32.

Kempler, D., Mart, Y., Herut, B., McCoy, F.W., 1996. Diapiric features in the southeastern Mediterranean Sea: possible indication of extension in a zone of incipient continental collision. Marine Geology, 134, 237–248.

Keskin, M., 2003. Magma generation by slab steepening and breakoff beneath a subduction–accretion

complex: an alternative model for collision-related volcanism in Eastern Anatolia, Turkey, Geophysical Research Letters, 30, 8046, doi:10.1029/2003GL018019.

King, H., 2014. Miocene–Recent evolution of the Antalya Basin, Eastern Mediterranean Sea. Unpublished MSc thesis, Memorial University of Newfoundland. 198 pp.

Kissel, C., Poisson, A. 1986. Étude paléomagnetique des formations néogènes du bassin d'Antalya (Taurides occidentales-Turquie). Comptes Rendus Acadademie Science Paris 302, Série II, 711–716.

Kissel, C., Laj, C., 1988. The Tertiary geodynamical evolution of the Aegean arc: a paleomagnetic reconstruction. Tectonophysics, 146, 183–201.

Kissel, C., Averbuch, O., Frizon de Lamotte, D., Monod, O., and Allerton, S., 1993. First paleomagnetic evidence for a post-Eocene clockwise rotation of the Western Taurides thrust belt east of the Isparta reentrant (Southwestern Turkey). Earth and Planetary Science Letters, 117, 1–14

Kissel, C., Laj, C., Poisson, A., Görür, N., 2003. Palaeomagnetic reconstruction of the Cenozoic evolution of the Eastern Mediterranean. Tectonophysics 362, 199–217.

Khair, K., Tsokas, G.N., 1999. Nature of the Levantine (eastern Mediterranean) crust from multiple-source Werner deconvolution of Bouguer gravity anomalies. Journal of Geophysical Research, 104, Bll, 25469–25478.

Koçyiğit, A., Özacar, A., 2003. Extensional neotectonic regime through the NE edge of the outer Isparta Angle, SW Turkey: new field and seismic data. Turkish journal of Earth Sciences 12, 67–90.

Koçyiğit, A., Yılmaz, A., Adamia, S., Kuloshvili, S., 2001. Neotectonics of East Anatolian Plateau (Turkey) and Lesser Caucasus: implication for transition from thrusting to strike-slip faulting,

Geodinamica Acta, 14, 177–195.

Kopf, A, Mascle, J., Klaeschen, D., 2003. The Mediterranean Ridge: A mass balance across the fastest growing accretionary complex on Earth. Journal of Geophysical Research, 108: B8, 2372, Doi:10.1029/2001jb000473.

Kozlu, H., 1987. Structural development and stratigraphy of Misis–Andirin region. Proceedings of the 7th Petroleum Congress of Turkey. Turkish Association of Petroleum Geologists, pp. 104– 116.

Krijgsman, W., Hilgen, F.J., Raffi, I., Sierro, F.J., Wilson, D. S., 1999. Chronology, causes and progression of the Messinian salinity crisis. Nature 400, 652–655.

Krijgsman, W., Fortuin, A.R., Hilgen, F.J., Roep, T.B. and Sierro, F.J., 2001. Astrochronology for the Messinian Sorbas Basin (SE Spain) and orbital (precessional) forcing for evaporite cyclicity. Sedimentary Geology, 140, 43–60.

Krijgsman, W., Blanc-Valleron, M.M., Flecker, R., Hilgen, F.J., Kouwenhoven, T.J., Orszag-Sperber, F., Rouchy, J.M., 2002. The onset of the Messinian salinity crisis in the eastern Mediterranean (Pissouri Basin, Cyprus). Earth and Planetary Science Letters, 194(3–4), 299–310.

Krijgsman, W., Gaboardi, S., Hilgen, F.J., Iaccarino, S., De Kaenel, E., van der Laan, E., 2004. Revised astrochronology for the Ain el Beida section (Atlantic Morocco): no glacioeustatic control for the onset of the Messinian Salinity Crisis. Stratigraphy, 1, 87–101.

Krijgsman, W., Meijer, P.Th., 2008. Depositional environments of the Mediterranean "Lower Evaporites" of the Messinian salinity crisis: Constraints from quantitative analyses. Marine Geology 253, 73–81. Krijgsman et al., 2010

Lastras, G., M. Canals, J.E. Hughes-Clarke, A. Moreno, M. De Batist, D.G. Masson, and P. Cochonat, 2002. Seafloor imagery from the BIG'95 debris flow, western Mediterranean. Geol-

ogy, 30: 871-874.

Lazar, M., Schattner, U., Reshef, M., 2012. The great escape: an intra-Messinian gas system in the eastern Mediterranean. Geophysical Research Letters 39, L20309.

Le Pichon, X., Kreemer, ., 2010. The Miocene-to-Present Kinematic Evolution of the Eastern Mediterranean and Middle East and Its Implications for Dynamics, in Annual Review of Earth and Planetary Sciences, 38, 323–351.

Le Pichon, X., Angelier, J., Sibuet, J.-C. 1982. Plate boundaries and extensional tectonics. Tectonophysics, 81, 239–256.

Le Pichon, X., N. Chamot-Rooke, S. Lallemant, R. Noomen, G. Veis, 1995. Geodetic determination of the kinematics of central Greece with respect to Europe: Implications for eastern Mediterranean tectonics, Journal of Geophysical Research, 100, 12675– 12690.

Li, C., van der Hilst, R., Toksöz, M.N., 2006. Constraining P-wave velocity variation in the upper mantle beneath SE Asia, *Phys. Earth Planet. Int.* 154: 180–195.

Limonov, A.F., Woodside, J.M., Cita, M.B., Ivanov, M.K., 1996. The Mediterranean Ridge and related mud diapirims: a background. Marine Geology, 132, 7-19.

Lisiecki, L.E., Raymo, M.E., 2005. A Pliocene-Pleistocene stack of 57 globally distributed benthic δ18O records. Paleoceanography, 20, 1–17.

Livermore. A., Smith, A.G., 1985. Some boundary conditions for the evolution of the Mediterranean. In: Stanledy, G. and Wezelf, C. (eds). Geological Evolution of the Mediterranean Sea, Springer-Verlag, New York, 89-105.

Lofi, J., Berné, S., 2008. Evidence for pre-Messinian submarine canyons on the Gulf of Lions slope (western Mediterranean). Marine and Petroleum Geology, 25, 804– 817.

Lofi, J., Gorini, C., Berne, S., Clauzon, G., Dos Reis, A.T., Ryan, W.B.F., Steckler, M.S., 2005. Erosional processes and paleo-environmental changes in the western Gulf of Lions (SW France) during the Messinian Salinity Crisis. Marine Geology 217, 1–30.

Lofi, J., Déverchère, J., Gaullier, V., Gillet, H., Gorini, C., Guennoc, P., Loncke, L., Maillard, A., Sage, F., Thinon. I., 2011b. Atlas of the Messinian Salinity Crisis: seismic markers in the Mediterranean and Black seas. Commission for the geological map of the world 77, rue Claude-Bernard, 75055 Paris, France, 76 pp.

Lofi, J., Sage, F., Déverchère, J., Loncke, L., Maillard, A., Gaullier, V., Thinon, I., Gillet, H., Guennoc, P., Gorini, C., 2011a. Refining our knowledge of theMessinian salinity crisis records in the offshore domain through multi-site seismic analysis. Special Issue, Miocene–Pliocene geodynamics and paleogeography in the Mediterranean region: eustasy-tectonics interference. Bulletin de la Societe Geologique de France 182 (2), 163–180.

Loget, N., Davy, P., Van Den Driessche, J., 2006. Mesoscale fluvial erosion parameters deduced from modeling the Mediterranean sea level drop during the Messinian (late Miocene). Journal of Geophysical Research, 111, F03005, doi:10.1029/2005 JF000387.

Lohmann, H.H., 1972. Salt dissolution in subsurface of British North Sea as interpreted from seismograms. AAPG Bulletin, 56(3), 472–479.

Loncke, L., J. Mascle, and Fanil Scientific Parties, 2004. Mud volcanoes, gas chimneys, pockmarks and mounds in the Nile deep-sea fan (Eastern Mediterranean): Geophysical evidences, Marine and Petroleum Geology, 21, 669–689.

Loncke, L., Gaullier, V., Mascle, J., Vendeville, B., Camera, L., 2006. The Nile deep-sea fan: an example of interacting sedimentation, salt tectonics and inherited subsalt paleotopographic

features. Marine and Petroleum Geology 23, 297–315.

Loncke, L., Gaullier, V., Camera, L., Mascle, J., 2010. Nile Deep Sea Fan. In: Lofi, J., Déverchère, J., Gaullier, V., Gillet, H., Gorini, C., Guennoc, P., Loncke, L., Maillard, A., Sage, F., Thinon. I. (Eds), Atlas of the Messinian Salinity Crisis: seismic markers in the Mediterranean and Black seas. Commission for the Geological Map of the world 77, rue Claude-Bernard, 75055 Paris, France, 51–53, 76 pp.

Lugli, S., Manzi, V., Roveri, M., Schreiber, B.C., 2010. The Primary Lower Gypsum in the Mediterranean: a newfacies interpretation for the first stage of theMessinian salinity crisis. Palaeogeography, Palaeoclimatology, Palaeoecology 297, 83–99.

Lugli, S., Gennari, R., Gvirtzman, Z., Manzi, V., Roveri, M., Schreiber, B.C., 2013. Evidence of clastic evaporites in the canyons of the Levant Basin (Israel): implications for the Messinian Salinity Crisis. Journal of Sedimentary Research 83, 942–954.

Maillard, A., Gorini, C., Mauffret, A., Sage, F., Lofi, J., Gaullier, V., 2006. Offshore evidence of polyphase erosion in the Valencia Basin (Northwestern Mediterranean): scenario for the Messinian Salinity Crisis. Sedimentary Geology 188–189, 69–91.

Maillard, A., Hübscher, C., Benkhelil, J., Tahchi, E., 2011. Deformed Messinian markers in the Cyprus Arc: tectonic and/or Messinian Salinity Crisis indicators? Basin Research 23, 146–170.

Malinverno, A., Ryan, W.B.F., 1986. Extension on the Tyrrhenian Sea and shortening in the Apennines as result of arc migration driven by sinking of the lithosphere. Tectonics, 5: 227–245.

Mann, P., 1997. Model for the formation of large, transtensional basins in zones of tectonic escape. Geology 25, 211– 214.

Manzi, V., Lugli, S., Ricci Lucchi, F., Roveri,M., 2005. Deep-water clastic evaporites deposition in the Messinian Adriatic foredeep (northern Apennines, Italy): did theMediterranean ever dry out? Sedimentology 52, 875–902.

Manzi, V., Lugli, S., Roveri,M., Schreiber, B.C., 2009. A newfaciesmodel for the Upper Gypsum of Sicily (Italy): chronological and paleoenvironmental constraints for the Messinian salinity crisis in the Mediterranean. Sedimentology 56, 1937–1960.

Manzi, V., Gennari, R., Hilgen, F., Krijgsman, W., Lugli, S., Roveri, M., Sierro, F.J., 2013. Age refinement of the Messinian salinity crisis onset in the Mediterranean. Terra Nova, 25, 315–322.

Manzi, V., Lugli, S., Roveri, M., Dela Pierre, F., Gennari, F., Lozar, F., Natalicchio, M., Schreiber, B.C., Taviani, M., Turco, E., 2014. The Messinian salinity crisis in Cyprus: a further step towards a new stratigraphic framework for Eastern Mediterranean. Basin Research, 1–30, doi: 10.1111/bre.12107.

Mart, Y., Ben Gai, Y., 1982. Some depositional patterns at continental margin of southeastern Mediterranean Sea. Americal Association of Petroleum Geologists, Bulletin, 66: 460–470.

Martinez del Olmo, W., 1996. Yesos de margen y turbiditicos en el Messiniense del Golfo de Valencia: Una desecacion imposible. Revista de la Sociedad Geológica de España 9, 67–116.

Mascle, J., Cousin, M., Fleury, J., Le Cleac'h, A., Saint-Marc, G., 1986. Calcaires mésozoïques dans les fosses helléniques: implications paléogéographiques et géodynamiques. Marine Geology, 73, 323–341.

Mascle, J., Benkhelil, J., Bellaiche, G., Zitter, T., Woodside, J., Loncke, L., and Prismed II Scientifi c Party, 2000, Marine geologic evidence for a Levantine-Sinai plate, a new piece of the Mediterranean puzzle: Geology, v. 28, p. 779–782.

Mascle, J., Mary, F., Praeg, D., Brosolo, L., Camera, L., Ceramicola, S., Dupre, S., 2014. Distribution and geological control of mud volcanoes and other fluid/free gasseepage features in the Mediterranean Sea and nearby Gulf of Cadiz. Geo-Mar. Lett. 34, 89–110.

Mattei, M., Cifelli, F., D'Agostino, N., 2007. The evolution of the Calabrian Arc: evidence from paleomagnetic and GPS observations. Earth and Planetary Science Letters, 263, 259–274.

Meijer, P.Th. and Krijgsman, W. 2005. A quantitative analysis of the dessication and reflling of the Mediterranean during the Messinian Salinity Crisis. Earth Planet. Sci. Lett. 240, 510–520.doi:10.1016/j.epsl.2005.09.029.

Meijers, M.J.M., van Hinsbergen, D.J.J., Dekkers, M.J., Altıner, D., Kaymakcı, N., and Langereis, C.G., 2010. Pervasive Palaeogene remagnetization of the central Taurides fold-and-thrust belt (southern Turkey) and implications for rotations in the Isparta Angle. Geophysical Journal International, 184: 1090–1112.

McCallum, J.E. and Robertson, A.H.F., 1990. Pulsed uplift of the Troodos Massif - evidence from the Plio-Pleistocene Mesaoria Basin. In: J. Malpas, E.M. Moores, A. Panayiotou and C. Xenophontos (Eds.), Ophiolites, Oceanic Crustal Analogues. Proceedings of the Symposium "Troodos 1987". Geological Survey Department, Ministry of Agriculture and Natural Resources, Nicosia, Cyprus, p. 217–229; 733 pp.

McClusky, S., Balassinian, S., Barka, A., Demir, C., Ergintav, S., Georgiev, I., Gurkan, O., Hamburger, M., Hurst, K., Kahle, H., Kastens, K., Kekelidze, G., King, R., Kotzev, V., Lenk, O., Mahmoud, S., Mishin, A., Nadariya, M.,Ouzonis, A.m, Paradissis, D., Peter, Y., Prilepin, M., Reilinger, R., Sanli, I., Seeger, H., Tealeb, A., Toksöz, M.N., and Veis, G. 2000. Global Positioning System constraints on plate kinematics and dynamics in the eastern Mediterranean and Caucasus. Journal of Geophysical Research, 105: B3, 5695-5719.

McClusky, S., Reilinger, R., Mahmoud, S., Sari, D.B., Tealeb, A., 2003. GPS constraints on Africa (Nubia) and Arabia plate motions. Geophysical Journal International, 155, 126–138

McKenzie, D., 1972. Active tectonics of the Mediterranean region. Geophysical Journal of the Royal Astronomical Society, 30: 109–185.

McKenzie, J.A., Ricchiuto, T.E., 1978. Stable isotopic investigation of carbonate samples related to the Messinian Salinity Crisis from DSDP Leg 42A, Mediterranean Sea. Initial Reports of the Deep Sea Drilling Project XLII, Part I, p. 650–655, U.S. Government Printing Office, Washington.

Milliman, J.D., Syvitski, J.P.M., 1992. Geomorphic/tectonic control of sediment discharge to the ocean: the importance of small mountainous rivers The Journal of Geology, 100, 525–544.

Milliman, J.D., Farnsworth, K.L., 2011. River Discharge to Coastal Ocean: a Global Synthesis. Cambridge University Press, Cambridge, 383 pp.

Mitchum, R. M., Jr., Vail, P. R., Thompson, S., III, 1977. Seismic stratigraphy and global changes of sea-level, part 2: the depositional sequence as a basic unit for stratigraphic analysis. In: Payton, C. E. (ed.), Seismic Stratigraphy – Applications to Hydrocarbon Exploration. American Association of Petroleum Geologists Memoir 26, 53–62.

Mocochain, L., Clauzon, G., Bigot, J-Y., Brunet, P., 2006. Geodynamic evolution of the peri-Mediterranean karst during the Messinian and the Pliocene: evidence from the Ardèche and Rhône Valley systems canyons, Southern France. Sedimentary Geology 188–189: 219–233.

Monod, O., 1977. Recherces géologiques dans le Taurus occidentales au sud de Beyşehir (Turquie). Thèse de Doctorat d'État ès Sciences, Université de Paris-Sud, Orsay, France. 442 pp.

Monod, O., Kuzucuoğlu, C., Okay, A.I., 2006. A Miocene Palaeovalley network in the Western Taurus (Turkey). Turkish Journal of Earth Sciences 15, 1-23.

Montadert, L., Sancho J., Fail, J. P., Debyser, J., and Winnock, E., 1970. De l'àge tertiaire de la série salifère responsable des structures diapiriques en Méditerranée occidentale (nord-est des Baléares): C.R. Acad. Sci. Paris, v. 271, p. 812-815.

Montadert, L., Letouzey, J. and Mauffret, A., 1978. Messinian Event: seismic evidence. In: K.Hsü, L. Montadert et al. (Eds.), Initial Reports of the Deep Sea Drilling Project XLII, Part I, p. 1037-1050. U.S. Government Printing Office, Washington.

Montadert, L., O. Lie, P. H. Semb, and S. Kassinis, 2010. New seismic may put offshore Cyprus hydrocarbon prospects in the spotlight. First Break, 28, 91–101.

Montadert, L., Nicolaides, S., Semb, P.H., Lie, Ø., 2010. Petroleum Systems Offshore Cyprus, Search and Discovery Article #10279, Poster Presentation, AAPG Annual Convention and Exhibition, New Orleans, Louisiana, April 11–14, 2010.

Montadert, L., Nicolaides, S., Semb, P.H.; Lie, Ø., 2014, Petroleum systems offshore Cyprus, in L. Marlow, C. Kendall and L. Yose, eds., Petroleum systems of the Tethyan region. American Association of Petroleum Geologists, Memoir, 106, 301–334.

Natalicchio, M., Pierre, F.D., Lugli, S., Lowenstein, T.K., Feiner, S.J., Ferrando, S., Manzi, V., Roveri, M. and Clari, P., 2014. Did Late Miocene (Messinian) gypsum precipitate from evaporated marine brines? Insights from the Piedmont Basin (Italy). *Geology*, 42(3), pp.179-182.

Neev, D., Hall, J.K., 1982. The Pelusium megashear system across Africa and associated lineament swarms. Journal of Geophysical Research, 87, 1015–1030.

Netzeband, G., Hübscher, C., Gajewski, G., 2006. The structural evolution of the Messinian evaporites in the Levantine Basin, Marine Geology, 230, 249–273, doi:10.1016/j.margeo.2006.05.004.

Nilsson, C., Reidy, C.A., Dynesius, M., Revenga, C., 2005. Fragmentation and Flow Regulation of the World's Large River Systems. Science, 308, 405–408. Supporting Online Material

www.sciencemag.org/cgi/content/full/308/5720/405/ DC1.

Nur, A., Ben-Abraham, Z., 1978. The eastern Mediterranean and the Levant: tectonics and continental collision. Tectonophysics, 46: 297–311.

Omodeo Salé, S., Gennari, R., Lugli, S., Manzi, V. and Roveri, M., 2012. Tectonic and climatic control on the Late Messinian sedimentary evolution of the Nijar Basin (Betic Cordillera, Southern Spain). *Basin Research*, 24(3), pp.314-337.

Othman, A.A.A., Tharwat, A.H., Fathy., M., Negm, A.M., 2014. Petrophysical analysis for hydrocarbon exploration based on well log data, North Maryut, Mediterranean Sea, Egypt. Journal of American Science, 10(12), 58–68.

Örgülü, G., Aktar, M., Türkelli, N., Sandvol, E., Barazangi, M., 2003. Contribution to the Seismotectonics of the Eastern Anatolian Plateau from Moderate and Small Size Events, Geophysical Research Letters, 30 (24) 8040, doi:10.1029/2003GL018258.

Orszag-Sperber, F., Rouchy, J.-M., Bizon, G., Bizon, J.-J., Cravatte, J., Müller, C., 1980a. La sédimentation messinienne dans le bassin de Polémi (Chypre). Géol. Méditerr. VII, 91–102.

Orszag-Sperber, F., Rouchy, J.M., Bizon, G., Bizon, J.J., Cravatte, J., Müller, C., 1980b. La sédimentation messinienne dans le bassin de Polémi (Chypre). In: Orszag-Sperber, F., Rouchy, J.-M. (Eds.), Les aspects géodynamiques du passage Miocène-Pliocène en Méditerranée. Géologie Méditerranéenne, vol. VII, pp. 91–102.

Orszag-Sperber, F., Rouchy, J.-M., Elion, P., 1989. The sedimentary expression of regional tectonic events during the Miocene–Pliocene transition in the Southern Cyprus basins. Geol. Mag. 126 (3), 291–299.

Orszag-Sperber, F., Rouchy, J.M., Blanc Valleron, M.M., 2000. La transition Messinien–Plioce‘ne en Mediterranee orientale (Chypre): la periode du Lago-Mare et sa signification. Comptes

Rendus de l'Academie des Sciences. Sciences de la Terre et des Plane'tes 331, 483–490.

Orszag-Sperber, F., 2006. Changing perspectives in the concept of "Lago-Mare" in Mediterranean Late Miocene evolution. Sedimentary Geology 188–189, 259–277.

Orszag-Sperber, F., Caruso, A., Blanc-Valleron, M.M., Merle, D., Rouchy, J.M., 2009. The onset of the Messinian salinity crisis: insights from Cyprus sections. Sedimentary Geology, 217, 52–64.

Özacar, A.A., Gilbert, H., Zandt., G., 2008. Upper mantle discontinuity structure beneath East Anatolian Plateau (Turkey) from receiver functions, Earth planet. Sci. Lett., 269, 426–434.

Özacar, A.A., Zandt, G., Gilbert, H., Beck, S.L., 2010. Seismic images of crustal variations beneath the East Anatolian Plateau (Turkey) from teleseismic receiver functions, Journal Geological Society, London, Special Publications, 340, 485–496, doi:10.1144/SP34021.

Özer, G.P., 2009. Miocene To Recent Stratigraphy, Structural Architecture And Tectonic Evolution Of The Florence Rise,Eastern Mediterrenean Sea. Unpuplished MSc thesis. Dokuz Eylul University, Izmir, Turkey.

Özbey S., Bagnasco G., 1960. Antalya Area; Lithostratigraphic Section. Turkish Gulf Oil Company (Unpublished Report).

Papadimitriou, E.E. and Karakostas, V.G., 2006. Earthquake generation in Cyprus revealed by the evolving stress field. Tectonophysics, 423, 61–72.

Pearce, J.A., Bender, J.F., De Long, S.E., Kidd, W.S.F., Low, P.J., Güner, Y., Şaroğlu, F., Yılmaz, Y., Moorbath, S., Mitchell, J.G. 1990. Genesis of collision volcanism in Eastern Anatolia, Turkey. Journal of Volcanology and Geothermal Research, 44, 189–229.

Perinçek, D., Eren, A.G., 1990. Origin of the Amik Basin within the strike-slip East Anatolian

and Dead Sea fault zones. Proceedings of the 8th Petroleum Congress of Turkey, Turkish Association of Petroleum Geologists, pp. 180–192.

Perinçek, D., Günay, Y., Kozlu, H., 1987. New observations on strike-slip faults in east and south-east Anatolia. Proceedings of the 7th Petroleum Congress of Turkey, Turkish Association of Petroleum Geologists, pp. 89–103.

Pierre, C., Fontes, J.C., 1978 Isotope Composition of Messinian sediments from the Mediterranean Sea as indicators of paleoenvironments and diagenesis. Initial Reports, DSDP, 42 (1978), Washington, U.S. Government Printing Office, pp. 635–650.

Pierre, F.D., Clari, P., Cavagna, S. and Bicchi, E., 2002. The Parona chaotic complex: a puzzling record of the Messinian (Late Miocene) events in Monferrato (NW Italy). *Sedimentary Geology*, 152(3), pp.289-311.

Pierre, F.D., Festa, A., Irace, A., 2007. Interaction of tectonic, sedimentary, and diapiric processes in the origin of chaotic sediments: An example from the Messinian of Torino Hill (Tertiary Piedmont Basin, northwestern Italy). *Geological Society of America Bulletin*, 119(9-10), pp.1107-1119.

Pilidou, S., Priestley, K., Jackson, J. & Maggi, A., 2004. The 1996 Cyprus earthquake: a large, deep event in the Cyprean Arc. Geophysical Journal International, 158, 85–97.

Piper, J.D.A., Tatar, O., Gürsoy, H., Koçbulut, F. and Mesci, B.L., 2006. Paleomagnetic analysis of neotectonic deformation in the Anatolian accretionary collage, Turkey. Geological Society of America Special Papers 409: 417–439.

Piper, J.D.A., Gürsoy, H., Tatar, O., Beck, M.E., Raoa, A., Koçbulut, F. and Mesci, B.L., 2010. Distributed neotectonic deformation in the Anatolides of Turkey: a palaeomagnetic analysis. Tectonophysics, 488, 31–50.

Pişkin, O., Delaloye, M., Moritz, R., Selçuk, H., Wagner, J.-J., 1984. A tectonic approach of the Hatay and Baër-Bassit ophiolites. Ofioliti 11, 87–104.

Platt, J.P., Vissers, R.L.M., 1989. Extensional collapse of thickened continental lithosphere: A working hypothesis for the Alboran Sea and Gibraltar arc. Geology, 17: 540-543.

Poisson, A., 1977. Recherches geologiques dans Les Taurides occidentals (Turquie; : These d'Etat, Univ. Paris Sud,795 (unpublished), Orsay.

Poisson, A., Akay, E., Cravatte, J., Müller, C, ve Uysal, Ş., 1983. Donnés nouvelles sur la chronologie de mise en place des nappes d'Antalya au centre de L'Angle d'Isparta (Taurus occidental, Turquie): C.R. Acad. Sc. Paris, t. 296, 923–926.

Poisson, A., Akay, E., Dumont, J.F., ve Uysal, Ş., 1984. The İsparta angle (western Taurides-Turkey): a Mesozoik paleorift. In: O. Tekeli ve M.C. Göncüoğlu (Ed.), Geology of Taurus Belt: Proceedings Int. Sym., 26-29 Sptember, Ankara, Turkey 11–26.

Poisson, A., Wernli, R., Sağular, K., and Temiz, H., 2003a. New data concerning the age of the Aksu Thrust in the south of the Aksu valley, Isparta Angle (SW Turkey): consequences for the Antalya Basin and the Eastern Mediterranean. Geological Journal, 38: 311–327.

Poisson, A., Yağmurlu, F., Bozcu, M., Şentürk, M., 2003b. New insights on the tectonic setting and evolution around the apex of the Isparta Angle (SW Turkey). Geological Journal, 38, 257-282.

Poisson, A., Orszag-Sperber, F., Koson, E., Bassetti, M-A, Müller, C., Wernli, R. and Rouchy, J-M., 2011. The Late Cenozoic evolution of the Aksu Basin (Isparta Angle: SW Turkey). New Insights. Bulletin de la Société Géologique de France, 182: 133-148.

Polonia, A., Camerlenghi, A., Davey, F., Storti, F., 2002. Accretion, structural style and syn-contractional sedimentation in the Eastern Mediterranean Sea. Mar. Geol. 186, 127–144.

Popov, S.V., Rögl, F., Rozanov, A.Y., Steininger, F.F., Shcherba, I.G., Kovac, M., 2004. Lithological-Paleogeographic maps of Paratethys, 10 maps late Eocene to Pliocene. Courier Forschungsinstitut Senckenberg 250, 1–46 (Frankfurt).

Popov, S.V., Shcherba, I.G., Ilyina, L.B., Nevesskaya, L.A., Paramonova, N.P., Khondkarian, S.O., Magyar, I., 2006. Late Miocene to Pliocene palaeogeography of the Paratethys and its relation to the Mediterranean. Palaeogeography, Palaeoclimatology, Palaeoecology 238, 91–106.

Reiche, S., Hübscher, C., Ehrhardt, A., 2015. The impact of salt on the late Messinian to recent tectonostratigraphic evolution of the Cyprus subduction zone. Basin Res. 1(29), doi:10.1111/bre.12122.

Reilinger, R.E., McClusky, S.C., Souter, B.J., Hamburger, M.W., Prilepin, M.T., Mishin, A., Guseva, T., Balassanian, S., 1997. Preliminary estimates of plate convergence in the Caucasus collision zone from global positioning system measurements, Geophysical Research Letters, 24, 1815–1818.

Reilinger, R., Mcclusky, S., Vernant, P., Lawrence, S., Ergintav, S., Çakmak, R. et al. 2006. GPS constraints on continental deformation in the Africa–Arabia–Eurasia continental collision zone and implications for the dynamics of plate interactions. Journal of Geophysical Research, 111, V05411, doi:10.1029/2005JB004051.

Réhault, J.-P., Boillot, G., and Mauffret, A., 1984, The western Mediterranean basin geological evolution: Marine Geology, v. 55, p. 447–477.

Rezak, R., Bright, T., McGrail, C. 1985. Reefs and Banks of the Northwestern Gulf of Mexico: their Geological, Biological and Physical Dynamics. Wiley, New York.

Ricchiuto, T.E & McKenzie, J.A., 1978. Stable isotopic investigation of the Messinian sulfate samples from DSDP Leg 42 A, Eastern Mediterranean Sea Initial Reports of the Deep Sea

Drilling Project, 42 (1) (1978), pp. 657–660

Riding, R., Braga, J.C., Martín, J.M., and Sánchez-Almazo, I.M., 1998. Mediterranean Messinian Salinity Crisis: constraints from a coeval marginal basin, Sorbas, SE Spain. Mar. Geol.,146:1–20.

Robertson, A.H.F., 1998. Tectonic significance of the Eratosthenes Seamount: a continental fragment in the process of collision with a subduction zone in the eastern Mediterranean (Ocean Drilling Program Leg 160). Tectonophysics 298, 63–82.

Robertson, A.H.F. 2000. Mesozoic-Tertiary tectonic sedimentary evolution of a south Tethyan oceanic basin and its margins in southern Turkey. In: Bozkurt, E., Winchester, J.A., Piper, J.D.A. (eds) Tectonics and Magmatism in Turkey and the Surrounding Area. Geological Society, London, Special Publication, 173, 97–138.

Robertson, A.H.F. and Woodcock, N.H., 1986. The role of Kyrenia Range lineament, Cyprus, in the geological evolution of the eastern Mediterranean area. Philosophical Transactions-Royal Society of London, Series A 317, 141– 177.

Robertson, A.H.F., 1998a. Lithofacies evidence for the Cretaceous–Paleogene sedimentary history of Eratosthenes Seamount, Eastern Mediterranean in its regional tectonic context (ODP Leg 160, Sites 966 and 967). Proc. ODP, Sci. Results 160, 403–407.

Robertson, A.H.F., 1998b. Miocene shallow-water carbonates of the Eratosthenes Seamount, easternmost Mediterranean Sea. Proc. ODP, Sci. Results 160, 419–436.

Robertson, A.H.F., Cliff, P.D., Degnan, P., and Jones, G., 1991. Palaeogeographic and palaeotectonic evolution of the Eastern Mediterranean Neothethys, Palaeogeography, Palaeoclimotology, and Palaeoecology, 87, 289–344.

Robertson, A.H.F., Eaton, S., Follows, E.J., Payne, A.S., 1995. Depositional processes and basin analysis of Messinian evaporites in Cyprus. Terra Nova, 7, 233–253.

Rontogianni S., Konstantinou, K.I., Melis, N.S. and Evangelidis, C.P., 2011. Slab stress field in the Hellenic subduction zone as inferred from intermediate-depth earthquakes. Earth Planets Space, 63, 139–144.

Rosenbaum, G., Lister, G. S. and Duboz, C. 2002. Reconstruction of the tectonic evolution of the western Mediterranean since the Oligocene. In: Rosenbaum, G. and Lister, G. S. 2002. Reconstruction of the evolution of the Alpine-Himalayan Orogen. Journal of the Virtual Explorer, 8, 107–130.

Ross, A., Uchepi, E.. 1977. Structure and sedimentary history of the southeastern Mediterranean sea – Nile cone area. American Association of Petroleum Geologists Bulletin, 61, 872–902.

Rotstein, Y. and Kafka, A.L., 1982. Seismotectonics of the southern boundary of Anatolia, eastern Mediterranean region: subduction, collision and arc jumping. Journal of Geophysical Research, 87 (B9): 7694-7706.

Rouchy J. M., 1982. La genèse des évaporites messiniennes de Méditerranée. *Mém. Mus. Nat. Hist. Nat.* (Paris), Sciences de la Terre, L., 280 pp.

Rouchy, J.-M., Caruso, A., 2006. The Messinian salinity crisis in the Mediterranean basin a reassessment of the data and an integrated scenario. *Sedimentary Geology*, 188, 35–67.

Rouchy, J.-M., Orszag-Sperber, F., 1980. Les aspects géodynamiques du passage Miocène-Pliocène en Méditerranée. In: Orszag-Sperber, F., Rouchy, J.-M. (Eds.), Les aspects géodynamiques du passage Miocène–Pliocène en Méditerranée. Géologie Méditerranéenne, vol. VII, pp. 147–154.

Rouchy, J.M. and Saint Martin, J.P., 1992. Late Miocene events in the Mediterranean as recorded by carbonate-evaporice relations. *Geology*, 20(7), pp.629-632.

Rouchy, J.M., Orszag-Sperber, F., Blanc-Valleron, M.M., Pierre, C., Rivière, M., Combourieu-Nebout, N. and Panayides, I., 2001. Paleoenvironmental changes at the Messinian–Pliocene boundary in the eastern Mediterranean (southern Cyprus basins): significance of the Messinian Lago-Mare. *Sedimentary Geology*, 145(1), pp.93-117.

Roveri, M., Manzi, V., 2006. The Messinian salinity crisis: looking for a new paradigm? Palaeogeography, Palaeoclimatology, Palaeoecology 238, 386–398. Roveri et al., 2001

Roveri, M. and Manzi, V., 2006. The Messinian salinity crisis: Looking for a new paradigm? Palaeogeography, Palaeoclimatology, Palaeoecology, 238, 386–398.

Roveri, M., Lugli, S., Manzi, V., Schreiber, B.C., 2008a. The Messinian Sicilian stratigraphy revisited: toward a new scenario for the Messinian salinity crisis. Terra Nova, 20, 483–488.

Roveri, M., Lugli, S., Manzi, V., Schreiber, B.C., 2008b. The Messinian salinity crisis: a sequence–stratigraphic approach. Geoacta Special Publications, 1, 169–190.

Roveri, M., Bertini, A., Cosentino, D., Di Stefano, A., Gennari, R., Gliozzi, E., Grossi, F., Iaccarino, S.M., Lugli, S., Manzi, V., Taviani, M., 2008c. A high-resolution stratigraphic framework for the latest Messinian events in the Mediterranean area. Stratigraphy, 5, 323–342.

Roveri, M., Lugli, S., Manzi, V., Schreiber, B.C., 2008d. The Messinian salinity crisis: a sequence-stratigraphic approach. GeoActa Special Publication 1, 169–190.

Roveri,M., Gennari, R., Lugli, S., Manzi, V., 2009. The Terminal Carbonate Complex: the record of sea-level changes during the Messinian salinity crisis. GeoActa 8, 57–71.

Roveri, M., Flecker, R., Krijgsman, W., Lofi, J., Lugli, S., Manzi, V., Sierro, F.J., Bertini, A., Camerlenghi, A., De Lange, G.J., Govers, R., Hilgen, F.J., Hubscher, C., Meijer, P.T.H., Stoica, M., 2014a. The Messinian Salinity Crisis: past and future of a great challenge for marine sciences. Marine Geology, 352: 25-58.

Roveri, M., Lugli, S., Manzi, V., Gennari, R., Schreiber, B.C., 2014b. High-resolution strontium isotope stratigraphy of the Messinian deep Mediterranean basins: implications for marginal to central basins correlation. Marine Geology, 349, 113–125.

Roveri, M., Manzi, V., Bergamasco, A., Falcieri, F., Gennari, R., Lugli, S., 2014c. Dense shelf water cascading and Messinian canyons: a new scenario for the Mediterranean salinity crisis. American Journal of Science, 314, 751–784.

Ruggieri, G., 1962. Gli ostracodi marni del Tortoniano (Miocene medio superiore) de Enna, nella Sicilia central. Paleontogr. Ital., 56, p. 68

Ryan,W.B.F., 1978. Messinian badlands on the southeastern margin of theMediterranean Sea. Marine Geology 27, 349–363.

Ryan,W.B.F., 2008. Modeling themagnitude and timing of evaporative drawdown during the Messinian salinity crisis. Stratigraphy 5, 227–243.

Ryan, W.B.F., 2009. Decoding the Mediterranean salinity crisis. Sedimentology 56, 95-136.

Ryan, W.B.F., Cita, M.B., 1978. The nature and distribution of Messinian erosional surfaces: indicators of a several-kilometer-deep Mediterranean in the Miocene. Marine Geology, 27, 193–230.

Ryan, W.B.F., Hsü , K.J., Cita, M.B., Dumitrica, P., Lort, P., Maync, W., Nesteroff, W.D., Pautot, P., Stradner, H., Wezel, F.C., 1973. Initial Reports of the Deep Sea Drilling Project (Eds W.B.F. Ryan and K.J. Hsü), Vol. 13, 1447 pp. U.S. Government Printing Office, Washington, DC.

Ryan, W.B.F., Olauson, E., Fairbridge, R.W., 1966. Mediterranean Sea: The Encylopedia of Oceonagraphy. Newyork, Rainhold Publ. Corp. pp. 490–498

Ryan, W.B.F. and Hsü, K.J., et al., 1973. Initial Reports of the Deep Sea Drilling Project, Volume XIII, Washington, U.S. Government Printing Office, 1447 p.

Ryan, W.B.F., Kastens, K. and Cita, M.B., 1982. Geological evidence concerning compressional tectonics in the eastern Mediterranean. Tectonophysics, 86: 213-242.

Ryan, W.B.F., Carbotte, S.M., Coplan, J.O., O'Hara, S., Melkonian, A., Arko, R., Weissel, R.A., Ferrini, V., Goodwillie, A., Nitsche, F., Bonczkowski, J., Zemsky, R., 2009. Global multiresolution topography synthesis. Geochemistry, Geophysics, Geosystems 10, Q03014. http://dx.doi.org/10.1029/2008GC002332.

Şafak, Ü, Kelling, G., Gökçen, N.S. and Gürbüz, K., 2005. The mid-Cenozoic succession and evolution of the Mut basin, southern Turkey, and its regional significance. Sedimentary Geology, 173, 121-150.

Sage, L., Letouzey, J., 1990. Convergence of the African and Eurasian plate in the eastern Mediterranean. In: J. Letouzey (Ed.), Petroleum and Tectonics in Mobile Belts, Edition Technip, Paris, 49–68, 224 pp.

Said, R., 1993. The River Nile: Geology, Hydrology and Utilization, Oxford, Pergamon Press, 320 pp.

Salaün, A.,Villemant, B.,Semet, M.P.,Staudacher, T., 2010. Cannibalism of olivine-rich cu- mulate xenoliths during the 1998 eruption of Piton de la Fournaise (La Réunion hotspot): implications for the generation of magma diversity. Journal of Volcanology and Geothermal Research 198 (1), 187–204.

Salem, R., 1976. Evolution of Eocene–Miocene sedimentation patterns in parts of northern Egypt. Bulletin of the American Association of Petroleum Geologists, 60, 34–64.

Sandvol, E., Seber, D., Barazangi, M., Vernon, F., Mellors, R., Al-Amri A., 1998. Lithospheric seismic velocity discontinuities beneath the Arabian Shield, Geophysical Research Letters, 25(15), 2873–2876.

Satur, N., Kelling, G., Cronin, B.T., Hurst, A. and Gürbüz, K., 2005. Sedimentary architecture of a canyon-style fairway feeding a deep-water clastic system, the Miocene Cingöz Formation, southern Turkey: significance for reservoir characterisation and modelling. Sedimentary Geology, 173, 91-119.

Savaşçın, M.Y., Francalanci, L., Innocenti, T., Manetti, P., Birsoy, R., Dağ, N., 1995. Miocene-Pliocene potassic-ultrapotassic volcanism of the Afyon-Isparta region (central-western Anatolia, Turkey): Petrogenesis and geodynamic implications: International Earth Sciences Colloquium on the Aegean Region (IESCA-1995), Proceedings, V-II, pp. 487–502.

Savoye, B., Piper, D.J.W., 1991. The Messinian event on the margin of the Mediterranean Sea in the Nice area, southern France. Marine Geology, 97, 279–304.

Sen, S., Valet, J.-P. 1986. Magnetostratigraphy of late Miocene continental deposits in Samos, Greece. Earth and Planetary Science Letters, 80, 167–174.

Schattner, U., 2010. What trigger the early- to- mid Pleistocene tectonic transition across the entire eastern Mediterranean? Earth and Planetary Science Letter 289, 539-548.

Schattner, U. and Lazar, M., 2014. Flip convergence across the Phoenician basin through nucleation of subduction. *Gondwana Research*, 25(2), pp.729-735.

Schreiber, B.C., Friedman, G.M., Decima, A. and Schreiber, E., 1976. Depositional environments of Upper Miocene (Messinian) evaporite deposits of the Sicilian Basin. *Sedimentology*, 23(6), pp.729-760.

Sellier, N.C., Loncke, L., Vendeville, B.C., Mascle, J., Zitter, T., Woodside, J., Loubrieu, B., 2013a. Post-Messinian evolution of the Florence Ridge area (Western Cyprus Arc), Part I: Morphostructural analysis. Tectonophysics, 591: 131-142.

Sellier, N.C., Vendeville, B.C., Loncke, L., 2013b. Post-Messinian evolution of the Florence Rise area (Western Cyprus Arc) Part II: Experimental modeling. Tectonophysics, 591: 143-151.

Şenel, M., 1997a. Geological Map of Fethiye, L8 quadrangle, No:2, 1:100,000 General Directorate of Mineral Research and Exploration, Ankara, Turkey, 22 pp.

Şenel, M., 1997b. Geological Map of Fethiye, M8 quadrangle, No:4, 1:100,000 General Directorate of Mineral Research and Exploration, Ankara, Turkey, 15 pp.

Şenel, M., Bölükbaşı, A.S., 1997. Geological Map of Fethiye, M9 quadrangle, No:5, 1: 100,000 General Directorate of Mineral Research and Exploration, Ankara, Turkey, 11 pp.

Şengör, A.M.C., Yılmaz, Y. 1981. Tethyan evolution of Turkey: a plate tectonic approach. Tectonophysics, 75, 181–241.

Şengör, A.M.C., Görür, N., Şaroğlu, F. 1985. Strike-slip faulting and related basin formation in zones of tectonic escape: Turkey as a case study. In: Christie-Blick, N. (ed.) Basin Formation and Sedimentation. Society of Economic Paleontologists and Mineralogists Special Publications, 37, 227–264.

Şengör, A.M.C., Özeren, S., Genç, T., Zor, E. 2003. East Anatolian high plateau as a mantle support, North–South shortened domal structure. Geophysical Research Letters, 30, doi: 10.1029/ 2003GL017858.

Sgarrella, F., Sprovieri, R., Di Stefano, E., and Caruso, A., 1997, Paleo-ceanographic conditions at the base of the Pliocene in the Southern Mediterranean Basin. Rivista Italiana di Paleontologia e Stratigrafia, 103: 207–220.

Sheriff, E.G., Geldart, L.P., 1995. Exploration Seismolgy, 2nd Edition, Cambridge University Press, Cambridge, 592 pp.

Shipboard Scientific Party, 1978. Chapter 6. Sites 375 and 376: Florence Rise. In: Initial Reports of the Deep Sea Drilling Project (Eds. K.J. Hsü and L. Montadert), Vol. 42A, pp. 219–304. U.S. Government Printing Office, Washington, DC. doi:10.2973/dsdp.proc.42-1.106.1978.

Skiple, C, Anderson, E., Fürstenau, F., 2012. Seismic interpretation and attribute analysis of the Herodotus and the Levantine Basin, offshore Cyprus and Lebanon. Petroleum Geoscience, 18, 433–442.

Sprovieri, R., Di Stefano, E., Sprovieri, M., 1996a. High resolu- tion chronology for Late Miocene Mediterranean stratigraphic events. Riv. Ital. Paleontol. 102, 77–104.

Sprovieri, R., Di Stefano, E., Caruso, A., Bonono, S., 1996b. High resolution stratigraphy in the Messinian Tripoli Formation in Sicily. Palaeopelagos 6, 415–435.

Sprovieri, M., A. Bellanca, R. Neri, S. Mazzola, A. Bonanno, B. Patti, and R. Sorgente (1999), Astronomical calibration of late Miocene stratigraphic events and analysis of precessionally driven paleoceanographic changes in the Mediterranean Basin, Mem. Soc. Geol. Ital.,54,7–24.

Stern, R.J., Johnson, P., 2010. Continental lithosphere of the Arabian Plate: A geologic, petrologic, and geophysical synthesis. Earth Science Reviews, 101: 29-67.

Swarbrick, R.E., 1993. Sinistral strike-slip and transpressional tectonics in an ancient oceanic setting: the Mamonia Complex, southwest Cyprus. Journal of the Geological Society London 150, 381–392.

Tari, G., Hussein, H., Novotny, B., Hannke, K., Kohazy. R., 2012. Play types of the deep-water Matruh and Herodotus basins, NW Egypt. Petroleum Geoscience, 18, 443–455.

Tatar, O., Gürsoy, H., Piper, J.D.A., 2002. Differential neotectonic rotations in Anatolia and the Tauride Arc: palaeomagnetic investigation of the Erenlerdağ Volcanic Complex and Isparta

volcanic district, south–central Turkey. Journal of the Geological Society London, 159: 281-294.

Tay, P.L., Lonergan, L., Warner, M., Jones, K.A. and IMERSE Working Group, 2002. Seismic investigation of thick evaporite deposits on the central and inner unit of the Mediterranean Ridge accretionary complex. *Marine geology*, 186(1), pp.167-194.

Taymaz, T., Jackson, J., McKenzie, D., 1991. Active tectonics of the north and central Aegean Sea. Geophysical Journal International 106, 433–490.

Tekin, E., Varol, B. and Ayyıldız, T., 2010. Sedimentology and paleoenvironmental evolution of Messinian evaporites in the Iskenderun–Hatay basin complex, Southern Turkey. *Sedimentary Geology*, 229(4), pp.282-298.

ten Veen, J.H., Woodside, M., Zitter, T.A.C., Dumont, J.F., Mascle, J., Volkonskaia, A., 2004. Neotectonic evolution of the Anaximander Mountains at the junction of the Hellenic and Cyprus Arcs. Tectonophysics, 391: 35-65.

Toksöz, M.N., Van der Hilst, R.D., Sun, Y., Zhang, H., 2010. Seismic Tomography of the Arabian-Eurasian Collision Zone and Surrounding Areas. AFRL-RV-HA-TR-2010-1043, Air Force Research Laboratory, Space Vehicles Directorate, MA USA, 43 pp.

Toprak, Y., Gül, M., and Yaman, S., 2009. Miocene lacustrine succession of the Hoyran Lake Basin, Isparta, southwest Turkey. Acta Geologica Polonica, 59 245–259.

Türkelli, N., Horasan, G., Kuleli, H.S., Reiter, D., 1996. Preliminary results of velocity distribution study in eastern Turkey, EOS, Trans. Am. Geophys. Un., 77(46), p. 477.

Tüysüz, N., Erler, A. 1995. Geology and geotectonic implications of Kazikkaya area, Kagizman-Kars (Turkey). In: Örcen, S. (ed.) Geology of the Black Sea Region. Proceedings of the International symposium on the Geology of the Black sea Region, 7–11 September 1995, Ankara,

Turkey. General directorate of mineral research and exploration and chamber of geological engineering, Ankara, 76–81.

Tuzcu, S. and Karabıyıkoğlu, M., 2001. Batı Toros Kuşağı Miyosen Mercan Resiflerinin Paleontolojisi, Stratigrafisi, Fasiyesleri ve Çökelme Ortamları, MTA Genel Müdürlüğü, Jeoloji Etütleri Dairesi, Rapor No: 10438, Ankara.

Uffenorde, H., Lund, J.J., Georgi, K.H., 1990. Biostratigraphy of the Neogene in the Iskenderun Basin. Turkish Association of Petroleum Geologists. Proceedings of the 8th Petroleum Congress of Turkey, pp. 363–370.

Underhill, J.R., 1989. Late Cenozoic deformation of the Hellenide foreland, western Greece. Geological Society of America Bulletin, 101, 613– 634.

Urgeles, R., Camerlenghi, A., Garcia-Castellanos, D., De Mol, B., Garcés, M., Vergés, J., Haslam, I., Hardman, M., 2010. New constraints on the Messinian sea level drawdown from3D seismic data of the Ebro Margin, western Mediterranean. Basin Research 2010, 1-23, doi: 10.1111/j.1365-2117.2010.00477.x.

Vai, G.B., 1997. Cyclostratigraphic estimate of the Messinian stage duration. In: Miocene Stratigrapghy: an Integrated Approach (A.G. Montanari, S. Odin and R. Coccioni, eds). Development in Paleontology Stratigraphy, 15, 463–476.

van der Laan, E., Gaboardi, S., Hilgen, F.J., Lourens , L.J., 2005. Regional climate and glacial control on high-resolution oxygen isotope records from Ain El Beida (latest Miocene, NW Morocco): A cyclostratigraphic analysis in the depth and time domain: Paleoceanography, v. 20, PA1001, doi: 10.1029/2003PA000995.

van der Laan, E., Snel, E., de Kaenel, E., Hilgen, F.J., Krijgsman, W., 2006. No major deglaciation across the Miocene-Pliocene boundary: Integrated stratigraphy and astronomical tuning of

the Loulja sections (Bou Regreg area, NW Morocco): Paleoceanography, v. 21, PA3011, doi: 10.1029/2005PA001193.

van Hinsbergen, D.J.J., Dekkers, M.J., Koç, A., 2010a. Testing Miocene Remagnetization of Bey Dağları: Timing and Amount of Neogene Rotations in SW Turkey. Turkish Journal of Earth Sciences, 19, 123–156.

van Hinsbergen, D.J.J., Kaymakcı, N., Spakman, W., Torsvik, T.H., 2010b. Reconciling the geological history of western Turkey with plate circuits and mantle tomography. Earth and Planetary Science Letters, 297, 674–686.

van Hinsbergen, D.J.J., Dekkers, M.J., Bozkurt, E., Koopman, M., 2010c. Exhumation with a twist: Paleomagnetic constraints on the evolution of the Menderes metamorphic core complex, western Turkey. Tectonics, 29, TC3009, doi:10.1029/2009TC002596, 1-33.

van Hinsbergen, D.J.J., Langereis, C.G., Meulenkamp, J.E., 2005. Revision of the timing, magnitude and distribution of Neogene rotations in the western Aegean region. Tectonophysics, 396, 1–34.

van Hinsbergen, D.J.J., Krijgsman, W., Langereis, C.G., Cornee, J.J., Duermeijer, C.E., van Vugt, N. 2007. Discrete Plio–Pleistocene phases of tilting and counterclockwise rotation in the southeastern Aegean arc (Rhodos, Greece): early Pliocene formation of the south Aegean left-lateral strike-slip system. Journal of the Geological Society, London 164: 1133-1144.

Vendeville, B.C., Jackson, M.P.A., 1992a. The rise of diapirs during thin-skinned extension. Mar. Pet. Geol. 9, 331– 353.

Vendeville, B.C., Jackson, M.P.A., 1992b. The fall of diapirs during thin-skinned extension. Mar. Pet. Geol. 9, 354– 371.

Vidal N., Klaeschen, D., Kopf, A., Docherty, C., Von Huene, R., Krasheninnikov, V.A., 2000. Seismic images at the convergence zone from south of Cyprus to the Syrian coast, eastern Mediterranean, Tectonophysics, 329, 157–170.

Walsh-Kennedy, S., Aksu, A.E., Hall, J., Hiscott, R.N., Yaltırak, C. and Çifçi, G, 2014. Source to sink: the development of the Pliocene-Quaternary Cilicia and Adana Basins and their linkages with the onland Mut Basin, eastern Mediterranean. Tectonophysics, 622: 1-21.

Warren, J.K., 1999. Evaporites: their Evolution and Economics. Blackwell Science, Oxford.

Warren, J.K., 2006. Evaporites: Sediments, Resources and Hydrocarbons. Birkhäuser. p. 352, 1041 pp.

Warren, J.K., 2010. Evaporites through time: Tectonic, climatic and eustatic controls in marine and nonmarine deposits. Earth-Science Reviews 98, 217–268.

Watchorn, F., Nichols, G.J., Bosence, D.W.J., 1998. Rift-related sedi-mentation and stratigraphy, southern Yemen (Gulf of Aden). In: Purser, B.H., Bosence, D.W.J. (Eds.), Sedimentation and Tectonics of Rift Basins: Red Sea–Gulf of Aden. Chapman and Hall, London, pp.165–189.

Weiler, Y., 1969. The Miocene Kythrea flysch basin in Cyprus. G. Geol. 35, 213– 229.

Welford, J.K., Hall, J., Hübscher,C., Reiche, S., Louden, K., 2015. Crustal seismic velocity structure from Eratosthenes Seamount to Hecataeus Rise across the Cyprus Arc, eastern Mediterranean. Geophysical Journal International, 200: 933-951.

Westaway, R., 2004. Kinematic consistency between the Dead Sea Fault Zone and the Neogene and Quaternary left-lateral faulting in SE Turkey. Tectonophysics, 391, 203-237

Weijermars, R. (1988). Neogene tectonics in the western Mediterranean may have caused the Messinian salinity crisis and an associated glacial event: Tectonophysics, 211–219.

Wdowinski, S., Ben Avraham, Z., Arvidsson, R., and Ekström, G. 2006. Seismotectonics of the Cyprian Arc. Geophysical Journal International, 164, 176 181.

Wijermars, R., 1988. Neogene tectonics in the Western Mediterranean may have caused the Messinian Salinity Crisis and an associated glacial event. Tectonophysics 148, 211–219.

Williams, G.D., Ünlügenç, U.C., Kelling, G., Demirkol, C., 1995. Tectonic controls on stratigraphic evolution of the Adana Basin, Turkey. Journal of the Geological Society of London, 152, 873–882.

Wohl, E.E., 2007. Hydrology and Discharge. In: A. Gupta (ed), Large Rivers: Geomorphology and Management, John Wiley & Sons Ltd., West Sussex, England, 29–44, 705 pp.

Wortel, M.J.R., Spakman, W., 1992. Structure and dynamics of subducted lithosphere in the Mediterranean region. Proc. K. Ned. Akad. Wetensch. 95, 325–347.

Woodside, J.M., Ivanov, M.K., Limonov, A.F., 1997. Neotectonics and £uid £ow through seafloor sediments in the eastern Mediterranean and Black Seas. Intergovernmental Oceanographic Commission Technical Series, Vol. 48, Parts I and II, 226 pp

Woodside, J.M., Mascle, J., Zitter, T.A.C., Limonov, A.F., Ergun, M., Volkonskaia, A., Shipboard scientists of the PRISMED II expedition, 2002. The Florence Rise, the western bend of the Cyprus Arc. Mar. Geol. 185, 177– 194.

Yağmurlu, F., Savasçın, Y., and Ergün, M., 1997. Relation of alkaline volcanism and active tectonism within the evolution of the Isparta Angle, SW Turkey. The Journal of Geology, 105, 717–728.

Yalçın, M.N. and Görür, N., 1984. Sedimentological evolution of the Adana basin. Proc. Int. Symp. Geol. Taurus Belt, Ankara, 165–172.

Yaltırak, C., 2002. Tectonic evolution of the Marmara Sea and its surroundings. Marine Geology, 90: 493-529.

Yılmaz, Ö., 2001. Seismic Data Analysis: Processing, Inversion and Interpretation of Seismic Data (2 Volumes). Investigations in Geophysics No: 1O. Society of Exploration Geophysicists.

Yılmaz, Y. 1993. New evidences and model on the evolution of the southeast Anatolian orogen. Geological Society of America Bulletin, 105, 251–271.

Yılmaz, Y., Gürpınar, O., Yiğitbaş, E. 1988. Tectonic evolution of the Miocene basins at the Amanos Mountains and the Maraş region Turk. Assoc. Pet. Geol. Bull., 1/1 (1988), pp. 52–72

Yılmaz, Y., Güner, Y., Şaroğlu, F. 1998. Geology of the quaternary volcanic centers of east Anatolia. Journal of Volcanology and Geothermal Research, 85, 173–210.

Zitter, T.A.C., Woodside, J.M., Mascle, J., 2003. The Anaximander Mountains: a clue to the tectonics of southwest Anatolia. Geological Journal, 38, 375– 394.

Zor, E., 2008. Tomographic evidence of slab detachment beneath eastern Turkey and the Caucasus, Geophys. J. Int., 175, 1273–1282.

Zor, E., Sandvol, E., Gürbüz, C., Türkelli, N., Seber, D., Barazangi, M., 2003. The Crustal Structure of the East Anatolian Plateau from Receiver Functions, Geophys. Res. Lett., 30, 8044, doi:10.1029/2003GL018192.

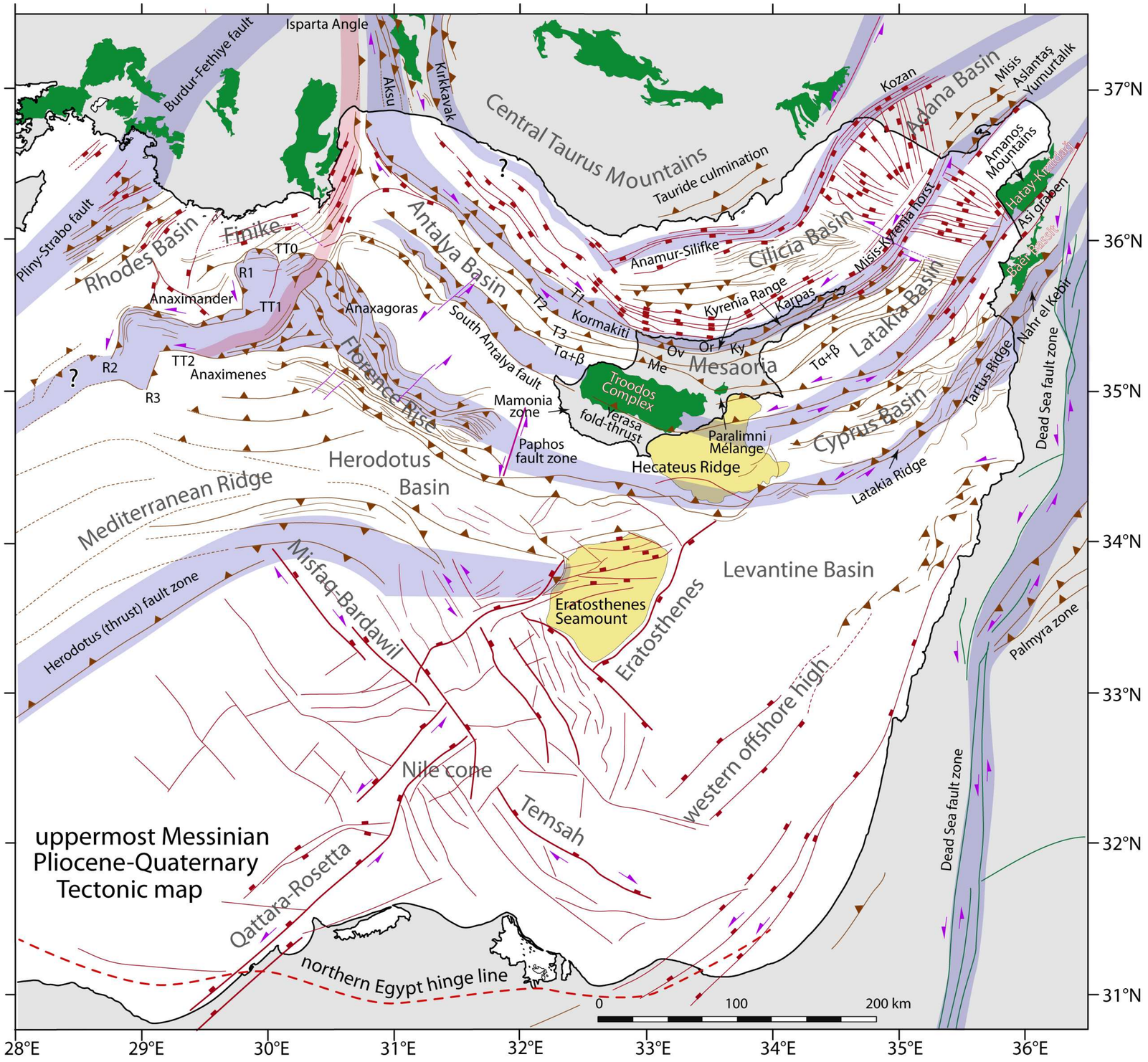

Figure A.1: Uppermost Messinian–Recent tectonic map of the eastern Mediterranean. Map is compiled by Aksu using data from (a) Florence Rise (Güneş, this thesis); (b) Rhodes and Finike basins, Anaximander Mountains (Hall et al., 2009, Aksu et al., 2009, Cranshaw, 2010, Barnes, 2015), (c) Adana, Cilicia, Latakia, Iskenderun basins (Aksu et al., 2005, 2014a,b, Hall et al., 2005a,b, Walsh-Kennedy et al., 2014), (d) offshore Israel, offshore Lebanon, Levantine Basin (Carton et al., 2009, Gvirtzman et al., 2010, Gardosh et al., 2008b), (e) Eratosthenes Seamount, Herodotus Basin (Montadert et al., 2010, Skiple et al., 2012), (f) offshore Syria (Bowmann 2011), and (g) Nile delta (Mascle et al., 2000, Abd-Allah et al., 2012). The coastline is from the International Bathymetric Charts of the Mediterranean (IOC, 1981). Brown lines = thrust faults with triangle ticks on hanging wall, red lines = normal faults with rectangular ticks on hanging wall, green lines = strike slip faults with purple half arrows showing slip direction, green fill = ophiolites. This figure is also shown in Figure 6.5.